ADVANCES IN
QUANTUM CHEMISTRY

ELECTRONIC STRUCTURE OF CLUSTERS

EDITOR-IN-CHIEF

PER-OLOV LÖWDIN

PROFESSOR EMERITUS

DEPARTMENT OF QUANTUM CHEMISTRY
UPPSALA UNIVERSITY
UPPSALA, SWEDEN

AND

QUANTUM THEORY PROJECT
UNIVERSITY OF FLORIDA
GAINESVILLE, FLORIDA

EDITORS

JOHN R. SABIN
MICHAEL C. ZERNER

QUANTUM THEORY PROJECT
UNIVERSITY OF FLORIDA
GAINESVILLE, FLORIDA

ERKKI BRÄNDAS

DEPARTMENT OF QUANTUM CHEMISTRY
UPPSALA UNIVERSITY
UPPSALA, SWEDEN

GUEST EDITORS

LASZLO KÖVÉR

INSTITUTE OF NUCLEAR RESEARCH OF
THE HUNGARIAN ACADEMY OF SCIENCES
DEBRECEN, HUNGARY

JUN KAWAI
HIROHIKO ADACHI

DEPARTMENT OF MATERIALS SCIENCE
AND ENGINEERING
KYOTO UNIVERSITY
KYOTO, JAPAN

VOLUME 29

ACADEMIC PRESS

San Diego London Boston New York Sydney Tokyo Toronto

This book is printed on acid-free paper. ♾

Academic Press
a division of Harcourt Brace & Company
525 B Street, Suite 1900, San Diego, California 92101-4495, USA
http://www.apnet.com

Academic Press Limited
24-28 Oval Road, London NW1 7DX, UK
http://www.hbuk.co.uk/ap/

International Standard Book Number: 0-12-034829-2

PRINTED IN THE UNITED STATES OF AMERICA
97 98 99 00 01 02 MM 9 8 7 6 5 4 3 2 1

Contributors

Hirohiko Adachi, Department of Materials Science and Engineering, Kyoto University, Kyoto 606-01, Japan

J. Anton, Theoretical Physics, Gesamthochschule Kassel, D-34109 Kassel, Germany

T. Bastug, Theoretical Physics, Gesamthochschule Kassel, D-34109 Kassel, Gemany

I. Cserny, Institute of Nuclear Research of the Hungarian Academy of Sciences, H-4001 Debrecen, Hungary

D. E. Ellis, Department of Chemistry and Materials Research Center, Northwestern University, Evanston, IL 60208

Hiroshi Endo, Isogo Engineering Center, Toshiba Corporation, Yokohama 235, Japan

B. Fricke, Theoretical Physics, Gesamthochschule Kassel, D-34109 Kassel, Germany.

Manabu Fujiwara, Department of Chemistry, Fukuoka University, Fukuoka 814-01, Japan

Kimichika Fukushima, Research and Development Center, Toshiba Corporation, Kawasaki 210, Japan

Gennady L. Gutsev, Quantum Theory Project, University of Florida, Gainesville, FL 32611

I. K. Gyémánt, Institute of Theoretical Physics, Jozsef Attila University, Szeged, Hungary

Eberhard Hartmann, Institute of Surface Modification, University of Leipzig, Leipzig, Germany

Akinori Hatamoto, Nakamura Yogyo Ltd., Okayama-ken 705, Japan

Yoshinori Hayafuji, Sony Corporation Research Center, Yokohama 240, Japan

Masaru Hirata, Oarai Research Establishment, Japan Atomic Energy Research Institute, Ibaraki 311-13, Japan

Syunji Imanaga, Sony Corporation Research Center, Yokohama 240, Japan

Fumikazu Kanamaru, The Institute of Scientific and Industrial Research, Osaka University, Ibaraki Osaka 567, Japan

Yuko Kato, Department of Chemistry, Fukuoka University, Fukuoka 814-01, Japan

Jun Kawai, Department of Materials Science and Engineering, Kyoto University, Kyoto 606-01, Japan

Hitoshi Kimura, Sony Corporation Research Center, Yokohama 240, Japan

Zs. Kovács, Institute of Theoretical Physics, Jozsef Attila University, Szeged, Hungary

L. Kövér, Institute of Theoretical Physics, Jozsef Attila University, Szeged, Hungary

Y. Kowada, Hyogo University of Teacher Education, Hyogo 673-14, Japan

Koichiro Koyama, Department of Materials Science and Engineering, Faculty of Engineering, Himeji Institute of Technology, Himeji 671-22, Japan

Masayoshi Kurihara, Ibaraki 311-41, Japan

Gao-Chao Lai, The Institute of Scientific and Industrial Research, Osaka University, Ibaraki Osaka 567, Japan

Christa Lauterbach, Institute of Surface Modification, University of Leipzig, Leipzig, Germany

Masahiko Morinaga, Department of Materials Science and Engineering, Kyoto University, Kyoto 606-01, Japan

Masao Morishita, Department of Materials Science and Engineering, Faculty of Engineering, Himeji Institute of Technology, Himeji 671-22, Japan

Takeshi Mukoyama, Institute for Chemical Research, Kyoto University, Kyoto 611, Japan

Ágnes Nagy, Institute of Theoretical Physics, Kossuth Lajos University, H-4010 Debrecen, Hungary

Hirohide Nakamatsu, Institute for Chemical Research, Kyoto University, Kyoto 611, Japan

Kazuyoshi Ogasawara, Department of Materials Science and Engineering, Kyoto University, Kyoto 606-01, Japan

Katsuhiro Ohta, The Institute of Scientific and Industrial Research, Osaka University, Ibaraki Osaka 567, Japan

Jun Onoe, The Institute of Physical and Chemical Research (RIKEN), Saitama 351-01, Japan

G. Paragi, Institute of Theoretical Physics, Jozsef Attila University, Szeged, Hungary

Arne Rosén, Department of Physics, Goteborg University and Chalmers University of Technology, S-412 96 Goteborg, Sweden

K. Schulze, Theoretical Physics, Gesamthochschule Kassel, D-34109 Kassel, Germany

Rika Sekine, Department of Chemistry, Shiuoka University, Shizuoka 422, Japan

W.-D. Sepp, Theoretical Physics, Gesamthochschule Kassel, D-34109 Kassel, Germany

Masao Takahashi, The Institute of Scientific and Industrial Research, Osaka University, Ibaraki Osaka 567, Japan

T. Takenaga, Department of Materials Science and Engineering, Waseda University, Tokyo 169, Japan

Isao Tanaka, Department of Materials Science and Engineering, Kyoto University, Kyoto 606-01, Japan

Kazuo Taniguchi, Osaka Electro-Communication University, Osaka 572, Japan

M. Uda, Department of Materials Science and Engineering, Waseda University, Tokyo 169, Japan

S. Varga, Theoretical Physics, Gesamthochschule Kassel, D-34109 Kassel, Germany

Zs. Varga, Institute of Theoretical Physics, Jozsef Attila University, Szeged, Hungary

Hisanobu Wakita, Department of Chemistry, Fukuoka University, Fukuoka 814-01, Japan

Toshio Yamaguchi, Department of Chemistry, Fukuoka University, Fukuoka 814-01, Japan

Tomoyuki Yamamoto, Department of Materials Science and Engineering, Waseda University, Tokyo 169, Japan

Seiichi Yamashita, Department of Chemistry, Fukuoka University, Fukuoka 814-01, Japan

H. Yukawa, Department of Materials Science and Engineering, Kyoto University, Kyoto 606-01, Japan

Foreword

Cluster type molecular orbital calculations have proven to be powerful tools for understanding the electronic structure of molecules, clusters and solids. The Discrete Variational Xα (DV-Xα) is one of the most versatile amongst these methods in interpreting spectroscopic results and for predicting properties of polyatomic systems of great practical importance.

This volume includes the papers of Keynote Lectures and Invited Contributions presented at the First International Workshop on DV-Xα Method (DV-Xα '96, with Special Emphasis on Inner-Shell Physics and Chemistry). The Workshop was organized by the Society for Discrete Variational Xα (Japan), the Institute of Nuclear Research of the Hungarian Academy of Sciences (ATOMKI), and the Department of Theoretical Physics of the L. Kossuth University of Debrecen, following numerous annual meetings on this topic in Japan.

DV-Xα '96 took place in the ATOMKI, Debrecen, Hungary, on 2–3 September 1996, ensuring a quiet place, good conditions, and a stimulating atmosphere for the lectures and discussions. The 40 invited participants (half of the attendance from Japan) represented six countries, and the scientific program involved 10 Keynote Lectures reviewing central issues in the development and application of the DV-Xα method, as well as 17 Invited Contributions focusing on the latest results.

During the meeting the limits and perspectives on the application of DV-Xα in describing the electronic structure of molecules, clusters, and solids, were discussed in detail, in an effort to find an explanation for the continuing popularity of the method. The specific issues represent three large, overlapping areas. Amongst these the first is the analysis and evaluation of the performance of the DV-Xα model in describing both electronic states and materials properties, including studies of the attainable accuracy of the approximation, careful comparisons with high resolution experiments as well as with other powerful theoretical methods, and overviews of new possibilities for improving the recent performance of the DV-Xα calculations. The second is concerned with a number of recent and prospective applications in the analysis of electronic structure of materials and for interpretation of related spectroscopic results, extended to the description of band structure and magnetic character of transition metals and their alloys and to calculations for systems with heavy elements. Revealing the nature of chemical bonds in compounds, interpretation of chemical effects on inner-shell, core-valence X-ray, Auger, energy loss, X-ray absorption and photoelectron spectra, as well as modeling charge transfer and core level shifts in alloy and metal clusters, belong to this group of topics. The third area involves

problems such as applicability of the method to improving properties of materials and to designing new materials of key importance.

The systematization above is reflected in the organization of the volume, with the titles of the chapters more or less corresponding to the respective sessions in the Workshop.

Enjoying the lively discussions during the meeting and reading the material of these Proceedings encourage me to conclude that DV-Xα '96 has been both very interesting and productive. A concise evaluation and forecast is given in the Closing Remarks of Prof. M. Uda at the end of the volume.

Finally, it is an especially great pleasure for me to warmly recommend this book to every reader interested to know more about the electronic structure of clusters and solids, on the occasion of the centennial of the discovery of the electron.

For supporting the Workshop and the publication of this volume, special thanks should be expressed to the Society of Discrete Variational Xα (Japan), and to the Institute of Nuclear Research of the Hungarian Academy of Sciences for providing the necessary facilities. The financial support of the Osaka Electro-Communication University, the SONY Corporation Research Center, the Hungarian National Committee for Technical Development, the Hungarian Scientific Research Foundation (OTKA), the Universitas Foundation, the Council of Debrecen City, and the Hotel Aranybika is also acknowledged.

Debrecen, 17 March, 1997.

Dr. L. Kövér
Co-Chairman
Organizing Committee of DV-Xα '96

Twenty to thirty years of DV-Xα calculations: A survey of accuracy and applications

Arne Rosén

Department of Physics,
Göteborg University and Chalmers University of Technology,
S-412 96 Göteborg, Sweden.

Abstract

During the last twenty to thirty years, both the possibilities for accurate electronic structure calculations, and the access to improved experimental data for comparison have changed dramatically. In general, electronic structure calculations based on density functional methods can be structured as *i)* to find an accurate potential which adequately accounts for Coulomb, exchange, correlation and relativistic effects, *ii)* to develop computational methods which are powerful enough to handle realistic potentials, and *iii)* to extend the theory to account for static and dynamic properties. The search to obtain an accurate treatment of exchange and correlation effects has been very difficult and continues to be one of the greatest challenges in density-functional theory. Development of accurate computational methods represents, in a similar way, difficult problems which have been addressed for many years in an effort to obtain accurate total energies or potential energy surfaces for studies of chemical and catalytic reactions. There is furthermore a general interest in using these types of methods for basic studies as well as for prediction of properties to improve existing materials and to also develop new materials. This paper gives a short historical overview of different developments and presents some examples of calculations for simple molecules, surfaces, clusters and C_{60}.

ADVANCES IN QUANTUM CHEMISTRY, VOLUME 29

0065-3276/97 $25.00

I. INTRODUCTION

"It is **Materials** *that are the basis of possibilities in all fields. The development of advanced materials is so important that it is not much to say that advanced materials will be the key factor in determining the world in the 21st century."*

This quotation taken from a folder describing the research in a big Japanese industry is very general, but is probably valid for every high technology industry a likely goal for their survival in the future. There are certainly many ways to develop high technological systems with advanced materials, and each company hopes that their decision represents a better choice compared to their competitors. Agencies for funding of research worldwide are today pushing university scientists to focus their work on applications, in this way contributing to the development of new materials. This would benefit national industries in creating new jobs and increase the general welfare of nations.

One of the main questions is how to proceed to achieve the visions and goals outlined above ? Can for example electronic structure calculations be one way, and which method should be used to get reliable results ? Can for example calculations based on Density Functional Theory, DFT, be one of the solutions or is this method not accurate enough ? Let us go back to a review article by Slater in 1972 [1], where he discusses the Statistical Exchange-Correlation in Self-Consistent-Field, SCF, calculations. In this article, Slater goes back to his derivation from 1951 [2,3] of the approximate exchange term for the Hartree-Fock exchange, which he found to be proportional to the one-third power of the local electronic density, $\rho(\mathbf{r})$. The use of this approximation for the exchange interaction, often referred to as the Hartree Fock Slater, HFS, approximation formed the basis of the Xα method and opened also up the possibilities for extensive electronic structure calculations for atoms, molecules and solids, as summarized in Refs. [1,4]. The most extensive calculations for atoms at that time were those summarized by Herman and Skillman [5], in which one could find tables of eigenvalues, potentials, wavefunctions and relativistic correction factors for elements from hydrogen to lawrencium with an atomic number of 103.

Slater summarized the power of the Xα method at the end of the article from 1972 by stating that: *The Xα method provides a practical starting point for an a priori theory of such problems, as magnetism, a starting point which has not been practical with earlier techniques.* The power of the Xα method was further accentuated in an article by Johnson on "Scattering-Wave Theory of the Chemical Bond" in 1973 [6], where he gives an overview of the traditional Hartree-Fock, HF, SCF method and also semi-empirical ones. He points out that the new Xα technique based on Scattering Wave Theory has

allowed a new theoretical approach, the so-called MS-Xα method to calculate the electronic structure of polyatomic molecules and solids from first principles [7,8]. Today, very few people use the MS-Xα method for electronic structure calculations mainly due to the limitations in accuracy by the muffin-tin approximation. This is in contrast to the use of different forms of density functional methods which are more popular than ever and are used in several academic and commercial computer codes [9–12]. It is unfortunate for the whole field of electronic structure calculations that the MS-Xα method was put on the market so extensively at that period so that the Xα method for some time had a bad rumour. My feeling is that this has also delayed the use of density functional based methods for calculations within physics, chemistry and materials science.

It may for the reader be interesting to know why I choose the title *Twenty to thirty years of DV-Xα calculations: A survey of accuracy and applications*, for my introductory talk at this *First International Workshop on DV-Xα Method with Special Emphasis on Inner Shell Physics and Chemistry.* One of the reasons is that I started with electronic structure calculations about thirty years ago [13–15]. At that time my work was focused on calculation of accurate expectation values of r^{-3}, to be used in evaluation of nuclear moments from experimental hyperfine structure constants. After my doctor's degree, Dr. Adachi and I worked together as postdoctors in the groups of Professor Jim Waber and Professor Don Ellis at Northwestern University from 1973-1974. We developed, in cooperation with Don Ellis and Frank Averill, the Self Consistent Charge, SCC, method [16], which has since that time been used extensively in electronic structure calculations by many groups. During that period Don Ellis and I also developed the theory and computer programs for relativistic electronic structure calculations for molecules containing heavy atoms based on the four-component formalism [17,18].

Another reason for the choice of the title is the above-mentioned introduction of the Xα-method and the MS-Xα method by Slater and coworkers. There are, however, in particular two other reasons for choosing the title. The first is the formulation of the Density Functional Theory by Hohenberg and Kohn in 1964 [19], which today is probably one of the most quoted papers in electronic structure calculations. This basic work was followed by another important paper in 1965 by Kohn and Sham [20], where they showed how one could use the method for practical calculations and introduced the Kohn-Sham, KS, exchange potential. Exactly the same expression for the exchange potential had previously been derived by Gaspar [21]. This exchange potential is therefore often known as the Gaspar-Kohn-Sham, GKS, potential. Another very important reason for choice of the title is the introduction of the three dimensional numerical integration method by Ellis and Painter in 1968-1970 [22–24]. This

numerical integration technique known as the Discrete Variational Method, DVM, forms the basic idea of many integration techniques used today in various programs for molecular electronic structure calculations. The choice of an accurate numerical integration method and a good description of the exchange potential defines also two of the main words in the title of this paper. The success of the application of the DV-Xα method in a number of calculations of basic and industrial related nature is also the reason for the organization of the DV-Xα Physical Society in Japan [25].

An example of a general discussion of electronic structure calculations in the scientific literature almost thirty years ago can be found in an article by Herman, van Dyke and Ortenburger in 1969 [26]. This article introduces a new exchange potential known as X$\alpha\beta$, with a discussion of gradient corrections based on the earlier work by Hohenberg and Kohn from 1964 [19]. The article contains references to a number of the works mentioned above and also to different kinds of exchange potentials such as the Optimized Hartree-Fock-Slater, OHFS, potential introduced by Lindgren [27,28] and also to relativistic self-consistent-field calculations known as use of the Dirac-Slater, DS, method [29] or the relativistic version of Optimized Hartree-Fock-Slater, ROHFS [13]. Today many of the problems associated with the choice of exchange-correlation potential, and use of gradient corrections are extensively discussed in the scientific literature [30]. The choice of a good exchange correlation potential and an accurate method for evaluation of the molecular charge density or molecular potential also defines the problems and challenges of electronic structure calculations, which can be structured into the following points.

- To find an accurate potential which adequately accounts for the terms in the molecular hamiltonian;

  i) Coulomb potential, v_n and v_e from nuclei and electrons, respectively.

  ii) Exchange and correlation potential, v_{xc} between the electrons.

  iii) Inclusion of relativistic effects either by perturbation theory, using some transformation or in a fully relativistic treatment with four-component wavefunctions.

- Development of computational methods which are powerful enough to handle realistic potentials. This last point can be divided into

  i) basis set dependent techniques

  ii) integration techniques

  iii) treatment of Coulomb potential

  iv) pure numerical methods such as the Finite Element Methods, FEM, and Finite Difference Methods, FDM.

This paper gives a short overview of density functional calculations mainly based on the DV-Xα approach organized as follows. A short overview of Density Functional Theory, DFT, and Kohn-Sham equations is given in section II followed by a summary of different ways of solution of the Kohn-Sham equations in Sec. III. Comparisons of results from some old and some up-to-date density functional electronic structure calculations made by our group to show applications to clusters, surfaces, adsorbates on surfaces and C_{60} are given in Sec. IV. Conclusions and outlook are summarized in Sec. V.

II. KOHN-SHAM EQUATIONS

The geometrical and electronic structure for molecular systems in general will depend on the balance between the different terms in the Hamiltonian i.e. electron-nucleus, electron-electron and nucleus-nucleus interaction including the valence as well as the core electrons of the constituent atoms. The full Hamiltonian for the molecular system is normally separated into a Hamiltonian $\hat{H}_N$ for the nuclei and another one $\hat{H}_{el}$ for the electrons with fixed positions for the nuclei according to Born Oppenheimer approximation [31].

$$\hat{H} = \hat{H}_N + \hat{H}_{el} \,, \tag{1}$$

$$\hat{H}_N = \sum_{\alpha=1}^{N} \left\{ \frac{\mathbf{P}_\alpha^2}{2M_\alpha} + \frac{1}{2} \sum_{\beta(\neq\alpha)=1}^{N} \frac{(Z_\alpha)(Z_\beta)e^2}{|\mathbf{R}_\alpha - \mathbf{R}_\beta|} \right\} \tag{2}$$

$$\hat{H}_{el} = \sum_{i=1}^{ZN} \left\{ \frac{\mathbf{p}_i^2}{2m} - \sum_{\alpha=1}^{N} \frac{Z_\alpha(e^2)}{|\mathbf{r}_i - \mathbf{R}_\alpha|} + \frac{1}{2} \sum_{j(\neq i)=1}^{ZN} \frac{e^2}{|\mathbf{r}_i - \mathbf{r}_j|} \right\} . \tag{3}$$

where the Coulomb potentials between the nuclei and electrons and electron-electron interactions are given by

$$v_{\text{ion}}(\mathbf{r}) = \sum_{\nu=1}^{N} \frac{-Z_\nu}{|\mathbf{r} - \mathbf{R}_\nu|} \,. \tag{4}$$

$$v_{\text{ee}}(\rho(\mathbf{r})) = \int \frac{\rho(\mathbf{r}')\, d\mathbf{r}'}{|\mathbf{r} - \mathbf{r}'|} \tag{5}$$

The exchange-correlation potential which includes the remaining exchange and correlation effects between the electrons will be discussed below. Solution of the Schrödinger equation is in general not simple, and a number of methods

have been used for a long time [4,32–34]. A very common approach for evaluation of the electronic structure of molecular systems has been to develop methods which are based on the electronic density $\rho(\mathbf{r})$ as the key parameter. This approach goes back to the early treatment of a uniform and non-uniform electron gas, the commonly used Thomas-Fermi model, TF, and the extension to inlcude exchange by Dirac, TFD, [35] as well as use of Slater's form of the HFS exchange potential including the Xα method [4].

The principal limitation of the earlier used TF and TFD models is the treatment of the kinetic energy which was handled in an approximate way, thereby giving less accurate values for atomic and molecular systems. This was solved by Hohenberg and Kohn in 1964 [19] when they used a variational procedure in the formulation of the modern form of density functional theory, DFT. This theory is based on two theorems which state that the total energy of an electronic system is a unique functional of the electronic density and that the ground state density determines the ground state energy:

$$E[\rho] = \int d\mathbf{r} v_{\mathrm{ext}}(\mathbf{r})\rho(\mathbf{r}) + F[\rho] \tag{6}$$

$$E_{\mathrm{GS}}[\rho_{\mathrm{GS}}] = \int d\mathbf{r} v_{\mathrm{ext}}(\mathbf{r})\rho_{\mathrm{GS}}(\mathbf{r}) + F[\rho_{\mathrm{GS}}]. \tag{7}$$

where $v_{\mathrm{ext}}(\mathbf{r})$ represents an external potential experienced by the electrons. F$[\rho]$ is a functional defined by:

$$F[\rho] = \min_{\Psi \to \rho} < \Psi | T + V_{ee} | \Psi > . \tag{8}$$

$\Psi(\mathbf{r}_1, \mathbf{r}_2, \mathbf{r}_N)$ is a many-electron antisymmetric wavefunction and the minimum is taken over all Ψ that result in a density $\rho(\mathbf{r})$. The functional F$[\rho]$ includes both the kinetic energy and Coulomb energy of the interacting system and is, according to Kohn and Sham [20], given by;

$$E[\rho] = T_0[\rho(\mathbf{r})] + \int d\mathbf{r}\rho(\mathbf{r}) \left(v_{ext} + \frac{1}{2}\Phi(\mathbf{r}) \right) + E_{xc}[\rho(\mathbf{r})], \tag{9}$$

which corresponds to

$$F[\rho] = T_0[\rho(\mathbf{r})] + \frac{1}{2} \int d\mathbf{r}\rho(\mathbf{r})\Phi(\mathbf{r}) + E_{\mathrm{xc}}[\rho(\mathbf{r})]. \tag{10}$$

$T_0[\rho(\mathbf{r})]$ defines the kinetic energy of a non-interacting electron gas which requires the density $\rho(\mathbf{r})$. $\Phi(\mathbf{r})$ is the classical (direct) Coulomb interaction which is equivalent to the Hartree potential. Using the constraints that the total number of electrons are conserved, Kohn and Sham [20] reduced the many electron Schrödinger equations to a set of one-electron equations known as the Kohn-Sham equations

$$(-\frac{1}{2}\nabla^2 + v_{\rm ext} + v_{\rm ee} + v_{\rm xc})\psi_i(\mathbf{r}) = \epsilon_i\psi_i(\mathbf{r}). \tag{11}$$

The total energy for the whole system using this scheme is given by:

$$E[\rho] = \sum_i \epsilon_i - \frac{1}{2}\int d\mathbf{r} v_{\rm ee}(\mathbf{r})\rho(\mathbf{r}) - \int d\mathbf{r} v_{\rm xc}(\mathbf{r})\rho(\mathbf{r}) + E_{xc}[\rho(\mathbf{r})]. \tag{12}$$

where

$$\rho(\mathbf{r}) = \sum_i |\psi_i(\mathbf{r})|^2, \tag{13}$$

$$v_{\rm xc} = \frac{\delta E_{\rm xc}}{\delta\rho(\mathbf{r})}. \tag{14}$$

Historically and still one of the challenging problems in the treatment of a uniform, non-uniform electron gas, an atomic or molecular system has been to find accurate expressions for the exchange and correlation energy among the electrons [30], i.e.

$$E_{\rm xc}[\rho] = \int d\mathbf{r}\varepsilon_{\rm xc}(\rho)\rho(\mathbf{r}), \tag{15}$$

or including the gradient corrections

$$E_{xc} = E_{xc}[\rho, \nabla\rho]. \tag{16}$$

Derivations of exchange and correlation energy formulas are in general based on the r_s value, (the Wigner-Seitz radius) which is related to the electron density by,

$$r_s = \left(\frac{3}{4\pi\rho}\right)^{1/3}. \tag{17}$$

In Slater's derivation in 1951 [2] of an exchange potential, a *local* potential was constructed from the *nonlocal* Hartree-Fock, HF, exchange potential by first using the weighted average of the HF potential and then approximating the electron orbitals/wave functions by plane waves. He found that the exchange potential could be given as a function of the electronic density $\rho(\mathbf{r})$ with the following expression.

$$V_{\rm HFS}(\mathbf{r}) = -C\left(\frac{3\rho(\mathbf{r})}{8\pi}\right)^{1/3} \tag{18}$$

where C is a constant which was determined to be equal to 1.0. This procedure does lead to a rather good and useful approximation to the HF exchange,

but it does not necessarily lead to the "best" local approximation since the variational procedure which leads to the HF equations is in Slater's treatment applied *before* the approximation is made. One might expect to get a better result, if the order between these two operations is reversed. This can be done by constructing an *energy* expression instead of a potential based on the free-electron-gas model and by using the variational principle to determine the orbitals that minimize this energy. This was the procedure used by Kohn and Sham in 1965 [20] in the derivation of an exchange potential which was found to be identical to the HFS potential derived by Slater in 1951 except for a multiplicative factor of two thirds. Exactly the same expression for the exchange potential was also derived by Gaspar as discussed before. This exchange potential is therefore often known as the GKS potential with the following relation to the HFS potential;

$$V_{\mathrm{GKS}}(\mathbf{r}) = \frac{2}{3} V_{\mathrm{HFS}}(\mathbf{r}) \tag{19}$$

It was soon realized, in the late sixties, that this kind of potential did not give a minimum in total energy for atomic systems. Actually an improvement could be obtained using a different value of the constant C compared with the $\frac{2}{3}$. Different kinds of parameter were introduced with the values determined by either minimizing the statistical total energy or by determining a parameter which gave a value of the exchange energy which was equal to the HF exchange. This was the basic idea behind the Xα exchange potential [4], where the constant C in Eq.(18) was denoted by α. Many calculations gave values scattered around a value of 0.70 which was not so far from the value of $\frac{2}{3}$ in the GKS potential. For quite some time, values of up to five decimals were extensively used and believed to be *the true values* for obtaining accurate and reliable results [36]. A somewhat different approach was used by Lindgren [27,28], who for atomic calculations introduced a potential with three parameters and determined the values of the parameters by minimizing the HF total energy. This was extended by Lindgren and the present author to relativistic calculations [13–15]. The potentials obtained are known as Optimized Hartree Fock Slater, OHFS, and in the relativistic case, ROHFS. Other commonly used potentials are due to Hedin [37], von Barth and Hedin [38] and Gunnarsson and Lundqvist [39].

At present the most frequently used parameterization for exchange and correlation are those of Perdew and Zunger [40] or Vosko, Wilk and Nusair [41]. These two functionals which are based on the Monte Carlo simulations by Ceperly and Adler [42] give rather similar results. There are deficiencies in the LDA schemes which are due to the wrong asymptotic behaviour of the exchange and correlation potential since it falls off exponentially and not as

1/r. This was solved in some approximate way in the early days by the so-called Latter correction [43]. Today a number of schemes have been introduced to reduce this failure, using gradient corrections [44]. The commonly used schemes today for this type of gradient corrections are due to Becke [45] and Perdew [46]. Other schemes commonly used are LYP [48] and a combination of the gradient corrections of Becke and the exchange in LYP, referred to as BLYP [45] or B3LYP [49]. The inclusion of gradient corrections has in a number of calculations been shown to improve the agreement with experimental data of spectroscopic constants, dissociation energies and diffusion barriers [50].

It should be noted that the eigenvalues ϵ_i obtained in the solution of the Kohn-Sham equations are not equal to the ionization energies as known by the Koopmans' theorem in Hartree Fock [51]. Slater found that ionization energies could be obtained by evaluation of the total energy for the neutral and ionized systems [4], which gives

$$\epsilon_i^{\mathrm{HF}} = E(n_1, \ldots, n_i, \ldots, n_N) - E(n_1, \ldots, n_i - 1, \ldots, n_N) \tag{20}$$

An approximate and rather accurate way to calculate ionization energies would be to use the so-called transition state method [4] and do SCF- calculations for each orbital when the occupancy has been reduced with half an electron.

Solution of the Kohn-Sham equations as outlined above are done within the static limit, i.e. use of the Born-Oppenheimer approximation, which implies that the motions of the nuclei and electrons are solved separately. It should however in many cases be of interest to include the dynamics of, for example, the reaction of molecules with clusters or surfaces. A combined *ab initio* method for solving both the geometric and electronic problem simultaneously is the Car-Parrinello method, which is a DFT dynamics method [52]. This method uses a plane wave expansion for the density, and the inner ions are replaced by pseudo-potentials [53]. Today this method has been extensively used for studies of dynamic problems in solids, clusters, fullerenes etc [54–61]. We have recently in a co-operation project with Andreoni at IBM used this technique for studying the existence of different isomers of transition metal clusters [62,63].

III. SOLUTION OF THE KOHN-SHAM EQUATIONS

The main challenge, after having defined the Kohn-Sham equations, is to solve them in an accurate way where the main problem is to find an accurate description of the multi-centre Coulomb potential. The method used is, to a large extent, determined by the character of the atoms involved in the bonding. The electronic structure of alkali and noble metals is for example rather simple

with the appearance of an outermost valence ns electron although the existence of the low lying $(n-1)d$ levels may influence the structure. A molecule containing other atoms such as carbon or silicon will give a quite different bonding character. I will in this article focus on the jellium model commonly used today [64–68] in evaluations of properties for metal clusters, III A. The main approach behind the earlier commonly used Muffin-tin potential [6] is also outlined to show the approximations used, III B. Finally, a short summary is given of the more standard method based on Molecular Orbital Linear Combination of Atomic Orbitals, MO-LCAO [32–34] in III C, the use of external fields in SCF calculations in III D and evaluation of polarizabilities in III E.

A. The Jellium Model

Using the jellium model, the ionic structure of the molecule is disregarded by smearing out the ionic charge obtained from the nuclei and core electrons into an effective, homogeneous positive background. This background can in principle be given any shape and is in the simplest version a spherical shape of the following form

$$\rho^{+}(r) = \rho_0\,\Theta(r-R) \tag{21}$$

where $\rho_0 = 3/4\pi r_s^3$ defines the positive background. Within this approximation the ionic potential, v_{ion}, in Eq. (4) is given;

$$v_{ion}(r) = \begin{cases} -\frac{N}{R}\left(\frac{3}{2} - \frac{1}{2}\left(\frac{r}{R}\right)^2\right) & r \le R \\ -\frac{N}{r} & r > R \end{cases} \tag{22}$$

$$R = r_s N^{1/3}$$

Using this potential the molecular many-centre problem is changed to a spherically symmetrical problem such as for atoms as visualized for an eight-atom cluster in Fig. 1.

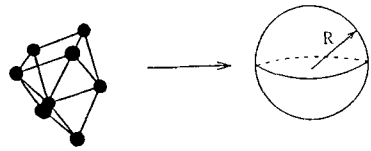

FIG. 1. A schematic overview of the jellium approximation for an eight atom cluster.

Ekardt [67] and Beck [68] used this approach and solved the Kohn-Sham equations self-consistently for this type of spherical jellium potential for Na clusters of various sizes. The results of such calculations are visualized for a 40-electron cluster of various metals or choices of r_s values in Fig. 2, [62]. Going down in the periodic table from sodium to potassium, the potential becomes shallower and the levels are more loosely bound. The valence electrons in the coinage metal copper has a much higher electron density which will give a smaller r_s value and more bound states.

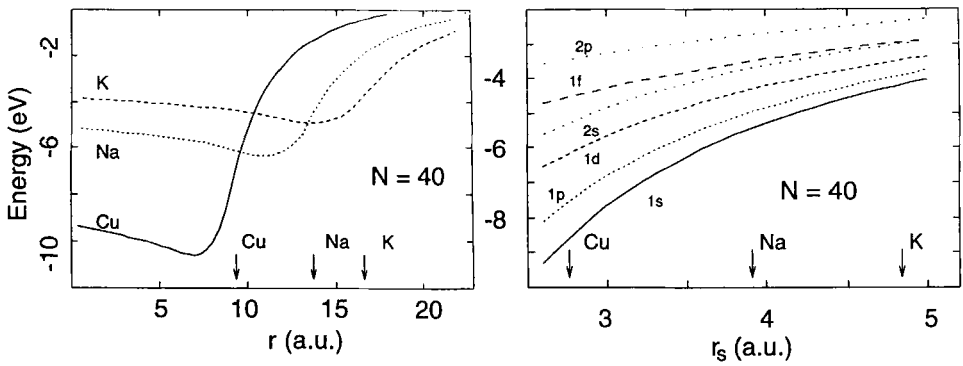

FIG. 2. Jellium for a cluster of a monovalent element with forty atoms. The self-consistent one-particle potential is shown for the three metals, K, Na and Cu to the left. The corresponding energy eigenvalues as a function of the r_s value is shown to the right.

An example of the potential and eigenvalue spectrum for a forty-atom cluster of Cu atoms is given in Fig. 3, [70]. We notice how the one-electron eigenvalues are characterized by main and orbital quantum numbers, the same as for atoms although the labeling and ordering of the main quantum numbers are somewhat different compared with atoms. As for atoms, there will be open and closed electronic shells where one can expect that closed shells will have a higher stability compared with open shells. Actually, the appearance of closed shells fits very nicely with experimental mass spectrum for clusters of sodium detected by Knight *et al.* [69,66], who found that clusters with the masses corresponding to 8, 20, 34, 40, 50 and 92 Na atoms are rather stable. We have also in more recent works found that the jellium model can be used for Cu clusters [62,70–73].

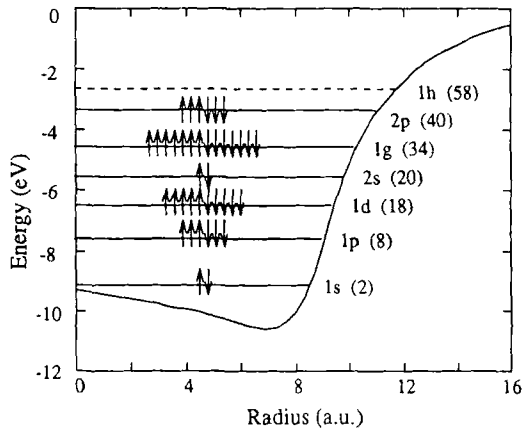

FIG. 3. Self-consistent electron potential, calculated for a spherical cluster of Cu with forty atoms. The calculated single-electron energy levels are also shown. The one-electron energy levels are denoted by the radial quantum number and angular momentum. The energy levels are occupied by electrons according to the Pauli principle.

B. The Muffin-tin potential

In the earlier mentioned Multiple-Scattering Xα Method [6], the molecule was geometrically partitioned into three fundamental types of region, Fig. 4:

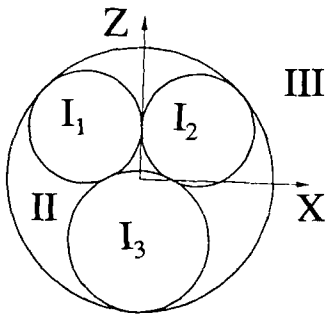

FIG. 4. A schematic overview of the muffin-tin potential in a molecule with the division of the space in three regions as described in the text.

- I) *Atomic*: The regions within non-overlapping spheres centered on the constituent atoms.
- II) *Interatomic*: The region between the "inner" atomic spheres and an "outer" sphere surrounding the entire molecule. The potential was assumed to be constant in this region.

- III) *Extramolecular*: The region exterior to the outer sphere.

The Schrödinger equation is solved for each of the regions, I, II, and III separately for a local potential, and the wavefunctions are matched at the boundaries. This approximation was found to describe the electronic structure quite satisfactorily for highly symmetric systems but gave in some cases very bad results, for example for diatomic molecules and the water molecule [75]. The main reason was the use of the constant potential in region II. Several attempts were made to solve this problem using overlapping spheres [76].

C. LCAO method

In calculations based on the MO-LCAO technique [32–34], the one-electron Kohn-Sham equations Eq. (11) are solved by expanding the molecular orbital wavefunctions $\psi_i(\mathbf{r})$ in a set of symmetry adapted functions $\chi_j(\mathbf{r})$, which are expanded as a linear combination of atomic orbitals i.e.

$$\psi_i(\mathbf{r}) = \sum_j \chi_j(\mathbf{r})\, C_{ji}\ . \tag{23}$$

$$\chi_j(\mathbf{r}) = \sum_{\nu,n,l,m} W_{nlm}^{j\nu}\, u_{nl}^{\nu}(r_\nu)\, Y_{lm}(\hat{r}_\nu)\ , \tag{24}$$

i.e. symmetry-adapted wavefunctions, $\chi_j(\mathbf{r})$, are projected from the atomic orbitals $u_{nl}Y_{lm}$ with coefficients $W_{nlm}^{j\nu}$. The variational coefficients, C_{ij}, are obtained from the matrix secular equation,

$$(\mathbf{H} - \epsilon\mathbf{S})\,\mathbf{C} = \mathbf{0} \tag{25}$$

where $\mathbf{H}$ and $\mathbf{S}$ are the Hamiltonian and overlap matrices, respectively. The matrix elements are given by

$$H_{pq} = \int \chi_p^*(\mathbf{r})\, h(\mathbf{r})\, \chi_q(\mathbf{r})\, d\mathbf{r} \tag{26}$$

$$S_{pq} = \int \chi_p^*(\mathbf{r})\, \chi_q(\mathbf{r})\, d\mathbf{r}\ , \tag{27}$$

In order to proceed we first need to know the atomic basis functions from which we can construct the symmetry orbitals and how to evaluate the one-centre and multi-centre integrals of $\mathbf{H}$ and $\mathbf{S}$. Finally one has to find an efficient and accurate way to describe the molecular potential in the self-consistent-field calculations.

i) Numerical Basis Sets

The standard procedure in LCAO calculations has been to use Gaussian Type Orbitals, GTO, or Slater Type Orbitals, STO, which are normally used in HF based codes but also in DFT codes. With such an approach the **H** and **S** could be given in closed forms. This was also partly the procedure used in the first molecular calculations using the DVM method by Baerends, Ellis and Ros [77]. The DVM method [22–24] is however quite general and very suitable for use of numerical basis functions, as first introduced by Averill and Ellis in 1973 [78]. They proposed that a first choice of basis functions for molecular calculations would be to solve the Schrödinger equation to self-consistency for the isolated atoms in a molecule, which will give

$$\left[-\frac{1}{2}\nabla^2 + v_{eff}(\vec{r}) + v_{ext}(\vec{r})\right]\varphi_j(\mathbf{r}) = \epsilon_i\varphi_j(\mathbf{r}), \tag{28}$$

$$\varphi_j(\mathbf{r}) = u_{nl}(\mathbf{r})Y_{lm}(\hat{r_\nu}). \tag{29}$$

where the different terms in the potential refer to the atoms. v_{ext} represents an external potential which is normally chosen equal to zero. The resulting self-consistent, one-electron Hamiltonian will only have a finite number of bound states since the Latter correction [43] is not normally applied. This type of basis set known as single-site orbitals, SSO, will define a minimal basis set in LCAO calculations. However, in order to gain a more accurate representation of the molecular orbitals, it is necessary to extend the basis with additional basis functions. Averill and Ellis accomplished this by superimposing upon the self-consistent potential a spherical well or barrier of sufficient depth V_S and with radius R_S defined by v_{ext} where,

$$v_{ext}(r) = \begin{cases} -V_S & r \leq R_S \\ 0 & r > R_S \end{cases} \tag{30}$$

Another way to extend the basis has been to generate basis functions for singly or doubly ionized atoms of the atoms in the molecule. In calculations for systems with carbon one obtains a basis set of (1s2s2p) functions for the neutral configuration with the addition of either (2s2p) functions for C^{2+} or (2s2p3s3p) functions for C^{3+}. The latter denoted as extended basis set. Averill and Ellis also introduced a simple way to avoid a direct evaluation of the kinetic energy by rewriting the Schrödinger equation in the following way.

$$-\frac{1}{2}\nabla^2\varphi_j(\mathbf{r}) = [\epsilon_i - v_{eff}(\vec{r}) - v_{ext}(\vec{r})]\varphi_j(\mathbf{r}) \tag{31}$$

ii) Numerical Integration Techniques

The computation of **H** and **S** requires use of efficient accurate three dimensional integration methods, in which the integration is performed numerically as a summation of the function values over a certain point distribution:

$$I = \int d\mathbf{r} f(\mathbf{r}) \approx \sum_i w(\mathbf{r}_i) f(\mathbf{r}_i). \tag{32}$$

where $w(\mathbf{r}_i)$ is a weighting function for each point at position $\mathbf{r}_i$ and $f(\mathbf{r}_i)$ the value of the function at that point. The basis functions of the constituent atoms in a molecule are strongly oscillating close to the nuclei. Consequently, the integration scheme should be accurate enough to include such oscillations which is particularly important if one should evaluate total energy properties. The integral will in general contain one-centre and multi-centre terms and the scheme should also be accurate enough to include all these terms. Ellis and Painter solved this problem partly in 1968-1970 by introducing the DVM method [22–24]. The error in the integration is proportional to N^{-1}, where N is the number of integration points.

The sampling of the points is usually taken as a sum of points centered around the atoms and given as the product of a certain adjustable constant sampling weight t_μ and spherical Fermi-Dirac distribution centered at each atomic site and given by

$$w_\mu(\mathbf{r}) = t_\mu v_\mu(\mathbf{r}) \tag{33}$$

$$v_\mu(\mathbf{r}) = A_\mu / 4\pi r_\nu^2 [1 + exp[\beta_\nu(r_\nu - R^\nu{}_0)]] \tag{34}$$

A schematic overview of the radial probability function $g(r) = 4\pi r^2 w_\mu(\mathbf{r})$ is given in Fig. 5. The shortcoming with this original DVM scheme is that it is difficult to attain accurate treatment of the core orbitals. The original DVM scheme can however be improved by employing a Gauss-Legendre integration scheme for the core region [79] and use of the original DVM scheme in the remaining space. Within this scheme the integration is done over a certain number of angular points and with a regular radial mesh up to a certain radial distance, R_e, chosen so that the spheres around each atomic site touch each other. More recently Boerrigter *et al.* [80] have improved the scheme by a discretization of the whole space in Voronoi cells, each containing one atom. A spherical integration is done as before and the remaining region inside the polyhedron is split into a sum of truncated pyramids where a threefold product formula is used.

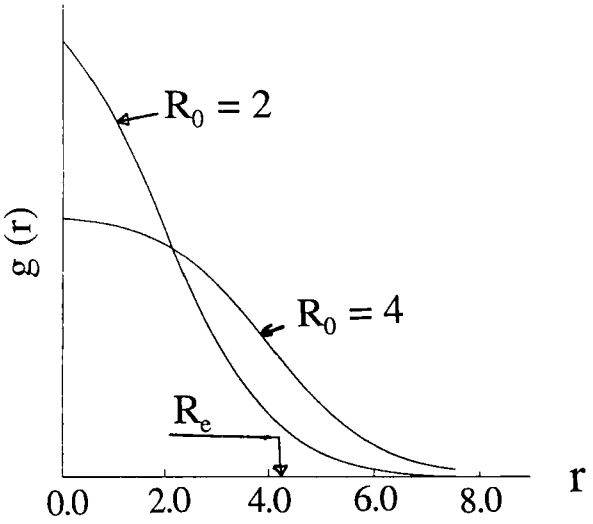

FIG. 5. Plot of the radial probability distribution function g(r) as a function of r for $\beta = 1.0$ and two different values of R_0 [78]. The location of the radius R_e is indicated.

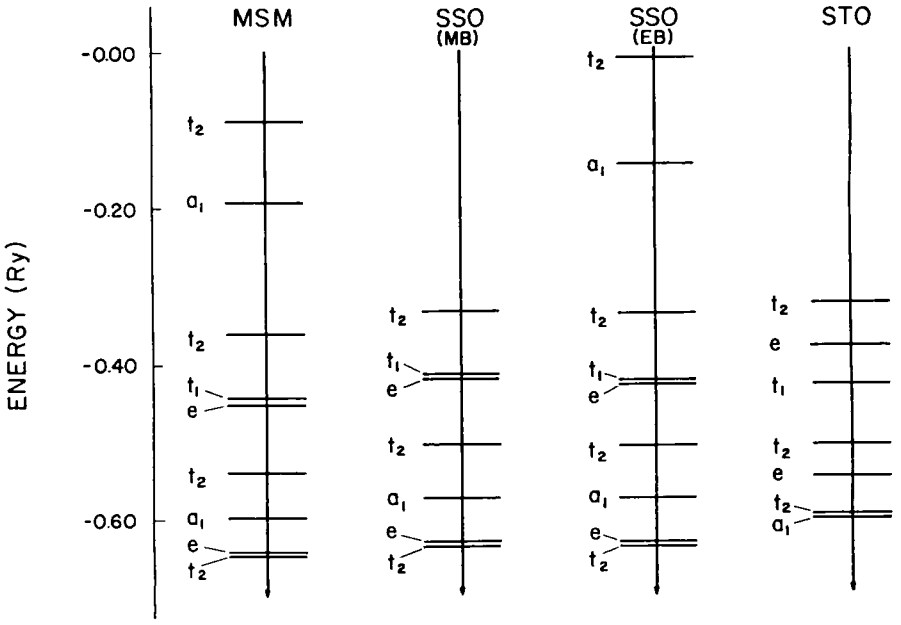

FIG. 6. The valence molecular eigenvalues,MSM, in the muffin-tin potential for $FeCl_4$ calculated using different basis sets as discussed in the text [78].

Averill and Ellis compared the accuracy of this kind of numerical basis with what was obtained with an STO type basis, Fig. 6, to the right. They generated for this analysis the eigenvalue spectrum for a $FeCl_4$ molecule with the MS-Xα potential and obtained the eigenvalues denoted by MSM and given to the left in Fig. 6. These eigenvalues would be the exact ones within this approximation. They used then the DVM method and evaluated the eigenvalue spectrum given in the middle of Fig. 6, using the numerical orbitals with mimimal basis, SSO(MB), extended basis, SSO(EB). The use of a SSO(MB) gives a good flexibility and a rather accurate description of the occupied states compared with the results obtained with STO. The accuracy is also improved for the unoccupied states with the SSO(EB).

iii) Evaluation of Molecular Potential.

For the self-consistent solution of these equations, the electronic Coulomb potential of the charge density must be calculated by solving the Poisson equation in three dimensions. This is a multi-centre problem which can be solved by a least-square-fit of the true charge density to some form of model density, which allows one-centre integration. We have in our work normally used the SCC approximation [16] with a division of the molecular charge density in terms of charges for the atomic basis function determined through a Mulliken analysis [81]. Using this method, the true charge density is projected on the radial basis functions and averaged over the different angular components used in the construction of the symmetry orbitals.

$$\rho_{SCC}(\mathbf{r}) = \sum_{\nu nl} q^{\nu}_{nl} |u^{\nu}_{nl}(r_\nu)|^2. \tag{35}$$

The Coulomb potential is obtained as a sum of each atomic contribution, for which standard one-dimensional integration can be performed. It should be stressed that this procedure does not imply spherical symmetry of the molecular potential around the atoms in the molecule, as for example is the case in the "muffin-tin" form used in the MS-Xα method. This is the reason why the SCC method gives rather good description of many experimental quantities. The exchange potential can be evaluated directly using the true charge density. Partition of the charge density is however an approximation since the Coulomb potential is assumed to be overlapping spherically. This type of shape approximation can be removed by augmenting the basis set with a multipole expansion as done within the SCM approximation [82].

$$\rho_{SCM}(\mathbf{r}) = \sum_{\nu nl} g^{\nu}_{nl} |u^{\nu}_{nl}(r_\nu)|^2 + \sum_{ilm} d^{i}_{lm} \rho_i(\mathbf{r}_i) Y_{lm}(\mathbf{r}_i). \tag{36}$$

Here the summation runs over ν atoms, and the sum over ilm is over the multipole expansion, which is distributed over symmetry unique points i, where r_i is the distance for these points. These multipole contributions can be handled with analytical integrations when they are for example given as piecewise parabolic functions. The expansion coefficients g_{nl}^{ν} and d_{lm} are determined by a least-square-fit to the true electron charge density. SCF calculations with this approach do not imply any strong shape approximation, and reasonably accurate results can be obtained. Two drawbacks are however, that the fitting procedure may be slow and that the result is influenced by the choice of the fitting functions. These disadvantages are avoided by projection techniques introduced by Becke [83] or Delley [84]. These methods are based on integration techniques originating from the DVM method, and the charge density is written as:

$$\rho_{\mathrm{PT}}(\mathbf{r}) = \sqrt{4\pi} \sum_{\nu,l,m} \sqrt{2l+1} Y_{l,m}(\mathbf{r} - \mathbf{R}_\nu) \rho_{\nu,l,m}(|\mathbf{r} - \mathbf{R}_\nu|) \tag{37}$$

where

$$\rho_{\nu,l,m} = \frac{1}{\sqrt{4\pi}\sqrt{2l+1}} \int d\Omega Y_{l,m}(\mathbf{r} - \mathbf{R}_\nu) w_\nu(\mathbf{r}) \rho(\mathbf{r}).$$

The model density is obtained by projecting the true density onto radial weighting functions w_ν centered at each atomic site. The projection can be done to arbitrary angular momentum l. This approach seems to be more accurate compared with the SCM method and is also faster.

D. Use of external fields in SCF calculations

It is also possible to include in addition to the ionic part an additional external potential v_{ext} in the Hamiltonian in Eq. (11) in the self-consistent procedure. This could be the long-range static potential from a surrounding crystalline environment, as used in the embedded cluster method, Fig. 7. Clusters are here used to model a small section of an infinite solid or surface.

This technique has been applied in the analysis of the electronic structure of stoichiometric and non-stoichiometric (111) surfaces of BaF_2 and CaF_2 crystals [85–88] or in the case of Al_2O_3 crystals by Guo, Ellis and Lam [89–91]. v_{ext} could also represent an applied static electric field as used for evaluation of static polarizabilities as discussed below. In the latter case, we could evaluate the multipolar moments separately, thus obtaining the static polarizability, induced by a field of the form [92]

$$v_{ext} = \varepsilon_l r^l P_l(cos\theta) \tag{38}$$

where $l = 1$ for dipole and $l = 2$ for quadrupole fields of strength ε_l etc., and P_l is the Legendre polynomial of order l. In this study we have evaluated the induced dipole moment and dipole polarizability as a function of the electric field strength ε as discussed below for C_{60}.

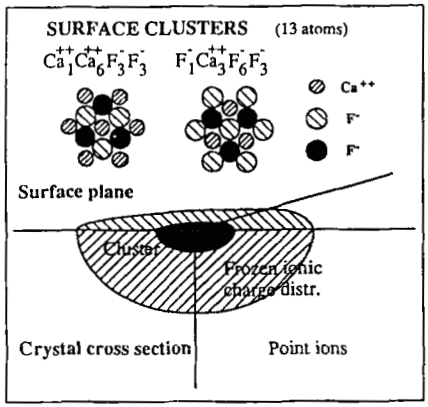

FIG. 7. Geometry of planar clusters used to represent the (111) surface of BaF_2 and CaF_2 as described in the text. Our model of the crystal environment is schematically shown for two types of cluster, M =Ca or Ba and X=F, [87].

E. Evaluation of polarizabilities

Using standard perturbation analysis [93,94] we evaluate the unscreened linear isotropic polarization from

$$\gamma^{(1)}(-\omega;\omega) = \frac{1}{3}\gamma^{(1)}_{\mu\mu}(-\omega;\omega) \tag{39}$$

where

$$\gamma^{(1)}_{\mu\alpha}(-\omega;\omega) = \sum_{gn}\rho_0(g)\left[\frac{r^{\mu}_{gn}r^{\alpha}_{ng}}{\Omega_{ng}-\omega-i\Gamma_{ng}} + \frac{r^{\alpha}_{gn}r^{\mu}_{ng}}{\Omega_{ng}+\omega+i\Gamma_{ng}}\right] \tag{40}$$

In the case of C_{60}, we have $\gamma^{(1)}_{xx} = \gamma^{(1)}_{yy} = \gamma^{(1)}_{zz}$. The ground state dipole matrix elements r^{α}_{nm} and transition frequencies Ω_{nm} are given by

$$r^{\alpha}_{nm} = \int dV \psi^{*}_{n}(\vec{r})\hat{r}_{\alpha}\psi_{m}(\vec{r}) \tag{41}$$

$$\Omega_{nm} = \epsilon_n - \epsilon_m \quad . \tag{42}$$

The phenomenological linewidth terms Γ_{nm} are introduced to ensure convergence of the response function and to describe damping processes which are

not explicitly considered here. For visualization of evaluated spectra, a constant as well as energy dependent broadening parameter Γ_{nm} is normally used. The electronic occupation of the system is taken into account by

$$\rho_0(g) = 2N_n(1 - N_m), \quad \text{where} \quad N_i = \left\{ \begin{array}{lll} 1 & if & i = \{g\} \\ 0 & if & i \neq \{g\} \end{array} \right\} \tag{43}$$

where the factor 2 arises owing to the spin degeneracy, and g denotes the ground state of C_{60}.

In practice, self-consistent calculations have been performed for different external dipole fields, $v_{ext} = -\varepsilon z$, and the evaluated induced moment has been fitted to the expression

$$P = \alpha\varepsilon + \gamma\varepsilon^3, \tag{44}$$

where α and γ are the linear and nonlinear static polarizabilities.

Having obtained the zero frequency limit of the dynamic polarizability i.e., $\alpha = \lim_{\omega\to 0} \gamma^{(1)}(-\omega;\omega)$, we use a simplified approach to evaluate the screened dynamic response. This is necessary, since the expression given above, Eq. (40), for the polarizability neglects the induced collective effects essentially due to direct and exchange terms of the Coulomb interaction. To treat this screening approximately, we have used the simplified approach of Bertsch *et al.* [96] to include the induced electron interaction in the C_{60} molecule, by a simple RPA type correction [92,95]

$$\gamma^{(1)}_{scr}(-\omega;\omega) = \frac{\gamma^{(1)}(-\omega;\omega)}{1 + \nu\gamma^{(1)}(-\omega;\omega)} \tag{45}$$

where $\nu = R^{-3}$ is an effective screening parameter of the applied external field. ν corresponds in a quantum mechanical description to the induced contribution from the Coulomb and exchange interaction terms. Classically ν corresponds to the centre of mass for the induced electronic charge distribution. An estimate of the magnitude can be obtained by taking the first term in a spherical expansion of the Coulomb potential and approximating the charge distribution of the C_{60} [96]. By use of the static polarizability calculated from first principle as described above and evaluated in a recent work [97], we can determine values of the effective screening ν, which will depend on the extension of the orbitals involved in the excitations. It seems that, in a first approximation, a constant value of ν can be used for all excitation energies in the evaluation of the dynamic response, oscillator strengths, dielectric constants etc. A more detailed analysis requires, however, different values for π and σ electrons. This estimate of the screening can be considered a first step towards a fully time-dependent LDA (TDLDA) calculation [92,98,99].

For comparison with experimental data [100–102], it is common to evaluate the oscillator strengths, photo absorption cross section and EELS (Electron Energy Loss Spectrum) defined here in terms of the imaginary part of the polarizability $\gamma^{(1)}$

$$\sigma(\omega) = \frac{df}{d\omega} = \frac{\omega}{\pi} Im\, \gamma^{(1)}(-\omega;\omega) \tag{46}$$

To describe local field effects associated with a crystalline environment, e.g. C_{60} arranged in a lattice of cubic symmetry, we use the Clausius-Mossotti relation [93] in the form

$$\chi^{(1)}(-\omega;\omega) = N\frac{\gamma^{(1)}(-\omega;\omega)}{1 + CN\gamma^{(1)}(-\omega;\omega)} \tag{47}$$

where $C = -\frac{1}{3}$ or $C = \frac{2}{3}$ depending on whether the external perturbation is of a transverse or longitudinal nature, with respect to the wave vector [103]. When evaluating the dielectric constant $\epsilon = 1 + \chi^{(1)}$ for C_{60}, we use 14.2 Å for the lattice constant [104]. The corresponding screened oscillator strengths, susceptibilities, etc. are obtained by using $\gamma^{(1)}_{scr}$ instead of $\gamma^{(1)}$ in Eqs. (46) and (47).

IV. RESULTS AND DISCUSSION

One general problem in molecular calculations has been to determine the optimum geometry for a molecular system for comparison with experimental bond distances and bonding energies. This will require evaluation of total energy properties which for a long time has been a difficult problem. A number of studies have however shown that useful information of bonding in a molecule can be obtained from analysis of one-electron properties which goes back to the approach used by Pauling [105] and Mulliken [81]. This has for example been the approach used by Pershina *et al.* [106] in prediction of chemical properties of superheavy elements.

Another standing topic during the last two decades has been to evaluate the electronic structure of solids, surfaces and adsorbates on surfaces. This can be done using standard band structure methods [107] or in more recent years slab codes for studies of surfaces. An alternative and very popular approach has been to model the infinite solid or surface with a finite cluster, where the choice of the form and size of the cluster has been determined by the local geometry. These clusters have in more advanced calculations been embedded in some type of external potential as discussed above. It should be noted that these types of cluster have in general quite different geometries compared with

the whole new groups of free metal clusters and ultrafine particles available today [108–114]. The development of methods for production of small free metal clusters with the laser vaporization technique [110,115,116] and studies of their properties such as; abundance, static dipole polarizabilities, photoionization and ionization potentials, photoelectron and electron affinities, optical properties, stability and fragmentation, magnetic moments, reactivity etc. have during the last decade opened up a totally new field of research.

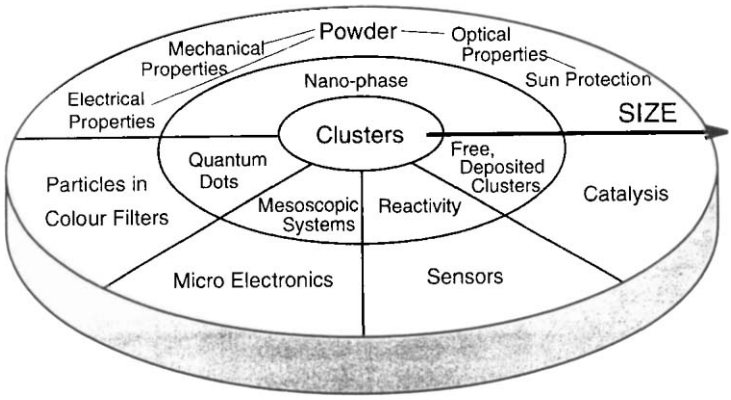

FIG. 8. A schematic overview of how clusters are related to many areas of modern materials science, micro electronics, mesoscopic physics when the sizes of the clusters increase.

One of the main goals in cluster science is to find out how many atoms are needed in a cluster to make its properties similar to what is known for solid materials. One could perhaps assume that the values of different properties would change smoothly when the number of atoms increases in a cluster from a few up to very large clusters comprising a large number of atoms. A more detailed analysis of these fluctuations shows, however, that there often exist some periodicities in this behaviour which in some cases can be understood as shell closing, geometric [117] or electronic [69], with the appearance of so-called "magic numbers" as was discussed in connection with the jellium model. Bigger clusters are related to powder [112,113] and to nanotechnology [118]. In addition to these clusters, also very unique species of carbon have been discovered such as the fullerenes [119], nanotubes [120], carbon onions [121], and metcars [122]. Actually clusters have many connections to materials science, nanotechnology and mesoscopic physics as schematically shown in Fig. 8. I will only in this short review give some examples mainly chosen from the work carried out by our group to show how the DV-Xα method can be used [72,97,88,123–131].

A. Results for Cl_2

As an example of application of the Xα method, I have chosen an early study of the effects of the exchange parameters on the binding energy curve of Cl_2 performed by Schwarz and Weinberger in 1974 [132]. The results from their analysis and use of the muffin-tin method in the evaluation of the binding energy curve are depicted to the left in Fig. 9. Obtaining bonding and reasonable agreement with the experimental bond length required the use of an α equal to 1.5 which was far from the value obtained from theory. The earlier mentioned α values with five decimals as calculated by Schwarz [36] failed totally. This was also the case for the $X\alpha\beta$ potential by Herman *et al.* [26]. The main reason was not the choice of the strength of the exchange potential but the use of the muffin-tin approximation in the evaluation of the molecular potential.

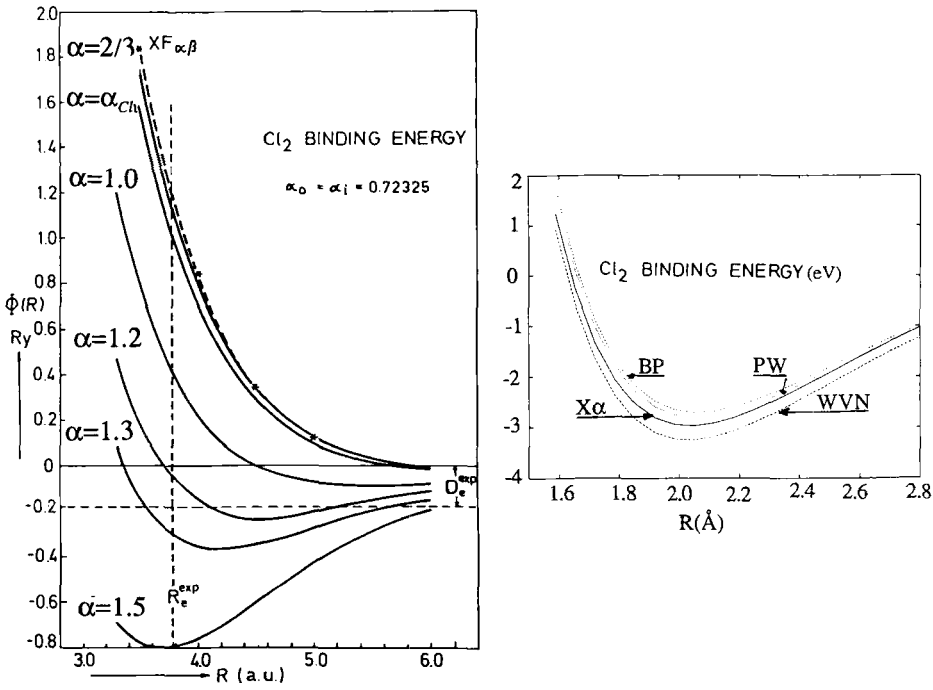

FIG. 9. a) The binding energy of Cl_2 as a function of the internuclear separation R The solid lines denote the α results using different parameters as shown in the figure. The experimental values [133] are given for comparison. b) Examples of calculation of binding energy curves for Cl_2 using different exchange correlation potentials as discussed in the text.

This is illustrated by Xα calculations using a reasonable approximation of the Coulomb potential as done in the ADF program [9]. Calculations have been done using the original Xα exchange potential with $\alpha = 0.70$ and modern forms of exchange correlation potentials by Vosko *et al.* [41], WVN, Becke and Perdew [45,46], BP and Perdew [47], PW, Fig. 9. We notice how the results as depicted to the right in Fig. 9, give with $\alpha = 0.70$ a comparatively good agreement with the experimental binding energy of 2.48 eV and bond length of 1.99Å [133] and with the results using other exchange correlation potentials. The failure of the MS method in calculations of total energies, eigenvalue spectrum and ionization energies opened up a market in the early 70s for improved methods to evaluate accurate molecular potentials. This coincided with Ellis and coworkers publishing the first results of the DV Xα method [77].

B. Electronic structure of clusters and surfaces

Access to clusters of principally all elements in the periodic table has opened new possibilities for test of calculations and comparison with available experimental data and what is known from surface science. The geometry of the free clusters will, as discussed above, be determined by the electronic properties of the constituent atoms. This means that clusters of alkali and coinage metals will in a first approximation be determined by the free electrons while clusters of transition elements will be determined by the balance between the *nd* and $(n+1)s$ valence electrons. Noble gas atoms will behave as hard spheres, which under certain thermodynamic conditions can form larger clusters of icosahedral symmetry [134,135]. The geometry of these free clusters are quite different what one obtains if the cluster is constructed as a piece of the lattice known for the corresponding solid.

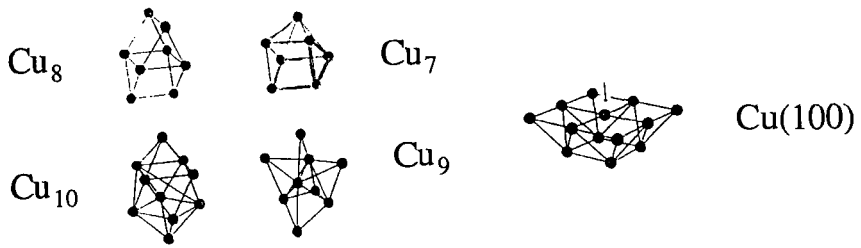

FIG. 10. Examples of geometries of four copper clusters Cu_7, Cu_8, Cu_9, Cu_{10} [136] and a cluster Cu_{13} modeling the Cu(100) surface [72,74].

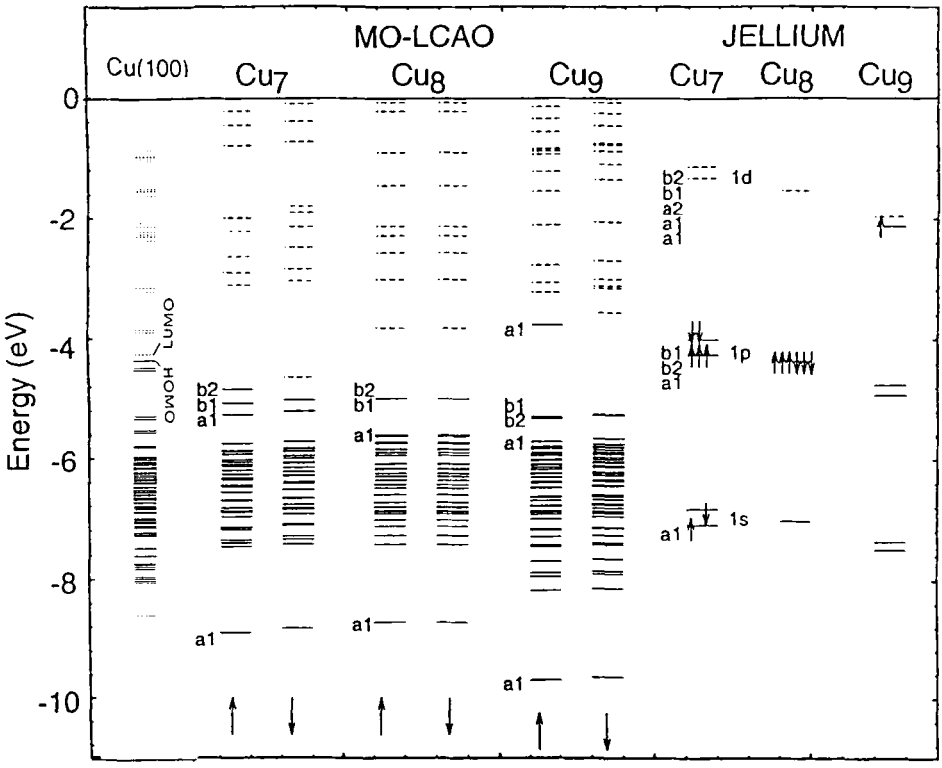

FIG. 11. Energy level diagram for the cluster modelling the Cu(100) surface, the bare clusters Cu_7, Cu_8 and Cu_9 evaluated with the standard MO-LCAO method to the left and the calculations for jellium to the right were done using the spherical jellium model [72,74]. The MO-LCAO results include contribution from the 3d levels while the jellium model only include the free 4s electrons. The one-electron orbitals are characterized by the symmetry notation corresponding to C_{2v} symmetry. Since the calculation for jellium were performed within the LSD scheme the one electron levels are split.

Particularly exciting in cluster science has been how the simple jellium model has been able to in first order explain many quantities for clusters of alkali and noble metals as the appearance of magic numbers. Examples were given in Fig. 3. We have in connection with our studies of the reactivity of

free metal clusters [70,71] made a number of calculations [62,72–74] to investigate such problems. Example of the geometries for some small clusters of Cu determined by Nygren *et al.* [136] with a comparison with the geometry of a Cu(100) surface is shown in Fig. 10, [72,74]. We notice how the geometries for the Cu clusters are quite different compared with what one would obtain by choosing the geometry as a part of the fcc solid. Recently Massobrio *et al.* [137,138] have determined the ground state structure of small Cu clusters using a plane wave expansion and pseudo-potentials and got somewhat different results compared with Nygren *et al.* [136].

A comparison of how the energy levels change for a cluster model of Cu(100) surface, and the Cu_7 to Cu_9 clusters is illustrated in Fig. 11 [72,74]. We notice the quite diffferent electronic structure of the free clusters compared with the Cu_{13} cluster modelling the surface and the large separation in energy for the HOMO and LUMO levels for Cu_8 compared with the other clusters. The copper clusters are free electron like and we have therefore investigated how the energy level diagram would change if the bare clusters were treated within the jellium model as illustrated for the Cu_7, Cu_8 and Cu_9 clusters to the right in Fig. 11. It seems that the jellium model can give a reasonable description of the electronic properties of these clusters .

Some characteristics of the electronic structure and bonding of transition metal clusters as illustrated for Nb_4 is shown in Fig. 12. These structures have been calculated by Andersson *et al.* [139] using the Dmol code [10]. For the bare tetramer three different isomers were investigated with different symmetries: a tetrahedron (C_{3v}), a square (D_{4h}) and a rhombus (D_{2h}). The C_{3v} isomer is a pyramid with equal bond lengths in the base triangle, but somewhat longer bonds to the top atom. The nearest-neighbour distance for the rhombus and the square are smaller than for the C_{3v} isomer. These distances should be compared with the nearest-neighbour distance in the niobium bcc bulk crystal 5.6 a.u.

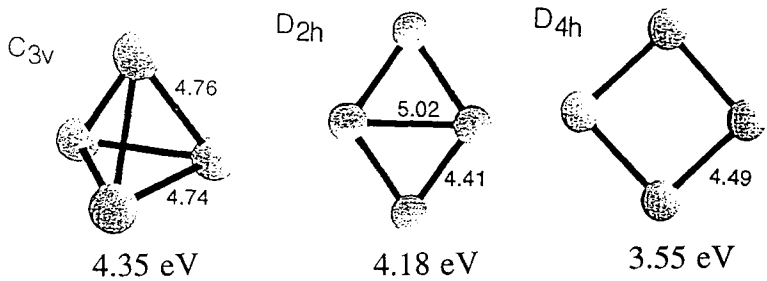

FIG. 12. Three possible Nb_4 with calculated equilibrium bond lengths in a.u. and binding energies in eV [139].

Calculations with the ADF program [9] give the same ordering of the isomers but with a reduction of the bond length to 4.65 a.u. due to inclusion of scalar-relativistic effects in the pseudo potential. These results are in agreement with calculations using the Car-Parrinello method [63]. The results for these tetramers should be compared with calculations for clusters of alkali and noble metals for which the rhombus gives the lowest energy [34]. The appearance of the three dimensional structure is the result of the balance between the 4d and 5s electrons.

C. Reactivity of molecules on clusters

Studies of the reactivity in terms of chemisorption of molecules on surfaces and clusters have been an important subject in surface and cluster science since the 60s. Knowledge of the reactivity of clusters is also an important property in the objective to use clusters as building blocks in new materials and as catalysts. We have in our group in recent years [70,71] studied the reactivity towards various diatomic molecules and compared those results with molecular calculations.

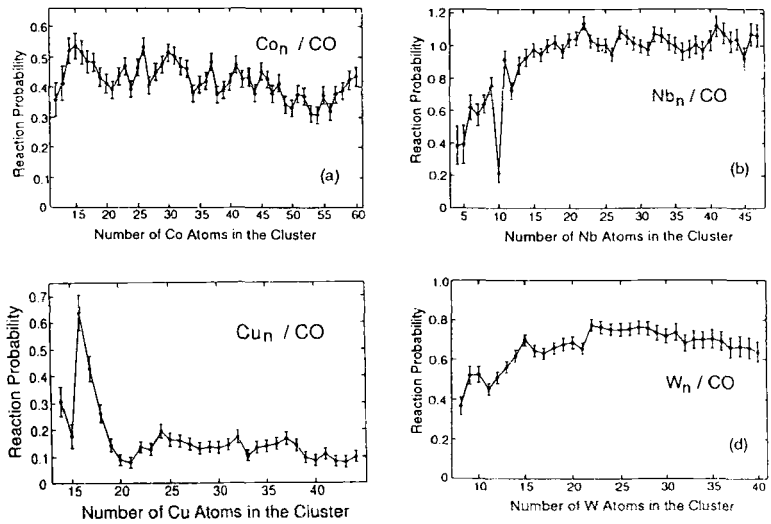

FIG. 13. Measured reaction probability with CO for clusters of (a) Co, (b) Nb, (c) Cu and (d) W, [139–141].

Data shown in Fig. 13 exemplify the reaction probability, S, of CO on small clusters of Co, Nb, Cu and W [139–141]. The reaction probability is generally high for clusters of all four metals except for Cu with n> 20. For

Co_n the reaction probability seems almost independent of cluster size while it seems to be an increase for Cu_n with a maximum at the size of 16 followed by a minimum at 20 with some small variations. For Nb_n there seems to be an increase in S with size for n< 15 followed with distinct variations in S around n= 10.

TABLE I. Comparison of chemisorption energies for small clusters of Cu in eV, calculated with the jellium model [141] and an *ab initio* method [136].

Method	Cu_6	Cu_7	Cu_8	Cu_9
jellium	-1.16	-0.43	-0.22	-0.75
ab initio	-1.06	-0.59	-0.44	-0.72

We have analyzed the chemisorption of CO on clusters of Cu and Nb using the MO-LCAO method described above. A cluster of Cu was described as a jellium sphere and the chemisorbed system was modelled with a tri-atomic molecule, Cu_nCO [72,140]. Calculated chemisorption energies shown in Fig. 14 reproduce the main trend of the experimental reaction probability. We have also tested the accuracy of the jellium model by doing calculations for some smaller clusters of Cu and compared the results with *ab initio* calculations by Nygren and Siegbahn [136], Table I. Evaluted chemisorption energies calculated within the simple jellium model as given in Table I are in comparatively good agreement with the *ab initio* results. The jellium model [72] was also found to give a comparatively good description of measured reaction probabilities [140] for clusters characterized as closed or close to closed shells.

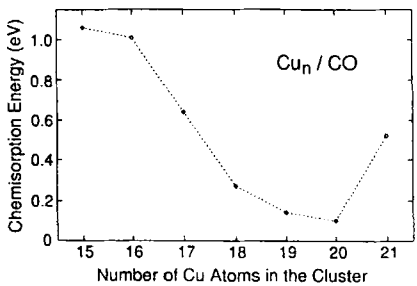

FIG. 14. Chemisorption energy of CO on jellium Cu Clusters n =15-21, [141]

The Dmol program [10] has also been used to optimize the geometries for clusters of Nb_n with n = 2-10 [125] (Fig. 15), as well as to determine the bond dissociation energies. A rather good agreement is obtained with experimental values determined from collision induced dissociation energies by Hales *et al.* [142] as shown in Fig. 16.

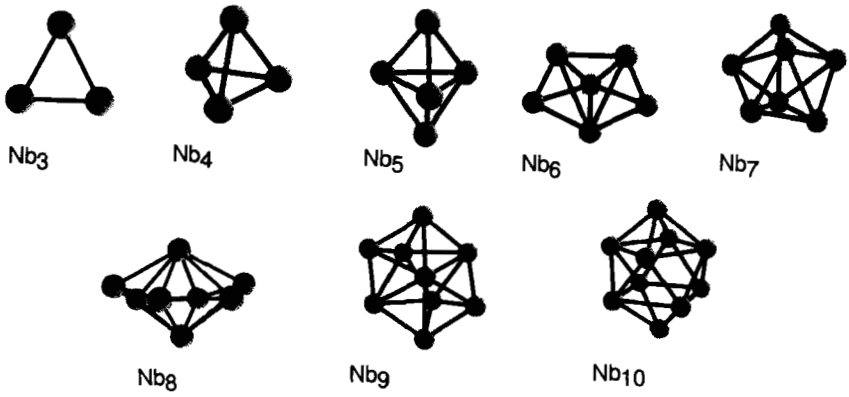

FIG. 15. Optimized cluster geometries for clusters of Nb n =3-10, [125].

TABLE II. Data for CO chemisorbed at various sites on the Nb_4 cluster [63]. The free CO molecule is also included for comparison.

Adsorption site	E_b (eV)	d(CO) (a.u.)	ω (cm^{-1})
Top	1.17	2.19	1917
Hollow	2.43	2.26	1761
Bridge	2.87	2.38	1584
CO		2.14	2117
CO(Exp.[133])		2.13	2170

The chemisorption geometries for the CO molecule in hollow and top position on the Nb_n clusters were also determined as given to the right in Fig. 16. For all clusters, the hollow site is predicted as the preferred chemisorption site. In order to investigate the accuracy of these results calculations were also done using the *ab initio* molecular dynamics Car-Parrinello method for some of the Nb_n clusters [63]. In this study extensive search were done for ground geometries using molecular dynamics. For Nb_8 two close lying iosmers were found which differ in energy by 0.12 eV. Calculations were also done to investigate the chemisorption energy of CO on Nb_4 with a comparison with results determined in MO-LCAO calculations as discussed above. The results summarized in Table II show that adsorption in bridge position gives the most preferred position.

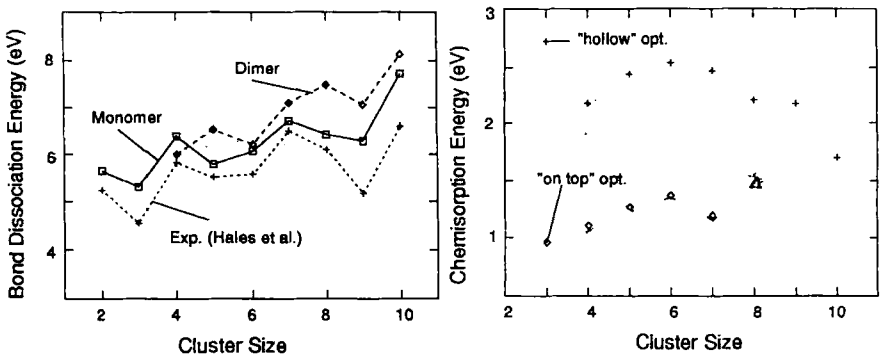

FIG. 16. a) Comparison of evaluated fragmentation energies with experimental values determinend by Hales *et al.* [142]. b) Adsorption energies for different clusters and adsorption sites in hollow and top position.

D. Electronic Structure of C_{60}

The access to the laser vaporization technique [115,116] made it possible to produce clusters of carbon of various sizes as first done by Rohlfing *et al.* [143]. Clusters of carbon became particularly exciting after further experiments with the laser vaporization technique and the discovery of C_{60} in 1985 by Kroto, Curl, Heath, O'Brien and Smalley [119]. The new carbon molecule C_{60} was proposed to have a closed cage structure like a soccerball or truncated icosahedron with 60 vertices, where the carbon atoms were located, 12 pentagonal

faces, 20 hexagonal faces and 90 bonds [119]. The structure can be obtained by cutting each corner on the regular icosahedron. Such a spherical structure which was estimated to have a diameter of 7Å was expected to have many unique properties. Fig. 17 gives a schematic overview of C_{60}, obtained from a stick model and from electronic structure calculations.

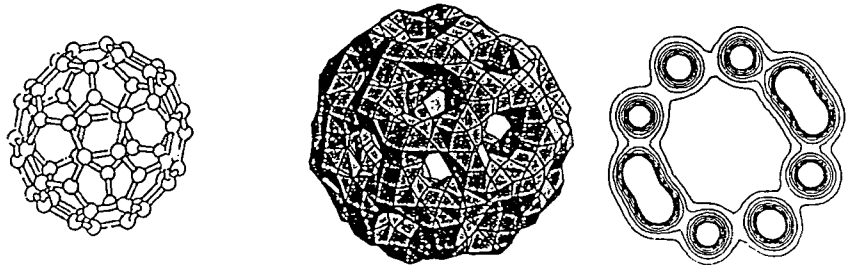

FIG. 17. A schematic overview of C_{60} represented by a stick model, 3D and 2D contour plots of the electron density. In the 3D plot in the middle the single contour has been chosen to show how the electrons are distributed in the bonds. The 2D contour plot shows the electron density in a plane that includes the center of the molecule. We clearly see that there is a void, which means that C_{60} constitutes a spherical shell.

The quantities produced with the laser vaporization method were however not even sufficient for doing experiments to verify the proposed structure. This was solved by Krätschmer, Huffman and their students who had as early as in 1982, [144–146] i.e. three years before the discovery of C_{60} in 1985, produced C_{60} without knowing it. They used an electric arc in a helium atmosphere of 150 torr and produced a special kind of soot with a unique type of optical absorption known as "*the camel hump smoke*" in the UV region. Their recorded spectrum fitted however very nicely to some predictions of the present author [147]. After a number of trials, they found in 1990 [148] that "the special carbon soot" could be dissolved in benzene, which provided the possibility to separate C_{60} from the carbon particles [149], record a UV visible spectrum and even fabricate crystals of C_{60} and C_{70} and determine the crystal structure. Suddenly a new kind of carbon material had been found in addition to the commonly known diamond and graphite.

The unique structure of C_{60} and access to an effective method for the production of macroscopic quantities opened up a new era of carbon research compared with what was known up to that date [150,151]. The field of fullerenes is a truly interdisciplinary area which has been covered in a number of proceedings, review articles and books [152–164]. As examples of some recent

discoveries can be mentioned how Martin *et al.* [165] have been able to produce clusters of C_{60} using a gas evaporation source. By coevaporating C_{60} with different metals as Li, Ca, Sr and Ba, Martin and coworkers [166,167] were also able to produce species covered with metal as $Li_{12}C_{60}$, $Ca_{32}C_{60}$, Fig. 18. I will in this article only be able to present a few examples on fullerenes to give some idea of this highly interdisciplinary field.

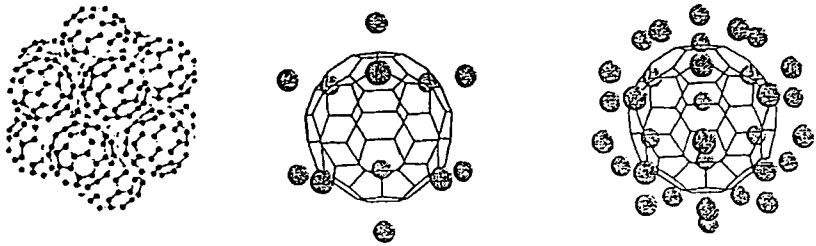

FIG. 18. Clusters of C_{60} [114,165] and two specific models of metal covered C_{60} with 12 and 32 metal atoms outside the pentagons and hexagons.

i) Ground state properties

Our first calculations for C_{60} and its doped species [128–131] were performed using the DVM method and a minimal basis set composed of the 1s, 2s and 2p orbitals of the neutral carbon atom and the 2s, 2p orbitals of the C^{2+} ion. The 1s orbital was kept frozen in all calculations. We have in more recent work [97] used an extended basis set by including either 3s, 3p, 3d or 3s, 3p and 3p, 3d functions generated for the N^{7+} ion in the basis set used previously. This basis set is similar to the one used by Freeman *et al.* [168]. The more recent calculations were performed using the three-dimensional integration method of Boerrigter *et al.* [80] with 600 points for each carbon atom. This should be compared with our earlier calculations using about 250 points per carbon atom and the original DVM scheme. The increased accuracy made it possible, not only to obtain more accurate molecular eigenvalues, but also to evaluate the induced electric dipole moment as a function of an external electric field and in this way evaluate the static polarizability from first principles as described below. The calculations were performed in D_{2h} symmetry using the SCC [16] as well as the SCM [82] method for the treatment of the molecular charge density.

Fig. 19 gives an overview of the eigenvalues determined with the SCC approximation using the minimal basis set and the addition of some of the basis functions determined for the N^{7+} ion. Results from the earlier calculations [130] are given in column 1. All these calculations were performed using the

Hedin- Lundqvist, HL, exchange-correlation potential [37], which is equivalent to our earlier use [130] of the von Barth-Hedin potential, vBH, [38] with parameter values as used by Hedin and Lundqvist. Calculations were also performed using the Xα form, with $\alpha = 0.7$ [4] and the Vosko-Wilk-Nusair form of v_{xc} [41]. A somewhat lower total energy was obtained by inclusion of the 3d, and in particular the 3p and 3d, basis functions, compared with the results obtained using the minimal basis set.

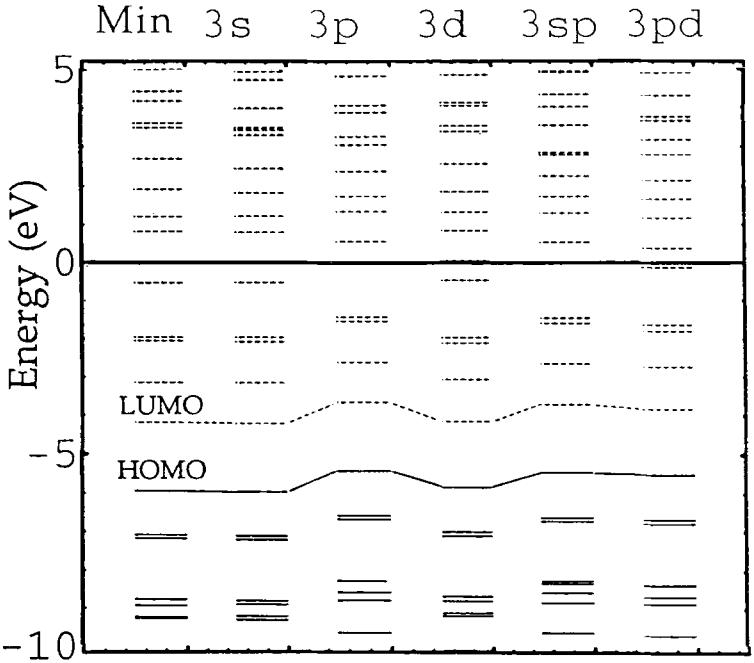

FIG. 19. Ground state properties of C_{60} evaluated with the SCC method using the minimal basis set and with the addition of 3s, 3p, 3d, (3s,3p) or (3p,3d) basis functions generated for the hydrogenic N^{7+} ion [97].

Fig. 20 illustrates the change in position of the molecular eigenvalues obtained when using the minimal and largest extended basis set, 3p 3d, as well as when using the SCC and SCM method for the description of the molecular charge density. Extension of the basis set and the use of different models for the treatment of the molecular charge density give a uniform shift compared with our earlier calculations, as depicted in column 1. The molecular charge density has been fitted with spherical harmonics of $l = 1$ and $l = 2$. Inclusion of s functions in the fit failed due to close linear dependency on the occupation

numbers determined in the Mulliken analysis and used in the least-squares-fit of the molecular charge density

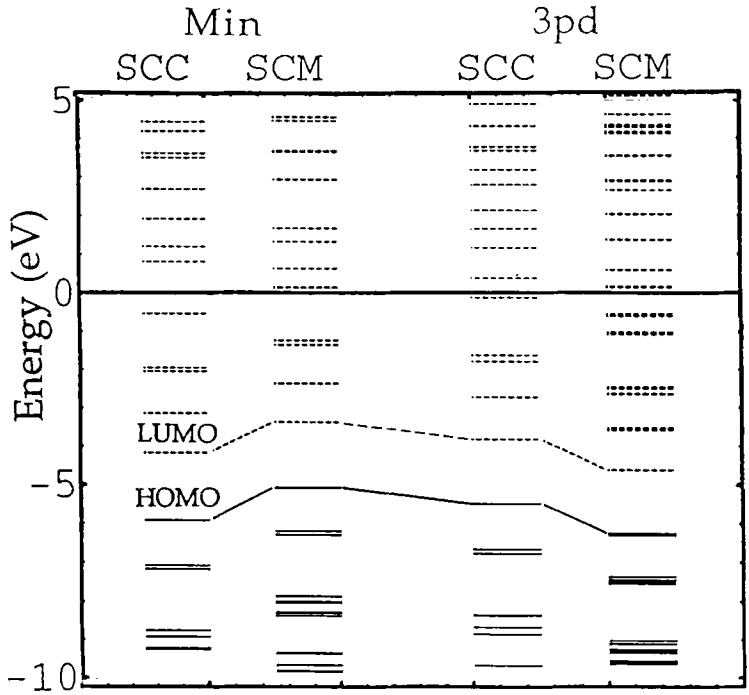

FIG. 20. Ground state properties of C_{60} evaluated with the SCC and SCM method using the minimal basis set and with the addition of 3p 3d basis functions generated for the hydrogenic N^{7+} ion, [97].

All these calculations were performed for the experimental bond distances of 1.458(6) Å and 1.401(10) Å as determined by electron diffraction [169]. The use of slightly different bond distances as in our earlier calculations [130] gave only minor changes in the eigenvalues. The best agreement with the experimentally determined first ionization potential (7.54 ± 0.04 eV) [170] and electron affinity (2.70 eV) [171] is obtained with the Hedin-Lundqvist exchange-correlation potential and the minimal basis set as defined above.

ii) Static polarizabilities

When discussing the electronic spectra and optical properties of C_{60}, it is important to include the effect of screening of the external field. Using the ground state single-particle wavefunctions and energy levels, the dipole transition matrix elements and transition frequencies have been evaluated in order

to obtain the free dynamic polarizability or oscillator strength distribution as a function of the excitation energy Eqs. (46) and (47). The static polarizability α, can then be evaluated from the dynamical polarizability in the limit $\alpha = \lim_{\omega \to 0} \gamma^{(1)}(-\omega;\omega)$, according to Eq. (39). Static polarizabilities evaluated using this sum-over-states technique for different exchange-correlation potentials are given in Table III.

The dynamic polarizability or theoretical optical spectrum calculated with this sum-over-states technique for C_{60}, [88,127] is however, not in particularly good agreement with the available experimental spectra obtained from C_{60} in solution [100] or as thin films [101] owing to the omission of screening effects. The experimental spectrum [100] is characterized by a strong peak at about 6 eV, which is totally missing in the the theoretical spectrum. The reason for this significant discrepancy may be that screening due to the Coulomb and exchange interaction has been neglected.

An alternative way of calculating the static polarizability is to evaluate the induced electric dipole moment by applying an external electric field in the SCF calculations, as described in section III. Variation of the induced dipole moment as a function of the applied electric field in the SCF calculations for C_{60} is shown in Fig. 21 for the Hedin–Lundquvist exchange-correlation potential and an extended basis set. The calculations were performed using an electric field of strength up to 0.032 a.u. corresponding to $0.16 \cdot 10^{11}$ Vm^{-1}.

TABLE III. Calculated free and screened static polarizabilities for C_{60} in atomic units, using different exchange-correlation potentials [97].

exc-corr pot		SCC min	SCM min	SCM ext
HL	screened	555.5	671.1	677
	free	1900	1857	1873
Xα	screened	567.3	685.4	649.8
BH	screened	526.5	636.3	631.7
VWN	screened	555.2		

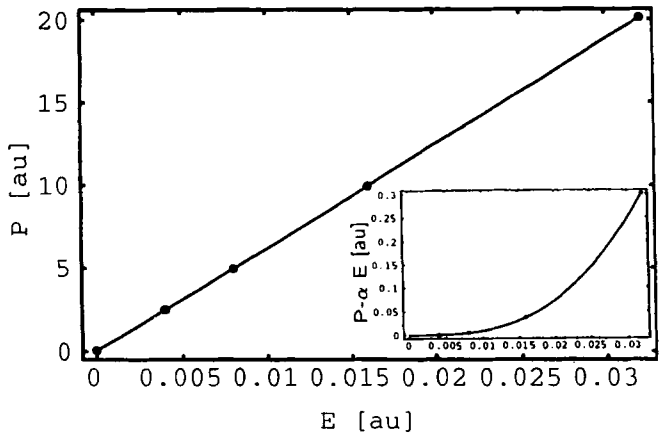

FIG. 21. Plot of the induced dipole moment for C_{60} evaluated from the self-consistent calculations using different external electric fields as discussed in the text. A plot of the third-order nonlinear contribution is given as an inset, [97].

A least-squares fit to Eq. (44) gives a value of 677 a.u. (100 $Å^3$) for the linear static polarizability and 15.6×10^3 a.u. ($8.1 \times 10^{-36} esu$) for the first nonlinear static hyperpolarizability. The calculated values are also somewhat sensitive to the form of the exchange correlation potential. Our values of the polarizability which include screening, are in rather good agreement with the value, 558 a.u. obtained by Pederson *et al.* [172] from extensive LDA total energy calculations, using a somewhat different computational method and exchange-correlation potential. Calculations [97] using the ADF program [9] gave a value of 552 a.u. for the linear static polarizability and 11.3×10^3 a.u. for the first nonlinear static hyperpolarizability using the Vosko-Wilk-Nusair form of exchange correlation potential [41]. A comparison of the polarizabilities evaluated with the sum-over-states technique, Table III, with those evaluated using an external electric field shows a dramatic effect on the polarizability with a change of the free polarizability from 1900 to 555.5.

Using the experimentally determined dielectric constant for films of C_{60} and the Lorentz local field factor $f_L = 1/(1 + N\alpha_{exp}/3)$, the experimental values of the polarizability were found to be 79.3 $Å^3$ (535 a.u.) or 85.2 $Å^3$ (575 a.u.) from UV absorption [101] and from EELS spectra [104], respectively. These values are not too far from our theoretical values determined with the SCC method, Table III. It seems, however, that use of an extended basis and more accurate description of the molecular charge density, as obtained within the SCM method, gives somewhat large values.

Classically, the static polarizability of a spherical charge distribution is proportional to the outer radius. Thus, taking 3.6 Å as the radius of the shell

and 1.4 Å as the shell thickness of C_{60} the static polarizability of C_{60} is given as 79.3 $Å^3$ [173]. These theoretical values should be compared with a value of 65 $Å^3$ calculated by Fowler *et al.* [174] using *ab initio* methods. Bertsch *et al.* [96] found a too small value of 37$Å^3$ for the static polarizability in the evaluation of the dynamical polarizability using the tight-binding method within an RPA approach.

iii) Optical spectra and dielectric constants

As discussed above, straightforward use of the sum-over-states approach for the calculation of optical absorption, oscillator strength or dispersion of the dielectric constants does not give a particularly good agreement with experimental data due to the neglect of screening. Inclusion of screening via the parameter $\nu = R^{-3}$ in Eq. (45) and the use of r= 6.8 a.u. i.e. the radius of the shell, gives a too large screening effect as obtained by Bertsch *et al.* [96].

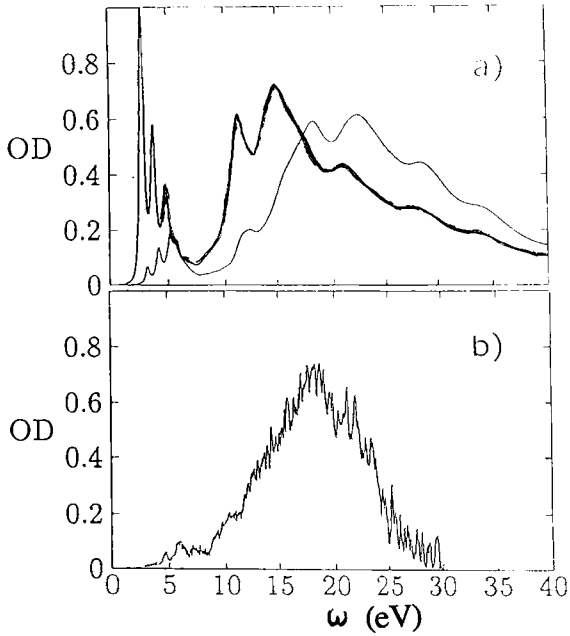

FIG. 22. a) Calculated free (thick curve) and screened R= 9.3 a.u. thin curve) response oscillator strength distributions with a linewidth parameters $\Gamma = 0.06\ \Omega$. b) Experimental oscillator strength distribution as measured by Burose *et al.* [175].

However, we can treat $\nu = R^{-3}$ in Eq. (45) as an adjustable parameter and make a least-squares- fit of the dynamic polarizabilites in the limit $\omega = 0$

to the static polarizabilities evaluated by inclusion of an external electric field in the SCF calculations. Such a procedure [97] gives values of $R = 9.3 - 9.5$ and $9.8 - 10$ using the polarizabilites evaluated with the minimal basis set and the SCC and SCM methods, respectively. A value of $R = 9.3$ a.u. also gives an overall good description of the dispersion of the absorption spectra and dielectric constants.

A comparison of theoretical spectra evaluated using the free response and a screening of $R = 9.3$ a.u. with linewidth parameter $\Gamma = 0.06\ \Omega$ is depicted in Fig. 22 with a comparison of the experimental oscillator strength distribution as measured by Burose *et al.* [175]. The theoretical result is in rather good agreement with the experimental data when screening has been included.

Having established the molecular linear response with the RPA type of screening, as discussed above, we can evaluate a dielectric function, $\epsilon(\omega)$ of crystalline C_{60} from the polarizability by using the Lorentz local field factor defined in the previous section, Eq.(47). The real and imaginary parts of the calculated dielectric function are denoted by ϵ_1 and ϵ_2, respectively and shown in Fig. 23.

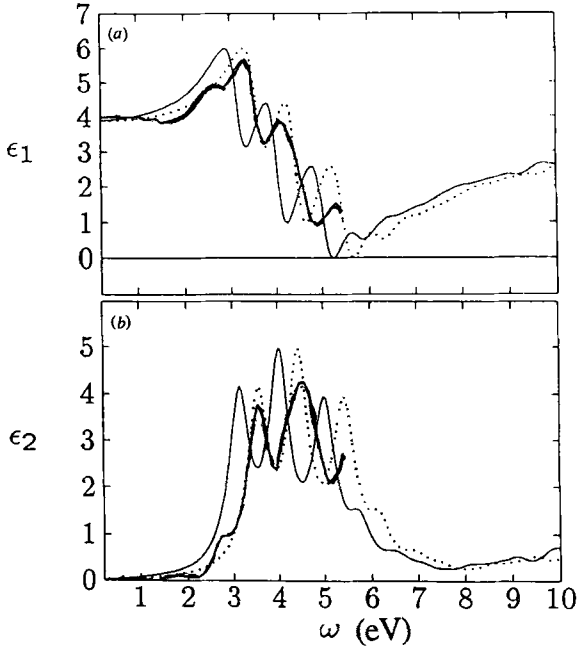

FIG. 23. A comparison between the experimentally determined dielectric function of Ren *et al.* (solid line) and the calculated function ($R = 9.3$ a.u. dotted line) using $\Gamma_{nm} = 0.3eV$ and with all transitions shifted +0.4 eV, see text. a) Real part, $\epsilon_1(\omega)$. b) Imaginary part, $\epsilon_2(\omega)$.

In these plots a linewidth of Γ =0.14eV is used to resolve details of the calculation. The effective screening corresponds to $R = 9.3$ a.u. which means that $\epsilon(0) = 3.8$. The imaginary part of ϵ shows pronounced peaks at 3.3, 4.2, 5.1 and 5.9 eV . The first weak transition at 2.85 eV corresponds to the strongly screened transition at 2.80 eV. Fig. 23 shows a comparison of our calculated spectrum with the Lorentz oscillator fit used by Ren *et al.* [101] used to present their ellipsometric data. Except for a shift of about 0.4 eV there is a good agreement between the experimental data and our calculated spectrum. In order to visualize this agreement, we have introduced an energy shift of 0.4 eV as shown in the figure. Excitation energy spectra have also been determined by Sohmen *et al.* [104] in the energy range $0 - 40eV$, using EELS spectroscopy on films of C_{60}. An overall agreement with the EELS experiments of Sohmen *et al.* has been found.

V. CONCLUSIONS

Twenty to thirty years ago comparatively few people worked with electronic structure calculations based on the DV-Xα method. Most of the calculations for molecules were based on HF and CI methods or the MS-Xα method, which for a certain period was a very promising approach to evaluate the electronic structure for big molecular systems and molecules modeling a solid or a surface. The situation is however quite different today mainly due to the development of accurate methods to treat molecular potentials of arbitrary shape and the access to accurate exchange and correlation potentials. Today people who in earlier time have been totally devoted to HF, MCHF, and CI methods have in recent years started to use density functional methods. Another important fact has been the power of simple models as the jellium model, which has been very successful in the analysis of properties of alkali and coinage metal clusters. We have recently in our group [176] used the jellium model and adopted a numerically stable technique, introduced by Salomonson and Öster [177] in atomic calculations, to evaluate the complete spectrum of occupied and unoccupied eigenstates of systems with cylindrical symmetry as nanotubes and nanowires. The calculations give a similar type of quantization which is known for mesoscopic systems as quantum dots. Another important reason for the possibilites of electronic structure calculations for different molecules and materials has been the development of powerful computers. One of my graduate students, Henrik Grönbeck summarized that in the conclusion of his thesis [62] by the following sentences, *From the computational point of view, the last decade has involved tremendous achievements. Some of them are thanks to the rapid development of computers. The workstation I am working at has been replaced three times during my five years as a graduate student,*

becoming increasingly faster. Parallel computer facilities is another example of the possibility to perform very extensive computations. This is quite different compared with the situation twenty to thirty years ago when one had to work with cards and rewrite the program in overlay structure for big calculations. Another also important factor is the possibilites for quick representations of the results in plots and three dimensional pictures which can be in colour and rotated to arbitrarily angles. However, the calculations done with the DV- Xα method today would not have been possible without the pioneering work on numerical integration methods done by Ellis in 1968. This is unfortunately forgotten in developments of new methods.

VI. ACKNOWLEDGMENTS

The author wants to in particular thank Professor Don Ellis for introducing me to molecular calculations more then 20 years ago and the very good collaboration we have had since that time. Special thanks should also be given to Professor Hirohiko Adachi for nice collaboration and the possibilities to visit him and Japan to see the spread and the impact of electronic structure calculations at Japanese universities and industries. My present research on electronic structure calculations have benefitted from contributions of earlier and present graduate students. Special thanks should be given Bo Wästberg, Erik Westin, Henrik Grönbeck and Daniel Östling. I will in particular thank Henrik Grönbeck and Daniel Östling for valuable comments and help with figures and equations in this article. Financial support for the cluster research is acknowledged from NUTEK, The National Swedish Board for Industrial and Technical Development, and NFR, The Swedish Natural Science Research Council Materials Science Consortium, "Clusters and Ultrafine Particles".

VII. REFERENCES

[1] J. C. Slater, Advan. Quantum Chem. **6**, 1 (1972).
[2] J. C. Slater, Phys. Rev. **81**, 385 (1951).
[3] J. C. Slater, Phys. Rev. **82**, 538 (1951).
[4] J. C. Slater, *The Self-consistent Field for Molecules and Solids; Quantum Theory of Molecules and Solids*, Vol. 4., McGraw-Hill, New York (1974).
[5] F. Herman and S. Skillman, *Atomic Structure Calculations*, Prentice-Hall, Englewood Cliffs, N.J. (1963).

[6] K. H. Johnson, Advan. Quantum Chem. **7**, 143 (1973).
[7] K. H. Johnson, J. Chem. Phys. **45**, 3085 (1966).
[8] J. C. Slater and K. H. Johnsson, Phys. Rev. **B5**, 844 (1972).
[9] *Amsterdam Density Functional, ADF relase 2.1*, Theoretical Chemistry, Vrije Universiteit, Amsterdam, E. J. Baerends *et al.*, Chem. Phys. **2**, 41 (1973); G. Te Velde and E. J. Baerends, J. Comp. Phys. **99**, 84 (1992); C. Fonesca Guerra *et al.* METECC-95, 305 (1995).
[10] *DMol* is a registered software product of Molecular Simulations Inc. San Diego. The computational method is described by B. Delley, J. Chem. Phys. **92**, 508 (1990).
[11] *DMon* is described by A. St-Amant and D. R Salahub, Chem. Phys. Lett., **169**, 387 (1990). A. St-Amant, These de doctorat, Université de Montreal, 1992.
[12] *Gaussian* Gaussian 94, Version B.3, M. J. Frisch, *et al.*, and J. A. Pople, Gaussian Inc., Pittsburgh PA, 1995.
[13] A. Rosén and I. Lindgren, Phys. Rev. **176**, 114 (1968).
[14] A. Rosén , *A Study on Atomic and Nuclear Structure by means of Experimental and Theoretical Investigations of Atomic Hyperfine Interactions*, Abstract of Gothenburg Dissertations in Science 35, Acta Universitatis Gothoburgensis 1973.
[15] I. Lindgren and A. Rosén, Case Studies in Atomic Physics **4**, 93 (1974).
[16] A. Rosén, D.E. Ellis, H. Adachi and F.W. Averill, J. Chem. Phys. **65**, 3629 (1976).
[17] A. Rosén and D.E. Ellis, Chem. Phys. Lett. **27**, 595 (1974).
[18] A. Rosén and D.E. Ellis, J. Chem. Phys. **62**, 6069 (1975).
[19] P. Hohenberg and W. Kohn, Phys. Rev. **136**, 864 (1964).
[20] W. Kohn and L.J. Sham, Phys. Rev. **140**, A1133 (1965).
[21] R. Gaspar, Acta. Phys. Acad. Sci. Hung. **3**, 263 (1954).
[22] D.E. Ellis, Int. J. Quantum. Chem. **IIS**, 35 (1968).
[23] G. S. Painter and D.E. Ellis, Int. J. Quantum. Chem. **IIIS**, 801 (1970).
[24] D.E. Ellis and G. S. Painter, Phys. Rev. **B2**, 2887 (1970).
[25] The Society of DV- Xα, H. Adachi, Dept of Materials Science and Engineering, Kyoto University Yoshidahonmachi, Sakyo-ku, Kyoto 606-01, Japan.
[26] F. Herman, J. P. Van Dyke and I. B. Ortenburger, Phys. Rev. Lett. **22**, 807 (1969).
[27] I. Lindgren, Phys. Lett. **19**, 382 (1965).
[28] I. Lindgren, Arkiv Fysik **39**, 59 (1966).
[29] D. Liberman, J. T. Waber and D. T. Cromer, Phys. Rev. **137**, A27 (1965).
[30] There are various reviews which demonstrate the strength (and weakness) of the DFT, for example, R. O. Jones, O. Gunnarsson, Rev. Mod. Phys. **61**, 689 (1989). W. Kohn, A.D. Becke and R.G. Parr, J. Phys. Chem. **100**, 12974 (1996). Several books have also been published on these matters, for example:

R.G. Parr,W. Yang, *Density-Functional Theory of Atoms and Molecules* Oxford University Press (1989). R.M. Dreizler,E.K.U. Gross, *Density-Functional Theory An Approach to the Quantum Many Body Problem* Springer-Verlag 1990.

[31] M. Born and R. Oppenheimer, Ann. Physik **87**, 457 (1929).

[32] H. F. Schaefer III, *The Electronic Structure of Atoms and Molecules; A Survey of Rigorous Quantum Mechanics Results*, Addison-Wesley Publ. Comp. 1972.

[33] *Density Functional Methods in Chemistry*, J. K. Labanowski, J. C. Andzelm Eds.Springer-Verlag, New York, Berlin, 1991.

[34] V. Bonačić-Koutecký, P. Fantucci and J. Koutecký, Chem Rev. **91**, 1035 (1991).

[35] See for instance, D. Pines, *The Many-Body Problem*, Benjamin Inc., New York 1961; M. Gell-Mann and K. A. Brueckner, Phys. Rev., **106**, 364 (1957). R.G. Parr, W. Yang, *Density-Functional Theory of Atoms and Molecules* Oxford University Press (1989).

[36] K. Schwarz, Phys. Rev. B **5**, 2466 (1972).

[37] L. Hedin and B. I. Lundqvist, J. Phys. **C4**, 2064 (1971)

[38] U. von Barth and L. Hedin, J. Phys. **C5**, 1629 (1972)

[39] O. Gunnarsson, and B.I. Lundqvist Phys. Rev B **13**, 4274 (1976).

[40] J. P. Perdew and A. Zunger, Phys. Rev B **23**, 5048 (1981).

[41] S.H. Vosko, L. Wilk and M. Nusair, Can. J. Phys. **58**, 1200 (1980).

[42] D. M. Ceperly and B. J. Adler, Phys. Rev. Lett. **45**, 566 (1980).

[43] R. Latter, Phys. Rev. **99**, 510 (1955).

[44] W. Kohn, A.D. Becke and R.G. Parr, J. Phys. Chem. **100**, 12974 (1996).

[45] A.D. Becke, Phys. Rev. A **38**, 3098, (1988);

[46] J.P. Perdew, Phys. Rev. B **33**, 8822, (1986).

[47] J.P. Perdew, Phys. Rev. B **436**, 6671, (1992).

[48] C. Lee, W. Yang and R.G. Parr, Phys. Rev. B **37** 785, (1988).

[49] A.D. Becke, J. Chem. Phys. **98**, 5648 (1993).

[50] B. Hammer, K.W. Jacobsen and J.K. Nørskov, Phys. Rev. Lett. **70**, 3971 (1993).

[51] T. Koopmans, Physica, **1**, 104 (1933).

[52] R. Car and M. Parrinello, Phys. Rev. Lett. **55**, 2471 (1985).

[53] M. C. Payne *et al.*, Rev. Mod. Phys. **64**, 1045 (1992).

[54] G. Galli, M. Parrinello, *Computer Simulations in Materials Science*, M. Meyer, V. Pontikis, (Eds.) Kluwer 1991.

[55] Review papers on the Car-Parrinello, and related *ab initio* molecular dynamics methods are: M.E. Tuckerman, P.J. Ungar, T v. Rosenvinge and M.L Klein, J. Phys. Chem. **100**, 12878 (1996); M.C. Payne, M.P. Teter, D.C. Allan, T.A. Arias and J.D. Joannopoulos, Rev. Mod. Phys. **64**, 1045 (1992).

[56] P. Ballone, W. Andreoni, R. Car and M. Parrinello, Phys. Rev. Lett. **60**,

271 (1988); W. Andreoni and G. Pastore, Phys. Rev. B **41**, 10243 (1990); U. Röthlisberger, W. Andreoni and M. Parrinello, Phys. Rev. Lett. **72** 665 (1994).
[57] U. Röthlisberger and W. Andreoni, J. Chem. Phys. **94**, 8129 (1991).
[58] U. Röthlisberger, W. Andreoni and P. Giannozzi, J. Chem. Phys. **96**, 1248 (1992).
[59] W. Andreoni, Phys. Rev. B **45**, 4203 (1992); W. Andreoni, Z. Phys. D **19**, 31 (1991).
[60] W. Andreoni, F. Gygi and M. Parrinello, Phys. Rev. Lett. **68**, 823 (1992); W. Andreoni, F. Gygi and M. Parrinello Chem. Phys. Lett. **190** 159 (1992); K. Laasonen, W. Andreoni and M. Parrinello, Science **258** 1916 (1992); W. Andreoni and A. Curioni, Phys. Rev. Lett. **77**, 834 (1996).
[61] R. Car, M. Parrinello and W. Andreoni, *Fundamental Approach to New Materials Phases: Microclusters*, S. Sugano, Y. Nishina and S. Ohnishi (eds.), Springer, Berlin, 1987,
[62] H. Grönbeck, *On the structure of and bonding in metal clusters* PhD Thesis, Göteborg University 1996.
[63] H. Grönbeck, A. Rosén and W. Andreoni, Z. Phys. D , (1997).
[64] M. Brack, Rev. Mod. Phys. **65**, 677 (1993).
[65] W. A. de Heer, Rev. Mod. Phys. **65**, 611 (1993).
[66] W.A. de Heer, W. A. Knight, M. Y. Chou, and M. L. Cohen, Eds. H. Ehrenreich and D. Turnbull, *Solid State Physics*, Academic Press , New York Vol. 40, p 93 1987.
[67] W. Ekardt, Phys. Rev. B **29**, 1558 (1984).
[68] D. E. Beck, Solid. State. Commun. **49**, 381 (1984).
[69] W Knight, K. Clemenger, W. A. de Heer, W. Saunders, M. Chou and M. Cohen, Phys. Rev. Lett. **52**, 2141 (1984).
[70] M. Andersson, *Metal Cluster Reactivity: Adsorption of small molecules in bimolecular collisions*, Thesis Chalmers University of Technology, Göteborg, 1995.
[71] M. Andersson, J. L. Persson and A. Rosén, J. Phys. Chem. **100**, 1222 (1996).
[72] H. Grönbeck and A. Rosén, Chem. Phys. Lett. **227** , 149 (1994).
[73] H. Grönbeck and A. Rosén, Surf. Rev. Lett. **3** , 687 (1996).
[74] H. Grönbeck and A. Rosén, Comp. Mater. Science. **2** , 607 (1994).
[75] J. W. D. Connolly and J. R. Sabin, J. Chem. Phys. **56**, 5529 (1972).
[76] J. C. Slater and J. W. D. Connolly, Int. J. Quant. Chem. **10S**, 141 (1976).
[77] E.J. Baerends, D.E. Ellis and P. Ros, Chem. Phys. **2**, 41 (1973).
[78] F. W. Averill and D. E. Ellis, J. Chem. Phys. **59**, 6412 (1973).
[79] A.H. Stroud, *Approximate Calculation of Multiple Integrals*, Prentice Hall, 1971.
[80] P.M. Boerrigter, G. Te Velde and E.J. Baerends, Int. J. Quant. Chem. **33**, 37 (1988).

[81] R.S. Mulliken, J. Chem. Phys. **23**, 1833 (1955).
[82] B. Delley and D.E. Ellis, J. Chem. Phys. **76**, 1949 (1982).
[83] A. D. Becke, J. Chem. Phys. **88**, 2547 (1988).
[84] B. Delley, J. Chem. Phys. **92**, 508 (1990).
[85] E. Matthias, H. B. Nielsen, J. Reif, A. Rosén and E. Westin, J. Vac. Sci. Technol. **B 5**,1415 (1987).
[86] A. Rosén, E. Westin, E. Matthias, H. B. Nielsen and J. Reif, Physica Scripta **T23**, 184 (1988).
[87] E. Westin, A. Rosén and E. Matthias, in *Desorption Induced by Electronic Transitions, DIET IV*, Springer Series in Surface Science, Vol. 19.
[88] E. Westin, *Calculations of Linear and Nonlinear Optical Properties of Ionic Crystal Surfaces and Fullerenes* Thesis Chalmers University of Technology, Göteborg, 1995.
[89] J. Guo and D. E. Ellis and D. J. Lam, Chem. Phys. Lett. **184**, 418 (1991).
[90] J. Guo and D. E. Ellis and D. J. Lam, Phys. Rev. **B 45**, 13 647 (1992).
[91] J. Guo and D. E. Ellis and D. J. Lam, Phys. Rev. **B 45**, 3204 (1992)
[92] G. D. Mahan and K. R. Subbaswamy, *Local Density Theory of Polarizability*, Plenum Press, New York 1990.
[93] C. J. F. Böttcher, *Theory of electric polarisation*, Elsevier, Amsterdam 1952.
[94] R.W. Boyd, *Nonlinear Optics*, Academic Press, Inc, San Diego 1993.
[95] G. D. Mahan, *Many Particle Physics*, Plenum, New York 1981.
[96] G.F. Bertsch, A. Bulgac, D. Tománek and Y. Wang, Phys. Rev. Lett. **67**, 2690 (1991).
[97] E. Westin, A. Rosén, G Te Velde and E. J.Baerends, J. Phys. **B29**, 5087 (1996).
[98] A. Zangwill and P. Soven, Phys. Rev. A **21**, 1561 (1980).
[99] A. Zangwill, J. Chem. Phys. **78**, 5926 (1983).
[100] S. Leach *et al.* Chem. Phys. **160**, 451 (1992).
[101] S. L. Ren *et al.* Appl. Phys. Lett. **59**, 2678 (1991).
[102] G. Gensterblum, Li-Ming Yu, J.J. Pireaux, P.A. Thiry, R. Caudano, Ph. Lambin, A.A. Lucas, W. Krätschmer and J.E. Fischer, J. Phys. Chem. Solids. **53**, 1427 (1992).
[103] U. Fano, Rev. Mod. Phys. **64**, 313 (1992).
[104] E. Sohmen, J. Fink and W. Krätschmer, Z. Phys. B **86**, 87 (1992).
[105] L. Pauling, *The Nature of the the Chemical Bond* , 3rd Ed., Cornell University Press, Ithaca, N. Y. 1960.
[106] V. Pershina, W.-D Sepp, B. Fricke and A. Rosén, J. Chem. Phys. **96**, 8367 (1992).
[107] N. W. Ashcroft, N. D. Mermin, *Solid State Physics*, Saunders College, CBS Publ. Asia Ltd. Philadelphia 1976.
[108] ISSPIC 1, J. Phys. **38**, (1977); ISSPIC 2, Surf. Sci. **106**, (1981); ISSPIC 3, Surf. Sci. **156**, (1981); ISSPIC 4, Z. Phys. D **12**, (1989); ISSPIC 5, Z. Phys. D

19, (1991); ISSPIC 6, Z. Phys. D **26**, (1993); ISSPIC 7, Surf. Rev. and Lett. **3**, (1996); ISSPIC 8, Z. Phys. D , (1997)
[109] J. Jortner, Z. Phys. D **24**, 247 (1992).
[110] *Clusters of Atoms and Molecules I and II*, Ed. H. Haberland, Springer Chemical Series in Chemical Physics 52 and 56 1994
[111] A. W. Castleman, Jr. and K. Bowen, J. Phys. Chem. **100**, 12911 (1996).
[112] R. W. Siegel, Physics Today. **Oct 93**, 64 (1993).
[113] R. W. Siegel, Nanostr. Mater. **4**, 121 (1994).
[114] T. P. Martin, Physics Reports. **273**, 199 (1996).
[115] R. E. Smalley, Laser Chem. **2**, 167 (1983). T. G. Dietz, M. A. Duncan, D. E. Powers and R. E. Smalley, J. Chem. Phys. **74**, 6511 (1981). J. B. Hopkins, P. R. R. Landgridge-Smith, M. D. Morse and R. E. Smalley, J. Chem. Phys. **78**, 1267 (1984).
[116] V. E. Bondybey and J. H. English, J. Chem. Phys. **76**, 2165 (1982).
[117] O. Echt, K. Sattler and E. Recknagel, Phys. Rev. Lett. **47**, 1121 (1981).
[118] *Nanostructures and Mesoscopic Systems*, Eds. W. P. Kirk, and M. A. Reed, Academic Press, San Diego, 1992.
[119] H.W. Kroto, J.R. Heath, S.C. O'Brien, R.F. Curl and R.E. Smalley, Nature **318**, 162 (1985).
[120] S. Ijima, Nature **354**, 56 (1991).
[121] D. Ugarte, Nature **359**, 707 (1992).
[122] B. C. Guo, K. P. Kerns and A. W. Castleman, Jr., Science **255**, 1411 (1992).
[123] B. Wästberg, *Calculations of electronic properties of metal clusters, fullerenes and molecules on Surfaces*, PhD Thesis, Chalmers University of Technology 1991
[124] D. Östling, *Electronic Strucuture and Optical Properties of C_{60} Nanotubes and Carbon Onions*, PhD Thesis, Göteborg University 1996.
[125] H. Grönbeck and A. Rosén, Phys. Rev. **B54**, 1549 (1996).
[126] T.T. Rantala, B. Wästberg and A. Rosén, Chem. Phys. **109**, 261 (1986).
[127] E. Westin and A. Rosén, Int. J. Mod. Phys. **B6**, 3893 (1992).
[128] A. Rosén and B. Wästberg, J. Chem. Phys. **90**, 2525 (1989).
[129] A. Rosén and B. Wästberg, J. Am. Chem. Soc. **110**, 8701 (1989).
[130] B. Wästberg and A. Rosén, Physica Scripta 44, 276 (1991).
[131] A. Rosén and B. Wästberg, Surf. Sci. **269/270**, 1121 (1992).
[132] K. Schwarz and P. Weinberger, Chem. Phys. Lett. **27**, 415 (1974).
[133] K. P. Huber and G. Herzberg, *Molecular Spectra and Molecular Structure, Constans of Diatomic Molecules*, van Nostrand Reinhold Comp, New York 1979.
[134] O. Echt, O. Kandler, T. Leisner, W. Miehle, and E. Recknagel, Faraday Symposium No. 25 on Large gas phase Clusters, University of Warwick, December 12-14,1989

[135] J. Farges, M. F. De Feaudy, B. Raoult and G. Torchet, J. Chem. Phys. **84**, 3491 (1986).
[136] M. A. Nygren and P. Siegbahn, J. Chem. Phys. **96**, 7579 (1992).
[137] C. Massobrio, A. Pasquarello and R. Car, Chem. Phys. Lett. **238**, 215 (1995).
[138] C. Massobrio, A. Pasquarello and R. Car, Phys. Rev. Lett. **75**, 2104 (1995).
[139] M. Andersson, H. Grönbeck, L. Holmgren and A. Rosén, SPIE Proc. **2548**, 157 (1995).
[140] L. Holmgren, H. Grönbeck, M. Andersson and A. Rosén, Phys. Rev. B **53**, 16644 (1996).
[141] L. Holmgren, M. Andersson, J. L. Persson and A. Rosén, NanoStructured Materials **6**, 1009 (1995).
[142] D. A. Hales, L. Lian, and P. B. Armentrout, Int. J. Mass Spectrom. Ion Phys. **102**, 269 (1990).
[143] E. A. Rohlfing, D. M. Cox and A. Kaldor, Chem. Phys. Lett. **99**, 161 (1983); J. Phys. Chem. **88**, 4497 (1983).
[144] D.R. Huffman, Physics Today **Nov 91**, 22 (1991).
[145] W. Krätschmer, Z. Phys. **D19**, 405 (1991).
[146] D.R. Huffman and W. Krätschmer, Mater. Res. Soc. Symp. **206**, 601 (1991).
[147] S. Larsson, A. Volosov and A. Rosén Chem. Phys. Lett. **137**, 501 (1987).
[148] W. Krätschmer, K. Fostiropoulos and D.R. Huffman, Chem. Phys. Lett. **170**, 167 (1990).
[149] W. Krätschmer, L.D. Lamb, K. Fostiropoulos and D.R. Huffman, Nature **347**, 354 (1990).
[150] H. Palmer and M. Shelef, *Chemistry and Physics of Carbon* , Walker, J. R. , Jr., Ed. Marcel Dekker: New York, 1967, Vol. 4 pp 85-135.
[151] W. Weltner and R. J. Van Zee, Chem. Rev. **89**, 1713 (1990).
[152] H. Kroto, A. W. Allaf and S. P. Balm, C_{60}*: Buckminsterfullerene*, Chem. Rev. **91**, 1213 (1991).
[153] H. Kroto, C_{60}*: Buckminsterfullerene, The Celestical Sphere that Fell to Earth*, Angew. Chem. **31**, 111 (1992).
[154] *Special Issue on Fullerenes*, Ed. H. Kroto, Pergamon Press, New York 1992, Carbon **30**, 1139 (1992).
[155] *Clusters and Fullerenes*, Proc. Adriatico. Res. Conf. Eds. V. Kumar, T. P. Martin and E. Tosatti, World Scientific, Singapore 1992, Int. J. Mod. Phys. B **6**, (1992).
[156] *Fullerenes*, Ed. H. Kroto, MRS Bulletin, Nov **XIX**, No 11, (1994).
[157] A. Hirsch, *The Chemistry of the Fullerenes*, Georg Thieme Verlag 1994.
[158] *The Fullerenes*, Eds. H.W. Kroto, J.E. Fischer and D.E. Cox, Pergamon Press, Exeter, Great Britain 1993.
[159] *Physics and Chemistry of the Fullerenes*, Ed. K. Prassides, NATO ASI series, Kluwer Acad. Pub., Dordrecht, The Netherlands 1994.

[160] Eds. H. Ehrenreich and F. Spaepen, *Solid State Physics (Fullerenes)*, **48**, Academic Press, London 1994.
[161] M.S. Dresselhaus, G. Dresselhaus, and P.C. Eklund, *Science of Fullerenes and Carbon Nanotubes* Academic Press, San Diego, 1996.
[162] *The Chemical Physics of Fullerenes 10 (and 5) Years Later*, Ed. W. Andreoni, NATO ASI series, Kluwer Acad. Pub., Dordrecht, The Netherlands 1996.
[163] *Perfect Symmetry*, J. Baggott, Oxford University Press, Oxford 1996.
[164] T. W. Ebbesen, Physics Today **June**, (1996)
[165] T.P. Martin, U. Näher, H. Schaber and U. Zimmermann, *Phys. Rev. Lett.* **70**, 3079 (1993).
[166] T.P. Martin, N. Malinowski, U. Zimmermann, U. Näher and H. Schaber, *J. Chem. Phys.* **99**, 4210 (1993).
[167] U. Zimmermann, N. Malinowski, A. Burkhardt and T.P. Martin, *Carbon* **33**, 995 (1995).
[168] A. J. Freeman, L. Ye and B. Delley, Chem. Phys. Lett. **160**, 415 (1992).
[169] K. Hedberg, L. Hedberg, D. S. Bethune, C. A. Brown, H. C. Dorn, R. D. Johnson and M. de Vries, Science, **254**, 410 (1991).
[170] I. V. Hertel *et al.* Phys. Rev. Lett. **68**, 784 (1992).
[171] S. Yang *et al.* Chem. Phys. Lett. **139**, 233 (1987).
[172] M. A. Pederson and A. A. Quong, Phys. Rev. **B46**, 13584 (1992).
[173] D. Östling, P. Apell and A. Rosén Europhys. Lett. **21**, 539 (1993).
[174] P.W. Fowler, P. Lazzeretti and R. Zanasi, Chem. Phys. Lett. **165**, 79 (1990).
[175] A. W. Burose, T. Dresch and A. M. G. Ding, Z. Phys. D **26**, S294 (1993).
[176] D. Östling, D. Tománek and A. Rosén, Phys. Rev. B **55** , May (1997).
[177] S. Salomonson and P. Öster, Phys. Rev. A **40** , 5559 (1989).

Electronic State Calculation of Transition Metal Cluster

Hirohiko Adachi

Department of Materials Science and Engineering,
Kyoto University, Kyoto 606-01, Japan

abstract

The electronic states of transition metal elements have been studied by the use of discrete variational (DV) Xα cluster model calculation. It is found that the valence band of the element is constructed by superimposing a narrow *d* band with high density on rather broadly spread *s* and *p* bands. The covalent interaction between the *d* orbitals of the neighbouring atoms is very important in their valence electronic state. Thus the valence band structure strongly depends upon the short-range covalent bonding between the near neighobours. The effect of the size of the cluster model on the valence electronic state is investigated for some elements. It is confirmed that the band structure of the cluster approaches that of the bulk crystal when the cluster size increases. The dependence of the electronic state on the geometrical structure of the cluster is also examined and it is found that the change in the band structure with the different structure is caused by the difference of the nature of the covalent bonding between the neighbouring atoms. In order to study the fundamental properties of magnetism of the transition element, the spin-polarized calculation for simple clusters has been carried out. The mechanisms of the spin polarization and the magnetic interaction between the atomic spins in the cluster are explained by a spin-polarized molecular orbital description. The relativistic Dirac-Slater calculation

ADVANCES IN QUANTUM CHEMISTRY, VOLUME 29

0065-3276/97 $25.00

has been made within DV-Xα framework to examine the importance of the relativistic effects and it is indicated that the relativistic effects are very important in determining the valence electronic state for heavy elements like *5d* transition elements.

1. Introduction

Recent development of the computational technique for electronic state of materials enables us to calculate the accurate valence electronic structure of fairly large and complicated systems from the first principles. However, it is still very important to investigate the electronic state and chemical bonding of a simple and small cluster model of metal element, because the basic understanding of the essential properties of the metal elements is not sufficient. It is also very useful to investigate a small cluster model in understanding various kinds of properties and phenomena of more complicated metallic materials like alloys and intermetallic compounds, because the fundamental electronic state is reflected in their properties.

In the present work, we study the electronic state and chemical bonding of transition elements by the aid of the simple and small cluster model using discrete variational (DV) Xα method[1]. First we describe the computational method and the cluster model very shortly. Second the valence level structure of the small cluster model of Ni_6 and its chemical bonding are investigated showing the wave function of molecular orbital (MO) in somewhat details. Next we research the change of *d* band structure when the atomic number increases in the 3d transition series. We also investigate the change of the *d* band structure when the atomic number increases within the same group in the periodic table. In these argument, it can be suggested that the chemical bonding is very important to determine the *d* band structure of the transition metal elements. Further we study the effects of the cluster size and geometrical structure on the valence level structure.

The transition metal atom has a possibility to possess a magnetic moment in metallic material, then an investigation of the spin polarization of the cluster from a microscopic point of view is very important in understanding the magnetism of the metallic materials. We try to explain the spin polarization and the magnetic interactions of the cluster in terms of the molecular orbital. For the heavy element in the periodic table whose atomic number is beyond 50, it is mentioned that the relativistic effects become very important even in the valence electronic state. We perform the relativistic DV-Dirac-Slater calculation[2] in addition to the nonrelativistic DV-Xα calculation for the small clusters of the *3d*, *4d* and *5d* transition elements to clarify the importance of the relativistic effects on the valence state especially for the *5d* elements.

2. Computational method

We use the simple Xα potential[3] written by

$$V_{xc\uparrow}(\mathbf{r}) = -3\alpha\left\{\frac{3}{4\pi}\rho_{\uparrow}(\mathbf{r})\right\}^{1/3}$$

with the scaling parameter α of 0.7. The MO wave function is expressed by an LCAO as

$$\phi_\ell = \sum_i C_{i\ell}\chi_i$$

The numerical atomic orbital generated by solving the Schrödinger equation for "atom in molecule" is employed as a basis function χ_i of LCAO, which is renewed for each SCF iteration taking a modification of charge density into account[1]. The atomic orbitals up to *nd*, *(n+1)s* and *(n+1)p* are utilized for *nd* transition elements, where *n* is 3, 4 and 5. The MO energy and the wave function are obtained by solving the secular equation,

$$\mathbf{H}\,\mathbf{C} = \varepsilon\,\mathbf{S}\,\mathbf{C} \quad ,$$

where the matrix elements of **H** and **S** are evaluated by the DV numerical integration[4,5] as

$$H_{ij} = \sum_k \omega(\mathbf{r}_k)\chi_i(\mathbf{r}_k)\, H\, \chi_j(\mathbf{r}_k)$$

$$S_{ij} = \sum_k \omega(\mathbf{r}_k)\chi_i(\mathbf{r}_k)\, \chi_j(\mathbf{r}_k)$$

The simplified and convenient self-consistent-charge (SCC)[1,6] scheme is used to obtained an approximate SCF potential. By the use of Mulliken population analysis[7], we estimate the effective charge on each atom in the cluster from the orbital population and also estimate the strength of the covalent bonding between atoms from the overlap population.

3. Cluster Model

Figure 1 shows the small cluster models employed in the present work. These are the typical cluster models of metal taken from the crystal fcc and bcc lattices. The clusters (a)-(f) are taken from fcc lattice and those of (g)-(k) from bcc lattice. The cluster (f) and (k) are sometimes used for models of metal (001) surfaces of fcc and bcc crystals, respectively. For some purpose, we need lager cluster or that with a different structure to be used.

4. Electronic state and chemical bonding of octahedral M_6 clusters of transition elements

First we investigate the valence level structure and chemical bonding of transition metal M_6 clusters with O_h symmetry shown in Fig.1(a). The valence levels and their atomic orbital components of Ni_6 cluster, as

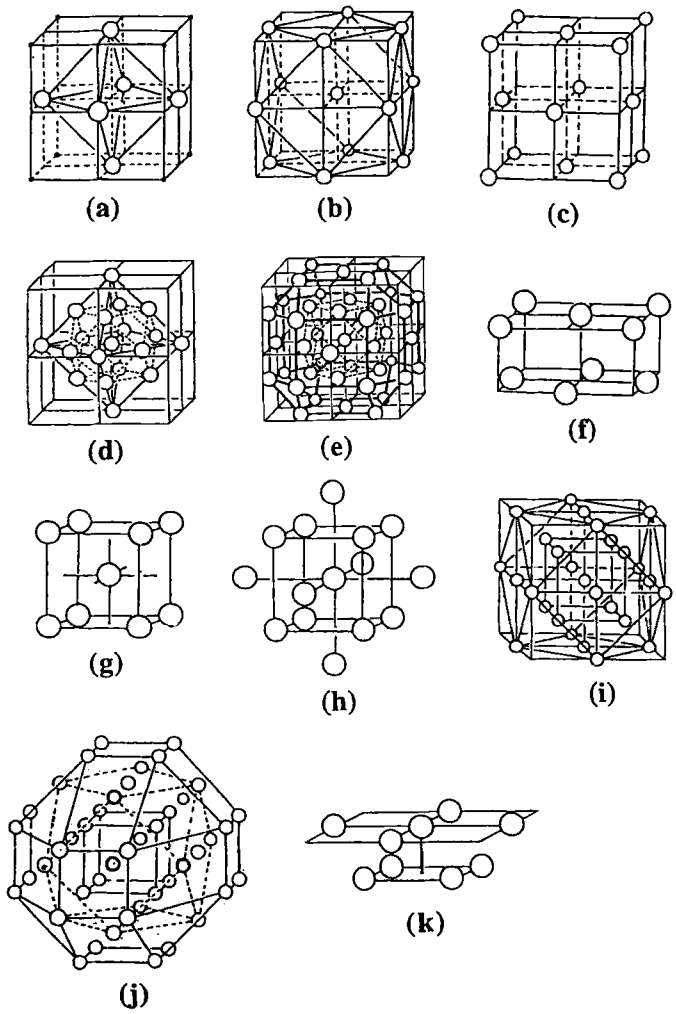

Fig.1 Model clusters of fcc and bcc metals

an example, are indicated in Fig.2. The valence band is constructed by overlapping of a narrow *3d* band with high density and rather widely spread *4s* and *4p* bands. It is convenient for visualization to represent the level structure as a density-of-states (DOS) diagram by substituting the discrete MO level by a distribution function like Gaussian given by

$$\exp\{-(\varepsilon-\varepsilon_\ell)/2\sigma^2\}/2\pi\sigma \quad ,$$

where ε_ℓ is the eigenvalue of the ℓ th MO. The density of states of Ni_6 cluster is illustrated in Fig.3, where 0.5 eV is used for the width parameter σ of each Gaussian. Next, we look into the details of the valence state examining the MO wave functions. Figure 4 shows the valence levels again, but with contour maps of the MO wave functions for the some typical levels. The low lying $7a_{1g}$ is of strongly π-type bonding between *d* orbitals of the nearest neighbours and also σ-type

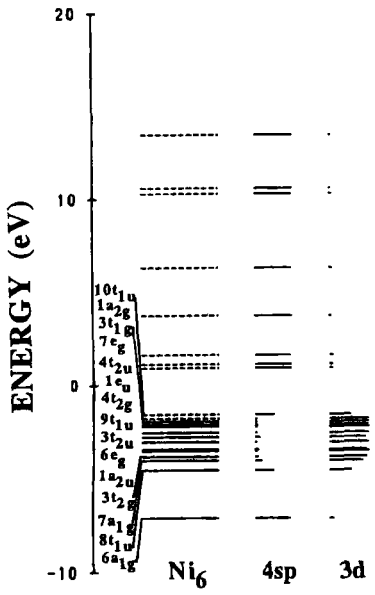

Fig.2 Valence levels and atomic components of Ni_6 cluster

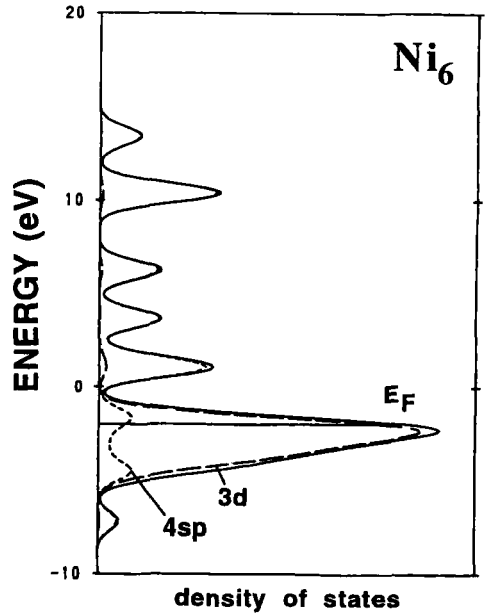

Fig.3 Density of states of Ni_6 cluster

bonding of the second nearest neighbours. The level $9t_{1u}$ which is situated at an intermediate energy is a mixture of bonding and antibonding nature, namely the interaction between the nearest neighbours is of bonding, while that between the second neighbours of rather strong antibonding. The upper lying $3t_{1g}$ is of typical antibonding both between the nearest and second nearest neighbours. This means that the valence level structure strongly depends upon the covalent

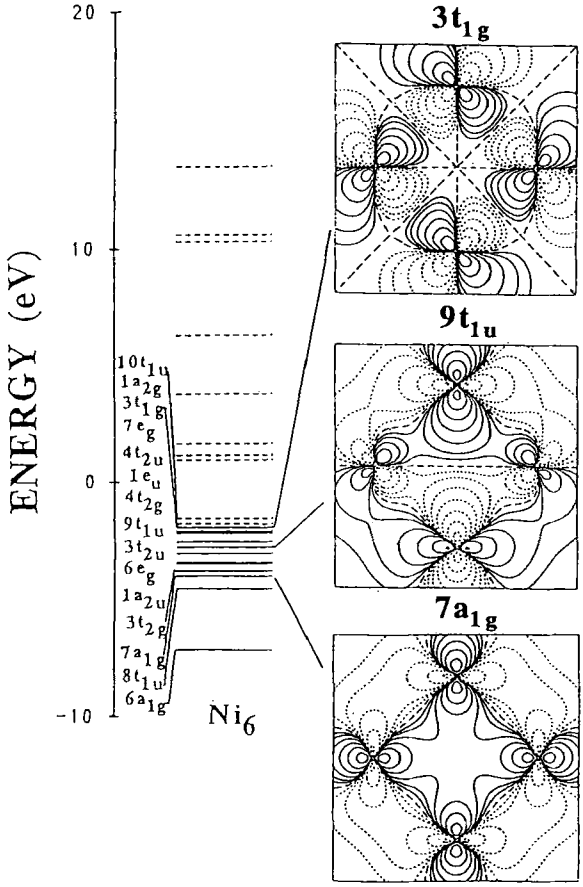

Fig.4 Valence levels and MO wave functions of Ni_6 cluster

interactions of *d* orbitals between the neighbouring atoms.

In the *3d* transition metal series, the electronic state gradually changes with the atomic number, though these elements possess similar properties. Because the valence electronic state of these elements essentially depends upon the nature of the *3d* atomic orbital, we depict the radial wave functions, namely the spatial distribution of the *3d* atomic orbitals of the elements from Sc to Zn in Fig.5. From the figure,

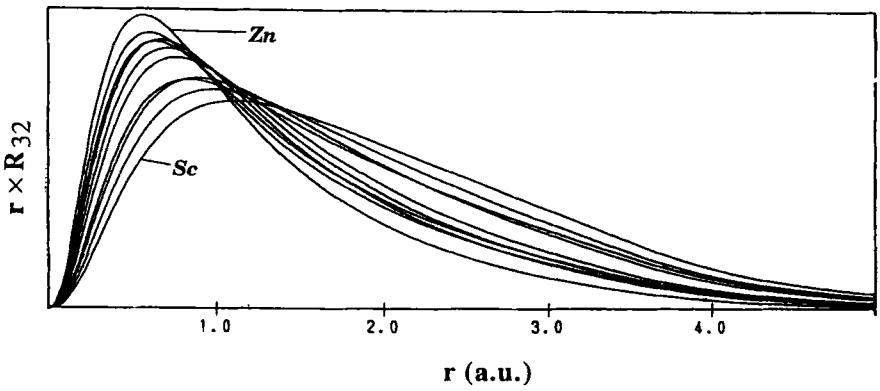

Fig.5 Radial wave functions for *3d* transition elements

the spatial extent and its change of the *3d* orbital are clearly seen. For the lightest element, Sc, the *3d* orbital extends its tail to considerably long distance. The stretch of the *d* orbital is reduced when the atomic number increases, and for Zn, the heaviest element in this series, the *d* orbital is relatively contracted as shown in this figure. The covalent interaction depends upon the orbital overlap between the neighbouring atoms, then the extension of the *3d* orbital is very important in determining the valence electronic structure of these elements. Then we investigate the change of DOS of M_6 clusters in the *3d* transition series and exhibit it in Fig.6. The energy scale is shifted so that the

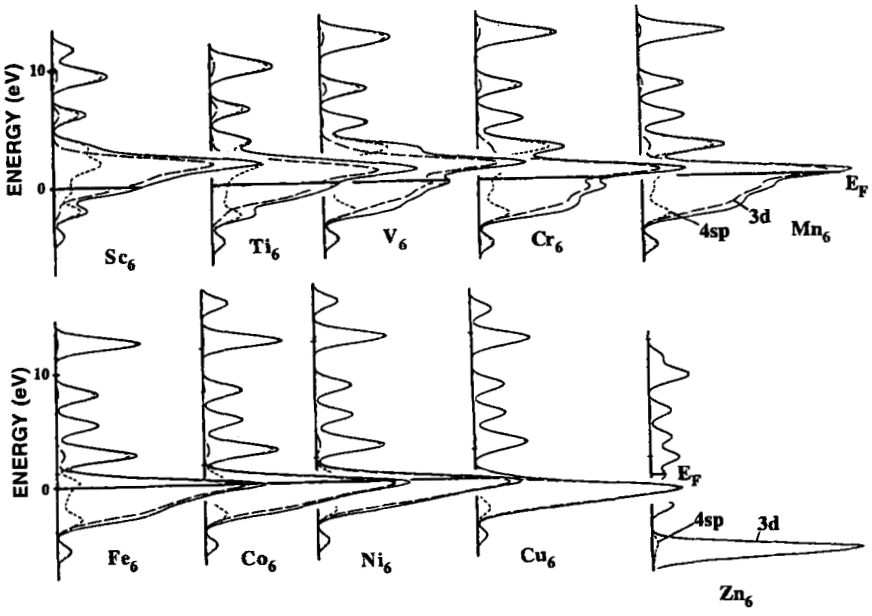

Fig.6 Density of states for M_6 clusters of *3d* transition metal elements

Fermi levels (E_F) are aligned. We note two points. One is that the relative position of the *d* band gradually lowers downward in energy. When coming to Cu, the *d* band almost sinks under E_F. This is due to n the increment of the occupation number of the *d* orbital with atomic number. The second is the change of width and shape of the *3d* band. In the early part of this series, namely from Sc to Cr or Mn, the *d* band is broadened and its structure becomes complicated when the atomic number increases, while in the later part the width of the *d* band is decreased and the shape gradually becomes simpler with atomic number. This is essentially caused by the change of covalent bonding between atoms in the cluster.

In the augment of Ni_6 cluster, we mentioned that the bonding interaction between atoms is very important to determine the valence

electronic structure. Then we look into the details of the covalent bonding of the clusters of the *3d* elements. Figure 7 shows the contour maps of the electronic charge density of Ti_6 cluster on a plane which contains four Ti atoms, and the difference density between the densities

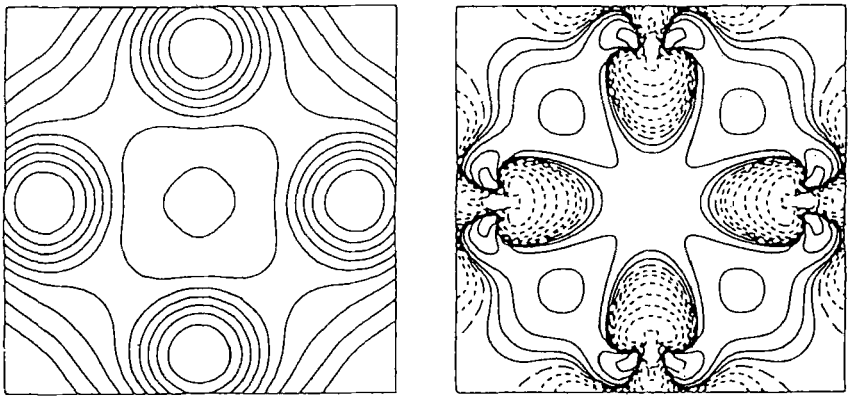

Fig.7 Contour maps of charge density ρ and difference density Δρ for Ti_6 cluster

of Ti_6 cluster and the summation for six Ti atoms. Thus the difference density represents the charge reconstruction when the cluster is formed. We can see the increments of the charge density in the areas between atoms. This is attributed to the covalent interactions between Ti atoms. For more quantitative discussion on this problem, we evaluate the overlap populations between atoms for each valence level, by the aid of Mulliken population analysis. The value of the bond overlap population for the level can be plotted at the corresponding level energy. A positive value of the bond overlap population indicates bonding interaction, while a negative value antibonding. The plot of the bond overlap population can be represented by a broadening with a Gaussian like DOS curve. Figure 8 exhibits an energy distribution of the bond

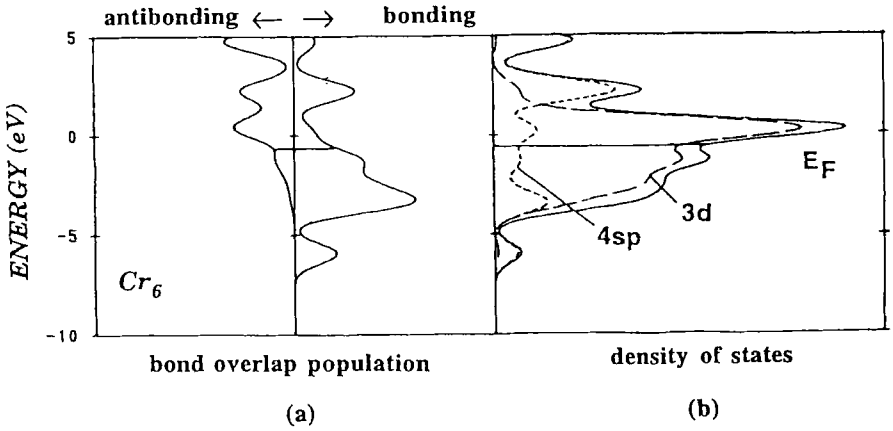

Fig.8 Energy distribution of bond overlap population (a) and DOS (b) of Cr_6 cluster

overlap population thus obtained for Cr_6 cluster as well as DOS. From this, it is found that the *d* band consists of bonding states at lower part of the band and of antibonding states at upper part. Thus the E_F of early elements like Sc and Ti is situated at lower parts of the band, namely the bonding states, while that of later elements at upper part, then the antibonding state. The strength of the covalent bonding of the cluster is estimated by the summation of the overlap populations up to E_F. Figure 9 plots the bond overlap population thus calculated. The value of the bond overlap population increases with atomic number until Cr, and then decreases. The bond overlap population is determined by two factors, one of which is orbital overlap between neighbouring atoms and the other is occupation number of the *d* electrons, and the value is something of multiplication of the two factors. In Fig.9, we plot the melting points[8] of these elements experimentally determined. A good correlation can be seen between the bond overlap population and the melting point of the elements. It is difficult to clarify this with a definite

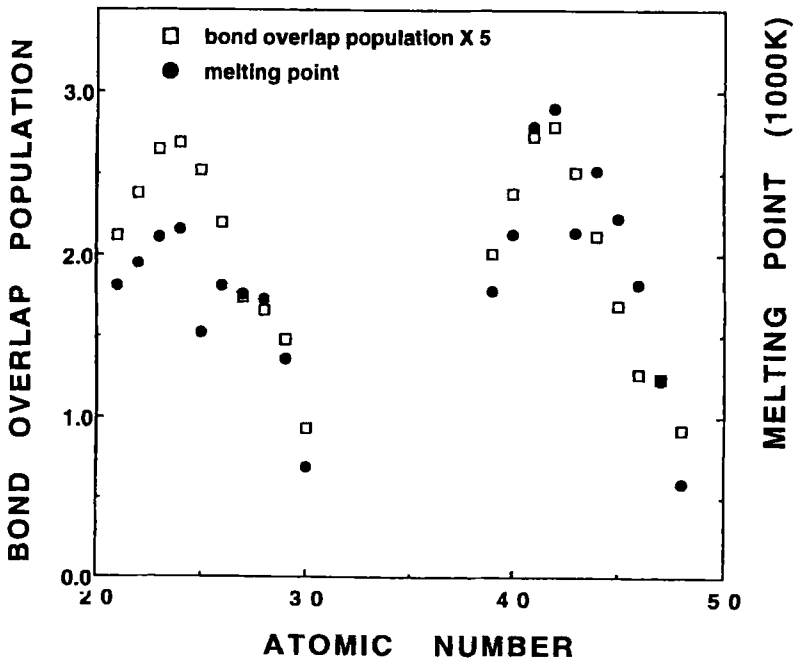

Fig.9 Plots of bond overlap populations of M_6 clusters and melting points of transition elements

interpretation, but it can be said that the covalent bonding is a very important factor in determining the melting points of these elements. For *4d* elements, we can find similar change and correlation as shown in the figure.

Usually the electronic properties of the elements in the same group in the periodic table are considered to be similar since they take an isoelectronic configuration. Then it is interesting to compare DOS of the *3d*, *4d* and *5d* elements in the same group. Figure 10 compares DOS of Ti, Zr and Hf clusters. The valence bands of these elements are similar to each other and the Fermi levels lie at similar positions of the bands. However, the *d* band is broadened and fine structures become

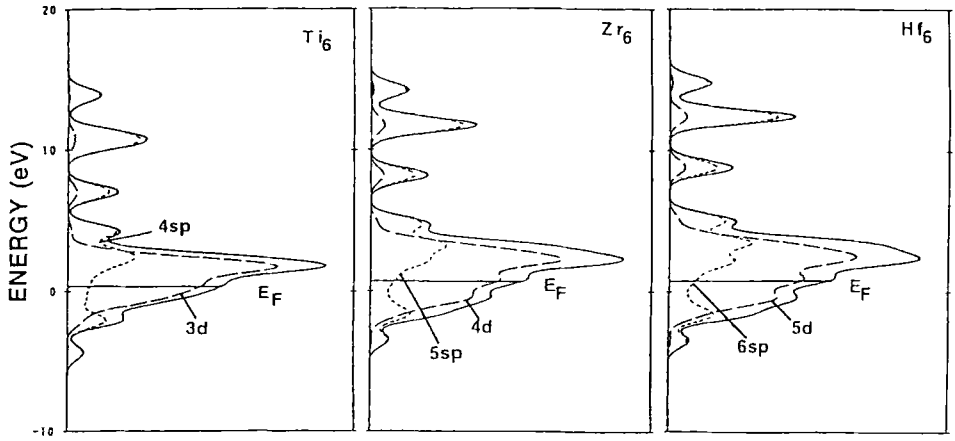

Fig.10 Comparison of density of states among Ti_6, Zr_6 and Hf_6 clusters

remarkable when the atomic number increases. Figure 11 displays the comparison among Cr, Mo and W. In this group the band width is large and the fine structures are clearly found even in Cr, but the *d* bands are split into three bands for Mo and W.

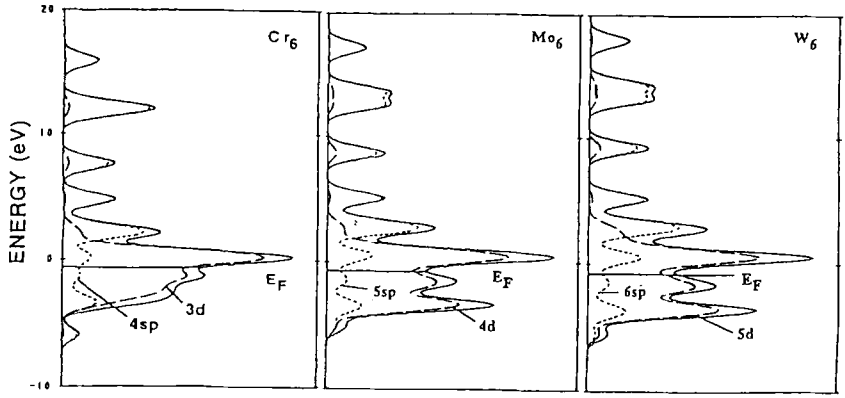

Fig.11 Comparison of density of states among Cr_6, Mo_6 and W_6 clusters

5. Effects of cluster size and geometrical structure on valence electronic state

Next we study the effects of the cluster size on DOS. When the cluster size is increased, the interactions between neighboring atoms with long distances are taken into account, then the electronic state approaches that of bulk. Figure 12 compares DOS of the clusters Ni_6, Ni_{13}, Ni_{19} and Ni_{43}, as well as bulk crystal[9] by a band structure calculation. Usually the band structure of the bulk crystal can be rather well reproduced if we take several ten atoms in the model cluster for transition elements, though the small cluster model provides somewhat narrower *d* band. In the case of the element with a *d* band which is almost completely occupied, for example the case of silver, the size effect is not very large, but a small cluster already well represents the band structure of bulk as shown in Fig.13.

Further investigation has been made for dependence of the valence electronic structure upon the geometrical structure. As an example, we take two model clusters, one of which is for fcc lattice and the other bcc. These clusters are shown in Fig.14; (a) is fcc cluster model M_{19} and (b) bcc cluster M_{15}. In order to compare the electronic states and to clarify the difference between fcc and bcc lattices, we take Fe metal as an example, and DOS curves are displayed in Fig.15. In this figure, (a) is the case of crystal and (b) of cluster. The solid line denotes DOS for fcc crystal and dotted line for bcc. These results for the crystals havebeen obtained by band structure calculations[10,11] by other authors. In the case of bcc, roughly speaking the *d* band is split into three bands, and the difference between two structures are clearly seen. If we use the cluster model to investigate the difference of the *d* band between the two lattice structures, we obtain the DOS for fcc and bcc clusters as shown in Fig.15(b). As is mentioned above, the width of the *d* band of these small clusters are somewhat narrower compared with that of bulk, but the essential characteristics of the band structure of the fcc and bcc

are satisfactorily reproduced by these small cluster models. We can compare the DOS of solid line for bulk fcc of figure (a) with the solid line of (b) and also dotted line of bcc of (a) with that of (b).

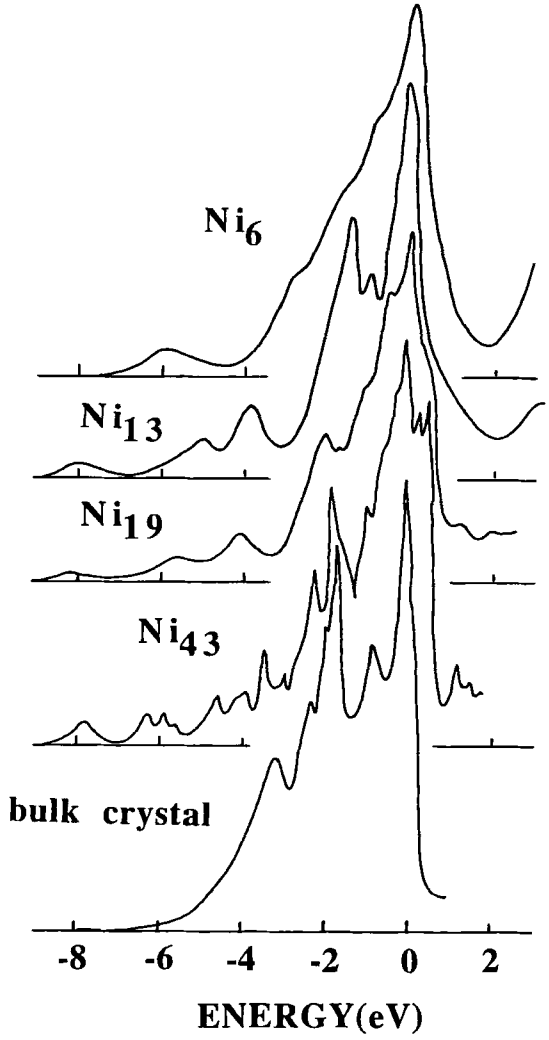

Fig.12 Density of states for various sizes of clusters and bulk crystal

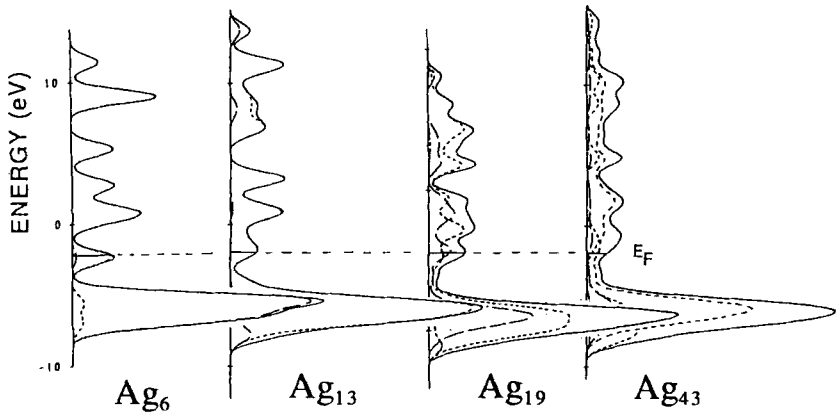

Fig.13 Density of states of silver clusters

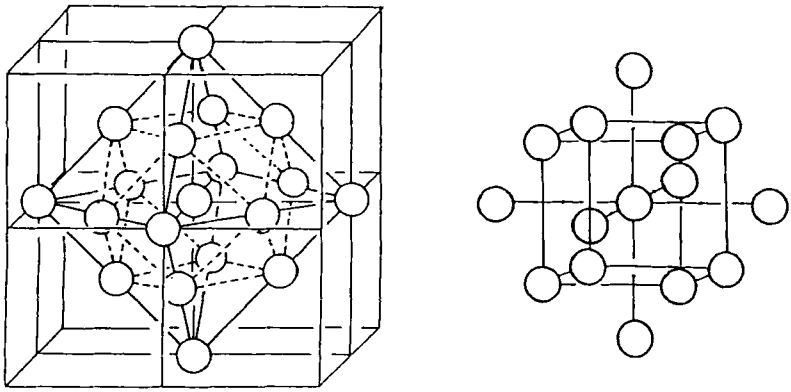

Fig.14 Cluster models for fcc (a) and bcc (b) structures

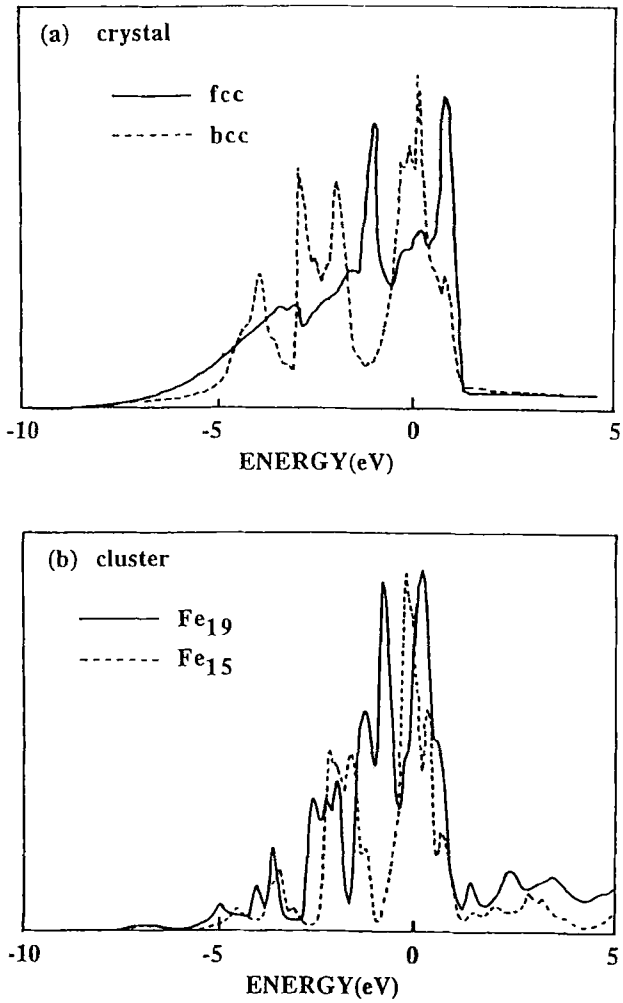

Fig.15 Comparison of density of states for fcc and bcc structures between crystal and cluster

Since the valence electronic state of a different lattice structure can be represented by a rather small cluster, we are able to study the origin of the band structure difference by the use of small cluster model. Figure 16 demonstrates the overlap integrals between Fe *3d* atomic

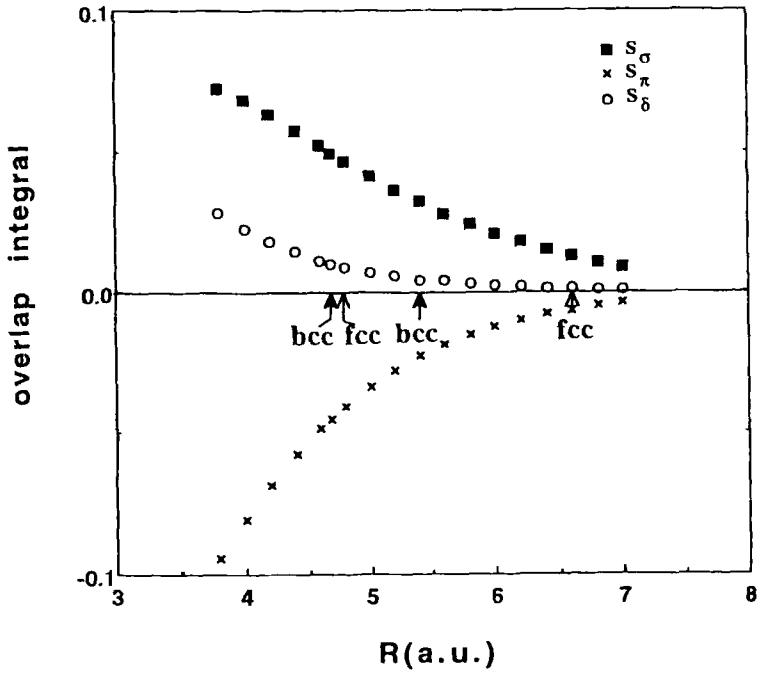

Fig.16 Overlap integrals between Fe *3d* orbitals versus Fe-Fe distance

orbitals of neighbouring atoms as a function of Fe-Fe distance. In the case of *d* orbital interactions, there are three types of interactions, namely σ, π and δ. The distances to the nearest and second nearest neighbors are pointed by arrows for bcc and fcc. In the bcc lattice, the second neighbor is rather closer than the fcc case, then the overlap integrals are still large so that the interactions are relatively strong, while the second neighbor in fcc lattice is far resulting in large reduction of the interactions. This is strongly reflected on the difference of the *d* band structures, which in turn is substantially determined by the difference of quite local structure. In order to look into the details, we again show the valence electronic structures of the fcc and bcc clusters

as the form of MO levels in Fig.17. For the bcc cluster, the valence band is split into three bands. In this case, the electronic states of the cluster can be distinguished by the character of the covalent interaction between atoms. This can be confirmed from the wave functions shown in Fig.18. The bonding states like $8e_g$ and $10t_{2g}$ are of bonding both with the nearest and second nearest neighbours and are situated at the

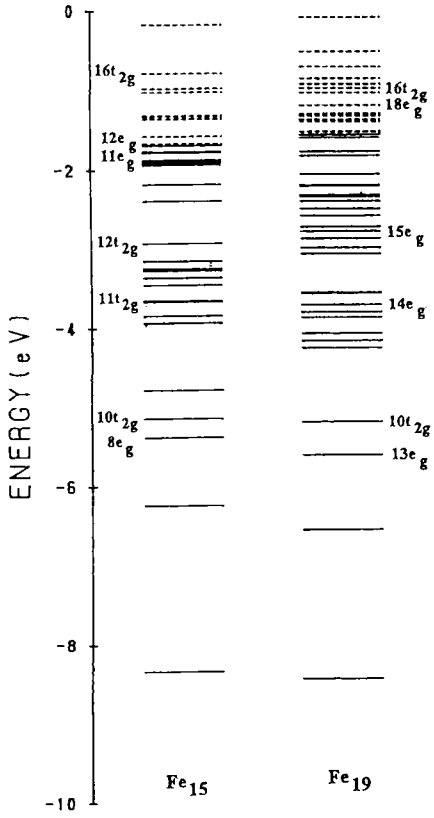

Fig.17 Valence level structures of bcc Fe_{15} and fcc Fe_{19} clusters

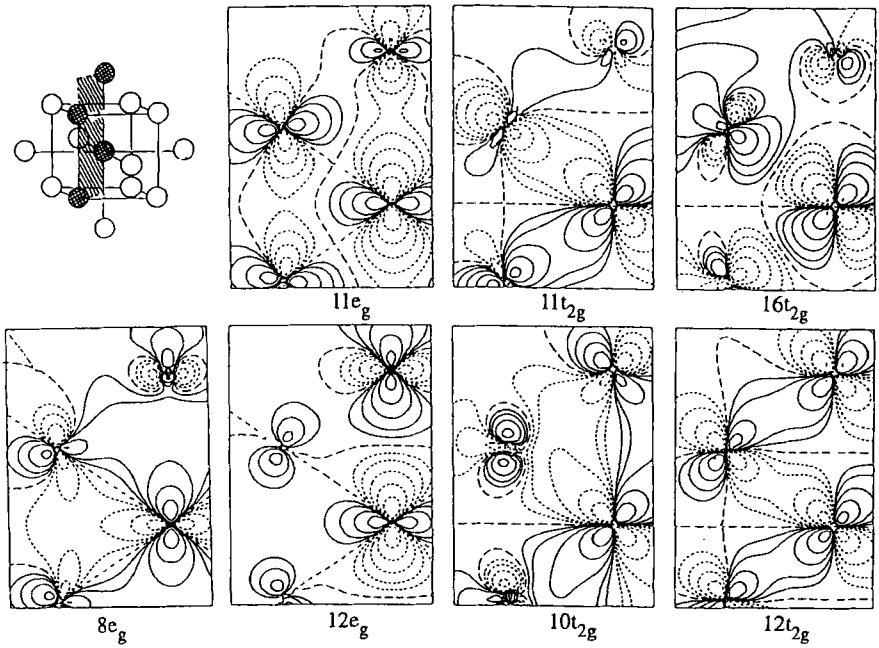

Fig.18 Contour maps of MO wave functions for Fe_{15} cluster

lowest energies. The states $11t_{2g}$ and $12t_{2g}$ located at intermediate energies are mixtures of bonding and antibonding, and those at higher energies, $11e_g$, $12e_g$ and $16t_{2g}$ are of strong antibonding nature. On the other hand, the bonding nature of the MO states for fcc cluster changes rather gradually. This difference is ascribed to that of the bonding interaction caused by the local structure difference between fcc and bcc.

6. Spin polarization and magnetic interaction

The magnetism of matter is one of the most basic but very important property in materials science. Transition elements have the *d* orbital which is partially occupied, then it is possible to possess magnetic moments. Thus the spin polarization in the valence electronic state takes place for the transition metal atom. The spin polarization brings about a modification of the electronic structure, because a level splitting of up and down spins occurs. The energy separation of this spin splitting is approximately proportional to the magnitude of spin polarization, namely the magnetic moment as shown in Fig.19. We make spin polarized DV-Xα calculations[12] for diatomic clusters of transition metals and obtain their level structures as shown in Fig.20. The cluster Sc_2 which is made of atoms A and B shows the

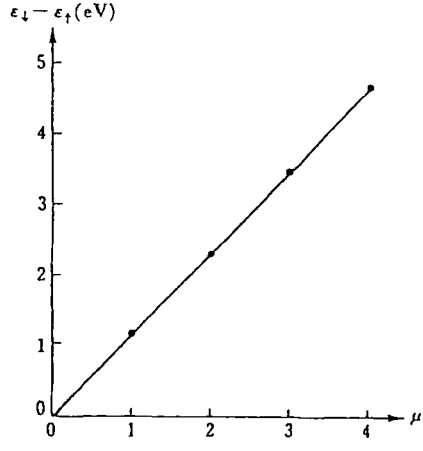

Fig.19 Level splitting Δε by spin density μ of *3d* orbital for Fe^{2+} ion
($\Delta\varepsilon=\varepsilon_\uparrow-\varepsilon_\downarrow$, $\mu=n_{3d\uparrow}-n_{3d\downarrow}$)

just mentioned can be explained by an analysis of the constitution of spin-polarized MO states. Figure 22 schematically illustrates the mechanism of spin-spin coupling between two atoms. First we consider

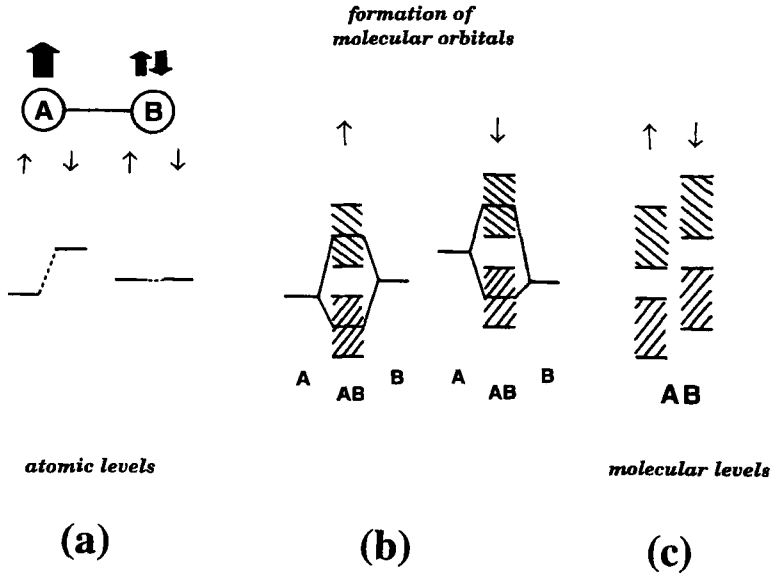

Fig.22 MO explanation for mechanism of spin-spin coupling between two atoms

spin-polarized atomic levels assuming the atom A is spin-polarized while B is free, namely not polarized (see figure(a)), then examine the spin state after the formation of molecular orbitals. The atomic orbital interacts with that of the same spin to form the MO, then the bonding and antibonding MO levels of up-spin are formed and similarly the MO levels of down-spin as well (see figure (b)). In the result, we obtain the MO level diagram of up and down spins as shown on the right (figure(c)). Next we consider what happens when the electrons are filling these MO states. For Sc, two *d* electrons from two atoms occupy only up-spin *d* levels, thus the cluster is polarized with up spin. For Ti, two more

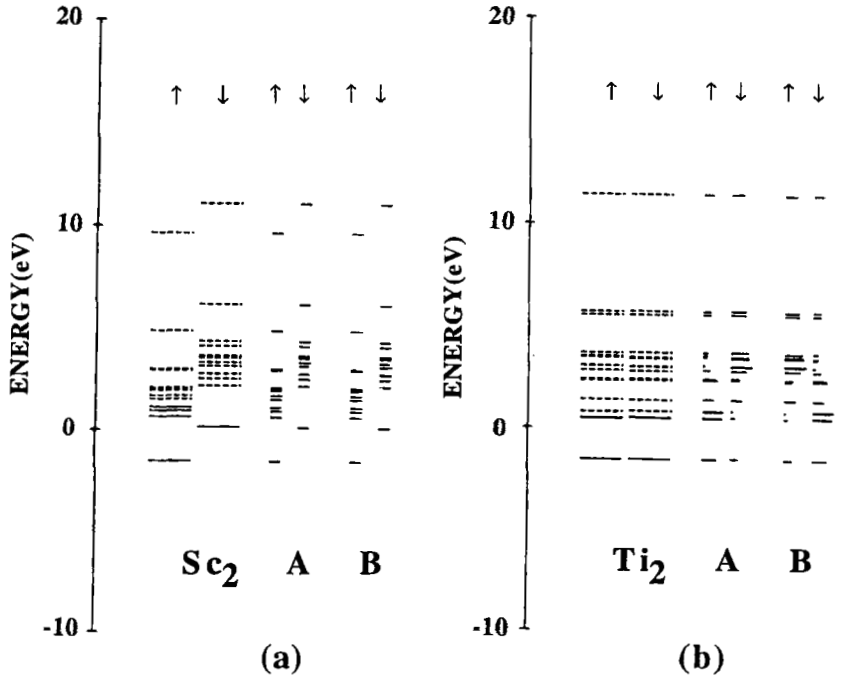

Fig.20 Valence level structures and spin polarization of Sc_2 and Ti_2 clusters

level structure where the spin-up and -down levels are split in energy and only some of the up-spin *d* levels are occupied, then the spin polarization takes place as shown in Fig.20(a). By Mulliken population analysis, it is found that the spin polarization for both of atoms A and B are the same, namely both are polarized with up spin. In this case, two Sc atoms are ferromagnetically coupled. On the other hand, the cluster Ti_2 shows a different feature as indicated in Fig.20(b). The up- and down-spin levels of each MO state have the same energy, thus it looks as if any spin polarization did not occur when we only look at the MO levels shown in the left column of Fig.20(b). However, it is found not to be the true if we examine the components of atoms A and B. The

atoms A and B are polarized in opposite spin direction, in other words, atom A has up-spin density and B down-spin. It can be said that A and B are antiferromagnetically coupled in this case. We make similar calculations for other elements in the *3d* transition series, and plot the magnitudes of the spin density of atoms A and B in Fig.21. It is found

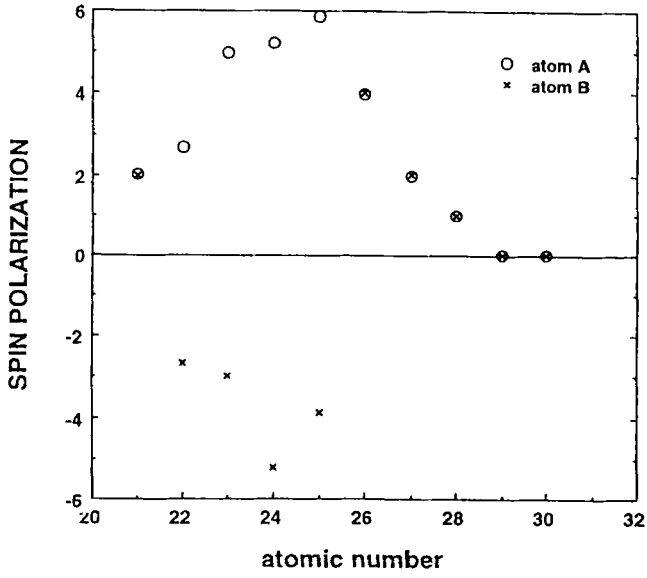

Fig.21 Spin density of atoms in M_2 clusters of *3d* elements

that A and B are coupled ferromagnetically for Sc_2 as mentioned above, while those are antiferromagnetically coupled for the elements from Ti to Mn. However the spins are arranged again in the same direction for later elements from Fe, though the magnetic moment is reduced with atomic number and vanishes beyond Cu.

It is very interesting and important to understand the origin of these magnetic interactions between atomic spins. The phenomena

electrons fill the down-spin levels as well as the up-spin levels already occupied. In this case, the wave function for up-spin leans and has higher amplitude on atom A. On the contrary, the down-spin wave function is partial towards atom B. By this reason, the atom A has up-spin and B down-spin resulting in an antiferromagnetic coupling. However for later elements with more than half-filled band, electrons occupy again up-spin levels of antibonding, where the orbital components of atom B is larger than that of A, contrary to the up-spin bonding levels, thus a ferromagnetic coupling is achieved. Further filling by electrons leads to reduction of spin density because the down-spin levels are also occupied so that the up-spin density cancels out. Next we try to calculate the spin polarization of M_6 clusters of the *3d* metals. Figure 23 shows the results of the calculations. From the result, it is found that the interactions between atomic spins are very

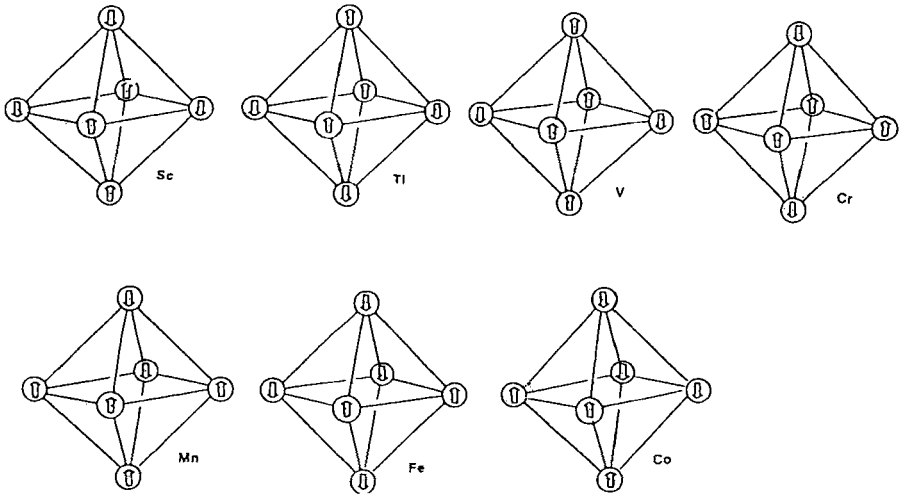

Fig.23 Spin polarization of each atom in M_6 clusters of *3d* elements

complicated. Both of ferromagnetic and antiferromagnetic interactions are mixed in very complicated manner. Figure 24 summarizes the magnitudes of the spin polarization of each atom in the M_6 clusters.

Further we examine how the spin polarization changes when the structure of cluster is different. We take up the small cluster Fe_6, but both for fcc and bcc. For fcc lattice, the Fe_6 cluster is the same as that used so far. Thus it has O_h symmetry, while the bcc cluster D_{4h} symmetry from a viewpoint of geometrical arrangement. There are two kinds of near neighbours with different distances in the bcc cluster. The distance from an atom on the horizontal Fe_4 plane to the top or bottom atom is somewhat shorter than that to the atom within the plane. The structural difference of two clusters is not very large. However we obtain considerably different result calculated for spin polarization. Figure 25 depicts the direction and magnitude of the spins

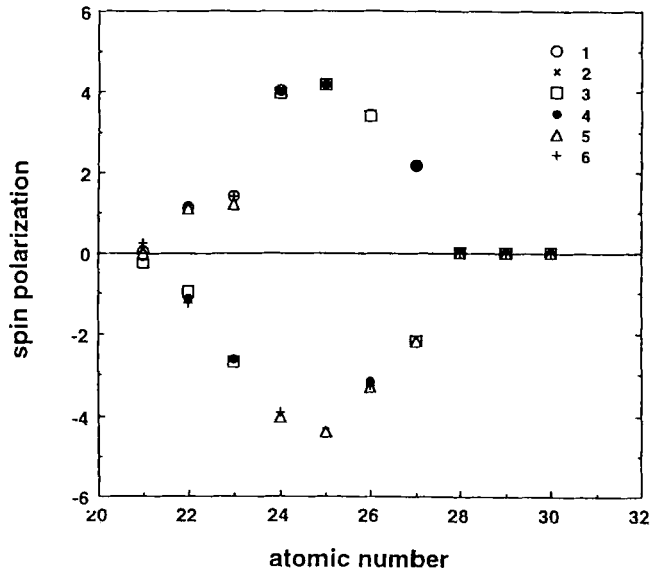

Fig.24 Change of spin density for M_6 clusters of *3d* elements

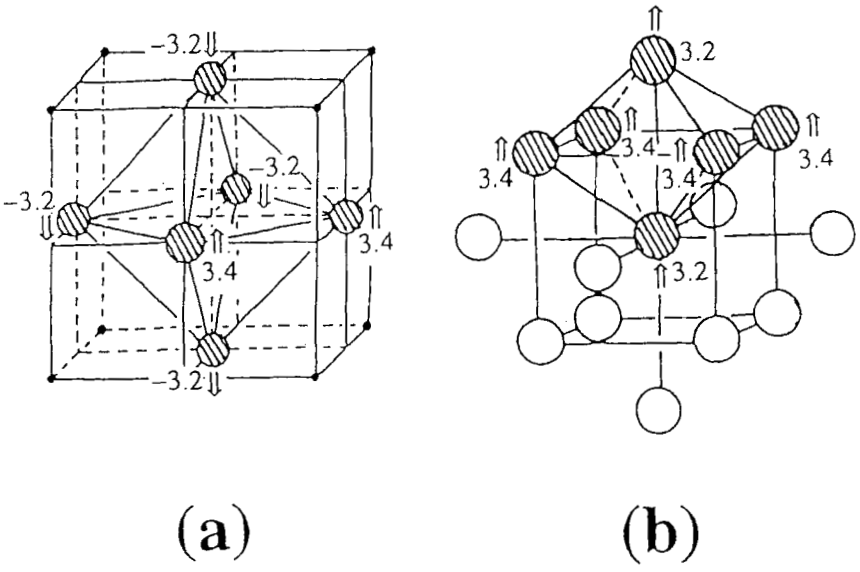

Fig.25 Spin polarization and density for fcc and bcc Fe_6 clusters

of each atom in the clusters. For the fcc cluster, both of ferromagnetic and antiferromagnetic couplings are found as above mentioned. In contrast with this, only ferromagnetic coupling exists in the bcc cluster. Thisresult is consistent with the fact that bcc Fe metal shows ferromagnetism while fcc Fe metal does not, though the magnetic moments of these small clusters are usually larger[13] than that in bulk. The DOS of the bcc cluster with ferromagnetism is shown in Fig.26. The spin-up and -down bands are split, and show some resemblance to the bulk band structure[14].

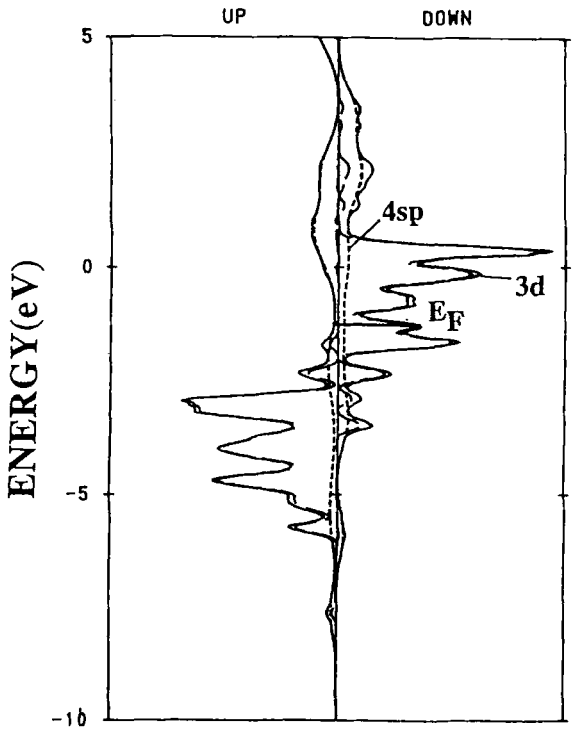

Fig.26 Density of states of spin-polarized Fe_6 cluster for bcc lattice

7. Relativistic effects on valence electronic state

For a heavy element whose atomic number is beyond 50, the relativistic effects (error caused by the nonrelativistic approximation) on the valence state can not be ignored. In such a case, it is necessary to solve Dirac equation instead of nonrelativistic Schrödinger equation usually used for the electronic state calculation. The relativistic effects

can be considered to consists of level shifts by so-called mass-velocity and Darwin terms, and level splitting by spin-orbit coupling from an analysis taking nonrelativistic limit of Dirac equation. By these effects, the valence *s* level shifts downwards, and *p* and *d* levels are split, and these also bring about indirect effects of electronic charge reconstruction as a consequence.

Figure 27 demonstrates the comparison of valence level structures of Ti_6, Zr_6 and Hf_6 clusters obtained by nonrelativistic and relativistic calculations[2]. From the figure, it can be seen that the relativistic effects are not appreciable almost at all for the *3d* metal. For *4d* element, the effects are still very small, while they become considerably large and the band structure is largely reconstructed for *5d* element.

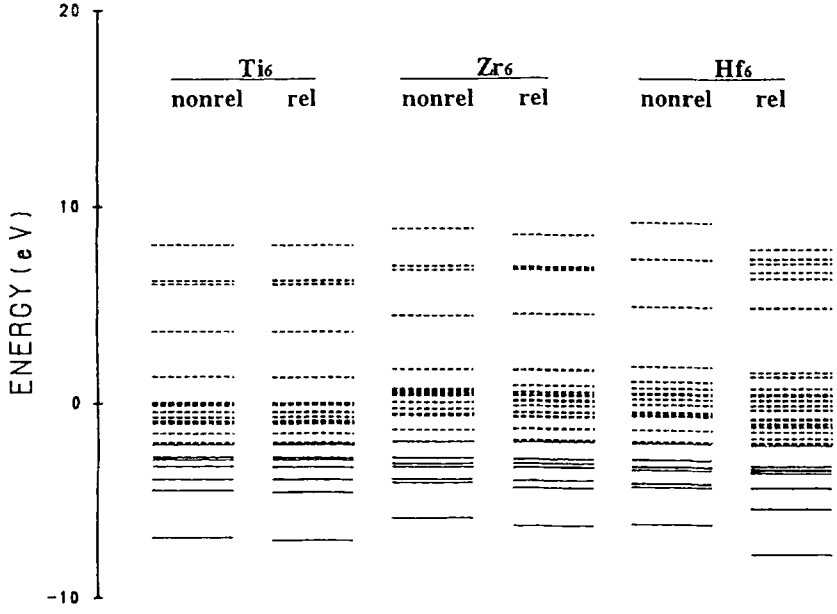

Fig.27 Comparison of relativistic and nonrelativistic level structures for Ti_6, Zr_6 and Hf_6 clusters

Table 1 shows the relativistic effects in the orbital populations of M_6 clusters. As mentioned above, the charge reconstruction due to the relativistic effects can be seen. When we compare them in the same group, it is found that the decrease of the d orbital population and the increases of the s and p orbital populations become remarkable for the elements with large atomic number. Then the relativistic effects bring about very large changes in the orbital populations for the $5d$ elements. For the elements where the d band is almost filled, namely Cu, Ag and Au, the relativistic effects appear in a little different manner. For Au, the d band is rather clearly split into two bands by the spin-orbit

Table 1 Relativistic effects in orbital populations for M_6 clusters

	Ti_6		Fe_6		Cu_6	
	nonrel	rel	nonrel	rel	nonrel	rel
3d	2.544	2.522	6.828	6.792	9.761	9.731
4s	0.864	0.882	0.683	0.706	0.802	0.831
4p	0.588	0.595	0.486	0.501	0.436	0.438
	Zr_6		Ru_6		Ag_6	
	nonrel	rel	nonrel	rel	nonrel	rel
4d	2.706	2.624	7.183	7.101	9.893	9.865
5s	0.838	0.896	0.511	0.577	0.750	0.800
5p	0.455	0.483	0.303	0.325	0.357	0.335
	Hf_6		Os_6		Au_6	
	nonrel	rel	nonrel	rel	nonrel	rel
5d	2.768	2.374	7.174	6.669	9.974	9.841
6s	0.838	1.069	0.520	0.866	0.859	1.055
6p	0.457	0.560	0.309	0.467	0.167	0.104

coupling as shown in Fig.28. Usually the Fermi level rises with an increase of the atomic number, but it lowers when going from Ag to Au because of the relativistic effects. Thus the position of the Fermi level of Au becomes closer to that of Cu, rather than to that of Ag. It may correspond with the similarities of various physical and chemical properties between Cu and Au.

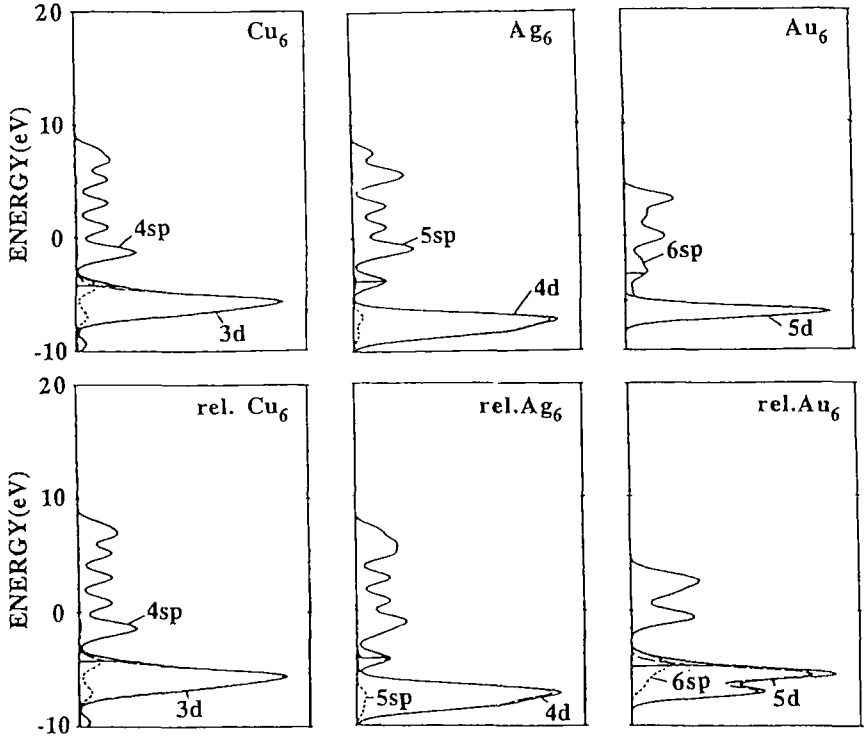

Fig.28 Comparison of relativistic and nonrelativistic densities of states for Cu_6, Ag_6 and Au_6 clusters

8. Conclusion

The electronic state calculations of transition metal clusters have been carried out to study the basic electronic properties of these elements by the use of DV-Xα molecular orbital method. It is found that the covalent bonding between neighboring atoms, namely the short range chemical interaction is very important to determine the valence band structure of transition element. The spin polarization in the transition metal cluster has been investigated and the mechanism of the magnetic interaction between the atomic spins has been interpreted by means of the spin polarized molecular orbital description. For heavy elements like *5d* transition metals, the relativistic effects are found to be very important even in the valence electronic state.

Acknowledgement

This work was supported in part by Grant-in-Aid for General Science Research from Ministry of Education, Sports, Science and Culture of Japan.

References

[1] H. Adachi. M. Tsukada and C. Satoko, J. Phys. Soc. Jpn **45**, 875, (1978).
H. Adachi, *Introduction to Quantum Materials Chemistry-Approach with DV-Xα Method-*, Sankyo, Tokyo, (1991).

[2] A. Rosen and D.E. Ellis, J. Chem. Phys. **62**, 3039,(1975).

[3] J. C. Slater, *Quantum Theory of Molecules and Solids* , McGraw-Hill, (1974), Vol.4.

[4] D. E. Ellis and G. S. Painter, Phys. Rev. B**2**, 2887, (1970).

[5] F. W. Averill and D. E. Ellis, J. Chem. Phys. 59, 6412, (1973).

[6] A. Rosén, D. E. Ellis, H. Adachi and F. W. Averill, J. Chem. Phys . **65**, 3629, (1976).

[7] R. S. Mulliken, J. Chem. Phys. **23** 1833 (1955).

[8] *CRC Handbook of Chemistry and Physics* Ed. by D. R. Lide, CRC Press, (1990).

[9] J. Callaway and C. S. Wang, Phys. Rev. B **7**,1076, (1973).

[10] J. H. Wood, Phys. Rev. **126**, 517, (1962).

[11] F. J. Pinski, J. Staunton, B. L. Gyorffy, D. D. Johnson and G. M. Stocks, Phys. Rev. Lett. **56**, 2096, (1986).

[12] H. Adachi, S. Shiokawa, M. Tsukada, C. Satoko and S. Sugano, J. Phys. Soc. Jpn. **47**, 1528, (1979).

[13] S. Nasu, T. Takano, K. Takanashi, H. Yasuoka and H. Adachi, Hyperfine Interactions **28**, 1071, (1986).

[14] S. Wakoh and J. Yamashita, J. Phys. Soc. Jpn. **25**, 1272, (1968)

The Nature of the Chemical Bond in Hydrogen Storage Compounds

H.Yukawa and M.Morinaga

Department of Materials Science and Engineering
Nagoya University
Furo-cho, Chikusa-ku,
Nagoya, Aichi, 464-01, JAPAN

Abstract

The electronic structures of $LaNi_5$ and Mg_2Ni both containing a variety of alloying elements, M, are investigated by the DV-Xα cluster method in order to understand alloying effects on the hydrogen absorption and desorption characteristics of them. It is found that hydrogen atoms make a strong chemical bond with Ni atoms rather than La or Mg atoms in pure $LaNi_5$ or in pure Mg_2Ni, despite the larger affinity of La or Mg atoms for hydrogen than Ni atoms in the binary metal-hydrogen system. It is also shown that the nature of the chemical bond between the constituent atoms determines the stability of $LaNi_5$ and Mg_2Ni hydrides. For example, for the $LaNi_5$ system, the ratio of the La(M)-Ni bond order to the Ni(M)-Ni bond order correlates well with the experimental data of the equilibrium plateau pressure of hydrogen. Similar results are also obtained for other systems, $CaNi_5$, TiFe and $ZrMn_2$. On the other hand, for the Mg_2Ni system, both the Ni(M)-Mg bond strength and the Ni(M)-H bond strength correlate well with the measured enthalpy of formation for the hydride. In addition, an empirical rule between the unit cell volume and the stability of the hydrides is explained consistently on the basis of the present calculation. The present electronic approach is useful even in the systems where an empirical rule is violated (e.g., $CaNi_5$ and Mg_2Ni).

ADVANCES IN QUANTUM CHEMISTRY, VOLUME 29

0065-3276/97 $25.00

1. Introduction

Hydrogen storage compound is an important material for the development of clean energy systems. This is because, the hydrogen fuel is one of the most clean energy resources obtained easily by the electrolysis of water. Among a variety of compounds, $LaNi_5$ is one of the most important hydrogen storage compounds [1,2]. Recently, clean secondary batteries with a high capacity have been developed using this compound [3]. Also, Mg_2Ni is a promising compound due to the light weight and the higher capacity of hydrogen [4]. In fact, it can absorb hydrogen by 3.6% in the weight percent [5]. However, the desorption pressure of this hydride is inconveniently low at room temperature. Therefore, in order to make use of this compound for practical applications, it is firstly necessary to improve its dehydriding behavior.

Recently, a variety of ternary compounds have been investigated experimentally [1,6-13]. For example, extensive studies have been carried out in the $LaNi_5$ system by substituting ternary alloying elements for either the Ni atoms or the La atoms in it [6,7]. This is because the hydrogen absorption and desorption characteristics are very sensitive to the ternary elements added into the mother compounds. Therefore, it is very important to understand the alloying effect on the hydriding or dehydriding behavior in order to design and develop new hydrogen storage compounds. However, despite great effort, as yet the alloying effect has not been elucidated on the hydriding properties of ternary compounds.

On the other hand, theoretical calculations on the electronic structures of $LaNi_5$ have been preformed by several investigators [14-16]. However, there are very few reports concerning the hydrides of $LaNi_5$ [14,15] and Mg_2Ni [17]. This is mainly due to the complexity of its crystal structure and also due to the poor understanding on the positions of hydrogen atoms in them.

Recently, the positions of hydrogen atoms in $LaNi_5$ with a lower hydrogen content, α-$LaNi_5H_{0.15}$, have been investigated using an inelastic neutron scattering technique [18]. There seems preferential occupancy on the 3f sites in the P6/mmm space group. Similar results are also reported for $LaNi_5H_{0.08}$ [19,20]. Also, the crystal structure of hydrogen-rich compound, β-$LaNi_5D_x$($x>5$), has been studied by a couple of groups [21,22] using a neutron scattering technique, and shown that it has the hexagonal structure of the $P6_3mc$ space group. Employing these crystallographic data, Gupta [14] has calculated the electronic structure of $LaNi_5H_7$ and shown the

importance of the Ni-H interaction more than the La-H interaction. Also, Suenobu *et al* [15] have calculated the electronic structure of hydrogenated YNi_5 and $LaNi_5$, and shown that the Ni-Ni chemical bond is stabilized by a small amount of lattice expansion to be introduced during the hydrogenation, but such stabilization never occurs in the YNi_5 system.

On the other hand, for Mg_2Ni system, crystal structures of Mg_2NiD_4 have been studied using a neutron scattering technique, and determined for the low-temperature phase and the high-temperature phase as well [23-25]. The hydride formed above about 520K is a cubic high-temperature (HT) phase (the Fm3m space group) with the lattice constant, a=0.6507nm, and it transforms at the temperature between 518 and 483K into the monoclinic low-temperature (LT) phase (the C2/c space group) [26,27]. Employing the crystallographic data of the high temperature phase of the Mg_2Ni hydride, Gupta [17] has calculated the electronic structure, and shown that there is a strong Ni-H interaction primarily originated from the bonding between Ni-d(e_g) and H-s electrons [17].

However, to the best of our knowledge, any clear correlation has not been obtained between the electronic structures and the hydriding properties of pure and alloyed compounds. In this study, the electronic structures of hydrogenated $LaNi_5$ and of Mg_2Ni hydrides, both containing various alloying elements, are first calculated in order to understand the alloying effect on the hydrogen absorption and desorption behavior in a fundamental manner. The DV-Xα cluster method [28,29] is employed in this calculation.

2. DV-Xα cluster method and cluster models

The DV-Xα cluster method is a molecular orbital calculating method, assuming a Hartree-Fock-Slater (HFS) approximation. In this calculation, the exchange-correlation between electrons, V_{XC}, is given by the following Slater's Xα potential,

$$V_{XC} = -3\alpha\left[\frac{3}{8\pi}\rho(r)\right]^{1/3} \tag{1}$$

where $\rho(r)$ is the density of electrons at position r, the parameter α is fixed at 0.7 and the self-consistent charge approximation is used in this calculation. The matrix elements of Hamiltonian and the overlap integrals are calculated by a random sampling method. The molecular orbitals are constructed by a linear combination of numerically generated atomic orbitals (LCAO). The atomic orbitals used in this

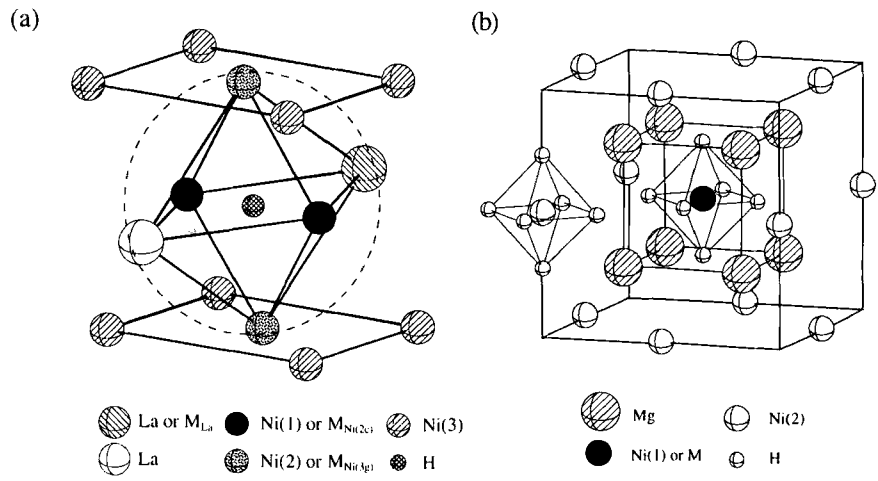

Fig.1 Cluster models used in the calculation; (a) ($HM_2Ni_{10}La_2$) and ($HMNi_{12}La$) cluster for $LaNi_5$ and (b) ($MNi_{12}Mg_8H_{78}$) cluster for Mg_2Ni.

calculation are 1s-4p for 3d transition metals, 1s-5p for 4d transition metals, 1s-6p for lanthanide elements, 1s-3d for Mg and 1s for hydrogen.

The cluster models used are shown in Fig.1(a) for $LaNi_5$ and (b) for Mg_2Ni. Both of them are hydrogenated clusters constructed on the basis of the crystal structure of α-$LaNi_5H_x$ ($x<0.4$) and Mg_2NiH_4 hydride [18,24,30-32]. For $LaNi_5$ system, a hydrogen atom occupies the 3f site in the crystal with the P6/mmm space group, which corresponds to the central site of the octahedron with the frame of four Ni atoms and two La atoms. Therefore, as shown in Fig.1(a), a hydrogen atom is located at the center of the octahedron. As shown in Fig.1(a), Ni(1), Ni(2) and Ni(3) are the first, second and third neighbour Ni atoms from the central H atom in the cluster, respectively. The interatomic distances in the cluster are, $d_{H\text{-}Ni(1)}$=0.1448nm, $d_{H\text{-}Ni(2)}$=0.1994nm, $d_{H\text{-}La}$=0.2509nm, $d_{Ni(1)\text{-}Ni(2)}$=0.2464nm, $d_{La\text{-}Ni(1)}$=0.2897nm and $d_{La\text{-}Ni(2)}$=0.3204nm. It is noticed here that the Ni(1)-Ni(2) distance is slightly shorter in this compound than in pure f.c.c. Ni ($d_{Ni\text{-}Ni}$=0.2498nm).

In order to examine alloying effects on the electronic structures, a variety of alloying elements are substituted for either the Ni atoms or the La atoms in the cluster. It is known that the Ni substitutional alloying elements occupy both the 2c and the 3g sites in the crystal lattice. For example, it is reported that the occupancy percentages of Co in $LaNi_4Co$ are 23% at the 2c site and 77% at the 3g site [33]. The

2c and 3g sites correspond to the Ni(1) and the Ni(2) atom sites shown in Fig.1(a), respectively. Therefore, in case of the Ni substitution, either the two Ni(1) atoms or the two Ni(2) atoms are substituted for various alloying elements, M, (M=Cr, Fe, Co, Cu, Pd and Ag). On the other hand, in case of the La substitution, one of the two La atoms are substituted for various alloying elements, M, (M=Y, Zr, Nd, Gd and Er). Therefore, the cluster models for the Ni substitution and the La substitution are expressed as, $HM_2Ni_{10}La_2$ and $HMNi_{12}La$, respectively.

On the other hand, for Mg_2Ni system, the hydrogen atoms occupy randomly two thirds of their equivalent positions in the crystal lattice. But because of the difficulty in the calculation involving random arrangements, hydrogen atoms are assumed here to occupy every equivalent position in it, so that each Ni atom is surrounded completely by six hydrogen atoms in this model. Therefore, this is the Mg_2NiH_6-type model instead of the Mg_2NiH_4-type model. The full occupancy of hydrogen atoms may not alter essential features of the electronic structures, as explained later [17,34]. As shown in Fig.1(b), Ni and Mg atoms occupy the cation and the anion sites in the CaF_2-type structure respectively, in which six hydrogen atoms form a small octahedron around each Ni atom as shown in the figure. The respective interatomic distances are, $d_{H\text{-}Ni}$=0.149nm, $d_{H\text{-}Mg}$=0.231nm, $d_{Mg\text{-}Ni}$=0.282nm and $d_{H\text{-}H}$=0.211nm. It is noticed here that the Mg-Mg distance of 0.325nm is slightly longer in this compound than in pure h.c.p. Mg ($d_{Mg\text{-}Mg}$=0.321nm), and the Ni-Ni distance of 0.460nm is much longer in this compound than in pure f.c.c. Ni ($d_{Ni\text{-}Ni}$=0.2498nm). In order to examine alloying effects on the electronic structures, a central Ni atom in the cluster is substituted for various alloying elements, M, (M=V, Cr, Fe, Co, Ni, Cu, Zn). Therefore, the cluster model for the Ni substitution, i.e., $Mg_2Ni_{1-x}M_x$, is expressed as $MNi_{12}Mg_8H_{78}$. Needless to say, the cluster model without any alloying elements is expressed as $NiNi_{12}Mg_8H_{78}$.

For a characterization of the electronic structure, the spatial electron density distributions, the bond order between atoms and ionicities of each atom in the cluster are estimated according to the Mulliken population analysis [35]. The overlap population, $Q_{\nu\nu'}$, of electrons between two atoms ν and ν' is defined as,

$$Q_{\nu\nu'} = \sum_l \sum_{ij} C_{il}^{\nu} C_{jl}^{\nu'} \int \Psi_i^{\nu} \Psi_j^{\nu'*} dV \tag{2}$$

where Ψ_i^{ν} and $\Psi_j^{\nu'}$ are the wavefunctions of the i and j orbitals of ν and ν' atoms, respectively. C_{il}^{ν} and $C_{jl}^{\nu'}$ are coefficients which show the magnitude of the linear

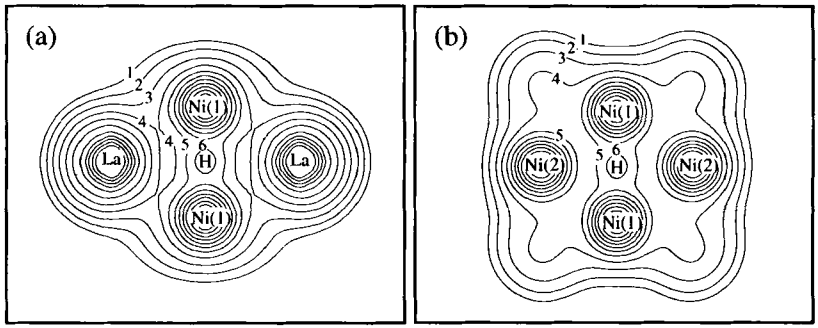

Fig.2 Contour maps of the electron density distributions in pure $LaNi_5$ system, (a) on the (0001) atomic plane containing both the La and the Ni(1) atoms and (b) on the $(\bar{1}2\bar{1}0)$ atomic plane containing both the Ni(1) and the Ni(2) atoms. The denoted numbers, 1, 2, 3, 4, 5 and 6 correspond to the electron density values, 0.005, 0.01, 0.02, 0.04, 0.08 and 0.16 in electrons per cube of the atomic unit, respectively.

combination of atomic orbitals in the lth molecular orbital. The sum over l runs only over the occupied orbitals. Here, this $Q_{\nu\nu'}$ is called the bond order and used as a measure of the strength of the covalent bond between ν and ν' atoms. Further detailed explanation of the calculation method is given elsewhere [36-41].

3. Results

3.1 $LaNi_5$ system

3.1.1 Spatial electron density distributions in pure $LaNi_5$ system

The contour maps of the electron densities on the two atomic planes are shown in Fig.2; one is the (0001) atomic plane containing both the Ni(1) and the La atoms as shown in (a), and the other is the $(\bar{1}2\bar{1}0)$ atomic plane containing both the Ni(1) and the Ni(2) atoms as shown in (b). In each figure, the hydrogen atom is located at the center of the map. As is evident from these figures, the relatively high electron-density region extends from the H atom site towards the Ni(1) atom site, but does not towards the La atom site. Also, the electron density distributions around the La atom site seem to extend towards the Ni(1) atom site but not towards the H atom site, although the La-H distance is shorter than the La-Ni(1) distance. These results clearly indicate that the hydrogen atom exhibits a larger affinity with Ni atoms rather than La atoms in pure $LaNi_5$ system.

3.1.2 Bond order between atoms in alloyed $LaNi_5$ system

The bond order is the overlap population of the electrons between atoms. As explained earlier, this is a measure of the strength of the covalent bond between atoms. The respective bond orders between atoms around the hydrogen atom change with alloying elements as shown in Fig.3 for the Ni(2c) substitution, in Fig.4 for the Ni(3g) substitution and in Fig.5 for the La substitution. Every bond order shown in these figures is the value per atomic bond in the cluster.

In Fig.3(a) and Fig.4(a), the bond order between the hydrogen atom and the La atom is always negative for every alloying element, irrespective of the Ni(2c) or the Ni(3g) substitution, indicating that there is a repulsive interaction operating between these atoms. On the other hand, the bond order between the hydrogen atom and the Ni(1) atoms (or the alloying element, M, on the Ni(1) site) is large and positive. The magnitude of this bond order shows a little change with alloying elements except for Pd as shown in Fig.3(a). In case of Pd, the bond order decreases largely, indicating that the strength of the chemical bond is relatively weak between the hydrogen and the Pd atoms in the Pd-containing compound. However, in case of the Ni(3g) substitution, the Ni(1)–H bond order shows the less change with M, as might be expected from the M atom site, which is the second-nearest-neighbour site from the central H atom in the cluster. On the other hand, in case of the La substitution as shown in Fig.5(a), all the bond orders between the hydrogen and surrounding metal atoms scarcely change with alloying. This result indicates that any La substitutional elements scarcely modify the nature of the chemical bond with the hydrogen atom.

From these results, it is clear that the hydrogen atom makes a stronger bond with the Ni(1) atoms (or M atoms on the Ni(1) sites) rather than the La atoms (or M atom on the La site) regardless of the Ni or the La substitutional elements. This is consistent with the results of the electron density distributions shown in Fig.2.

Fig.3(b), Fig.4(b) and Fig.5(b) show the changes in the bond orders between the metal-metal pairs for the three cases. In Fig.3(b), there are large changes in the M-Ni(2) and the La-M bond orders. For example, the M-Ni(2) bond order changes from about 0.23 for Cr to about 0.14 for Ag. Similar results are also obtained for the case of the Ni(3g) substitution as shown in Fig.4(b). On the other hand, for the La substitutional elements shown in Fig.5(b), the M-Ni(1) bond order changes remarkably with M. It is large for Y, Zr and Er, but small for La, Nd and Gd.

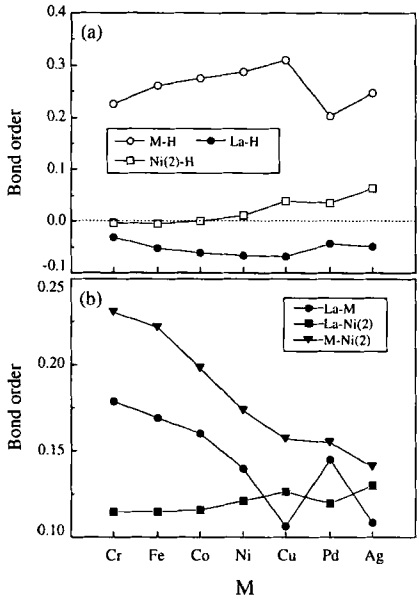

Fig.3 Changes in the bond orders with the Ni(2c) substitutional elements, (a) H-metal bond orders and (b) metal-metal bond orders.

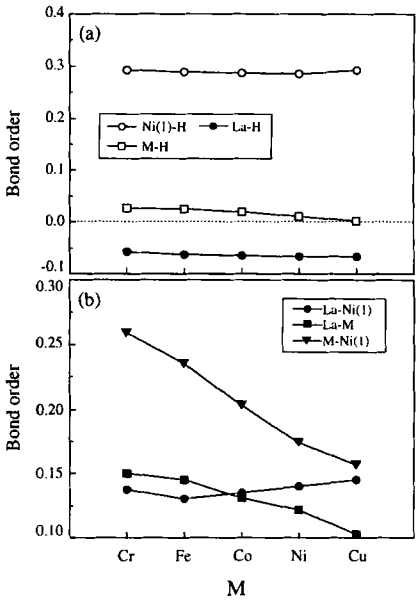

Fig.4 Changes in the bond orders with the Ni(3g) substitutional elements, (a) H-metal bond orders and (b) metal-metal bond orders.

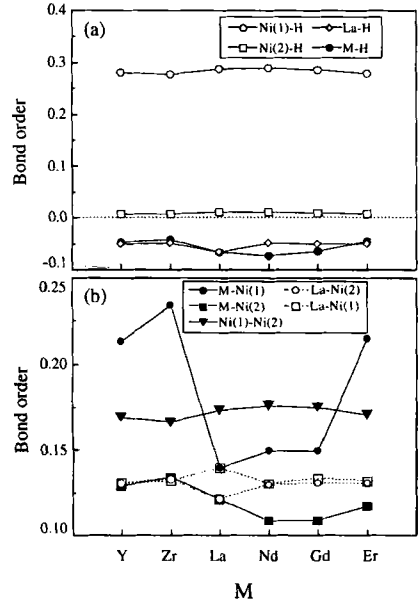

Fig.5 Changes in the bond orders with the La substitutional elements, (a) H-metal bond orders and (b) metal-metal bond orders.

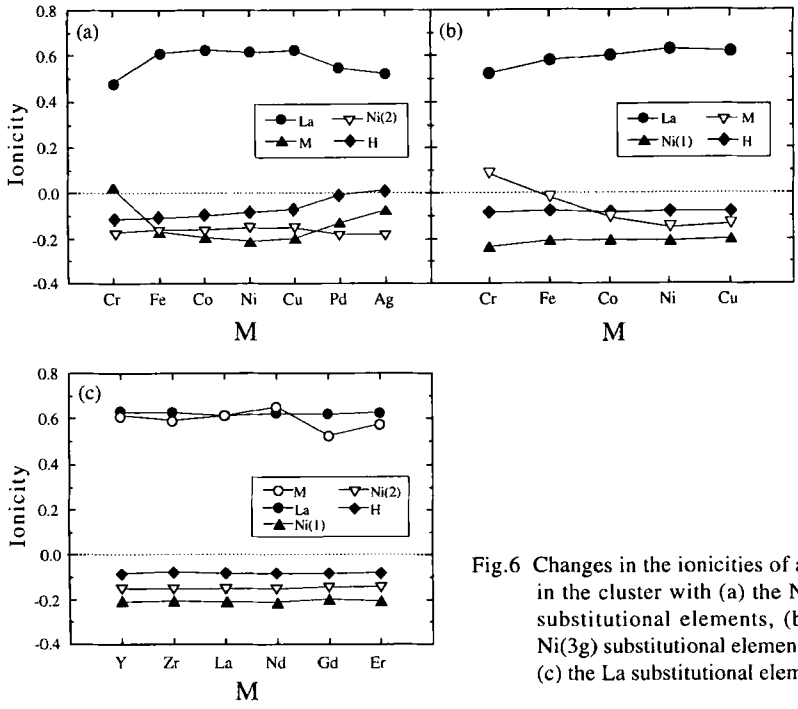

Fig.6 Changes in the ionicities of atoms in the cluster with (a) the Ni(2c) substitutional elements, (b) the Ni(3g) substitutional elements and (c) the La substitutional elements.

3.1.3 Ionicities of atoms in alloyed $LaNi_5$ system

The ionicity of each atom in the cluster near the hydrogen atom is estimated according to the Mulliken population analysis [35]. The results are shown in Fig.6 (a) for the Ni(2c) substitution, (b) for the Ni(3g) substitution and (c) for the La substitution. As shown in these figures, the ionicities of the La-site atoms (La or M atom on the La site) are always positive. On the other hand, all the ionicities of the hydrogen atom, the Ni atom and the alloying element on the Ni-site are always negative or nearly nil. These results indicate that charge transfer takes place from the La atom (or M atom on the La site) towards the hydrogen atom and other metal atoms in the cluster. The ionicity of the hydrogen atom is about -0.1 and its change with the alloying elements is small except for Pd and Ag in Fig.6(a). For Pd and Ag, it is almost nil, and also in response to this change in the hydrogen ionicity, the ionicities of La and M (Pd or Ag) atoms shift towards the less ionized side. This means that ionic interactions between the hydrogen and these elements are probably weak.

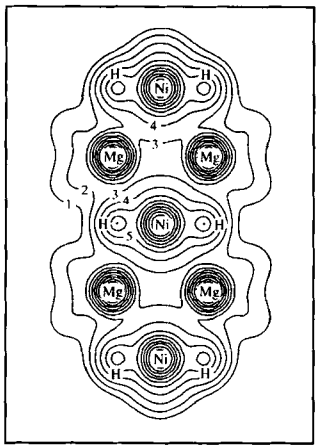

Fig.7 Contour map of the electron density distributions on the (110) atomic plane in pure Mg_2Ni hydride. The denoted numbers, 1, 2, 3, 4, 5 and 6 correspond to the electron density values, 0.005, 0.01, 0.02, 0.04, 0.08 and 0.16 in electrons per cube of the atomic unit, respectively.

3.2 Mg_2Ni system

3.2.1 Spatial electron density distributions in pure Mg_2Ni hydride

The contour map of the electron densities on the (110) atomic plane is shown in Fig.7 for pure Mg_2Ni hydride. As shown in this figure, it is evident that relatively high electron-density regions extend from the H atom site towards the Ni atom site, but do not towards the Mg atom site. Also, the electron density distributions around the Mg atom site seem to show an extension towards the Ni atom site but does not towards the H atom site, although the Mg-H distance is shorter than the Mg-Ni distance. These results clearly indicate that hydrogen atoms exhibit a larger affinity with Ni atoms rather than Mg atoms in this system.

Further, from the present calculation using a Mg_2NiH_6-type cluster model, it is found that there is a strong bonding-type interaction operating between the Ni-d(e_g) and the H-s electrons, whereas non-bonding interaction exists between the Ni-d(t_{2g}) and the H-s electrons. These results are is in good agreement with the previous results of Mg_2NiH_4 [17].

3.2.2 Bond order between atoms in alloyed Mg_2Ni hydride

The changes in the bond order with alloying elements are shown in Fig.8. Referred to 'H' in this figure are the hydrogen atoms sitting on the six corner sites of the octahedron around an alloying element, M (see Fig.1(b)).

As shown in this figure, both the Ni(2)-H and the M-Ni(2) bond orders are

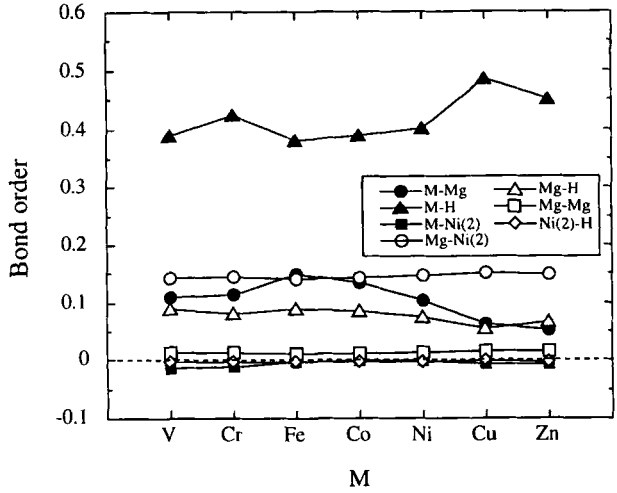

Fig.8 Changes in the bond orders with the Ni substitutional elements in the Mg_2Ni system.

very small because of the long interatomic distances between them. Also, it is noticed that the Mg-Mg bond order is positive, but very small despite the fact that the Mg-Mg distance in the hydride is very similar to the one in pure h.c.p. Mg. The Mg-Ni(2) and the Mg-H bond orders are positive and larger than the above three bond orders. However, all these bond orders are nearly constant without showing any large dependence on the alloying elements.

On the other hand, the M-H bond order is significantly large, indicating that there is an attractive and strong interaction operating between the alloying element and the hydrogen atom. The magnitude of this bond order changes with M. In response to this change, the M-Mg bond order varies in a reverse way. Namely, the alloying elements which have a strong affinity with the hydrogen atom, tend to interact weakly with the surrounding Mg atoms.

From these results, it is evident that the hydrogen atom makes a stronger bond with M atoms on the Ni site rather than Mg atoms, regardless of alloying elements. This is consistent with the results of the electron density distributions shown in Fig.7. In addition, although the Ni-Ni bond order is not shown in the figure, it is very small and negative (~-0.001) due to the much larger distance between them (~0.460nm), as compared to the distance in pure f.c.c. Ni (~0.2498nm). Also, as mentioned above, the Mg-Mg interaction is very weak. Therefore, the structural

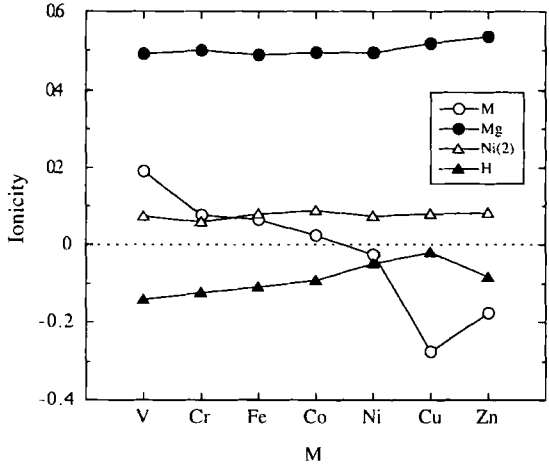

Fig.9 Changes in the ionicities of atoms in the cluster with the Ni substitutional elements in Mg_2Ni system.

stability of this Mg_2Ni hydride will be attributable mainly to the existence of strong Ni-Mg interactions in it.

3.2.3 Ionicities of atoms in alloyed Mg_2Ni hydride

The changes in the ionicities with alloying elements are shown in Fig.9. As shown in this figure, the ionicities of the Mg and the Ni(2) atoms are always positive, and they scarcely vary with alloying elements, M. On the other hand, the ionicities of the alloying elements change considerably. For example, V, Cr, Fe and Co, all of which are the left-side elements from Ni in the periodic table take the positive value and gradually decrease with increasing the atomic number of M. For the right-side elements, such as Ni, Cu and Zn, all the ionicities take negative values, while having a minimum at the Cu substitution, in agreement with the order of the electronegativity of the elements. These results indicate that for the left-side elements charge transfer takes place from every metal atom towards the hydrogen atom, but for the right-side elements it does from the Mg and the Ni atoms towards the alloying element and the hydrogen atom. As a result, the effective charge on the H atom site varies in the range of -0.14 to -0.02, depending on the alloying elements. It is noted here that the ionicity of the hydrogen atom varies with M in an approximately opposite way as that of the alloying elements.

4. Discussion

4.1 Hydrogen-metal interaction

Most hydrogen storage compounds such as $LaNi_5$, Mg_2Ni, $CaNi_5$ and TiFe consist of both endothermic and exothermic elements in view of the heat of formation of their hydrides. For example, an exothermic element, La, has a strong attractive interaction with hydrogen and hence forms easily the hydride, LaH_2. The endothermic elements (e.g., Ni) may work to reduce such an attractive interaction, so that the hydrogen desorption process could be activated by the presence of them.

However, this naive understanding is not true. This is, because an antibonding interaction is operating between the hydrogen and the La atoms in the $LaNi_5$ system as shown in Figs.3(a), 4(a) and 5(a). On the other hand, a strong bonding interaction is dominant between the hydrogen and the Ni(1) atoms. Similar results are also obtained in the Mg_2Ni system. For example, a strong bonding interaction is operating between the hydrogen and the Ni atoms, whereas the interaction between the Mg and the hydrogen atoms is relatively weak as shown in Fig.8 (M=Ni). These results clearly indicate that the hydrogen atom makes a strong chemical bond with the Ni atom rather than the La or Mg atoms in pure $LaNi_5$ and Mg_2Ni systems, despite the larger affinity of La or Mg atoms for hydrogen than Ni atoms in the binary metal-hydrogen system. These results are in good agreement with the previous calculations [14,17] in which the H-s bonding state appears in the low energy region, and participates in the formation of the strong bond with Ni atoms but the weak bond with La or Mg atoms. This trend has also been observed in the other hydrogen storage compounds, for example, TiFe where Fe atoms interact more strongly with hydrogen atoms than Ti atoms [42,43].

However, it is still true that the mixing of endo- and exo-thermic elements forms appropriate hydrogen storage compounds. In the present discussion, important is probably the location of hydrogen in the hydride. For example, in case of $LaNi_5H_6$, the hydrogen is closer to the Ni atoms rather than the La atoms. This inevitably makes the Ni-H interaction larger than the La-H interaction. However, this Ni-H interaction in $LaNi_5H_6$ is still weaker, compared to the La-H interaction in LaH_2, judging from the enthalpy of formation of each hydride; ΔH=-30 kJ/mol H_2 for $LaNi_5H_6$ and -209 kJ/mol H_2 for LaH_2. But this weak Ni-H interaction is very favorable for activating the hydrogen desorption process readily in $LaNi_5H_6$. Thus the existence of such a weak interaction with hydrogen is supposed to be characteristic of hydrogen storage compounds.

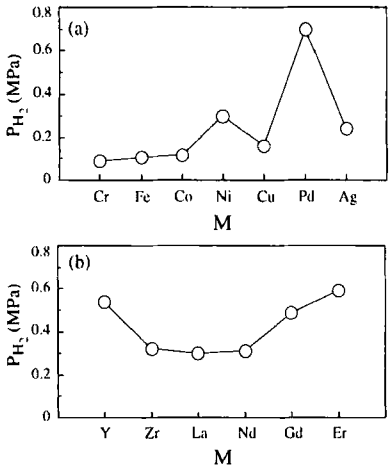

Fig.10 Equilibrium plateau pressures at 313K for (a) $LaNi_4M$ alloys and (b) $La_{0.8}M_{0.2}Ni_5$ alloys, where M is the alloying element (after Van Mal *et al*).

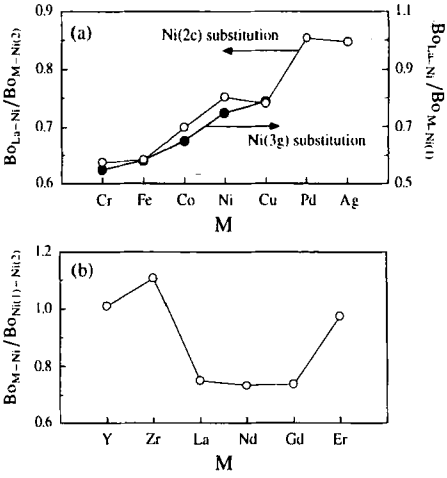

Fig.11 Changes in the bond order ratios with (a) the Ni substitutional elements and (b) the La substitutional elements.

4.2 Alloying effect on the hydrogen absorption and desorption characteristics

4.2.1 $LaNi_5$ system

The alloying effect on the hydriding properties has been studied extensively [1,6-13], because of the fundamental interest as well as the practical interest for the hydrogen storage application. The changes in the equilibrium plateau pressure at 313K with alloying elements (M), obtained by Van Mal *et al* [6] are shown in Fig.10 (a) for $LaNi_4M_1$ and (b) for $La_{0.8}M_{0.2}Ni_5$. These experimental results are interpreted by using the bond orders shown in Figs.3, 4 and 5. Namely, it is found that the measured hydrogen pressures change following the variation of the bond orders between metal atoms sitting on the small octahedron around the hydrogen atom. For example, when compared Pd with Ni in Fig.10(a), the hydrogen pressure is higher for Pd than for Ni. In this case, as shown in Fig.3(b), the La-Pd bond order is comparable to the La-Ni bond order, but the Pd-Ni(2) bond order is smaller than the Ni-Ni(2) bond order. Similarly, when compared Cu with Pd, the hydrogen pressure is lower for Cu than for Pd. In this case, the Cu-Ni(2) bond order is comparable to the Pd-Ni(2) bond order, but instead the La-Cu bond order is much smaller than the La-Pd bond order. In case of the La substitution, as shown in Fig.5(b) and Fig.10(b),

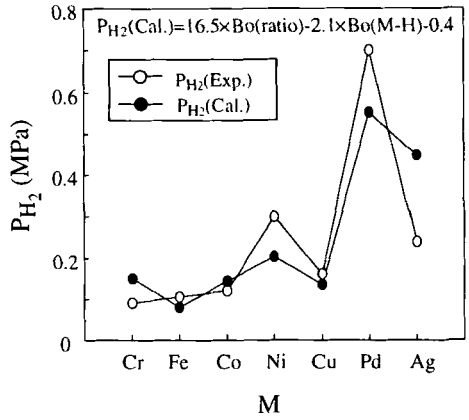

Fig.12 Comparison between calculation and experimental data of the equibrium plateau pressures at 313K for $LaNi_4M$ alloys.

those elements which have a stronger M-Ni(1) bond order show the higher hydrogen pressure with an exception of Zr. Therefore, it seems that the alloying element which increases the Ni-Ni interaction but decreases the La-Ni interaction in the octahedron tends to have the lower equilibrium pressure of hydrogen. Then, the ratios of these bond orders are calculated, and the results are shown in Fig.11(a) for the Ni(2c) and the Ni(3g) substitution and (b) for the La substitution. In the figures, the ratio of the bond orders (Bo) is defined as Bo(La-Ni)/Bo(M-Ni) for the Ni substitution and Bo(M-Ni)/Bo(Ni-Ni) for the La substitution, respectively. Therefore, as this ratio increases, the hydrogen pressure is supposed to increase. In accordance with this expectation, the results shown in Fig.11 are approximately similar to the experimental results of the equilibrium plateau pressure of hydrogen shown in Fig.10(a) and (b) with an exception of Zr. The reason for the discrepancy in Zr is unknown, but it may be true that Zr atoms goes preferentially into the grainboundary instead of substituting for La atoms, resulting in the less modification of the hydrogen pressure by the Zr addition [44].

Also, in case of the Pd substitution for Ni atoms, the weak Pd-H interaction shown in Fig.3(a) will give an additional effect on the increasing hydrogen pressure, as explained earlier. In fact, the agreement is further improved by taking into account the M-H interaction. Here, the equilibrium plateau pressure of hydrogen is assumed to be expressed as,

$$P_{H_2}(\text{Cal.}) = A \times \text{Bo(ratio)} + B \times \text{Bo(M-H)} + C \qquad (3)$$

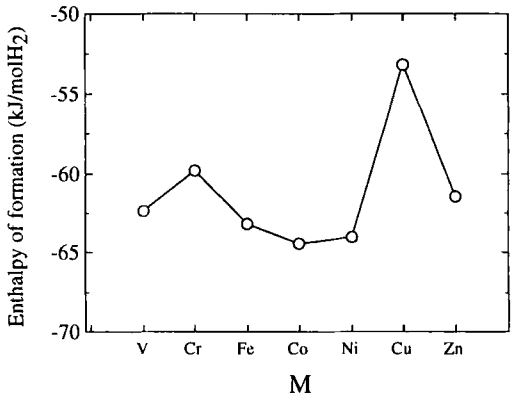

Fig.13 Enthalpy of formation for $Mg_2Ni_{0.75}M_{0.25}$ hydrides, where M is the alloying element (after Darnaudery *et al*).

where the Bo(ratio) and the Bo(M-H) are the bond order ratio and the M-H bond order, respectively. The coefficients are determined to be A=1.65, B=-2.12 and C=-0.42 by the least squares method and the results are shown in Fig.12. The agreement is fairly good between the calculation and the experiment.

In addition to the covalency mentioned above, the charge transfer will contribute to the chemical bond between atoms [45,46]. However, as shown in Fig.6, the ionicities of the hydrogen atom and other atoms in the cluster are less dependent on M except for Cr, Pd and Ag, indicating that there may be a small modification by alloying in the chemical bond strength originating from the charge transfer between the hydrogen and the surrounding metals.

4.2.2 Mg_2Ni system

Fig.13 shows the changes in the enthalpy of formation for the hydrides, ΔH, with alloying elements (M) in $Mg_2Ni_{0.75}M_{0.25}$, reported by Darnaudery *et al* [12]. The values of ΔH change significantly with the alloying elements substituted for Ni atoms. There may be a certain correlation between the values of ΔH and the M-Mg or M-H bond orders which change largely with M as shown in Fig.8. For example, the value of ΔH for $Mg_2Ni_{0.75}Cu_{0.25}$ shows the largest value among the alloyed compounds, which means that the Cu substitution makes the hydride most unstable among them. This may be attributable to the small Cu-Mg and the large Cu-H interactions. In fact, there is a general trend that the smaller M-Mg interaction and the larger M-H

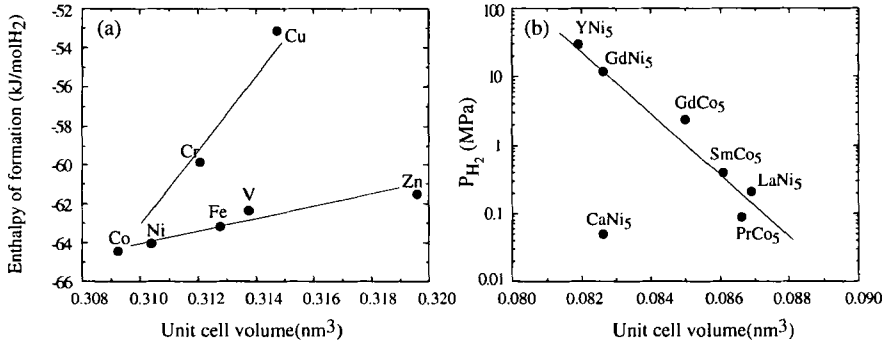

Fig.14 Correlation between the unit cell volume and the hydriding properties for (a) $Mg_2Ni_{0.75}M_{0.25}$ (M : the alloying element), and (b) AB_5 compounds.

interaction make the hydride more unstable. It is interesting that the change in the ΔH with M shown in Fig.13 quite resembles the change in the M-H bond order shown in Fig.8.

The charge transfer between atoms may act to moderate this bond order change with M, but such a moderation effect may not be large in this system [34].

4.3 Comparison in the hydride stability between the $LaNi_5$ and the Mg_2Ni system

There are some empirical rules to account for the stability of hydrides formed in the hydrogen storage compounds. One of the rules is concerned with a correlation between the unit cell volume (or the interstitial hole size) and the hydriding properties of $CaCu_5$-type compounds [47,48]. That is to say, the larger the unit cell volume is, the more stable the hydride is. In order to test this correlation in the present system, the unit cell volumes of alloyed Mg_2Ni (i.e., $Mg_2Ni_{0.75}M_{0.25}$ [12]) are plotted against the enthalpy of formation, ΔH, for their hydrides as shown in Fig.14 (a). For comparison, a similar figure is also given in Fig.14(b) for typical hydrogen storage AB_5 compounds with the $CaCu_5$-type crystal structure [47,48], where the equilibrium plateau pressure of hydrogen are used instead of the ΔH. The large ΔH corresponds to the high hydrogen pressure. Therefore, in both figures the vertical axis is an index to show the stability of the hydrides, and the compounds locating in the lower part of these figures tend to make more stable hydrides by the hydrogenation.

When compared Fig.14 (a) with (b), there is a clear difference between them. The rule mentioned above is generally satisfied for the AB_5 compounds except for

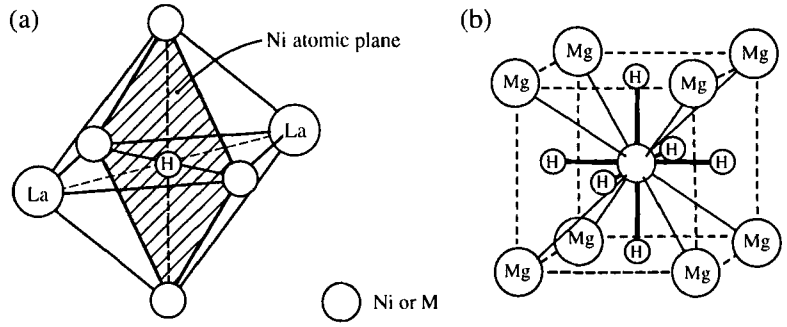

Fig.15 Schematic illustration of showing the magnitude of the bond strangths between atoms in the metal framework of (a) $LaNi_5$ hydride and (b) Mg_2Ni hydride.

$CaNi_5$. However, for $Mg_2Ni_{0.75}M_{0.25}$, data is scattered, but still there is a tendency that the compounds become unstable with increasing unit cell volume. Thus, the empirical rule is no longer valid in $Mg_2Ni_{0.75}M_{0.25}$.

This difference lying between AB_5 and $Mg_2Ni_{0.75}M_{0.25}$ may arise from the difference in the crystal structural evolution as the hydrogenation proceeds.

4.3.1 $LaNi_5$ system

For the AB_5 system, the crystal structure of the hydride, AB_5H_x, does not change essentially up to x=4, since the hydrogen atoms occupy interstitial sites in the $CaCu_5$-type crystal lattice, while accompanying a small lattice expansion and lattice distortion as well. The lattice keeps expanding while the hydrogenation proceeds. As mentioned before, the ratio of the La-Ni bond order to the Ni-Ni bond order correlates well with the stabilities of $LaNi_5$ hydride. All these metal atoms are the constituent atoms in the framework of an octahedron around the hydrogen atom. Therefore, the most important crystal unit to determine the phase stability of this hydride is a small octahedron as shown in Fig.15(a). In the figure, the bond strengths between atoms are shown by using the thickness of lines. The thicker line means the stronger bond, whereas the thinner line means the weaker bond, and the dotted line means the further weak bond existing between them.

As shown in Fig.15(a), both the La-Ni and Ni-Ni interactions are strong enough to hold the framework of this octahedron. When hydrogen is absorbed into the compound, the crystal lattice may expand so as to optimize the Ni-Ni interaction. In

Table 1 Lattice parameters, unit cell volume for $CaNi_5$, YNi_5 and $LaNi_5$.

Compound (RNi_5)	Lattice parameter		Unit cell volume(nm^3)
	a (nm)	c (nm)	
YNi_5	0.4883	0.3967	0.0819
$CaNi_5$	0.4930	0.3925	0.0826
$LaNi_5$	0.5017	0.3987	0.0869

fact, according to the previous calculation [15], the Ni-Ni interaction is reduced by the hydrogenation, but it is recovered to some extent by introducing a small expansion to the Ni atomic plane where the hydrogen atom is located. However, the situation is different if the La-Ni interaction is significantly large. As is evident from the atomic arrangement in the octahedron shown in Fig.15(a), this La-Ni interaction acts to suppress such a lattice expansion on the Ni atomic plane, so that the Ni(M)-Ni bond order is never recovered, resulting in the remarkable reduction in the total chemical bond strengths in the octahedral framework by the hydrogenation. As a result, the stability of the hydrides decreases with increasing La(M)-Ni bond order and with decreasing Ni(M)-Ni bond order. Thus, the ratio of the La(M)–Ni bond order to the Ni(M)–Ni bond order is indeed a good indication to show the hydride stability, as shown in Fig.10 and Fig.11.

As shown in Fig.14(b), there is a large deviation in $CaNi_5$ from other compounds. This is also understood consistently following the present inference. The electronic structures of $CaNi_5$, YNi_5 and $LaNi_5$ are calculated using a small octahedral cluster, R_2Ni_4(R=Ca, Y and La) which is the same as the one shown in Fig.15(a). The lattice parameters used in the calculations for each compound are shown in Table 1 together with the unit cell volume. The results of the bond order ratio for each compound are shown in Fig.16. The calculated bond order ratio changes similarly as the observed hydrogen pressure does. The lower hydrogen pressure of $CaNi_5$ compared to the other compounds is simply due to the weaker Ca–Ni interaction. On the contrary, the higher hydrogen pressure of YNi_5 is attributable to the stronger Y–Ni interaction. Thus, as far as the present approach is employed, there is no difficulty in understanding experimental results of AB_5 compounds as shown even in $CaNi_5$.

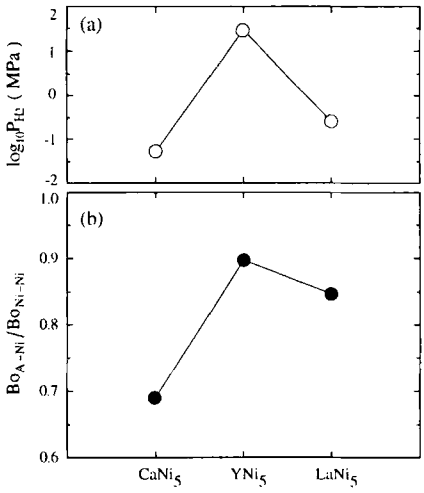

Fig.16 Correration between (a) observed hydrogen pressures at room temperature and (b) bond order ratios for $CaNi_5$, YNi_5 and $LaNi_5$.

4.3.2 Mg_2Ni system

In case of the Mg_2Ni system the situation is completely different from the $LaNi_5$ system. This is because, a low-temperature phase of the hydride is hexagonal and its metals framework somewhat resembles the Mg_2Ni crystal framework. But, it is no longer stable above about 500K, and instead the high-temperature phase of Mg_2NiH_4 appears when the hydrogenation proceeds at the temperature around 573K. This crystal structure is very different from that of Mg_2Ni. In particular, the atomic volume per metal atom is about $2.3\times10^{-2}nm^3$, which is much larger than that of Mg_2Ni ($1.7\times10^{-2}nm^3$) or $LaNi_5$ ($1.4\times10^{-2}nm^3$) or $LaNi_5H_6$ ($1.8\times10^{-2}nm^3$). As a result, the hydrogen atoms easily occupy a portion of the corner sites in the small octahedron existing around a Ni atom, as shown in Fig.1(b). This occupancy of hydrogen atoms may not accompany any significant lattice expansion because of the large atomic volume, and the occupied portions of the octahedral sites will simply increase as the hydrogenation proceeds.

As explained before, the metal framework of pure Mg_2Ni hydride is held mainly by the Ni-Mg interactions. Therefore, as shown in Fig.15(b), a small cube containing Ni and Mg atoms is the important crystal unit to determine the phase stability of this hydride. The atomic interactions in the cube are modified considerably by alloying mainly due to the change in the M-H and M-Mg interactions as shown in Fig.8. If the M-H interaction becomes stronger, the M-Mg interaction becomes weaker,

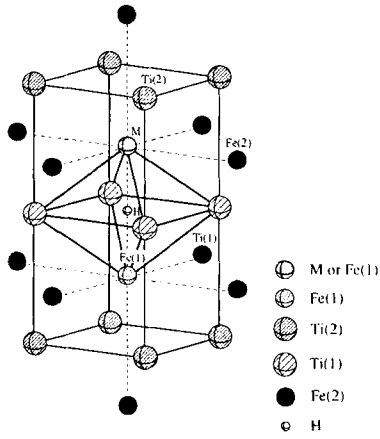

Fig.17 ($HMFe_{11}Ti_{12}$) cluster model used for TiFe system.

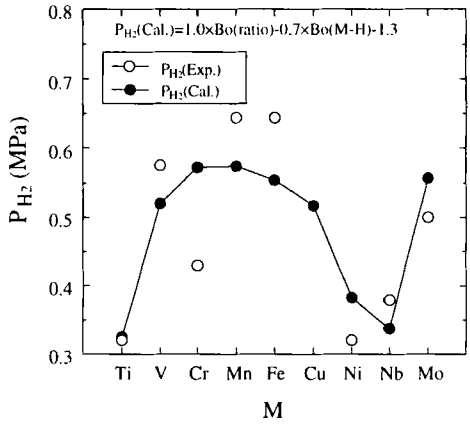

Fig.18 Comparison between calculation and experimental data of the equibrium plateau pressures at room temperature for $TiFe_{0.96}M_{0.04}$ alloys.

resulting in the instability of the framework of the cube. As a result, the stability of the hydrides decreases with decreasing M-Mg bond order, even though the M-H interaction may act to increase the stability of the hydride to some extent.

Thus, the hydrogen absorption and desorption characteristics are very different between $LaNi_5$ and Mg_2Ni, but both of them are well understood in terms of the nature of the chemical bond between atoms in the small polyhedron in which the absorbed hydrogen atom is located.

4.4 Other hydrogen storage compounds

The present approach is applicable to other hydrogen storage compounds. Here, two examples will be shown briefly.

4.4.1 TiFe system

A cluster model used for the calculation of TiFe system is shown in Fig.17. For simplicity, this is constructed on the basis of the CsCl-type crystal structure of TiFe [49], although the hydrogenation induces a small distortion in the crystal structure. In this model a hydrogen atom is located on the central site of the octahedron consisting of two Fe(1) atoms and four Ti atoms. In order to examine alloying effects on the hydriding properties, one of the two Fe(1) atoms is substituted

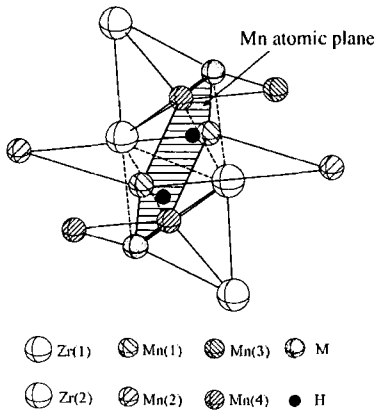

Fig.19 ($H_2M_2Zr_4Mn_8$) cluster model used for $ZrMn_2$ system.

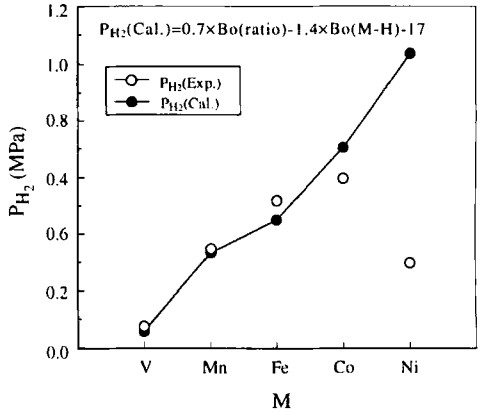

Fig.20 Comparison between calculation and experimental data of the equibrium plateau pressures at 473K for $ZrMn_{1.8}M_{0.2}$ alloys.

for various alloying elements, M. Therefore, the cluster model is expressed as $HMFe_{11}Ti_{12}$.

In this system, the most important crystal unit is the octahedron where a hydrogen atom is located. Therefore, the ratios of the M-Ti bond order to the Ti-Ti bond order are calculated. Using this bond order ratio and also the M-H bond order, the equilibrium hydrogen pressures are examined for $TiFe_{0.96}M_{0.04}$ alloys [49]. As shown in Fig.18, the calculated pressures of hydrogen are approximately similar to the experimental ones. A discrepancy observed at Cr may be attributable to the difficulties in the activation process of this compound [50,51].

4.4.2 $ZrMn_2$ system

A similar analysis is also performed for $ZrMn_2$ Laves phase. A cluster model used is shown in Fig.19, which is constructed on the basis of the C14-type crystal structure of $ZrMn_2H_y$ hydride [52,53]. The positions of the hydrogen atoms have been studied using a neutron scattering technique [53], and there is a preferential occupancy of hydrogen atoms on the 12k site in the $P6_3/mmc$ space group. This site corresponds to the center of the tetrahedron consisting of two Zr atoms and two Mn atoms as shown in Fig.19. It is seen from this cluster model that two tetrahedra exist closely and form the Mn atomic plane as is indicated by the shadow in the figure. In order to examine the alloying effect on the hydriding properties, two Mn atoms are

substituted for various alloying elements, M. Therefore, the cluster model used is expressed as $H_2M_2Mn_8Zr_4$.

For $ZrMn_2$, the most important crystal unit is a tetrahedron where a hydrogen atom is located at the center. As shown in Fig.19, the hydrogen atoms are on the Mn atomic plane and the lattice expansion on the Mn atomic plane may take place so as to optimize the Mn-Mn interaction. The Zr-Mn interaction acts to suppress such a lattice expansion on the Mn atomic plane. Then, the ratio of the Zr-Mn bond order to the Mn-Mn bond order is calculated in this tetrahedron. Using this bond order ratio and also the M-H bond order as well, the equilibrium hydrogen pressures are examined for $ZrMn_{1.8}M_{0.2}$ alloys [54] and the results are shown in Fig.20. As shown in this figure, the calculated pressures of hydrogen are in agreement with the experimental data except for Ni.

A two-step plateau is observed experimentally in such a Ni-containing $ZrMn_2$ [54]. This implies that one hydride, which is supposed to be the hydride commonly observed in the other alloyed compounds, is very unstable and no longer formed, but instead another hydride appears as the hydrogenation proceeds. In addition, an empirical rule between the unit cell volume and the hydrogen pressure is valid for the other alloyed compounds, but invalid only for the Ni-containing compound. These experimental results appear to support the present calculation.

In addition to these system, the present approach is found to be valid in the $CaNi_5$ system.

5. Conclusion

The alloying effects on the electronic structures of $LaNi_5$ and Mg_2Ni intermetallic hydrides are investigated by the DV-Xα cluster method in order to understand the hydrogen absorption and desorption characteristics of these compounds.

The hydrogen atom is found to make a strong chemical bond with the Ni atoms rather than the La or the Mg atoms in pure $LaNi_5$ and in pure Mg_2Ni hydride. For $LaNi_5$ system, the La(M)-Ni and Ni(M)-Ni bond strengths in the small octahedron containing a hydrogen atom play the most dominant role to determine the hydride stability, where M is the alloying element substituted for the Ni or the La atoms in the compound. In fact, the ratio of the La(M)-Ni bond order to the Ni(M)-Ni bond order correlates well with the experimental data of the equilibrium plateau pressures

of hydrogen. Similar correlations are also obtained for other systems, TiFe, $ZrMn_2$ and $CaNi_5$.

On the other hand, for Mg_2Ni system, the Ni-Mg bond strength is most dominant since both the Ni-Ni and the Mg-Mg bond strengths are rather weak. It is shown that the hydride become unstable for those alloying elements, M, which are substituted for the Ni atoms and reduce the M-Mg bond strength. In fact, the change of the M-Mg bond strength with M correlates well with the measured change in the enthalpy of formation for the hydride.

In addition, a correlation between the unit cell volume and the hydriding properties for $LaNi_5$ and Mg_2Ni is discussed from a view of the nature of the chemical bond between atoms in small polyhedra and also of the possible lattice expansion induced by the hydrogenation.

Acknowledgments

The authors would like to appreciate Messrs. Y.Takahashi, T.Muto and T.Matsumura for their assistance in the calculations of electronic structures. We also acknowledge the Computer Center, Institute for Molecular Science, Okazaki National Institutes for the use of the SX-3/34R computer. This research was supported by the Grant-in-Aid for Scientific Research from the Ministry of Education, Science, Sports and Culture of Japan.

References

1. J.H.N.Van Vucht, F.A.Kuijpers and H.C.A.M.Bruning, *Philips Res. Rep.*, **25**, 133 (1970)
2. H.Sakaguchi, Y.Yagi, J.Shiokawa and G.Adachi, *J. Less-Common Met.*, **149**, 185 (1989)
3. T.Sakaki, H.Ishikawa, H.Miyamura, N.Kuriyama, S.Yamada and T.Iwasaki, *J. Electrochem. Sic.*, **138**, 908 (1991)
4. D.Lupu, A.Biris and E.Indrea, *Int. J. Hydrogen Energy.*, **7**, 783 (1982)
5. J.J.Reilly and R.H.Wiswall , *Inorg. Chem.*, **7**, 2254 (1968)
6. H.H.Van Mal, K.H.J.Buschow and A.R.Miedema, *J. Less-Common Met.*, **35**, 65 (1974)
7. K.R.Clay, A.J.Goudy, R.G.Schweibenz and A.Zarynow, *J. Less-Common Met.*, **166**, 153 (1990)

8. A.Zarynow, A.J.Goudy, R.G.Schweibenz and K.R.Clay, *J. Less-Common Met.*, **172-174**, 1009 (1991)
9. S.Orimo, H.Fujii and M.Tabata, *J. Alloys Comp.*, **210**, 37 (1994)
10. L.Zaluski, A.Zaluska and J.O.Ström-Olsen, *J. Alloys Comp.*, **217**, 245 (1995)
11. L.Zaluski, A.Zaluska, P.Tessier, J.O.Ström-Olsen and R.Schulz, *J. Alloys Comp.*, **217**, 295 (1995)
12. J.P.Darnaudery, B.Darriet and M.Pezat, *Int. J. Hydrogen Energy.*, **8**, 705 (1983)
13. T.Hirata, T.Matsumoto, M.Amano and Y.Sasaki, *J. Less-Common Met.*, **89**, 85 (1983)
14. M.Gupta, *J. Less-Common Met.*, **130**, 219 (1987)
15. T.Suenobu, I.Tanaka, H.Adachi, and G.Adachi, *J. Alloys Comp.*, **221**, 200 (1995)
16. S.K.Malik, F.Arlinghaus and W.E.Wallace, *Phys. Rev. B*, **25**, 6488 (1982)
17. M.Gupta, E.Belin and L.Schlapbach, *J. Less-Common Met.*, **103**, 389 (1984)
18. R.Hempelmann, D.Richter, G.Eckold, J.J.Rush, J.M.Rowe and M.Montoya, *J. Less-Common Met.*, **104**, 1 (1984)
19. D.Richter, R.Hempelmann and C.Schonfeld, *J. Less-Common Met.*, **172-174**, 595 (1991)
20. C.Schonfeld, R.Hempelmann, D.Richter, T.Springer, A.J.Dianoux, J.J.Ruch, T.J.Udovic and S.M.Bennington, *Phys. Rev. B*, **50**, 853 (1994)
21. P.Thompson, J.J.Reilly, L.M.Corliss, J.M.Hastings and R.Hempelmann, *J. Phys. F*, **16**, 765 (1986)
22. C.Schonfeld, R.Hempelmann, D.Richter, T.Springer, A.J.Dianoux, J.J.Ruch, T.J.Udovic and S.M.Bennington, *Phys. Rev. B*, **50**, 853 (1994)
23. J.Schefer, P.Fischer, W.Hälg, F.Stucki, L.Schlapbach, J.J.Didisheim, K.Yvon and A.F.Andersen, *J. Less-Common Met.*, **74**, 65 (1980)
24. K.Yvon, J.Schefer and F.Stucki, *Inorg. Chem.*, **20**, 2776 (1981)
25. P.Zolliker, K.Yvon, J.D.Jorgensen and F.J.Rotella, *Inorg. Chem.*, **25**, 3590 (1986)
26. Z.Garva, M.H.Mintz, G.Kimmel and Z.Hardi, *Inorg. Chem.*, **18**, 3595 (1979)
27. M.L.Post and J.J.Murray, *J. Less-Common Met.*, **134**, 15 (1987)
28. J.C.Slater, *Quantum Theory of Molecules and Solid. Vol. 4*, Wiley, New York, (1974)
29. F.W.Averill and D.E.Ellis, *J. Chem. Phys.*, **59**, 6413 (1973)
30. J.L.Soubeyroux, A.Percheron-Guegan and J.C.Achard, *J. Less-Common Met.*, **129**, 181 (1987)

31. K.H.J.Buschow and H.H.Van Mal, *J. Less-Common Met.*, **29**, 203 (1972)
32. P.Villars and L.D.Calvelt, *Pearson's Handbook of Crystallographic Data for Intermetallic Phases. Vol.1-3*, ASM, Metas Park, (1985)
33. E.Gurewitz, H.Pinto. M.P.Dariel and H.Shaked, *J. Phys. F: Met. Phys.*, **13**, 545, (1983)
34. Y.Takahashi, H.Yukawa and M.Morinaga, *J. Alloys Comp.*,**242**, 98 (1996)
35. R.S.Mulliken, *J. Chem. Phys.*, **23**, 1833, 1841, 2338, 2343 (1955)
36. H.Adachi, M.Tsukada and C.Satoko, *J. Phys. Soc. Japan*, **45**, 874 (1978)
37. H.Adachi, S.Shiokawa, M.Tsukada, C.Satoko and S.Sugano, *J. Phys. Soc. Japan*, **47**, 1528 (1979)
38. M.Tsukada, H.Adachi and C.Satoko, *Progr. in Surface Sci.*, **14**, 113 (1983)
39. M.Morinaga, N.Yukawa and H.Adachi, *J. Phys. Soc. Jpn.*, **53**, 653 (1984)
40. M.Morinaga, N.Yukawa and H.Adachi, *J. Phys. F*, **15**, 1071 (1985)
41. M.Morinaga, N.Yukawa, H.Adachi and T.Mura, *J. Phys. F.*, **17**, 2147 (1987)
42. M.Gupta, *J Less-Common Met.*, **103**, 103 (1984)
43. M.Gupta, *Materials Science Forum Vol.3*, Trans Tech publications, Swizerland, 77 (1988)
44. T.Sakai, private communication.
45. L.Pauling, Nature of the Chemica Bond 3rd edn, Ithaca, N.Y., Cornell University Press, (1960)
46. A.R.Miedema, *J. Less-Common Met.*, **32**, 117 (1973)
47. C.E.Lundin, F.E.Lynch and C.B.Magee, *J. Less-Common Met.*, **56**, 19 (1977)
48. M.H.Mendelsohe, D.M.Gruen and A.E.Dwight, *J. Less-Common Met.*, **63**, 193 (1979)
49. F.Reidinger, J.F.Lynch and J.J.Reily, *J. Phys. F*, **12**, L49 (1982)
50. J.J.Reilly and R.H.Wiswall, Jr., *Inorg. Chem.*, **13**, 218 (1974)
51. H.Y.Zu, J.Wu and Q.D.Wang, *J. Alloys Comp.*, **215**, 91 (1994)
52. L.Pontonnier, S.Miraglia, D.Fruchart, J.Soubeyoux, A.Baudry and P.Boyer, *J. Alloys Comp.*, **186**, 241 (1992)
53. J.Soubeyroux, L.Pontonnier, S.Miraglia, O.Isnard, D.Fruchart, E.Akiba, H.Hayakawa, S.Fujitani and I.Yonezu, *Z. Phys. Chem.*, Bd. **186**, 187 (1993)
54. S.Fujitani, I.Yonezu, T.Saito, N.Furukawa, E.Akiba, H.Hayakawa and S.Ono, *J. Less-Common Met.*, **172-174**, 220 (1991)

USE OF THE DV Xα-METHOD IN THE FIELD OF SUPERHEAVY ATOMS

B. Fricke, W.-D. Sepp, T. Bastug, S. Varga, K. Schulze, J. Anton
Fachbereich Physik, Universität Kassel, D-34109 Kassel

and

V. Pershina
GSI-Darmstadt, Postfach 110 552, D-64220 Darmstadt

Abstract:

We are discussing our manner to calculate the total energy for small molecules within the DV-Xα approximation by using only the monopol part of the potential in the solution of the Poisson equation. A discussion of the relativistic effects, including our results for heavy diatomic molecules, is followed by remarks on the choice of the exchange-correlation potential together with our results of calculations on molecules for the element 106 and their chemical interpretation. We conclude with results on very heavy correlation diagrams for collision systems with a united Z above 110.

1. Introduction

The DV Xα-method has been first proposed and formulated more than 25 years ago by Ellis and Painter[1] at Northwestern University. This method allows to calculate relatively large systems with medium accuracy. However the knowledge of energy eigenvalues, electron distributions, effective charges or overlap populations etc. are a valid tool for physical and chemical interpretations.
1971 was the first time one of us (B.F.) learned about this method at Northwestern University as a Post-Doc where he had strong connections to Don Ellis. However, as at that time only atoms were of any interest that method was not put to use. About one year later, Adachi and Rosen joined Don Ellis and the three worked together and developed the relativistic DV Xα-code[2], still in use today and absolutely necessary to handle molecules composed of atoms with relatively large nuclear charges.
When our present group became interested in quasi-molecules, which are generated in atomic collision systems, we started to use the relativistic DV Xα-method. With the help of Arne Rosen we were the first to calculate correlation diagrams of relatively heavy systems[3].

ADVANCES IN QUANTUM CHEMISTRY, VOLUME 29

0065-3276/97 $25.00

But already at that point we realized that the accuracy of this method was not very good. Many physical and chemical quantities, like binding energy or chemical bond distances, could not be calculated directly with this method. When we finally also started calculations of real molecules at chemical distances this deficiency became even more obvious and we began to improve the method itself in order to calculate the total energy of a system within the Xα-approximation.

2. The Dirac-Fock-Slater (DFS) Method

The energy functional of any many-electron system in the one-particle approximation with the single-particle wavefunction Φ_i can be written as

$$E[\Phi] = \sum \langle \Phi_i | t | \Phi_i \rangle + \int \rho \, V^N \, d^3r + \tfrac{1}{2} \int \rho \, V^C \, d^3r + \tfrac{1}{4} \int \rho \, V^{ex} \, d^3r + \sum (Z_1 Z_2) / |R_n - R_m| \qquad (1)$$

with the kinetic energy $t = \boldsymbol{\alpha}\, \mathbf{p} + \beta$,
the electron density $\rho(\mathbf{r}) = \Sigma\, n_i \, |\Phi_i(\mathbf{r})|^2$,
the direct Coulomb potential $V^C(\mathbf{r}) = \int \rho(\mathbf{r}) \,/\, |\mathbf{r} - \mathbf{r}'| d^3r$
and the local exchange potential $V^{ex}(\mathbf{r}) = -\, 3\, X_\alpha \, (3\pi\, \rho(\mathbf{r})/4)^{1/3}$.
If this functional is varied with respect to the single particle functions Φ_i one obtains the Dirac-Fock-Slater equations

$$(t + V^N + V^C + V^{ex}) \, |\Phi_i\rangle = \epsilon_i \, |\Phi_i\rangle \qquad i = 1, \; M \qquad (2)$$

where M is the number of electrons.
The $|\Phi_i\rangle$ are expanded in numerical atomic relativistic wave-functions $|\xi_j\rangle$ as a basis $|\Phi_i\rangle = \sum c_{ij} \, |\xi_j\rangle$.
The total energy E can then be re-written as

$$E = \sum n_i \, \epsilon_i - \tfrac{1}{2} \int \rho \, V^C \, d^3r - \tfrac{1}{4} \int \rho \, V^{ex} \, d^3r + \sum (Z_n Z_m) / |R_n - R_m| \; . \qquad (3)$$

During the iterations in the SCF process one has to calculate the Coulomb potential V^C from the electron density $\rho(\mathbf{r})$ of the last iteration, i.e. the Poisson equation must be solved

$$\Delta \, V^C = -\, 4\pi \, \rho(\mathbf{r}) \; .$$

So far so good, but in any real 3-dimensional calculation we are then faced with the problem of the Poisson equation having only an approximate solution either in terms of a Mullikan charge analysis or a least square fit with a multipole expansion. An exact solution would take too much time.

As a consequence we are unable to calculate the quantity E and V^C but approximated quantities $\hat{E}$ resp. $\hat{U}^C$. So in reality we calculate the quantity

$$\hat{E} = \langle \Phi_i | t + V^N + \hat{U}^C + V^{ex} | \Phi_i \rangle - \tfrac{1}{2} \int \rho \, \hat{U}^C \, d^3r - \tfrac{1}{4} \int \rho \, V^{ex} \, d^3r + \sum (Z_n Z_m) / |R_n - R_m| \qquad (4)$$

What is the error?
If we write $V^C = \hat{U}^C + V^C_{rest}$ and $\rho = \rho_0 + \rho_{rest}$ the total energy is $E = \hat{E} + \tfrac{1}{2} \int \rho \, V^C_{rest} \, d^3r$ which implies an error of first order. On the other hand one can re-write the exact total energy in the following form

$$E = \langle \Phi_i | t + V^N + \hat{U}^C + V^{ex} | \Phi_i \rangle - \tfrac{1}{2} \int \rho_0 \, \hat{U}^C \, d^3r - \tfrac{1}{4} \int \rho \, V^{ex} \, d^3r + \sum (Z_n Z_m) / |R_n - R_m| + \tfrac{1}{2} \int \rho_{rest} \, V^C_{rest} \, d^3r \, . \qquad (5)$$

The last part in this formula is the energy E_{rest} being the difference between calculated and exact value. This introduces an error in the total energy of second order only, because both terms in the integral are small quantities. In order to reduce this error even more this term can be minimized as well. This leads to an additional variational equation to be solved. Details of this complicated but very effective procedure can be found in Ref. 4.
The second important improvement we introduced to our calculations is the 3-dimensional integration scheme of Baerends et al.[5-7], which allows the calculation of highly accurate matrix elements.
The third change in the program was the implementation of a frozen core approximation. Unfortunately, this procedure does not save much computing time and space because during the first iteration - defining the frozen core part - all electrons must be taken into account to achieve orthogonalization of the valence orbitals to the core orbitals.
The main improvement to the calculation of the total energy is already achieved by using formula (5) instead of (4). The first improvement in combination with the second now allows to calculate potential energy curves of small molecules and systems.

3. Relativistic effects

If one or more atoms with large nuclear charges are part of a molecule, relativistic effects become very important. Just to remind ourselves, we would like to list here those relativistic effects which are known since about 30 years but which have to be kept in mind in this discussion in order to understand the effects which occur in relativistic molecular calculations.
The main effect is the so-called 'direct relativistic effect', a strong decrease of the radial distribution of the atomic wavefunctions with an angular momentum 1/2,

i.e. all $s_{1/2}$ and $p_{1/2}$ electrons contract towards the nucleus. And for an element Hg, for instance, this would be a 15% decrease. The $p_{3/2}$ electrons are less affected and all other outer electrons with higher angular momenta show very little decrease in their charge radii compared to a non-relativistic calculation with the same potential.

The second but often dominant effect is the so-called 'indirect relativistic effect'. This occurs as a change in the radial distribution of the wavefunctions because in a many-electron atom the inner electrons contract and thus shield the outer ones more effectively. As a result, this effect often compensates the direct relativistic effect for the d-wavefunctions; for the 5f-wavefunctions, however, this leads to an increased radius and the 4f-wavefunctions are hardly affected at all. As a consequence, the 5f-wavefunctions are chemically much more active in the Actinides than the 4f-wavefunctions in the Lanthanides.

The third effect is the relativistic spin-orbit (L-S) splitting of the shells with angular momenta $l=1$ and higher. In the case of the 2p elements the 2p shell is first filled with 3 electrons possessing parallel spin and then with the remaining 3 electrons with anti-parallel spin. This still holds true for the 3p and 4d series as well. In the case of the 5p elements the relativistic effect of the spin-orbit splitting is already so large that first 2 electrons fill the complete $5p_{1/2}$ shell then followed by the four $5p_{3/2}$ electrons. The subshells of these heavy elements have very little similarity with the non-relativistic wavefunctions and thus behave very differently in every self-consistent relativistic calculation. This is indicative of every non-relativistic calculation yielding quite unrealistic results.

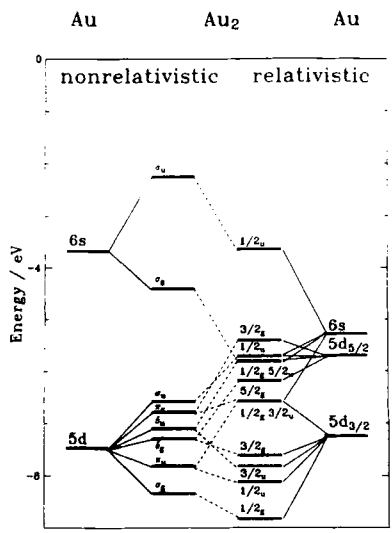

Fig.1 Energy eigenvalues of the outermost levels of Au and Au_2 from non-relativistic and relativistic DV-Xα calculations.

An example can be seen in Fig. 1: it shows the results for the diatomic system Au_2, both with a non-relativistic and a relativistic calculation for the atoms as well

as for the molecule[4]. As expected, the relativistic atomic calculation shows a strong increase in binding of the 6s electrons in the atom as well as a moderate indirect relativistic effect which decreases the binding of both 5d subshells. In addition, the $5d_{3/2}$ and $5d_{5/2}$ subshells show a strong spin-orbit splitting. In case of the molecular calculations the various linear combinations of these basis functions lead to quite a different pattern of the molecular levels in both cases.

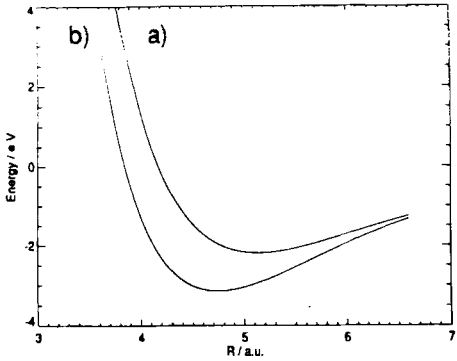

Fig. 2 Potential energy curve of the Au_2 molecule a) non relativistic b) relativistic.

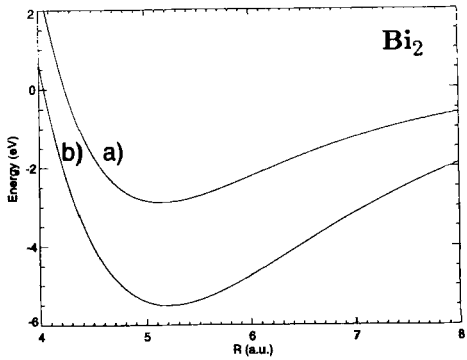

Fig. 3 Potential energy curve of the Bi_2 molecule a) relativistic b) non-relativistic.

Fig. 2 presents the potential energy curves of the Au_2 system from our molecular calculations, both non-relativistic and relativistic. The relativistic curve shows a strong decrease in bond length and an increase in binding, both of which can be attributed mainly to the direct relativistic effects of the outer 6s electrons.Tab. 1 compares the results of the non-relativistic and relativistic calculations for the three homologue molecules Cu_2, Ag_2 and Au_2 as well as the total relativistic effect in bond length ΔR_e, bond energy ΔD_e and vibrational frequency $\Delta\omega_e$. Fig. 3 shows the analogue potential energy curves[8] for the 5p-element diatomic molecule Bi_2.

	relativistically			non-relativistically		
Molecule	$R_e[a.u.]$	$D_e[eV]$	$\omega_e[cm^{-1}]$	$R_e[a.u.]$	$D_e[eV]$	$\omega_e[cm^{-1}]$
Cu_2	4.16 (4.20)	3.07 (1.97)	269.0 (264.5)	4.23	2.91	261.1
Ag_2	4.82 (4.67)	2.57 (1.66)	206.2 (192.4)	4.94	2.18	190.2
Au_2	4.75 (4.67)	3.16 (2.37)	191.2 (190.9)	4.23	2.91	261.1

Molecule	$\Delta R_e[a.u.]$	$\Delta D_e[eV]$	$\Delta\omega_e[cm^{-1}]$
Cu_2	0.07	0.16	8
Ag_2	0.12	0.39	16
Au_2	0.39	0.98	42

Tab. 1 a) Spectroscopic parameters R_e (bond length), D_e (bond depth) and ω_e (vibrational frequency) for Cu_2, Ag_2 and Au_2 from relativistic and non-relativistic calulations compared to experimental values. b) Relativistic effects for the spectroscopic parameters for the same diatomic molecules.

In this case the upper curve is the relativistic one because in the molecular calculation the dominant binding is via the $p_{3/2}$ basis functions which are somewhat less strongly bound compared to the non-relativistic p-electrons. Tab. 2 shows the differences between the relativistic and non-relativistic results for the first three 5p-electron diatomic molecules Tl_2, Pb_2 and Bi_2.

Molecule	$\triangle R_e[a.u.]$	$\triangle D_e[eV]$	$\triangle \omega_e[cm^{-1}]$
Tl_2	0.11	0.78	9.9
Pb_2	0.05	2.02	9.1
Bi_2	0.07	2.35	13.7

Tab. 2 Relativistic effects for the spectroscopic parameters for the diatomic molecules Tl_2, Pb_2 and Bi_2.

We should mention here that even for the diatomic molecule Hg_2, which is dominantely bound via van der Waals binding, our calculation[7] in terms of the Xα-approximation is valid to some extent. At least it results in a binding of the two atoms, which is non-trivial. The largest system so far is Hg_3, which we calculated in terms of a total energy calculation[7]. The two dimensional potential energy surface with its relatively flat minimum is presented in Fig. 4.

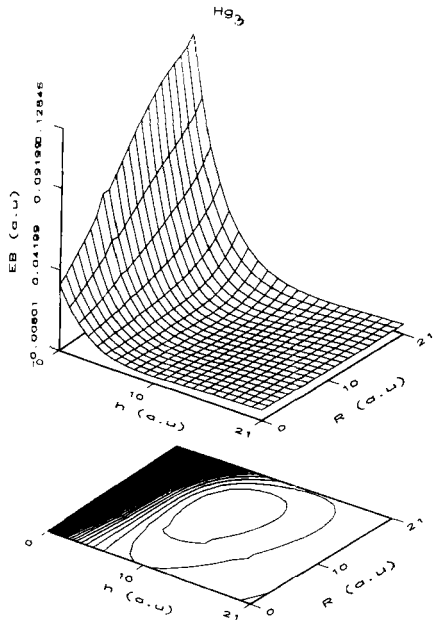

Fig. 4 Potential energy surface of the Hg_3 molecule from relativistic calculations. R is the length of one of the sides of the isosceles triangle and h is its height.

4. Comments on the exchange-correlation potential and the geometry optimization

All these examples so far show a consistent overbinding - the question is why ? We believe that the reason for this behaviour is caused by the special assumption of the Xα-approximation which we use and which originally was introduced by Slater in his local exchange approximation $\sim(\rho(\mathbf{r}))^{1/3}$. Even with the parameter α, which we always choose to be 0.7, this is only a rough approximation of the correct exchange and correlation potential. In principle, according to the Hohenberg-Kohn theorem, such an expression should exist. Up to now, however, only proposals for the exchange and correlation potential have been published and tried in actual calculations. The results improve staedily but are still far from satisfactory. Examples are the exchange correlation potentials of Barth-Hedin or Becke etc. The calculation of the more sophisticated ones is quite complicated because the gradient terms of first and sometimes second order are needed[9].
Automatic geometry optimization is one additional feature any molecular program used to calculate total energies should have nowadays. At the moment we are in the process of developing this feature for our molecular code but it proves to be a difficult task, because this procedure might conflict with the numerical accuracy achievable today.

5. Application to complicated many-electron molecules

The photoionisation spectrum of the OsO_4 molecule[10] is one example were we definitely see the relativistic influence. Fig. 5 compares the experimental results with our DVM-DFS method and extensive HF-CI calculations. The splitting of the $3t_2$ levels (originating from the spin-orbit splitting of the 5d-wavefunctions of Os) are quite well-reproduced.

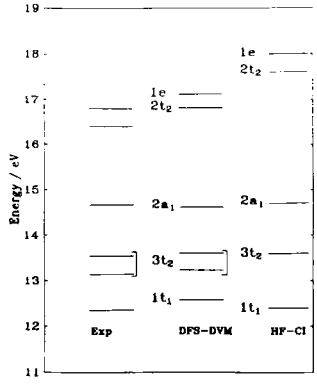

Fig. 5 Photo-ionization energies of the OsO_4 molecule from experiment, from V-Xα calculations and Hartree Fock-Configuration Interaction (HF-CI) calculations.

The relativistic effects become much stronger for even heavier elements. A real chemical experiment with the highest charge number ever undertaken is an experiment[11] with element 106, nowadays called Seaborgium (Sg). Element 104 is Rutherfordium (Rf) and element 105 Hahnium (Ha). Owing to the short half lives of their nuclei (minutes or less), the chemical procedure must be very fast. In addition one has to keep in mind that there is only one atom in the apparatus at any time. The chemical questions concerning chromatography experiments are the stability of Sg-halides and -oxyhalides in the gas-phase and those for extraction chromatography experiments are the stability of Sg complexes and their extraction behaviour in aqueous acid solutions.

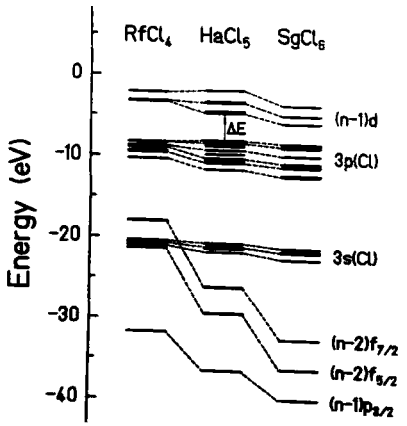

Fig. 6 Energy eigenvalues of the outermost levels of the group 4 to 6 highest chlorides from DV-Xα calculations.

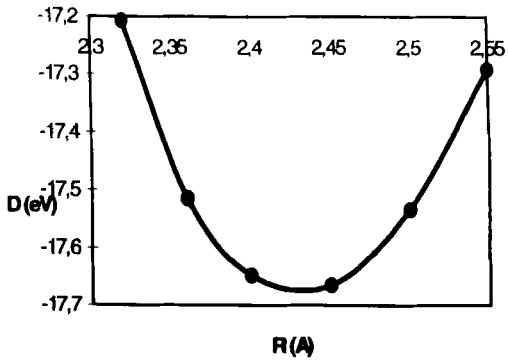

Fig. 7 Potential energy curve for $RfCl_4$ calculated with the DV-Xα total energy code. D is the binding.

To tackle these questions we have started on DV-Xα calculations[12]. The energy eigenvalues of the outer molecular orbitals for the group 4 to 6 highest chlorides are given in Fig. 6, where trends in the group can be seen already. Results of the Mullikan analysis and calculated effective charges Q_M and overlap populations for the molecules $M\text{-}Cl_n$ are presented in Tab. 3 for the group 4 to 6 and the homologues within the same groups. These are results[12] which allow to estimate thermochemical M-Cl bond energies and thus predict trends. One of the conclusions is

	MCl_4	MCl_5	MCl_6
Q_M	Zr 1.18	Nb 0.93	Mo 0.79
	Hf 1.04	Ta 0.95	W 0.74
	Rf 1.07	Ha 0.81	Sg 0.59
OP(M-CL)	Zr 0.48	Nb 0.41	Mo 0.36
	Hf 0.55	Ta 0.50	W 0.46
	Rf 0.57	Ha 0.52	Sg 0.45

Tab. 3 Effective charges (QM) and overlapp populations (OP) for MCl_4.

that there should be a decrease in the metal-halogen bonding within the 6d row: $RfCl_4$ > $HaCl_5$ > $SgCl_6$. Thus it is predicted that $SgCl_6$ will decompose into the compound $SgCl_5$ plus ½ Cl_2. The same procedure is used to predict the behaviour of Oxy-Halides like $SgOCl_4$, where we expect also a decomposition into $SgOCl_3$ plus ½ Cl_2. In addition we calculated all compounds with 2 Oxygen atoms. Those results led us to conclude that SgO_2Cl_2 will be relatively stable and thus can be used to extract element 106 in the gas-phase chromatography experiments. First results for the molecule $RfCl_4$ have been achieved with our total energy program. Fig. 7 presents a one-dimensional potential energy curve where the same distance to all four Cl atoms.
This is just a glimpse at the large number of calculations with the DV-Xα code for this type of complex molecules in the region of superheavy atoms. Details can be found in the references 12 - 15.

6. Results for Superheavy correlation diagrams and MO X-rays

A very different application of DV-Xα calculations are correlation diagrams for very heavy ion-atom collision systems. These correlation diagrams present the molecular energy eigenvalues as function of internuclear distance and thus give a basis for the description of the behaviour of electrons or holes during the collision. If one of the collision partners is highly ionized, holes can be brought into the collision system and transferred at small internuclear distances to levels of the partner causing a transfer to occur. Of course, such a correlation diagram is only a static description; in reality this is a dynamic system following the solution of the time-dependent Dirac-equation which allows a direct exchange of electrons between all molecular levels of the correlation diagram in the collision. One example we would like to discuss.
The latest results we can present are calculations[16] for the system Ni-Pb measured by Schuch et al.[17] and Pb-Ni by Mokler et al.[18]. For the corresponding correlation diagram see Fig. 8. In the experiments the Ni K X-rays and the Pb L X-rays are observed. The interesting fact is that here the hole transfer occurs (in the one-particle picture) from the Pb M-shell via the $3d_\sigma$-coupling to the Ni K-shell and via the radial coupling at the internuclear distance R≈0.14 a.u. to the Pb L-subshells. M. Zoran et al.[19] have been especially interested in this system and measured a number of cross sections. We performed coupled channel calculations taking into account as many as 90 molecular levels in the coupled channel calculations. The problem is that the incoming ion brings only empty O-levels into the collision system. Various calculations at large internuclear distances gives us an idea of the hole distribution of the ion during its passage inside the solid. The vacancy production probability Ni_K and Pb_L from the system Pb^{42+} on Ni is presented in Fig. 9. There is no perfect agreement but a reasonably good one considering the complexity of the problem.

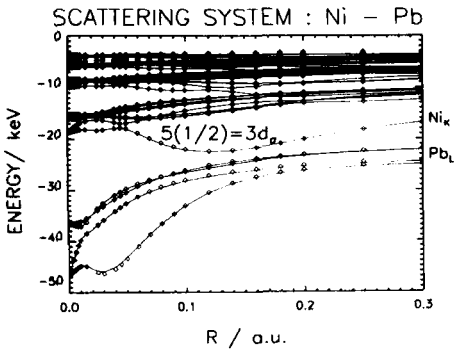

Fig. 8 Correlation diagram for the system Ni on Pb taking into account 80 electrons.

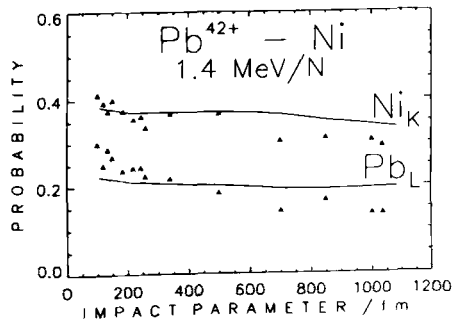

Fig. 9 Vacancy production probability for Pb^{42+} on Ni solid targets. The triangles are the experimental values from Ref. 17.

Another possibility to obtain direct information from such a collision system is the observation of Molecular orbital (MO) X-rays resulting from electronic de-excitations between the molecular levels during the collision under emission of non-characteristic photons. The result of our many-particle calculation[20] is given in Fig. 10 where the spectrum of the collision system 20 MeV Cl^{16+} on Ar is compared with the experiment[21]. In this calculation the radiation field was coupled to the system by first order perturbation theory but the wavefunctions were taken from the solution ot the time-dependent relativistic DV-Xα calculations[20].

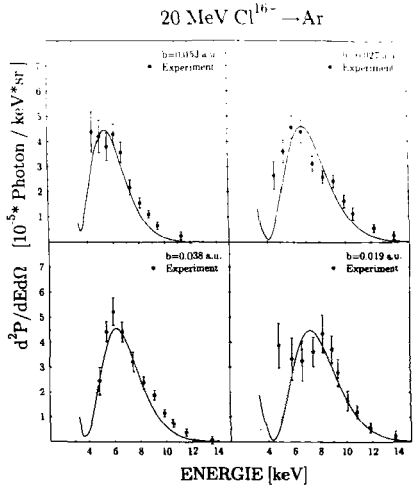

Fig. 10 MO X-ray spectrum for the system 20 MeV Cl^{16+} on Ar for four different impact parameters. The full curve is our calculation[20] scaled by a factor of 0.5. The experiment is from Schuch et al.[19]. b is the impact parameter.

Keeping this in mind we propose now to initiate experiments for very heavy ion-atom collisions in order to learn about the behaviour of the innermost levels of systems with a united Z in the superheavy region. The quality of the theoretical description within our DV-Xα method is now so good that

- accurate correlations diagrams can be calculated,
- full coupling treatment including all rotational and radial couplings of the inner shells can be performed and
- a many-particle interpretation is possible which allows to take into account the electron excitation and transfer in a collision of a naked projectile in a solid state target.
- In addition MO X-ray calculations and experiments are under way which also should provide information about the inner level structure.

Hopefully, this experiment then will allow to determine the level behaviour of the innermost levels of united systems like the one in Fig. 11 (U on Pb). First theoretical attempts in this direction have been made already many years ago by Kirsch et al.[22], in comparing Pb-Pb collision systems (which first were calculated as a many-electron system in Ref. 23) with only small initial ionizations[24].

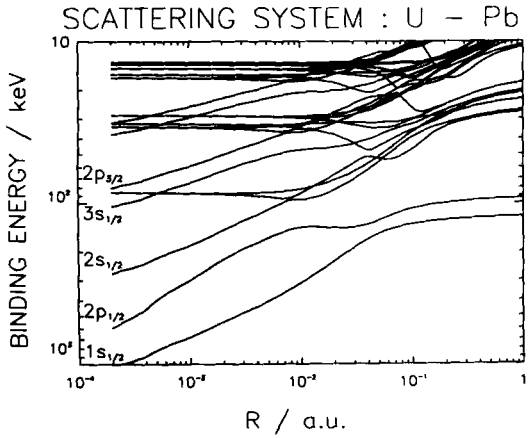

Fig. 11 Correlation diagram of the system U on Pb which takes into account 96 electrons. The point of interest is the behaviour of the innermost levels at small internuclear distances which is very different to correlation diagrams for small Z.

In time improved measurements and analysis are expected to yield also information on QED corrections, level structure or any of the other missing influences like the transient magnetic field.

7. Conclusions

The DV-Xα method is very useful to obtain results

- on systems where one would like to have a first approximation and where Quantum chemical calculations are too time consuming
- on systems where Quantum Chemical calculations are not yet possible, i.e.

- very large systems and
- relativistic systems, where up to now only pseudo-potential calculations are possible.

- The DV-Xα method needs further strong improvements in the development of the method in order to
  - improve the quality of the integration
  - calculate total energies
  - improve the eschange-correlation approximation
    - the Xα approximation used so far has the disadvantage that the binding always comes out to be too strong
    - the angular binding is not described very accurately
  - and one needs an automatic geometry optimization.

This summary of applications from chemical calculations to heavy-ion collision physics shows that DV-Xα calculations are an important tool in all of these fields and thus shows the usefulness of this method.

Acknowledgement

T.B. and S.V. thank the Deutsche Forschungsgemeinschaft (DFG) and K.S. and J.A. the Gesellschaft für Schwerionenforschung (GSI) for financial support.

References

1. D.E. Ellis and G.S. Painter, Phys. Rev. **B2**, 2887 (1970)
2. A. Rosen, D.E. Ellis,H. Adachi and F.W. Averill, J. Chem. Phys. **65**, 3629 (1976)
3. B. Fricke, T. Morovic, W.-D. Sepp, A. Rosen and D.E. Ellis, Phys. Lett. **A59**, 375 (1976)
4. T. Bastug, D. Heinemann, W.-D. Sepp, D. Kolb and B. Fricke, Chem. Phys. Lett. **211**, 119 (1993)
5. P.M. Boerigter, G. te Velde and E.J. Baerends, Int. J. Quantum Chem. **33**, 87 (1988)
6. G. te Velde and E.J. Baerends, J. Comp. Phys. **99**, 84 (1992)
7. T. Bastug, W.-D. Sepp, D. Kolb, B. Fricke, E.J. Baerends and G. te Velde, J. Phys. **B28**, 2325 (1995)
8. T. Bastug, W.-D. Sepp, D. Kolb, B. Fricke and K. Rashid, Phys. Rev. A in print
9. a summary is given in the book: R.M. Dreizler and E.K.U. Gross, Density Functional Theory, Springer Verlag Berlin 1990

10. P. Pyykkö, J. Li, T. Bastug, B. Fricke and D. Kolb, Inorg. Chem. **32**, 1525 (1993)
11. H.W. Gäggeler et al., GSI Scientific report 1991, GSI 92-1
12. V. Pershina and B. Fricke, J. Phys. Chem. **98**, 6468 (1994)
13. V. Pershina, B. Fricke, J.V. Kratz and G.V. Ionova, Radiochim. Acta **64**, 37 (1994)
14. V. Pershina and B. Fricke, J. Phys. Chem. **99**, 144 (1995)
15. V. Pershina and B. Fricke, J. Phys. Chem. **100**, 8748 (1996)
16. J. Anton, K. Schulze, P. Kürpick, W.-D. Sepp, B. Fricke, Proc. 2. Euroconf. Atom. Phys. with Stored Highly charged Ions, Stockholm Juni 1996
17. V. Zoran, A. Enulescu, I. Piticu, G. Wintermeyer, T. Kambara, M. Gabr, R. Schuch, Phys. Rev. Lett. **64**, 527 (1990)
18. A. Warczak, D. Liesen, D. Maor, P.H. Mokler, W.A. Schönfeldt, J. Phys. **B16**, 1575 (1983)
19. V. Zoran et al., EAS **16**, 33 (1995)
20. K. Schulze, J. Anton, W.-D. Sepp, B. Fricke and P. Kürpick, J. Phys. B in print
21. R. Schuch et al., Phys. Rev. **A37**, 3313 (1988)
22. J. Kirsch, W. Betz, J. Reinhardt, B. Müller, W. Greiner, Z. Phys. **A292**, 227 (1979)
23. W.-D. Sepp, B. Fricke, T. Morovic, Phys. Lett. **A81**,258 (1981)
24. W.E. Meyerhof, T.K. Saylor, S.M. Lazarus, A. Little, B.B. Triplett, L.F. Chase, R. Anholt, Phys. Lett. **32**, 1279 (1974)

Electronic Structures of Metal Carbides TiC and UC: Similarity and Dissimilarity

Rika Sekine

Department of Chemistry, Shizuoka University, Ohya 836, Shizuoka, 422 Japan

Hirohide Nakamatsu, Takeshi Mukoyama

Institute for Chemical Research, Kyoto University, Uji, Kyoto, 611 Japan

Jun Onoe

The Institute of Physical and Chemical Research (RIKEN), 2-1 Hirosawa, Wako, Saitama, 351-01 Japan

Masaru Hirata

Oarai Research Establishment, Japan Atomic Energy Research Institute, 3607 Narita, Oarai, Ibaraki, 311-13 Japan

Masayoshi Kurihara

4-27-12 Futabadai, Mito, Ibaraki , 311-41, Japan.

Hirohiko Adachi

Department of Material Science and Engineering, Kyoto University, Yoshidahonmachi, Sakyo-ku, Kyoto, 606 Japan

Abstract

To elucidate the nature of chemical bonding in metal carbides with the NaCl structure, the valence electronic states for TiC and UC have been calculated using the discrete-variational (DV) Xα method. Since relativistic effects on chemical bonding of compounds containing uranium atom become significant, the relativistic Hamiltonian, i.e., the DV-Dirac-Slater method, was used for UC. The results

ADVANCES IN QUANTUM CHEMISTRY, VOLUME 29

0065-3276/97 $25.00

obtained using a neutral cluster model of C-M6-C12-C6 with *Oh* symmetry are compared with each other. The present calculations for the UC and TiC reproduce fairly well the peak position of the experimental valence X-ray photoemission spectrum, indicating that the cluster model is appropriate to treat with the bulk properties of the metal carbides. The Mulliken population analysis demonstrated that the ionicity of UC is greater than that of TiC, while the covalency of UC is weaker than that of TiC. This discrepancy between the bond nature of the two compounds is discussed in connection with the similarity and dissimilarity of their physical properties.

1. Introduction

Metal carbides with the NaCl structure have been paid much attention to its remarkable physical properties, such as extreme hardness, very high melting points, and metallic-like electric conductivity [1,2]. Being significantly less reactive than most metals, the compounds have been used as cold cathode emitters. It is essential to understand the bond nature of these compounds for practical use of their physical properties. However, few attempts to study the chemical bonding of these compounds have been made until now. The aim of the present work is to examine TiC and UC as typical examples of transition and heavy metal carbides and to compare their bond natures in connection with their physical properties.

Table 1 summarizes physical properties of TiC and UC. The M-C bond length of UC is 2.481 Å, while that of TiC is 2.164 Å. The difference of 0.317 Å between their bond lengths is comparable to that of 0.222 Å between the atomic radii of the corresponding metal elements. Both compounds have high melting points, but there is a quite difference in micro-hardness and resistivity between TiC and UC. Since the valence electrons of Ti atom are attributed to the 3d-electrons and those of U atom to the 5f- and 6d-electrons, it is valuable to consider how these valence electrons contribute to the physical properties of their compounds.

Table 1. Physical properties of TiC and UC

	TiC	UC
M-C bond length [Å]	2.164 a)	2.481 c)
Atomic radius (metal) [Å]	1.32 b)	1.542 d)
Melting point [°C]	3067 a)	2250-2590 e)
Micro-hardness [kg/mm^2]	2900 a)	750-800 e)
Resistivity [$\mu\,\Omega$ cm]	50-250 b)	5-99 e)

a) ref. [1], b) ref. [2], c) ref. [3], d) ref. [4], e) ref. [5]

In the present study, we used a neutral C-M6-C12-C6 cluster model (abbreviated as MODEL I) for TiC and UC compounds in order to compare their electronic structures and bond natures. However, this model does not represent the bulk state of TiC and UC strictly, because outermost atoms of the cluster are not located in their bulk potential. In order to calculate solid-state electronic structures more accurately than MODEL I, we developed a chemically complete cluster model (abbreviated as MODEL II) by introducing periodic potentials to MODEL I and examined this modified model for TiC. We compared the valence electronic structure of TiC between the two cluster models and demonstrate the advantages of MODEL II in this work.

2. Computational Method

We used the DV Hartree-Fock-Slater method for TiC, while for UC we used the DV Dirac-Slater (DV-DS) method taking fully relativistic effects into account. The basis functions used were 1s-2p for C atom, 1s-4p for Ti atom, and 1s-7p for U atom. The bond nature of TiC and UC compounds were studied by Mulliken population analysis [6,7]. The details of the nonrelativistic and relativistic DV-Xα molecular orbital methods have been described elsewhere [7,8,9].

In the present calculation, we employed a neutral C-M6-C12-C6 cluster model (MODEL I) as shown in Fig. 1. The bond lengths between M and C were taken

from the values of the bulk crystals (Ti-C: 2.164 Å and U-C: 2.481 Å). The cluster has *Oh* symmetry.

In order to consider the ***periodic crystal*** potential in ***cluster*** calculations, we developed the "chemically complete cluster model" (MODEL II) [10], which is similar to that proposed by Goodman et al. [11]. In our cluster model, atoms in the cluster are classified into three types. Type I atoms are "seed atoms" of which basis functions are obtained by the self-consistent procedure. The seed atoms are chemically complete. Namely, they are put in a potential environment similar to that in the bulk. Type II atoms are "passive atoms" of which basis functions are solved in the same potential field as for the type I atoms of the same species. Type III atoms have atomic potentials which are the same as in the type I atoms, but their wavefunctions are not included in molecular orbital calculations. The validity of MODEL II is tested for TiC in comparison with the results obtained using MODEL I.

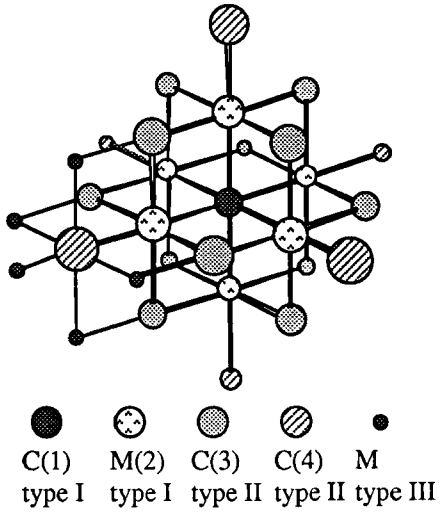

Figure 1. C-M_6-C_{12}-C_6 cluster (M = Ti, U).
A part of type III atoms is shown.

Figure 1 shows C-M_6-C_{12}-C_6 cluster model used in the present calculation The central C and six Ti atoms are categorized into type I atoms and chemically complete. Both C and Ti are surrounded by six Ti atoms and the same number of C atoms, respectively. The outermost eighteen C atoms are classified as type II atoms. Though these atoms are the edge or the corner ones in the cluster model, their potentials are duplicates of that of the central C. Surrounding the type II of C atoms, type III of fifty-six Ti atoms with the potential of "the seed" Ti atoms are situated, though the only a few examples of type III atoms are displayed in Fig. 1. No further external potential was used for C-M_6-C_{12}-C_6 cluster, since polarization between Ti and C was expected to be very small (and really was small) and the long range Coulomb potential was thought to be negligible for the present system. The self-consistent calculation was performed for the C-M_6-C_{12}-C_6 cluster until the neutral condition is achieved between the central C and the surrounding Ti.

3. Results and Discussion

3. 1. Electronic structure of TiC

In order to interpret the bond nature of TiC, we examined the contribution of each atomic orbital to the total density of states (DOS) in the valence region. Figure 2 shows total and partial DOS of TiC which are composed of the central C and the adjacent Ti atoms for MODEL II, where the components of Ti are multiplied by 1/6 for normalization. Figure 2 (a)~(d) show the total DOS, partial DOS of the Ti4s-C2s, Ti4p-C2p, Ti3d components, respectively, in units of [electrons per (unit cell)•eV]. The solid and broken lines represent the Ti and C components. It is found that the peak I of the total DOS consists of only the C2s component, the peak II contains the Ti3d and C2p components. The peak III constitutes mainly from the Ti3d and Ti4p components. The present results agree with those reported by Neckel et al. [12]. It is remarkable that the states just below Fermi level in Fig. 2(a), which are marked with *, include mainly the Ti3d component. Didziulis et al. [13] have obtained valence photoemission spectra of TiC with different incident photon energies and concluded that the peak marked

with * consists of only the Ti3d component. This is consistent with our results. The calculated DOS obtained in the present work well reproduced experimental spectra [10].

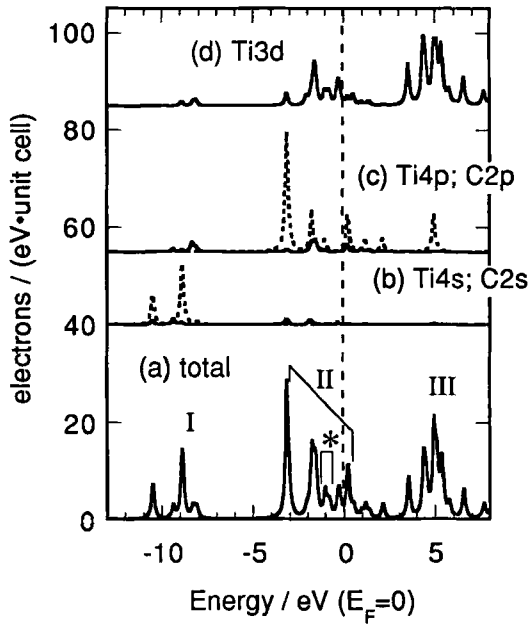

Figure 2. DOS of TiC for MODEL II. Where, (a), (b), (c), and (d) represent the total DOS, the partial DOS of Ti4s & C2s, Ti4p & C2p, and Ti3d, respectively. The solid lines exhibit the Ti atom component, while the broken lines exhibit the central C atom component.

Table 2 shows the effective charge and orbital populations for each atom of TiC for MODEL I and II. The MODEL I and II have two types of C atoms: the central

C atom (type I) and the corner and edge C atoms (type II). The latter ones are not chemically complete, and we will consider the results obtained for the former C atom in the following discussion. It is found that the charge neutrality of the stoichiometric pairs Ti-C is almost satisfied using MODEL II. The effective charges on the Ti and C atoms are obtained to be +0.42 and -0.42, respectively. These values are comparable to the reported values of +0.5 and -0.5 by Neckel [14]. The advantage of MODEL II is seen in comparison with the values obtained using MODEL I (the third column) for TiC. The difference between the absolute values of effective charges on C (-0.50) and Ti (+0.59) is large for MODEL I. This fact indicates that MODEL II is indispensable for the charge neutrality.

Table 2. Orbital populations and effective charges for TiC and UC compounds.

	MODEL II	MODEL I		MODEL I
C2s	1.60	1.52		1.51
C2p	2.82	2.99		3.13
Effective charge	-0.42	-0.50		-0.64
			U5f	2.33
Ti3d	2.45	2.41	U6d	2.43
Ti4s	0.44	0.39	U7s	0.35
Ti4p	0.71	0.62	U7p	0.34
Effective charge	+0.42	+0.59		+0.65

Table 3 shows the bond overlap populations for the Ti-C and Ti-Ti bonding. Bond overlap population is a good indicator for strength of covalent bonds [6,15]. The positive and negative values of the bond overlap population represent "bonding" and "antibonding" characters, respectively. The bond overlap population between Ti and C is +0.36, while that between Ti and Ti is +0.07.

Considered that the conductive electrons screen the ionic interaction between Ti and C, it is concluded that the Ti-C covalent bonding mainly contributes to the cohesive energy of TiC [10]. In addition, we compared the results of MODEL I and II. It is found that the M-C bond overlap populations agree well with each other, while the M-M bond overlap populations are a little bit different.

From the results of Tables 2 and 3, we demonstrated that MODEL II is more suitable to reproduce the electronic structure of bulk compounds than MODEL I. The details of MODEL II applied to TiC have been discussed elsewhere [10].

Table 3. Bond overlap populations of TiC and UC [per bond].

	M-C	M-M
TiC MODEL II	+0.36	+0.07
TiC MODEL I	+0.36	+0.05
UC MODEL I	+0.29	-0.01

3.2. Electronic structure of UC

Figure 3 shows the density of states obtained for UC using MODEL I. The partial DOS of each atomic orbital component is also plotted. The DOS indicates the metallic character and the U5f component are located around the Fermi level (E_F). The $U5f_{5/2}$ and $U5f_{7/2}$ components are largely separated by spin-orbital interaction. The E_F lies in the $U5f_{5/2}$ atomic orbital, while most of the $U5f_{7/2}$ states constitute unoccupied molecular orbitals. The U6d atomic orbital also mainly contribute to unoccupied states, but a part of the U6d component is located in the occupied states in the range of 0 ~ -4 eV. The C2p component contributes to the peak at -4 eV. The C2s component has a main peak at -10 eV and a small peak located in the range of -7 ~ -8 eV. The latter peak arises from the surface atoms of the cluster, that is, MODEL II (Fig. 1) has two types of carbons; the central C atom and the surrounding C atoms in different circumstances. As a result, the

component of the central carbon, which is shown in Fig. 3, is hybridized with components of the surface carbons. This hybridization gives rise to small broad peaks at -7 ~ -8 eV. The present calculations of DOS and atomic orbital components are in qualitatively agreement with those reported by Weinberger [16] and Hasegawa et al. [17].

The top panel in Fig. 3 shows experimental spectra obtained by X-ray photoelectron spectroscopy (occupied states) and bremsstrahlung isochromat spectroscopy (unoccupied states) [18]. We can compare the present DOS (Fig. 3) with the experimental spectra. The peak A of the experimental spectra is assigned to the $U5f_{5/2}$ component, the shoulder B to the $U6d_{5/2}$ and $U6d_{3/2}$ components, and the broad hump C to the $C2s_{1/2}$ component. The $C2p_{1/2}$ and $C2p_{3/2}$ components are not observed in the XPS, because its photoelectric cross section [19] is very small for excitation by X-ray photon energy (Al Kα, 1486.5 eV) used in their experiment.

We next examine the nature of chemical bonding in UC. The effective charges on the atoms and the orbital population of each atomic orbital are shown in the fifth column in Table 2. Although we did not apply MODEL II to this compound, the absolute values of the C (-0.64) and U (+0.65) effective charges were almost equal to each other. This allow us to compare the effective charges of UC for MODEL I with those of TiC for MODEL II. Compared the effective charges between TiC and UC compounds, it is found that the charge transfer from the metal atoms to the carbon atoms for UC is larger than that for TiC. In other words, the ionicity of UC is greater than that of TiC. The bond overlap populations for UC (MODEL I) is shown in Table 3. The bond overlap population between U and C is +0.29, while that between U and U is almost zero. In case of UC, the M-C interaction mainly contributes to the chemical bonding and the M-M interaction is negligibly small.

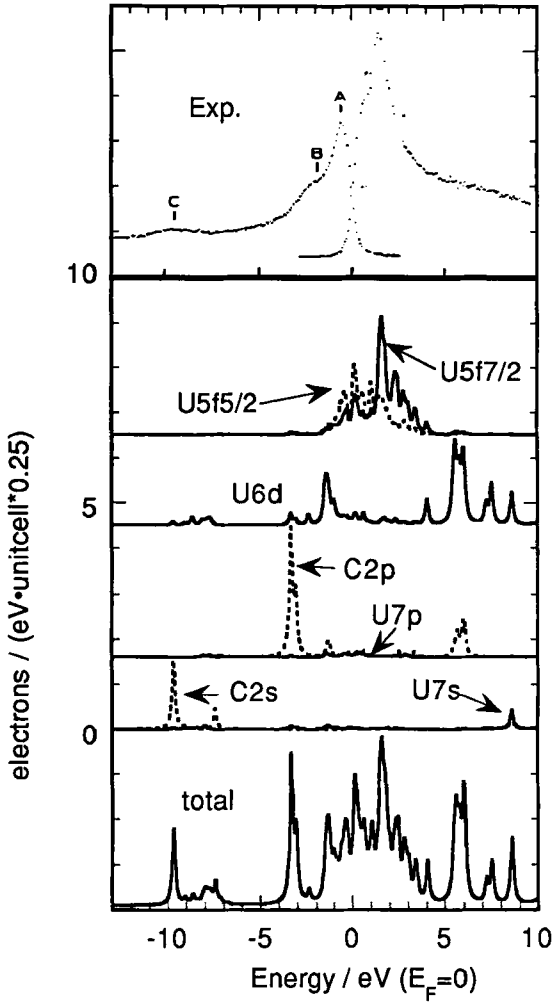

Figure 3. Valence DOS of UC for MODEL I.
The top panel shows XPS and BIS for UC, taken from ref.[18]

3.3. Comparison of the bond nature between TiC and UC

We showed the bond overlap populations for TiC and UC compounds in Table 3. To characterize the bonding nature of each compound, we examine the overlap populations between the atomic orbitals and the energy for these atomic orbitals. Tables 4 and 5 show the overlap populations between the atomic orbitals for TiC and UC, respectively.

For TiC, the orbital overlap population (+0.16) between Ti3d and C2p is the largest. The corresponding combination for UC is the U6d-C2p (+0.10). However, the U5f-C2p overlap population is small to be +0.05. The differences in bonding between these compounds is further analyzed in terms of energies for atomic orbitals. Atomic orbital energies in clusters without covalent interaction are taken from the diagonal elements of the Fock matrix. The energies of the C2p and Ti3d atomic orbitals for TiC were -1.8 eV and 9.1 eV, respectively. On the other hand, the energies of the C2p (the average of $C2p_{3/2}$ and $C2p_{1/2}$), U6d (the average of $6d_{3/2}$ and $6d_{5/2}$), $U5f_{5/2}$, and $U5f_{7/2}$ for UC were -6.0 eV, 0.2 eV, 0.4 eV, and 1.3 eV, respectively. The energy difference (10.9 eV) between the Ti3d and C2p is larger than those (6.2 eV ~ 7.3 eV) between C2p and U6d, 5f, while the overlap population of the Ti3d-C2p pair is the largest as indicated in Tables 4 and 5. The off-diagonal elements in the Fock matrix produce the strong Ti3d-C2p interaction. Large overlaps among the Ti3d and C2p atomic orbitals cause the widely dispersed Ti3d band and the significant mixing of Ti3d and C2p bands as shown in Fig. 2. In contrast, the separation of the U and C bands for UC are large, as shown in Fig. 3. The mixing between the Ti3d and C2p atomic orbitals in the lower energy region of the Ti3d band results in a bonding interaction. The strong Ti3d-C2p covalent interaction is attributed to the hardness of this compound. This is consistent with the fact that the micro-hardness of TiC is stronger than that of UC, as shown in Table 1.

Here, we go back to the other physical properties indicated in Table 1. Both the TiC and the UC compounds have high melting points. The melting point relates to the Coulomb and the covalent interactions. The Coulomb interaction is larger for UC than TiC: the effective charge for the former is ±0.65, while that for the latter is ±0.42. On the other hand, as discussed in the previous paragraph, the

covalent interaction is larger for TiC. As a result, the melting points are comparable with each other. As to the resistivity, the value is a little larger for TiC. The conductivity, which is the inverse of the resistivity, relates on the density of states (DOS) at the Fermi level (E_F). We can simply compare the height of DOS at the E_F, since the FWHM used for the lorentzian curve is the same for TiC (Fig. 2) and UC (Fig. 3). As shown in Fig. 2, the height is 4 for TiC, while the value is 12 for UC (Fig. 3). Since the DOS at E_F is larger for UC than TiC, the resistivity is smaller for the former than the latter.

Table 4. Orbital overlap populations for MODEL II [per bond].

	C2s	C2p	Ti4s	Ti4p	Ti3d
Ti4s	0.02	0.05	0.00		
Ti4p	0.02	0.08	0.01	0.01	
Ti3d	0.04	0.16	0.01	0.02	0.03

Table 5. Orbital overlap populations for MODEL I [per bond].

	C2s	C2p	U6s	U6p	U7s	U7p	U6d	U5f
U6s	-0.01	-0.02	0.00					
U6p	-0.02	-0.02	0.00	0.00				
U7s	0.03	0.01	0.00	0.00	0.00			
U7p	0.02	0.06	0.00	0.00	-0.01	0.02		
U6d	0.03	0.10	0.00	0.00	0.00	0.00	0.01	
U5f	0.01	0 .05	0.00	0.00	0.00	0.00	0.01	0.00

4. Summary

The similarity and dissimilarity in physical properties between TiC and UC metal carbides have been studied using the nonrelativistic and relativistic discrete-variational (DV) Xα methods. To elucidate the nature of chemical bonding in the metal carbides, the valence electronic states for TiC and UC have been calculated using two cluster models. The following conclusions were obtained in the present study.

1) The present calculations for the UC and TiC reproduce fairly well the peak position of the experimental valence X-ray photoemission spectrum, indicating that the cluster models used are appropriate to treat with the bulk properties of the metal carbides.

2) The Mulliken population analysis demonstrated that the ionicity of UC is greater than that of TiC, while the covalency of UC is weaker than that of TiC. This discrepancy between the bond nature of the two compounds is connected with their physical properties.

3) It is demonstrated that the chemically complete cluster model (MODEL II) reproduces the electronic structure of bulk TiC more accurately than the conventional cluster model (MODEL I). This MODEL II is useful to study the electronic structure and chemical bonding of solid-state materials.

References

[1] L. E. Toth, Transition Metal Carbides and Nitrides; Academic Press: New York, (1971).

[2] D. R. Lide (Ed.), CRC Handbook of Chemistry and Physics, 74th Ed., CRC Press (1993).

[3] P. Chiotti, V. V. Akhachinskij, I. Ansara and M. H. Rand, The Chemical Thermodynamics of Actinide Elements and Compounds, Part 5, The actinide Alloys, IAEA, Vienna, STI/PUB/424/5 (1981).

[4] J. J. Katz, G. T. Seaborg and L. R. Morss, The Chemistry of the Actinide Elements, 2nd Ed., Vol. 2, p.1450, London, New York, Chapman and Hall, (1986).

[5] J. H. Gittul, Uranium, Series of Metallurgy of the Rarer Metals, Vol. 8, p.434, London, Butterworths, (1963).

[6] R.S. Mulliken, J. Chem. Phys. 23 (1955) 1833, 1841, 2338, 2343

[7] H. Adachi, M. Tsukada, and C. Satoko, J. Phys. Soc. Jpn., 45 (1978) 875.

[8] A. Rosén and D. E. Ellis, J. Chem. Phys., **62**, 3035 (1975).

[9] H. Nakamatsu, H. Adachi, and T. Mukoyama, Bull. Inst. Chem. Res. Kyoto Univ., **70**, 16 (1992).

[10] R. Sekine, E. Miyazaki, H. Nakamatsu, and T. Mukoyama, in preparation.

[11] G. L. Goodman, D. E. Ellis, E. E. Alp, and L. Soderholm, J. Chem. Phys., **91**, 2983 (1989).

[12] A. Neckel, P. Rastl, R. Eibler, P. Weinberger and K. Schwarz, J. Phys. C: Solid State Phys., **9**, 579 (1976)

[13] S. V. Didziulis, J. R. Lince, T. B. Stewart, E. A. Eklund, Inorg. Chem. **33**, 1979 (1994) .

[14] A. Neckel, Int. J. Quantum Chemistry, **23**, 1317 (1983).

[15] V. Pershina, W.-D. Sepp, B. Fricke and A. Rosén, J. Chem. Phys., **96**, 8367 (1992).

[16] P. Weinberger, Ber. Bunsenges. Phys. Chem., **81**, 905 (1977).

[17] A. Hasegawa and H. Yamagami, J. Phys. Soc. Jpn., **59**, 218 (1990).

[18] T. Ejima, K. Murata, S. Suzuki, T. Takahashi, S. Sato, T. Kasuya, Y. Ônuki, H. Yamagami, A. Hasegawa, and T. Ishii, Physica B, **186-188**, 77 (1993).

[19] J. H. Scofield, J. Electron Spectrosc., Relat. Phenom., **8**, 129 (1976) .

Numerical Pseudopotentials within DV-X_α Framework

Gennady L. Gutsev[1]

Quantum Theory Project, P. O. Box 118435, University of Florida, Gainesville, FL 32611, USA

ABSTRACT

Construction of numerical pseudopotentials from HF or HFS solutions to the atomic Hamiltonians and their incorporation into the program suites based on direct numerical integration schemes are presented. Several test calculations have shown the pseudopotential approach to be reliable in reproduction of the all-electron eigenvalues of free molecules. The most promising application of numerical pseudopotentials and pseudoorbitals appears to be the simulation of bulk and surfaces. A solid is simulated by a cluster embedded in a surrounding lattice, whose nodes are supplied with pseudopotentials which do not allow the cluster wavefunction to decay exponentially. Some $(MgO)_n$ clusters were considered as the test examples. The results of calculations demonstrate good performance of the approach in simulating the bulk and surface of the MgO crystal.

1. Introduction

The pseudopotential concept was advanced a long ago [1] and is based on the natural energetic and spatial separation of core and valence electrons. The concept allows a significant reduction in computational efforts without missing the essential physics of phenomena provided the interaction of core and valence electrons is well described by some effective (model) Hamiltonian. Traditionally, pseudopotentials are widely used in the band structure calculations [2], because they allow convenient expansions of the wavefunctions in terms of plane waves suited to describing periodical systems. For molecular and/or nonperiodical systems, the main advantage of pseudopotentials is a

[1] Also at: *Institute of Chemical Physics at Chernogolovka of the Russian Academy of Sciences, Chernogolovka, Moscow Region 142432, Russian Federation*

ADVANCES IN QUANTUM CHEMISTRY, VOLUME 29

0065-3276/97 $25.00

serious reduction in the size of basis sets, which is especially important when studying compounds with a large number of core electrons such as transition metals [3].

A great number of different schemes, generally based on the use of the classic Phillips-Kleinman operator [4] for the core-valence separation, was suggested for constructing "*ab initio*" atomic pseudopotentials [5] – [27]. Such a huge variety of pseudopotentials and pseudofunctions is related to the absence of some strict formal criteria to be satisfied, so the construction of effective Hamiltonians can be accomplished in numerous ways. However, all reasonably generated pseudopotentials lead to close computational results as was shown by Klobukowski [28]. In order to be used in standard programs of quantum chemical calculations, the atomic pseudoorbitals and pseudopotentials are usually fitted by Gaussian type functions.

Within the density functional theory (DFT), several schemes for generation of pseudopotentials were developed. Some of them construct pseudopotentials for pseudoorbitals derived from atomic calculations [29] – [31], while the others make use [32] – [36] of parameterized analytical pseudopotentials. In a specific implementation of the numerical integration for solving the DFT one-electron equations, named Discrete-Variational Method (DVM) [37]– [41], one does not need to fit pseudoorbitals or pseudopotentials by any analytical functions, because the matrix elements of an effective Hamiltonian can be computed directly with either analytical or numerical basis set (or a mixed one).

Two pseudopotential schemes were developed in the framework of the DV-X_α method. One of them [42], [43] is based on the explicit inclusion of core atomic orbitals in the valence pseudoorbitals (the Phillips-Kleinman ansatz)

$$\psi_i^{PS}(\mathbf{r}) = \psi_i^{val}(\mathbf{r}) + \sum_j a_{ij}\Phi_j^{core} \tag{1}$$

These pseudopotentials are inconvenient because the resulting pseudoorbitals are eigenfunctions to different Hamiltonians. We developed a more suitable scheme [44], [45] based on the Christiansen-Lee-Pitzer approach [9]. Let us consider first the construction of pseudopotentials, then their use for molecular systems, and, finally, for simulating surfaces and bulk of solids.

2. Generation of atomic pseudopotentials

Within the pseudopotential approach, one replaces N all-electron equations

$$(-\frac{1}{2}\nabla^2 + V[\rho(\mathbf{r})] + V_{ext})\psi_i(\mathbf{r}) = \epsilon_i\psi_i(\mathbf{r}) \tag{2}$$

by a system of equations of a lower dimensionality M, where typically $M = N(\text{all}) - N'(\text{core})$

$$(-\frac{1}{2}\nabla^2 + V[n(\mathbf{r})] + V'_{ext} + V_{PS})\psi_i^{PS}(\mathbf{r}) = \epsilon_i \psi_i^{PS}(\mathbf{r}) \tag{3}$$

Here, all equations for core states are explicitly removed. V_{PS} is a projection operator and the pseudodensity reads

$$n(\mathbf{r}) = \sum_i^M |\psi_i^{PS}(\mathbf{r})|^2 \tag{4}$$

The external potential corresponds to the effective nuclei charges

$$V'_{ext}(\mathbf{r}) = \sum_A \frac{Z_A}{|\mathbf{r} - \mathbf{R}_A|} - \sum_A \frac{Z_A^{core}}{|\mathbf{r} - \mathbf{R}_A|} = \sum_A \frac{Z_A^{val}}{|\mathbf{r} - \mathbf{R}_A|} \tag{5}$$

Usually, one assumes that a multicenter molecular pseudopotential can be represented by a superposition of one-center atomic pseudopotentials placed at corresponding atomic sites:

$$V^{PS}(\mathbf{r}) = \sum_A \sum_l V_l^{PS}(\mathbf{r} - \mathbf{R}_A)\hat{P}_l \tag{6}$$

In order to construct atomic pseudopotentials, one needs to formulate some requirements on a pseudoorbital which is to be an eigenfunction to the atomic pseudopotential equation with the same eigenvalue as in the all-electron case. We assume that outermost part of a pseudoorbital coincides with the numerical Hartree-Fock-Slater (HFS) function as close to the nucleus as possible. The pseudoorbital should be nodeless and normalized.

According to these requirements, the pseudoorbital of each outer atomic shell is constructed from the corresponding numerical HFS radial function $R_{nl}(r)$ by substituting its portion for $r < r_c$, where r_c is some core radius to be determined, by the five-term polynomial. The polynomial coefficients are chosen so as to match the amplitude and the first three derivatives of the inner portion and the remaining part of $R_{nl}(r)$. The matching point r_c is chosen to be the innermost point at which the matching results in a nodeless function with no more than two inflections in the entire region. This can be attained when the "smoothness" index

$$SMI = n_1 * 10^4 + n_2 * 10^3 + n_3 * 10^2 + n_4 * 10^1 + n_5 * 10^0 \tag{7}$$

where n_j is the number of nodes in the inner region of the jth derivative, is minimal, i. e., the radial part of a pseudoorbital is

$$R_{nl}^{PS} = \begin{cases} \sum_{i=1}^{i=5} a_i r^{\lambda+i-1} & r \le r_c \\ R_{nl}(r) & r > r_c \end{cases}$$

$\lambda \geq l+1$, where l is the angular momentum of the atomic shell considered and

$$\int_0^\infty (R_{nl}^{PS}(r))^2 r^2 dr = 1 \tag{8}$$

Typical pseudoorbitals constructed from the HFS $3s$ and $3p$ orbitals of the chlorine atom are presented in Fig. 1 and 2, respectively. Since a pseudoorbital constructed in such a way has no nodes, Eq. 3 can be inverted to represent explicitly the corresponding pseudopotential

$$V_{nl}^{PS} = \epsilon_{nl} - \frac{l(l+1)}{2r^2} + \frac{Z^{val}}{r} + \frac{(\psi_{nl}^{PS})''}{\psi_{nl}^{PS}} - \frac{V_{el} + V_{X\alpha}}{\psi_{nl}^{PS}} \tag{9}$$

The total atomic pseudopotential reads

$$V_{PS} = \sum_l V_l^{PS} * \hat{P}_l \tag{10}$$

where $\hat{P}_l$ is an angular projector

$$\hat{P}_l = \sum_{m=-l}^{l} |lm><lm| \tag{11}$$

and $|lm>$ denotes the spherical harmonic $Y_{lm}(\theta, \phi)$. Note that the pseudopotentials constructed from the HF or HFS equations are similar because the corresponding all-electron valence orbitals are nearly identical. However, there is a small difference, namely, all the V_l^{PS} for $l \geq L$, where L is the maximal angular momentum of the valence shells, although are nearly the same [46] but somewhat different in the HF case, whereas they are exactly equal in the HFS case [47].

Having in mind that $V_l^{PS} = V_L^{PS}$ for $l \geq L$, where $L = l_{max}$, and the identity

$$\sum_l \hat{P}_l = \sum_{l=0}^{\infty} \sum_{m=-l}^{l} |lm><lm| \equiv 1 \tag{12}$$

one can rewrite the total atomic pseudopotential in a convenient way

$$V^{PS} = V_L^{PS} + \sum_{l=0}^{L} [V_l^{PS} - V_L^{PS}] \sum_{m=-l}^{l} |lm><lm| \tag{13}$$

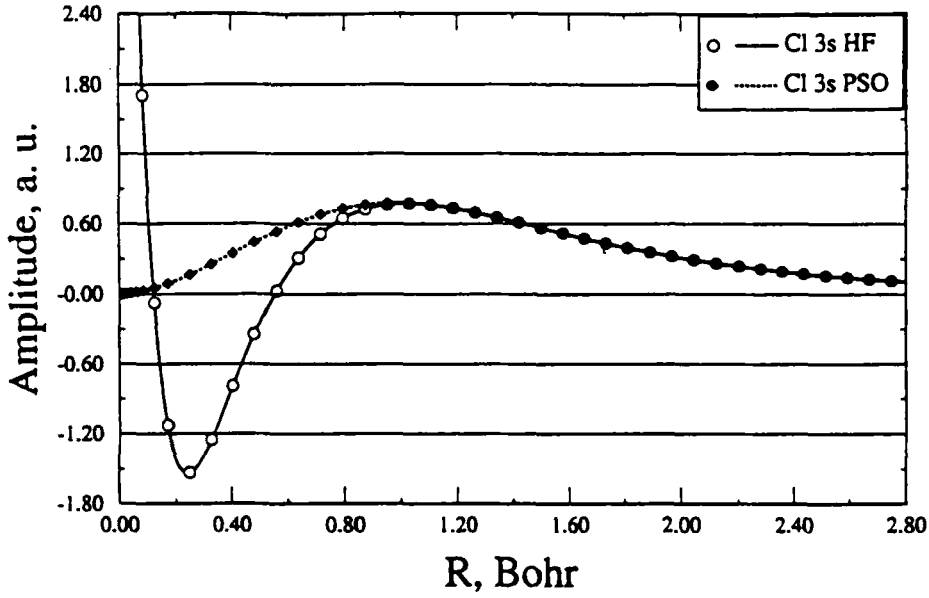

Fig. 1. *Cl* 3*s* HFS orbital and pseudoorbital.

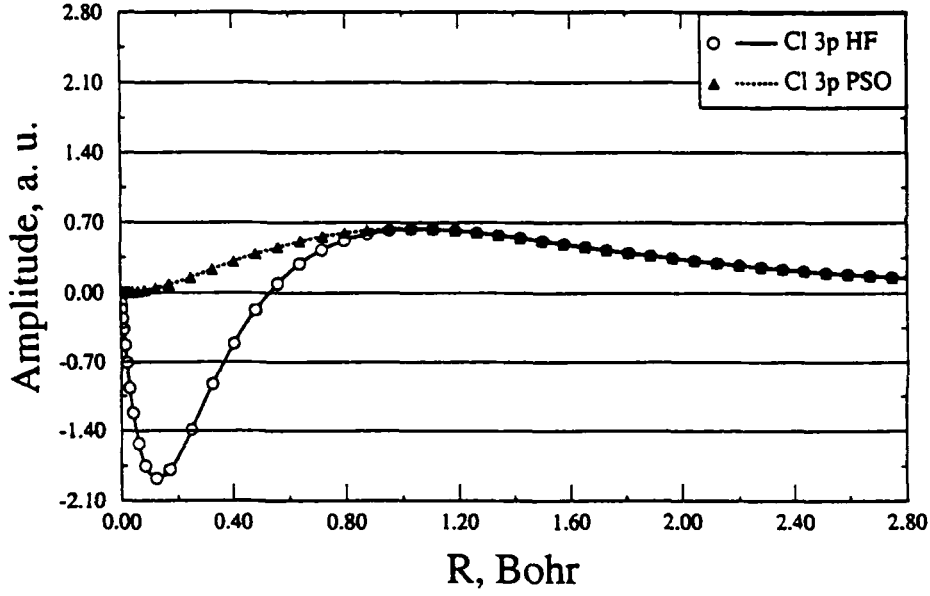

Fig. 2. *Cl* 3*p* HFS orbital and pseudoorbital.

3. Pseudopotential matrix elements

The molecular pseudopotential equation (Eq. 3) may be rewritten as

$$(-\frac{1}{2}\nabla^2 - \sum_A \frac{Z_A^{val}}{|\mathbf{r}-\mathbf{R}_A|} + \int \frac{n(\mathbf{r}')}{|\mathbf{r}-\mathbf{r}'|}d\mathbf{r}' + V_{xc}[n(\mathbf{r})] + \sum_A \sum_l V_A^{PS}(\mathbf{r}-\mathbf{R}_A)\psi_i^{PS}(\mathbf{r}) = \epsilon_i \psi_i^{PS}(\mathbf{r}) \quad (14)$$

where V_{xc} is the exchange-correlation potential. which reads in the X_α approximation as $-\frac{9}{8}\alpha(3\rho/\pi)^{1/3} = -C\rho^{1/3}$. The evaluation of the matrix elements for all operators in Eq. 14 but the pseudopotential is described elsewhere [37]–[41]; so, we need to consider only the evaluation of the pseudopotential matrix elements, which include in a general case the following integrals

$$P_{ij} = \int \chi_i^*(\mathbf{r}-\mathbf{R}_A)|Y_{lm}^*(\hat{r}_C) > R_l(r_C) < Y_{lm}(\hat{r}_C)|\chi_j^*(\mathbf{r}-\mathbf{R}_B)d\mathbf{r} \quad (15)$$

where R_l is the radial constituent of the lth partial component of the atomic pseudopotential, $\hat{r}_C$ is the angular variable and r_C is the radial one in the local coordinate system of the atom C, and χ_l are the basis functions. Let us expand [48] – [51] the basis functions located at A and B relative to the C center as follows

$$\frac{\chi_i^*(\mathbf{r}-\mathbf{R}_A)}{r_A} = \frac{R_{nl}(r_A)}{r_A} Y_{LM}(\theta_A,\phi_A) = \sum_{l=0}^{\infty}\sum_{m=-l}^{l} \frac{1}{r_C}\alpha_l(nlLM|R,r_C)Y_{lm}(\theta_C,\phi_C) \quad (16)$$

where $R = |\mathbf{R}_A - \mathbf{R}_C|$ and α_l coefficients are defined as

$$\alpha_l(nlLM|R,r_C) = \left(\frac{R}{r_C}\right)^l \frac{1}{R}\sum_{s=0}^{l+L} Q_{slLM}(R,r_C)\int_{|R-r_C|}^{|R+r_C|} R_{nl}(t)\left(\frac{t}{R}\right)^{2s-L} dt \quad (17)$$

and Q_{slLM} are polynomials of $(r_C/R)^2$. Such integrals can be evaluated with the use of a direct numerical integration. We have used the Gauss quadratures [52]. Having expanded both atomic orbitals, one is left with the one-dimensional integral over r_C due to the orthogonality of spherical harmonics.

The total pseudoenergy has the familiar $X\alpha$ representation

$$E_{PS} = \sum_{vale}\epsilon_i - \frac{1}{2}\int\int \frac{n(\mathbf{r})n(\mathbf{r}')}{|\mathbf{r}-\mathbf{r}'|}d\mathbf{r}d\mathbf{r}' - \frac{1}{4}C\sum_\sigma \int n_\sigma(\mathbf{r})(n_\sigma(\mathbf{r}) + \frac{1}{2}\rho_c(\mathbf{r}))^{\frac{1}{3}}d\mathbf{r} + \frac{1}{2}\sum_{A\neq B}\frac{Z_A^{val}Z_B^{val}}{|\mathbf{R_A}-\mathbf{R_B}|} \quad (18)$$

where some core density is added when evaluating the exchange-correlation energy [53] and the summation is over both $\sigma = \alpha$ and β electrons.

4. Results of test calculations

In order to estimate the reliability of the pseudopotential variant of our DVM package [40], [54], [55], the molecules O_2, O_3, Cl_2 as well as the complex anions $PdCl_4^{-2}$ and $PdCl_6^{-2}$ are considered. The following valence configurations of the neutral atoms were assumed: O $(2s^22p^4)$, Cl $(3s^23p^5)$, and Pd $(4p^64d^95s^1)$ when constructing the pseudopotentials, and the α parameters are the Schwartz's [56] α_{HF} ones. We made use of the numerical pseudoorbitals as the basis functions. Several calculations were performed with adding some diffuse STOs from Roetti-Clementi's *double-ζ* basis [57] to our numerical bases.

Table 1 compares the orbital eigenvalues of the O_2 molecule obtained from the all-electron and pseudopotential computations.

Table 1. DV-X_α orbital energies (in eV) of the valence and the lowest unoccupied MOs of the O_2 molecule, R_e = 1.21 Å.

Basis	Approach	$1\sigma_g$	$1\sigma_u$	$2\sigma_g$	$1\pi_u$	$1\pi_g$	$2\sigma_u^*$
Numerical	All-El	-33.86	-23.05	-16.03	-15.18	-9.09	+2.60
	PsPot	-33.69	-23.10	-15.97	-15.14	-9.05	+3.74
Extended[a])	All-El	-33.28	-22.18	-15.39	-14.43	-8.16	+3.29
	PsPot	-33.07	-22.24	-15.32	-14.34	-8.08	+4.77

[a]) *Extended* stands for the numerical pseudoorbitals augmented by some diffuse STOs of Roetti-Clementi's *double-ζ* basis set.

As is seen, the difference in the eigenvalues calculated with both approaches does not exceed 0.1 eV, as a rule. We did not find any essential dependence on the form of the core density added to the valence pseudodensity when calculating the X_α exchange (i. e., as a superposition of the numerical atomic densities or simulated by a spherical Bessel function $\rho_c = Asin(Br)/r$ [58]). The orbital energy of the $2\sigma_u^*$ LUMO calculated in both approaches differs by 1 eV, and the difference depends on the shape of the innermost section of the pseudoorbitals. Such a behavior is rather common [59] – [61].

In order to further check the dependence of the difference in the eigenvalues calculated in the all-electron and pseudopotential approaches, we compare the

results of calculations of the ground-state O_3 molecule in Table 2 performed nonself- and self-consistently, since the nonselfconsistent computations present a pure effect from the replacement of the all-electron consideration by a pseudopotential one. One can see that the self-consistent procedure, which employs the projection of pseudodensity onto specially fitted STO sets [40], [54], does not deteriorate seriously the differences in the corresponding eigenvalues, obtained in the non-selfconsistent case.

Table 2. DV-X_α orbital energies (in eV) of the valence and lowest unoccupied MOs of the ozone molecule for $R_e(O-O) =$ 1.28 Å, $\angle OOO =$ 116.5 °.

	Superposition		SCF	
Symm.	All-El	PsPot	All-El	PsPot
$1a_1$	-32.40	-32.30	-35.60	-35.49
$1b_2$	-26.77	-26.75	-28.77	-28.72
$2a_1$	-19.67	-19.65	-22.40	-22.37
$3a_1$	-13.88	-13.85	-17.01	-16.99
$1b_1$	-13.63	-13.63	-16.83	-16.87
$2b_2$	-14.78	-14.76	-16.77	-16.79
$3b_2$	-9.14	-9.14	-10.99	-11.03
$4a_1$	-8.52	-8.49	-10.98	-11.01
$1a_2$	-9.63	-9.63	-10.68	-10.65
$2b_1^*$	-5.99	-5.99	-8.44	-8.47
$5a_1^*$	1.31	2.12	-0.99	-0.13
$4b_2^*$	3.35	3.84	0.53	0.97

The calculations for the Cl_2 molecule were performed at the all-electron, pseudopotential and combined levels. In the latter case, the pseudopotential and pseudofunctions were chosen at only one of the chlorine atoms. Such a variant could be considered as a prototype for large-scale cluster computations where external coordination shells of a cluster have to be replaced by pseudoatoms, whereas the innermost "important" area is represented by the all-electron atoms. Table 3 shows that the combined approach does not lead

to any appreciable deviation of the eigenvalues from those calculated either in the all-electron approach or the pseudopotential one.

Table 3. DV-X_α orbital energies (in eV) of the valence and lowest unoccupied MOs of the Cl_2 molecule for R_e = 1.99 Å.

Approach	$1\sigma_g$	$1\sigma_u$	$2\sigma_g$	$1\pi_u$	$1\pi_g$	$2\sigma_u^*$
All-El	-23.72	-19.52	-11.52	-10.65	-7.94	-2.71
PsPot+All-El	-23.69	-19.51	-11.51	-10.61	-7.92	-2.84
PsPot	-23.67	-19.58	-11.49	-10.65	-8.04	-2.93

Another application of such a combined approach is presented by the results our calculations on the electronic structure of the $PdCl_4^{-2}$ dianion in Table 4. The calculations were performed both selfconsistently and nonselfconsistently with the superimposed atomic electronic densities and potentials [54]. In the pseudopotential calculations, all four chlorine atoms were considered as pseudoatoms.

Finally, Table 5 presents the results of all-electron and all-pseudopotential calculations on the valence electronic structure of the $PdCl_6^{-2}$ dianion.

As is seen, the most noticeable differences between the all-electron and pseudopotential eigenvalues are observed for the molecular orbitals containing the s-type AOs of Pd by symmetry. It appears to be related to the "non-core" character of the $4s$ states in the second transition series atoms; therefore, one could take into account for the subvalence shells when constructing pseudopotential [17] or to use some extended basis in such cases.

Briefly summarizing the results presented in Tables 1 – 5, one could conclude that the pseudopotential approach is promising for simulations of large-scale systems. A special advantage appears to be presented by a combined approach when some region of a large system is considered all-electronically, whereas the rest is replaced with pseudoatoms. The latter will lead to a drastic reduction in computational efforts without the loss of accuracy.

Table 4. DV-X_α orbital energies (in eV) of the $PdCl_4^{-2}$ dianion calculated within the all-electron and pseudopotential approaches. The latter includes the atomic pseudopotentials and pseudoorbitals on the chlorine atoms only. $R(Pd-O) =$ 2.30 Å.

	Superposition		SCF	
Symm.	All-El	PsPot	All-El	PsPot
$1a_{1g}$	-20.87	-20.89	-8.42	-8.43
$1e_u$	-20.46	-20.49	-7.98	-7.99
$1b_{1g}$	-20.43	-20.48	-7.92	-7.94
$2b_{1g}$	-10.67	-10.67	1.14	1.11
$2a_{1g}$	-10.53	-10.51	1.21	1.20
$1b_{2g}$	-10.15	-10.17	1.34	1.30
$1e_g$	-9.22	-9.22	1.99	1.93
$2e_u$	-9.31	-9.28	2.63	2.67
$1a_{2u}$	-8.82	-8.82	2.92	2.94
$3a_{1g}$	-7.05	-7.05	3.45	3.36
$1b_{2u}$	-8.22	-8.22	3.70	3.73
$3e_u$	-8.14	-8.14	3.92	3.96
$1a_{2g}$	-7.70	-7.73	4.42	4.42
$2e_g$	-6.83	-6.83	4.47	4.45
$2b_{2g}$	-6.80	-6.80	4.54	4.48
$3b_{1g}^*$	-4.30	-4.27	7.66	7.60
$4a_{1g}^*$	0.76	1.27	13.05	13.00
$2a_{2u}^*$	2.88	2.88	16.15	19.31
$4e_u^*$	8.05	8.54	19.47	19.89

Table 5. DV-X_α orbital energies (in eV) of the valence and lowest unoccupied MOs of the $PdCl_6^{-2}$ dianion for $R(Pd-O)$ = 2.29 Å.

	Superposition		SCF	
Symm.	All-El	PsPot	All-El	PsPot
$1a_{1g}$	-21.17	-21.14	-10.04	-10.26
$1e_g$	-20.52	-20.57	-9.30	-9.55
$1t_{1u}$	-20.52	-20.52	-9.26	-9.45
$2e_g$	-10.86	-10.78	-1.43	-1.49
$2a_{1g}$	-10.58	-10.09	0.01	0.28
$1t_{2g}$	-10.31	-10.28	-1.30	-1.49
$2t_{1u}$	-9.61	-9.58	1.15	1.06
$1t_{2u}$	-8.33	-8.30	2.68	2.61
$3t_{1u}$	-8.11	-8.08	2.86	2.83
$1t_{2g}$	-7.73	-7.73	3.35	3.29
$2t_{2u}$	-6.88	-6.86	2.61	2.51
$2e_g^*$	-4.35	-4.27	5.35	5.40
$3a_{1g}^*$	2.99	4.87	12.79	15.85
$4t_{1u}^*$	5.96	7.99	16.15	19.31

5. Cluster models

Several typical approaches are widely in use when simulating bulk or surface phenomena [62], [63]. In the case of covalent crystals like silicon, one takes usually some cluster surrounding a lattice defect and saturates external broken bonds of the cluster with pseudo or hydrogen atoms [64] –[69]. In the case of ionic crystals like alkali halides, a common approach is to place the selected cluster into a field of point charges [70] sited at the lattice nodes. The DVM method allows more flexible lattice simulations, because it employs the numerical integration schemes. One of the first pseudopotential approach, so-called embedding cluster technique, has been suggested by Ellis *et. al.* [71] – [73] and is widely employed when simulating magnetic alloys [74]. Also, this embed-

ding technique was used for interpreting the Auger spectra of stoichiometric and non-stoichiometric refractory compounds [75] – [78].

With this embedding technique, one selects a representative cluster representing a solid, and embeds the cluster in a surrounding portion of the crystalline lattice, usually consisting of several coordination shells. The corresponding Hamiltonian reads

$$\hat{H}^{EC} = \hat{H}^{C} + \sum_{A} \frac{Z_A}{|\mathbf{r} - \mathbf{R}_A|} + \sum_{A} \int \frac{\rho_A^*(\mathbf{r}')}{|\mathbf{r} - \mathbf{r}'|} d\mathbf{r} \tag{19}$$

where H^C is the (all-electron) Hamiltonian of a cluster and the second and third terms describe the Coulomb interaction with surrounding effective atoms A. The effective electronic densities of the embedding environment can be fixed (e. g., corresponding to some pure ionic states of free atoms [75], [76]) or selfconsistently with the use of Mulliken population analysis data obtained for the cluster atoms [71].

The pseudopotential formalism developed above allows a more uniform and consistent way for simulating solids and their surfaces. Again one chooses a cluster representing the system under study and embeds the cluster into a set of pseudopotentials sited at the lattice nodes of several coordination shells. The purpose of these pseudopotentials is to project out those components of the cluster wavefunction which result in the non-physical exponential decay of a free-cluster wavefunction. Some point charges could be added also at the environmental nodes in order to simulate Coulomb potentials in ionic solids. To reduce the possible inaccuracy, one can select a bigger cluster consisting of the all-electron inner part and pseudopotentially-treated next-neighbor shells.

As an example of a pseudopotential simulation of boundary conditions for clusters representing some ionic compounds, let us consider the MgO case [79], which has been considered previously [80], [81] within a bare cluster model. The MgO crystal (the rock-salt lattice) was simulated by a cluster Mg_9O_9 (see Fig. 3) placed in several embeddings comprised of a different number of pseudoatoms possessing the effective potentials and placed at the lattice sites.

The effective potential W consists of pseudopotentials and point charges

$$W(\mathbf{r}) = \sum_{S} [\sum_{l} V_l^{PS}(\mathbf{r} - \mathbf{R}_A)\hat{P}_l + \sum_{nl} \Delta q_{nl} V_C^{nl}(\mathbf{r} - \mathbf{R}_A)] \tag{20}$$

where V_l^{PS} is the lth atomic pseudopotential, $\hat{P}_l$ is the corresponding projector onto the l-th atomic spherical harmonics, Δq_i is the difference between the populations of the nl-th shell in the atomic calculations used for the pseudopotential construction and in the cluster, and V_C^{nl} is the Coulomb potential generated by the atomic nl-shell

$$V_C^{nl}(\mathbf{r}-\mathbf{R}_A)=\frac{R_{nl}^2}{|\mathbf{r}-\mathbf{R}_A|} \tag{21}$$

We made use of the numerical pseudopotentials obtained from atomic calculations of the O^- and Mg^+ ions. The cluster basis consists of the numerical HFS AOs $1s, 2s, 2p$ of O^- and $1s, 2s, 2p, 3s$ of Mg^+.

Three clusters were chosen: **(I)** Mg_9O_9 embedded in the field of the first cationic coordination sphere (each anion of the cluster has coordination number 6); **(II)** Mg_9O_9 embedded in the whole first coordination sphere of the cluster plus the second cationic sphere; **(III)** is obtained from **(II)** by deleting all the pseudoatoms attached above the upper plane of the Mg_9O_9 cluster. Embedded clusters **(I)** and **(II)** could be considered as models of the MgO bulk, whereas **(III)**as modeling the MgO surface. The number of embedding centers is 21, 58, and 41 in **(I)**, **(II)**, and **(III)**, respectively.

The results of calculations on all three embedded clusters are presented in Table 6.

Table 6. Mulliken charges on anions (Q_O), the gap, and the maximal splitting of the core O $1s$ levels ($\Delta\epsilon_{O1s}$). calculated for the Mg_9O_9 cluster embedded in three different surroundings (clusters I, II and III, see text above)

Property	I	II	III
Q_O^{3c} [a)]	1.85	1.83	1.75
Q_O^{4c}	1.93	1.80	1.78
Q_O^{5c}	1.78	1.74	1.63
Gap[b)], eV	6.34	6.31	5.28
$\Delta\epsilon_{O1s}$, eV	2.27	0.45	0.90

[a)] Note that the Mg_9O_9 cluster contains three types of non-equivalent oxygen anions which coordinated to three ($3c$), four ($4c$), or five ($5c$) magnesium cations.

[b)]Gap is evaluated as the difference in the orbital energies of the LUMO and HOMO.

As expected, cluster **II** presents a more realistic description of the MgO crystal compared to cluster **I**, since the charges on the anions with different coordination numbers are more uniform and the change in the energies of the core O $1s$ levels, reflecting the homogeneity of the MgO lattice, is smaller (0.45 in **II** vs 2.27 eV in **I**). Partial densities of the O $2p$ states of both clusters **I** and **II** are presented in Fig. 4. As is seen, the densities of different anions differ somewhat but there is no indication of any artificial surface cluster states appearing in the bare-cluster calculations.

The gap, estimated as the difference in the orbital energies of the highest occupied and lowest vacant MOs of the clusters is by 20% underestimated compared to the experimental value, which is typical for the LSDA approximations [82]. When going from the "bulk" cluster **II** to the "surface" cluster **III**, the gap decreases by 1 eV in agreement with the experimental findings [83].

In order to calculate the binding energy and bulk modulus of the MgO crystal, we have used the smallest cluster, namely, the diatomic MgO unit, embedded into two coordination spheres, whose nodes have effective potentials described by Eq. 20. Table 7 compares our results with the experimental data and the results of other calculations. One could see that even the smallest cluster embedded in the pseudopotential environment allows a decent reproduction of the bulk properties. Let us note that we have used also the smallest basis consisting of the numerical HFS orbitals of the O^- and Mg^+ ions.

Table 7. Binding energies (BE) and bulk modulus (BM) of MgO.

Compound	Method	Ref.	$R_e(Mg-O)$, Å	BE, eV	BM, hPa
MgO, cryst.	Band HF	[84]	2.11	7.40	184
Mg_9O_9, **II**	DV-X_α	*tw*	2.11	9.94	202
MgO, cryst.	Exper.	[84]	2.11	10.45	156
MgO	CI	[85]	1.87	2.65±0.16	...
MgO	DV-X_α	*tw*	1.87	2.15	...
MgO	Exp.	[86]	1.75	(3.5)	...

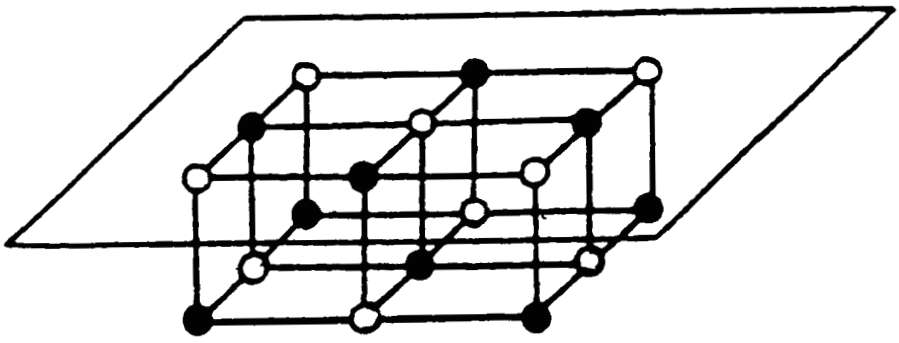

Fig. 3. The Mg_9O_9 cluster.

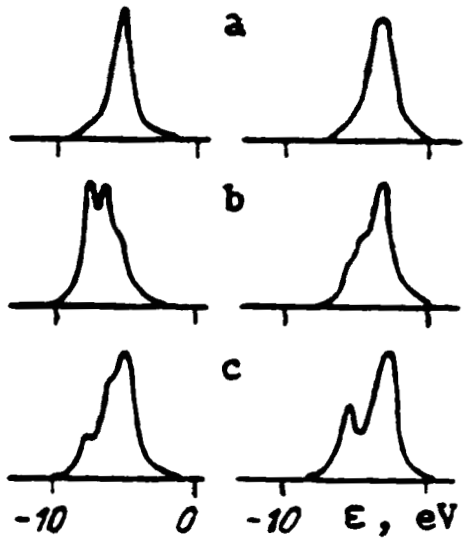

Fig. 4. Partial densities of the O $2p$ states for cluster I on the left side and for cluster II on the right side: a — O_{3c}; b — O_{4c}; c — O_{5c}. Nc denotes the coordination number of magnesium cations in the Mg_9O_9 cluster.

6. Conclusions

Numerical integration schemes allow an opportunity to test the numerical nonempirical pseudopotentials without their fit by analytical functions, which can lead to a considerable reduction in computational efforts. Employment of atomic pseudopotentials only at some selected atoms of a system while treating the rest "all-electronically" makes an impression of the consistency and reliability of such a combined approach. The results obtained for the MgO clusters embedded in some effective pseudopotential surroundings demonstrate a promise of the approach for compensation of broken bond effects. Specifically, the approach offers a tool for a substantial reduction of the artificially introduced nonequivalence of partial densities and the effective charges for atoms equivalent in the lattice. It is worth to mention that our approach can be modified further in many ways because numerical integration schemes can be easily applied/adapted even in those cases where the analytical methods become too complicated.

REFERENCES

References

[1] H. Hellmann, J. Chem. Phys. **3**, 61 (1935).

[2] W. A. Harrison, *Solid State Theory* (Mc-Graw-Hill, New York, 1970).

[3] G. Frenking, I. Antes, M. Böhme, S. Dapprich, A. W. Ehlers, V. Jonas, A. Neuhaus, M. Otto, R. Stegmann, A. Veldkamp, and S. F. Vyboishikov *Pseudopotential Calculations of Transition Metal Compounds: Scope and Limitations*, Rev. Comp. Chem. **8**, 63 (1996).

[4] J. C. Phillips and L. Kleinman, Phys. Rev. **116**, 287 (1959).

[5] C. F. Melius and W. A Goddard III, Phys. Rev. A**10**, 1528 (1974).

[6] V. Bonifacic and S. Huzinaga, J. Chem. Phys. **60**, 2779 (1974).

[7] J. C. Barthelat and Ph. Durand, Gaz. Chim. Ital. **108**, 225 (1978).

[8] P. J. Hay, W. R. Wadt, and L. R. Kahn, J. Chem. Phys. **68**, 3059 (1978).

[9] P. A. Christiansen, Y. S. Lee, and K. S. Pitzer, J. Chem. Phys. **71**, 4445 (1979).

[10] Y. Sakai and S. Huzinaga, J. Chem. Phys. **76**, 2537 (1982).

[11] G. B. Bachelet, D. R. Hamann, and M. Schlütter, Phys. Rev. B**26**, 4199 (1982).

[12] D. R. Hamann, Phys. Rev. B**40**, 2980 (1989).

[13] S. Huzinaga, M. Klobukowski, and Y. Sakai, J. Phys. Chem. **88**, 4880 (1984).

[14] W. J. Stevens, H. Bash, and M. Krauss, J. Chem. Phys. **81**, 6026 (1984).

[15] P. S. Bagus, C. W. Baushlicher Jr., C. J. Nelin, B. C. Laskowski, and M. Seel, J. Chem. Phys. **81**, 3594 (1984).

[16] J. Andzelm, E. Radzio, and D. R. Salahub, J. Chem. Phys. **83**, 4573 (1985).

[17] P. J. Hay and W. R. Wadt, J. Chem. Phys. **82**, 270; 284; 299 (1985).

[18] J. Schnitker and P. J. Rossky, J. Chem. Phys. **86**, 3462 (1987).

[19] C. Woodward and A. B. Kunz, Phys. Rev. B**37**, 2674 (1988).

REFERENCES

[20] Z. Barandiaran, L. Seijo, and S. Huzinaga, J. Chem. Phys. **93**, 5843 (1990).

[21] D. Andrae, U. Häussermann, M. Dolg, H. Stoll, and H. Preuss, Theor. Chim. Acta **77**, 123 (1990).

[22] R. B. Ross, J. M. Powers, T. Atashroo, W. C. Ermler, L. A. LaJohn, and P. A. Christiansen, J. Chem. Phys. **93**, 6654 (1990).

[23] W. J. Stevens, M. Krauss, H. Bash, and P. G. Jasien, Can. J. Chem. **70**, 612 (1992).

[24] A. Bergner, M. Dolg, W. Küchle, H. Stoll, and H. Preuss, Mol. Phys. **80**, 1431 (1993).

[25] G. Ortiz and P. Ballone, Phys. Rev. B**43**, 6376 (1991).

[26] D. M. Bylander and L. Kleinman, Phys. Rev. B**43**, 12070 (1991); B**46**, 9837 (1992).

[27] Á. Nagy and I. Andrejkovics, Phys. Rev. A**53**, 3656 (1996).

[28] M. Klobukowski, Theor. Chim. Acta **83**, 239 (1992).

[29] A. Zunger and M. L. Cohen, Phys. Rev. B**18**, 5449 (1978).

[30] A. Zunger, J. Vac. Sci. Technol. **16**, 1339 (1979).

[31] S. Topiol, A. Zunger, and M. A. Ratner, Chem. Phys. Lett. **49**, 367 (1977).

[32] H. Preuss, H. Stoll, U. Wedig, and Th. Krüger, Int. J. Quantum Chem. **19**, 113 (1981).

[33] S. Katsuki and M. Inokuchi, J. Phys. Soc. Japan, **51**, 3652 (1982).

[34] M. L. Cohen, *Applications of the Fermi Atomic Pseudopotentials to the Electronic Structure of Nonmetals*, in Highlights of Condensed matter Theory, Corso, Soc. Italiana di Fisica, Bologna **89**, 16 (1985).

[35] R. Car, R. A. Meuli, and J. Buttet, J. Chem. Phys. **73**, 4511 (1980).

[36] A. Savin, U. Wedig, H. Stoll, and H. Preuss, Chem. Phys. Lett. **92**, 503 (1982).

[37] F. W. Averill and D. E. Ellis, J. Chem. Phys. **59**, 6412 (1973).

REFERENCES

[38] E. J. Baerends, D. E. Ellis, and P. Ros, Chem. Phys. **2**, 41 (1973).

[39] A. Rosén, D. E. Ellis, H. Adachi, and F. W. Averill, J. Chem. Phys. **65**, 3629 (1976).

[40] G. L. Gutsev and A. A. Levin, Chem. Phys. **51**, 49 (1980).

[41] B. Delley and D. E. Ellis, J. Chem. Phys. **76**, 1949 (1982).

[42] J. G. Snijders and E. J. Baerends, Mol. Phys. **33**, 1651 (1977).

[43] W. Ravenek and E. J. Baerends, J. Chem. Phys. **81**, 865 (1984).

[44] V. A. Nasluzov, G. L. Gutsev, and V. K. Gryaznov, Struct. Chem. **31**, 3 (1990).

[45] G. L. Gutsev, V. K. Gryaznov. and V. A. Nasluzov, Chem. Phys. **154**, 291 (1991).

[46] C. F. Melius, B. D. Olafson, and W. A. Goddard III, Chem. Phys. Lett. **28**, 457 (1974).

[47] A. Zunger, S. Topiol, and M. Ratner, Chem. Phys. **39**, 75 (1979).

[48] H. J. Silverstone, J. Chem. Phys. **47**, 537 (1967).

[49] R. R. Sharma, Phys. Rev. A**13**, 517 (1976).

[50] H. W. Jones and C. A. Weatherford, Int. J. Quantum Chem. Symp. **12**, 483 (1978).

[51] H. W. Jones, Phys. Rev. A**30**, 1 (1984).

[52] V. I. Krylov and L. T. Shul'gina, *The Handbook for Numerical Integration* (Science, Moscow,1966).

[53] J. Bernholc and N. A. W. Holzwarth, J. Chem. Phys. **81**, 3987 (1984).

[54] G. L. Gutsev and A. A. Levin, Struct. Chem. **19**, 976 (1978).

[55] V. K. Gryaznov, A. N. Ivanova, G. L. Gutsev, A. A. Levin, and A. V. Krestinin, Struct. Chem. **30**, 132 (1989).

[56] K. Schwartz, Phys. Rev. B**5**, 2466 (1972).

[57] C. Roetti and E. Clementi, J. Chem. Phys. **60**, 4725 (1974).

[58] S. G. Louie, S. Froyen, and M. l. Cohen, Phys. Rev. B**26**, 1738 (1982).

REFERENCES

[59] L. Pettersson and U. Walgren, Chem. Phys. **69**, 185 (1982).

[60] O. Gropen, U. Walgren. and L. Pettersson, Chem. Phys. **66**, 459 (1982).

[61] L. G. M. Pettersson, U. Walgren, and O. Gropen, Chem. Phys. **80**, 7 (1983).

[62] J. Sauer, Chem. Rev. **89**, 199 (1989).

[63] J. M. Vail, J. Phys. Chem. Solids **51**, 589 (1990).

[64] M. J. Burnard and G. G. DeLeo, Phys. Rev. B**47**, 690 (1993).

[65] L. Spiess, S. P. Tang, A. J. Freeman, B. Delley, K. M. Schirm, Z. Hurych, and P. Soukiassian, Appl. Surf. Sci. **65**, 690 (1993).

[66] G. S. Myaken'kaya, G. L. Gutsev, and N. N. Gerasimenko, Semiconductors **24**, 1024 (1990).

[67] G. S. Myaken'kaya, G. L. Gutsev, N. P. Afanas'eva, V. A. Evseev, and R. F. Konopleva, Phys. Stat. Sol. (b) **161**, 91 (1990).

[68] G. S. Myaken'kaya and G. L. Gutsev, Semiconductors **27**, 35; 218 (1993).

[69] G. S. Myaken'kaya, G. L. Gutsev, N. N. Gerasimenko, V. V. Frolov, M. A. Chubisov. and J. W. Corbett, Rad. Eff. Def. Solids **129**, 199 (1994).

[70] N. W. Winter, R. M. Pitzer, and D. K. Temple, J. Chem. Phys. **86**, 3549 (1987).

[71] D. E. Ellis, G. A. Benesh, and E. Byrom, Phys. Rev. B**16**, 3308 (1977).

[72] D. E. Ellis, G. A. Benesh, and E. Byrom, Phys. Rev. B**20**, 1198 (1979).

[73] D. E. Ellis, J. Guo, and J. J. Low, in *Quantum Chemistry Aproaches to Chemisorption and Heterogeneous catalysis*, ed. F. Ruette (Kluwer, Amsterdam, 1992), p. 69.

[74] D. Guenzburger and D. E. Ellis, Phys. Rev B**82**, 13390 (1995).

[75] G. L. Gutsev, Yu. M. Shul'ga, and Yu. G. Borod'ko, Phys. Stat. Sol. (b) **121**, 595 (1984).

[76] G. L. Gutsev and Yu. M. Shu'ga, J. Phys. C**17**, 3269 (1984).

[77] Yu. M. Shul'ga and G. L. Gutsev, Solid State Phys. **26**, 945; 1083 (1984).

REFERENCES

[78] Yu. M. Shul'ga, G. L. Gutsev, and V. I. Rubtsov, Phys. Stat. Sol. (b) **129**, 683 (1985).

[79] V. A. Nasluzov, G. L. Gutsev, V. V. Rivanenkov, K. M. Neiman, and A. G. Anshits, Struct. Chem. **33**, 157 (1992).

[80] C. Satoko, M. Tsukada, and H. Adachi, J. Phys. Soc. Jpn. **45**, 1333 (1978).

[81] M. Tsukada, H. Adachi, and C. Satoko, Prog. Surf. Sci. **14**, 113 (1983).

[82] J. P. Perdew, Int. J. Quantum Chem. S**19**, 497 (1986).

[83] V. E. Henrich, Rep. Prog. Physics **48**, 1481 (1985).

[84] B. Silvi, M. Causa, R. Dovesi, and C. Roetti, Mol. Phys. **67**, 891 (1989).

[85] C. W. Baushlicher, Jr., B. H. Lengsfield III, and B. Liu, J. Chem. Phys. **77**, 4084 (1982).

[86] K. P. Huber and G. Herzberg, *Constants of Diatomic Molecules* (Van Nostrand Reinhold, New York, 1979).

Density functional theory for excited states

Á. Nagy
Institute of Theoretical Physics, Kossuth Lajos University
H–4010 Debrecen, Hungary

Abstract

Self-consistently determined ensemble exchange-correlation parameters α are applied to calculate the first excitation energies of atoms. Several ground-state local density approximations are tested in obtaining excitation energies. The dependence of the ensemble α parameters on the weighting factor w is studied. Accurate ensemble exchange potential for Si multiplets is presented as a function of the radial distance. The w dependence of the ensemble exchange energy for multiplets is explored.

1 Introduction

The density functional theory was originally formalized for the ground-state [1]. It was soon noticed [2] that the original theory can also be applied to the lowest excited states with different symmetries. To calculate excitation energies Slater[3] introduced the so-called transition state method. It proved to be a very efficient and simple approach and was used to solve a large variety of problems. The density functional theory was first rigorously generalized for excited states by Theophilou [4]. Formalisms for excited states have also been provided by Fritsche[5] and English et al. [6]. A more general treatment was given by Gross, Oliveira and Kohn [7] . The relativistic generalization of this formalism has also been done [8].

Gross, Oliveira and Kohn [7] calculated the excitation energies of He atom using the quasi-local-density approximation of Kohn [9]. The first excitation energies of several atoms [10] have been calculated with the parameter-free exchange potential of Gáspár [11]. Higher excitation energies have also been studied [12]. Other ground-state local density approximations have been tested [13] , too. The coordinate scaling for the density matrix of ensembles has been explored [14]. The ground-state adiabatic connection formula has been extended to the ensemble exchange-correlation energy. A simple local

ADVANCES IN QUANTUM CHEMISTRY, VOLUME 29

0065-3276/97 $25.00

$X\alpha$ ensemble exchange potential has been proposed [15]. Accurate ensemble exchange potentials have been calculated as a function of the radial distance from the Hartree-Fock ensemble electron density [16].

In section 2 the theory of ensembles is reviewed. Section 3 summarizes the parameter-free theory of Gáspár[11]. The self-consistently determined ensemble α parameters of the ensemble $X\alpha$ potential are presented. In section 4 spin-polarized calculations using several ground-state exchange-correlation potentials are discussed. In section 5 the w dependence of the ensemble α parameters is studied. It is emphasized that the excitation energy can not generally be calculated as a difference of the one-electron energies. The additional term $\frac{\partial E_{xc}}{\partial w}\Big|_{n_w}$ should also be determined. Section 6 presents accurate ensemble exchange potential for Si multiplets as a function of the radial distance. In section 7 the w dependence of the ensemble exchange energy for multiplets is explored.

2 Density functional theory for ensembles

The density functional theory for ensembles is based on the generalized Rayleigh-Ritz variational principle [7]. The eigenvalue problem of the Hamiltonian $\hat{H}$ is given by

$$\hat{H}\Psi_k = E_k\Psi_k \qquad (k = 1, ..., M) \tag{1}$$

where

$$E_1 \leq E_2 \leq ... \tag{2}$$

are the energy eigenvalues. The generalized Rayleigh-Ritz variational principle [7] can be applied to the ensemble energy

$$\mathcal{E} = \sum_{k=1}^{M} w_k E_k \,, \tag{3}$$

where $w_1 \geq w_2 \geq ... \geq w_M \geq 0$. The weighting factors w_i are chosen as

$$w_1 = w_2 = ... = w_{M-g} = \frac{1 - wg}{M - g} \tag{4}$$

$$w_{M-g+1} = w_{M-g+2} = ... = w_M = w \,, \tag{5}$$

$$0 \leq w \leq \frac{1}{M} \,, \tag{6}$$

and

$$1 \leq g \leq M-1 \,. \tag{7}$$

The limit $w = 0$ corresponds to the eigenensemble of $M - g$ states ($w_1 = ... = w_{M-g} = 1/(M-g)$ and $w_{M-g+1} = ... = w_M = 0$). The case $w = 1/M$ leads to the eigenensemble of M states ($w_1 = w_2 = ... = w_M = 1/M$).

The generalized Hohenberg–Kohn-theorems read as follows:

(i) The external potential $v(r)$ is determined within a trivial additive constant, by the ensemble density n defined as

$$n = \sum_{k=1}^{M} w_k n_k \,. \tag{8}$$

(ii) For a trial ensemble density $n'(r)$ such that

$$n'(r) \geq 0 \tag{9}$$

and

$$\int n'(\mathbf{r}) d\mathbf{r} = N \tag{10}$$

$$\mathcal{E}[n] \leq \mathcal{E}[n'] \,. \tag{11}$$

The ensemble functional $\mathcal{E}$ takes its minimum at the correct ensemble density n.

Using the variation principle the Euler-equation can be obtained:

$$\frac{\delta \mathcal{E}}{\delta n} = \mu \,. \tag{12}$$

Kohn-Sham equations for the ensemble can also be derived:

$$\left[-\frac{1}{2}\nabla^2 + v_{KS}\right] u_i(\mathbf{r}) = \epsilon_i u_i(\mathbf{r}) \,. \tag{13}$$

The ensemble Kohn-Sham potential

$$v_{KS}(\mathbf{r}; n_w) = v(\mathbf{r}) + \int \frac{n_w(\mathbf{r})}{|\mathbf{r} - \mathbf{r}'|} d\mathbf{r} + v_{xc}(\mathbf{r}; w, n_w) \,, \tag{14}$$

is a functional of the ensemble density

$$n_w^I(\mathbf{r}) = \frac{1 - w g_I}{M_{I-1}} \sum_{m=1}^{M_I - g_I} \sum_j \lambda_{mj} |u_j(\mathbf{r})|^2 + w \sum_{m=M_I-g_I+1}^{M_I} \sum_j \lambda_{mj} |u_j(\mathbf{r})|^2 \,. \tag{15}$$

g_I is the degeneracy of the Ith multiplet.

$$M_I = \sum_{i=1}^{I} g_i \tag{16}$$

is the multiplicity of the ensemble and

$$0 \leq w \leq 1/M_I \,. \tag{17}$$

λ_{mj} are the occupation numbers. The ensemble exchange-correlation potential v_{xc} is the functional derivative of the ensemble exchange-correlation energy functional E_{xc}

$$v_{xc}(\mathbf{r}; w, n) = \frac{\delta E_{xc}[n, w]}{\delta n(r)} \,. \tag{18}$$

The excitation energies can be expressed with the one-electron energies ϵ_j as

$$\bar{E}^I = \frac{1}{g_I} \left.\frac{d\mathcal{E}^I(w)}{dw}\right|_{w=w_I} + \sum_{i=2}^{I-1} \frac{1}{M_I} \left.\frac{d\mathcal{E}^I(w)}{dw}\right|_{w=w_i} , \tag{19}$$

where

$$\frac{d\mathcal{E}^I(w)}{dw} = \sum_{j=N+M_{I-1}}^{N-1+M_I} \epsilon_j - \frac{g_I}{M_{I-1}} \sum_{j=N}^{N-1+M_{I-1}} \epsilon_j + \left.\frac{\partial E_{xc}^I}{\partial w}\right|_{n_w} \tag{20}$$

and

$$0 \leq w_i \leq 1/M_I \,. \tag{21}$$

It is emphasized that the excitation energy can not generally be calculated as a difference of the one-electron energies. There is an extra term $\left.\frac{\partial E_{xc}}{\partial w}\right|_{n_w}$ to be determined.

To solve the Kohn-Sham equations (13) one needs the ensemble exchange-correlation potential. In the following sections several approximate forms are discussed.

3 $X\alpha$ ensemble potential with self-consistent parameter α

Several years ago Gáspár [11] proposed a parameter-free exchange potential in the ground-state theory. This method is applied to determine the

first and higher excitation energies of several atoms [10, 12]. As the method has already been detailed in earlier papers [17-19], here only a short summary is presented.

The method is based on the free-electron gas theory, where the exchange potential is given by

$$v_x^{FE} = -4F(\eta)\left(\frac{3}{8\pi}n\right)^{1/3}, \tag{22}$$

$$\eta = \frac{p}{p_F}, \tag{23}$$

$$F(\eta) = \frac{1}{2} + \frac{1-\eta^2}{4\eta} ln|(1+\eta)/(1-\eta)| . \tag{24}$$

p_F is the Fermi momentum. To get rid of the momentum dependence, as it is usual, an average is performed in the momentum space:

$$v_x = -4\left(\frac{3}{8\pi}n\right)^{1/3}[\frac{1}{2}(\eta^3+\eta) - \frac{1}{4}(\eta^2-1)^2 ln|(1+\eta)/(1-\eta)|]_{\eta_1}^{\eta_2}[(\eta^3)_{\eta_1}^{\eta_2}]^{-1}. \tag{25}$$

If the average is done over the whole Fermi sphere, i.e. $\eta_1 = 0$ and $\eta_2 = 1$, the $X\alpha$ exchange potential of Slater [20] with $\alpha = 1$ is obtained. An average for a thin shell near the Fermi sphere, the thickness of which going to zero, i.e. $\eta_1 = (p_F - \epsilon)/p_F$, $\eta_2 = 1$ and $\epsilon \to 0$, leads to the $X\alpha$ exchange potential proposed by Gáspár [21] and later by Kohn and Sham [22], corresponding to $\alpha = 2/3$. As Gáspár [11] pointed out, a physically more acceptable average must be between these two extreme cases: the average is taken near the Fermi sphere for a layer containing the reference electron, i.e. $\nu_j = u_j^* u_j$, in the unit volume [$\eta_1 = (1 - 2\nu_j/n)^{1/3}$ and $\eta_2 = 1$]. So the exchange potential for the orbital u_j has the form

$$v_x^G = -3\left(\frac{3}{8\pi}n\right)^{1/3}\alpha_j , \tag{26}$$

where

$$\alpha_j = \frac{n}{2\nu_j}[1 - \frac{1}{2}\eta_j^3 - \frac{1}{2}\eta_j + \frac{1}{4}(\eta_j^2-1)^2 ln|(1+\eta_j)/(1-\eta_j)|] \tag{27}$$

and

$$\eta_j = (1 - 2\nu_j/n)^{1/3} . \tag{28}$$

If we do not want to use different potentials for different orbitals, an average for the shells is performed leading to the potential

$$v_x^G = -3\left(\frac{3}{8\pi}n\right)^{1/3}\alpha\,, \tag{29}$$

where

$$\alpha = \frac{\sum_j \lambda_j \alpha_j}{\sum_j \lambda_j}\,. \tag{30}$$

λ_j is the occupation number of the shell j. Though α is a function of the radial distance, it is very close to a constant value [19]. α can be determined self-consistently [17, 18]. As this potential depends explicitly on the spin orbitals it is very flexible and can be succesfully applied not only in ground-state but also in ensemble-state calculations.

Making use of this potential the first excitation energies of several atoms have been determined [10]. Table I presents these results. In these calculations the excitation energy is approximated by

$$E_2 - E_1 = \frac{1}{g_2}\sum_{j=N+g_1}^{N-1+M_2}\epsilon_j - \frac{1}{g_1}\sum_{j=N}^{N-1+g_1}\epsilon_j \tag{31}$$

that is the extra term in Eq. (20) does not appear. This must be one of the reasons for the difference between the calculated and the experimental excitation energies[23]. Table I also contains the self-consistently determined values of α.

Table I.

Ground- and excited state configurations, excitation energies and exchange-correlation parameters α_{SCF} (in Ry).

Atoms	ground-state configurations	excited-state configurations	calculated this work	experimental	α_{SCF}
O	$2p^4$	$3s$	0.762	0.698	0.72912
F	$2p^5$	$3s$	1.088	0.946	0.71725
Na	$3s$	$3p$	0.151	0.154	0.69827
Mg	$3s^2$	$3p$	0.256	0.259	0.70473
Al	$3p$	$4s$	0.168	0.231	0.70340
P	$3p^3$	$4s$	0.487	0.512	0.69948
Cl	$3p^5$	$4s$	0.707	0.665	0.70071

Higher excitation energies have also been studied [12]. Gáspár's parameter-free potential proved to be remarkably good in these calculations.

4 First excitation energies determined from ground-state exchange-correlation potentials

There are a number of model exchange-correlation functionals for the ground-state. How do they perform for ensemble states? Recently, several local density functional approximations have been tested [24]. The Gunnarsson–Lundqvist–Wilkins (GLW) [26], the von Barth–Hedin (VBH)[25] and Ceperley–Alder [27] local density approximations parametrized by Perdew and Zunger [28] and Vosko, Wilk and Nusair (VWN) [29] are applied to calculate the first excitation energies of atoms.

Table II presents the first excitation energies obtained from spin- polarized calculations [24]. As ground-state exchange-correlation potentials were used the extra term in Eq.(20) does not appear. This is, certainly, one of the reasons for the difference between the calculated and the experimental excitation energies. There is a definite improvement comparing with the non-spin-polarized results [13]. Still, in most cases the calculated excitation energies are highly overestimated. The results provided by the different local density approximations are quite close to each other. The best one seems to be the Gunnarson–Lundqvist–Wilkins approximation. (In non-spin-polarized case the Perdew–Zunger parametrization gives results closest to the experimental data[30].)

In these calculations the minimum ($w = 0$) and the maximum possible values of the weighting factor were applied. The results obtained with different weighting factors w are different. However, any value of w satisfying inequality (6) is appropriate. If we knew the exact exchange-correlation energy functional, any value of w satisfying condition (6) would lead to the same result. As the exact form of the exchange-correlation energy is, however, unknown and we have to use approximate functionals, different values of w provide different excitation energies. The effect of w on the excitation energies has also been studied [13, 24]. In certain atoms it causes only a small change while in other cases there is a considerable change in the excitation energy. The change is monotonic in all the approximations studied. We mention that a special choice of w, in certain cases, corresponds to Slater's transition-state method.

Relativistic calculation have also been performed [8]. A simple $X\alpha$ potential was used with the parameter $\alpha = 0.7$ to obtain the first six excitation energies of the Cs atom. A comparison with experimental data shows that this simple approximation provides quite adequate results.

Table II

Electron configurations of ensemble states and calculated (spin-polarized) and experimental first excitation energies of atoms (in Ry). The upper rows contain the results belonging to $w = 0$, the lower rows contain the results belonging to $w = 1/(g_1 + g_2)$.

Atom	Ensemble state	Xα	GLW	VBH	VWN	Exp
B	$2s^2\ 2p_\uparrow$	0.285	0.326	0.340	0.335	0.262
	$2s_\uparrow\ 2s_\downarrow^{\frac{1}{3}}\ 2p_\uparrow^{1\frac{2}{3}}$	0.034	0.184	0.202	0.191	
C	$2s^2\ 2p_\uparrow^2$	0.306	0.403	0.423	0.413	0.307
	$2s_\uparrow\ 2s_\downarrow^{\frac{9}{14}}\ 2p_\uparrow^{2\frac{5}{14}}$	0.168	0.321	0.341	0.327	
O	$2p_\uparrow^3\ 2p_\downarrow\ 3s_\uparrow^0$	0.488	0.549	0.562	0.533	0.672
	$2p_\uparrow^3\ 2p_\downarrow^{\frac{9}{14}}\ 3s_\uparrow^{\frac{5}{14}}$	0.570	0.642	0.643	0.629	
F	$2p_\uparrow^3\ 2p_\downarrow^2\ 3s_\uparrow^0$	0.746	0.780	0.788	0.756	0.933
	$2p_\uparrow^3\ 2p_\downarrow^{1\frac{1}{3}}\ 3s_\uparrow^{\frac{2}{3}}$	1.013	1.051	1.051	1.040	
Na	$3s_\uparrow\ 3p_\uparrow^0$	0.152	0.166	0.162	0.159	0.155
	$3s_\uparrow^{\frac{1}{4}}\ 3p_\uparrow^{\frac{3}{4}}$	0.156	0.167	0.164	0.162	
Mg	$3s^2\ 3p_\uparrow^0$	0.244	0.254	0.253	0.249	0.199
	$3s_\uparrow\ 3s_\downarrow^{\frac{1}{10}}\ 3p_\uparrow^{\frac{9}{10}}$	0.045	0.143	0.152	0.149	
Al	$3p_\uparrow\ 4s_\uparrow^0$	0.174	0.216	0.210	0.196	0.230
	$3p_\uparrow^{\frac{3}{4}}\ 4s_\uparrow^{\frac{1}{4}}$	0.183	0.216	0.209	0.202	
Si	$3s^2\ 3p_\uparrow^2$	0.318	0.370	0.387	0.381	0.302
	$3s_\uparrow\ 3s_\downarrow^{\frac{9}{14}}\ 3p_\uparrow^{2\frac{5}{14}}$	0.238	0.320	0.340	0.332	
P	$3p_\uparrow^3\ 4s_\uparrow^0$	0.427	0.459	0.446	0.434	0.512
	$3p_\uparrow^{2\frac{1}{4}}\ 4s_\uparrow^{\frac{3}{4}}$	0.538	0.554	0.544	0.541	
Cl	$3p_\uparrow^3\ 3p_\downarrow^2\ 4s_\uparrow^0$	0.538	0.600	0.606	0.585	0.656
	$3p_\uparrow^3\ 3p_\downarrow^{1\frac{1}{3}}\ 4s_\uparrow^{\frac{2}{3}}$	0.639	0.699	0.703	0.694	

5 Ensemble $X\alpha$ exchange potential

As we have seen in the previous sections the currently existing exchange-correlation potentials do not always perform well for ensemble-states. Recently, a simple $X\alpha$ ensemble potential has been proposed [15]. In this section this potential is discussed and results for other atoms are presented. The form of the $X\alpha$ ensemble exchange potential is

$$v_x(n_w, w) = -3\alpha(w)\left(\frac{3}{8\pi}\, n_w\right)^{1/3} . \tag{32}$$

The w-dependence is incorporated in the parameter α. The corresponding exchange energy has the form

$$E_x[n_w, w] = -\frac{9}{4}\left(\frac{3}{8\pi}\right)^{1/3} \alpha(w) \int n_w^{4/3} d\mathbf{r} . \tag{33}$$

Only the first excitation energies are studied. The ensemble energy is given by

$$\mathcal{E}(w) = (1 - wg_2)E_1 + wg_2E_2 , \tag{34}$$

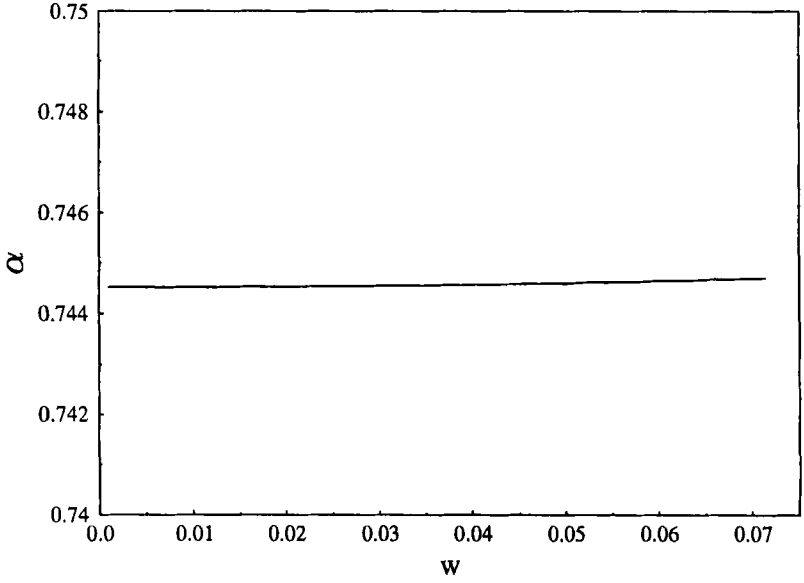

Fig.1. The exchange-correlation factor α versus the weighting factor w for the atom S

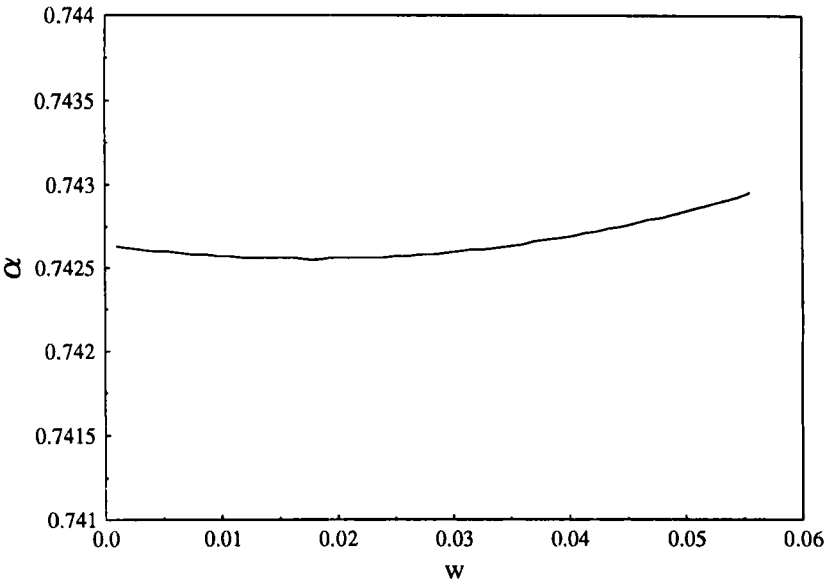

Fig.2. The exchange-correlation factor α versus the weighting factor w for the atom Cl

where g_1, E_1 and g_2, E_2 are the degeneracy and the total energy of the ground- and the first excited states, respectively. Using the experimental energies for E_1 and E_2, $\mathcal{E}$ can be determined for any value of w. $\alpha(w)$ is determined so that the ensemble energy calculated with Eq.(33) be equal to the ensemble energy obtained from the experimental energies. The calculations have been performed for selected light atoms. Figs.1. and 2. present two typical cases. Fig.1. shows the function $\alpha(w)$ for the atom S . The functions α for the atoms B, C, O, Mg, Si and P have almost the same form, i.e. slight almost monotonic dependence on w. For the atom S α is almost constant. Fig.2. presents the function α for the atom Cl. It has a a very shallow minimum. Similar functions can be obtained for the atoms F and Na.

The excitation energy is the difference of the total energies

$$\Delta E = E_2 - E_1 \,. \tag{35}$$

As we have already seen it can be determined using the single-particle energies:

$$\Delta E = \epsilon_{N+1} - \epsilon_N + \frac{1}{g_2} \left. \frac{\partial E_{xc}}{\partial w} \right|_{n_w} , \tag{36}$$

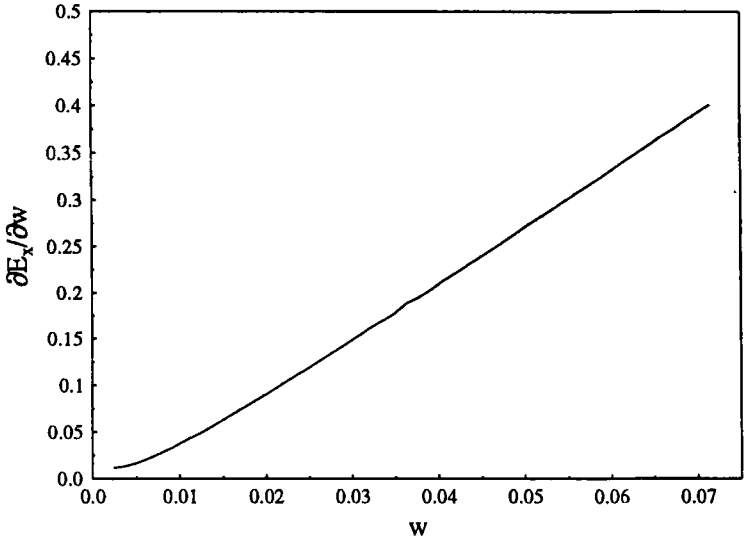

Fig.3. The partial derivative of the exchange energy with respect to the weighting factor w for the atom S

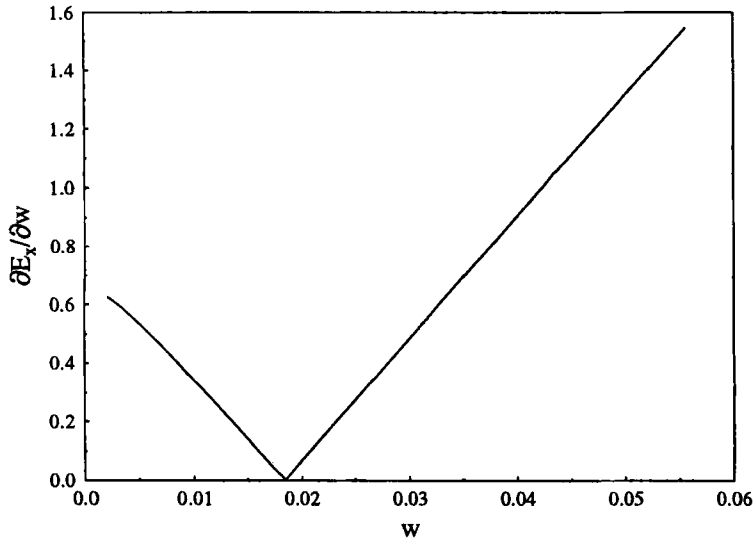

Fig.4. The partial derivative of the exchange energy with respect to the weighting factor w for the atom Cl

i.e. not simply the difference of the one-electron energies. The extra term is generally not zero. At certain values of w it gives a significant contribution. Figs.3. and 4. present $\frac{\partial E_{xc}}{\partial w}\Big|_{n_w}$ as a function of w for atoms S and Cl, respectively. The function $\frac{\partial E_{xc}}{\partial w}\Big|_{n_w}$ for atoms B, C, O, Mg, Si and P has approximately the same form as the function in Fig. 3. The function $\frac{\partial E_{xc}}{\partial w}\Big|_{n_w}$ in Fig.4. shows a completely different behaviour. There is a value $w = w_0$, where it disappears. It means that at w_0 the excitation energy can be simply given by the difference $\epsilon_{N+1} - \epsilon_N$. The importance of the existence of this w_0 lies in the fact that it is possible to determine the excitation energy simply as a difference of one-electron energies at a certain value of w.

The value of w_0 is 0.0144 for the F, 0.113 for the Na and 0.0178 for the Cl. The corresponding values of α are 0.76100, 0.75198, 0.74256 for the atoms F, Na and Cl, respectively.

Table III.

Ground- and excited state configurations and the value of α corresponding to the maximal weighting factor w.

Atoms	ground-state configurations	excited-state configurations	α
B	$^2P_{1/2}(2p)$	$^4P_{1/2}(2s2p^2)$	0.80210
C	$^3P_0(2p^2)$	$^5S_0(2p3s)$	0.79115
O	$^3P_2(2p^4)$	$^5S_0(2p^33s)$	0.77350
F	$^3P_{3/2}(2p^5)$	$^4P_{3/2}(2p^43s)$	0.76390
Na	$^2S_{1/2}(3s)$	$^2P_{1/2}(3p)$	0.75198
Mg	$^1S_0(3s^2)$	$^3P_0(3s3p)$	0.75105
Al	$^2P_{1/2}(3p)$	$^2S_{1/2}(4s)$	0.74810
Si	$^3P_0(3p^2)$	$^5S(3s3p^3)$	0.74832
P	$^4S_{3/2}(3p^3)$	$^4P(3p^24s)$	0.74623
S	$^3P_2(3p^4)$	$^5S(3p^34s)$	0.74472
Cl	$^3P_{3/2}(3p^5)$	$^4P_{5/2}(3p^44s)$	0.74295

Naturally, calculations can be performed at any value of w (satisfying the condition (21)). One can select e.g. the maximum possible value of w, (i.e. the one corresponding to the subspace theory of Theophilou [4]). Table III.

contains the values of α corresponding to $w_{\max}$ for selected atoms. Comparing these values of α with the values of α_{SCF} we see that there is a considerable difference between them(α_{SCF} is always smaller.) The difference is large even in the cases, where the excitation energies calculated with α_{SCF} are close to the experimental values. This is because the excitation energy is given by an energy difference, i.e. there is a rather complicated dependence on α.

6 Ensemble exchange potential for multiplets

The multiplet structure has already been treated using the density functional theory. The most important approaches have been proposed by Bagus and Bennett [31], Ziegler, Rauk and Baerends [32] and von Barth [33]. All these methods have the same feature of not being completely within the frame of the density functional theory.

The method of fractionally occupied states can be used to treat the multiplet problem, too. However, the exchange energy and potential are not known even for the ground state. They are unknown for the ensemble of excited states, too.

There is a growing interest in determining the exact exchange, exchange-correlation and Kohn-Sham potential in the knowledge of the density[31-35]. The present author has also proposed a method that enables one to calculate these potentials if the density is known [37]. This method can be applied to ensemble states without any difficulty [16].

The method can be summarized as follows. The ensemble density

$$n_w = \sum_i \lambda_i |u_i|^2 \tag{37}$$

can be calculated with one-particle wavefunctions u_i of the Kohn–Sham equations (13). The occupation numbers can be determined from g_i and w. If the ensemble density n_w is known the ensemble exchange and the exchange-correlation potentials can be calculated as follows: Starting out from an appropriate (e.g. an $X\alpha$) potential.the Kohn–Sham equations are solved and the density of the first iteration is calculated. The potential of the ith iteration can be given by

$$V^{(i)} = V^{(i-1)} \frac{n^{\text{input}}}{n^{(i-1)}} \tag{38}$$

and an appropriate damping is applied to obtain a stable convergence. Then the Kohn–Sham potential of the second iteration is constructed. The process goes on until the density equals to the input density. If the input density is the exact density, the exact Kohn–Sham potential and the exact exchange-correlation potential are obtained. If the input density is the Hartree–Fock density an exchange potential extremely close to the exact one is gained. Starting out from the Hartree–Fock densities [39] the ensemble exchange potentials for multiplets have been calculated.

In a previous paper [16] the ensemble exchange potentials are studied for the following multiplets: ^3P, ^1D, ^1S for the atoms O and S and ^4S, ^2D and ^2P for the atoms N and P. Here, the ensemble exchange potentials are presented for the Si atom. The ensemble exchange potentials are written in the form

$$v_{xc}^{M,g}(w,n;r) = -3\alpha^{M,g}(w)\left(\frac{3}{8\pi}n_w\right)^{1/3} . \tag{39}$$

The factors $\alpha^{M,g}(w)$ are functions of the radial distance r. The exchange factors $\alpha^{M,g}(w)$ for the Si atom are presented in Fig. 5 versus the square of the radial distance. For comparison the ground-state functional α is shown (solid line). The upper line is for ^3P. The exchange factor α of the ensemble obtained from ^3P and ^1D is the middle (point) line. The lower function corresponds to the ensemble arising from ^3P, ^1D and ^1S (dashed line). In these calculations the maximum possible value of w is used, i.e., the ensemble density is given by

$$n = (g_1 n_1 + g_2 n_2)/(g_1 + g_2) \tag{40}$$

for the middle and

$$n = (g_1 n_1 + g_2 n_2 + g_3 n_3)/(g_1 + g_2 + g_3) , \tag{41}$$

for the lower line, respectively. It corresponds to the subspace theory of Theophilou [4].

This figure shows a shell structure. For the ground state the shell structure has already been demonstrated [37]. Though the ensemble exchange potentials are different from the ground state one, the difference is not too much and the factors α show a very similar behaviour.

The fact that the exact exchange potential has similar behaviour for the ensemble of multiplets suggests that approximations might also be similar. Probably, a small change in the ground-state exchange functionals might lead

to good approximation for ensembles of multiplets.

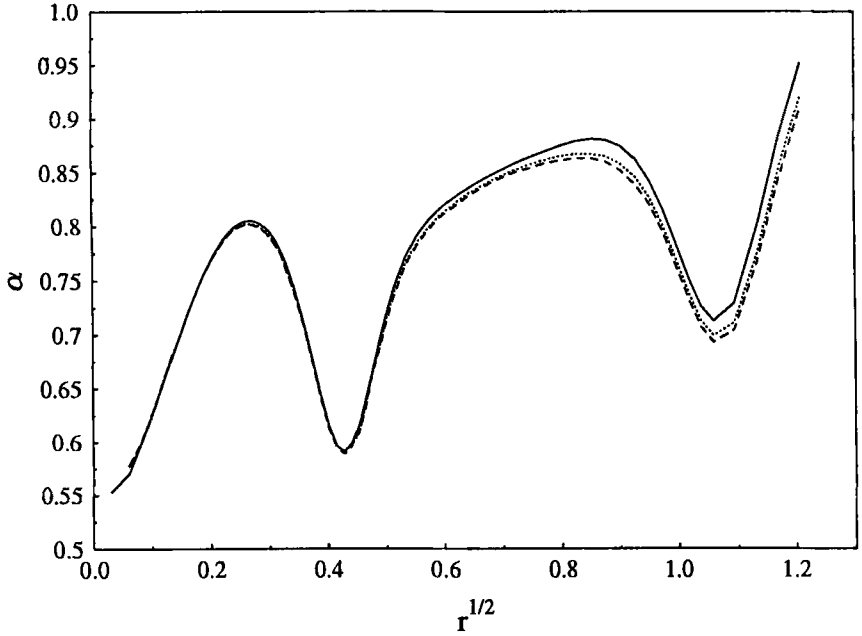

Fig.5. The exchange factors α of the Si atom for the ground-state (^3P) (—) the ensemble obtained from ^3P and ^1D (...) and the ensemble gained from ^3P, ^1D and ^1S (- - -) as a function of the square of the radius.

Fig.6. presents the factors α as functions of the density. The shell structure can be clearly seen, too. If the ensemble exchange potential were a unique function of the ensemble density alone (for different ensembles) the curves α would be exactly the same. However, we can also see that the ensemble exchange potential is not the same function of the ensemble density. Though the curves are very close together, they are not exactly the same. So the ensemble exchange potential has a different dependence on the ensemble densitites for different ensembles.

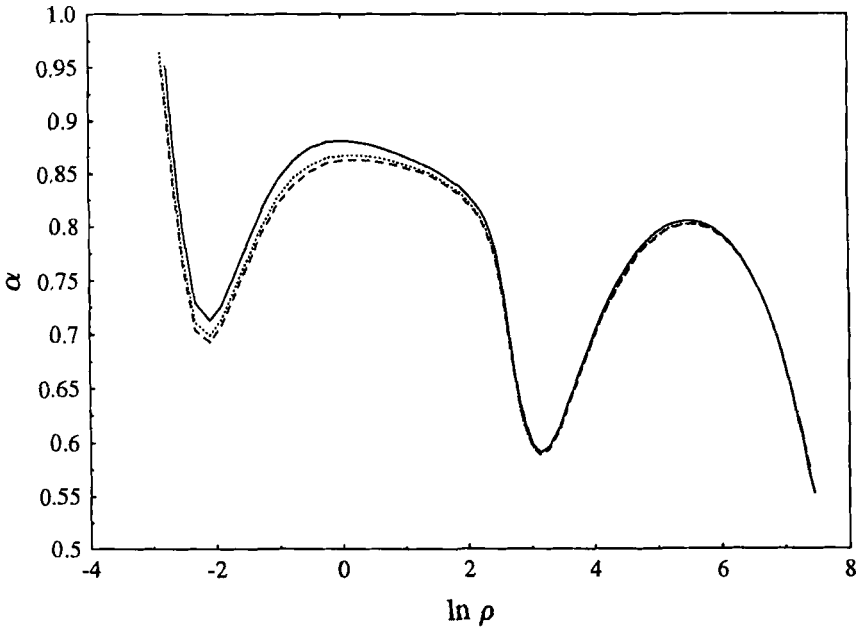

Fig.6. The exchange factors α of the Si atom for the ground-state (^3P) (—), the ensemble obtained from ^3P and ^1D (...) and the ensemble gained from ^3P, ^1D and ^1S (- - -) as a function of the electron density.

It was emphasized in the theory of Gross, Oliveira and Kohn [7] that the ensemble exchange potential depends on w. In a previous paper [16] it was shown that the ensemble exchange factor for multiplets is different for different values of w.

The method described here makes it possible to calculate the ensemble energy (details can be found in [16]). The ensemble exchange energies are very close to the Hartree–Fock ones, the latter being somewhat lower as it is expected.

7 The w dependence of the ensemble exchange energy for multiplets

We have already seen that the w dependence of the ensemble exchange energy is not negligible. In case of multiplets it can be explicitly determined. The first excitation energy (Eq. (19)) takes the form

$$\Delta E^2 = \epsilon_{N+1} - \epsilon_N + \frac{1}{g_2} \frac{\partial E^2_{xc}}{\partial w}\bigg|_{n^2_w} . \tag{42}$$

The electron configuration is the same for the multiplets so $\epsilon_{N+1} = \epsilon_N$. Integrating Eq. (42) with respect to w we obtain for the ensemble exchange energy

$$E^2_{xc} = c_2 w + E^1_{xc} , \tag{43}$$

where

$$c_2 = g_2 \Delta E^2 , \tag{44}$$

and E^1_{xc} is the ground-state exchange energy. Similarly, the second excitation energy reads

$$\Delta E^3 = \frac{1}{g_3} \frac{\partial E^2_{xc}}{\partial w}\bigg|_{n^3_w} + \frac{1}{g_1 + g_2} \frac{\partial E^3_{xc}}{\partial w}\bigg|_{n^2_w} , \tag{45}$$

After integration the second ensemble exchange energy has the form

$$E^3_{xc} = c_3 w + E^1_{xc} , \tag{46}$$

where

$$c_3 = g_3 (\Delta E^3 - \frac{g_2}{g_1 + g_2} \Delta E^2) . \tag{47}$$

So the ensemble exchange energy for multiplets is linear in w. Using the Hartree-Fock values for the ground-state exchange energy E^1_{xc} and the multiplet separation energies ΔE^2 and ΔE^3, the constants c_2 and c_3 can be calculated. Table IV presents these values for several atoms.

Table IV.
Values of constants c_2 and c_3.

Atoms	c_2	c_3
C	0.2865	0.1186
N	1.048	0.5880
O	0.4007	0.1698
Si	0.1963	0.08179
P	0.6994	0.3933
S	0.2633	0.1115
As	0.6660	0.3752
Se	0.2430	0.1030

In Section 5 the w-dependence of the ensemble exchange energy has already been discussed. In that case we have also found a linear dependence for certain light atoms using a very simple $X\alpha$ potential. For a couple of atoms, however, the w-dependence is non-linear. We cannot compare these results with the ones obtained in this section, because both the potentials ($X\alpha$ and almost exact exchange) and the systems are different.

8 Concluding remarks

The study of several ground-state approximations for determining excitation energies leads to the conclusion that the excitation energy cannot generally be calculated as a difference of the one-electron energies. One either try to approximate the extra term or find new forms for the ensemble exchange-correlation potential. This potential should depend on the value of w. For multiplets the ensemble exchange energy depends linearly on w. However, for ensembles of other states the w-dependence might be more complicated.

If it turns out that there are values of w at which the $\frac{\partial E_{xc}}{\partial w}\Big|_{n_w}$ is zero, the excitation energy can be calculated as a difference of the one-electron energies at these values of w. It would correspond to a quasi-particle picture, resulting a simpler way of computing.

9 Acknowledgments

This work was partly made during a visit to Osaka Electro-Communication University (Neyagawa, Japan) in August of 1996. It is a pleasure to thank Professor Taniguchi (Osaka Electro-Communication University, Neyagawa) and Professor Adachi and Professor Mukoyama (Kyoto University) for much stimulation and encouragement, and for generous hospitality. This work was also supported by the grants OTKA No T16623 and F16621 and Foundation for Hungarian Higher Education and Resarch No. 351/95.

References

[1] P. Hohenberg and W. Kohn, Phys. Rev. **B 136**, 864 (1964).

[2] O. Gunnarsson and B.I. Lundgvist, Phys. Rev. **B 13**, 4274 (1976).

[3] J. C. Slater, Quantum Theory of Molecules and Solids vol.4. (McGraw-Hill, New York, 1974.)

[4] A.K. Theophilou, J. Phys. **C 12**, 5419 (1978).

[5] L. Fritsche,Phys. Rev. **B 33**, 3976 (1986); Int. J. Quantum. Chem. **21**, 15, (1987).

[6] H. English, H. Fieseler and A. Haufe, Phys. Rev. **A 37**, 4570 (1988).

[7] E.K.U. Gross, L.N. Oliveira and W. Kohn, Phys. Rev. **A 37**, 2805, 2809, 2821 (1988).

[8] Á. Nagy, Phys. Rev. **A 49**, 3074 (1994).

[9] W. Kohn, Phys. Rev. **A 34**, 737 (1986).

[10] Á. Nagy, Phys. Rev. **A 42**, 4388 (1990).

[11] R. Gáspár, Acta Phys. Hung. **35**, 213 (1974).

[12] Á. Nagy, J. Phys. **B 24**,4691 (1991).

[13] Á. Nagy and I. Andrejkovics, J. Phys. **B 27**, 233 (1994).

[14] Á. Nagy, Int. J. Quantum. Chem.. **56**, 225 (1995).

[15] Á. Nagy , J. Phys. **B 29**, 389 (1996).

[16] Á. Nagy , Int. J. Quantum. Chem.S. **29**, 297 (1995).

[17] R. Gáspár and Á. Nagy, Acta Phys. Hung. **53**, 247 (1982); **58**, 107 (1985); **65**, 405 (1988).

[18] R. Gáspár and Á. Nagy, Theor. Chim. Acta **72**, 393 (1987); J. Phys. **B 20**, 3631 (1987).

[19] Á. Nagy , Int. J. Quantum. Chem. **31**, 269 (1987).

[20] J. C. Slater, Phys. Rev. **81**, 385 (1951).

[21] R. Gáspár, Acta Phys. Hung. **3**, 263 (1954).

[22] W. Kohn and L. J. Sham, Phys. Rev. **140**, A1133 (1965).

[23] A. A. Radzig and B. M. Smirnov, Reference Data on Atoms, Molecules and Ions (Springer-Verlag), Berlin, 1985)

[24] I. Andrejkovics and Á. Nagy , Acta Phys. et Chim. Debr. **29**, 7 (1994).

[25] U. von Barth and L. Hedin, J. Phys. **C 5**, 1629 (1972).

[26] O. Gunnarsson, B.I. Lundgvist and J. W. Wilkins, Phys. Rev. **B 10**, 1319 (1974).

[27] D. M. Ceperley and B. J. Alder, Phys. Rev. Lett. **B 45**,566 (1980).

[28] J. P. Perdew and A. Zunger, Phys. Rev. **B 23**, 5048 (1981).

[29] S. H. Vosko, L. Wilk and M. Nusair, J. Phys. **B 58**, 1200 (1980).

[30] S. Bashkin and J. O. Stoner,Jr, Atomic Energy Levels (North-Holland, Amsterdam, 1975).

[31] P.S. Bagus and B.I. Bennett, Int. J. Quantum Chem. **9**, 143 (1975).

[32] T. Ziegler, A. Rauk and E.J. Baerends, Theor. Chim. Acta (Berl) **43**, 261 (1977).

[33] U. von Barth, Phys. Rev. **A 20**, 1693 (1979).

[34] C. O. Almbladh and A. P. Pedroza, Phys. Rev. A **29**, 2322 (1984).

[35] F. Arysetiawan and M. J. Stott, Phys. Rev. B **38**, 2974 (1988); J. Chen and M. J. Stott, Phys. Rev. A **44**, 2816 (1991); J. Chen, R. O. Esquivel and M. J. Stott, Phil. Mag. B **69**, (1994).

[36] Q. Zhao and R. G. Parr, J. Chem. Phys. **98**, 543 (1993); R. G. Parr, Phil. Mag. B **69**, 737 (1994).

[37] Á. Nagy, J. Phys. B **26**, 43 (1993); Phil. Mag. B **69**, 779 (1994).

[38] A. Görling, Phys. Rev. A **46**,3753 (1992);**51**,4501 (1995).

[39] E. Clementi and A. Roetti, At. Data Nucl. Data Tables **14**, 177 (1974).

Theoretical Calculation of Molecular Photoelectron Spectrum by the First-Principles DV-Xα Molecular Orbital Method

Hirohiko Adachi

Department Materials Science and Engineering, Kyoto University, Yoshida-honmachi, Sakyo-ku, Kyoto 606-01, Japan

Abstract

Theoretical photoelectron spectrum has been calculated by the use of DV-Xα molecular orbital method combined with the calculation of atomic photoionization cross section in Hartree-Fock-Slater model. A calculation of the photoionization cross section has been performed for flexible numerical atomic orbitals including the excited atomic orbitals which are employed for basis functions in the molecular orbital calculation. Some variation of the photoionization cross section is seen when a reconstruction of the atomic orbital due to change in the effective charge takes place. This affects the molecular photoelectron spectrum to a certain extent.

1. Introduction

Photoelectron spectroscopy is known to be very efficient for chemical analysis of the materials[1]. The x-ray photoelectron spectroscopy (XPS) measurement for the chemical shift of the core level is often used to estimate the oxidation state of an

ADVANCES IN QUANTUM CHEMISTRY, VOLUME 29

0065-3276/97 $25.00

atom in molecule or solid. Although the inner-shell level is sensitive to the valence state effective charge of the element, its chemical shift is rather qualitative for the chemical state analysis, because of its insensibility to the element and coordination number of the ligand. On the other hand, the valence-state photoelectron spectrum is strongly affected by the chemical environment. By recent development of the experimental technique for photoelectron spectroscopy, the valence-state spectrum as well as the chemical shift of the core level is considered to be very useful for chemical state analysis of various kind of materials. Because it is difficult to completely understand the chemical state of an unknown material only from the experimental spectrum, a reliable analysis from theoretical calculation of the electronic state is inevitable for the most efficient use of the photoelectron spectroscopy. Discrete variational(DV) Xα cluster method[2] has been proved to be one of the most effective technique to calculate an accurate electronic state of matter. The DV-Xα method has been employed to calculate the theoretical XPS spectra for various kind of molecules and solid state compounds such as free molecules[3], metal oxides[4,5,6] and oxyanions[7,8]. In these calculations, Slater's transition state method[9] is useful to obtain the ionization energies of the molecular orbital electrons, and reproduces well the experimental peak energy in the spectrum. The peak intensity can be estimated by a semiemprical manner, where the photoionization cross section for free atomic subshell is utilized in Gelius's formula[10]. However, recent high resolution XPS spectrum has very clearly shown the valence-band fine structure, and more realistic model calculation seems to be required. Recently, Cserny et al.[8] have reported the theoretical calculation of valence state XPS spectra for phosphate ions employing realistic cluster models based on the crystallographic data. The calculated spectra have shown very good correspondence with the high resolution XPS measurements[11] even for the detailed structure.

However, there has still been problem in their calculation. In the molecular orbital calculation, the basis set is often expanded so as to include some excited atomic orbitals in order to achieve a high accuracy. For estimation of the peak intensity of the XPS spectrum, information of the ionization cross section for the atomic orbital employed for the basis function is required. By the use of Hatree-Fock-Slater model, the ionization cross sections for atomic sub-shell orbitals have been calculated by several authors[12,13]. Although these data are very useful for evaluation of the XPS

peak intensity, they are limited within the occupied atomic orbitals in the ground state for the neutral atom. Furthermore, the effective charge on each atom in molecule obtained by self-consistent-field(SCF) procedure is different from that on the neutral atom. For typical ionic compounds such as alkali halides, the effective charges are very near the formal charges in the compounds, namely ±1, and higher valent ions have larger effective charges. The spatial distribution of the atomic orbital in a potential field of such a material is very different from that for neutral atom, in other word, an orbital contraction or expansion takes place. This naturally causes the photoionization cross section to change. Therefore, an accurate estimation of XPS peak intensity requires an information of the photoionization cross section which includes the effect of SCF potential not only for the occupied atomic orbital but also for excited state orbitals.

In the present paper, first we investigate the photoionization cross sections for atomic orbitals calculated with different scaling parameters of exchange-correlation potential, and for those of different oxidation states, namely different charge densities. We discuss the effect of the variation of the spatial extension of the atomic orbital on the photoionization cross section. Next we make LCAO (linear combination of atomic orbitals) molecular orbital (MO) calculations for some compounds by the SCF DV-Xα method with flexible basis functions including the excited atomic orbitals. We calculate theoretical photoelectron spectrum using the atomic orbital components of MO levels and the photoionization cross sections evaluated for the flexible atomic orbitals used in the SCF MO calculation. The difference between the present result and that calculated with the photoionizaion cross section previously reported is discussed.

2. Computational method

In DV-Xα MO method used in the present study, the ℓth molecular orbital ϕ_ℓ is expressed by an LCAO as

$$\phi_\ell = \sum_i C_{i\ell}\chi_i \,. \qquad (1)$$

For the basis function χ_i, we use a numerical atomic orbital which is generated by

solving Shrödinger equation for *atom in molecule* [2]. During the SCF process, the effective charge on the atom varies. In the present method, the atomic orbital is computed at every SCF iteration, taking the reconstruction of the charge density into account so as to provide an optimum basis function being flexible to any case of the different effective charge. The matrix elements of **H** and **S** in the secular equation,

$$\mathbf{H}\,\mathbf{C} = \varepsilon\,\mathbf{S}\,\mathbf{C}, \qquad (2)$$

are evaluated by the usual DV numerical integration procedure[14] given by

$$H_{ij} = \sum_k \omega(\mathbf{r}_k)\chi_i(\mathbf{r}_k)\,H\,\chi_j(\mathbf{r}_k) \ , \qquad (3)$$

$$S_{ij} = \sum_k \omega(\mathbf{r}_k)\chi_i(\mathbf{r}_k)\,\chi_j(\mathbf{r}_k) \ . \qquad (4)$$

By solving the secular equation, we obtain the orbital energy ε_ℓ and its wave function ϕ_ℓ for ℓth MO. For a molecule, an accurate peak energy of the photoionization can be evaluated by the use of Slater's transition state concept[8]. Slater has suggested that the wave function for the transition state also provides an accurate transition probability[15]. The Slater transition state concept can be utilized to estimate the ionization energy, then the negative sign of the ionization energy corresponds to the MO energy for Slater's transition state. The peak intensity of photoelectron spectrum can be estimated by a semi-empirical method as proposed by Gelius[9]

$$I_\ell = \sum_i Q_i^\ell \cdot \sigma_i \ , \qquad (5)$$

where Q^ℓ_i is the component of atomic orbital i in the ℓth MO, and σ_i is a photoionization cross section for an electron in the atomic orbital i. The value of Q^ℓ_i is estimated by the Mulliken orbital population[16] for MO level ℓ. The photoionization cross section for atomic orbital i is written (in atomic units) by (within the dipole approximation)

$$\sigma_i(\varepsilon_f) = \frac{8\pi^2\alpha_0}{3}\left(\varepsilon_f - \varepsilon_i\right)\left|\langle\chi_i\,|\,\mathbf{r}\,|\,\chi_f\rangle\right|^2 \ , \qquad (6)$$

where α_0 is the fine structure constant, i and f denote the initial and the final states, respectively. Then ε_i is the energy of the atomic orbital i and ε_f is the kinetic energy

of photoelectron. If we put the photon energy as hν, then $\varepsilon_f = h\nu + \varepsilon_i$. The atomic functions χ_i and χ_f are expressed as

$$\chi_i = R_{n_i\ell_i}(r)Y_{\ell_i m_i}(\hat{r}),\ \chi_f = R_{\varepsilon_f\ell_f}(r)Y_{\ell_f m_f}(\hat{r}), \qquad (7)$$

where χ_i is the usual atomic orbital with $\varepsilon_i < 0$, but χ_f is wave function for a continuum state at $\varepsilon_f > 0$ (see Fig.1), both of the radial function for initial and final states can be calculated as the solution R of the equation

$$\left[-\frac{1}{2}\frac{d^2}{dr^2} - \frac{1}{r}\frac{d}{dr} + V(r) + \frac{\ell(\ell+1)}{2r^2}\right] R(r) = \varepsilon\, R(r)\,. \qquad (8)$$

Then, when r is sufficiently large, the function R_f for the final state behaves as

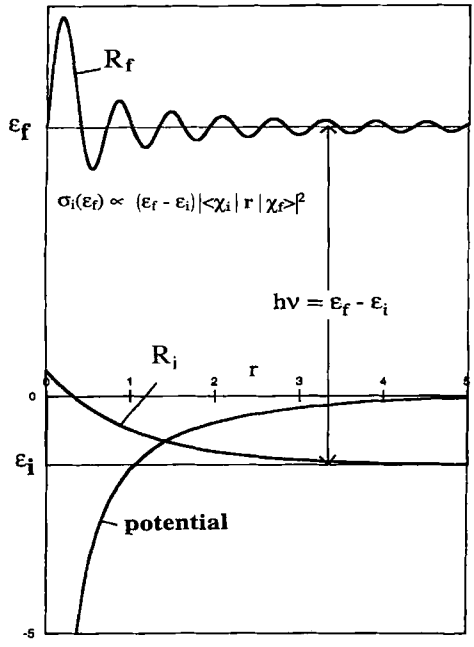

Fig.1 Schematic representation of photoionization process.

$$r \cdot R_f \rightarrow \sqrt{\frac{2}{\pi k}} \sin\left(kr - \frac{\pi \ell}{2} + \delta\right) ,$$

where k is the wave number. The photoionization cross section is calculated by the equation

$$\sigma_i(\varepsilon_f) = \frac{32\pi^3}{9}(\varepsilon_f - \varepsilon_i)\left\{R_{n_i\ell_i}(\varepsilon_f)\right\}^2 \sum_{M=-1}^{1} \left\{C_{1M}(\ell_f m_f; \ell_i m_i)\right\}^2 \qquad (9)$$

where

$$R_{n_i\ell_i}(\varepsilon_f) = \int_0^\infty R_{\varepsilon_f \ell_f}(r) r R_{n_i\ell_i}(r) r^2 dr \qquad (10)$$

and

$$C_{LM}(\ell m; \ell' m') = \int Y_{\ell m}(\hat{r})\, Y_{LM}(\hat{r})\, Y_{\ell' m'}(\hat{r})\, d\hat{r} . \qquad (11)$$

As a consequence, the photoionization cross section of the atomic orbital electron is evaluated by

$$\sigma_i(\varepsilon_f) = \frac{8\pi^3 \alpha_0}{3} \frac{h\nu}{2\ell_i + 1}\left[\ell_i \left\{R_{n_i\ell_i - 1}(\varepsilon_f)\right\}^2 + (\ell_i + 1)\left\{R_{n_i\ell_i}(\varepsilon_f)\right\}^2\right] , \qquad (12)$$

In calculating a theoretical photoelectron spectrum, the atomic ionization cross section σ_i is usually taken so far from the theoretical values calculated for a neutral free atom in the ground state. However, the MO calculation by DV-Xα method is carried out self consistently and provides Q^{ℓ}_i by Mulliken population analysis using the SCF MO wave function calculated. In the present calculations, the atomic orbital χ_i used for the basis function flexibly expands or contracts according to reorganization of the charge density on the *atom in molecule* in the self-consistent field. Furthermore, excited state atomic orbitals are sometimes added to extend the basis set. In such a case, the estimation of peak intensity of the photoionization using the data of σ_i previously published is not adequate. Thus a calculation of the photoionization cross section is required for the atomic orbital used in the SCF calculation in order

to obtain an accurate peak intensity of photoelectron spectrum. In the present work, we calculate σ_i of equation (9) with the χ_i used in the SCF MO calculation and then employ it to estimate peak intensity I_i by equation (5).

3. Result and discussion

The calculations of the photoionization cross section of the atomic subshell have previously been performed using Hartree-Fock-Slater one-electron model by several workers[12,13]. Table 1 compares the photoionization cross sections of the atomic orbital electrons obtained in the present work with those previously reported by Scofield[12] for some atoms. Scofield has used the relativistic wave functions. The

Table 1 Comparison of photoionization cross sections of atomic orbitals for several elements at hv=1486.6eV(Mb)

atomic subshell		Present	Scofield	atomic subshell		Present	Scofield
C	1s	0.0136	0.0136	Se	2p	0.589	0.57
	2s	0.000645	0.000649		3s	0.0194	0.0194
	2p	0.000021	0.000020		3p	0.0602	0.0616
					3d	0.0313	0.0312
Si	2s	0.0130	0.0130		4s	0.00210	0.00218
	2p	0.0110	0.0110		4p	0.00276	0.00286
	3s	0.00116	0.00110				
	3p	0.000338	0.000301	Cs	3s	0.0565	0.0507
					3p	0.227	0.227
Cu	2s	0.0762	0.0743		3d	0.552	0.547
	2p	0.339	0.345		4s	0.0154	0.0147
	3s	0.0129	0.0130		4p	0.0502	0.0521
	3p	0.0329	0.0337		4d	0.0721	0.0714
	3d	0.00802	0.00801		5s	0.00251	0.00251
	4s	0.000338	0.000301		5p	0.00629	0.00682
					6s	0.000075	0.000080

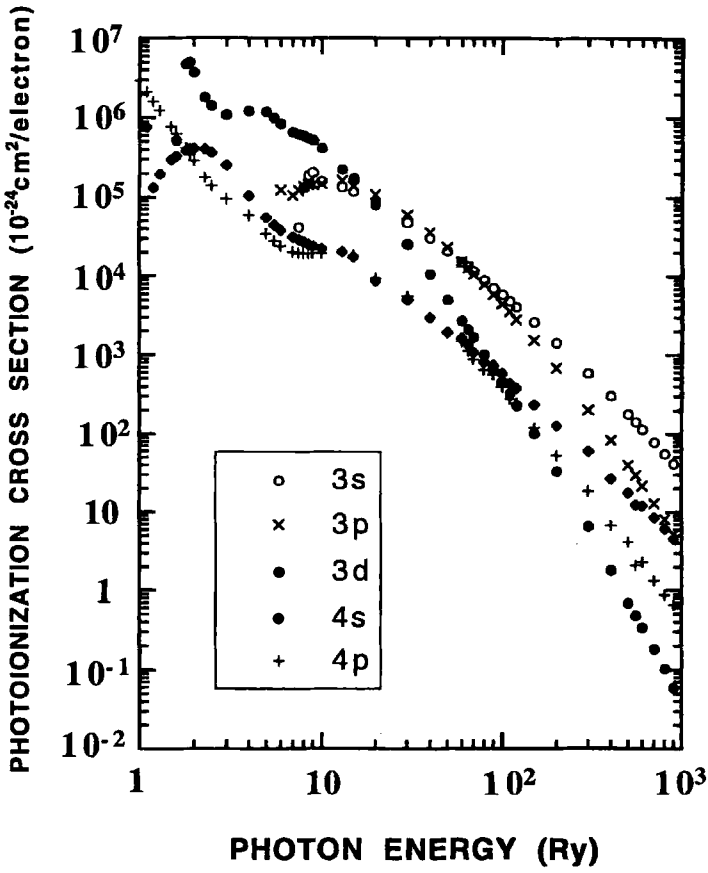

Fig. 2 Photon energy dependence of photoionization cross sections of Fe atomic orbitals

present values involve a certain error due to the nonrelativistic approximation, especially for the inner-shell orbitals of heavy elements. A reasonably good agreement can be seen between the present and previous works.

The value of the photoionization cross section varies for a different photon energy. Figure 2 plots the photoionization cross sections of the atomic orbitals for Fe atom as a function of the photon energy. Yeh and Lindau[13] have reported the photoionization cross sections of atomic subshells for various photon energies. The present result is in a good agreement with the previous calculations.

Next we examine the dependence of the photoionization cross section of atomic orbital on some parameters. The atomic orbital expands or contracts when the electron configuration, namely the effective charge varies, as mentioned above. In the Hatree-Fock-Slater model, we use Slater's exchange-correlation potential with the scaling parameter α. Then the atomic orbital is affected by the parameter α. For DV-Xα MO calculation, we usually use 0.7 for α, which gives an accurate MO energy. However, the photoionization cross sections have mostly been calculated with α = 1.0. The variation of an atomic orbital can be estimated by examining the radius of the atomic orbital which is defined by an average of its radial distribution. Table 2 shows the change in the radius of the atomic orbital for neutral Fe atom calculated with α = 1.0 and 0.7, and for ions in various oxidation states, namely Fe^{+}, Fe^{2+}, Fe^{3+} and Fe^{4+}.

The deep inner shell orbitals such as 1s, 2s and 2p are not very sensitive both to the scaling parameter α and to the oxidation state. On the other hand, the shallow inner shells like 3s and 3p and outer-shell orbitals 3d and 4s strongly depend upon α and the effective charge. Accordingly, the theoretical photoionization cross section computed by equation (12) is affected by the change of spatial extent of the atomic orbital. The theoretical photoionization cross sections for Fe orbitals shown in Table 2 are calculated for the photon energy of hν = 1487eV (Al Kα) and indicated in Table 3. In the case of α=1.0, the atomic orbitals are somewhat contracted compared with

Table 2 Atomic orbital radii for Fe in various oxidation states (a.u.)

state	α	1s	2s	2p	3s	3p	3d	4s	4p
Fe(0)	1.0	0.059	0.268	0.234	0.808	0.843	1.039	2.820	3.833
Fe(0)	0.7	0.059	0.270	0.237	0.820	0.861	1.130	3.040	4.804
Fe(I)	0.7	0.059	0.270	0.237	0.821	0.861	1.104	2.740	3.468
Fe(II)	0.7	0.059	0.270	0.237	0.821	0.861	1.074	2.518	3.004
Fe(III)	0.7	0.059	0.270	0.237	0.813	0.848	0.983	2.271	2.593
Fe(IV)	0.7	0.059	0.270	0.237	0.804	0.832	0.915	2.088	2.318

the case of α=0.7, then the photoionization cross sections are overestimated, when we evaluate the molecular spectra from DV-Xα MO calculation with α=0.7.

When the atom is oxidized and becomes an ion, the spatial expansion of the atomic orbitals are decreased by the reduction of the electronic shielding effect. In such a case, the photoionization cross sections are increased. Although the change is not very large for inner shell electrons, it becomes significant for the outer shells. In the case of a high valent ion like Fe^{4+}, the increments amount to 30% and 90% for the 3d and 4s orbitals, respectively, compared with the neutral atom. On the contrary, the orbitals are expanded and the ionization cross sections decrease for an anion like O^{2-}. The molecular orbital calculation for ClO_4^- anion cluster has been calculated by DV-Xα method with Slater's scaling parameter α=0.7. The valence state levels and their atomic orbital components for the ground state are listed in Table 4. In this calculation, we include the excited Cl 3d orbital in the basis set in order to obtain an accurate MO. The present result is in a good agreement with those previously reported[7] and the valence levels show good correspondence with the experimental XPS peak positions.

The peak intensity can be estimated by the equation (5) using the atomic photoionization cross section of equation (12). The result is summarized in Table 5. We also evaluate the peak intensities using the photoionization cross sections given by Scofield[12] and compare them with the present values. The difference between these results is not very significant, but some discrepancy is appreciable in the valence

Table 3 Theoretical photoionization cross sections for the atomic orbitals of Fe in various oxidation states ($10^{-24}cm^2$/electron)

state	α	2s	2p	3s	3p	3d	4s	4p
Fe(0)*	1.0	31076	37218	5066	3783	388	326	
Fe(0)	1.0	31286	36926	5008	3704	385	478	305
Fe(0)	0.7	30280	35452	4874	3566	329	438	279
Fe(II)	0.7	30341	35110	4884	3554	338	506	282
Fe(III)	0.7	30318	35069	4976	3655	384	676	422
Fe(IV)	0.7	30300	35025	5109	3791	433	853	566

* From reference 12

Table 4 Valence levels and orbital populations for ClO_4^- anion cluster

		Cl			O	
level	ε(eV)	3s	3p	3d	2s	2p
$4a_1$	-23.73	0.491			0.397	0.112
$3t_2$	-18.43		0.174	0.032	0.748	0.046
$5a_1$	-10.40	0.237			0.588	0.175
$4t_2$	-6.71		0.320	0.007	0.183	0.490
1e	-2.67			0.116		0.884
$5t_2$	-2.28		0.000	0.094	0.011	0.895
$1t_1$	-0.77					1.000

Table 5 Theoretical XPS peak intensity for ClO_4^- anion cluster

MO level	Present		Scotfield	
$4a_1$	0.0513	(0.460)	0.0504	(0.425)
$3t_2$	0.1116	(1.000)	0.1185	(1.000)
$5a_1$	0.0425	(0.380)	0.0438	(0.370)
$4t_2$	0.0507	(0.454)	0.0501	(0.423)
1e	0.0046	(0.041)	0.0058	(0.049)
$5t_2$	0.0084	(0.075)	0.0105	(0.089)
$1t_1$	0.0075	(0.067)	0.0099	(0.084)

The number in the parenthesis indicates the relative intensity with respect to the $3t_2$ peak

peak intensities.

We also examine a transition metal oxide cluster with high valence because the atomic photoionization cross section can be expected to change due to the large orbital reconstruction. Figure 3 illustrates the theoretical spectra for FeO_6^{8-} cluster with O_h symmetry. We compare the present spectrum and that obtained with Scofield's values for σ_i. The valence state is constructed by O 2p band overlaying Fe 3d band located at the top of the valence band. The photoionization cross section for Fe 3d electron is considerably affected by the charge reconstruction as mentioned above. Therefore, some discrepancy between the two theoretical spectra can be seen, though it is not very serious.

4. Conclusion

The theoretical calculation for peak intensity of photoelectron spectrum has been carried out in the framework of DV-Xα method. First we calculate the atomic subshell photoionization cross sections. The photoionization cross section for atomic orbital

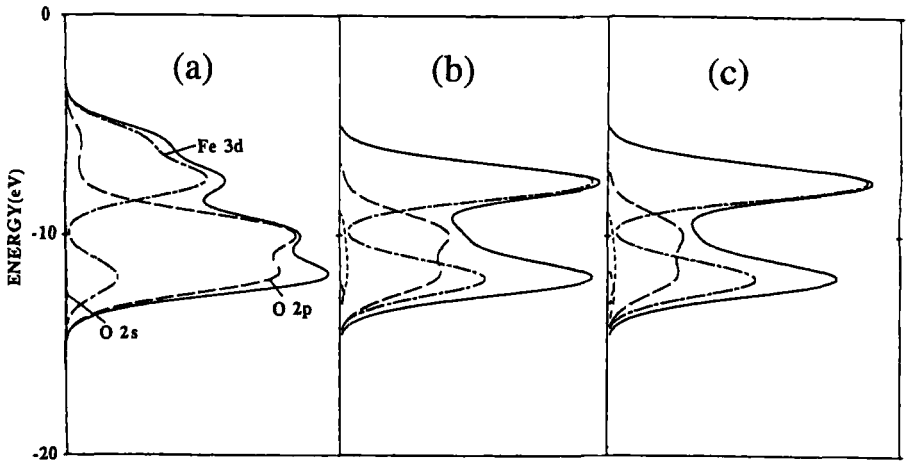

Fig.3 Theoretical valence state XPS spectra of FeO_6^{8-} cluster. (a) density of states, (b) theoretical spectrum with Scofield value for σ_i and (c) present result.

varies when the reconstruction of the electronic charge density of the *atom in molecule* takes place. We calculate the atomic orbital photoionization cross section taking account of the variation of the atomic orbital due to the use of different scaling parameters for exchange-correlation potential, and also due to the charge reconstruction by oxidation of the atom.

Next the DV-Xα molecular orbital calculation has been made using the flexible atomic orbital for the basis function which is numerically generated by solving Schrödinger equation for *atom in molecule* at each SCF iteration. The numerical atomic orbital is contracted or expanded reflecting the charge reorganization of the *atom in molecule* during the SCF iterations. We estimate the peak intensity of the photoelectron spectrum for molecule by a semi-emprical method. The molecular peak intensity is evaluated as the sum of the atomic orbital components multiplied by the atomic orbital photoionization cross sections. The orbital reconstruction somewhat affects the peak intensity in the molecular photoelectron spectrum, though the change in the peak intensity is not very significant. In the MO calculation, the basis set is often extended to include the excited atomic orbitals, then the photoionization cross sections for the excited orbitals are also calculated to involve it in estimating the peak intensity of the molecular photoelectron spectrum. Thus the present method is convenient to produce a theoretical photoelectron spectrum which is consistent with the SCF MO calculation in DV-Xα framework.

Acknowledgment

We thank Prof. T.Mukoyama for his helpful discussion. This work was supported in part by Grant-in-Aid for General Science Research from Ministry of Education, Sports, Science and Culture of Japan.

References

[1] K.Siegbahn, C.Nording, A. Fahlman, R.Nordberg, K.Hamrin, J.Hedman, G.Johansson, T.Bergmark, S.-E.Karlsson, I.Lindgren and B.Lindberg, *ESCA Atomic, Molecular and Solid State Structure Studies by Means of Electron*

Spectroscopy, Nova Acta Regiae Soc. Sci., Upsaliensis, Ser. IV, **20** (1967)

[2] H. Adachi. M. Tsukada and C. Satoko, J. Phys. Soc. Jpn **45**, 875 (1978), H. Adachi, *Introduction to Quantum Materials Chemistry-Approach with DV-Xα Method-* (in Japanese), Sankyo, 1991

[3] H. Nakamatsu, T. Mukoyama and H. Adachi, J. Electr. Spectr., **53**, 265 (1991)

[4] H. Nakamatsu, H. Adachi and S. Ikeda, J. Electr. Spectr., **24**, 149 (1981)

[5] L. Kövér, G. Moretti, Zs. Kovács, R. Sanjinés, I. Cserny, G. Margaritondo, J. Palinkas and H. Adachi, J. Vac. Sci. Technol., **A13**, 1382 (1995)

[6] L. Kövér, Zs. Kovács, R. Sanjinés, G. Moretti, I. Cserny, G. Margaritondo, J. Pálinkás and H. Adachi, Surface and Interface Analysis **23**, 461 (1995)

[7] T. Sasaki and H. Adachi, J. Electr. Spectr., **19**, 261 (1980)

[8] I. Cserny, L. Kövér, A. Némethy, H. Adachi, I. Tanaka, R. Sanjinés, C. Coluzza and G. Margaritondo, Surface and Interface Analysis **23**, 477 (1995)

[9] J.C. Slater, *Quantum Theory of Molecules and Solids* , McGraw-Hill, Vol.4 (1974)

[10] U. Gelius, *Electron Spectroscopy*, ed. by D.A. Shirley, North-Holland, Amsterdam (1972) p.311

[11] A. Le Beuze, R. Lissillour, A. Quemerais, D. Agliz, R. Marchand and H. Chermette, Phys. Rev. **B39**, 11055 (1989)

[12] J.H. Scofield, J. Electr. Spectr. Relat. Phenom. **8**,129 (1976)

[13] J.J. Yeh and I. Lindau, Atomic Data and Nuclear Data Table **32**,1 (1985)

[14] D.E. Ellis and G.S. Painter, Phys. Rev. **B2**, 2887 (1970)

[15] J.C. Slater, *The Calculation of Molecular Orbitals*, John Wiley and Sons,1979

[16] R.S. Mulliken, J. Chem. Phys. **23** (1955) 1833

The Electronic Structure of Silicon Clusters

Hitoshi Kimura, Syunji Imanaga and Yoshinori Hayafuji
Sony Corporation Research Center
134 Goudo-cho, Hodogaya-ku, Yokohama 240 Japan

Hirohiko Adachi
Department of Materials Science and Engineering, Kyoto Universiry
Yoshida honmachi, Sakyo-ku, Kyoto 606-01 Japan

Abstract

The electronic structure of microcrystalline silicon of one-dimensional (1-D), 2-D, and 3-D clusters were calculated using the Discrete-Variational (DV)-$X\alpha$ Molecular-Orbital method. The calculated results are discussed with respect to the effect of the size and the number of dimensions on the energy levels of molecular orbitals. The energy-gap (Eg) between the highest-occupied molecular orbital (HOMO) and the lowest-unoccupied molecular orbital (LUMO) decreases with the increase of cluster size and the number of dimensions. It is found that including silicon $3d$ orbitals as basis sets decreases the Eg value. The results show that the components of silicon $3d$ orbitals in the unoccupied levels near LUMO are over 50 per cent. The calculated results predict that the Eg value will be close to the band gap of crystalline silicon when a 3-D cluster contains more than 1000 silicon atoms with a diameter of 4nm.

ADVANCES IN QUANTUM CHEMISTRY, VOLUME 29

0065-3276/97 $25.00

1 Introduction

Crystalline silicon is well known as one of the most useful semiconductors for electronic devices. Many theoretical calculations on the electronic structure of crystalline silicon have been done by the band structure calculation or the cluster method.

In the cluster method, the cluster is cut out of the crystal, and the surface of the cluster is terminated by hydrogen atoms. However, the energy gap (Eg) between the highest-occupied molecular orbital (HOMO) and the lowest-unoccupied molecular orbital (LUMO) is much larger than the energy-band gap of crystalline silicon (if we ignore the defect energy levels)[1]-[6]. This discrepancy is a serious problem with the cluster method. Estreicher suggested that the HOMO is usually associated with the top of the valence band, and that the LUMO has nothing to do with the bottom of the conduction band [2]. Another explanation is that the Eg value may be affected by the size of the cluster.

Properties such as photoconductivity[7]-[9] and photoluminescence [10],[11] of silicon polymers have been reported because of their wider optical band gap compared with crystalline silicon. Theoretical investigations of silicon polymers have been also reported [12]-[21]. Takeda, Matsumoto and Fukuchi calculated the electronic structure of polysilane chains using the semi-empirical approach called the Complete Neglect of Differential Overlaps (CNDO) Molecular-Orbital (MO) method [12]. They discussed the dependence of the size and geometrical structure of polysilane on the energy level.

Silicon microcrystals [22]-[26] also have a wider optical band gap than that of crystalline silicon and show photoluminesce in the visible region. The Raman spectrum indicated that these hydrogen terminated clusters are mostly crystallized [23]-[25]. On the other hand, there have been many reports on the geometric properties of silicon microclusters. Silicon microclusters, which are not terminated their surfaces with hydogen atoms, are not just small crystals

of bulk silicon but are reconstructed to more compact structure in order to minimize their surface dangling bonds [27]-[32].

Recently, attention have been paid to the properties nano-porous silicon. Canham observed the strong luminescence from porous silicon[33]. A number of photo-luminescent(PL) and/or electro-luminescent(EL) devices have been reported. Steiner et al. reported not only red/orange luminescence but also green/blue electro luminescence from the devices[34]. The quantum confinement or the localized centers at the surface have been reported as the luminescence mechanism. They suggested that the luminescence mechanism depends of the fabrication process of the porous silicon[34].

In this paper, we only focus on the properties of hydrogen-terminated silicon clusters and the surface reconstructions are ignored. All the cluster models, we used in the present work, were cut out of crystalline silicon and the surfaces were terminated with hydrogen atoms.

In order to elucidate the relation between the Eg value and both of the number of dimensions and size of silicon clusters, we treated three types of clusters, that is, one-dimensional (1-D), 2-D, and 3-D silicon clusters, where we defined a 1-D cluster as a zig-zag chain, a 2-D cluster as a planar cluster, and a 3-D cluster as a ball-shaped cluster. The infinite size of 3-D cluster is close to crystalline silicon.

We used the Discrete Variational (DV)-$X\alpha$ Molecular-Orbital (MO) method to calculate the electronic structures of 1-D, 2-D, and 3-D silicon clusters[35] and studied the effect of size and number of dimensions on their Eg values.

2 Theoretical Model

The electronic structures of 1-D, 2-D, and 3-D silicon clusters were calculated using DV-$X\alpha$ MO method[36]-[40]. In the $X\alpha$ method, the exchange-correlation term $\hat{V}_x(\mathbf{r})$ in the one-electron Hamiltonian is written in terms of

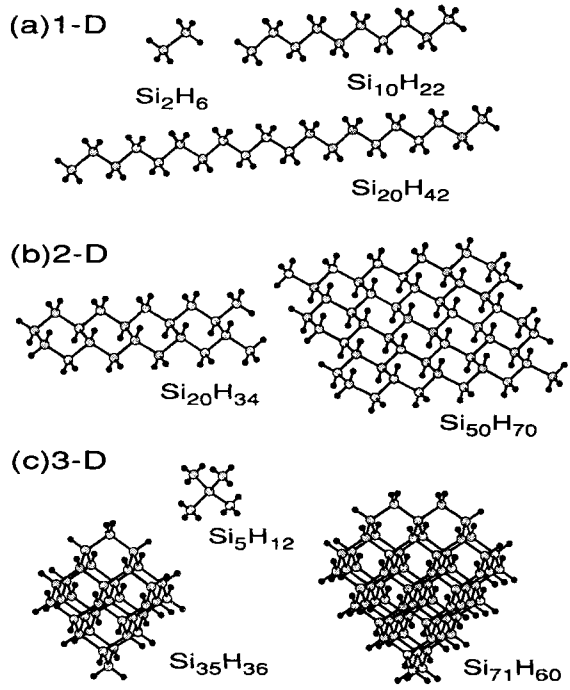

Figure 1: Models of (a) 1-D, (b) 2-D, and (c) 3-D silicon clusters. Si_2H_6, $Si_{10}H_{22}$, and $Si_{20}H_{42}$ are shown as examples for 1-D clusters, $Si_{20}H_{3}$, , $Si_{50}H_{70}$ are shown as examples for 2-D clusters, and Si_5H_{12}, $Si_{35}H_{36}$, and $Si_{71}H_{60}$ are shown as examples for 3-D clusters.

the statistical local potential

$$\hat{V}_x(\mathbf{r}) = -3\alpha[(\frac{3}{8\pi})\rho(\mathbf{r})]^{1/3}, \tag{1}$$

where $\rho(\mathbf{r})$ is the local charge density at $\mathbf{r}$. The coefficient α is the scaling parameter in the DV-$X\alpha$ MO method and was set to α=0.7 throughout the present work. In the $X\alpha$ method, the excitation energy is usually evaluated by Slater's transition-state method [41]-[46] in which a half electron is moved from the ground configuration to an excited configuration.

The method can partly take account of the electronic relaxation effects in the excitations. However, for the 1-D clusters of Si_2H_6 and $Si_{32}H_{68}$, the

calculated Eg values of the transition state did not change from those of the ground state. Therefore, the Eg values in this paper were evaluated from the calculations of the ground configurations.

The surfaces of all silicon clusters used for the calculations were terminated with hydrogen atoms in order to eliminate the dangling bonds. One-dimensional clusters are assumed to be zig-zag chains such as $(SiH_2)_nH_2$(n = 2 to 20) shown in Figure 1(a); the skeletons of the 1-D clusters were cut out of crystalline silicon along the (110) direction. Two-dimensional clusters are planar clusters such as $Si_{20}H_{34}$ and $Si_{50}H_{70}$ shown in Figure 1(b); the skeletons of the 2-D clusters were cut out of crystalline silicon perpendicular to (111) direction. Three-dimensional clusters are ball-shaped clusters such as Si_5H_{12}, $Si_{35}H_{36}$ and $Si_{71}H_{60}$ with T_d symmetry as shown in Figure 1(c). The silicon atoms in these clusters are tetrahedrally coordinated just as those in the crystal. The length of the Si-Si bond was assumed to be 2.35Å on the basis of that in crystalline silicon and the length of the Si-H bond was assumed as 1.48Å based on that of the SiH_4 molecule. In the present work, the calculations were done with and without taking into account silicon $3d$ orbitals. The calculation with silicon $3d$ orbitals were done so as to see the effect of higher-polarized d-type basis function for silicon. $4s$ and $4p$ orbitals were not considered because of those higher energies than $3d$'s. The DV-$X\alpha$ MO calculations were carried out by using an ALLIANT FX/2800GT mini-super computer.

3 Results and Discussion

Figure 2 shows the energy-level diagram of the molecular orbitals of the 1-D silicon clusters $(SiH_2)_nH_2$ with silicon $3d$ orbitals. The levels shown by broken lines are unoccupied. These unoccupied levels correspond to the conduction band in crystalline silicon. The occupied levels shown by solid lines around -17 to -13eV and -11 to -9eV are the valence orbitals mainly localized on silicon $3s$ and $3p$ orbitals, respectively. The unoccupied levels are the

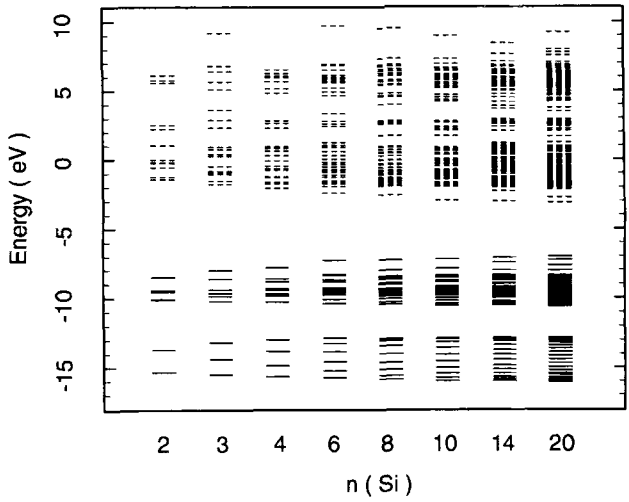

Figure 2: Energy levels of the calculated occupied (solid line) and unoccupied (broken line) levels of molecular orbitals in 1-D silicon clusters with silicon $3d$ orbitals. The number of silicon atoms was varied from 2 to 20.

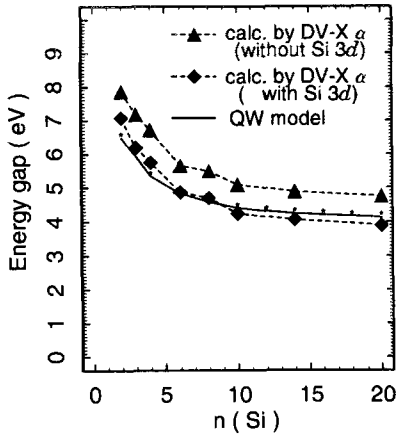

Figure 3: Eg values of 1-D silicon clusters as a function of the size. The calculated Eg values are with (◆) and without (▲) silicon $3d$ orbitals plotted by broken curves. The solid curve shows the Eg values evaluated from Matsumoto's QW model.

antibonding orbitals consist of silicon $3s$, $3p$ and $3d$ orbitals. As the number of silicon atoms increases, the number of orbitals increases and the Eg value decreases.

Figure 3 shows the Eg values of 1-D silicon clusters as a function of size. The calculated Eg value decreases with increase of the number of silicon atoms, that is, the cluster size. Figure 3 also indicates the Eg values evaluated by Matsumoto's quantum-well (QW) model[17] in which the wavefunctions are confined in the potential well and asolute Eg values were determined by interpolating the experimental Eg values of disilane (6.5eV) and polysilane (4eV) by the size dependance of the energy levels of the wavefunctions.

The Eg value derived from the QW model also decreases with an increase in size and the size dependence of the Eg value is similar to our calculated result.

Figures 4 and 5 show the Eg values of 2-D and 3-D silicon clusters also as a function of their size, respectively. The Eg values of of QW-model derived 1-D, 2-D, and 3-D silicon clusters of infinite size were determined by the experimental Eg values of disilane (6.5eV), polysilane (4eV), siloxene (2.5eV) and crystalline silicon (1.1eV), respectively. When the cluster size increases, the Eg values in 2-D and 3-D clusters decrease similar to the decrease in the Eg values in 1-D clusters. Also, the Eg values decrease as the number of dimensions of the cluster increases. These decrease in Eg values have been explained by the fact that the delocalized skeleton σ-electrons form both band edge levels including HOMO and LUMO.

Figures 3, 4 and 5 also show the Eg values when silicon $3d$ orbitals are added to the basis sets. All of the calculated Eg values without Si $3d$ orbitals are about 1eV higher than those of the QW model. However, when Si $3d$ orbitals are taken into account, the calculated Eg values decrease by about 1eV and good agreement with the values given by the QW model is obtained. These results imply that the energy levels around HOMO and LUMO of silicon clusters are well modeled by the quantum confinement of delocalized wavefunc-

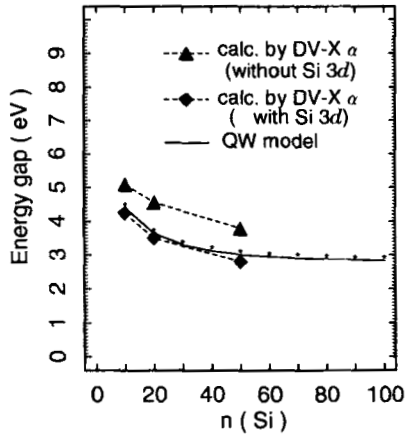

Figure 4: Eg values of 2-D silicon clusters as a function of the size. The calculated Eg values are with (◆) and without (▲) silicon $3d$ orbitals plotted by broken curves. The solid curve shows the Eg values evaluated from Matsumoto's QW model.

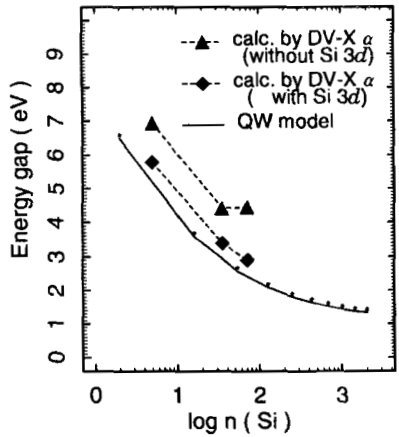

Figure 5: Eg values of 2-D silicon clusters as a function of the size. The calculated Eg values are with (◆) and without (▲) silicon $3d$ orbitals plotted by broken curves. The solid curve shows the Eg values evaluated from Matsumoto's QW model.

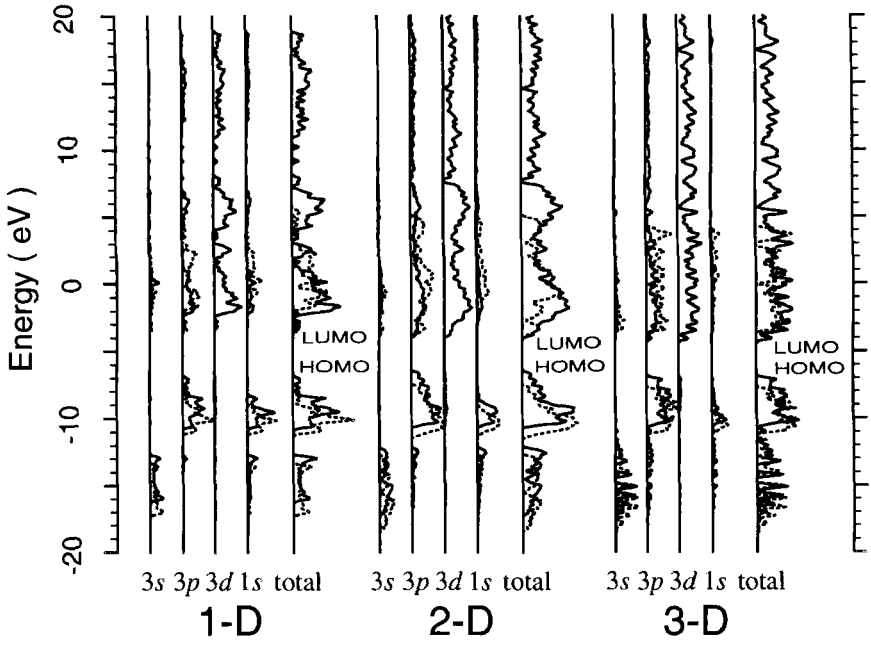

Figure 6: Partial and total Density of States (DOS) of molecular orbitals of 1-D ($Si_{20}H_{42}$), 2-D ($Si_{50}H_{70}$), and 3-D ($Si_{71}H_{60}$) clusters calculated with (solid curve) and without (broken curve) silicon $3d$ orbitals as basis sets. Partial DOS's indicate the contribution of silicon $3s$, $3p$, $3d$ and hydrogen 1s orbitals. The DOS's are drawn by superposition of Gaussian functions for each orbital with a half width of 0.1eV.

tions in the potential well. We think, these size dependances on Eg values are characteristic in the silicon clusters which the covalent bondings form delocalized wavefunctions in the cluster, and not so much in the clusters consist of more ionic bonding.

Figure 6 shows the density of states (DOS) of the molecular orbitals of 1-D, 2-D, and 3-D clusters calculated with (solid curve) and without (broken curve) silicon $3d$ orbitals as basis sets. The partial DOS of silicon $3s$, $3p$, $3d$ and hydrogen $1s$ orbitals in the clusters are also shown in Figure 6. As can

be seen in Figure 6, the DOS of 1-D, 2-D, and 3-D clusters is similar. The occupied levels lower than -12eV mainly consist of silicon $3s$ orbitals, while the occupied levels from -6 to -11eV including HOMO mainly consist of silicon $3p$ orbitals. When silicon $3d$ orbitals are included in the calculations, the occupied levels shift to higher energy by about 1eV. However the mixings of silicon $3d$ orbitals in the occupied levels are small. On the other hand, the mixings of silicon $3d$ orbitals in the unoccupied levels including LUMO were great — over 50%. This suggests that the conduction band of the silicon clusters and silicon crystal can be also well described by taking account of silicon $3d$ orbitals. Takeda, Matsumoto and Fukuchi also calculated the electronic structure of polysilane using semi-empirical CNDO MO method [17]. They suggested the existence of the d-state hybridization into the sp coupling, but details were not reported. The calculated results in the present work clearly show the large contribution of $3d$ orbitals to the unoccupied levels. The Eg values derived from the QW model agreed well with our calculated results including silicon $3d$ orbitals. We think, therefore, that the Eg value approaches that of bulk crystalline silicon (1.1eV) when the 3-D cluster contains more than 1000 silicon atoms, or a ball-shaped cluster has a diameter more than 4nm.

4 Conclusion

We calculated the electronic structure of 1-D, 2-D, and 3-D silicon clusters using (DV)-$X\alpha$ MO method. The calculated energy gap (Eg) between HOMO and LUMO decreases with increase of the cluster size and the number of dimensions of the cluster. It is found that including silicon $3d$ orbitals as basis sets results in lowering the Eg values by about 1eV. The results also show that the components of silicon $3d$ orbitals in the unoccupied levels near LUMO are over 50%. In the case of silicon clusters, the size effect on the Eg value is well described by the quantum-well(QW) model in which the delocalized wavefunctions are confined in the potential well. The calculated results predict that Eg

values will be close to the band gap of bulk crystalline silicon when the 3-D cluster contains more than 1000 silicon atoms or the ball-shaped cluster has a diameter more than 4nm.

References

[1] F. P. Larkins, J. Phys. **C 4,** (1971) 3065.

[2] S. Estreicher, Phys. Rev. **B 36,** (1987) 9122.

[3] P. Deák, L. C. Snyder, R. K. Singh, and J. W. Corbett, Phys. Rev. **B 36,** (1987) 9612.

[4] S. Estreicher, Phys. Rev. **B 37,** (1988) 858.

[5] A. A. Bonapasta, C. Battistoni, A. Lapiccirella, N. Tomassini, S. L. Altmann, and K. W. Lodge, Phys. Rev. **B 37,** (1988) 3058.

[6] M. Saito, A. Oshiyama, Phys. Rev. **B 38,** (1988) 10711.

[7] R. West, L. D. David, P. I. Djurovich, K. L. Stearley, K. S. V. Srinivasan, and H. Yu, J. Am. Chem. Soc. **103,** (1981) 7352.

[8] S. Furukawa and N. Matsumoto, Solid State Commun. **51,** (1984) 833.

[9] R. G. Kepler, J. M. Zeigler, L. A. Harrash, and S. R. Kurtz, Phys. Rev. **B 35,** (1987) 2818.

[10] N. Matsumoto, S. Furukawa, and K. Takeda, Solid State Commun. **53,** (1985) 881.

[11] T. Kagawa, M. Fujino, K. Takeda, and N. Matsumoto, Solid State Commun. **57,** (1986) 635.

[12] K. Takeda, N. Matsumoto, and M. Fukuchi, Phys. Rev. **B 30,** (1984) 5871.

[13] K. Takeda and N. Matsumoto, J. Phys. C: Solid State Phys. **18,** (1985) 6121.

[14] K. A. Klingensmith, J. W. Downing, R. D. Miller, and J. Michl, J. Am. Chem. Soc. **108,** (1986) 7438.

[15] K. Takeda, H. Teramae, and N. Matsumoto, J. Am. Chem. Soc. **108,** (1986) 8186.

[16] K. Takeda, M. Fujino, K. Seki, and H. Inokuchi, Phys. Rev. **B 36,** (1987) 8129.

[17] N. Matsumoto, K. Takeda, H. Teramae, and M. Fujino, *Int. Topical Workshop "Advances in Silicon-Based Polymer Science",* in Hawaii (1987), OS 5-1. Advances in Chemistry, **224**, ACS Books, Chap. 28, (1989) p515.

[18] K. Takeda and K. Shiraishi, Phys. Rev. **B 39,** (1989) 11028.

[19] H. Teramae and K. Takeda, J. Am. Chem. Soc. **111,** (1989) 1281.

[20] K. Takeda, K. Shiraishi, and N. Matsumoto, J. Am. Chem. Soc. **112,** (1991) 5043.

[21] N. Matsumoto and H. Teramae, J. Am. Chem. Soc. **113,** (1991) 4481.

[22] H. Richter and L. Ley, J. Appl. Phys. **52,** (1981) 7281.

[23] S. Furukawa and T. Miyasato, Phys. Rev. **B 38,** (1988) 5726.

[24] S. Furukawa and T. Miyasato, Jpn. J. Appl. Phys. **27,** (1988) L2207.

[25] S. Furukawa and T. Miyasato, Superlattices and Microstructures **5,** (1989) 317.

[26] H. Takagi, H. Ogawa, Y. Yamazaki, A. Ishizaki, and T. Nakagiri, Appl. Phys. Lett. **56,** (1990) 2379.

[27] S. Saito, S. Ohnishi, C. Satoko, and S. Sugano, J. Phys. Soc. Jpn. **55,** (1986) 1791.

[28] D. Tománek and M. A. Schlüter, Phys. Rev. Lett. **56,** (1986) 1055.

[29] D. Tománek and M. A. Schlüter, Phys. Rev. **B 36,** (1987) 1208.

[30] W. L. Brown, R. R. Freeman, K. Raghavachari, and M. Schlüter, Scince **235,** (1987) 860.

[31] C. H. Patterson and R. P. Messmer, Phys. Rev. **B 42,** (1990) 7530.

[32] M. A. Jarrold, Science **252,** (1991) 1085.

[33] L. T. Canham, Appl. Phys. Lett., **57,** (1990) 1046.

[34] P. Steiner, W. Lang, F. Kozlowski, and H. Sandmaier, Mat. Res. Soc. Symp. Proc., **Vol. 298,** (1993) 397.

[35] H. Kimura, S. Imanaga, Y. Hayafuji, and H. Adachi J. Phys. Soc. Jpn., **62,** (1993) 2663.

[36] D. E. Ellis and G. S. Painter, Phys. Rev. **B 2,** (1970) 2887.

[37] E. J. Baerends, D. E. Ellis, and P. Ros, Chem. Phys. **2,** (1973) 41.

[38] E. J. Baerends and P. Ros, Chem. Phys. **2,** (1973) 52.

[39] F. W. Averill and D. E. Ellis, J. Chem. Phys. **59,** (1973) 6412.

[40] A. Rosén, D. E. Ellis, H. Adachi, and F. W. Averill, J. Chem. Phys. **65,** (1976) 3629.

[41] J. C. Slater, J. B. Mann, T. M. Wilson, and J. H. Wood, Phys. Rev. **184,** (1969) 672.

[42] J. C. Slater, *Computational Methods in Band Theory,* edited by P. M. Marcus, J. F. Janak, and A. R. Williams(Plenum Press), (1971) p447.

[43] J. C. Slater and K. H. Johnson, Phys. Rev. **B 5,** (1972) 844.

[44] J. C. Slater, *Advances in Quantum Chemistry*, edited by P. O. Löwdin (Academic Press) **Vol. 6,** (1972) p1.

[45] J. C. Slater, *Quantum Theory of Molecules and Solids*, (McGraw-Hill) **Vol. 4,** (1974).

[46] P. G. Ellis, and O. Goscinski, Physica Scripta **9,** (1974) 104.

Studies of the Valence Band of Tetrahedral Oxyanions

I. Cserny

Institute of Nuclear Research of the Hungarian Academy of Sciences, P.O.Box. 51, H-4001 Debrecen, Hungary

Abstract

Following a short review of early studies of the valence band of tetrahedral oxyanions of types XO_4^{n-} some recent results of this field are discussed. High resolution XPS measurements of the valence band of phosphorus and sulphur oxyanions made possible a rigorous test of various theoretical models. For DV-Xα cluster MO calculations, experimentally determined crystal structure information were used to set up realistic model clusters. In the case of the SO_4^{2-} cluster, the results of several model calculations (*ab initio*, DV-Xα, hybrid models) are presented. From the comparison of these results a better understanding of the role of the contributions from different effects to the MO one-electron energies can be obtained.

Introduction

The electronic structure of tetrahedral oxyanions and their derivatives has been extensively studied by many authors during the past decades. The earlier attempts were summarized by Prins [1]. Since the work of Walsh [2] and that of Wolfsberg and Helmholz [3] several semi-empirical theoretical studies have been published [4-7]. Later *ab initio* [8-10] and scattered wave calculations [11] have been also reported. Among the experimental investigations, Prins mentioned the electron spin resonance measurements of radicals formed by ejection or addition of an electron from or to certain oxyanions, obtaining information on just those molecular orbitals which contained unpaired electrons. [12] X-ray absorption and emission studies provided useful information on a limited number of molecular orbitals in the valence band [13-19].

The application of X-ray photoelectron spectroscopy (XPS) [1, 20-22], has considerably extended the possibilities. The main advantage of XPS is that, in contrast to the spectroscopic techniques mentioned above, it can in principle provide information on all valence levels. A drawback is that the energy resolution of spectra of solid samples is low, especially when a non-monochromated X-ray source (Al Kα radiation with a natural width of ~1 eV) is used.

ADVANCES IN QUANTUM CHEMISTRY, VOLUME 29

0065-3276/97 $25.00

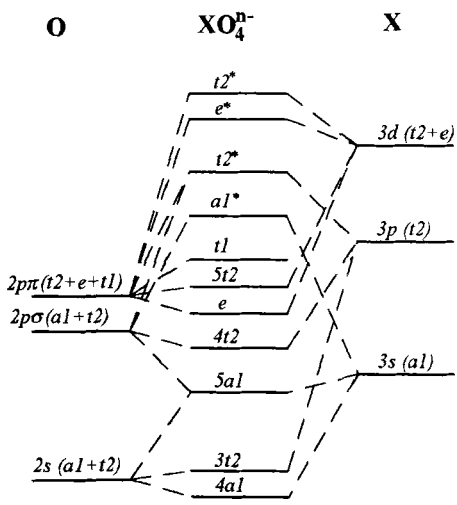

Fig 1. Energy level diagram of tetrahedral oxyanions of elements from the 3rd period.

The assignment of the photoelectron lines (i. e. the identification of the MO levels) is usually done by the help of molecular orbital calculations and X-ray fluorescence data. The schematic LCAO view of the energy level diagram is shown in Fig 1. As an example, the identification of the Li_2SO_4 MO levels [23] is illustrated in Fig 2.

The pioneering work [20] of Connor *et al* provided a set of ionization energies of the valence electrons of the ions PO_4^{3-}, SO_4^{2-}, ClO_4^-, ClO_3^-, CO_3^{2-}. Aqueous solution of lithium salts was deposited and dried on gold foil. The spectra were recorded by an AEI ES100 spectrometer using Al Kα radiation. All electron *ab initio* SCF-MO calculations were performed and correlated to the experimental results by the use of Koopmans' theorem [24] Due to the lack of the formal selection rules in the photoelectron emission, and the limited energy resolution caused by the broadening solid state effect and the natural width of the non-monochromated ionization source, such an assignment can be ambiguous. In order to overcome this problem the experimental data was completed with published X-ray emission data on the ions studied.

Another systematic study of the X-ray photoelectron spectra of the valence region of several oxyanions has been carried out by Prins [1]. XPS valence band spectra of the lithium salts of SiO_4^{4-}, PO_4^{3-}, SO_4^{2-}, ClO_4^-, ClO_3^-, ClO_2^-, SO_3^{2-}, $S_2O_3^{2-}$, MnO_4^- and CrO_4^{2-} were measured. Besides the identification of the photoelectron lines, the intensities were also analyzed with the aid of a LCAO-type model that related the molecular to atomic orbital photoionization cross-sections and atomic population in the molecular orbitals. This intensity model gave a quite satisfactory interpretation of the valence band spectra of these oxyanions. As a function of the atomic number of the central atom, the contribution of the oxygen 2s orbitals was observed. The increase in the *e*, $3t_2 - t_1$ energy separation from SiO_4^{4-} to ClO_4^- was attributed to the increased π backbonding between the oxygen *2p* and central atom *3d* orbitals.

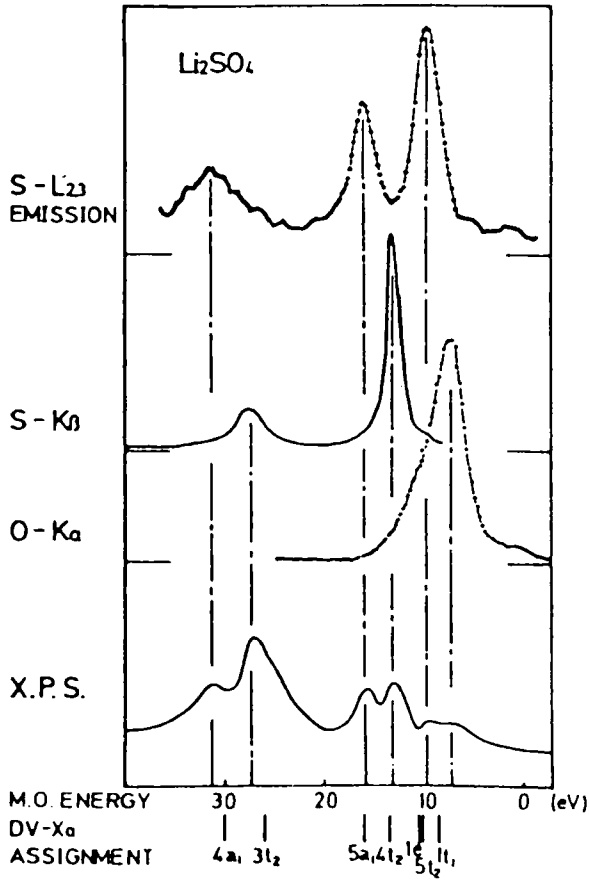

Fig 2. Assignment of spectral lines of S $L_{2,3}$, S Kβ, O Kα X-ray and photoelectron spectra of Li_2SO_4.

Similar investigation in a broader atomic number range was presented by Nefedov *et al* [22], in which lithium salts of PO_4^{3-}, SO_4^{2-}, ClO_4^-, AsO_4^{3-}, SeO_4^{2-}, SO_3^{2-}, ClO_3^-, BrO_3^-, SeO_3^{2-}, IO_3^-, TeO_3^{2-}, AlF_6^{3-}, SiF_6^{2-}, AsF_6^- and SF_6 were measured using a Varian VIEE-15 spectrometer and Al Kα radiation. These spectra were measured with a good statistics revealing minor details not observed in the previous experiments. For example, the oxygen *2s* region of the XPS valence band spectra of Li_3PO_4 contains three peaks (this was not mentioned in the paper), though the MO theories predict only two levels ($4a_1$ and $3t_2$). From the other experimental studies [21, 25, 26] we will discuss the important works of Le Beuze et al [26] and that of from Calabrese and Hayes [21] later.

During the past decade the developments in the experimental technique made possible high resolution measurements of the XPS valence band spectra with a good statistics. The use of these measurements for a more rigorous comparison between the theoretical and experimental data are illustrated by recent results obtained for phosphorus [27, 28] and sulphur [29] oxyanions. In these studies the theoretical interpretation was obtained from DV-Xα cluster MO calculations. Experimental data on crystal structure information from X-ray diffraction measurements were used to set up realistic model clusters. In the case of the SO_4^{2-} cluster, the results of several model calculations (ab initio, DV-Xα, hybrid models) are also presented. From the comparison of these results a better understanding of the role of the contribution from different effects to the MO one-electron energies can be obtained.

Theoretical interpretation of the photoelectron spectra

As a consequence of the significance of the XPS in the investigation of the electronic structure of molecules and solids, the theoretical model calculations of photoionization spectra became an important area of quantum chemistry [30-35]. One possible way of description of the photoionization process is the perturbation theory. The description of the model would exceed the limits of this paper, so we refer to the textbook of Fulde [36] for the details of the formalism and the applied terminology. In this model the excitations are given by the poles of the Green's matrix $G_{\nu\nu}(\omega)$, i. e. by

$$\omega = \varepsilon_\nu + \Sigma_{\nu\nu}(\omega) \qquad (1)$$

where ω is the excitation energy, ε_ν are the energies of the νth spin orbital and $\Sigma_{ij}(\omega)$ denote the elements of the self-energy matrix which has to be calculated as a function of the residual interactions [37]. The structure of $\Sigma_{\nu\nu}(\omega)$ is schematically illustrated in [32]: it contains a sequence of poles and smooth regions between them, leading to different forms of ionization spectra depending on whether one is considering outer valence, inner valence, or core ionization.

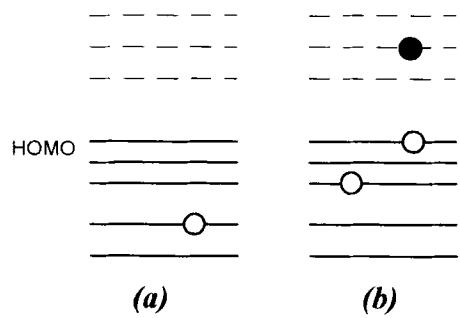

Fig 3. Two electronic configurations of a molecule. Configurations like *(b)* that have almost the same energy as the initial hole state *(a)* are strongly admixed to the final state, resulting in a multipeak structure in the spectrum.

Ionization of outer valence orbitals: When an electron is removed from an orbital close to the highest occupied molecular orbital (HOMO), the spectrum is dominated by the contribution from only one solution of Eq. 1, since in that energy regime the self energy has no poles.

Ionization of inner valence orbitals: In this regime, where several matrix elements have comparable strength, the self energy has a sequence of poles, and has several solutions with comparable residues. A qualitative explanation is given in Fig 3: there are configurations shown in part (b) of the figure that have the same energy as the hole state shown in part (a).

The strong admixture of such states results in a multipeak structure in the spectra and the independent particle approximation MO model may break down completely. A good example for this case is the carbonyl sulfide demonstrated in [35]. In the case of tetrahedral oxyanions, the *O 2s* region of the valence band spectra may also belong to this group.

Core ionization: The core orbitals are localized at one of the atoms of the molecule. The main effect of $\Sigma_{vv}(\omega)$ is true relaxation. It may cause energy shifts of the order of 10 eV, while the remaining correlation effect is usually of the order of 1 eV [34].

Even the lowest order approximation describes three physical processes which take place following the creation of an inner shell hole by the photoionization:

Relaxation: When an electron is removed from an orbital, the remaining orbitals relax toward the nuclei. In other words, the MOs of an (N-1) electron system differ from those of the N electron system, so they adjust themself upon the removal of an electron. This process lowers the excitation energy.

Correlation loss: When an electron is removed from the system, some of the correlations which were present in the ground state can be lost. This is illustrated on Fig 4. Configuration interaction method is the most general of various theories for treating electron correlations. In most cases only single

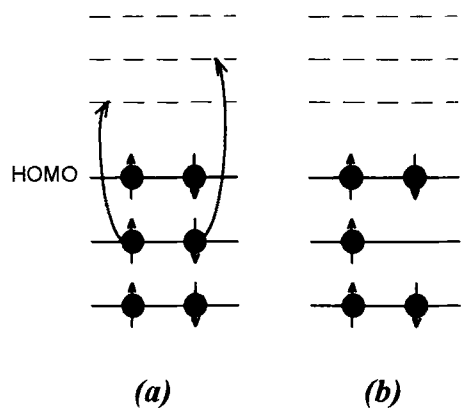

Fig 4. The change of the correlation due to ionization: the two-electron excitation which is present in the ground state *(a)* is missing when an electron has been removed *(b)*.

and double substitutions are considered, i.e. the basis system is constructed from one and two-electron excitations admixed to the SCF ground state. The double substitutions which are present in the ground state (Fig 4.a) cannot take place when one of the electrons has been removed (Fig 4.b). Losses of ground state correlations result in an increase of the excitation energy.

Polarization effects: The vacancy created by photoionization will be surrounded by a polarization cloud. This process is different from the charge redistribution due to relaxation mentioned above. This process results in a decrease in the excitation energies.

It is important to note, that for the accurate estimation of spectral intensities of the theoretical spectra it is not sufficient to consider only the lowest order processes. A sufficiently accurate yet relative simple computational scheme is the two-particle-hole Tamm-Dancoff approximation [36]. Due to the difficulties and complications involved in the computations there are only few such studies [32-35]. The majority of the authors use a simplified model for the estimation of the ionization energies, based on one of the following approximations:

Koopmans' theorem [24] relates the ionization energies to the one-electron orbital energies of the ground state:

$$I_i = E^+ - E^0 \approx - \varepsilon_i$$

where E^+ is the total energy of the ionized molecule, E^0 is the total energy of the molecule in the ground state, ε_i is the ground state one-electron orbital energy of the level considered. The major drawback of this approximation is the complete neglection of the relaxation and correlation effects.

The failure of the Koopmans' theorem has been observed in many cases. As a general tendency, the orbital energies calculated by the HF method are usually larger than the experimental values. The opposite tendency is true for the Xα method. A very simple semiempirical correction, which is often called the "92 % rule" is mentioned in [38]

$$I_i \approx -0.92\varepsilon_i$$

which is suitable for the correction of HF results. On the other hand, in our studies of the PO_4^{3-} and SO_4^{2-} oxyanions [27-29] the following rule was found for the Xα method:

$$I_i \approx -1.1\varepsilon_i$$

A more accurate approximation is the transition state calculation scheme proposed by Slater [39].

$$I_i \approx -\varepsilon_i(n=1/2)$$

where the ε_i one-electron spin orbital energies of states in which half of an electron is removed from the orbital considered, are calculated. A generalized transition state calculation scheme was proposed by Williams *et al* [40]:

$$I_i \approx -[\varepsilon_i(n=1) + 3\varepsilon_i(n=1/3)]/4.$$

In this method the ionization energy is calculated from the weighted mean of the one-electron energies of the ground state and of a transition state in which 2/3 of an electron is removed from the spin orbital considered. The transition state calculations should be carried out through spin unrestricted calculations.

While a great deal of effort has been spent on the interpretation of energies, a much less number of studies have been published of the corresponding intensities in photoelectron spectra of molecules. Due to the lack of information on the molecular photoionization cross-sections, in most cases the simple semiempirical formula proposed by Gelius is used [41]:

$$I_j \propto \sum_i \sigma_i P_{ij}$$

where I_j is the intensity of the photoelectrons originated from the *j*th molecular orbital, P_{ij} denotes the Mullikan gross population values for the *i*th atomic orbital obtained from the MO calculations, and σ_i is the photoionization cross-section of the *i*th atomic orbital. Such atomic photoionization cross-sections were obtained for free atoms from theoretical calculations [42]. In few cases experimentally determined photoionization cross-sections were used [1, 21, 41].

Studies of the valence band of phosphorus oxyanions

The important role of the phosphates in many practical fields as water softening agents, corrosion inhibitors, phosphate glasses, thin film insulators on semiconductors, etc. attracted a great deal of attention, and their electronic structure has been studied so far by many authors by applying different analytical techniques like XPS [1, 20, 22, 25], X-ray spectroscopy [43, 44] and X-ray excited Auger-electron spectroscopy [27]. The spectra of the tetrahedral PO_4^{3-} anion was successfully interpreted by means of molecular orbital calculations [45]. These calculations, however, represented a challenge to the experiments, reliable, high-resolution data were needed for a more rigorous testing of the theoretical models.

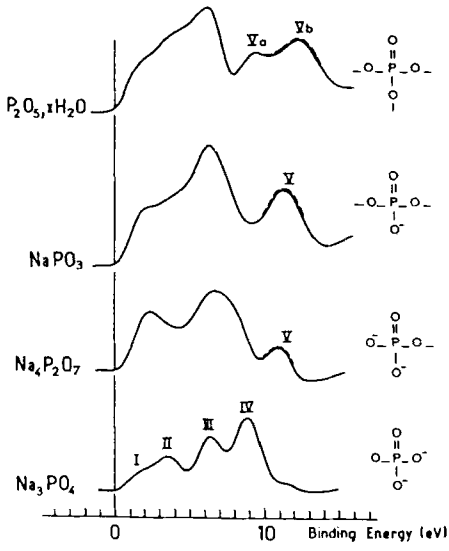

Fig 5. XPS valence band spectra of Na_3PO_4, $Na_4P_2O_7$, $(NaPO_3)_n$ and P_2O_5 (from [26]). The separable lines are labeled in the order of their binding energy. The most characteristic features are underlined by dashed line.

From the point of view of practical applications, the understanding of the electronic structure of condensed phosphates (consisting of different numbers of PO_4 tetrahedra linked by oxygen bridges) is important. The first systematic analysis of the evolution of the valence band within a series of condensed phosphates was carried out by Le Beuze *et al* [26]. In their study, experimental XPS spectra of standard phosphorus oxides like Na_3PO_4, $Na_4P_2O_7$, $(NaPO_3)_n$ and P_2O_5 were measured. The spectra of pressed powder samples were recorded by using a WSW HA 100 hemispherical analyzer and Mg Kα radiation as photon source. In order to compensate the broadening effect of the non-monochromated excitation source, resolution enhancement technique (deconvolution by means of a fast-Fourier transformation program) was applied. The experimental data were compared to theoretical spectra obtained from band structure calculations using the extended Hückel theory and tight-bonding approach. In spite of the limited energy resolution

obtained by the non-monochromatized Mg Kα photon source, the main features of the valence band of a series of phosphates were explored (Fig 5) and, in the case of condensed phosphates, the advent and the evolution of a new band (peak *V*th in Fig 5) was observed. The latter feature was assigned to the s-orbital interaction through the P–O–P bonds. As an example, the theoretical XPS valence band spectra is shown on Fig 6. Even in the case of Burns parametrization the relative energies (peak distances) are much smaller (by almost a factor of 2) than those in the experimental spectra. These deviations between the experimental data and the theoretical results stimulated further studies and the application of a more elaborated cluster MO method.

Kowada *et al* [46] published DV-Xα calculations for different phosphates that were supposed to exist in phosphate glasses. The published one-electron energies were in agreement with the earlier experimental results [26], although a detailed comparison was not possible because of the limited energy resolution of the experimental data available. These model calculation showed, that a new band appearing between the so called O 2s and O 2p region can be attributed to the bridging oxygen atoms (O_b), and the number of the MO levels in this region is equal to the number of these bridging atoms. The energy gap between the highest occupied (HOMO) and the lowest unoccupied (LUMO) MO levels was found to be decreasing with the increasing O_b/P ratio. From the Mullikan population analysis the dependence of the bond order (overlap population) on the O_b/P ratio was also obtained. In the case of the $P_4O_{13}^{6-}$ branch cluster which is supposed to exist in ultraphoshate glasses, the P-O_b bond was found to be less stable than that in the case of chain and ring clusters. This can explain the antibranching rule and the hygroscopic behavior of ultraphosphate glasses. Since in these calculations the emphasis was on the electronic structure and chemical bonding, the MO parentages required for the construction of theoretical XPS valence band spectra were not published. Moreover, the crystal parameters were different from

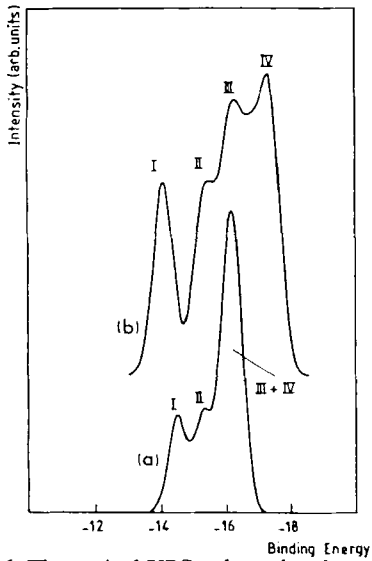

Fig 6. Theoretical XPS valence band spectra of PO_4^{3-} obtained by using *(a)* Slater parameters; *(b)* Burns parameters (Ref 26). The peak labeling is identical to that in Fig 5.

those obtained by X-ray diffraction experiments for the crystalline form of condensed phosphates. This facts and the increasing demands for high resolution XPS valence band data of condensed phosphates stimulated the further investigations of this field.

New experimental XPS valence band spectra of polycrystalline Na_3PO_4 and $(NaPO_3)_n$ obtained by using a Rigaku XPS-7000 instrument equipped with monochromated Al Kα X-ray source were published in [27]. To obtain more information about the local electronic structure, the X-ray excited P and O K-Auger (KLV, KVV) spectra of these compounds were also measured and the experimental results were interpreted by means of the DV-Xα cluster molecular orbital model and by semi empirical approximations. The similarity observed in the KLV Auger spectra of these compounds demonstrated that the local electronic structure around the core-ionized central atom is reflected in the K-V Auger spectra, showing the dominant effect of the local symmetry.

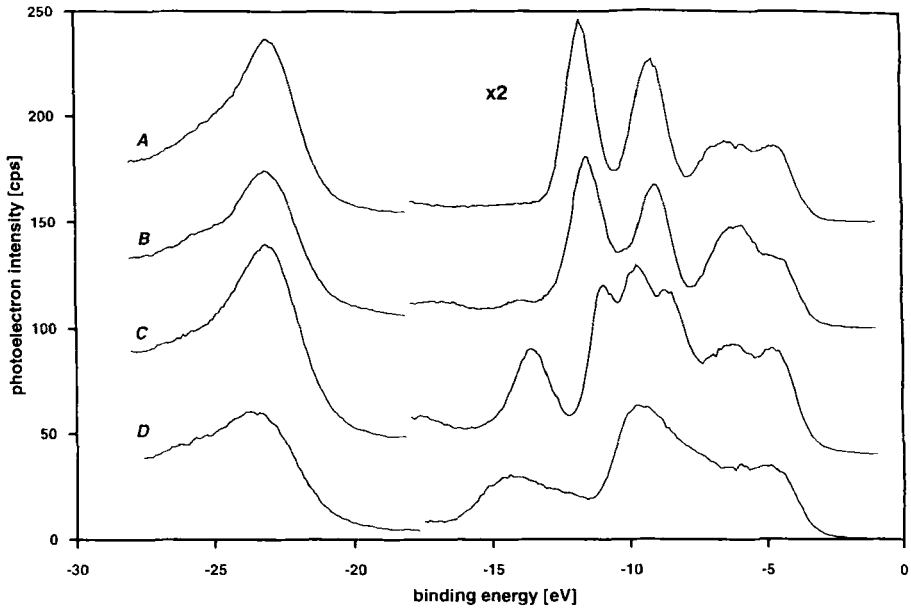

Fig 7. Monochromated XPS valence band spectra of *(A)* Li_3PO_4; *(B)* Na_3PO_4; *(C)* $Na_4P_2O_7$; *(D)* $(NaPO_3)_n$ (Ref 28) polycrystalline powder samples.

A more systematic study of the valence band structure of phosphorus oxyanions was published in [28]. In this study monochromated Al Kα XPS measurements of the valence band spectra of Li_3PO_4, Na_3PO_4 $Na_4P_2O_7$ and $(NaPO_3)_n$ (n>3) polycrystalline powder samples were performed. The spectra were recorded by using a SCIENTA ESCA-300 instrument equipped with a rotating anode X-ray source. The overall energy resolution of the instrument was ~0.4 eV. Correction for the charging effect was made by referencing to the adventitious C 1s line. It should be noted, however, that the differential charging (i.e. when different parts of the analyzed sample area are charged to different potentials) may lead to an extra broadening of the photopeaks. In order to minimize this contribution, a uniformly charged small area of the sample (typically 0.5x0.5 mm^2) was selected for analysis. Further details about the experiments are given in [28]. The measured XPS valence band spectra (without background subtraction) are shown in Fig 7. These spectra are somewhat different from those obtained earlier [26] (see in Fig 5). The most striking difference was observed in the case of the $Na_4P_2O_7$ compound, where the number of peaks were doubled.

For the interpretation of these spectra DV-Xα cluster MO calculations were performed using numerical basis set and the self-consistent charge (SCC) scheme. The Slater exchange potential $V_{exc} = -3\alpha(3\rho(r))/8\pi)^{1/3}$ was used, where α is the exchange scaling parameter and ρ is the charge density; α was fixed at 0.70 for all calculations. The details of the method have been described elsewhere [23, 45, 47]. A near minimal basis set was used: atomic orbitals *1s - 3d* for P, *1s-3p* for Na and *1s-2p* for O and Li. The theoretical photoelectron spectra were calculated from the local density of states (DOS), replacing the MO energy levels by energy distribution (Gaussian) functions. For the calculation of these distribution functions the linewidth parameters determined from the evaluation of the corresponding experimental spectra were used. The line intensities were obtained from the semi-empirical formula proposed by Gelius [41] using atomic photoionization cross-sections calculated for neutral free atoms [42]. Information on crystal structure from X-ray diffraction measurements available in the literature was used to set up realistic model clusters.

PO_4^{3-}

In Fig 8. the experimental XPS valence band spectra of Na_3PO_4 (curve B) is compared to the theoretical spectrum (curve A) obtained for a regular tetrahedron (P-O distance = 0.153 nm; O-P-O angle = 109.5° taken from Ref 48). The calculated spectrum is similar to those obtained earlier [45, 46] and it is in a good agreement with the experimental data if we use an empirical correction factor of 1.14. In other words: we found that the calculated ground state energies can excellently reproduce the experimental ionization energies if we apply the simple

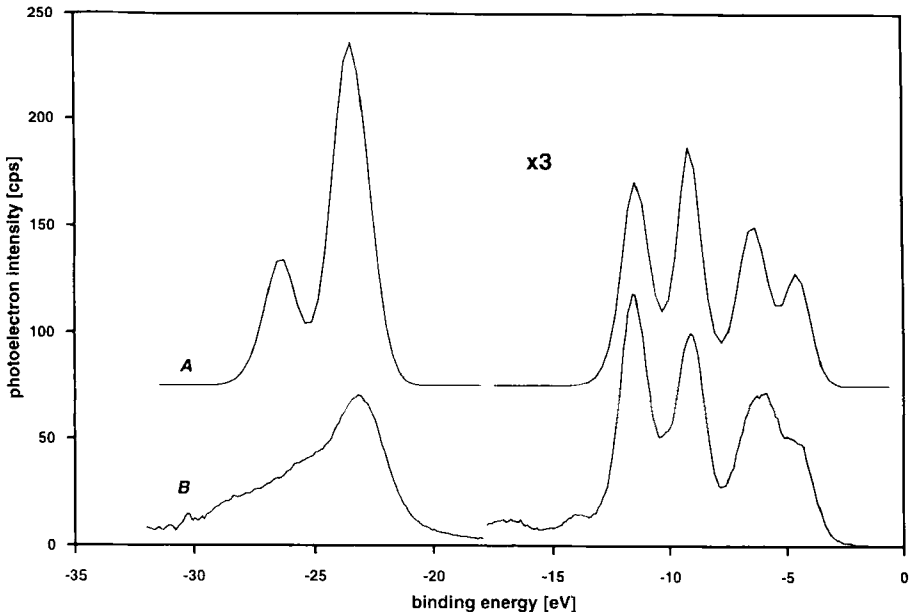

Fig 8. The PO_4^{3-} XPS valence band spectrum *(A)* calculated by using the DV-Xα cluster MO method, in comparison with the experimental valence band spectrum *(B)* of the Na_3PO_4 sample (Ref 28).

$I_i \approx -1.14\varepsilon_i$ empirical correction formula. The effect of the crystal forces was checked by performing DV-Xα calculation using a non-regular PO_4^{3-} cluster.

The atomic positions were taken from available X-ray diffraction data [49]. The results were almost identical to those of the regular PO_4^{3-} cluster, and the respective energy values were in agreement within 0.1 eV. Similar results were obtained from a $Li_{12}PO_4^{9+}$ cluster (one P atom surrounded by the nearest neighboring O and Li atoms, geometry parameters taken from [49]). These results proves the validity of the earlier supposition, that in the valence band spectra the local effects are dominating, the small distortions in the geometry and the neighboring cations (Na^+ or Li^+) play only a minor role.

$P_2O_7^{4-}$

The $P_2O_7^{4-}$ dimer pyrophosphate anion consists of two PO_4^{3-} units sharing one oxygen atom that is called the 'bridging oxygen' O_b. The other oxygen atoms are called non-bridging or terminal (O_t). Theoretical XPS valence band spectra based on two different cluster models are shown and compared to the respective

experimental data in Fig 9 [28]. The fine structure (i.e. the large number of separable lines) in this spectrum was not observed in the earlier study [26]. Curve A was obtained from a model cluster describing the structure of the anion in hydrated pyrophosphate ($Na_4P_2O_7 \cdot H_2O$), the parameters were taken from Ref 50 ($P–O_b$ distance = 0.161 nm; $P–O_t$ distance = 0.152 nm; $P–O_b–P$ angle = 134°). For the calculation of curve B another cluster geometry, characteristic of the anhydrous form of $Na_4P_2O_7$ was used ($P–O_b$ distance = 0.163 nm; $P–O_t$ distance = 0.151 nm; $P–O_b–P$ angle = 127.5° [51]). The most characteristic feature of these spectra is the single level near to 15 eV. The large shift of this level due to the changes in the cluster geometry (mainly in the $P–O_b$ –P angle) provides an opportunity to distinguish between the hydrous and anhydrous form of $Na_4P_2O_7$ from the XPS valence band spectra. The empirical $I_i/-\varepsilon_i$ ratio of value 1.12 was found [28].

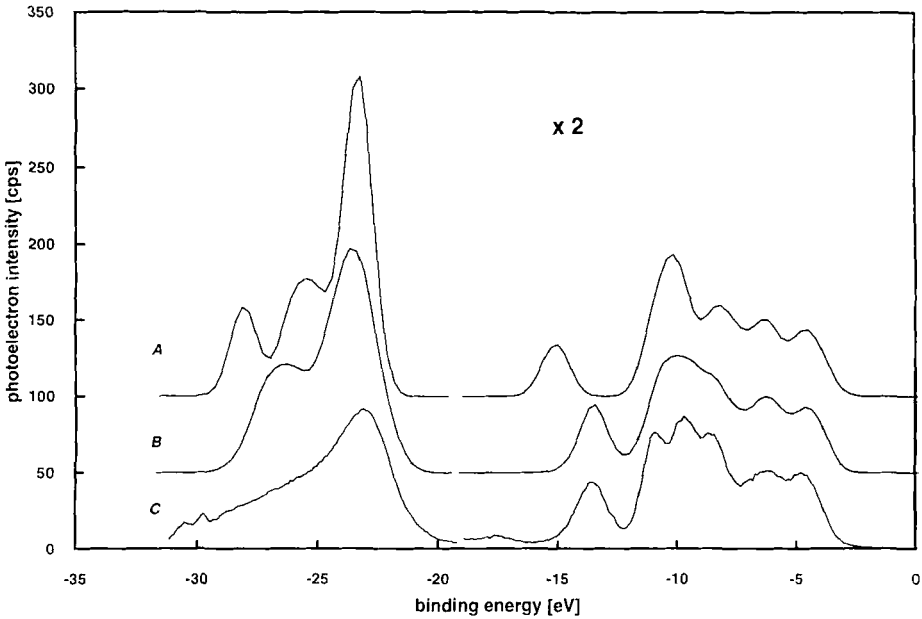

Fig 9. The $P_2O_7^{4-}$ XPS valence band spectra of anions corresponding to the hydrated *(A)* and anhydrous *(B)* forms of $Na_4P_2O_7$, calculated by using the DV-Xα cluster MO method, in comparison with the experimental valence band spectrum *(C)* of the $Na_4P_2O_7$ sample (Ref 28).

PO_3

In the case of metaphosphates, each tetrahedron shares two bridging oxygen atoms with their neighbors, thus forming rings, chains or spirals of various forms and size. Fig 10. shows calculated XPS valence band spectra based on two different model clusters together with our experimental data measured from $(NaPO_3)_n$ (n>3) sample [28]. Model A represents a hypothetical cyclic tetra-metaphosphate ring ($P_4O_{12}^{4-}$) while model B describes a realistic case, a $P_4O_{13}^{4-}$ spiral consisting of four PO_4^{3-} tetrahedra. The parameters were similar in both case ($P–O_b$ distance = 0.156 nm; $P–O_t$ distance = 0.148 nm; average O–O distance =0.25 nm [52]). In these spectra an increase of the number of levels and a band-like structure was observed. The large change in the spectra due to the changes in the cluster geometry illustrates a remarkable dependence on the bonding angles. The experimental data was in agreement with the theoretical spectrum obtained from model B. The empirical $I_i/-\varepsilon_i$ ratio of value 1.10 was found [28].

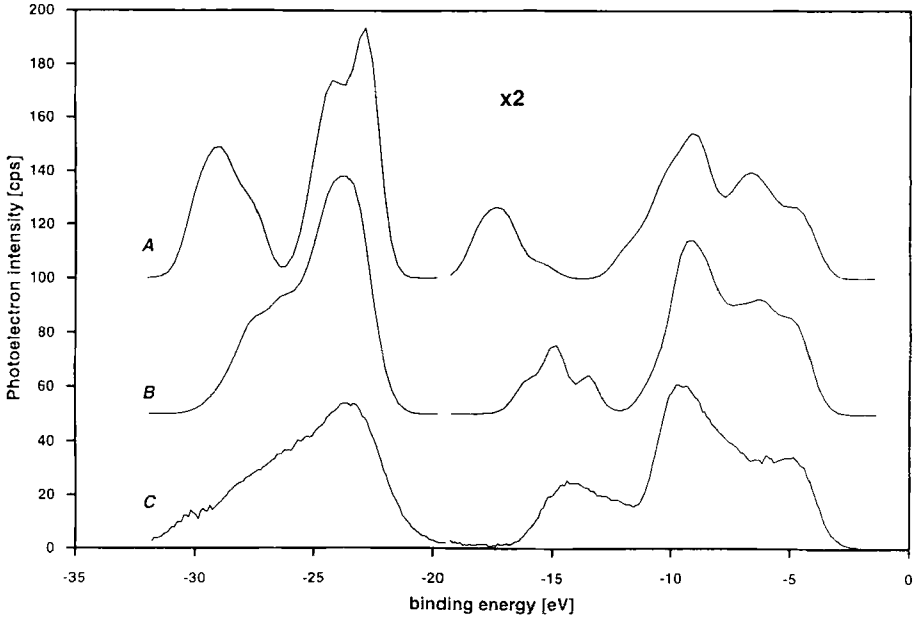

Fig 10. Theoretical XPS valence band spectrum of a $P_4O_{12}^{4-}$ cluster *(A)* and that of a PO_3^- cluster embedded into a $P_4O_{13}^{4-}$ cluster *(B)* calculated by using the DV-Xα cluster MO method, in comparison with the experimental valence band spectrum *(C)* of the $(NaPO_3)_n$ (n>3) sample (Ref 28).

Theoretical and experimental studies of the valence band of the SO_4^{2-} anion

The electronic structure of the SO_4^{2-} anion has been the subject of many theoretical studies of varied degrees of sophistication ranging from the *ab initio* SCF MO calculations to the scattered wave Xα approach. The result of the earliest studies [53, 54] was somewhat uncertain: the order of the molecular levels was dependent on the choice of the parameters of the basis set. However, they could conclude, that the highest filled orbital should be a triply degenerated level, and the sulphur *3d* orbital play an important role in the sulphur oxygen bonds. *Ab initio* calculations were reported by Hillier and Saunders [8] and also by Keeton and Santry [55]. Both of these calculations based on minimal *spd*-basis of Slater type orbitals, expanded in Gaussian functions. The main problems of these earlier works were summarized as [9]: *(a)* the *sp* approximation gives a very polar S-O bond with a sulphur charge of around +2. *(b)* the *spd* calculations give an almost neutral sulphur atom. These problems arose from the fact that a minimal *sp* basis was utilized. It is known that such calculations tend to overestimate the importance of the 3d orbitals. The aim of the MO-SCF-LCAO study of Gelius *et al* [9] was to investigate the effect of using a more extended *sp* basis. While the energy values obtained from this study were similar to those calculated earlier [8], the decreasing role of the 3d orbital (when the number of s and p type orbital is increased) was clearly demonstrated, and more realistic values of the net charges were obtained. The usefulness of the discrete variational Xα (DV-Xα) method for the theoretical study of the tetrahedral oxyanions was demonstrated in [45]. The numerical basis functions, the simple exchange functional and the discrete variational integration scheme makes this method very suitable for the easy extension of the cluster model as it was done in [29].

Among the earlier experimental XPS valence band studies of Li_2SO_4 [1, 11, 22, 45] we refer to the analysis done by Calabrese and Hayes [21]. In their study Mg Kα radiation was used for the excitation of the sample, thus obtaining a somewhat better resolution than that of the earlier studies. Comparing these data to the theoretical results [8] they found few minor problems (there are differences in the relative energies and in the intensity of the $4a_1+3t_2$ group). These problems stimulated further studies of this field.

Recently new, high resolution measurements were performed [29] and interpreted by means of both *ab initio* and DV-Xα cluster calculations. The experimental conditions were identical to those mentioned above in the previous section: monochromated Al Kα radiation was used, and the spectra were recorded by using a SCIENTA ES-300 spectrometer. Fig 11 shows the XPS valence band spectra of

powdered Na_2SO_4 and $Li_2SO_4 \cdot H_2O$ samples. We note, however, that in ultrahigh vacuum (according to our previous experiences) the crystalline water is lost (at least from the topmost layers) from samples of this kind, and the experimental spectra are in agreement with those calculated assuming crystal structure characteristic for the anhydrous crystal, and there is a disagreement with those for the hydrous crystal. The spectra shown in Fig 11 are almost identical (except of the strong Na 2p peak originated from the Na_2SO_4 sample) suggesting that the cations plays only a minor role, and the spectra is basically determined by the local structure of the SO_4^{2-} anion.

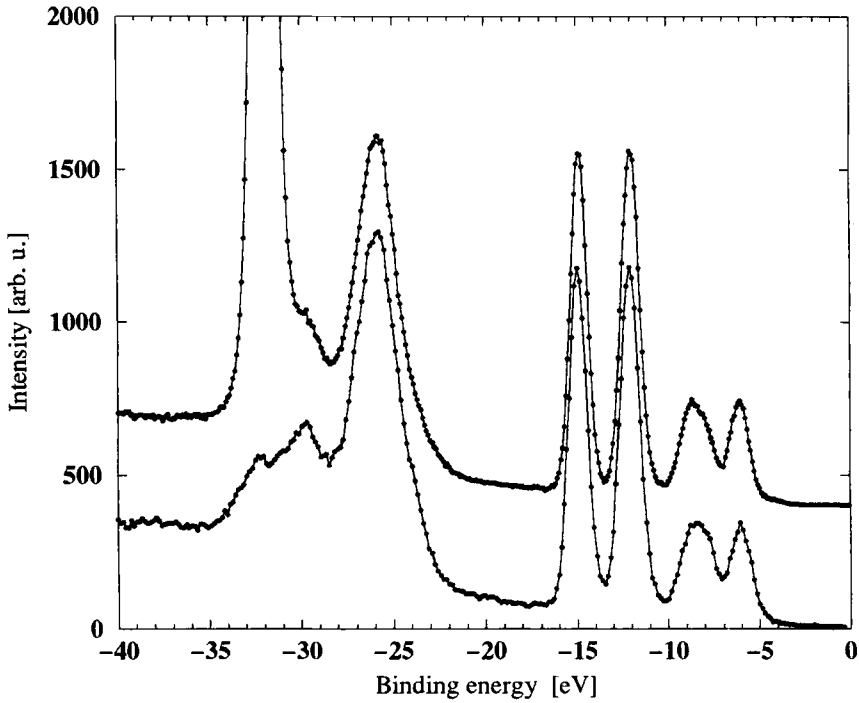

Fig 11. Monochromated XPS valence band spectra of *(A)* Na_2SO_4 and *(B)* Li_2SO_4 (Ref 29).

For the theoretical interpretation, the following cluster MO model calculations were performed:

Model A: a single SO_4^{2-} anion cluster, DV-Xα Hartree-Fock-Slater calculations and the self consistent charge (SCC) scheme was utilized. Atomic contributions

calculated from the population analysis and photoionization cross sections obtained for free atoms [42] were used for the estimation of the line intensities.

Model B: a more realistic cluster ($Li_8SO_4^{6+}$) was set up based on available crystal geometry data [56], the Madelung potential of the neighboring ions (the Coulomb field of point charges, with the formal charges of the respective ions from three layers of unit cells surrounding the model cluster) was also taken into account. As a result, the absolute energies came close to the experimental values, but the energy separation of the lines is still too small.

Model C: a single SO_4^{2-} anion cluster, ab initio HF SCF calculations were performed by using the GAMESS [57] package. An extended split valence band *sp* basis set of contracted Gaussian functions were used with 3d polarization functions (6-31G* basis).

The calculated and experimentally determined binding energies are shown in Table 1. As it was mentioned above, the best agreement between the absolute energies were obtained from Model B, when the potential field of the neighboring ions was also taken into account. Since the theoretical energy values in the literature have been obtained from ground state calculations, for the correct comparison we give ground state energies (which may be directly compared to the experiments only on the basis of the Koopmans' theorem).

Comparing these results to the experiments, a general tendency can be observed: in the case of the Xα results, the relative energies (to the HOMO level, for example) are systematically lower, than the experimental ones. These deviations from the experimental values are approximately proportional to the absolute energy values. The opposite tendency can be observed in the case of the *ab initio* calculations, where the relative energies are larger than the peak separations in the experiments. The difference in the basis sets and in the description of the electron-electron interaction are the possible sources of these deviations.

In the case of the *ab inito* calculations, the application of the Koopmans' theorem ignore the electron correlation in addition to the relaxation of the electron density. Though for a substantial number of molecules it appears that these two effects largely cancel, there still remains a small (10-15 %) difference, which is well observable due to the high resolution reached in the experiments.

In the case of the DV-Xα method, an *average* charge density is used which may not lead to the real energy minimum. On the other hand, this charge density contains the contribution of all electrons, even that one which is used to calculate the interaction with the charge cloud, so the simple functional proposed by Slater

contains an extra contribution, the self interaction as well. The relaxation effect can be taken into account through the transition state calculations, but the correlation effect are only partially included into the functional, and gradient corrections due to the non-local character of the exchange or the correlation term may be also required.

Table 1. Molecular orbital energies for the SO_4^{2-} oxyanion (Ref 29).

	Our result					Literature			
	Exp	Exp	***A***	***B***	***C***	Exp.[a]	Calc[b]	Calc[c]	Cal[d]
Orbital	*Na_2SO_4*	*Li_2SO_4*	*DV-Xα*	*DV-Xα*	*GTO*	*Li_2SO_4*	*MS-Xα*	*STO-3G*	*GTO*
4a1	-29.8	-29.4	-14.5	-28.1	-28.1	-30.7	-34.1	-27.1	-27.6
3t2	-25.7	-25.4	-10.6	-24.0	-23.3	-26.0	-30.1	-21.7	-22.7
5a1	-14.7	-14.5	-0.7	-13.7	-9.7	-14.9	-21.9	-6.2	-8.63
4t2	-11.9	-11.6	+1.9	-11.4	-6.0	-12.2	-18.8	-3.8	-5.0
1e	-8.7	-8.6	+4.7	-8.5	-2.4	-8.7	-15.1	0.0	-1.4
5t2	-7.9	-7.7	+5.2	-8.0	-1.5		-13.9	2.1	-0.3
1t1	-5.9	-5.6	+6.9	-6.2	+0.4	-6.6	-13.3	4.6	+1.39

[a] Ref. [21] [b] Ref. [11] [c] Ref. [8] [d] Ref. [9]

A: DV-Xα calculation for a SO_4^{2-} cluster of Td symmetry; ***B***: DV-Xα calculation for a $Li_8SO_4^{6+}$ cluster embedded into the potential field of neighboring ions; ***C***: all electron *"ab initio"* calculation using split valence (6-31G*) GTOs as basis. Note that the experimental values presented here are referenced to the Fermi level, so the work function of the sample material (ca 3-4 eV) should be subtracted for the correct comparison with the theoretical data being referenced to the vacuum level.

In a recent paper [58] we try to investigate the role of the local and nonlocal exchange and correlation terms. One-electron energies of SO_4^{2-} have been obtained from local and non-local density functional theory (DFT). The Gaussian92 program [59] was used, in which the general form of a hybrid density functional has the following form:

$$A \cdot E_x^{HF} + B \cdot E_x^{local} + C \cdot E_x^{non-local\ corr} + D \cdot E_c^{local} + E \cdot E_c^{non-local\ corr}$$

where E_x and E_c denote the exchange and the correlation terms, respectively, and the coefficients A trough E are adjustable parameters. Pre-configured sets of these parameters are built in the program and can be activated by keywords [59]. The results in Table 2 are the binding energy values relative to the HOMO level. For the comparison, the experimental values from [29] are also presented.

Table 2. SO_4^{2-} one-electron energies (relative to the $1t_1$ level) obtained from local and non-local density functional theory (DFT) and *ab initio* MO cluster calculations (Ref 58) compared to the experimental data (Ref 29).

Level	6-31G*	BH&HL	BH&H	Exp.	B3P86	B3LYP	BP86	BPL	Xα
$4a_1$	-28.46	-25.47	-25.48	**-23.8**	-23.67	-23.58	-22.39	-22.29	-22.28
$3t_2$	-23.65	-20.89	-20.81	**-19.7**	-19.25	-19.18	-18.12	-18.05	-17.90
$5a_1$	-10.07	-9.14	-9.11	**-8.9**	-8.54	-8.49	-8.10	-8.05	-7.98
$4t_2$	-6 42	-6.02	-6.09	**-6**	-5.77	-5.72	-5.55	-5.47	-5.54
$1e_1$	-2.83	-2.54	-2.60	**-3**	-2.38	-2.35	-2.25	-2.18	-2.27
$4t_2$	-1.91	-1.99	-2.05	**-2.1**	-2.02	-2.01	-2.03	-1.98	-2.08

The notation used in [59] were followed:

6-31G* - ab initio HF calculation using split-valence contracted Gaussian basis set with polarization functions,

BH&HL - Beckes's "half and half" [60] exchange functional with Lee, Yang and Perr (LYP) correction [61],

BH&H - Becke's "half and half" method [60] (where 50% of the HF and 50% of the Slater exchange term is taken),

B3P86 - Becke's 3 parameter functional [60] with Perdew gradient correction and local correlation [62],

B3LYP - Becke's 3 parameters functional [60] with LYP non-local correlation [61],

BP86 - Becke's exchange functional [63] with Perdew's correlation functional [62],

BPL - Becke's exchange functional [63] with Perdew's local correlation functional [64]

Xα - Slater exchange functional

It can be seen, that the Becke's "half and half" and the Becke's "three parameter" semi-empirical hybrid functionals give the best agreement with the experiment. It should be noted, however, that the net charges on the S and O atoms are far from the value determined from X-ray diffraction measurements (see Table 4). An interesting point is that the correlation functional of Lee, Yang and Parr affects very little the energy values (compare for example the BH&HL and BH&H columns in Table 2), suggesting that the effects of local an non-local correlation is negligible or is just compensated by other effects. On the other hand, the similarity of the results obtained by using the Becke's exchange functional with Perdew local correlation to those of the Xα functional proves the validity of the application of the local density functional theory, since the gradient correction has very little effect on the energy values.

The calculated and the experimentally determined line intensities are shown in Table 3. Generally a good agreement can be observed between our and the earlier results. The only exception is the O 2s group ($4a_1$ and $3t_2$ lines), where the experimental data from the earlier study of Calabrese and Hayes [21] are higher than our data, and differ from the calculated results as well. Supposing, that this difference was caused by the improper background treatment in [21], we tried to make a critical evaluation of the experimental Li_2SO_4 spectra.

The procedure is explained in the following figures. The structure of the inelastic background can be observed from the XPS spectra of a single peak. As an example, the XPS spectrum of O 1s level is shown in Fig 12 (Ref 29). If we make a deconvolution of the photopeak itself, we can get an energy loss function, characteristic for this sample. Using this loss function, one can estimate the energy distribution of the inelastically scattered electrons originated from the O 2p region of the valence band.

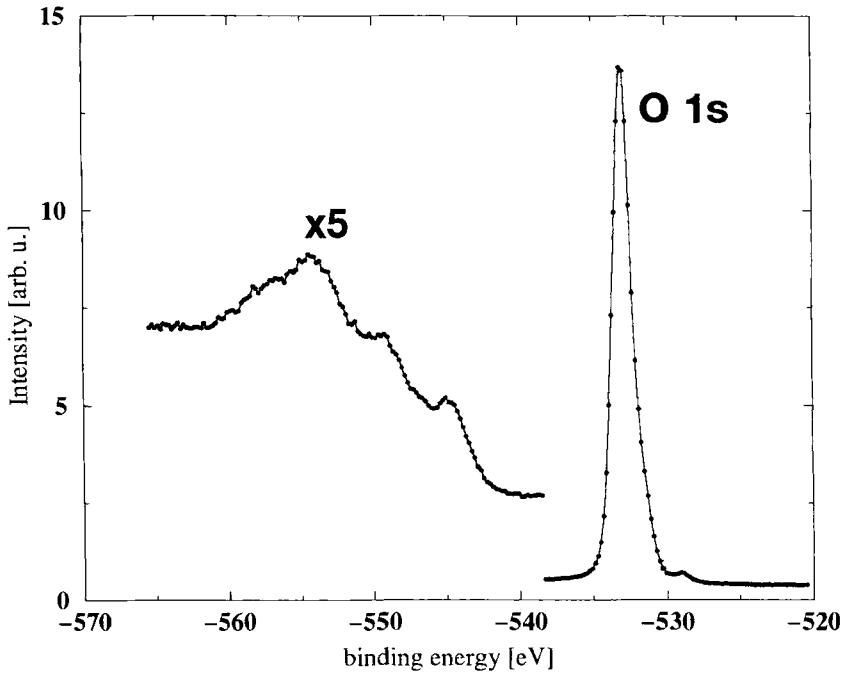

Fig 12. The O 1s XPS photoelectron spectrum from polycrystalline Li_2SO_4 (Ref 29). The loss part of the spectrum is enlarged by a factor of 5.

It is shown in Fig 13 that this distribution has a non-negligible contribution to the background of the O 2s region, and has a smooth, curved shape. It is obvious, that an analysis in which linear background correction is used will overestimate the intensity of lines $4a_1$ and $3t_2$. The difference between the experimental and theoretical intensities of these line observed in [21] was probably caused by inappropriate background subtraction procedure. Our method used for the background treatment eliminated this difference, and we came to the conclusion, that even the simplest SO_4^{2-} cluster model could reproduce the line intensities quite well.

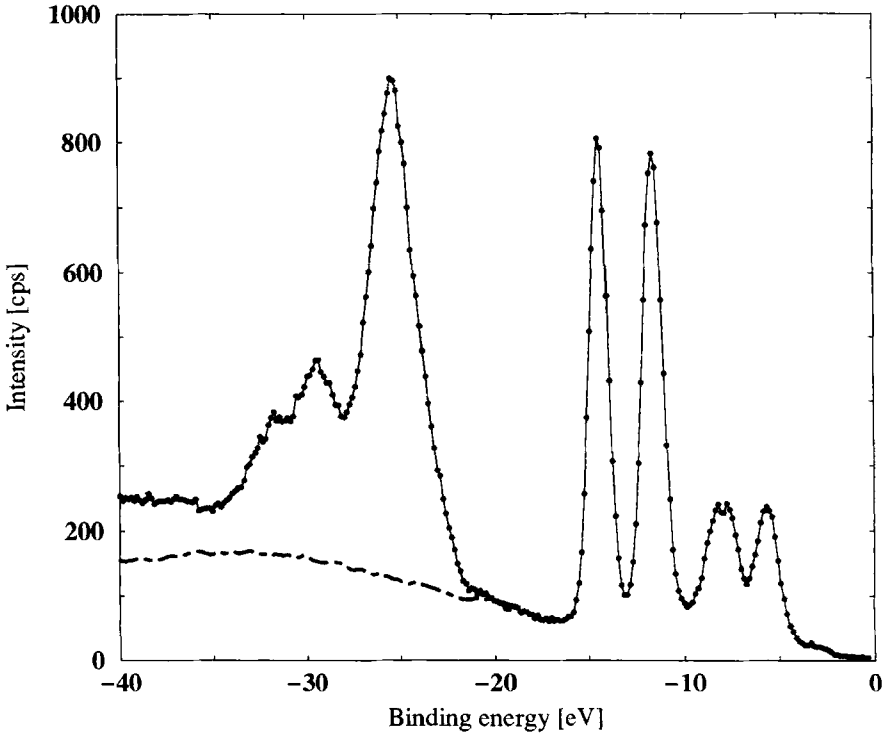

Fig 13. XPS valence band spectra of Li_2SO_4 (dots) and the inelastic background (dashed line) attributable to the O 2p region (Ref 29). For the background estimation we used a loss function obtained from the O 1s XPS spectrum (Fig 12).

Table 3. XPS valence band line intensities measured from Li_2SO_4 samples, compared to calculated intensities.

	This work		Literature	
Orbital	Exp[a]	Calc[b] *A*	Exp[c]	Calc[d] *B*
4a1	2.6	2.8	3.69	2.86
3t2	8.6	8.7	9.57	8.15
5a1	2.6	2.0	1.95	2.02
4t2	2.9	2.7	2.82	2.67
1e	1.5	0.6	1.56	1.59
5t2		1.0		
1t1	1.0	1.0	1.0	1.0

[a] Ref. [29] [b] Ref. [29] [c] Ref. [21] [d] Ref. [8]

A: DV-Xα calculation for a SO_4^{2-} cluster ***B***: all electron *"ab initio"* calculation for a SO_4^{2-} cluster using split valence GTOs basis set (6-31G*)

Experimental investigation of the electronic charge density in pyroelectric lithium sulphate monohydrate was reported in [65, 66]. In these experiments lithium sulphate monohydrate single crystal was studied by neutron [65] and X-ray diffraction [66] at different temperatures. Static deformation and charge density model refinements allowed an estimation of the differences in electron densities between 80 K and 298 K. Changes in the sulphate oxygen atom lone-pair deformation densities, caused by contraction in $SO_4^{2-} - Li^+$ contacts between 298 K and 80 K were also found.

Deformation density calculations [66] based on X-ray and neutron diffraction data indicated a substantial electron deficiency in the sulphur valence shell. Kappa refinement based on the point charge model relates a positive charge close to 1.8 to the sulphur, and about -1.0 on each of the sulphate oxygen atoms [66]. The comparison of these results to those obtained from MO cluster model calculations, provides an indication of the goodness of the applied atomic basis sets. Such a comparison is presented in Table 4.

While the net charges obtained from the DV-Xα model calculations are in good agreement with the experiments, the results from the semi-empirical hybrid models are differing from those obtained from diffraction experiments. These results, together with those presented in Table 1 indicate the weak points of the different theoretical models.

Table 4. Net atomic charges (in atomic units) in $Li_2SO_4 \cdot H_2O$ compared to calculated values obtained from different model cluster MO calculations.

	Exp.[a]	DV-Xα[b]	DV-Xα[c]	6-31G*[d]	BH&H[e]
S	1.83±0.1	1.79	1.65	1.53	1.09
O	-0.96±0.1	-0.89	-0.91	-0.88	-0.77
Li	1.0	0.97	—	—	—

[a] Averaged values of net atomic charges in $Li_2SO_4 \cdot H_2O$ (Ref 66)
[b] DV-Xα calculations for an embedded $Li_8SO_4^{6+}$ cluster (Ref 29)
[c] DV-Xα calculations for a SO_4^{2-} cluster (Ref 29)
[d] Ab initio calculations for a SO_4^{2-} cluster (Ref 29)
[e] Hybrid model calculations for a SO_4^{2-} cluster (Ref 58)

Summary

Taking the advantage of present day high intensity, monochromated X-ray sources, and the availability of high-resolution, small spot spectroscopic technique, new XPS valence band measurements of phosphates and sulphates were performed in order to provide high reliability data for rigorous testing of the theoretical cluster model MO calculations. These measurements revealed the fine structure of the XPS valence band spectra of $Na_4P_2O_7$ and helped us to resolve the lines in the valence band spectra of Li_2SO_4. The critical evaluation of the valence band spectra of Li_2SO_4 eliminated the discrepancy found earlier [21] between the theoretical and experimental line intensities.

Theoretical cluster model MO calculations were used for the interpretation of these spectra. The DV-Xα method combined with realistic cluster approach (in which the model clusters were set up using available crystal structure information from diffraction experiments) proved to be a powerful tool to interpret the structural changes in the valence band spectrum due to the changes in the superstructure of the consisting PO_4 tetrahedra. We found noticeable differences in the calculated spectra when the cluster geometry was changed, especially in the case of the hydrous and anhydrous pyrophosphate and similarly for the ring and spiral forms of the tetra-metaphosphate.

Acknowledgement

This work was partially supported by the Swiss National Foundation and research projects OTKA/T000-7274/1993 and COST/D5/12014.

References

[1] R. Prins, J. Chem. Phys., **61** No 7 (1974) 2580
[2] A. D. Walsh, J. Chem. Soc. **1953**, 2260, 2266, 2301, 2306
[3] M. Wolfsberg and L. Helmholz, J. Chem. Phys. **20** (1952) 837
[4] R. Manne, J. Chem Phys. **46** (1967) 4645
[5] D. P. Santry and G. A. Degal, J. Chem. Phys. **47** (1967) 158
[6] H. Basch, A. Vista and H. B. Gray, J. Chem. Phys. **44** (1966) 10
[7] J. P. Dahl and C. J. Ballhausen, Adv. Quantum Chem. **4** (1967) 170
[8] H. Hillier and V. R. Saunders, Int. J. Quantum Chem. **4** (1970) 203
[9] U. Gelius, B. Roos and P. Siegbahn. Theor. Chim. Acta **23** (1971) 59
[10] H. Johansen, Chem. Phys. Lett. **17** (1972) 569
[11] K. H. Johnson and F. C. Smith Jr., Chem. Phys. Lett. **7**, No 5 (1970) 541
[12] P. W. Atkins and M. C. R. Symons, The Structure of Inorganic Radicals, Elsevier, Amsterdam, 1967
[13] P. E. Best, J. Chem. Phys. **49** (1968) 2797
[14] Y. Takahashi , Bull. Chem. Soc. Japan **42** (1969) 3064; **44** (1971 587; **45** (1972) 4
[15] V. I. Nefedov and V. A. Fomichev, J. Struct. Chem. USSR **9** (1968) 107
[16] B. L. Henke and E. N. Smith, J. Appl. Phys. **37** (1966) 922
[17] E. Schnell, Monatsh. Chemie 93 (1962) 1383; **94** (1963) 703
[18] P. E. Best, J. Chem Phys. **44** (1966) 3248
[19] D. W. Fischer, Appl. Spectrosc. **25** (1971) 263; J. Phys. Chem Solids **32** (1971) 2455
[20] J. A. Connor, L. H. Hillier, V. R. Saunders and M. Barber, Mol. Phys. 23 (1972) 81
[21] A. Calabrese and R. G. Hayes, J. Electron Spectrosc. Relat. Phenom. **6** (1975) 1
[22] V. I. Nefedov, Yu. A. Buslaev, N. P. Sergushin, Yu. V. Kokunov, V. V. Kovalev and L. Bayer, J. Electron Spectrosc. Relat. Phenom. **6** (1975) 221
[23] H. Adachi and K. Taniguchi, J. Phys. Soc. Jpn. **49** (1980) 1944
[24] T. Koopmans, Physica **1** (1933) 104
[25] M. K. Benett, J. S. Murday and N. H. Turner, J. Electron Spectrosc. Relat. Phenom. **12** (1977) 375
[26] A. Le Beuze, R. Lissilour, A. Quemerais, D. Agliz, R. Marchand and H. Chermette, Phys. Rev. B **39** (1989) 11055
[27] L. Kövér, A. Némethy, I. Cserny, A. Nisawa, Y. Ito and H. Adachi, Surf. Interface Anal. **22** (1994) 45
[28] I. Cserny, L. Kövér, A. Némethy, H. Adachi, I. Tanaka, R. Sanjinés, C. Coluzza and G. Margaritondo, Surf. Interface Anal. **23** (1995) 477
[29] I. Cserny, L. Kövér, R. Sanjinés, H. Berger, C. Coluzza, G. Margaritondo, H. Adachi and I. Tanaka, *to be published*

[30] B. T. Pickup and O. Goscinski, Mol. Phys. **26** (1973) 1013
[31] J. Lindberg and Y. Öhrn, Propagators in Quantum Chemistry, Academic, London, 1973
[32] L. S. Cederbaum, W. Domcke, J. Schirmer and W. von Niessen, Phys. Scr. **21** (1980) 481
[33] L. S. Cederbaum and W. Domcke, Adv. Chem. Phys. **36** (1977) 205
[34] G. Wendin, Breakdown of the One-Electron Pictures in Photoelectron Spectra, Structure and Bonding, Vol. 45, Springer, Berlin, Heidelberg, 1981
[35] L. S. Cederbaum, W. Domcke, J. Schirmer and W. von Niessen, Adv. Chem. Phys. **65** (1986) 115
[36] P. Fulde, Electron Correlations in Molecules and Solids, 3rd edition, Springer-Verlag, Heidelberg, 1995
[37] P. Fulde (*ibid,* subchapter 8.6)
[38] A. Hinchcliffe, *Ab Initio* Determination of Molecular Properties, Adam Hilger, Bristol, 1987
[39] J. C. Slater, Adv. Quant. Chem. **6** (1972) 1
[40] A. R. Williams, R. A. deGroot and C. B. Sommers, J. Chem. Phys. **63** (1975) 628
[41] U. Gelius, in Electron Spectroscopy, ed. by D. A. Shirley. p. 311, North-Holland, Amsterdam, 1972
[42] J. H. Scofield, J. Electron Spectrosc. Relat. Phenom. **8** (1976) 129; I. M. Band, Yu. I. Kharitonov and M. B. Trzhaskovskaya, Atomic Data and Nuclear Data Tables **23,** No 5 (1979) 443
[43] N. Kosuch, E. Tegeler, G. Wiesch and A. Faessler, Chem. Phys. Lett. **47** (1977) 96
[44] K. Taniguchi, Bull. Chem. Soc. Jpn. **57** (1984) 909, 915
[45] T. Sasaki and H. Adachi, J. Electron Spectrosc. Relat. Phenom. **19** (1980) 261
[46] Y. Kowada, H. Adachi and T. Minami, J. Phys. Chem. **97** (1993) 8989
[47] H. Adachi, M. Tsukada and Ch. Satoko, J. Phys. Soc. Jpn. **45,** No 3 (1978) 875
[48] W. H. Baur, Acta Crystallogr. Sect. B **30** (1974) 1195
[49] C. Keffer, A. Mighell, F. Mauer, H. Swanson and S. Block, Inorg. Chem. **6** (1967) 119
[50] A. F. Wells, Structural Inorganic Chemistry, 4th Ed., p689, Clanderon Press, Oxford, 1975
[51] K. Y. Leung and C. Calvo, Can. J. Chem. **50** (1972) 2519
[52] K. H. Jost, Acta Crystallogr. **16** (1963) 640
[53] D. M. Bishop, M. Randic and J. R. Morton, J. Chem. Phys. **45** (1966) 1880; **48** (1968) 1878
[54] D. M. Bishop, Theor. Chim. Acta **8** (1967) 285

[55] M. Keeton and D. P. Santry, Chem. Phys. Lett. 7 (1970) 105
[56] A. G. Nord, Acta Crystallogr. Sect. B **32** (1976) 982
[57] M. W. Schmidt, K. K. Baldridge, J. A. Boatz, S. T. elbert, M. S. Gordon, J. H. Hensen, S. Koseki, N. Matsunaga, K. A. Nguyen. S. Su, T. L. Windus, M. Dupuis and J. A. Montgomery Jr., J. Comp. Chem. **14**, No 11 (1993) 1347
[58] Á. Nagy and I. Cserny, *to be published*
[59] Gaussian 92/DFT, Rev. G.1., M. Frisch, G. W. Trucks, H. B. Schlegel, P. M. W. Gill, B. B. Johnson, M. W. Wang, J. B. Foresman, M. A. Robb, M. Head-Gordon, E. S. Replogle, R. Cgomperts, J. L. Andres, K. Raghavachari, J. S. Binkley, C. Gonzalez, R. L. Martin, D. J. Fox, D. J. Defrees, J. Baker, J. J. P. Stewart and J. A. Pople, Gaussian Inc., Pittsburgh, Pennsylvania, 1993
[60] A. D. Becke, J. Chem. Phys. **98** (1993) 5648
[61] C. Lee, W.Yang and R. G. Parr, Phys. Rev. B **37** (1988) 785
[62] J. P. Perdew, Phys. Rev. B **33** (1986) 8822; **34** (1986) 7046
[63] A. D. Becke, J. Chem. Phys. **88** (1988) 2457; Phys. Rev. A **38** (1988) 3098
[64] J. P. Perdew and A. Zunger, Phys. Rev. B **23** (1981) 5048
[65] J.-O. Lundgren, A. Kvick, M. Karppinen, R. Liminaga and S.C. Abraham, J. Chem. Phys. **80** (1), (1984) 423
[66] M. Karppinen, R. Liminaga, J.-O. Lungdgren, A. Kvivk and S. C. Abraham, J. Chem Phys **85** (9), (1986) 5221

Application of the Embedded Cluster Method to the Electronic State of Silicate Glasses

Y. Kowada* and D. E. Ellis

Department of Chemistry and Materials Research Center, Northwestern University, Evanston, Illinois 60208

** Permanent address: Hyogo University of Teacher Education, Yashirocho, Hyogo 673-14, Japan*

Abstract

The discrete variational (DV) Xα method is used to investigate the electronic structure of silicate glasses in the embedded cluster model. Effects of the cluster size and the size of embedding units on electronic states are discussed. The embedding unit greatly improves the electronic state description compared with an isolated SiO_4^{4-} cluster, which is a structural unit of silicate glasses; e.g., the Fermi energy becomes -7.20 eV in the embedded cluster, while that of the isolated charged cluster is +23.8 eV. More importantly, both Si and O ions become more ionic in the embedded clusters. The size of both embedding units and variational cluster, however, is not very critical to electronic states localized around the center of the clusters.

1 Introduction

Silicate glasses have a very long tradition as popular materials for the application of optical devices. Recently silicate glass has become even more attractive, because of the usefulness of optical components in

ADVANCES IN QUANTUM CHEMISTRY, VOLUME 29

0065-3276/97 $25.00

communications. Nowadays our communications, such as telephone, fax, Internet and etc., are almost completely dependent on transmission by optical fiber, largely replacing copper wire. Optical communication is the fastest among the variety of available communication methods; the weak point of this method, however, is lack of good amplifiers of the optical signals. Since presently the optical signals need to be converted to electronic signals, then amplified electronically and reconverted, the total communication speed becomes slow. When good optical amplifiers become available, the communication could become much faster and more useful. Thus, many people have been studying optical amplification in the past several years. One approach is the development of non-linear optical materials.[1] Furthermore, non-linear optical devices are expected to be critical for the application of optical switching and optical memory devices in order to construct optical computers.

The non-linear optical properties of a glass depend not only on the occupied electronic states but also on the unoccupied orbitals, demanding a theory which can treat both sets of states. The unoccupied molecular orbitals are typically diffuse in nature, a "local excitation" involving atomic orbitals of a considerable group of neighboring ions. So crystal field or highly localized models may seem inappropriate. Electronic states of oxide glasses, moreover, are difficult to study by all traditional theoretical methods because of their structural randomness; i.e., lack of long-range order. Taking silicate glasses as a typical case, the glass structure is defined by SiO_4 tetrahedral units which are connected by sharing one corner oxygen ion. [2, 3] This structural unit is very similar to that occurring in corresponding silicate crystals; i. e. the short-range structure of silicate glasses is similar to that of silicate crystals.

There are several theoretical methods available to study the electronic state of oxide materials, including band calculations and molecular orbital methods. [4-9] In the band approach, randomness is a problem since translational symmetry of the unit cell is required; a

large super-cell may be chosen, at the cost of increased computer time and possible spurious interactions between cells. On the other hand, the molecular orbital (MO) approach is usually applied to isolated molecules, and can not handle the infinite numbers of atoms found in the solid state. Among improvements of the molecular orbital methods introduced in order to study solid state materials is the embedding potential method. [10] Basically, the Hamiltonian of the cluster is modified by adding pseudo potentials representing the solid state environment, and constraints are applied to localize cluster orbitals. This method has been used in many materials and many useful results have been obtained. [10,11] In order to apply this embedding method to glassy materials, several problems should be clarified, one of the most important being size effects of embedding units. To describe the glassy state, we need in principle many distinct embedding potentials and can't use translational symmetry. Consequently, it is necessary to study the appropriate embedding conditions which will give a reasonable description of the potential in the glassy state. Therefore we need to study size effects of both variational clusters and embedding units.

In this work we will discuss the effects of embedding units and the cluster size, using several related clusters. We have already calculated the Si-O-Si bond angle dependence of electronic structure of silicate clusters. The Si-O-Si bond angle effects, however, are being discussed in a more complete report, owing to the limited space.

2 Computational Details

We used the discrete variational (DV-Xα) method which uses a linear combination of atomic orbitals (LCAO) expansion of molecular orbitals to calculate electronic states of silicate clusters. [12, 13] In this method the exchange-correlation potentials are approximated by the simple Kohn-Sham-Slater form

$$V_{ex}(r) = -\alpha\left[\frac{3\rho}{4\pi}\right]^{\frac{1}{3}} \quad (1)$$

where α is a constant, fixed at 0.7, and ρ is the electronic density of the cluster. The basis sets are formed from numerical solutions of the Schrödinger equation for free atoms/ions in a potential well.

Mulliken population analysis was used for the evaluation of the net charge of each atom and the bond overlap populations of each cluster. The Fermi energy E_F of each cluster was evaluated as the midpoint of the energy gap between the highest occupied molecular orbital (HOMO) and the lowest unoccupied molecular orbital (LUMO). In order to discuss the bonding nature, we used the familiar chemist's bond order which is the sum of the bond overlap populations between each pair of atoms in the cluster.

Five clusters shown in Figure 1 were used to discuss the effects of the embedding, the cluster size, and the Si-O-Si bond angles. Basically, the silicate random glass structure has a wide distribution of Si-O-Si bond angles and a rather restricted range of Si-O bond lengths. Since it is very complex to study both the size effects and Si-O-Si bond angles at the same time, we first used a Si-O-Si bond angle of 180° for both the variational cluster and the embedding units to discuss the size effects on electronic states. Next, the Si-O-Si bonds were varied from 180° to 124° in a certain cluster, simulating the observed distribution of Si-O-Si bond angles in the SiO_2 glass. Cluster (a) is an isolated SiO_4^{4-} cluster, the smallest possible structural unit ; cluster (b) is a same as (a) with the addition of four embedding SiO_3^{+} units. We can observe the most basic effects of embedding by comparing clusters (a) and (b). Cluster (c) includes five SiO_4 units ($Si_5O_{16}^{12-}$) in the variational space and twelve embedding SiO_3^{+} units. There are four bridging oxygens in this cluster. In clusters (b) and (c), the charge of each embedding Si ion was fixed at +3.4 and that of the O ion was -0.8. These charge values were optimized by calculations on clusters (a)-(e) and the charge of the O anion was

decreased in order to make neutral clusters, as discussed in more detail below. Cluster (d) has twenty four more embedding SiO_3 units than cluster (c). In this case, the charges of the embedded Si and O ions in the first sheath are +3.4 and -1.8 respectively. The charge of the O ions in the second sheath was again decreased to make a neutral cluster; then the embedding Si and O ions in the second sheath have charge +3.4 and -0.76 respectively. Cluster (e) is a $Si_{17}O_{52}^{36-}$ variational unit with embedding consisting of twelve $SiO_2^{1.7+}$ units which are connected to two oxygen ions and twelve $SiO_3^{1.3+}$ units connected to one oxygen ion in the cluster. It is possible to discuss the variational cluster size effects and the embedding unit size effects on electronic states by using clusters (b)-(e).

The Si-O bond length was fixed to 1.62 Å and the Si-O-Si bond angle was fixed to 109°28' in clusters (a)-(e). These are average values measured by X-ray and neutron diffraction in SiO_2 glass. [14] Charges of embedded units were fixed in the all clusters.

We used HP 9000/735 workstation for the calculations. The number of sample points were 3000 for clusters (a) and (b), 18000 for clusters (c) and (d), and 48000 for the cluster (e).

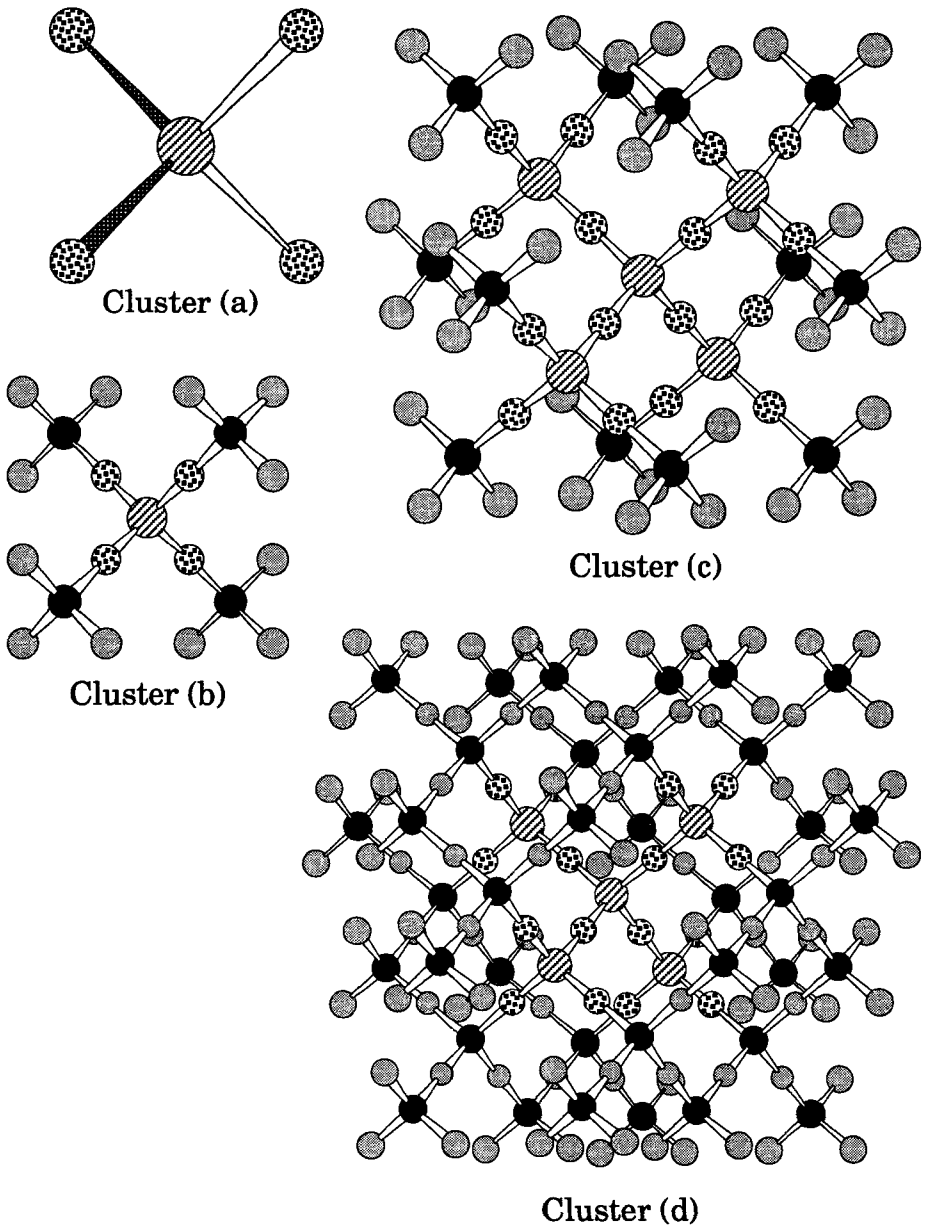

Figure 1. Structures of the model clusters: (a) isolated SiO_4^{4-}, (b) embedded SiO_4^{4-}, (c) embedded $Si_5O_{16}^{12-}$, (d) embedded $Si_5O_{16}^{12-}$ with second sheath of embedding units, (e) embedded $Si_{17}O_{52}^{36-}$.

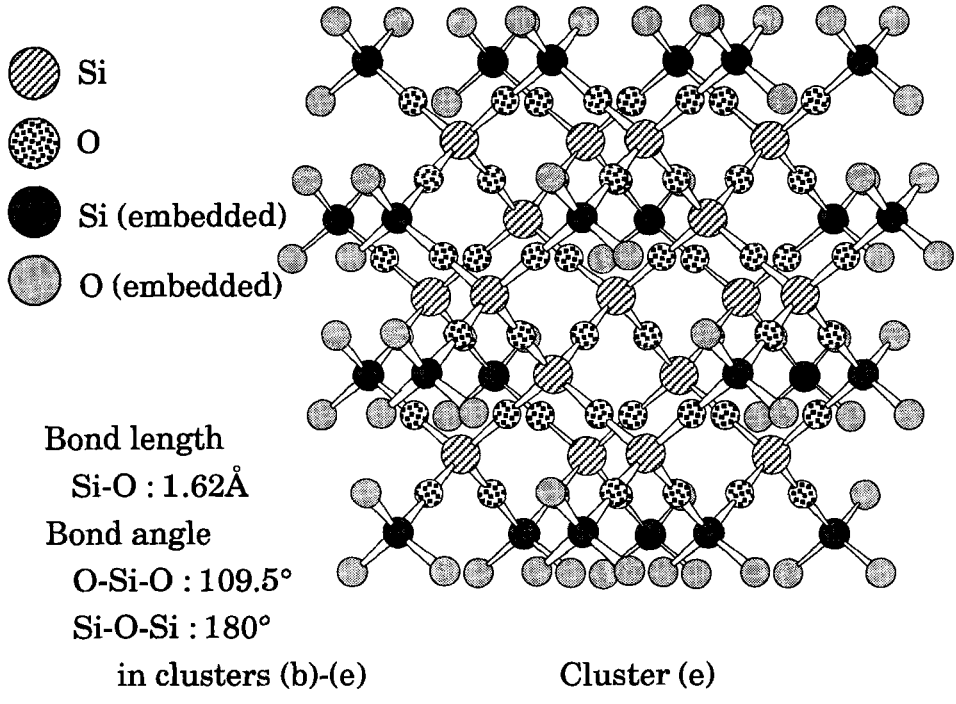

(Figure 1. continued)

3 Results and Discussion

Fig. 2 shows the MO energy level structures for valence states in clusters (a)-(e). The ordinate shows the energy of each MO in eV.

For the isolated SiO_4^{4-} unit in cluster (a), occupied MOs are mainly constructed by O 2s and 2p orbitals, while unoccupied MOs are dominated by Si 3s-3d orbitals, as could be expected from the nominal Si^{4+}, O^{2-} ionic charge states. The Fermi energy of this cluster is +23.8 eV since the nominal total charge of (a) is -4 and there is no external environment. The HOMO- LUMO energy gap is 12.8 eV. As a result of the additional four SiO_3^{+} embedding units, cluster (b) becomes electrically neutral. Charge neutrality lowers the Fermi energy of this cluster to -7.20 eV, and potential effects reduce the HOMO- LUMO gap

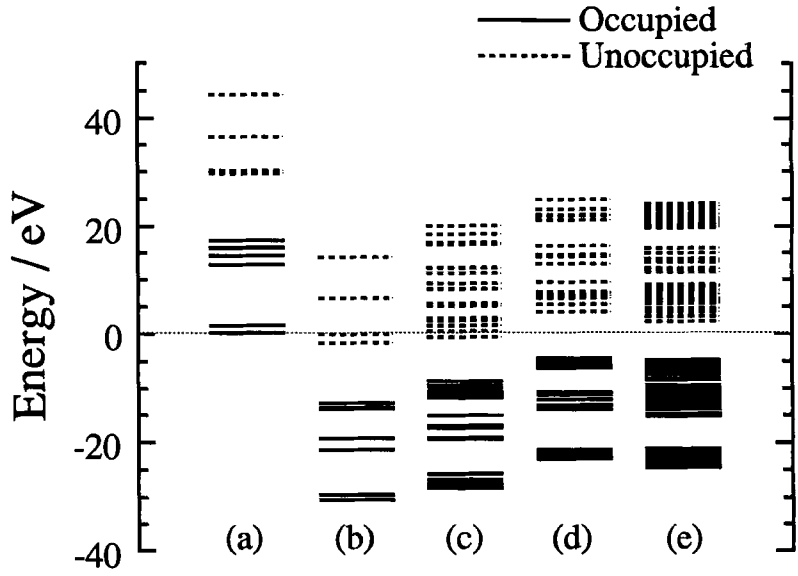

Figure 2. Valence energy level diagram for clusters (a)-(e).

to 11.0 eV. The energy gap in cluster (b) is larger than the 7.7 - 8.2 eV value found by experiment in bulk SiO_2 glass [15, 16], suggesting that the only one SiO_4 unit is not enough to represent the quantitative energy level structure of the bulk state. Though it is necessary to use transition state calculations and non-local functionals to compare precisely the HOMO-LUMO band gap with experimental results, the embedding method clearly improves the energy level structure of the SiO_4 cluster [17, 18].

There is another notable difference of energy level structure between cluster (a) and (b). That is, the occupied "O 2p" band in cluster (b) near the HOMO is split into two sub-bands. The top band (near to HOMO) is due to lone pair electrons and MOs which have p type interaction with the embedding Si ions. The bottom band is due to s type interactions with the embedding Si ions, corresponding to the formation of bridging oxygens. Except for the Fermi energy shift and the splitting of the occupied band, the level structure of cluster (b) is similar to that of cluster (a). This result suggests that we can use isolated clusters to discuss qualitatively the electronic states of silicate glasses. We need, however, to use the embedding method to discuss electronic properties such as energy gap and absorption spectra to compare with experimental measurements.

Cluster (c) is a larger $Si_5O_{16}^{12-}$ variational unit with embedding ions which gives a much denser set of MO levels and a presumably better description of the energy bands of the solid. In this cluster, occupied orbitals are again constituted from O 2s and 2p orbitals and unoccupied orbitals arise primarily from Si 3s-3d orbitals. Basically, the energy level structure of cluster (c) is same as that of cluster (b); the Fermi energy, however, shifts down to -4.64 eV, and the HOMO-LUMO energy gap is further reduced to 8.15 eV, quite close to that found in the SiO_2 glass. There are several studies about SiO_2 crystals by the band calculation[19,20] and the SW-Xα method[21]. In these studies, the energy gap was 5.7-8.0 eV for SiO_2 crystals. Cluster (c) has almost the same energy gap as the band calculation, though the cluster contains

only 21 atoms. The result suggests that the cluster (c) already has similar energy level structure to that of the bulk. Cluster (d) has a second sheath of embedding units added; this cluster should have electronic states still more similar to the silicate bulk, since now second and third neighbor interactions are included. The level structure of this cluster is very similar to (c) with E_F rising, however, to ~ 0 eV. These results now appear quite satisfactory, both in relative and absolute energy distribution. Cluster (e) is the largest considered in this work; here, MO level density in each band is considerably greater than in the smaller clusters. The HOMO-LUMO band gap of 7.53 eV is slightly smaller than that in cluster (d), with E_F of -7.10 eV returning close to that of cluster (b). Thus the lesser number of embedding units for this cluster has primarily an effect on the absolute position of energies, and might be improved by an additional sheath as in cluster (d).

The effects of embedding units have obviously appeared in energy level shifts and sub-band formation. More subtle changes of net charge and bond order are also interesting, since these parameters are very important to understand the ionicity and bonding nature of silicate glasses. Fig. 3 (a) and (b) show net ionic charge in clusters (a)-(e). There are three kinds of Si and O ions in these clusters: every cluster has a central silicon shown as Si_C in Fig. 3 (a) and four nearest-neighbor oxygens, shown as O_I in Fig. 3 (b). Clusters (c) and (d) have four silicon and twelve oxygen ions around the central SiO_4 unit; these outer ions are shown as Si_O and O_O. Cluster (e) has an additional twelve Si and thirty six O ions around the Si_5O_{16} unit, of which two kinds of oxygen ions are distinguished. One (Non-bridging) is connected to $SiO_3^{1.3+}$ units and the other (Bridging) is connected to $SiO_2^{1.7+}$ units by sharing that unit by two oxygens. These "third shell" ions are shown as Si_{O2}, O_{ONB} and O_{OB} in Fig. 3.

Net charge of the Si ion in the naked cluster (a) is 2.04 in comparison to the nominal +4 value; embedding units drastically change the net Si charge. Thus, in cluster (b) the net Si_C charge becomes 3.52, which is

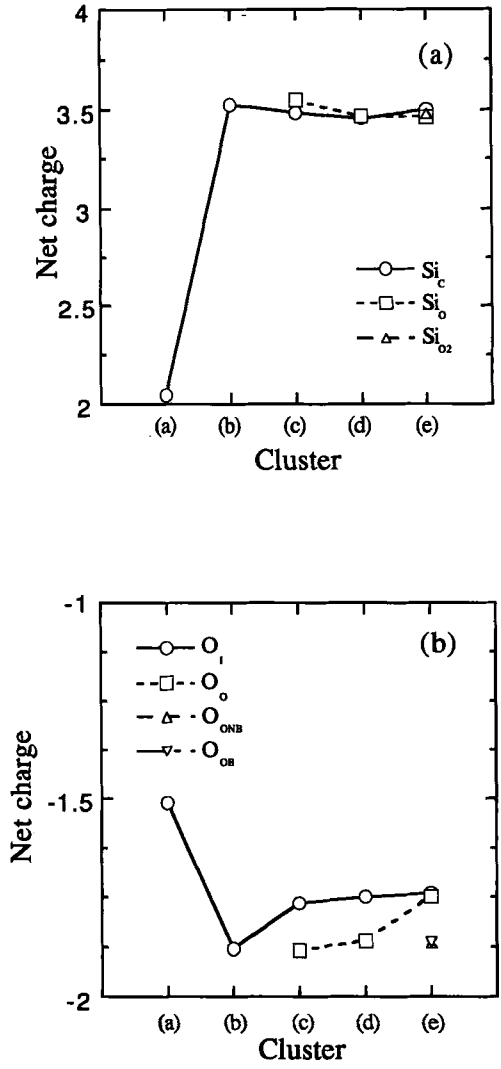

Figure 3. Net charge of Si (a) and O (b) ions in the clusters (a)-(e).

much closer to the expected or nominal value. In cluster (c), however, the Si_C ion charge is not much different from that in cluster (b), and the charge of the four Si_O is near to that of Si_C. This result means that these two Si ions are in similar conditions in this cluster. Since one of the most important purposes of embedding is to locate the cluster into the same environment as in the solid, these results show that the embedding units are very effective to improve the electronic state of the silicate clusters. Cluster (d) has two sheaths of embedding SiO_3 units. This increase of embedding units makes net charge of both Si_C and Si_O almost the same, marking an improvement of environment around these two ions. In cluster (e) Si_C, Si_O and Si_{O2} have almost the same charges, though the net charges of Si_O and Si_{O2} are a bit smaller than that of Si_C. This result suggests that the embedding method is very useful to improve the environment around the silicate clusters, while the electronic state around the cluster center is not very sensitive to its size.

Net charges of oxygen ions are shown in Fig. 3 (b). In cluster (a), O_I has charge of -1.51, and increases to -1.88 with the embedding units in cluster (b). This change obviously corresponds to that of Si in Fig. 3 (a). In cluster (c), the charges of O_I and O_O ions become -1.77 and -1.88, respectively. The charge of O_O is larger than that of O_I here, showing the different effect of the embedding units: since cluster electrons are attracted toward the "surface" by the positive charge of embedding units, the O_O ions become more negative. The net charge of O_I ions, however, is almost same as that in cluster (c), so the net balance is reasonable. In cluster (e), the O_O ions have almost same charge as the O_I ions, while the O_{ONB} and O_{OB} ions have larger negative charge than the others. These results suggest that the embedding units make drastic changes on net charge of peripheral oxygen ions, while the charge of O_I around the cluster center is only weakly affected, similar to the case of Si ions.

Fig. 4 shows bond orders between Si_C and O_I (Si_C-O_I), between Si_O and O_I ions (Si_O-O_I), between Si_O and O_O ions (Si_O-O_O). In the case of

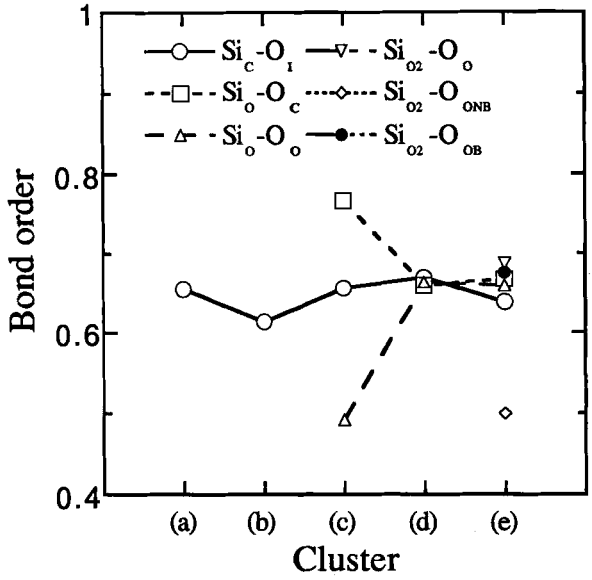

Figure 4. Bond order of Si-O in the clusters (a)-(e).

cluster (e), there are in addition Si_{O2}, O_{ONB} and O_{OB} ions.; their bond orders are shown as Si_{O2}-O_{ONB} and Si_{O2}-O_{OB}, respectively.

In cluster (a) the bond order between Si_C and O_I is 0.655, and decreases with embedding units to 0.614 in cluster (b). This result is consistent with the net charge of Si and O ions, that is, these charges are increased with embedding; i. e., they become more ionic. In cluster (c) there are three different kinds of Si-O bonding, including Si_C-O_I, Si_O-O_I, and Si_O-O_O, each with a corresponding bond order. The relative order, Si_O-O_O (0.767) > Si_C-O_I (0.656) > Si_O-O_I (0.492) is correlated to the effects of embedding units. Thus Si_O-O_O receives the largest embedding influence, therefore the bond order of Si_O-O_O becomes larger; on the contrary to this, Si_O-O_I becomes smaller by that influence. The

Si_C-O_I bonding, however, has almost the same bond order as that in cluster (c), suggesting that the central region Si_C-O_I bonding has less influence from embedding than the peripheral structure. This means that electronic states near the cluster center are little affected by both the cluster size and the embedding units. In other words, electronic states localized near the center are stable in silicate clusters, and thus suitable for extraction of glass properties.

The results for cluster (c) suggest that one sheath of embedding units is useful to put the isolated cluster into a bulk-like state, but not sufficient to give the solid state environment to the "surface-layer" Si and O ions. After the addition of a second sheath of embedding units, the bond orders of Si_O-O_O are much improved. In cluster (d), the three different Si-O bonding structures have almost the same value of bond order. This result shows that variational cluster (d) comes close to the bulk-like state and that the second sheath of embedding units is needed to discuss quantitative details of the electronic states of solid state silicates. Of course we can't regard the cluster (d) as a complete model of the solid state, because the variational cluster has 12 negative charges and outside oxygen ions have larger negative charge than interior oxygen. We can discuss quantitatively, however, the electronic state of silicate clusters by using the results around the center of cluster (d).

In cluster (e) the Si-O bond orders are: Si_C-O_I, Si_O-O_I, Si_O-O_O, and Si_{O2}-O_O with values 0.635, 0.697, 0.659, and 0.609, respectively. These interior bonding structures are satisfactorily close to each other; however, the bonding of terminal groups Si_{O2}-O_{OB} and Si_{O2}-O_{ONB} are different from the others. The Si_{O2}-O_{OB} bond order is 0.827; i. e., much larger than interior values, while in contrast, the Si_{O2}-O_{ONB} bond order is 0.513 and is thus much smaller than interior bonding of cluster (e). Analysis of these differences reveals combined effects of number of bonds shared and embedding unit charges. Since O_{ONB} is connected to one embedding $SiO_3^{1.3+}$ unit, it feels less attraction to electrons of the variational cluster and makes the Si_{O2}-O_{ONB} bond order smaller. On

the other hand, two O_{OB} share one embedding $SiO_2^{1.7+}$ unit, which has a larger positive charge; consequently, this larger charge causes a larger Si_{O2}-O_{OB} bond order. In order to improve the bond order of Si_{O2}-O_{OB} and Si_{O2}-O_{ONB}, we could add the second sheath of embedding units or optimize the charge of the embedding ions. The observed stability of the central region, and the easily separated boundary-condition effects on the surface of the variational cluster thus permits quantitative discussion of the electronic states of solid state silicate using embedding methods.

Fig. 5 shows the density of states (DOS) in clusters (a)-(e) and an experimental ultra-violet photoelectron spectrum (UPS) for SiO_2 glass reported by Distefano et al. [22] The energy scale is normalized to the Fermi energy and then shifted by + 3 eV in order to compare with experimental UPS.

In cluster (a), there are 4 peaks in the energy range from -12 to +3 eV. These peaks are dominated by O 2p AO and can be divided into two groups. The first group contains the lower energy peaks below -5 eV. These peaks are contributed by Si 3s and 3p AOs. The second group includes the higher energy peaks above -5 eV. The Si 3p and 3d orbitals contribute to these peaks. As seen in Fig. 2, there is no obvious energy separation between these two groups. In the case of cluster (b), however, the DOS features are drastically changed. As the result of the shift to lower energy of the lower energy group, there now appears a clear energy gap between two groups. DOS of cluster (c) is similar to that of cluster (b), while the density develops extended structure, according to the larger number of atoms in the cluster. In this case, there are three peaks in the lower energy group, whose number and position are due to the increase of the variational cluster size and the lesser number of embedding units. This means that the number of embedding units in cluster (c) is not enough to put the variational cluster into the desired pseudo-solid state environment. In cluster (d), the energy gap between the lower energy and the higher energy groups is increased, compared to

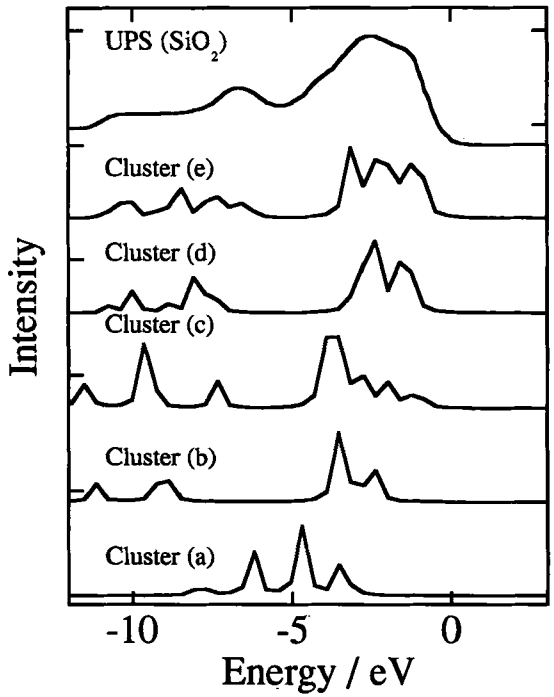

Figure 5. Density of state (DOS) for clusters (a)-(e) and experimental UPS spectrum for SiO_2 glass. All DOS are shifted +3 eV to compare with UPS.

(c), with the upper group of levels shifting to higher energy. DOS of cluster (e) is almost the same as that of (d) except for the extended structure of both the lower and the higher energy group. In the DOS of cluster (e), the peak positions and intensities are very similar to those in the experimental UPS of SiO_2 glass. This result shows that we can adequately discuss peak assignments of UPS and local structure of

SiO_2 glass by comparison of cluster (e) DOS with UPS. However, since the DOS of the smaller cluster (d) already reproduces the main features of the UPS of SiO_2 glass, it is also adequate to discuss details of UPS. So cluster (d) is the most convenient among clusters (a)-(e) for further experimentation on properties such as bond-angle dependence of spectra, as the computational time is much shorter.

Thus we find the embedded cluster method, with a modest number of atoms in the variational space, is very useful to discuss experimental UPS spectra quantitatively and we can get reliable electronic state information on silicate clusters with reasonable computational time.

4 Conclusion

We have used the DV-Xα method to analyze a number of silicate clusters in order to study effects of the cluster size, embedding units and the Si-O-Si bond angles on the electronic structure of silicate glasses. Clusters with a single sheath of $(SiO_4)^Q$ embedding units already show level structure and Fermi energy compatible with the bulk system. Addition of the second sheath of embedding units improves the net charge and the bond order in silicate clusters, particularly near the cluster surface.

References

[1] E. M. Vogel, S. G. Kosinski, D. M. Krol, J. L. Jackel, S. R. Friberg, M. K. Oliver, and J. D. Powers, J. Non-Cryst. Solids, **107,** 244 (1989).

[2] J. Wong and C. A. Angell, "Glass Structure by Spectroscopy, " Marcel Dekker, New York p864 (1976).

[3] S. Sakka and K. Matusita, J. Non-Cryst. Solids, **22**, 57 (1976).

[4] R L. Mozzi and B. E. Warren, J. Appl. Crystal., **2**, 164 (1969).

[5] E. Ellis, D. W. Johnson, A. Breeze, P. M. Magee and P. G. Perkins, Phil. Mag. B **40**, 105 (1979).

[6] P. M. Schneider and W. B. Fowler, Phys. Rev. Lett., **36**, 425 (1976).

[7] J. A. Tossell, D. J. Vaughen, K. H. Johnson, Chem. Phys. Lett., **20**, 329 (1973).

[8] S. T. Pantelides and W. A. Harrison, Phys. Rev. B, **13**, 2667 (1976).

[9] J. R. Chelikowsky and M. Schlüter, Phys. Rev. B, **15**, 4020 (1977).

[10] Understanding Chemical Reactivity Vol.12, "Density Functional Theory of Molecules, Clusters, and Solids," Edited by D. E. Ellis 1995; Kluwer Academic Publishers, Dordrecht.

[11] D.E. Ellis, J. Guo, and J.J. Low, in "Quantum Chemistry Approaches to Chemisorption and Heterogeneous Catalysis", p 70; Edited by F. Ruette, 1992, Kluwer Academic Publishers, Dordrecht.
D.E. Ellis, in "Physics and Chemistry of Metal Cluster Compounds", p 135; Edited by L.J.de Jongh, 1994, Kluwer Academic Publishers, Dordrecht.

[12] D. E. Ellis and G. S. Painter, Phys. Rev. B, **2**, 2887 (1970).

[13] A. Rosen, D. E. Ellis, H. Adachi, and F. W. Averill, J. Chem. Phys., **65**, 3629 (1976).

[14] Y. Waseda, "The Structure of Non-Crystalline Materials" McGraw-Hill, New York, p. 133 (1980).

[15] G. H. Sigel Jr., J. Phys. Chem. Solids, **32**, 2373 (1971).

[16] G. H. Sigel Jr., J. Non-Cryst. Solids, **13**, 372 (1973/1974).

[17] J. P. Perdew and A. Zunger, Phys. Rev. B, **23**, 5048 (1981).

[18] O. Gunnarsson, M. Jonson, B. I. Lundqvist, Phys. Rev. B, **20**, 3136 (1979).

[19] P. M. Schneider and W. B. Fowler, Phys. Rev. Lett. **36**, 425 (1976).

[20] Y. Xu and W. Y. Ching, Phys. Rev. B **44**, 11048 (1991).

[21] J. A. Tossell, D. J. Vaughan, and K. H. Johnson, Chem. Phys. Lett. **20**, 329 (1973).

[22] T. H. DiStefano, D. E. Eastman, Phys. Rev. Lett., **27**, 1560 (1971).

Bond Strength and Thermal Stability of Transition Metal Nitrides

Masao Takahashi, Gao-Chao Lai, Katsuhiro Ohta and Fumikazu Kanamaru

The Institute of Scientific and Industrial Research, Osaka University, 8-1 Mihogaoka, Ibaraki Osaka 567, Japan

To clarify the origin of thermal stability of transition metal nitrides, an empirical approach and the DV-Xα molecular orbital calculation for several transition metal nitride have been executed. Thermally stable crystal phases in $Mo_{1-x}M_xN$ (M =Nb, Zr, Ti) solid solution and simple transition metal nitrides are classified using the radius ratio of nonmetal to metal atoms and the number of valence electrons. The relationship of the generalized number of valence electrons instead of the average number of valence electrons per atom to the thermal stability of transition metal nitride has been discussed. It has been found that the bond overlap population of metal-metal bond plays an important role on the thermal stability of transition metal nitride.

1. Introduction

Metal nitrides, such as Si_3N_4, AlN, TiN, Fe_4N, GaN, ZrN and NbN have attracted much interest recently from the practical uses, ie., application to high-temperature materials, electronic devices and catalysts. These nitrides show high melting points, high hardness and electric properties ranging from metallic conductor to insulator. Such properties are mainly due to the diversity of chemical bonding in metal nitrides; metal nitrides can take their chemical bonding state in which plural bonding character among ionic, covalent and metallic bonding co-exist. Several metal nitrides are listed in Table I in order of atomic number of the metal. Such alkaline or alkaline earth metal nitrides as Li_3N, Ca_3N_2 and Sr_3N_2 have the ionic bonding between metal and nitrogen, and the covalent bonding mainly contributes to the main group nitrides as BN, AlN and Si_3N_4. Transition metal nitrides are so-called interstitial compounds having metallic bonding character. The combination of these nitrides with different bonding character is expected to yield new functional materials, and preparations

ADVANCES IN QUANTUM CHEMISTRY, VOLUME 29

0065-3276/97 $25.00

Table I Periodic table of metal nitrides.

1	2	3	4	5	6	7	8	9	10	11	12	13	14
Li_3N	Be_3N_2											BN	
Na_3N	Mg_3N_2											AlN	Si_3N_4
K_3N	Ca_2N Ca_3N_2 $Ca_{11}N_8$ Ca_3N_4	ScN	Ti_2N TiN	V_3N V_2N VN	Cr_2N CrN	Mn_4N Mn_2N Mn_3N_2 Mn_6N_5	$Fe_{16}N_2$ Fe_4N $Fe_{2-3}N$ Fe_2N $FeN_{0.9}$	Co_4N Co_3N Co_2N Co_3N_2 CoN	Ni_4N Ni_3N Ni_2N Ni_3N_2	Cu_3N	Zn_3N_2	GaN	Ge_3N_4
Rb_3N	Sr_3N_2	YN	ZrN	Nb_2N Nb_4N_3 NbN	$Mo_{16}N_7$ Mo_2N MoN	TcN					Cd_3N_2	InN	
	Ba_3N_2	*Ln*N	Hf_3N_2 Hf_4N_3 HfN	Ta_2N TaN Ta_3N_5	W_2N	Re_2N					Hg_3N_2	TlN	

of new double metal nitrides have been conducted by many researchers. These metal nitrides look like a promising practical materials to all appearance, however, some controversy arise; simple nitrides of 3d-transition metals between Mn to Cu, some of which are attracting an attention as new magnetic materials, are not stable at an elevated temperature and metal nitrides such as Li_3N, BN, AlN and Ca_3N_2, highly react with water and/or oxygen gas and form corresponding metal oxides or metal oxynitrides. It has been attempted to stabilize chemical bond in those 3d-transition metal nitrides by forming bimetallic nitrides with strong ionic or covalent ones. The addition of another metal has succeeded in the improvement of both the durability against oxidation for TiN and the water resistance for AlN in the Ti-Al-N system.[1-6]

The thermal stability of compounds is able to be evaluated by discussion based on the thermodynamic data and/or the electronic structures. As for the search of new materials, one can get information on the electronic structure using either the molecular orbital or the band calculations, though the thermodynamic data may not be obtainable in some cases.

In this paper the thermal stability of several metal nitrides is discussed firstly with the number of valence electrons based on the information acquired experimentally. In the second part, the thermal stability is investigated by the electron theory using results of the discrete variational (DV)-Xα molecular orbital calculations for some transition metal nitrides.

2. Experimental and empirical approach for thermal stability of transition metal nitride

2.1 Thermal stability of NaCl-type $Mo_{1-x}M_xN$ (M=Nb, Zr)[7]

The NaCl-type MoN prepared by the rf-sputtering remained unchanged after annealing in both NH_3 and N_2 gases below 773K for 5 hours. A WC-type phase was formed by annealing the NaCl-type MoN in both NH_3 and N_2 gases at 873K. The WC-type phase remained in NH_3 gas up to 1173K, while it converted to γ-Mo_2N or β-Mo_2N phases by an annealing in N_2 gas above 1073K. These results indicate that (1) the NaCl-type MoN cannot exist above 873K in these gases and (2) the WC-type phase is formed easily in the sample with stoichiometric composition, ie., N/Mo =1.0. Below 773K, diffusion coefficient of molybdenum and nitrogen atoms may be so small that the phase

transition cannot take place. Phase transition begins at 873K and becomes fast above 1073K because the migration of molybdenum and nitrogen atoms is enhanced with an increase in temperature. The formation of γ-Mo_2N rather than the WC-type MoN in N_2 gas above 1073K can be explained by the release of nitrogen from the sample. Theses results are comparable with the relation between the lattice parameter of the sputter-deposited MoN film and the deposition temperature, reported by both Linker et al.[8] and Yamamoto et al[9], ie., their findings are as follows: the NaCl-type MoN was formed at the substrate temperature around 773K, the lattice constant value decreased with increasing the substrate temperature, and the NaCl-type phase did not form at all for the substrate temperature above 1073K.

The relationship between crystal phase of the solid solution and annealing temperature is summarized in Fig. 1. The NaCl-type ZrN showed no change in both their crystal phase and the lattice parameter after the annealing. The annealed NbN films showed no phase transition until 1173K, but only a small decrease in lattice parameter was observed above 1073K. The present results are consistent with that reported by Talvacchio et al.[10] who annealed a NbN single crystal with NaCl-structure under a high vacuum ($< 10^{-8}$ Pa) between 1073 and 1373K. They reported that no phase transition was observed and only nitrogen loss was found after the annealing, particularly at the temperature of 1373K. This fact that the hexagonal phase was not formed though it is a stable one below 1503K may be due to the nitrogen deficiency of the NaCl-type NbN induced during the annealing.

It is obvious that the stability of the NaCl-type phase in these solid-solution systems increases with the content of NbN or ZrN, whose number of valence electrons is one or two less than that of MoN. That is to say, the stability of the NaCl-type phase in these systems decreases with increasing the number of valence electrons, N_{VE}. In the higher N_{VE} regions, the NaCl-type phase in the MoN-NbN system transforms to the WC-type phase in NH_3 gas and to γ-Mo_2N-type phase in N_2 gas. These phase transformations take place in the samples with $x \leq 0.5$, ie., $N_{VE} > 10$, of the $Mo_{1-x}Zr_xN$ and in the samples with $x \leq 0.38$, ie., $N_{VE} > 10.38$, of the $Mo_{1-x}Nb_xN$ system. The annealed Nb-rich films showed a small reduction in lattice parameter, although the NaCl-type structure was remained until 1173K.

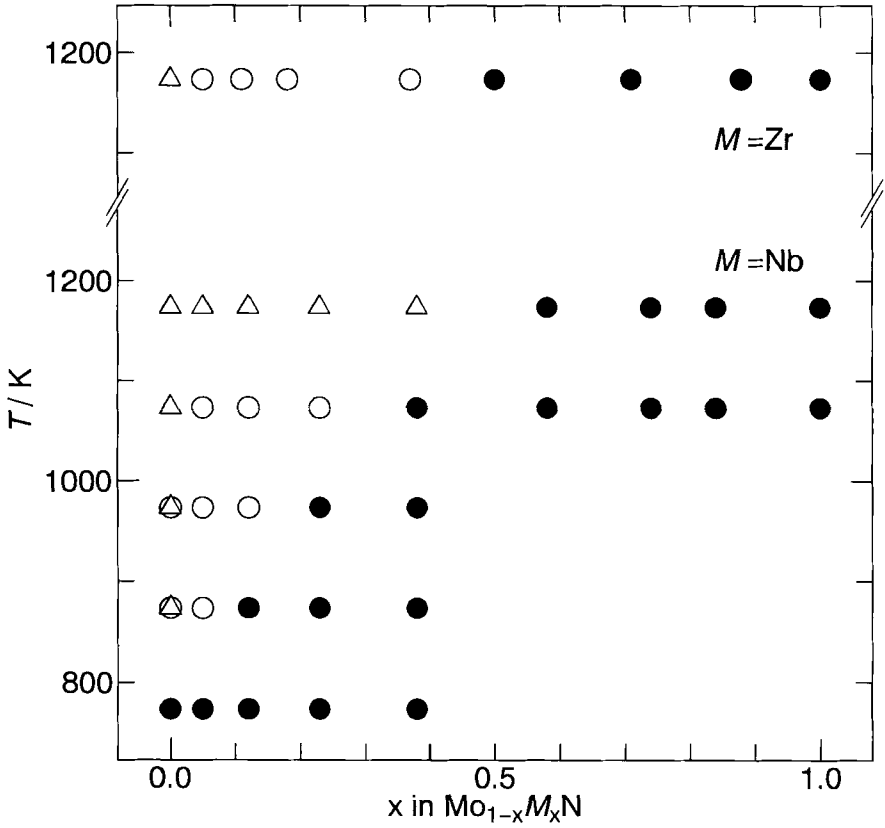

Fig. 1. Crystal phases in the $Mo_{1-x}M_xN$ (M=Nb, Zr) solid solution annealed at 723 - 1173K for 5 - 24 hours. Closed circle, triangle and open circle indicate NaCl-type, WC-type and γ-Mo_2N-type phase, respectively.

For the NaCl-type M(C, N), many investigations suggest that they all have similar band structure and their properties can be associated with N_{VE}, ie., a rigid band model is applicable to the characterization[11]. Bilz[12] proposed first a model for the energy band scheme of the NaCl-type M(C, N), which consisted of 4 energy bands; s band, p-d band (bonding), d band and $(p-d)^*$ band (antibonding). The d band overlays slightly with both the p-d and the $(p-d)^*$ bands. It may be explained well by the Bilz's model that the NaCl-type M(C,

N) have high melting point and hardness, even though they exhibit metallic conductivity. However, the Bilz's model cannot give a good explanation for the instability of the NaCl-type phase in the compounds with $N_{VE} > 10$ and the contribution of d-electrons of metals to these bands is not yet clear, because his band model is too simple to discuss the physical and chemical properties.

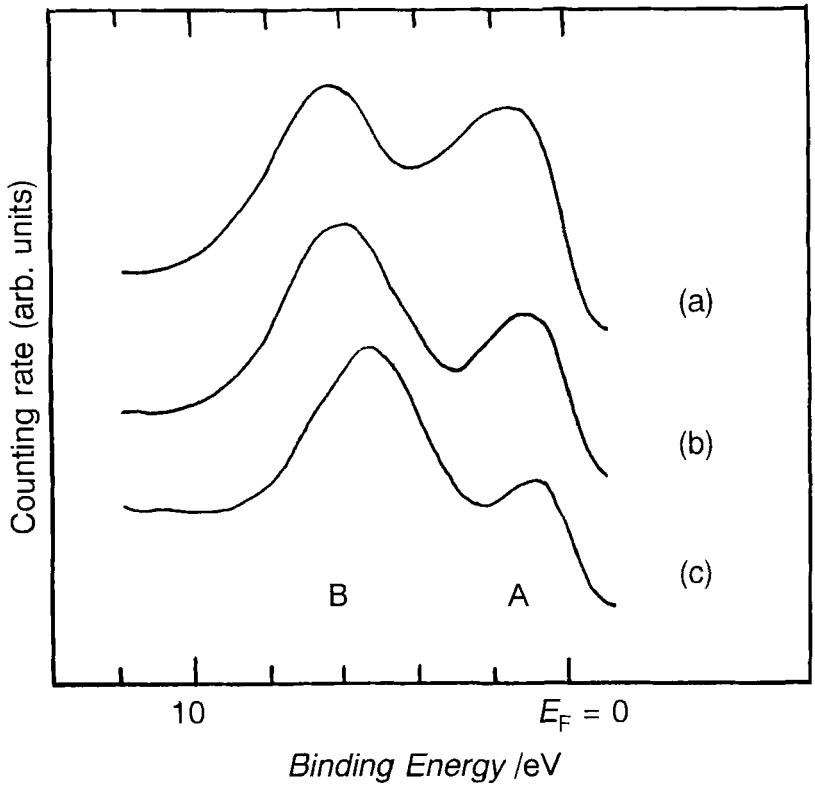

Fig. 2. Valence band region of XPS for (a) MoN, (b) NbN and (c) ZrN films partially etched by Ar ion.

Three typical XPS valence band spectra of MoN (N_{VE}=11), NbN (N_{VE}=10) and ZrN (N_{VE}=9), are shown in Fig. 2. The valence bands of XPS in these nitrides consist of two main bands; according to several band-structure

considerations[11,13-21], one is the N2p-M4d band, being denoted as B band and the other denoted as A band is the M4d-band in Fig. 2. It can be seen that $N(E_F)$ increases in the order of ZrN, NbN and MoN, or with increasing N_{VE}, indicating that the number of electrons occupying d-band or $(p-d)^*$ band increases with an increase of N_{VE}. The XPS results also show that the energy levels of the B band shift to the high binding energy side with increasing N_{VE}. This suggests that the rigid band model is also applicable to the present solid-solution systems with N_{VE} up to 11. The instability of the NaCl-type phase in the solid solution with N_{VE} above 10 implies a partial contribution of the anti-bonding $(p-d)^*$ band to the chemical bond in these systems.

2.2 Empirical classification of transition metal nitride

According to Hägg's rule[22], the crystal structure of M(C, N) depends on the radius ratio of nonmetal(X) to metal(M) atoms r_X/r_M. Hägg's rule can be explained as follows; In M(C, N), metal atoms take cubic or hexagonal close packing with nonmetal atoms at the interstitial sites. In order to make the bonding between X and M and also between M and M, shorter interatomic distance as possible is desirable for both atom pairs. The distance between the metal atoms increases as the value of r_X/r_M increases, so the bonding between the metal atoms becomes weaker and the crystal structure with cubic and hexagonal packing of metal atoms becomes unstable. Hägg's rule indicates that the upper limit of r_X/r_M for the formation of the simple structures such as NaCl-type, WC-type and NiAs-type ones is 0.59, based on a lot of experimental results.

In order to clarify the relation between N_{VE} and r_X/r_M, the structural type are plotted as functions of these two parameters for the present systems together with the other related compounds of M(C, N) in Fig. 3. In this figure the data for the present systems obtained after the annealing under NH_3 at 1173K was used. It is seen that there are two regions of structural type according to sample's N_{VE} and r_X/r_M; one is the NaCl-type and another is the WC-type phase. In the case of N_{VE} less than 10, only the NaCl-type phase with stoichiometric composition is formed independently of r_X/r_M. At N_{VE}=10, the WC-type phase and the other hexagonal phases are formed in addition to the NaCl-type phase. In the case of N_{VE} larger than 10, the WC-type phase, the

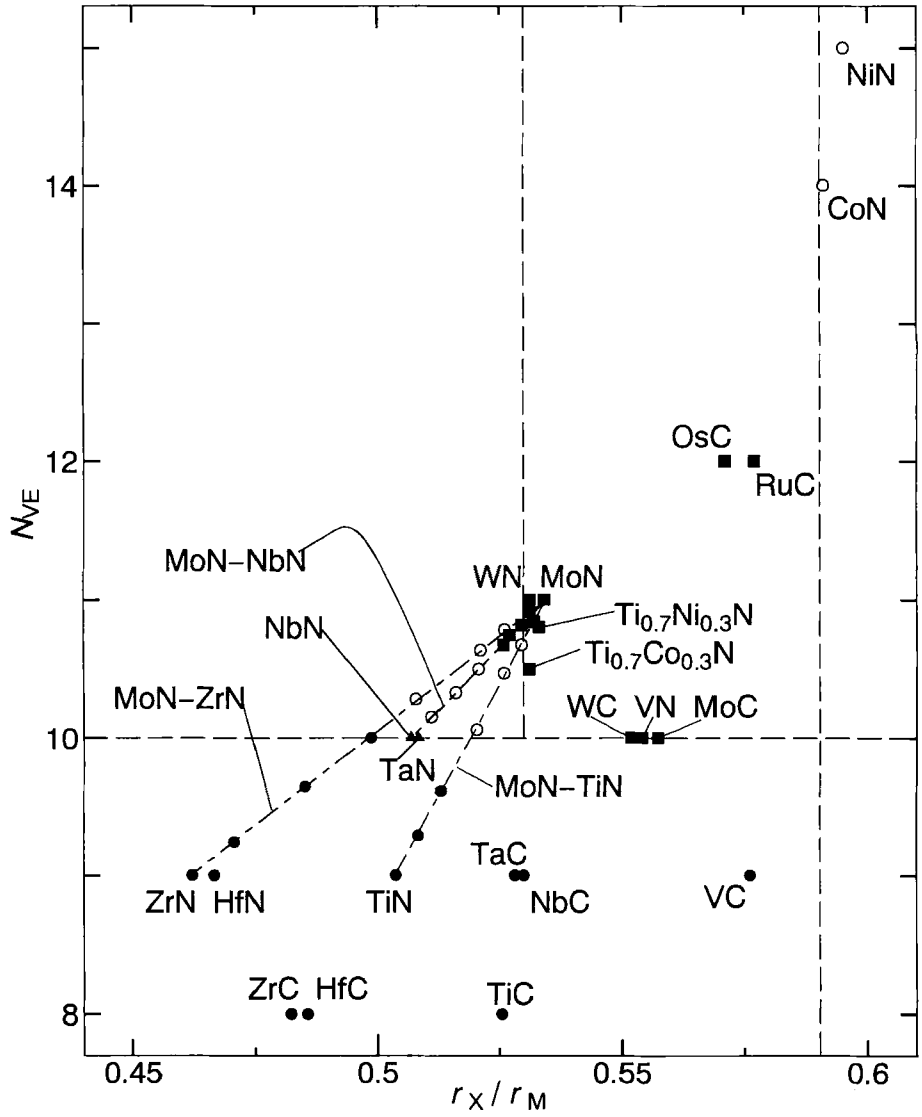

Fig. 3. Crystal phases of the $Mo_{1-x}M_xN$ (M=Nb, Zr, Ti) solid solution and the related M(C, N) plotted against N_{VE} and r_X/r_M. Closed circle, closed square, closed triangle and open circle denote NaCl-type, WC-type, other-type for MN and other-type for MN_y, respectively.

NaCl-type phase with nonstoichiometric composition and γ-Mo_2N-type phase are formed. The WC-type region and the other region can be separated simply by r_X/r_M, eg., in the region of r_x/r_M larger than 0.53, only the WC-type phase is formed, in which there exists not only simple nitrides and carbides, such as WN, MoN, OsC and RuC, but also solid-solution compounds, such as MoN-NbN, MoN-TiN, TiN-CoN and TiN-NiN systems. It is of interest to note that $Ti_{0.7}Co_{0.3}N$ and $Ti_{0.7}Ni_{0.3}N$ have the WC-structure while the end members, TiN, CoN and NiN do not take the WC structure.

The effect of N_{VE} and r_X/r_M on the crystal structure of M(C, N) can be explained as follows. Firstly let us consider the difference between the NaCl and WC structures in view of crystal chemistry. In the NaCl structure metal atoms take cubic closest packing and MX_6 octahedra link each other by sharing edges, but in the WC structure metal atoms only take a simple hexagonal packing and face-sharing is taken between the MX_6 trigonal prisms. This geometrical arrangement may result in that the WC structure has higher lattice energy than the NaCl one, thus the NaCl-type phase rather than the WC-type one is formed in the condition of lower N_{VE}. However, the contribution of antibonding in the NaCl-type phase increases with increasing N_{VE}, resulting in the decrease in the total energy and structural stability in the NaCl-type phase. On the other hand, the increase of N_{VE} may have little effect on the total energy in the WC structure which has a different band structure as compared with the NaCl one. So the WC structure becomes stable compared to the NaCl structure when $N_{VE} \geq 10$. The formation of the WC-type MoN will be limited by the geometrical factor as well, ie., $r_X/r_M > 0.53$. This corresponds well to the fact that only the WC-type phase is formed in the region of $r_X/r_M > 0.53$, while the other structures occur in $r_X/r_M < 0.53$.

2.3 Relation between number of valence electrons and thermal stability

The definition of the valence electron concentration introduced by Bilz[12] has been used as N_{VE} in the foregoing discussion, ie., both the valence electron concentration and N_{VE} for simple nitride, MN is defined as the sum of number of valence electrons for both metal, M and nitrogen. The number of valence electrons, N_{VE} is hereafter redefined as follows so as to generalize the idea of the number of valence electrons not only for simple nitride but for several metal

nitride, $M_{1-x}M'_xN_y$,

N_{VE} = number of valence electrons of $M \times (1-x)$
+ number of valence electrons of $M' \times x + 5y$,

where 5 is the number of electrons in 2s and 2p orbitals of nitrogen and y is the fraction of nitrogen expressed by the proportion of nitrogen content to total metal content. According to the present definition of N_{VE}, such alkaline metal nitrides as Li_3N, Na_3N, K_3N and Rb_3N takes N_{VE} of 2.67, alkaline earth metal nitrides, eg., Be_3N_2, Mg_3N_2 and Ca_3N_2, have N_{VE} of 5.33, and Mn_6N_5 and Fe_4N, kinds of transition metal nitrides, takes N_{VE} of 11.17 and 9.25, respectively. As for binary metal nitrides, for example, N_{VE} of LiCaN, Fe_3NiN, $Co_{0.3}Ti_{0.7}N$ is 4, 9.75 and 10.5, respectively.

Table II Number of valence electrons, N_{VE} and decomposition temperature under N_2 atmosphere, T_{dec}.

	N_{VE}	T_{dec} / K
AlN	8.0	3173*
$Ti_{1-x}Al_xN$ (0<x<1.0)	8 ~ 9	1173
TiN	9.0	3223
$Ti_{1-x}Cu_xN$ (x=0.25)	10.75	673
Cu_3N	12.67	523
γ'-Fe_4N	9.25	953
ζ-Fe_2N	10.5	723
γ"-FeN	13.0	543
Ni_2N	12.5	463
FeNiN	11.5	>673
CaNiN	8.5	>1173
Ca_3N_2	5.33	1468*

*Sublimation temperature.

N_{VE} for several metal nitrides are listed in Table II together with their decomposition temperature under nitrogen gas atmosphere. The temperature of

AlN and Ca_3N_2 listed in Table II is not the decomposition temperature but the sublimation temperature and that of FeNiN and CaNiN in Table II is the lowest temperature at which those nitrides are synthesized. As found in the previous discussion for the thermal stability of $Mo_{1-x}M_xN$ and N_{VE}, the lower N_{VE} is, the higher the decomposition temperature is, indicating that the idea based on the rigid band model may be still applicable to these metal nitrides. As is evident from Table II, the decomposition temperature of iron nitrides decreases with increasing nitrogen content, y, and the order is consistent with the above relation of N_{VE} to the thermal stability whereas such trends for MN_y with different y cannot be derived by the average number of valence electrons per atom, n_e, which is used for the investigations on the cohesive properties of transition metal carbides and nitrides[23-26]; the relationship between the thermal stability and N_{VE} or n_e for MN_y with different metal is identical each other but that for MN_y with different y varies in opposite manner each other, eg., n_e of γ'-Fe_4N, ζ-Fe_2N, and γ''-FeN is 7.4, 7.0, and 6.5, respectively. In the system of FeNiN and CaNiN, however, the electronic structures might be different each other since these nitrides take different crystal structures. Therefore, the information on the bonding state for these metal nitrides is necessary to insight the thermal stability of metal nitrides.

3. DV-Xα molecular orbital approach for thermal stability of transition metal nitride

3.1 Computations

The non-spin polarized DV-Xα molecular orbital calculations were done with the self-consistent charge procedure and the basis set generated numerically, described by Adachi, et al[27-30]. The exchange scaling parameter, α, in the Xα potential given by Slater[31] was fixed at 0.70 for all atoms throughout the present calculation. Figure 4 shows model clusters used in the calculations. $MTi_{12}N_{14}$ with O_h symmetry(a) represents the model for nitrides in the Ti-*M*-N system (*M* =Ti, V, Cr, Cu, and Al). NiM_8N_2 with D_{4h} symmetry(b) and $Ca_8Ni_2N_3$ with D_2 symmetry(c) depict the model for both Ni_2N and FeNiN, and CaNiN, respectively. Each bond length in these model clusters is taken from crystal structural data of TiN[32], Ni_2N[33], FeNiN[33] and CaNiN[34],

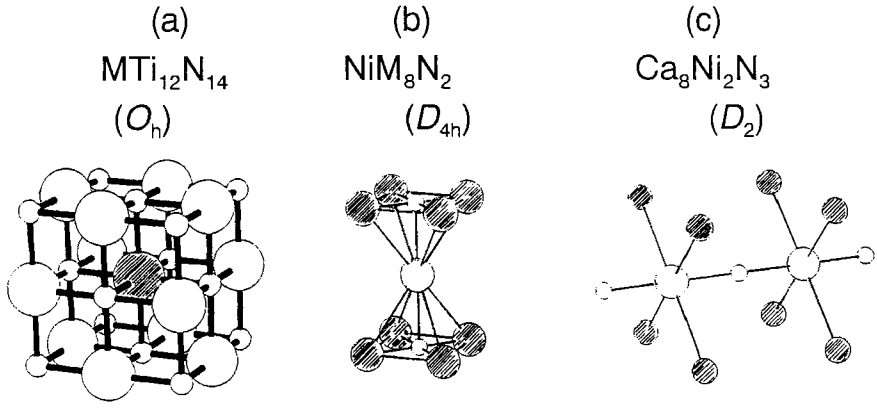

Fig. 4. Model clusters used for the present DV–Xα calculations. Hatched circles for $MTi_{12}N_{14}$, NiM_8N_2 and $Ca_8Ni_2N_3$ depict *M*, *M* and Ca, respectively. Small and large circles for $MTi_{12}N_{14}$ are nitrogen and Ti and those for both NiM_8N_2 and $Ca_8Ni_2N_3$ are nitrogen and Ni, respectively.

respectively. That means both Ti–N and *M*–N bond lengths are fixed to 0.2120nm for the Ti–*M*–N system. The number of basis function used are minimal, ie., 1s to 2p orbitals for N, 1s to 3p orbitals for Al, 1s to 4s orbitals for Ca and 1s to 4p orbitals for Ti, V, Cr and Cu.

3.2 Overlap population and thermal stability of transition metal nitrides

3.2.1 Ti–M–N system.

The overlap populations and charge obtained by the Mulliken population analyses included in the calculation procedure are listed in Table III. Net charge on the central atom, M becomes smaller in the order of the atomic number from Ti to Cu, while that on surrounding Ti changes little on altering central atom. On the other hand, net charge on nitrogen atom, which is the mean value of all nitrogen atoms, is around −1.70 except M=Cu, for which net charge on nitrogen is smaller and −1.64. Correspondingly net charge on Cu is rather small as to $CuTi_{12}N_{14}$ cluster, indicating that such tendency that d–electrons of Cu localize on Cu atom is remarkable. The tendency is also notable for Cu_3N[35]. It has been experimentally found that the width of d band in the valence band region of XPS of Cu_3N is quite sharp as compared with Cu and other metal nitrides.

Table III Charge and overlap populations for $MTi_{12}N_{14}$ cluster.

	M	Al	Ti	V	Cr	Cu
Charge	M	1.58	1.88	1.73	1.67	1.15
	N	−1.72	−1.74	−1.72	−1.70	−1.64
	Ti*	1.71	1.67	1.67	1.67	1.68
Overlap population	M–N	1.50	0.17	0.63	0.47	0.34
	M–Ti	0.30	0.27	0.31	0.31	0.10

*surrounding Ti atoms.

It has also been confirmed by the preliminary calculation[36] for a comparison of valence band structure of Cu_3N with that of Cu metal that incorporating nitrogen into Cu cluster makes d–electrons of Cu atoms localized more. As for M=Ti, ie., $Ti_{13}N_{14}$ cluster, net charge on central Ti atom differs from that of surrounding Ti atoms, which is due to a surface effect, ie., surrounding Ti atoms have so–called dangling bonds because no Madelung potential has been used in the present calculations.

Overlap populations between M and N is somewhat small for M=Ti, medium value for M=V, Cr and Cu and quite large for M=Al, whilst overlap population between M and surrounding Ti atoms is about 0.30 except $CuTi_{12}N_{14}$, for which the value is only 0.10. These results show the followings. (1) Substitution of V or Cr for Ti leads an increment of covalency on metal–nitrogen bond and does not affect the bonding character in metal–metal bond. (2) By replacing Ti by Al, the covalency in the metal–metal bond increases slightly, while such replacement introduces the covalency into metal–nitrogen bond pronouncedly. This finding is in agreement with results obtained by means of the band–structure calculations for (Ti, Al)N by D. V.–Pawelczak et.al[37]. (3) Such covalency in the metal–nitrogen bond somewhat increases but the bond strength of metal–metal bond decreases by substituting Cu for Ti. Considering that the thermal stability for the solid solution in the Ti–Cu–N system is lower than in the Ti–Al–N system[35], it appears that the bond strength, ie., the bond overlap

population of metal–metal bond plays an important role for the thermal stability of the transition metal nitride.

3.2.2 Metal nitrides having linear N–Ni–N bond.

There is some nitrides having linear N–Ni–N bond, eg., Ni_2N, FeNiN, CaNiN and so on. As listed in Table II, Ni_2N decomposes at around 460K in N_2 gas atmosphere[33] while FeNiN and CaNiN does not decompose at least 673 and 1173K, respectively, ie., FeNiN and CaNiN are synthesized higher than 673 and 1173K in a nitrogen gas flow, respectively. Overlap populations of model clusters for these nitrides are tabulated in Table IV. The M–N bond overlap

Table IV Overlap populations for nitrides having linear N–Ni–N bond

	Ni_9N_2	$NiFe_8N_2$	$Ca_8Ni_2N_2$
Ni–N	0.32	0.10	0.39
Ni_c–N	0.18	–	–
Fe–N	–	0.10	–
Ca–N	–	–	0.21
Ni–Ni_c	0.06	–	–
Ni_c–Fe	–	0.10	–
Ni–Ca	–	–	0.11
Ca–Ca	–	–	0.24

Ni_c denotes Ni atoms occupying corner site.

population is quite large for Ni_9N_2 cluster and $Ca_8Ni_2N_2$ cluster but rather small for $NiFe_8N_2$ cluster. The M–M overlap population is around 0.1 for both Ni–Fe and Ni–Ca bonds and 0.24 for Ca–Ca bond though the overlap population for Ni–Ni in Ni_2N is smaller and only 0.06. These facts indicate that Ni_2N with weak metal–metal bond can not be thermally stable. Although the thermal stability for $Mo_{1-x}M_xN$ (M =Nb, Zr) with $N_{VE} > 10$, being discussed in the section 2.1, has been accounted for the contribution of the antibondign $(p–d)^*$

band based on the electronic structural considerations[11-21], the present DV–Xα molecular orbital calculations point out that the interaction between metal atoms influences the stability of the transition metal nitride rather than the interaction between metal and nitrogen atoms. The relative importance of metal–metal versus metal–nitrogen bonds on bonding in transition metal carbides and nitrides is still controversial[8,20,21]. These indicate that the electronic structural investigations for more several nitride systems based on the molecular orbital schemes are needed for interpreting the chemical bond in the metal nitride and will be described elsewhere.

4. Conclusion

It has been found for examining empirically the thermal properties of the metal nitrides that the number of valence electrons is more advantageous than the average number of valence electrons per atom. DV–Xα molecular orbital calculations for several metal nitrides reveal that the thermal stability of transition metal nitride is intensely dominated by the bond overlap population of the metal–metal bond.

A part of computations was carried out at the computation center, Osaka University and the computation center, the Institute of Protein Research, Osaka University. XPS measurements were conducted with microlab III, VG scientific, co., at Materials Analysis Center, the Institute of Scientific and Industrial Research, Osaka University.

References

1) H.A. Jehn, S. Hofmann, V.E. Rückborn and W.D. Münz, *J. Vac. Sci. Technol.* **A4** (1986) 2701.
2) W.D. Münz, *J. Vac. Sci. Technol.*, **A4** (1986) 2717.
3) H. Randhawa, P.C. Johnson and R. Cunnungham, *J. Vac. Sci. Technol.*, **A6** (1988) 2173.
4) S. Inamura, M. Takahashi, K. Nobugai, F. Kanamaru and D. Miyamoto, *J. Soc. Mater. Sci. Jpn*, **37** (1988) 83.
5) M. Takahashi, S. Inamura, K. Nobugai and F. Kanamaru, *Corrosion/Coating of Adv. Mater.*, **1989** 307.
6) D. McIntyre, J.E. Greene, G. Hâkansson, J.–E. Sundgren and W.D. Münz, *J.Appl. Phys.*, **67** (1990) 1542.

7) G.-C. Lai, Thesis, Osaka University (1990); a part of the section 2.1 has also been appeared in G.-C. Lai, M. Takahashi, K. Nobugai and F. Kanamaru, *J. Solid State Chem.*, **82**, (1989) 1.
8) G, Linker, R. Smithey and O. Meyer, *J. Phys.*, **F14** (1984) L115.
9) H. Yamamoto, T. Miki and M. Tanaka, *Adv. Cry. Eng.*, **32**, (1986) 671.
10) J. Talvacchio, S. Sinharoy and A.I. Braginski, *J. Appl. Phys.*, **62** (1987) 611.
11) L.E. Toth, "Transition Metal Carbides and Nitrides", Academic Press, New York (1971).
12) H. Bilz, *Z. Phys.*, **153** (1958) 338.
13) J. Klima, G. Schadler, P. Weinberger and A. Neckel, *J. Phys. F*, **15** (1985) 1307.
14) D.A. Papaconstantopoulos, W.E. Pickett and B.M. Klein, L.L. Boyer, *Phys. Rev. B*, **31** (1985) 752.
15) P. Marksteiner, J. Redinger and P. Weinberger, *Z. Phys. B*, **62** (1986) 443.
16) A.L. Ivanovskii, D.L. Novikov and V.A. Gubanov, *Phys. Stat Sol (b)*, **141** (1987) 9.
17) K. Schwarz, *CRC Critical Rev, Solid State Mater. Sci.*, **13** (1987) 211.
18) W.A. Harrison and G.K. Straub, *Phys. Rev. B*, **36** (1987) 2695.
19) V.P. Zhukov, N.I. Medvedeva and V.A. Gubanov, *Phys. State Sol. (b)*, **151** (1989) 407.
20) J. Häglund, A.F. Guillermet, G. Grimval and M. Körling, *Phys. Rev. B*, **48** (1993) 11685.
21) L. Benco, *Solid State Commn.*, **94** (1995) 861.
22) G. Hägg, *Z. Phys. Chem. Abt.*, **B12** (1931) 33.
23) A.F. Guillermet and G. Grimval, *Phys. Rev. B*, **40** (1989) 10582.
24) J. Häglund, G. Grimvall, T. Janlborg and A.F. Guillermet, *Phys. Rev. B*, **43** (1991) 14400.
25) A.F. Guillermet and G. Grimvall, *J. Phys. Chem. Solids*, **53** (1992) 105.
26) A.F. Guillermet and K. Frisk, *J. Alloys Compds.*, **203** (1994) 77.
27) H. Adachi, M. Tsukada and C. Satoko, *J. Phys. Soc. Jpn.*, **45** (1978) 875.
28) C. Satoko, M. Tsukada and H. Adachi, *J. Phys. Soc. Jpn.*, **45** (1978) 1333.
29) H. Adachi, S. Shiokawa, M. Tsukada, C. Satoko and S. Sugano, *J. Phys. Soc. Jpn.*, **47** (1979) 1528.
30) H. Adachi and K. Taniguchi, *J. Phys. Soc. Jpn.*, **49** (1980) 1944.
31) J.C. Slater, "The Self-consistent Field for Molecules and Solids, Quantum Theory of Molecules and Solids", Vol. 4, McGraw-Hill, New Tork (1974).
32) JCPDS, Inter. Center for Diffraction Data, 6-642.
33) K. Ohta, *Master Thesis*, Osaka University (1992).
34) M.Y. Chern and F.J. Disalvo, *J. Solid State Chem.*, **88** (1990) 459.
35) M. Takahashi, S. Izumi and F. Kanamaru, *J. Soc. Mater. Sci. Jpn.*, **40** (1991) 1093.
36) M. Takahashi, S. Izumi and F. Kanamaru, *Proc. Fall Meeting, Cer. Soc. Jpn.*, **1990** 550.
37) D.V.-Pawelczak, P.Herzig and J. Klíma, *Z. Phys. B*, **84** (1991) 211.

Electronic States of Impurities and Their Effect on Material Properties

Kimichika Fukushima

Research and Development Center, Toshiba Corporation
4–1 Ukishima-cho, Kawasaki-ku, Kawasaki 210, Japan

Hiroshi Endo

Isogo Engineering Center, Toshiba Corporation
8 Sinsugita-cho, Isogo-ku, Yokohama 235, Japan

Abstract

Electronic structure calculations were performed to study the effect of impurity on material properties by using the DV-Xα molecular orbital method. Firstly, calculations were carried out for halogen atoms (cluster) substituted for oxygen atoms in a Cu-O plane in copper oxides. It was found that the energies of the orbitals belonging to F atoms make a small contribution to the highest occupied orbital, whose energy corresponds to the Fermi energy. A small amount of charge carriers therefore can enter F impurity sites. Thus, it is expected that F impurities will work effectively as pinning centers and enhance the critical current density in superconductors.

Secondly, we focused on the role of oxygen impurities in element-selective corrosion of austenitic stainless steels in liquid sodium. Calculation was carried out for an oxygen impurity associated with an Na atom located at the site on top of a Cr atom at the Fe(001) surface in sodium. The result shows that a positively charged Cr atom will be released selectively into sodium by an O anion.

Thirdly, we examined the ion-implantation effect on the bond between composite atoms of Si_3N_4. When Fe, Mo and Hf atoms are supposed to be ion-implanted, d energy levels of these atoms appear in the energy gap or near the gap. A transfer of the Mulliken charge between the implanted atoms and surrounding atoms occurs due to the mixing between the d orbitals of the

ADVANCES IN QUANTUM CHEMISTRY, VOLUME 29

0065-3276/97 $25.00

implanted atom and *sp* orbitals of surrounding atoms. Due to the reduced ionicity of Si, the attack on ceramics atoms by O (oxygen) in liquid sodium becomes weak. At the same time, however, the covalent bond strength between Si and N becomes weaker, which may in some cases depress corrosion resistance.

1. Introduction

Impurities in materials often present important effects on material properties. Previous work has demonstrated that calculating electronic structure is a useful way to investigate material properties and to synthesize improved and advanced materials [1-7]. The DV-Xα method [8] is a reliable tool for studying local electronic states around impurities and their role in material properties. Further, the highly accurate total energy can be catlulated by the GQ(Gaussian quadrature)-Xα method [9]. Using this method, we focus here on (1) the role of halogen impurities in pinning magnetic flux lines in copper oxide superconductors to enhance the critical current density in magnetic fields, (2) the role of oxygen impurities in element-selective corrosion of stainless steels in liquid metal, and (3) the problem of implanting ions into ceramics to improve corrosion resistance.

The first materials we focus on are high-T_c copper oxide superconductors which have the potential to be used at high temperatures and in high magnetic fields. In order to achieve the application of oxide superconductors under such conditions, we need the enhancement of the critical current density, J_c. In high magnetic fields over 77K, a sufficient J_c has not been obtained. It is necessary to introduce the stronger pinning centers for magnetic flux lines to improve J_c. We expect to use impurities and insulating inclusions for stronger pinning centers for magnetic flux lines, because most of the charge carriers do not enter impurity sites and insulating inclusions, and superconducting order parameters will have small or null values there. It is then expected that impurity atoms and insulating inclusions would be effective as strong pinning centers for magnetic flux lines. We have also predicted theoretically such candidate impurities to pin magnetic flux lines, and an optimal size for the insulating inclusion [5,6,10]. In fact, experimental results have been reported supporting the enhancement

of J_c by the impurity addition in high magnetic field at 77K [11]. By electronic structure calculations, we first examine theoretically the possibility of applying halogen impurities as pinning centers for magnetic flux lines. We selected F atoms substituted for O (oxygen) atoms as candidate impurities.

The second materials we focus on are austenitic stainless steels which are one of the most useful materials for such as plant piping. Austenitic stainless steels are excellent materials, but they have some defects which need improvement. Experiments indicate that alloying elements such as chromium and nickel in the steels are released selectively when the steels are exposed to liquid sodium [12]. The element-selective corrosion brings about a change in surface compositions, and then the surface of austenitic stainless steels loses its excellent qualities. The improvement of the corrosion resistance is required for the use of more severe conditions where strong stress is exerted on steels. It is suggested in experiments that the corrosion rate of austenitic stainless steels is affected by the concentration of oxygen impurities in liquid sodium. At the microscopic level, however, this corrosion mechanism is not yet fully understood. The second study was aimed at examining the mechanism of element-selective corrosion of austenitic stainless steels in liquid sodium. An understanding of the corrosion mechanism makes it easier to synthesize materials with improved corrosion resistance.

The third materials we focus on are ceramics which have excellent characteristics such as a high degree of hardness at high temperatures, friction resistance, low thermal expansion and low density. We expect, therefore, to use ceramics as a thermal shield at high temperatures and as a contact material between structural components which enhance the reliability with mutual contact. In order to use ceramics for such materials, they need resistance against corrosion such as by liquid metal. In order to improve the corrosion resistance of materials, ion-implantation is expected to be a new useful tool. In the third study, we calculated the electronic states of simulated ion-implanted atoms in ceramics and examined the effect of ion-implantation on the properties of ceramics. The material we considered was β-Si_3N_4. Since SiAlON is produced by replacing some amounts of Si and N in β-Si_3N_4 by Al and O (oxygen), the essential properties of SiAlON are obtained from calculations for Si_3N_4.

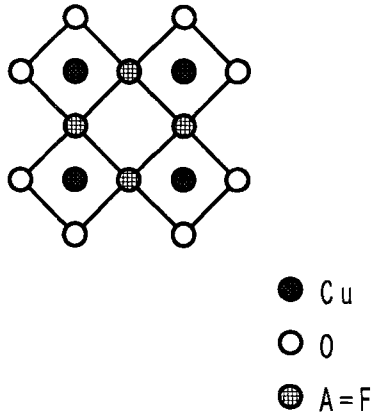

Fig.1 Atomic configuration of the model $Cu_4O_{16}A_4$ in the ab plane, where A is an impurity atom substituted for an O (oxygen) atom.

2. Magnetic flux pinning effect of impurities in copper oxide superconductors

The electronic structure calculations in this section were carried out by means of the non-spin-polarized molecular orbital method. We adopted the model cluster $Cu_4O_{16}A_4$ (A=F) for which halogen atoms were substituted for O atoms. The model was obtained from Cu_4O_{20} by substituting four impurity atoms for four O atoms. Figure 1 depicts the atomic configuration in the ab plane for the cluster $Cu_4O_{16}A_4$. The cluster is composed of four octahedra with a central Cu atom and six O ligands. The Cu-O distance in the ab plane and along the c axis are 1.894 Å and 2.428 Å, respectively, and the values are presented in Ref. [13]. The basis set used was numerical atomic orbitals consisting of $1s$-$2p$ for O (oxygen) and F, and $1s$-$4p$ for Cu. The initial charges assigned in self-consistent iterations were +2 and −2 for Cu and O atoms, respectively, and −1 for the F atom. In producing symmetry orbitals, we used the point group D_{4h}. The present study deals with the metallic state, so that

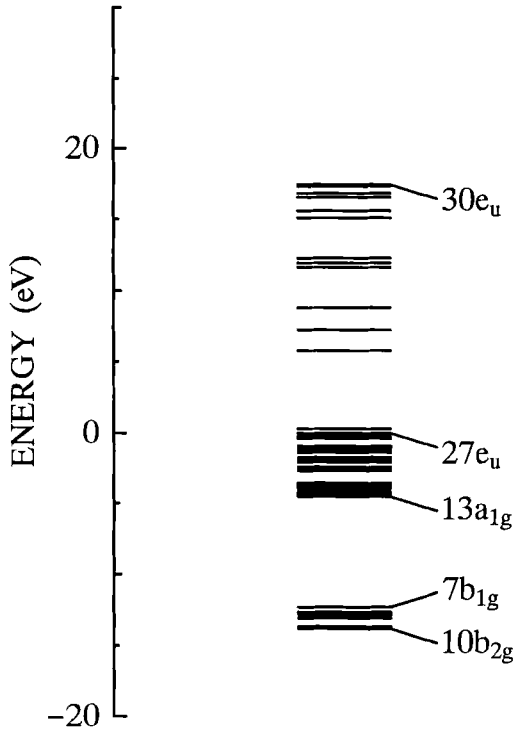

Fig.2 Energy levels for F atoms substituted for O atoms in Cu oxides.

one hole was introduced into the cluster. The long-range electric field produced by the ions out of the cluster was included in the Hamiltonian as a form of a Madelung potential evaluated in $11\times11\times3$ unit cells arrayed in the a, b, and c directions with the K_2NiF_4 lattice structure.

Figure 2 shows the energy levels for $Cu_4O_{16}F_4^{27-}$. The energy levels from $13a_{1g}$ to $27e_u$ are for the mixed states between O $2p$ and Cu $3d$ atomic orbitals, and these states are occupied by electrons. The orbital $27e_u$ is the highest occupied molecular orbital (HOMO). The energy levels from $10b_{2g}$ to $7b_{1g}$ are originated mainly from the F $2p$ atomic orbitals. These orbitals occupied by electrons are lower in energy than the minimum energy of the mixed states

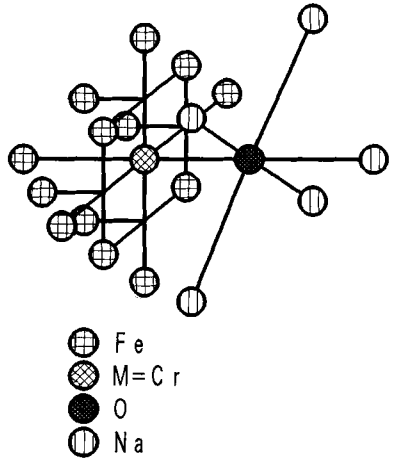

Fig.3 Atomic configuration of the model $Fe_{13}MONa_5$.

between the O $2p$ and Cu $3d$ atomic orbitals. The Mulliken population [14] of the F atoms in HOMO is less than 1% per atom. The region over the sites, where O (oxygen) atoms are replaced by F atoms, has a small amount of charge carriers and it is rather extended with the superconducting state being broken. Accordingly, the F atoms will be effective as pinning centers for magnetic flux lines in Cu oxide superconductors. In fact, by the F addition, the superconducting critical current is observed experimentally to be substantially enhanced at 77K in the magnetic field and to be maintained up to 3.5T, which is a practical magnetic field in engineering [11].

3. Mechanism of the element-selective corrosion of austenitic stainless steels

Austenitic stainless steels have an fcc crystal structure and they are stabilized by the addition of some amounts of chromium and nickel to iron. Figure 3 illustrates the cluster $Fe_{13}MONa_5$, which is a model for the element M (M=Cr in the present case) substituted for Fe at the Fe(001) surface that is attacked

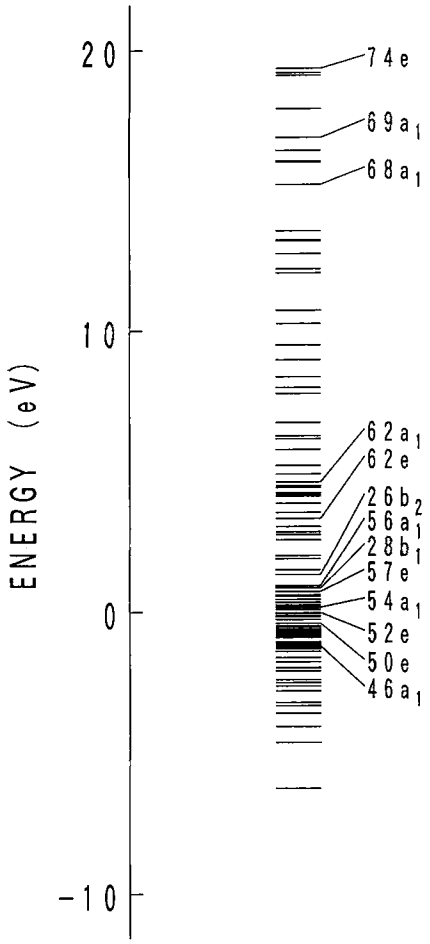

Fig.4 Energy levels for Cr at the (001) surface of the austenitic stainless steels exposed to liquid sodium with oxygen impurities.

by an O (oxygen) impurity accompanied by sodium atom in liquid sodium. The positions of the Fe atoms in the cluster are $(a/2, a/2, 0)$, $(-a/2, a/2, 0)$, $(-a/2, -a/2, 0)$, $(a/2, -a/2, 0)$, $(a/2, 0, -a/2)$, $(-a/2, 0, -a/2)$, $(0, a/2, -a/2)$, $(0, -a/2, -a/2)$, $(a, 0, 0)$, $(-a, 0, 0)$, $(0, a, 0)$, $(0, -a, 0)$ and $(0, 0, -a)$. Here,

a is a lattice constant, which has the value of 3.64 Å. Taking into account the atomic radii [15,16], the positions for the O atom and for the Na atom associated with it are set to $(0,0,b)$ and $(0,0,c)$, respectively, where b=3.09 Å and c=6.75 Å. The other four liquid Na atoms are positioned at the bridge sites, (d,d,e), $(-d,d,e)$, $(-d,-d,e)$ and $(d,-d,e)$, where d and e are 2.73 Å and 3.19 Å, respectively. At the beginning of the self-consistent iterations, the charges of the atoms were all neutral. The symmetry point group used was C_{4v} for the cluster.

Figure 4 shows the energy level diagram for the cluster $Fe_{13}CrONa_5$, whose levels are attributed to the orbitals $3d$, $4s$, and $4p$ of the Fe and Cr atoms, the O $2p$ orbitals and the $3s$ and $3p$ orbitals of the Na atoms. Tle energy level $52e$ is for HOMO, and its main origin is the Fe $3d$ orbitals. The orbitals $57e$, $28b_1$, $56a_1$ and $26b_2$ are originated mainly from the Cr $3d$ orbitals, and these energies are higher than the Fermi energy. The average energy of Cr $3d$ is 0.9 eV higher than the Fermi energy. On the other hand, the orbitals $46a_1$ and $50e$— which are composed mainly of the O $2p$ orbitals — are all lower than the Fermi energy. The average energy of these orbitals is 0.6 eV lower than the Fermi energy. The orbital with the main component of the $3s$ atomic orbital of the Na atom coupled with the O atom is $54a_1$, with energy higher than the Fermi energy. These energy differences cause the charge transfer from the Cr atom to the Fe atoms and from the Na atom to the O atom. The net charges on the Cr and O atoms are +0.40 and −0.90, respectively, and an ionic interaction becomes attractive between the positively charged Cr and the O anion. This shows that the selective transfer into liquid sodium of a positively charged element Cr at the (001) surface of the austenitic stainless steel will be brought about by the attack of an O anion accompanied by a positively charged Na atom.

4. Effect of ion-implanted atoms on the corrosion resistance of ceramics

The material considered in the third study was β-Si_3N_4. The implanted atoms we dealt with here were Fe, Mo and Hf located at an interstitial site. The crystal structure of β-Si_3N_4 is hexagonal phenacite-like, and the unit lengths

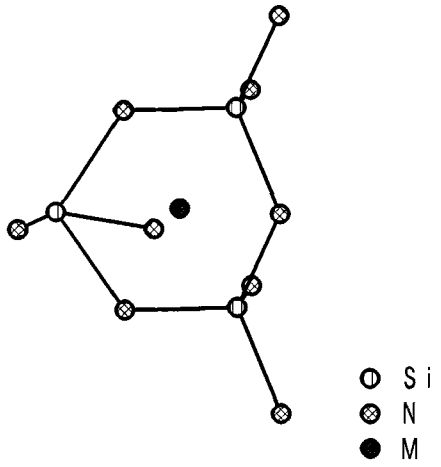

Fig.5 The atomic configuration of the model Si_3N_9M, where M indicates Fe, Mo and Hf.

in the dirctions of the a and c axes are 7.606 Å and 2.909 Å, respectively [17]. The model cluster adopted was Si_3N_9M as shown in Fig. 5, where M indicates Fe, Mo and Hf. The initial values of the ionic charges were set to $+4$ and -3 with Si and N, respectively. The initial charges for ion-implanted Fe, Mo and Hf atoms were set to neutral values. Calculations were also carried out with the initial ionic charge of $+2$ for the implanted Fe atom. The atomic basis functions used were $1s$-$3p$ for Si, $1s$-$2p$ for N, $1s$-$3d$ for Fe, $1s$-$4d$ for Mo and $1s$-$5d$ for Hf. The point group adopted in calculations was C_s. Calculations were performed at electronic temperatures of 900 K.

When Fe, Mo and Hf are ion-implanted into β-Si_3N_4, it is expected that the effect of the implanted atoms on ceramic properties are determined from the relative positions of the energy levels of the d electrons to the valence and conduction levels. Figure 6 shows the energy levels for a neutral Fe ion-implanted into β-Si_3N_4. The valence states from $23a'$ to $26a''$, occupied by electrons, consist mainly of N $2sp$ orbitals, while the conduction states from

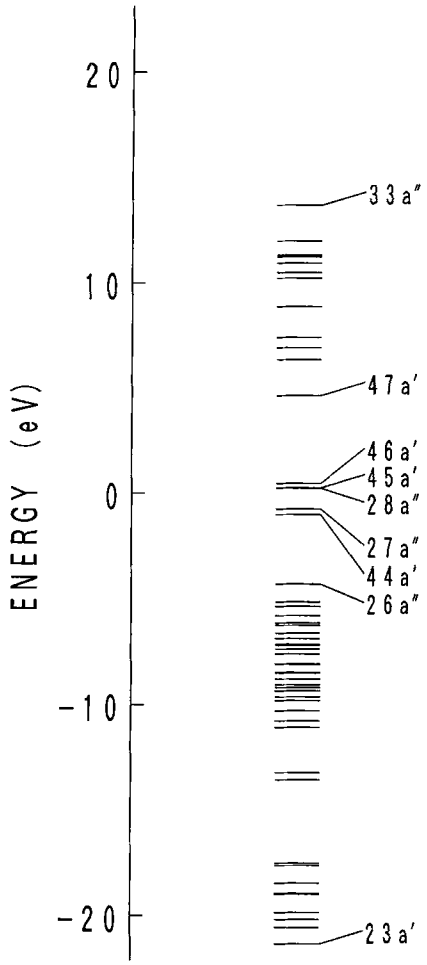

Fig.6 Energy levels for an ion-implanted neutral Fe in β-Si_3N_4.

$47a'$ to $33a''$ comprise Si $3sp$ orbitals. The energy levels originated from the Fe $3d$ atomic orbitals ($44a'$, $27a''$, $28a''$, $45a'$ and $46a'$) are all located in the energy gap. Since the neutral Fe atom has eight $3d$ electrons, the orbitals up to $45a'$ are occupied by electrons. The mixing between Fe $3d$ and Si $3sp$

causes a transfer of the Mulliken charge from the Fe atoms to the Si atom. The net charge of Si surrounding Fe is +1.780, which is lower than the corresponding value of +1.992 for the non-ion-implantation case. (The net charge of N surrounding Fe amounts to −2.030, and the change is slight from the value of −1.992 for the non-ion-implantation.) The weakened ionicity due to the charge transfer between the Fe and Si atoms will interfere with the attack of ceramics by the O (oxygen) ions in liquid sodium, and this will enhance the corrosion resistance of the ceramics. A problem occurs, however, in the covalent bond. The Mulliken overlap population per bond between the Si and N atoms surrounding the Fe atom takes the smaller value of 0.387 compared to the corresponding value of 0.497 in the non-ion implantation case. This weakened covalent bond between the Si and N atoms is due to the fact that the Fe $3d$ orbitals occupied by electrons are mixed with the unoccupied conduction states, and the Mulliken charge is transferred from Fe $3d$ to the antibonding conduction states. Furthermore, the average overlap population per bond between Fe and N and between Fe and Si is −0.067, indicating the covalent bond strength between Fe and N and between Fe and Si is weak. This weak covalent bond between Fe and N and between Fe and Si is partially because both the bonding and the antibonding orbitals between Fe $3d$ and N $2sp$ are almost all occupied by electrons, and the bond by the bonding orbitals is cancelled by the antibonding orbitals. The other reason for the weak covalent bond strength is that the Fe $3d$ orbitals cannot form a bond with the antibonding conduction states. The weakened covalent bond between the Si and N atoms may interfere with the improvement of the corrosion resistance by the ionicity suppression.

As for the Fe^{2+} case, the energy levels are depicted in Fig. 7. The energy levels consisting mainly of the Fe $3d$ orbitals ($44a'$, $45a'$, $27a''$, $28a''$ and $46a'$) are also cited in the energy gap, but they are lower in energy than in the neutral Fe case. The Si neighboring Fe has a net charge of +1.727 with little difference from the neutral Fe case, while the N around Fe has a reduced value of −1.771. The covalent bond strength (overlap population) between the Si and N atoms around the Fe atom in the case of Fe^{2+} is 0.391, and little larger than that in the case of neutral Fe. The average covalent bond strength between Fe and N and between Fe and Si has the almost same value of −0.029 as in the neutral

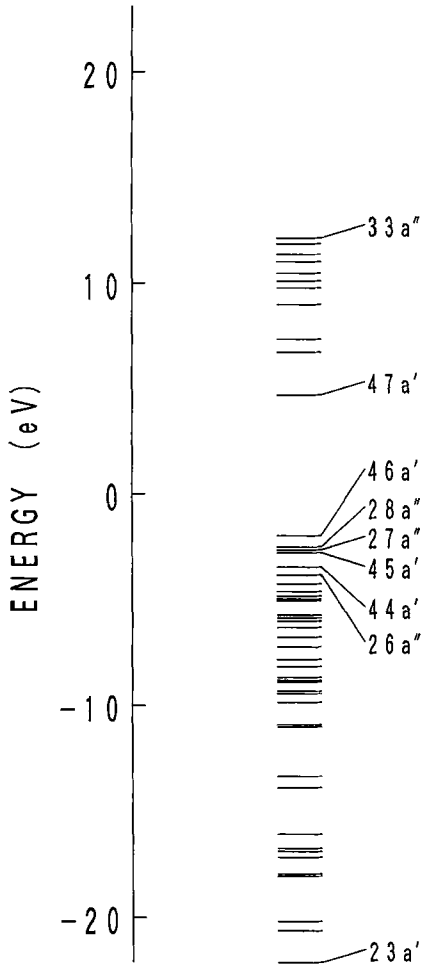

Fig.7 Energy levels for an ion-implanted Fe^{2+} in β-Si_3N_4.

Fe case. Concerning the neutral interstitial Mo, the d energy levels are all in the energy gap with higher energies than the neutral Fe. Among the d energy levels for Hf, two lower levels for the orbitals occupied by electrons are in the energy gap, while the other three levels for the unoccupied orbitals are in the

conduction levels. The net charges of the Si neighboring Mo and Hf take the reduced values of +1.710 and +1.642, respectively, while those of N for the Mo and Hf cases are not so different from the values for the Fe cases and take the values of −2.005 and −1.956, respectively. The covalent bond strength between the Si and N surrounding Mo and Hf becomes smaller with values of 0.275 and 0.187, respectively. The average covalent bond strength between the ion-implanted atom and neighboring N and Si atoms are −0.137 and −0.089 for the Mo and Hf cases, respectively, and the covalent bond is not formed between the implanted atom and surrounding atoms in these cases.

As has been indicated in this section, when Fe, Mo and Hf atoms are implanted into the β-Si_3N_4, the ionicity of Si around the implanted atom becomes weaker in the order Hf, Mo and Fe. The weakened ionicity will enhance the corrosion resistance of the β-Si_3N_4 against the ionic O (oxygen). At the same time, however, the weakened covalent bond may in some cases interfere with the improvement of the corrosion resistance.

5. Conclusions

With the use of the DV-Xα molecular orbital method, electronic structure calculations have been performed to investigate the impurity effect on material properties. Firstly, calculations were done for F atoms substituted for O (oxygen) atoms in copper oxide superconductors. It was found that the population of the atomic orbitals of F atoms is small in HOMO (highest occupied molecular orbital) and a small fraction of charge carriers enters the impurity sites. The F impurities are therefore expected to be effective for pinning magnetic flux lines in Cu oxide superconductors.

Secondly, we examined the mechanism of element-selective corrosion of austenitic stainless steels in liquid sodium. We performed calculations for a system where an O impurity atom accompanying Na atom approaches Cr atom at an Fe(001) surface exposed to liquid sodium. The energy levels attributed to the Cr 3*d* orbitals are located above the Fermi level, while the energy levels originated from the O 2*p* orbitals are below the Fermi level. Furthermore, the level for the Na 3*s* orbital is above the Fermi level. By the energy differences of these orbitals, the Cr atom is charged positively, while an O atom accompa-

nying an Na atom is ionized negatively. The charging of the Cr and O atoms causes an attractive ionic interaction between Cr and O. This shows that an attack by an O anion accompanied by Na atom will bring about a selective transfer of Cr at the steel surface into the liquid sodium. The model is highly consistent with the experimentally obtained results.

Thirdly, we investigated the effect of an ion-implanted atom on the corrosion resistance of ceramics. We carried this out for the model clusters comprising the implanted atom and its neighbor atoms in the ceramics, and examined the ionicity of these atoms and the covalent bond strength between the atoms neighboring the implanted atom. The material considered was β-Si_3N_4, the model of SiAlON. The supposed implanted atoms were Fe, Mo and Hf located at an interstitial site. The calculated energy levels showed that the material is an insulator (semiconductor) having valence states consisting of N $2p$ atomic orbitals and conduction states composed of Si $3sp$ orbitals. The valence states are all occupied by electrons, while the conduction states are all empty, so that N atoms are ionized negatively and Si atoms are ionized positively. From the viewpoint of material corrosion in liquid metal, strong ionicity will cause the corrosion. When Fe, Mo and Hf atom are ion-implanted into the ceramics, the energy levels originated from the d orbitals of the implanted atoms are located around the energy gap and the energy of the d orbitals are in the order Fe $<$ Mo $<$ Hf. The orbital mixing between the d orbitals of implanted atoms and the Si $3sp$ orbitals leads to the charge transfer from the implanted atoms to the Si atoms. The weakened ionicity of Si due to the charge transfer will enhance the corrosion resistance against an attack by an O anion. At the same time, the covalent bond strength between Si and N is weakened, which may in some cases interfere with the corrosion resistance.

References

[1] K. Fukushima, H. Adachi and S. Imoto, J. Nucl. Mater. **137**, 154 (1986).

[2] K. Fukushima, H. Adachi and S. Imoto, J. Nucl. Mater. **158**, 253 (1988).

[3] K. Fukushima and H. Adachi, Jpn. J. Appl. Phys. **28**, 1851 (1989).

[4] K. Fukushima and H. Adachi, in *Advances in Superconductivity III*, edited by T. Kagoshima and H. Hayakawa (Springer-Verlag, 1991), p. 65.

[5] K. Fukushima and H. Adachi, Physica C **207**, 119 (1993).

[6] K. Fukushima, Physica C **212**, 407 (1993).

[7] K. Fukushima and H. Endo, Jpn. J. Appl. Phys. **33**, 2613 (1994).

[8] H. Adachi, M. Tsukada and C. Satoko, J. Phys. Soc. Jpn. **45**, 875 (1978).

[9] K. Fukushima, J. Mizuno, K. Fujima and H. Adachi, J. Phys. Soc. Jpn. **51**, 4028 (1982).

[10] N. Takezawa and K. Fukushima, Physica C **228**, 149 (1994).

[11] K. Tachikawa, A. Kikuchi, T. Kinoshita and S. Komiya, in *Advances in Superconductivity VII*, edited by K. Yamafuji and T. Morishita (Springer-Verlag, 1995) p. 461; K. Tachikawa *et al.*, Cryogenics (to be published).

[12] T. Suzuki, I. Mutoh, T. Yagi and Y. Ikenaga, J. Nucl. Mater. **139**, 97 (1986).

[13] J. D. Jorgensen, H.-B. Schüttler, D. G. Hinks, D. W. Capone, II, K. Zhang, M. B. Brodsky and D. J. Scalapino, Phys. Rev. Lett. **58**, 1024 (1987).

[14] R. S. Mulliken, J. Chem. Phys. **23**, 1833 (1955).

[15] L. Pauling, *The Nature of the Chemical Bond and the Structure of Molecules and Crystals* (Cornell University Press, New York, 1960).

[16] R. D. Shannon, Acta Cryst. **A32**, 751 (1976).

[17] R. W. G. Wyckoff, *Crystal Structures* (Interscience, New York, 1964).

Electronic States of Oxygen Ions of Molten Slags Used for Iron and Steel Making

Masao Morishita*[1], Koichiro Koyama*[1], Akinori Hatamoto*[2], Masahiko Morinaga*[3] and Hirohiko Adachi*[4]

*[1] Department of Materials Science and Engineering, Faculty of Engineering, Himeji Institute of Technology.
2167 Shosha, Himeji, 671-22 Japan.

*[2] Formerly Graduate Student of Himeji Institute of Technology.
Now at Nakamura Yogyo Ltd., Urai-gun, Bizen, Okayama-ken, 705 Japan.

*[3] Department of Materials Science and Engineering, Faculty of Engineering, Nagoya University.
Furocho, Chigusa-ku, Nagoya, 464-01 Japan.

*[4] Department of Materials Science and Engineering, Kyoto University.
Yoshida Honmachi, Sakyo-ku, Kyoto, 606-01 Japan.

Abstrart

Regarding molten slags used for iron and steel making, discrete anion models, SiO_4^{4-} and $Si_2O_7^{6-}$, coordinating metal ions such as Na^+, K^+, Ca^{2+} and Mg^{2+} were examined by the DV-X α method. The bond order which is a measure of the covalent bond and the ionicity which is a measure of the charge transfer were calculated. The bond orders between the Si ions and non-bridging oxygen ions were found to be very high. On the other hand, the bond orders between the Si ions and the oxygen ions coordinating the metal ions were very low, that is, the covalent bonds between them are weak. The metal ions such as Na^+, K^+, Ca^{2+} and Mg^{2+} are necessary for the formation of the free oxygen ions as well as the decomposition of polymerized structures. As a result, the bond orders between the Si ions and the oxygen ions

ADVANCES IN QUANTUM CHEMISTRY, VOLUME 29

0065-3276/97 $25.00

coordinating the metal ions were found to be correlated with reactivity such as sulphide capacity of molten slags. The values of ionicity of the non-bridging oxygen ions were -1.0～-1.4. These values of non-bridging oxygen ions are approximately equal to the valences obtained from the statistical thermodynamics studies.

1. Introduction

Molten slags are important substances for iron and steel making. Thus much effort has been made for clarifying the nature of molten slags. The structures of molten slags were investigated by X-ray diffraction analyses[1)-3)] and molecular dynamics calculations[4,5)]. The properties such as viscosity[6)] , surface tension[6)], activity of oxygen ions[7)], sulphide[8,9)], phosphate[10)] and carbonate[11)] capacities, and optical basicity[12)] were measured by physico-chemical methods. Activities of metal oxides were also theoretically calculated by statistical thermodynamics[13,14)]. However, many problems have been left unsolved because molten slags are generally high temperature liquid. In the previous statistical thermodynamics studies[13,14)], the valences of the bridging (O_B), non-bridging (O_{NB}) and free oxygen ions were assumed as 0, -1 and -2, respectively, and on the basis of this assumption thermodynamic properties such as activities of metal oxides were evaluated. The figures, 0, -1 and -2 mean, however, only formal charges. We considered that one of the important problems to be solved is the change in the valence of oxygen ion at local sites near metal ions such as Na^+, K^+, Mg^{2+} and Ca^{2+}. Thus we undertook to clarify the change in the valence of oxygen ion at local sites near metal ions by calculating the electronic configuration among O, Si and metal ions.

Previously we calculated the electronic states of molten chlorides of alkali metals, magnesium and zinc[15)] as well as molten SiO_2[16-17)], and found that the mechanism of formation of complex ions and their polymerization, and also the viscosity can be well explained in terms of

the bond order and densitiy of states calculated by the DV-X α molecular orbital method[18,19]. Furthermore, the DV-X α method advantageous over the semi-empirical method and the *ab initio* Hartree-Fock method in the terms that empirical parameters are unnecessary and also computing time is much shorter not only for simple molecules but also for large clusters containing metal atoms. Thus we adopted the DV-X α molecular orbital method in the present investigation.

2. Cluster model

The covalent bonds between Si^{4+} ions and O^{2-} ions are very strong in molten SiO_2. This is the reason for the formation of the highly polymerized network structure of the molten SiO_2. However, when large amount (more than 60mol%) of basic metal oxides such as Li_2O, Na_2O, K_2O, CaO and MgO are added to the molten SiO_2, the Si^{4+} ions capture the O^{2-} ions of the metal oxides to have an electron configuration of Ar-like closed shell[14,20], and then the polymerized network structure decomposes to discrete anions, SiO_4^{4-}, $Si_2O_7^{6-}$, $Si_3O_{10}^{8-}$, etc. [13,14,20] On the other hand, the metal ions such as Na^+, K^+ and Ca^{2+} coordinate edge-shared sites of the unit cell of tetrahedron

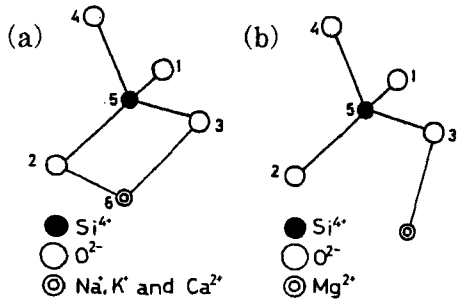

Fig.1 Monomer cluster models adopted in the calculation.

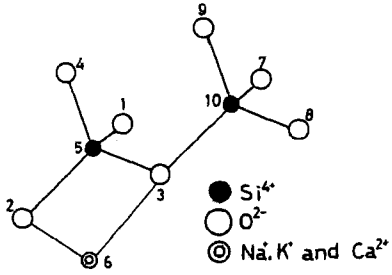

Fig. 2 Dimer cluster model adopted in the calculation.

SiO_4^{4-} [21,22]. In the same manner, the Mg^{2+} ion coordinates corner-shared sites of the unit cell of tetrahedron SiO_4^{4-} [21,22].

Figure 1(a) shows the cluster models adopted for the calculation for the SiO_4^{4-} coordinating Na^+, K^+ and Ca^{2+}, and Fig. 1(b) the cluster model adopted for the SiO_4^{4-} coordinating Mg^{2+}. Figure 2 indicates the cluster models adopted for the calculation for the $Si_2O_7^{6-}$ coordinating Na^+, K^+ and Ca^{2+}. In these cluster models, the configurations and interatomic distances obtained from the X-ray diffraction[1)-3)] are adopted. The basis sets are constructed by 1s～3d atomic orbitals for Si, 1s～2p for O, 1s～3d for Na, 1s～4p for K, 1s～4p for Ca and 1s～3d for Mg.

3. Results and discussion

Figure 3 shows the calculated results of the ionicity of the oxygen ions. The ionicity is a kind of effective charge, defined as the difference between the calculated electron population on the atom in a cluster and the atomic number[19)]. For SiO_4^{4-}, the symbols of ○ show the ionicities of the oxygen ions coordinating the metal ions (No.3 in Fig. 1(a) and (b)), and the symbols of □ show the ionicities of O_{NB} (No.1 in Fig. 1(a) and (b)). For $Si_2O_7^{6-}$, the symbols of ● show the ionicities of O_B coordinating the metal ions (No.3 in Fig. 2), and the symbols of ▲ show the ionicities of O_{NB} (No.1 in Fig. 2). In the case of SiO_4^{4-}, the ionicities of the oxygen ions coordinating the metal ions (○) were about -1.1～-1.3, and the ionicities of O_{NB} (□) were about -1.0～-1.4. In the case of $Si_2O_7^{6-}$, the ionicities of O_B coordinating the metal ions (●) were about -1.1～-1.3, and the ionicities of O_{NB} (▲) were about -1.3～-1.4.

The previous statistical thermo-dynamics studies[13,14)] treated the valences of O_B, O_{NB} and free oxygen ions as 0, -1 and -2, respectively, and succeeded in the estimation of thermodynamic properties such as activities of CaO, MnO, PbO and FeO. In the both cases of SiO_4^{4-} and $Si_2O_7^{6-}$, the present calculations of the ionicity (□ and ▲) of O_{NB} (No.1 in Fig. 1(a)(b) and Fig. 2) support the assumption of the statistical thermodynamics studies[13,14)]. On the other side, the

ionicity (●) of O_B coordinating the metal ions (No.3 in Fig. 2) of $Si_2O_7^{6-}$ were lager than the valence of the bridging oxygen ion[13,14] but can be regarded to be similar to that of the non-bridging ion[13,14]. From the structural studies by X-ray diffraction[1)-3)], it has been considered that the polymerized structure is decomposed near the metal ions. Judging from the calculation of the ionicity and the experiments of X-ray diffraction, O_B coordinating the metal ion was

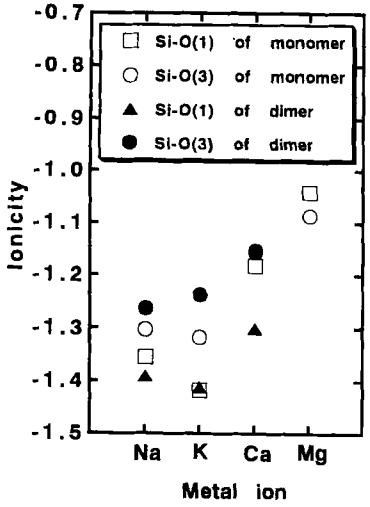

Fig. 3 Changes in ionicity of oxygen ion with local sites in SiO_4^{4-} and $Si_2O_7^{6-}$ clusters coordinating metal ions.

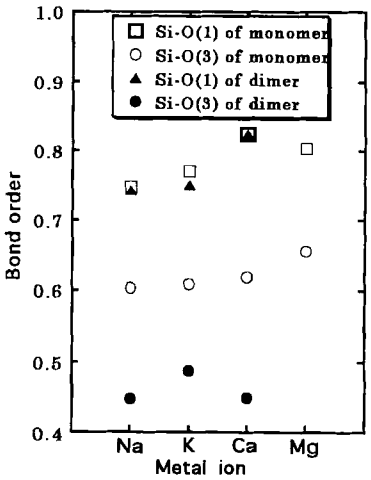

Fig. 4 Changes in bond order between Si ion and oxygen ion with local sites in SiO_4^{4-} and $Si_2O_7^{6-}$ clusters coordinating metal ions.

considered to becomes a non-bridging oxygen ion after the decomposition of the polymerized structure. Therefore, we calculated the bond order between the Si ions and the oxygen ions. Further, the ionicities (○) of the oxygen ions coordinating the metal ions (No.3 in Fig. 1(a)(b)) of SiO_4^{4-} will be discussed later.

Figure 4 shows the bond orders, that is, the two-centered charges called overlap population[19]. For SiO_4^{4-}, the symbols of ○ shows the bond orders between the Si ions and oxygen ions coordinating the metal

ions (No.3 in Fig. 1(a) and (b)), and the symbols of □ show the bond orders between the Si ions and O_{NB} (No.1 in Fig. 1(a) and (b)). For $Si_2O_7^{6-}$, the symbols of ● show the bond orders between the Si ions and O_B coordinating the metal ions (No.3 in Fig. 2), and the symbols of ▲ show the bond orders between the Si ions and O_{NB} (No.1 in Fig. 2). In the both cases of SiO_4^{4-} and $Si_2O_7^{6-}$, the bond orders between the Si ions and O_{NB} (□ and ▲) were very high. This means that the covalent bond between the Si ions and O_{NB} is very strong. On the other hand, the bond orders between the Si ions and O_B coordinating the metal ions (●) of $Si_2O_7^{6-}$ were very small. This means that the metal ion weakens the covalent bond between the Si ion and O_B to which the metal ion attaches, and then the covalent bond between them is readily destroyed. Furthermore, the bond orders between the Si ions and oxygen ions coordinating the metal ions of SiO_4^{4-} (○) were small. Especially, the bond order between the Si ion and O_{NB} which coordinate Na^+ ion was small.

For the SiO_4^{4-} cluster coordinating Na^+, the contour map of the charge difference, $\triangle\rho$ ($\rho(SiO_4Na^{3-}) - \rho(SiO_4^{4-})$), was calculated, in order to obtain better understanding of a decrease in the bond order

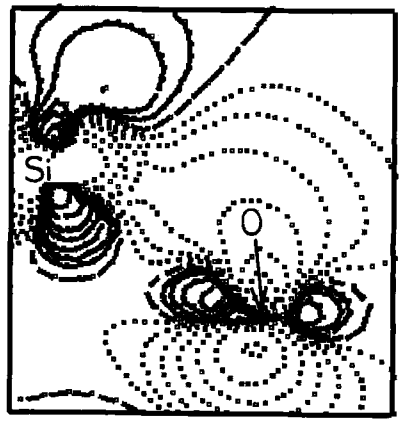

Fig. 5 Contour map of difference charge density, $\Delta\rho(\rho(SiO_4Na^{3-})) - \rho(SiO_4^{4-})$), around Si(5) and O(3) ions. Solid, dotted and dashed lines indicate positive, negative and zero contour lines, respectively.

between the Si ion and the oxygen ion. Figure 5 shows the contour map of the charge difference around the Si and O(3) ions (Fig. 1(a)). The solid, dotted and dashed lines indicate positive, negative and zero contour lines, respectively. The area between the Si ion and O(3) ion shows negative difference charge. Therefore, it can be said that Na^+ ion decreased the charge density in the area between the Si ion and O(3) ion.

Masson[14] considered that, as the silica content in an oxide melt was increased, a series of polycondensation reactions might be envisaged in which SiO_4^{4-} ions at first dimerize and then further react with higher members of the series, and at last formed linear and branched polyionic chains, with the elimination of an oxygen ion at each step as shown in eq.(1):

$$\begin{aligned} SiO_4^{4-} + SiO_4^{4-} &= Si_2O_7^{6-} + O^{2-} \quad (K_{1,1}) \\ SiO_4^{4-} + Si_2O_7^{6-} &= Si_3O_{10}^{8-} + O^{2-} \quad (K_{1,2}) \\ SiO_4^{4-} + Si_3O_{10}^{8-} &= Si_4O_{13}^{10-} + O^{2-} \quad (K_{1,3}) \end{aligned} \qquad (1)$$

In his calculation, it was assumed that all of the equlibrium constants, $K_{1,1}$, $K_{1,2}$, $K_{1,3}$---, were equal to the same value, K. The activities of the metal oxides such as CaO and FeO can be evaluated by using the equilibrium constant, K.

Although thermodynamic properties can be evaluated by these statistical thermodynamics studies[13,14], effects of metal ions on the equilibria among SiO_4^{4-}, $Si_2O_7^{6-}$, $Si_3O_{10}^{8-}$, $Si_4O_{13}^{10-}$ --- have not been directly clarified. We tried to interpret our present calculation in connection with the statistical thermodynamic studies[13,14]. Figure 6 shows the schematic models of the equilibrium between SiO_4^{4-} and $Si_2O_7^{6-}$. We considered that the mechanisms of polymerization and depolymerization were as shown in models I (a), (b) and models II (c), (d), respectively. Model I (a) shows interaction between a monomer of SiO_4^{4-} and a metal ion. As described above (Fig. 4 and 5), it was found that the metal ions decrease the electron densities between the Si and oxygen ions of SiO_4^{4-}. Therefore, we consider that the oxygen ion (Mark A in Fig. 6(a)) coordinating the metal ion can easily

dissociate. As a result, the oxygen ion (Mark B in Fig. 6(a)) combines the Si ion to form polymerized $Si_2O_7^{6-}$, as shown in Model I (b).

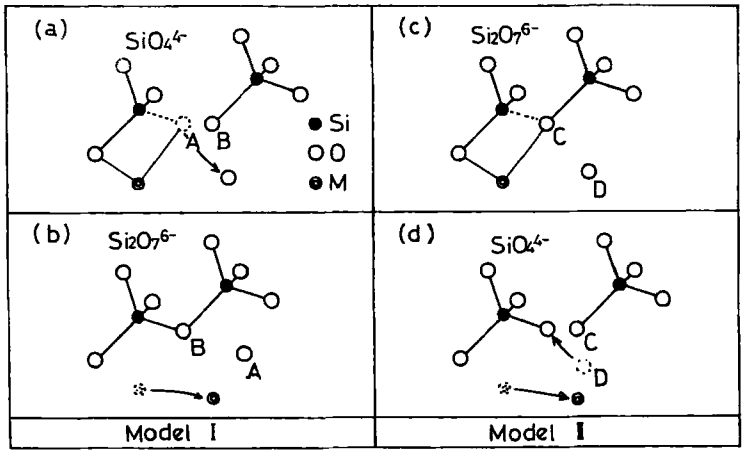

Fig.6 Schematic models of polymerization. Model I shows the polymerization of SiO_4^{4-} to $Si_2O_7^{6-}$ and Model II shows the depolymerization of $Si_2O_7^{6-}$ to SiO_4^{4-}.

Model II (c) shows the interaction between a dimer of $Si_2O_7^{6-}$ and a metal ion. The metal ion decreases the electron densitiy of $Si-O_B$ of $Si_2O_7^{6-}$ as shown in Fig. 4. Therefore, the covalent bond of $Si-O_B$ (Mark C in Fig. 6 (c)) is readily destroyed. As a result, two SiO_4^{4-} are formed by cooridinating a free oxygen ion (Mark D in Fig. 6(d)), as shown in Model II (d). Further the equilibrium constants, K in eq.(1) of Masson's statistical thermodynamics study was very small[14]. For example, for SiO_2-CaO binary system, K is 0.003[14]. This is the reason why, when metal oxides are added, the depolymerization proceeds more than the ploymerization. The bond orders between the Si ions and O_B coordinating the metal ions of $Si_2O_7^{6-}$ (Model II, ● in Fig.4) were smaller than those between the Si ions and oxygen ions coordinating the metal ions of SiO_4^{4-} (Model I , ○ in Fig.4). Furthermore, the ionicities (○) of the oxygen ions coordinating the metal ions (No.3 in Fig. 1(a)(b)) of SiO_4^{4-} does not yet reach to -2.0 of

the free oxygen ions. These calculated results support the fact that the decomposition proceeds more than the polymerization.

Further, concerning in our present study, Kowada et.al. investigated the optical properties of the solid states of silicate glassses from the energy level structures calculated by the DV-Xα method[23)-26)]. Besides the optical properties, the ionicity of O_{NB} was found to be from -1.4 to -1.5 and that of O_B was found to be from -1.2 to -1.3[23)]. Furthermore, it was found that Na^+ ion decreased the bond order between the Si ion and O_B[24)]. Therefore, the ionicities of O_{NB} and O_B, and the effect of Na^+ ion on the bond order between the Si ion and O_B[24)] obtained in the present study were similar to those of the pioneer studies for the silicate glasses[23)-26)]. However, the characteristics of the liquid states such as the dynamic equilibrium among the discrete anions and free oxygen ions have not yet been discussed[23)-26)]. We found that the metal ions were necessary for the formation of the free oxygen ions as well as the decomposition of polymerized structures as above described.

Finally, we will consider the relation between the sulphide capasity of molten slags and the present calculation. The sulphide capacity is the solubility of sulphur atoms into molten slags from molten irons. Sulphur make irons brittle. Therefore, it is necessary for molten slags to have the high sulphide capacity in order to produce high performance irons.

During iron making, sulphur atoms in molten irons react with free oxygen ions in molten slags and then dissolve into the molten slags[9)] as shown in eq.(2).

$$\underline{S}\ (\text{molten iron}) + O^{2-}\ (\text{molten slag}) = S^{2-}\ (\text{slag}) + 1/2\ O_2 \quad (2)$$

Therefore, when oxygen ions are dissociated easily from SiO_4^{4-} during the polymerization (Mark A in Fig.6(a)), sulphur atoms in molten irons can readily react with oxygen ions in molten slags, and then readily dissolve into the molten slags. The dissociation of oxygen ions from SiO_4^{4-} should be governed by the strength of the covalent bond between the Si and O(3) ions. Hence, when the bond orders of Si−O(3) in

SiO_4^{4-} are small, sulphur atoms in molten irons should readily react with oxygen ions in molten slags and readily dissolve into the molten slags. Thus we tried to evaluate experimental data of the sulphide capacities in terms of the bond order of Si−O(3) in SiO_4^{4-} (the symbols of ○ in Fig.4). Figure 7 shows correlation of the sulphide capacities of the molten SiO_2−55mol%Na_2O, SiO_2−55mol%CaO and SiO_2−55mol%MgO[9] with bond order for Si−O(3). It is found that the molten slag has higher sulphide capacity as the bond order decreases. The DV-X α molecular orbital calculation is expected to be a useful method for process design.

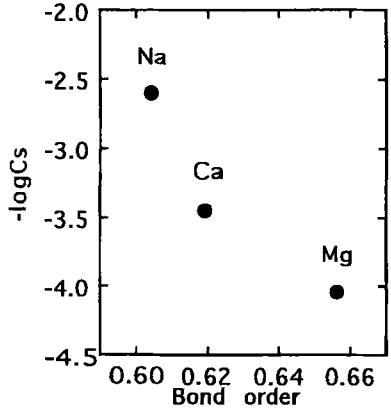

Fig.7 Correlation of sulphide capasities of SiO−55mol%Na_2O, SiO_2−55mol%CaO and SiO_2−55mol%MgO[9] with bond order for Si−O(3) in monomer cluster in Fig.1.

4.Conclusion

In order to clarify the electronic states of molten slags used for iron and steel making, discrete anion models, SiO_4^{4-} and $Si_2O_7^{6-}$, coordinating metal ions such as Na^+, K^+, Ca^{2+} and Mg^{2+} were calculated by the DV-X α method. The bond orders between the Si ions and non-bridging oxygen ions were found to be very high. On the other hand, the bond orders between the Si ions and the oxygen ions coordinating

the metal ions were very low, that is, the covalent bonds between them are weak, indicating that these oxygen ions appear to librated as free oxygen ions during the polymerization of the discrete anions. The metal ions such as Na^+, K^+, Ca^{2+} and Mg^{2+} are necessary for the formation of the free oxygen ions as well as the decomposition of polymerized structures. As a result, the bond orders between the Si ions and the oxygen ions coordinating the metal ions were found to be correlated with reactivity such as sulphide capacity of molten slags. The values of ionicity of the non-bridging oxygen ions were -1.0～-1.4. These values of non-bridging oxygen ions are approximately equal to the valences obtained from the statistical thermodynamics studies.

References

(1) Y.Waseda. and E.Suito : Tetsu to Hagane, 62(1976), 1493.
(2) Y.Waseda and J.M.Toguri : Met. Trans., 8B(1977), 563.
(3) Y.Waseda : *The structure of Non-crystalline Materials*, McGraw-Hill, New York, (1980), 138.
(4) I.Okada, Y.Matsui and K.Kawamura : Nippon KagakuKaishi, (1982), 910.
(5) T.Matsumiya, A.Nogami and Y.Fukuda : ISIJ. Int., 33(1993), 210.
(6) Y.Suginohara, T.Yanagase and H.Ito : Trans. JIM., 3(1962), 227.
(7) M.Nagano and A.Katou : Denkikagaku, 42(1974), 148.
(8) C.J.B.Fincham and F.D.Richardson : Proc. Roy. Soc., A223(1954), 40.
(9) M.Tokuda : Tetsu to Hagane, 69(1983), 1699.
(10) H.Suito and R.Inoue : Trans. ISIJ., 24(1984), 47.
(11) K.Koyama and Y.Hashimoto : High Temperature Mater. Processes, 9(1990), 163.
(12) J.A.Duffy and M.D.Ingram : J. American. Chem. Soc., 93(1971),
(13) C.W.Toop and C.S.Samis : Trans. Met. Soc. AIME., 224(1962), 878.

(14) C.R.Masson : Proc. Roy. Soc., A287(1965), 201.
(15) M.Morishita, K.Koyama, K.Yamazoe, M.Morinaga and H.Adachi : J. Jpn. Inst. Met., 58(1994), 276.
(16) M.Morishita, K.Koyama, M.Morinaga and H.Adachi : J. Jpn. Inst. Met., 58(1994), 1156.
(17) M.Morishita, K.Koyama, M.Morinaga and H.Adachi : Mater. Trans. JIM., 36(1995), 44.
(18) D.E.Ellis and G.S.Painter : Phys. Rev., 21(1970), 2887.
(19) H.Adachi : *Ryosi Zairyo Kagaku Nyumon*, Tokyo, (1991), 26.
(20) T.Yokokawa : Tetsu to Hagane, 68(1982), 26.
(21) E.M.Levin and S.Block : J. American Ceramic Soc., 40(1957), 95.
(22) K.Nakajima : Tetsu to Hagane, 80(1994), 1
(23) K.Kowada, H.Adachi, M.Tatsumisago and T.Minami : J. Non-Cryt. Solids, 150(1992), 318.
(24) K.Kowada, H.Adachi and T.Minami : J. Ceramic Soc. Jpn., 101 (1993), 1330.
(25) K.Kowada, H.Adachi, M.Tatsumisago and T.Minami : J. Non-Cryt. Solids, 177(1994), 286.
(26) K.Kowada, H.Adachi, M.Tatsumisago and T.Minami : J. Non-Cryt. Solids, 192&193(1995), 316.

X-Ray Emission in Molecules

Takeshi Mukoyama,[a] **Kazuo Taniguchi**[b] and **Hirohiko Adachi**[c]

[a]Institute for Chemical Research, Kyoto University, Uji, Kyoto, 611 Japan
[b]Department of Solid-State Electronics, Osaka Electro-Communication University, Neyagawa, Osaka, 572 Japan
[c]Department of Materials Science and Engineering, Kyoto University, Yoshida, Kyoto, 606 Japan

Abstract

The K-shell x-ray emission rates of molecules have been calculated with the DV-Xα method. The x-ray transition probabilites are evaluated in the dipole approximation by the DV-integration method using molecular wave functions. The validity of the DV-integration method is tested. The calculated values in the relaxed-orbital approximation are compared with those of the frozen-orbital approximation and the transition-state method. The contributions from the interatomic transitions are estimated. The chemical effect on the $K\beta/K\alpha$ ratios for $3d$ elements is calculated and compared with the experimental data. The excitation mode dependence on the $K\beta/K\alpha$ ratios for $3d$ elements is discussed.

ADVANCES IN QUANTUM CHEMISTRY, VOLUME 29

0065-3276/97 $25.00

1. Introduction

For long time the x-ray emission spectroscopy has been widely used to investigate electronic structures of materials. The x-ray emission spectrum is conventionally considered as a characteristic quantity of elements and most theoretical calculations of x-ray transition probabilities have so far been made for free atoms.

On the other hand, the chemical effect on x-ray spectrum has been known since early days of the x-ray spectroscopy. Extensive studies on transition energies and line profiles have been reported [1], but quantitative investigations on x-ray emission rates and relative x-ray intensities for various compounds are rather scarce.

With development of solid-state detectors, relative x-ray intensities, such as, $K\beta/K\alpha$ ratios, have been measured and compiled in the tabulated or graphical forms [2–4]. However, these values are still considered as an atomic property and compared with the theoretical calculations for free atoms [5]. This is because for calculation of x-ray emission rates in molecules it is necessary to perform multi-center integration for molecular wave function. Such calculations are tedious and require a lot of computation time and large memory capacity.

The experimental study on the chemical effect has been greatly promoted by the recent development of high-energy-resolution x-ray spectrometers. On the other hand, theoretical calculations of x-ray emission rates for molecules become possible by the use of modern high-speed large-memory computers. The x-ray spectroscopy for molecules is now a powerful tool to study molecular electronic structures.

For theoretical calculations of molecular x-ray emission rates, it is usual to neglect the contributions from interatomic transitions, sometimes called *crossover transitions*, and to use the single-center approximation [6]. This approximation is useful and can often reproduces the experimental spectra quite well. Using a simple molecular orbital (MO) approach, Urch [7,8] showed the validity of the single-center approximation for metal K x-ray emission rates in MX_4 and MX_6 molecules. On the other hand, Adachi and Taniguchi

[9] found that contributions from the crossover transitions are appreciable in their MO calculations for $L_{2,3}$ x-ray intensities of S in Li_2SO_4.

X-ray emission rates in simple molecules have been extensively studied by Larkins and his group [10,11]. Larkins and Rowlands [12] made the MO calculations with the complete-neglect-of-differential-overlap (CNDO/2) method and pointed out that there are significant contributions of interatomic transitions to the C K x-ray emission rates in CO, HCN, and CO_2 molecules, but relative intensities are less sensitive to inclusion of crossover transitions. Applying the *ab initio* MO method to CO, they also examined [13] various factors influencing the molecular x-ray emission rate, such as choice of basis set, choice of length and velocity forms, electronic relaxation effect, and interatomic contributions. Phillips and Larkins extended their calculations to other simple molecules [14,15].

Recently we have estimated [16] the interatomic contributions to molecular x-ray emission rates by the use of the discrete-variational (DV) Xα MO method [17]. For CO molecule, the C K x-ray emission rate increases significantly by taking into account the interatomic transitions. On the other hand, the interatomic transitions play a minor role for K x-ray emission process in the compounds of $3d$ elements.

Experimental studies on the $K\beta/K\alpha$ x-ray intensity ratio for $3d$ elements have shown [18–23] that this ratio changes under influence of the chemical environment of the $3d$ atom. Brunner *et al.* [22] explained their experimental results due to the change in screening of $3p$ electrons by $3d$ valence electrons as well as the polarization effect. Band *et al.* [24] used the scattered-wave (SW) Xα MO method [25] and calculated the chemical effect on the $K\beta/K\alpha$ ratios for $3d$ elements. They performed the SW-Xα MO calculations for different chemical compounds of Cr and Mn. The spherically averaged self-consistent-field (SCF) potential and the total charge of valence electrons in the central atom, obtained by the MO calculations, were used to solve the Dirac equation for the central atom and the x-ray transition probabilities were calculated.

We have studied the chemical effect on the $K\beta/K\alpha$ x-ray inten-

sity ratios for several Cr and Mn compounds both theoretically and experimentally [26,27]. The K x-ray spectra were measured with a double crystal spectrometer and the theoretical calculations were performed with the DV-Xα MO method. The calculated results indicate that the $K\beta/K\alpha$ ratio depends on the crystal symmetry and the ratio for compound with the tetrahedral symmetry is larger than that with the octahedral symmetry. This tendency is qualitatively in agreement with the experimental data.

On the other hand, Hansen *et al.* [28] measured K-x-ray intensity ratios for various elements following K-capture decay of radioactive nuclides and pointed out that the $K\beta/K\alpha$ ratios by electron capture (EC) decay are considerably different from those by photon and electron impact ionization. Paić and Pečar [29] found that the $K\beta/K\alpha$ ratios for Ti, V, Cr, and Fe by EC are smaller by almost 10% than those by photoionization (PI), but no appreciable difference was observed for Cu and Zn. A similar excitation mode dependence was measured for Mn by Arndt *et al.* [30]. They stated that the reason for the difference is due to the excess $3d$ electron in EC and the large shakeoff probability in PI. Rao *et al.* [31] also observed smaller $K\beta/K\alpha$ intensity ratios by EC for Mn and Fe. Since no appreciable difference was found for high-Z elements, they concluded that the difference observed for $3d$ elements can be ascribed to the chemical effect. It is usual that the chemical forms of the samples for EC measurements are different from those for PI. In order to elucidate the excitation mode dependence on the $K\beta/K\alpha$ ratios in $3d$ elements, it is necessary to perform theoretical calculations which takes into account the chemical effect as well as the difference in the electron configurations.

In the present paper, we calculated the x-ray emission rates in molecules with the DV-Xα method. We examine several factors affecting on the x-ray emission rates, estimate the chemical effect on the $K\beta/K\alpha$ ratios for $3d$ transition elements, and discuss the effect of the excitation modes on the $K\beta/K\alpha$ ratios.

2. X-Ray Transition Probability

The MO calculations are made with the DV-Xα method, which has been described in detail elsewhere [17]. First the Hartree-Fock-Slater (HFS or Xα) calculations are performed for each constituent atom in the molecule and the atomic wave functions obtained in the numerical form are used as the basis functions for the MO calculation. The molecular wave function for the λ-th MO is expressed as

$$\psi_\lambda = \sum_i c_{i\lambda}\, \phi_i \tag{1}$$

where ϕ_i is the i-th atomic orbital as a basis function and $c_{i\lambda}$ is the eigenvector corresponding to the expansion coefficient for the i-th atomic orbital in the λ-th MO.

In the MO calculations, the matrix elements in the secular equation are evaluated numerically with the DV-integration method [32] and this equation is then diagonalized to solve the generalized eigenvalue problem giving the MO energy eigenvalues and eigenfunctions.

Within the framework of the dipole approximation, the x-ray emission rate in $\sec^{-1}$ is given by [33]

$$T = 0.8888 \times 10^9\, N_i\, E_X^3\, D_\lambda^2 \tag{2}$$

where N_i is the number of electron in the initial state, E_X is the x-ray transition energy in Rydberg, and D_λ is the dipole matrix element in atomic units.

For K-shell x-ray emission, the dipole matrix element from the λ-th MO is expressed as

$$D_\lambda = \sum_i c_{i\lambda} < \phi_K | \boldsymbol{r} | \psi_i > \tag{3}$$

where ϕ_K is the K-shell wave function and $\boldsymbol{r}$ is the position vector. In the DV method, the integration in Eq. (3) is carried out as the weighted sum of the integrand values at the discrete points according to a certain sampling function [32].

3. Calculations of X-Ray Emission Rates

In the calculations of x-ray emission rates in molecules with the DV-Xα method, we have used various approximations and numerical techniques. We examine several factors which influence the theoretical calculations of molecular x-ray emission rates, i.e. the accuracy of the DV integration, the electronic relaxation effect, and the contributions from the interatomic transitions. The examination of other factors, such as the choice of dipole operators, basis-set dependence, and the vibrational effect, has been reported by Larkins [10,11] with the *ab initio* method.

3.1. Validity of the DV-Integration Method

In the present work, the calculations of the dipole matrix element in the x-ray emission rate, Eq. (3), have been performed with the DV-integration method [32]. In this method, the integral is evaluated as the weighted sum of the integrand values at the discrete points distributed randomly according to an appropriate sampling function. The advantage of the DV method consists in the fact that we can avoid the difficulties encountered in multi-center integration. The validity of the DV-integration method has been tested by calculating the overlap integrals and dipole matrix elements for single free atoms [34].

For this purpose, the wave functions were obtained with the computer program for the DV-Xα method. Using these wave functions, the overlap integrals between two orbitals were evaluated with the DV-integration method. For the wave functions given in Eq. (1), the overlap integral can be expressed as

$$S_{\lambda\mu} = \sum_{i,j} c_{i\lambda}\, c_{j\mu} \; < \phi_j | \phi_i > \quad . \tag{4}$$

In the case of a single free atom, the molecular wave function reduces to the atomic wave function ($\lambda = i$, $\mu = j$) and $S_{\lambda\mu} = 1$ for $\lambda = \mu$ and 0 for $\lambda \neq \mu$.

The calculated results of the square of the overlap integral for Cl atom indicate that $|S_{\lambda\mu}|^2$ is equal to unity for $\lambda = \mu$ within the

Table 1: Comparison of squares of dipole matrix elements (a.u.) between the values obtained by the DV integration method and numerical integration of HS wave function.

	Cl ($\times 10^{-2}$)		Mn ($\times 10^{-3}$)	
	HS	DV	HS	DV
$2p \rightarrow 1s$	0.417	0.417	2.181	2.197
$2p \rightarrow 2s$	17.50	17.52	66.37	66.15
$3s \rightarrow 2p$	1.316	1.328	3.681	3.687
$3p \rightarrow 1s$	0.025	0.025	0.194	0.195
$3p \rightarrow 2s$	1.150	1.169	8.701	8.684

accuracy better than 10^{-3} and becomes less than 10^{-5} for $\lambda \neq \mu$ for all possible combinations of atomic orbitals [34]. From this fact, it can be said that the DV-integration method can well reproduce the orthonormality of the atomic wave functions.

In the next step, the dipole matrix element, Eq. (3), for Cl (Z =17) and Mn (Z = 25) atoms were calculated with the DV-integration method for all possible dipole transitions. The obtained results for the square of the matrix element are shown in Table 1. For comparison, the nonrelativistic atomic HFS calculations were carried out by the use of the computer code of Herman and Skillman (HS) [35] and the dipole matrix elements corresponding to Eq. (3) were evaluated by the conventional numerical integration method. The calculated values are also listed in Table 1 and compared with the DV values.

It should be noted that the exchange scaling parameter in the original HS code is set to be $\alpha = 1$. On the other hand, it is usual to adopt $\alpha = 0.7$ in the DV-Xα method. In addition, the Latter tail correction for the atomic potential [36] is included in the HS code. However, in order to compare with the DV value, we modified the HS code and the calculations were made with $\alpha = 0.7$ and without the Latter correction. Accordingly, the x-ray emission rates obtained from the HS values in Table 1 are different from the

tabulated values of Manson and Kennedy [37].

It is clear from the table that the numerical values obtained with the present method are in good agreement with those calculated with the direct numerical integration of the HS wave functions. This means that the DV-integration method is useful to calculate the transition matrix elements between two wave functions.

3.2 Electronic Relaxation Effect

The x-ray emission process in atoms and molecules is considered in three steps. In the first step ($t = -\infty$), all the electrons are in their lowest energy states, the ground state (GS). Then an inner-shell vacancy is created at $t = 0$ in the second step. This state can be called the initial state (Init). After a certain period between this step and the next step, the vacancy in the inner shell moves to an outer shell accompanying x-ray emission. In the final step, the vacancy is assumed to remain in the outer shell ($t = \infty$). Let us call this state the final state (Fin).

In the Xα method, the dipole matrix element is often calculated using the Slater's *transition state* (TS) concept [38]. The TS for x-ray emission corresponds to the state where the electron concerned with the transition stays half in the initial state and half in the final state. The electron configurations for the ground state, the initial state, the transition state, and the final state are shown in Fig. 1.

Most theoretical calculations of x-ray emission rates in atoms and molecules have been performed in the *frozen-orbital* (FR) approximation, where the same atomic or molecular potential is used before and after the transition. It is usual to use the ground state configuration for this purpose. This approximation is convenient because we need only one atomic or molecular calculations and the wave functions for the initial and final states are orthogonal. However, the presence of vacancy is not taken into consideration. On the other hand, we have shown that the TS method is useful to predict x-ray transition energies, but is not so good approximation to the absolute x-ray transition probabilities [39].

It is more realistic to calculate transition matrix elements be-

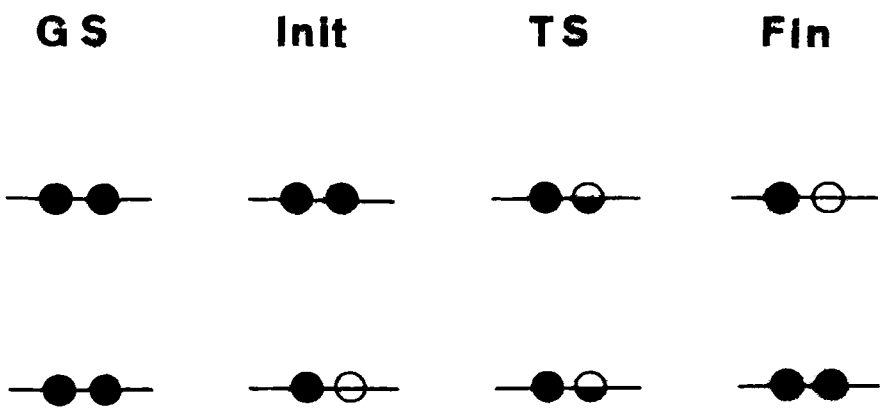

Figure 1: Electron configurations for the ground state (GS), initial state (Init), transition state (TS), and final state (Fin).

tween the initial and final states, taking into account the electron relaxation. In this case, called *relaxed-orbital* (RX) approximation, we must calculate wave functions separately for the initial state with an inner-shell vacancy and for the final sates with a vacancy in an outer shell. We have compared the K-x-ray emission rates of CO molecule for the FR approximation with GS, the TS method, and the RX approximation [40].

The x-ray emission rates with a $1s$ vacancy in O atom (1σ) were calculated with the DV-Xα method in the FR, TS, and RX approximations. The obtained results for all possible MO states by three approximations are listed in Table 2 and compared with each other. The x-ray transition energies were calculated with the TS method, because the energy eigenvalues in the Xα method do not correspond to the binding energy of the electron [38]. It can be seen that the FR gives the largest values for the transitions from 3σ and 4σ, while the RX values are largest for 1π and 5σ. The TS gives always the smallest transition probabilities.

In Table 3, the similar results for $1s$ vacancy in C (2σ) are given. In this case, the FR values are largest except for the $4\sigma \rightarrow$

Table 2: X-ray energies (eV) and emission rates (arbitrary units) for O $1s$ vacancy in CO.

		Emission rate		
Level	Energy	FR	TS	RX
3σ	512	30.63	22.09	26.60
4σ	529	174.9	144.6	168.7
1π	531	472.5	423.7	490.4
5σ	534	52.23	37.74	64.66

Table 3: X-ray energies (eV) and emission rates (arbitrary units) for C $1s$ vacancy in CO.

		Emission rate		
Level	Energy	FR	TS	RX
3σ	265	10.71	8.04	8.45
4σ	281	1.08	1.35	3.44
1π	283	52.69	48.11	44.03
5σ	287	51.30	31.26	39.37

Table 4: Comparison of relative K x-ray intensity ratios for oxygen atom in CO.

	DV-Xα^a			*Ab initio*^{b}		*Ab initio*^{c}		
Level	FR	TS	RX	FR^d	RX	FR	RX	Experiment^e
3σ	0.06	0.05	0.05	0.06	0.08	0.05	0.04	
4σ	0.37	0.34	0.34	0.37	0.51	0.42	0.20	0.38
1π	1.00	1.00	1.00	1.00	1.00	1.00	1.00	1.00
5σ	0.11	0.09	0.13	0.08	0.00	0.11	0.06	0.28

[a]Ref. 40.
[b]Ref. 41.
[c]Ref. 14.
[d]$1\sigma^{-1}$ state.
[e]Ref. 42.

2σ transition. The TS gives the smallest values except for the transition from 4σ. The RX value for 4σ is largest and others are between the FR and the TS values.

In order to compare with other theoretical calculations and the experimental data, the relative intensity ratios of x-ray emission rates with respect to the strongest component from the 1π orbital are estimated. The present results for O $1s$ vacancy (1σ) are listed in Table 4 and compared with the theoretical values of Phillips and Larkins [14] and of Ågren and Nordgren [41] and with the experimental data by Werme *et al.* [42]. Ågren and Nordgren [41] performed the *ab initio* calculations in the FR and the RX approximations, but their FR calculations were made for the state with the 1σ vacancy. Theoretical values of Phillips and Larkins [14] were also calculated in the *ab initio* method. It should be noted, however, that their RX calculations include the effect of exchange and overlap due to nonorthogonality of the initial and final wave functions. The similar comparison is made for the case of C $1s$ vacancy (2σ) in Table 5.

Table 5: Comparison of relative K x-ray intensity ratios for carbon atom in CO.

	DV-Xα^a			*Ab initio*^{b}		*Ab initio*^{c}		
Level	FR	TS	RX	FR^d	RX	FR	RX	Experiment^e
3σ	0.20	0.17	0.19	0.25	0.24	0.34	0.13	
4σ	0.02	0.03	0.08	0.04	0.03	0.10	0.00	
1π	1.00	1.00	1.00	1.00	1.00	1.00	1.00	1.00
5σ	0.97	0.65	0.89	0.91	0.84	1.11	0.91	0.59

[a]Ref. 40.
[b]Ref. 41.
[c]Ref. 14.
[d]$1\sigma^{-1}$ state.
[e]Ref. 42.

It can be seen from Tables 4 and 5 that, although the absolute x-ray emission rates depend on the approximations used, the relative intensity ratios are almost same for all theoretical calculations. The reason for the discrepancy between the theoretical and experimental values can be ascribed to the satellites due to multiple ionization which are included in the theoretical values [41].

It can be said that, when we are interested only in relative intensities for major transitions or shapes of x-ray spectra, all the theoretical models can give similar results.

3.3 Contributions from Interatomic Transitions

Most of old theoretical calculations for molecular x-ray emission rates have been performed in the single-center approximation and the contributions from the interatomic transitions have been neglected. On the other hand, Taniguchi and Adachi [9] and Larkins [10,11] pointed out that in some cases the contributions from the interatomic transitions are appreciable. In the present work, the

contributions of the interatomic transitions to the molecular x-ray emission rates have been estimated with the DV-Xα method.

The x-ray emission rate with the interatomic contributions is given by Eq. (2). On the other hand, the rate without the interatomic transitions can be obtained as follows. We calculate the x-ray emission rate by Eq. (2), but the summation over i in the dipole matrix element, Eq. (3), is restricted only for the atomic orbitals that belong to the same atom as the initial K-shell vacancy. This method may be different from the conventional single-center model, in which the square of D_λ is expressed as

$$D_\lambda^2 = \sum_j c_{j\lambda}^2 \mid < \phi_K | \boldsymbol{r} | \phi_j > \mid^2 , \tag{5}$$

where j denotes the atomic orbital in the same atom as ϕ_K.

The calculations were made for K-x-ray emission rates of C and O atoms in the CO molecule. The results with and without the interatomic transitions and the relative change in the emission rate due to interatomic transitions are listed in Table 6. In general, the K-x-ray emission rate increase by taking into account the existence of the interatomic transitions. Only one exceptional case is the $5\sigma \rightarrow 1\sigma$ transition for the K-shell vacancy in O atom. The decrease in this transition rate due to the two-center effect has already been pointed out by Rowlands and Larkins [13] in their CNDO/2 calculations.

The increase in the x-ray emission rates is significant for C K x rays. In this case, the single-center approximation is inadequate to predict the C K-x-ray emission process in CO. On the other hand, the interatomic transitions play less important role for O K-x-ray emission.

We have also studied the interatomic contributions to the K-x-ray emission rates for chemical compounds of $3d$ elements [16]. For the compounds with octahedral symmetry, such as $CrCl_3$ and $MnCl_2$, the interatomic transitions play a minor role. On the other hand, in the case of the compounds with tetrahedral symmetry, such as CrO_3 and $KMnO_4$, the interatomic transitions increase x-ray intensities of $4t_2$, $5t_2$, and $6t_2$ components of $3d$ transition metals. The $4t_2$ component corresponds to the $K\beta''$ peak and $6t_2$ to the $K\beta_{2,5}$

Table 6: K x-ray emission rates for carbon and oxygen of CO in the single-center approximation (I) and two-center calculation (II) (arbitrary units).

	C			O		
MO	I[a]	II[b]	Δ[c]	I	II	Δ
3σ	3.218	8.157	153.5	21.44	25.56	19.2
4σ	0.484	0.834	70.4	132.9	145.0	9.1
1π	33.04	40.86	23.6	390.8	394.5	3.3
5σ	31.83	38.54	21.2	43.47	43.14	−0.8
total	68.57	88.43	29.0	588.6	608.2	3.3

[a]Without interatomic contributions.
[b]With interatomic contributions.
[c]$\Delta = (\mathrm{II} - \mathrm{I}) \,/\, \mathrm{I} \times 100$.

peak, while the $5t_2$ component has not yet been observed experimentally. These components are generally very weak in comparison with the strong diagram lines. When we measure the $K\beta/K\alpha$ ratios for the chemical compounds of $3d$ elements, the contributions from the interatomic transitions are less than 0.3% and almost negligible.

4. Chemical Effect on the $K\beta/K\alpha$ Ratios of $3d$ Elements

The chemical effect on the $K\beta/K\alpha$ x-ray intensity ratios has been studied experimentally for various chemical compounds of $3d$ transition metals [18–23,26,27]. We choose several simple chemical compounds of Cr and Mn and calculate the $K\beta/K\alpha$ ratios with the DV-Xα method. For simplicity, we assume that all compounds are expressed as clusters with the tetrahedral (Td) or octahedral (Oh) symmetry, in which the central metal atom is surrounded by four or six ligand atoms, respectively. The compounds and clusters used

Table 7: Compounds and clusters used in the calculations.

Compound	Symmetry	Cluster	Bond length (Å)
K_2CrO_4	Td	CrO_4^{2-}	1.65
$K_2Cr_2O_7$	Td	CrO_4^{2-}	1.70
CrO_3	Td	CrO_4^{2-}	1.80
CrO_2	Oh	CrO_6^{8-}	1.90
Cr_2O_3	Oh	CrO_6^{9-}	2.00
$CrCl_3 \cdot 6H_2O$	Oh	$CrCl_6^{3-}$	2.38
$CrCl_2$	Oh	$CrCl_6^{4-}$	2.55
$KMnO_4$	Td	MnO_4^-	1.59
K_2MnO_4	Td	MnO_4^{2-}	1.81
MnO_2	Oh	MnO_6^{8-}	1.89
MnO	Oh	MnO_6^{10-}	2.22
$MnCl_2 \cdot 2H_2O$	Oh	$MnCl_6^{4-}$	2.51
MnS	Oh	MnS^{10-}	2.61

in the calculations are listed in Table 7 together with the crystal symmetry and the bond length between the metal and ligand atoms.

For metal atoms, the $1s$–$4p$ atomic orbitals are used as the basis functions, while the $1s$–$2p$ orbitals are used for oxygen and the $1s$–$3p$ orbitals for sulfur and chlorine. In all cases, the Slater's statistical exchange parameter was chosen to be $\alpha = 0.7$. The calculations were made for the FR approximation with the GS. The x-ray transition energies were obtained with the TS method.

In Fig. 2(a), the experimental $K\beta$ spectrum of Cr in K_2CrO_4 [26] is compared with the calculated one. The energy scale is normalized to the experimental data at the $K\beta_{1,3}$ line. The theoretical shape is assumed to be a Lorentzian function. There are two satellite lines in the high-energy side of the $K\beta_{1,3}$ diagram line, which originates from the $3p \rightarrow 1s$ transition in Cr atom. These satellite lines can be ascribed to the transitions from the MO levels. The $K\beta''$ line corresponds to the $4t_2 \rightarrow 1s$ transition and the $K\beta_{2,5}$ line

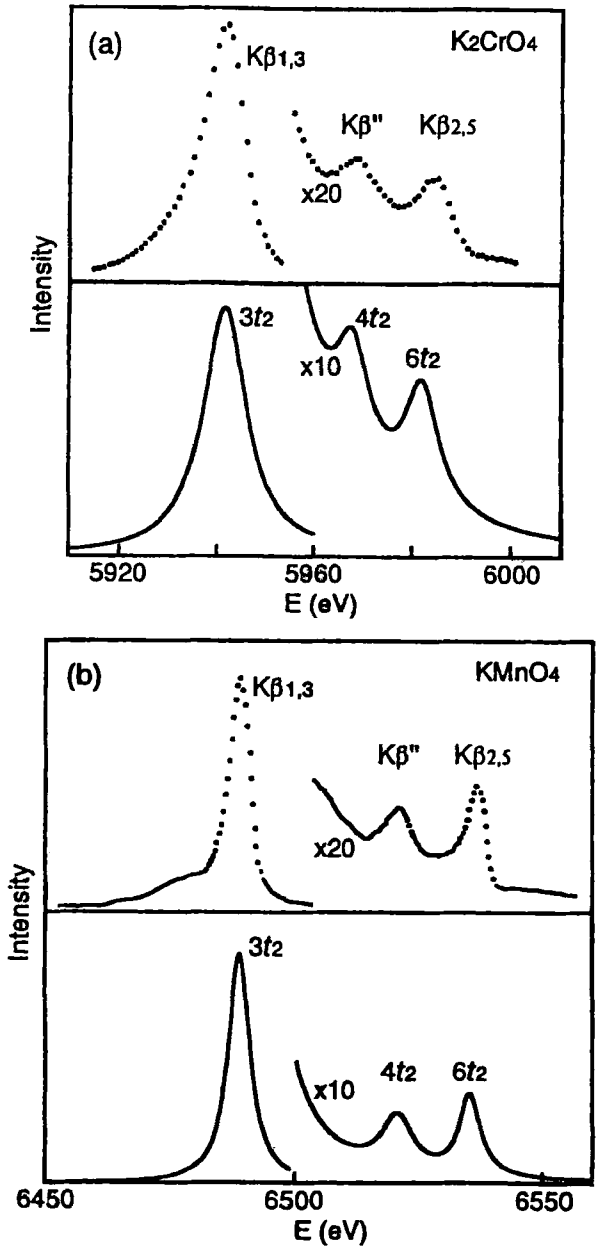

Figure 2: The experimental and calculated $K\beta$ x-ray emission spectra of Cr in K_2CrO_4 and Mn in $KMnO_4$. The assignments of the molecular states to the measured spectra are shown. The energy scale is adjusted to the experimental data at the $K\beta_{1,3}$ line.

is due to the transition from the $6t_2$ orbital. This assignment is the same as that proposed by Best [43]. There is another line from the $5t_2$ orbital in the theoretical calculation, but this line is too weak to be observed experimentally. Figure 2(b) shows the similar experimental and theoretical spectra for Mn in $KMnO_4$ [26]. It can be seen from the figure that the experimental spectra are in good agreement with the theoretical ones.

In the present work, we used the FR approximation with the GS, where the exchange and overlap effect is not taken into account. The $K\beta/K\alpha$ ratio calculated for a single atom is 0.1144 for Cr and 0.1184 for Mn. These values are slightly smaller than the HS values of Manson and Kennedy [37] obtained with the model similar to the present one. This difference is attributed to the difference in the choice of the Slater's statistical scaling parameter. In the present work, we used $\alpha = 0.7$, while Manson and Kennedy used the original HS wave functions with $\alpha = 1.0$.

On the other hand, according to the relativistic calculations by Scofield [5] with exchange and overlap effect, the $K\beta/K\alpha$ ratio for Cr atom is 0.1337 and for Mn 0.1385. His values are considerably larger than the present ones and are in good agreement with many experimental data for atoms. Scofield pointed out [5] that neglection of the exchange and overlap effect underestimates the $K\beta/K\alpha$ ratios for $3d$ elements. Considering this fact, it is not favorable to compare the present theoretical values for chemical compounds directly with the experimental results.

In order to compare with the measured values, we calculated the relative $K\beta/K\alpha$ ratios with respect to a standard compound. As for the standard, we chose K_2CrO_4 for Cr and $KMnO_4$ for Mn. The theoretical values for other compounds were divided by the theoretical value for the standard compound, while the experimental values were also expressed as the ratio to the measured value for the corresponding standard compound.

In Table 8, the calculated relative $K\beta/K\alpha$ ratios are compared with the relative measured values. For comparison, the theoretical values calculated by Band *et al.* with the MS-Xα method [24] are also shown.

Table 8: Comparison of calculated and measured relative $K\beta/K\alpha$ ratios.

	Theory		Experiment	
Compound	DV-Xα[a]	MS-Xα[b]	MTA[a]	
Cr (Relative to K_2CrO_4)				
$K_2Cr_2O_7$	1.020		1.039	1.022±0.021[c]
CrO_3	0.980		1.040	1.029±0.021[c]
CrO_2	0.949			
Cr_2O_3	0.952		0.975	0.978±0.020[c]
$CrCl_3 \cdot 6H_2O$	0.942	0.964	0.994	0.978±0.020[c]
$CrCl_2$	0.934			
Mn (Relative to $KMnO_4$)				
K_2MnO_4	0.978			0.933±0.021[c]
MnO_2	0.960		0.973	1.007±0.021[c]
MnO	0.944			
$MnCl_2 \cdot 2H_2O$	0.937			0.971±0.020[c]
MnS	0.935	0.966		0.950±0.007[d]
				0.953±0.003[e]

[a]Ref. 26.
[b]Ref. 24.
[c]Ref. 18.
[d]PIXE, Ref. 22.
[e]Fluorescence, Ref. 22.

The calculated results are qualitatively in agreement with the experimental data, except for CrO_3. The experimental value for CrO_3 is larger than unity, while the calculated one is smaller. In the case of MnO_2, the theoretical value agrees with the measured value of Mukoyama *et al.* [26], but smaller than the experimental value of Tamaki *et al.* [18]. It should be noted that the experimental studies of Tamaki *et al.* [18] and Brunner *et al.* [22] were performed with poor-energy-resolution Si(Li) detectors. On the other hand, a double crystal spectrometer with high energy resolution was used by Mukoyama *et al.* [26]. In the latter experiment, the $K\beta''$ and $K\beta_{2,5}$ peaks were observed separately from the $K\beta_{1,3}$ peak, as shown in Fig. 2. The MS-Xα values of Band *et al.* [24] are larger than the present results, but only two values are available for the chemical compounds listed in Table 8.

From Tables 7 and 8, it is clear that the $K\beta/K\alpha$ ratios of the compounds with the Td symmetry are in general larger than those with the Oh symmetry. This trend can be explained in the following reason. As can be seen in Fig. 2, for the compounds with the Td symmetry the satellite lines due to $4t_2$ and $6t_2$ orbitals have considerable contributions to the $K\beta$ x-ray intensity, while in the Oh symmetry the intensity of the corresponding satellite line from the $5t_{1u}$ orbital in oxides and from the $8t_{1u}$ orbital in sulfides and chlorides is weak.

The results in Table 8 indicate that the chemical effect on the $K\beta/K\alpha$ ratios is in order of several %. This means that the experimental studies on this effect should be made very carefully. In all experiments except for two, Paci-Mazzilli and Urch [20] and Mukoyama *et al.* [26], Si(Li) detectors were used to observe x-ray spectra. Owing to poor energy resolution of the solid-state detectors, $K\beta$ satellite peaks cannot be resolved from the $K\beta_{1,3}$ diagram line and the presence of these peaks should be taken into account in the data analysis of the experimental spectra. However, a single Gaussian shape has often been used for the $K\beta$ composite peak in most experiments. In order to compare with the present theoretical values, it is hoped that more systematic studies for the chemical effect on the $K\beta/K\alpha$ ratios for $3d$ elements be performed with high

Table 9: $K\beta/K\alpha$ ratios of Cr as a function of the number of $3d$ electrons.

	Number of $3d$ electrons	$K\beta/K\alpha$ ratio
Cr	5	0.1144
Cr^{+1}	4	0.1164
Cr^{+2}	3	0.1203
Cr^{+3}	2	0.1256
Cr^{+4}	1	0.1303
Cr^{+5}	0	0.1398

energy resolution spectrometers, which can observe the $K\beta''$ and $K\beta_{2,5}$ lines separately.

5. Effect of Excitation Modes on $K\beta/K\alpha$ Ratios

For $3d$ elements, it was experimentally observed [28–31] that the $K\beta/K\alpha$ x-ray intensity ratios by EC are systematically smaller than those by PI. The difference amounts to almost 10% at the largest case. The excitation mode dependence has been explained due to the excess $3d$ electron in EC and larger shakeoff probability in PI [30]. This conclusion was drawn based on the single-atom picture.

In order to examine the effect of the number of $3d$ electrons on the x-ray intensity ratios, we have calculated the $K\beta/K\alpha$ ratios for Cr atom as a function of the number of $3d$ electrons with the HS code. The calculations were made by removing the $3d$ electron one by one from the valence electron configuration of the Cr atom in the ground state, $(3d)^5(4s)^1$. The results are given in Table 9 and it is found that the decrease in the number of $3d$ electrons increases the $K\beta/K\alpha$ ratio. This fact indicates that the $K\beta/K\alpha$ ratio by EC is smaller than that by PI if the parent Mn atom in EC and the

Cr atom in PI are a single free atom.

However, the atom of the $3d$ elements in the radioactive sources and the targets used for PI is usually not a free atom, but in the chemical compounds. As has been shown in the previous section, the $K\beta/K\alpha$ ratios for $3d$ elements depend on the chemical environment of the x-ray emitting atom. In K-x-ray emission following EC, it can be assumed that the chemical form of the parent atom is preserved until x rays are emitted. In this case, the daughter atom is considered as an impurity atom embedded in the chemical compound of the parent atom and its chemical state is different from the state of the ordinary chemical compound of the parent atom as well as from that of the daughter atom. In addition, since the daughter atom is produced by EC of the parent atom, there is an extra electron in the valence shell of the daughter atom in comparison with the ordinary neutral atom. These facts suggest that the $K\beta/K\alpha$ ratios by EC should be estimated by taking into account both the chemical environment of the daughter atom and the presence of an additional electron.

In the present work, we calculate the $K\beta/K\alpha$ ratio by EC for $3d$ elements in different chemical compounds and compare them with the values by PI in the corresponding chemical compounds. In the chemical effect, the $K\beta/K\alpha$ ratios depend on the symmetric property of the compounds. Taking into account this fact, we choose the V and Cr compounds with the Td and Oh symmetry and calculate the $K\beta/K\alpha$ ratios by EC and PI. In the case of EC, the chemical compounds of the parent atom are used, but the atomic number of the central atom is decreased by one. The electron configuration of the parent atom is used for the daughter atom and the bond length is assumed not to change during EC.

For Cr K x rays after ^{54}Mn decay in $K_2\,^{54}MnO_4$, we used the cluster $Cr[MnO_4^{2-}]$, where the symbol $Cr[MnO_4^{2-}]$ means that the central Mn atom in MnO_4^{2-} cluster is replaced by Cr. The corresponding chemical compound of Cr for PI is K_2CrO_4 and the $K\beta/K\alpha$ ratio is calculated with the cluster CrO_4^{2-}. The pairs of the chemical compounds and clusters used for the calculations of the $K\beta/K\alpha$ ratios by EC and by PI are shown in Table 10. All the

Table 10: Pairs of the compounds and clusters used in the calculations.

Compound	Symmetry	Cluster	Bond length (Å)
$K_2{}^{54}MnO_4$	Td	$Cr[MnO_4^{2-}]$	1.81
K_2CrO_4	Td	CrO_4^{2-}	1.65
$K_2{}^{51}CrO_4$	Td	$V[CrO_4^{2-}]$	1.65
Na_3VO_4	Td	VO_4^{3-}	1.74
$^{54}MnO_2$	Oh	$Cr[MnO_6^{8-}]$	1.89
CrO_2	Oh	CrO_6^{8-}	1.90
$^{51}CrO_2$	Oh	$V[CrO_6^{8-}]$	1.90
VO_2	Oh	VO_6^{8-}	1.93
$^{54}MnCl_2$	Oh	$Cr[MnCl_6^{4-}]$	2.51
$CrCl_2$	Oh	$CrCl_6^{4-}$	2.55
$^{51}CrCl_3$	Oh	$V[CrCl_6^{3-}]$	2.38
VCl_3	Oh	VCl_6^{3-}	2.45

Table 11: Calculated results for $K\beta/K\alpha$ ratios.

EC	$K\beta/K\alpha$	PI	$K\beta/K\alpha$
$V[CrO_4^{2-}]$	0.1210	VO_4^{3-}	0.1201
$V[CrO_6^{8-}]$	0.1149	VO_6^{8-}	0.1154
$V[CrCl_6^{3-}]$	0.1125	VCl_6^{3-}	0.1133
$Cr[MnO_4^{2-}]$	0.1201	CrO_4^{2-}	0.1227
$Cr[MnO_6^{8-}]$	0.1171	CrO_6^{8-}	0.1172
$Cr[MnCl_6^{4-}]$	0.1127	$CrCl_6^{4-}$	0.1146

calculations were made in the manner similar to the case for the chemical effect in the previous section.

The calculated values of the $K\beta/K\alpha$ ratios for EC and PI are listed in Table 11. It is clear that the $K\beta/K\alpha$ ratio by EC is smaller than that by PI for all chemical compounds, except for the case of the $V[CrO_4^{2-}]$ and VO_4^{3-} pair. This is consistent with the experimental results of Hansen *et al.* [28], Paić and Pečar [29], Arndt *et al.* [30], and Rao *et al.* [31]. For only one exceptional case of $V[CrO_4^{2-}]$, it is interesting to note that its equivalent cluster for PI is not VO_4^{3-}, but VO_4^{2-}, whose crystal structure is not found in literature. The formal oxidation number of V atom in the former cluster is 5, while that in the latter is 6. It is pointed out [23] that the $K\beta/K\alpha$ ratio for the compounds of $3d$ elements increases with the formal oxidation number. From these facts it is expected that the $K\beta/K\alpha$ ratio for V in VO_4^{3-} is smaller than that in VO_4^{2-} and also in $V[CrO_4^{2-}]$.

As has been described above, the direct comparison of the calculated results with the experimental values is not favorable because the exchange and overlap effect is neglected in the present calculations. In order to compare with the experimental data, we calculated the theoretical $K\beta/K\alpha$ ratio by EC relative to that by PI, $(K\beta/K\alpha)_{EC}/(K\beta/K\alpha)_{PI}$, for different chemical compounds. The obtained results are listed in Table 12. The value for the $K_2{}^{51}CrO_4$

Table 12: Comparison of calculated and measured relative ratios, $(K\beta/K\alpha)_{EC}/(K\beta/K\alpha)_{PI}$.

Element	Compound	Calculated	Measured	Reference
V	VO_2	0.996		
	VCl_3	0.993		
	not specified		0.903 ± 0.020	29
Cr	K_2CrO_4	0.979		
	CrO_2	0.999		
	$CrCl_2$	0.983		
	not specified		0.948 ± 0.021	29

and Na_3VO_4 pair is not included in the table because of the difference in the formal oxidation number.

The relative $K\beta/K\alpha$ ratios, $(K\beta/K\alpha)_{EC}/(K\beta/K\alpha)_{PI}$, are less than unity for all chemical compounds in the table. It can be said from the table that the $K\beta/K\alpha$ ratios depend on the excitation modes. However, these relative values are very close to unity and the difference is less than a few %. This fact indicates that when the $K\beta/K\alpha$ ratios by EC and by PI are measured in the similar chemical states, it is very difficult to observe the excitation mode dependence.

In Table 12, the experimental results of Paić and Pečar [29] are also listed for comparison. They observed almost 10% decrease for V and about 5% decrease for Cr. These results are much larger than the present theoretical values. Unfortunately there is no description about the chemical forms of the samples they used. It is possible that the chemical forms of their radioactive sources are different from those of the targets for PI. If the chemical forms of the samples are different, the relative ratios become a sum of two effects, the chemical effect and the effect of excitation modes, and can be larger values than those for the latter effect alone. For example, if we choose the smallest value for EC and the largest value for PI from

Table 12, the relative ratio is 0.937 for V and 0.917 for Cr. These values are in better agreement with the values of Paić and Pečar. From these facts, it can be said that the experimental results of Paić and Pečar be ascribed to the sum of the chemical effect and the effect of the excitation modes.

Arndt *et al.* [30] proposed another reason for smaller $K\beta/K\alpha$ ratios by EC, i.e. larger shakeoff probability in PI. They demonstrated that if the number of $3d$ electrons in PI is assumed to be by two less than that in EC, the experimental results of Paić and Pečar and their own data for Mn can be explained. Smaller shake probabilities for EC than for PI have already been pointed out by Crasemann *et al.* [44]. It is important to compare the effect of the shake process on the $K\beta/K\alpha$ ratios by EC and by PI for V and Cr atoms.

When the nuclear charge changes due to radioactive decay and/or an inner-shell vacancy is produced, the bound electrons in the same atom or molecule experience the sudden change in the central potential and have a small but finite probability to be excited to an unoccupied bound state (shakeup) or ejected to the continuum (shakeoff). We calculated the shakeup-plus-shakeoff probabilities accompanying PI and EC using the method of Carlson and Nestor [45].

According to the sudden approximation, the shakeup-plus-shake-off probability for an atomic electron with the principal quantum number n and orbital angular momentum quantum number l is given by [45]

$$P_{nl} = 1 - \left[\left|\int \psi'^{*}_{nl}\psi_{nl}\, d\tau\right|^2\right]^N - P_F \qquad (6)$$

where ψ_{nl} represents the electron wave function of the orbital nl in the initial atom in the ground state, ψ'_{nl} is that in the daughter atom with an inner-shell vacancy, and N is the number of electrons in the nl orbital. The quantity P_F represents the probability for the transition to occupied bound states, which is forbidden by the Pauli principle. When the principal quantum number of the highest

Table 13: Shakeup-plus-shakeoff probabilities for K-shell photoionization and K-electron capture.

	V		Cr	
Shell	PI	EC	PI	EC
$1s$	$4.91(-5)^a$	$5.15(-4)$	$4.55(-5)$	$4.70(-4)$
$2s$	$1.59(-3)$	$1.13(-3)$	$1.52(-3)$	$1.03(-3)$
$2p$	$8.16(-3)$	$1.61(-4)$	$7.51(-3)$	$1.50(-4)$
$3s$	$6.79(-3)$	$1.16(-3)$	$6.59(-3)$	$9.54(-4)$
$3p$	$5.43(-2)$	$1.10(-4)$	$4.15(-2)$	$9.81(-5)$
$3d$	$8.45(-2)$	$5.17(-4)$	$1.49(-1)$	$3.75(-4)$
$4s$	$1.24(-1)$	$7.87(-4)$	$7.86(-2)$	$9.44(-4)$

$^a 4.91(-5)$ means 4.91×10^{-5}.

occupied state is x, this probability is written by

$$P_F = \sum_{n'=1}^{x} \frac{NN'}{2(2l+1)} \left| \int \psi'^{*}_{n'l} \psi_{nl} \, d\tau \right|^2 \tag{7}$$

where $n \neq n'$ and N' is the number of electrons in the $n'l$ orbital.

In the case of PI, the calculations were made with the HS wave functions in the manner similar to that of Mukoyama and Taniguchi [46]. On the other hand, for EC the change in the nuclear charge was taken into account in addition to the creation of a K-shell vacancy. In this case, the parent atom, i.e. Cr for V and Mn for Cr, was used as the initial state. The valence electron configurations of the ground state for V, Cr, and Mn were taken to be $(3d)^3(4s)^2$, $(3d)^5(4s)^1$, $(3d)^5(4s)^2$, respectively.

The calculated shakeup-plus-shakeoff probabilities for V and Cr following PI and EC are listed in Table 13. It is clear that the probabilities for EC are negligibly small and those for PI are about 5% for $3p$ electrons and about 10% for $3d$ electrons. Using the values of Table 13, we obtained the effective numbers of $3p$, $3d$, and $4s$ electrons after EC and PI and calculated the $K\beta/K\alpha$ ratios for atoms. There is no influence of the shake process on the $K\beta/K\alpha$

ratios by EC. On the other hand, the increase in the ratios due to the shake process for PI is less than 0.5% for V and less than 0.4% for Cr. This fact shows that the shake process plays a minor role in the excitation mode dependence of the $K\beta/K\alpha$ ratios for $3d$ elements. The dominant factor for the effect of excitation modes can be ascribed to the sum of the effect of the excess $3d$ electrons in EC and the effect of the difference in the chemical environments.

It should be noted, however, that in actual situations the final states of the shakeup process are molecular Rydberg states and should be described by the MO wave functions. We estimated the contributions from the shakeup probabilities for atoms accompanying K-shell PI to the total (shakeup-plus-shakeoff) probabilities. The shakeup probabilities were calculated with the HS wave functions as the overlap integrals by the method used in our previous work [47]. The shakeup probabilities in PI were found to be about 30~40% of the total probabilities for $3p$ electrons and about 40~50% for $3d$ electrons. These large shakeup probabilities suggest that the chemical effect on the shakeup process would be large if the shakeup probabilities are calculated with the MO wave functions and the contributions of the shake process in PI to the $K\beta/K\alpha$ ratios for $3d$ elements would be appreciable.

6. Summary

The main difficulty in MO calculations consists in evaluation of the multi-center integrals. The DV-integration method is one of the powerful methods to avoid such difficulty and has been successfully used in the MO method. When this technique is applied to the calculations of the transition matrix elements, it makes the evaluations of x-ray emission rates in complex molecules easier.

In the present work, the x-ray emission rates in molecules have been calculated with the DV-Xα MO method. The dipole matrix elements for x-ray emission are evaluated by the use of the DV-integration method. The validity of this procedure was tested and the DV-integration method was found to be useful to calculate the dipole matrix elements in x-ray emission. Comparison of the FR,

TS, and RX methods for x-ray transition probabilities was made and it is demonstrated that relative intensity ratios and shapes of x-ray emission spectra are not so sensitive to the method used. The contributions of the interatomic transitions was estimated for CO and compounds of $3d$ transition metals. For C K-x-ray emission rates in CO the multi-center effect is found to be important, but in the case of the $K\beta/K\alpha$ ratios for the $3d$ transition elements the interatomic transitions are almost negligible.

The chemical effect on the $K\beta/K\alpha$ ratios for $3d$ elements have been calculated for compounds with Td and Oh symmetry and are in qualitative agreement with the experimental data. It is found that the ratios for compounds with Td symmetry are larger than those with Oh symmetry. The excitation mode dependence on the $K\beta/K\alpha$ ratios for $3d$ elements was studied. For the same chemical compounds the $K\beta/K\alpha$ ratios by EC are smaller than those by PI due to the excess $3d$ electron in EC, but the difference is too small to explain the experimental results. It was pointed out that the large experimental values may be due to the sum of the effect of the excess $3d$ electron and the chemical effect. The larger shake process in PI plays a minor role for the excitation mode dependence.

From these studies, it can be concluded that the DV-Xα method is quite efficient to calculate x-ray emission rates in molecules.

References

[1] A. Meisel, G. Leonhardt, and R. Szargan, *Röntgenspektren und chemische Bindung* (Geest & Portig, Leipzig, 1977); *X-Ray Spectra and Chemical Binding* (Springer, Berlin, 1984).

[2] S. I. Salem, in *Proc. of the International Conference on Inner Shell Ionization Phenomena and Future Applications*, ed. by R. W. Fink, S. T. Manson, J. M. Palms, and P. V. Rao (USAEC, Oak Ridge, Tenn., 1973), pp. 285–316.

[3] S. I. Salem, S. L. Panossian, and R. A. Krause, At. Data Nucl. Data Tables **14**, 92 (1974).

[4] D. Berényi, Bull. Inst. Chem. Res., Kyoto Univ. **57**, 139 (1979).

[5] J. H. Scofield, Phys. Rev. A **9**, 1041 (1976).

[6] R. Manne, J. Chem. Phys. **52**, 5733 (1970).

[7] D. S. Urch, J. Phys. C **3**, 1271 (1970).

[8] D. S. Urch, in *Electron Spectroscopy: Theory, Techniques, and Applications*, Vol. 3, ed. by C. R. Brundle and A. D. Baker (Academic, New York, 1979), pp. 1 – 39.

[9] H. Adachi and K. Taniguchi, J. Phys. Soc. Jpn **49**, 1944 (1980).

[10] F. P. Larkins, in *X-Ray Spectroscopy in Atomic and Solid State Physics*, ed. by J. G. Ferreira and M. T. Ramos (Plenum, New York, 1988), pp. 201–213.

[11] F. P. Larkins, in *X-Ray and Inner-Shell Processes, Knoxville, TN, 1990* ed. by T. A. Carlson, M. O. Krause, and S. T. Manson (AIP, New York, 1990), pp. 817–832.

[12] F. P. Larkins and T. W. Rowlands, J. Phys. B **19**, 591 (1986).

[13] T. W. Rowlands and F. P. Larkins, Theor. Chim. Acta **69**, 525 (1986).

[14] R. A. Phillips and F. Larkins, Aust. J. Phys. **39**, 717 (1986).

[15] R. A. Phillips and F. Larkins, J. Phys. B **21**, 277 (1988).

[16] T. Mukoyama, K. Taniguchi, and H. Adachi, Phys. Rev. B **41**, 8118 (1990).

[17] H. Adachi, M. Tsukada, and C. Satoko, J. Phys. Soc. Jpn **45**, 875 (1978).

[18] Y. Tamaki, T. Omori, and T. Shiokawa, Radioanal. Lett. **20**, 255 (1975); *ibid.* **37**, 39 (1979); Jpn J. Appl. Phys. **17**, S245 (1978).

[19] E. Lazzarini, A. L. Lazzarini-Fantola, and M. Mandelli Betoni, Radiochim. Acta **25**, 81 (1978).

[20] B. Paci-Mazzilli and D. S. Urch, in *Inner Shell and X-Ray Physics of Atoms and Solids*, ed. by D. J. Fabian, H. Kleinpoppen, and L. M. Watson, (Plenum, New York, 1981), pp. 741–743.

[21] K. E. Collins, C. H. Collins, and C. H. Heitz, Radiochim. Acta **28**, 7 (1981).

[22] G. Brunner, M. Nagel, E. Hartmann, and E. Arndt, J. Phys. B **15**, 4517 (1982).

[23] Y. Tamaki, X-Ray Spectrometry **24**, 235 (1995).

[24] I. M. Band, A. P. Kovtun, M. A. Listengarten, and M. B. Trghaskovskaya, J. Electron Spectrosc. Relat. Phenom. **36**, 59 (1985).

[25] K. H. Johnson, Adv. Quantum Chem. **7**, 143 (1973).

[26] T. Mukoyama, K. Taniguchi, and H. Adachi, Phys. Rev. B **34**, 3710 (1986).

[27] K. Taniguchi, T. Mukoyama, and H. Adachi, J. Phys. (Paris) **48**, C9-77 (1987).

[28] J. S. Hansen, H. U. Freund, and R. W. Fink, Nucl. Phys. A **142**, 604 (1970).

[29] G. Paić and V. Pečar, Phys. Rev. A **14**, 2190 (1976).

[30] E. Arndt, G. Brunner, and E. Hartmann, in *Proceedings of the International Seminar on High-Energy Ion-Atom Collisions*, ed. by D. Berényi and G. Hock (Akadémiai Kiadó, Budapest, 1982), pp. 253 – 256; J. Phys. B **15**, L887 (1982).

[31] N. V. Rao, S. B. Reddy, and D. L. Sastry, Nuovo Cimento **97A**, 1 (1987).

[32] F. W. Averill and D. E. Ellis, J. Chem. Phys. **59**, 6412 (1973).

[33] H. A. Bethe and E. E. Salpeter, *Quantum Mechanics of One- and Two-Electron Systems* (Springer, Berlin, 1957), pp. 248–269.

[34] T. Mukoyama, K. Taniguchi, and H. Adachi, Bull. Inst. Chem. Res., Kyoto Univ. **62**, 13 (1984).

[35] F. Herman and S. Skillman, *Atomic Structure Calculations* (Prentice-Hall, Englewood Cliffs, N.J., 1963).

[36] R. Latter, Phys. Rev. **99**, 510 (1955).

[37] S. T. Manson and D. J. Kennedy, At. Data Nucl. Data Tables **14**, 111 (1974).

[38] J. C. Slater, *Quantum Theory of Molecules and Solids*, Vol. 4 (McGraw-Hill, New York, 1974).

[39] T. Mukoyama and H. Adachi, Bull. Inst. Chem. Res., Kyoto Univ. **65**, 23 (1987).

[40] T. Mukoyama, Bull. Soc. Discrete Variational Xα **9**, No. 1 (1996), in press.

[41] H. Ågren and J. Nordgren, Theor. Chim. Acta **58**, 111 (1981).

[42] L. O. Werme, J. Nordgren, H. Ågren, C. Nordling, and K. Siegbahn, Z. Phys. **A272**, 131 (1975).

[43] P. E. Best, J. Chem. Phys. **44**, 3248 (1966).

[44] B. Crasemann, M. H. Chen, J. P. Briand, P. Chevallier, A. Chetioui, and M. Tavernier, Phys. Rev. C **19**, 1042 (1979).

[45] T. A. Carlson and C. W. Nestor, Phys. Rev. A **8**, 2887 (1973).

[46] T. Mukoyama and K. Taniguchi, Phys. Rev. A **36**, 693 (1987).

[47] T. Mukoyama and K. Taniguchi, Bull. Inst. Chem. Res., Kyoto Univ. **70**, 1 (1992).

DV-$X\alpha$ Calculation of X-Ray Emission Spectra

Jun Kawai

Department of Materials Science and Engineering, Kyoto University, Sakyo-ku, Kyoto 606-01, Japan

Abstract It is demonstrated that the profile changes of x-ray emission spectra of various molecules and solids are successfully reproduced by the local and partial electron density of states calculated by the DV-$X\alpha$ molecular orbital method. Some successful examples of the materials characterization by way of comparing the measured x-ray spectra and the DV-$X\alpha$ calculations are also demonstrated.

1. Introduction

X-ray emission spectra of solids and molecules are methods of measuring electronic structure of matter [1-5]. The x-ray emission spectra reflect the occupied electronic structure as shown in Fig. 1, while the x-ray absorption spectra reflect the unoccupied molecular orbitals (MO). These x-ray spectra represent local (L) and partial (P) electron density of states (DOS) because of the electric dipole selection rule, and thus the x-ray spectroscopy is a powerful tool to study the electronic structure of matter. The development of

ADVANCES IN QUANTUM CHEMISTRY, VOLUME 29

0065-3276/97 $25.00

synchrotron radiation facilities makes it possible to measure the x-ray emission spectra more easily with using a resonance condition [6, 7], and we can get information on the detailed electronic structure of matter using the characteristics of synchrotron radiation such as resonance and polarization.

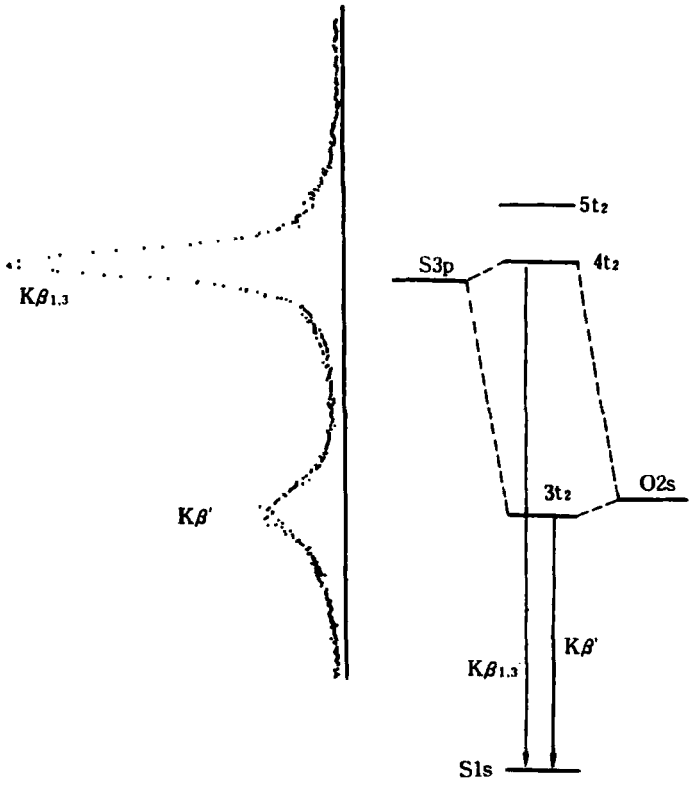

Fig. 1 Measured sulfur $K\beta$ (K-$M_{2,3}$) x-ray emission spectrum of Na_2SO_4 and the assignment of x-ray transitions for the SO_4^{2-} cluster. The x-ray intensity reflects the S $3p$ atomic orbital component in the molecular orbitals. (Taken and modified from Kawai *et al.* [1].)

The calculation of x-ray emission spectra of molecules or solids are one of the most successful applications of the discrete variational (DV) Hartree-Fock-Slater ($X\alpha$) MO method using cluster approximation [8-10], which was originally coded by Ellis and his coworkers [11-14] based on Slater's $X\alpha$ exchange potential [15]. The DV-$X\alpha$ method has several advantages for the calculation of x-ray transition process as follows.

Firstly, it can calculate the inner-shell hole state. The atomic orbitals as well as the molecular orbitals are relaxed by the inner-shell or valence shell hole in the self-consistent field (SCF) calculation. This is because the DV-$X\alpha$ method uses SCF numerical atomic orbitals as the basis set in an atomic potential in a cluster and thus the orbitals contract or expand according to the hole potential. They also self-consistently contract or expand due to the formation of chemical bonds. Figure 2 shows the Fe $3d$ atomic orbital used as one of the basis functions in the DV-$X\alpha$ method for the ground state or the $1s^{-1}$ hole state. It is found that the $3d$ wavefunction contracts due to the core hole potential. The Gaussian type orbital (GTO) basis sets are usually fixed and thus the relaxation effect due to the core hole is included either by the change of MO coefficients or by the configuration interaction. Thus the expression of core hole state by the fixed basis function requires a large basis set. On the other hand, the numerical atomic basis functions are self-consistent themselves, and thus are good eigenfunctions of the Hamiltonian. Therefore the DV-$X\alpha$ method usually needs only the minimal basis set for the MO calculations.

Figure 3 shows the electron density of states of $[MnO_6]^{10-}$ for the ground state and the $1s^{-1}$ core hole state [16]. This cluster is a model cluster of MnO. In the ground state, the Mn $3d$ and O $2p$ are separated in energy and the hybridization is week. Thus MnO is an

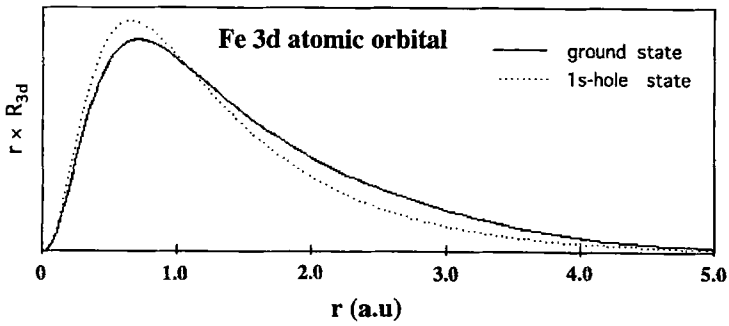

Fig. 2 Iron $3d$ atomic orbital used in the DV-$X\alpha$ method as a basis function. Solid line: ground state, and dotted line: $1s^{-1}$ hole state.

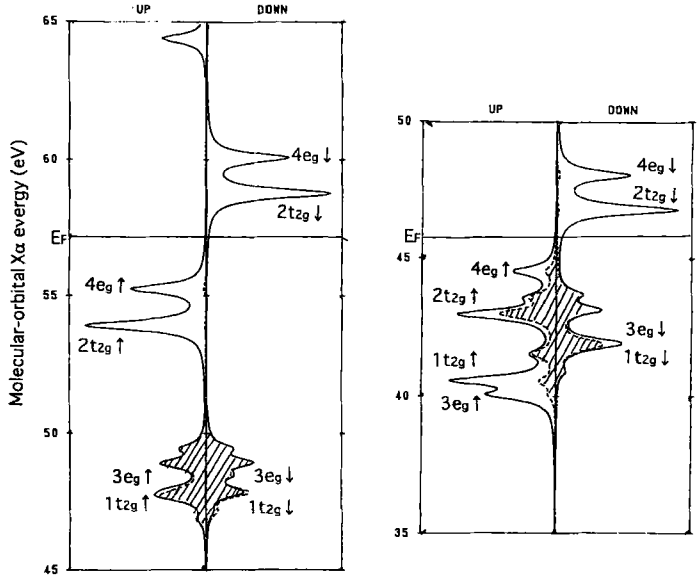

Fig. 3 Electron densities of states of $[MnO_6]^{10-}$ cluster for the ground state (left) and the $1s\uparrow^{-1}$ hole state (right) calculated by the spin-included DV-$X\alpha$ method. The shadowed area indicates oxygen $2p$ component. (Taken from Suzuki [16].)

ionic solid. In the $1s^{-1}$ core hole state, however, the Mn $3d$ orbital energy becomes as deep as that of the O $2p$ and they hybridize strongly each other. Thus we can know, using the DV-$X\alpha$ method, that the initial state of x-ray emission (or final state of photoionization) of MnO is no longer ionic but covalent.

The second advantage of the DV-$X\alpha$ method is that the basis functions of the DV-$X\alpha$ method are atomic orbitals. Thus the number of nodes is exact as shown in Fig. 4, where Si $2s$ GTO in GAUSSIAN method is compared with the numerical basis function used in the DV-$X\alpha$ method [17]. The use of the atomic orbital wavefunction makes it possible to perform the direct calculation of the electric dipole matrix elements, *e.g.* $<1s|\, r|\, 2p>$, using the DV-$X\alpha$ MO, yielding better result than when using a GTO basis MO.

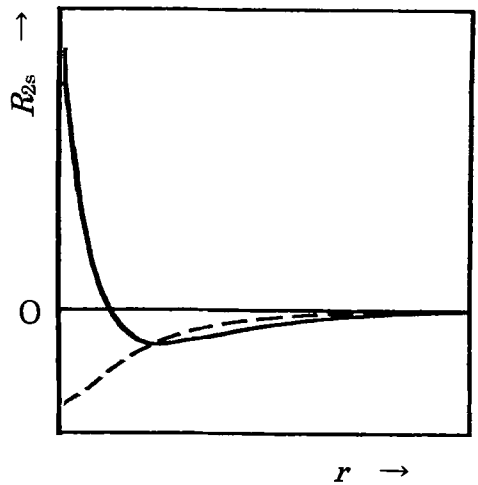

Fig. 4 Comparison of atomic basis functions of Si $2s$ used in the DV-$X\alpha$ (solid line) and GAUSSIAN 6-31G* (broken line). (Taken and modified from Nakamatsu [17].)

The third advantage of the DV-$X\alpha$ method is in the cluster approximation. The core hole state as the initial state of x-ray emission or final state of x-ray absorption is treated as an impurity atom in solid when using the band theory. However, since the core hole potential usually affects the next nearest neighbor atoms at most, it is enough for the calculation of x-ray emission spectra to use the clusters which include the second nearest neighbor atoms to the x-ray emitting atom as is described below.

The fourth advantage is that the precision of the DV calculation is comparable to the experimental precision. The energy resolution of x-ray optics is at most 0.01 eV, which is the comparable value to the DV-$X\alpha$ precision. Thus the infrared spectra cannot be reproduced by the DV-$X\alpha$ method.

We have calculated for these several years the x-ray emission spectra of solids and molecules and we have found that the calculation of x-ray emission spectra is one of the most successful applications of the DV-$X\alpha$ method. In the present paper, results of our ongoing research, as well as published results are described.

2. X-ray emission spectra and DOS

Fullerene The most successful examples of the application of the DV-$X\alpha$ method to the calculation of x-ray spectra are fullerenes. At the stage we have calculated the valence electron DOS of C_{60}, carbon $2p$ partial DOS was not measured or if it was measured [18], the reliability of the experiment was not sufficient [19]. We could suggest, based on our DV-$X\alpha$ calculation of C_{60}, that the measured C_{60} $K\alpha$ (K-L) x-ray emission spectrum in Ref. [18] was not correct and it contained some artifact because of the spectrometer fault [19].

Moreover, I calculated the electronic structure of C_{60} and C_{70} independently of the measurements of $K\alpha$ x-ray emission spectra by

Motoyama, and he and I finally compared the spectrum each other and the satisfactory agreement was published [20] as shown in Fig. 5. There were no adjustable parameters which affect the calculated results seriously.

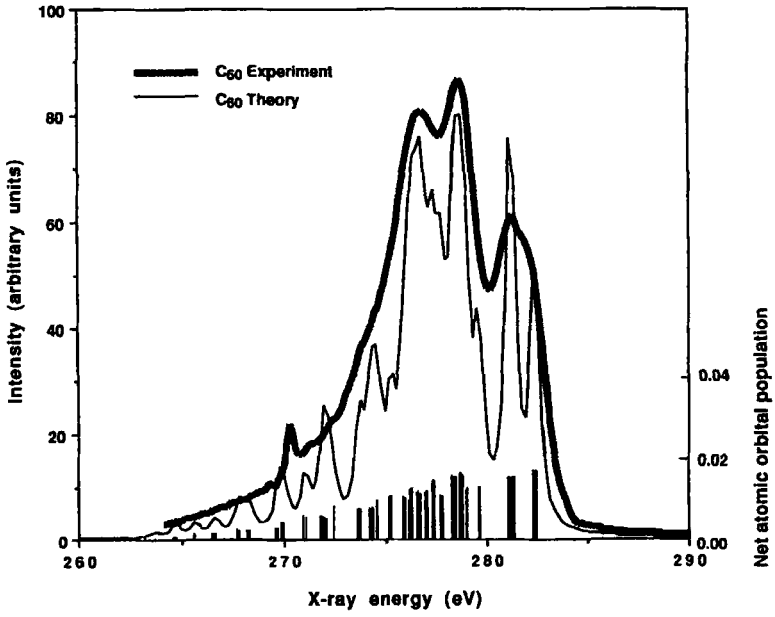

Fig. 5 Measured x-ray emission spectrum of C_{60} (heavy solid line) compared with carbon 2*p* DOS calculated by the DV-*Xα* method (thin solid line). Vertical line: net 2p atomic orbital population calculated by the DV-*Xα* method. The thin solid line is the result of the convolution of 0.5-eV FWHM Lorentzian function and the net atomic orbital population. The peak at 270 eV is a substrate signal. (Taken from Kawai and Motoyama [20].)

The method of calculation of the x-ray emission spectra is as follows after Manne [21] and Urch [22]. One-electron wavefunction φ_j of the *j*-th valence MO in the ground state of a molecule is expressed by a linear combination of atomic orbitals (LCAO),

$\varphi_j = \sum_i C_{ji}\chi_i$, where C_{ji} is the MO coefficient and χ_i the i-th atomic orbital. The electric dipole transition moment of the j-th transition T_j is then expressed as $T_j = <1s|ez_1|\varphi_j>$, where ez_1 is the electric dipole transition operator on electron 1. Here the z coordinate means that the emitted x-rays are z-polarized and $|1s>$ is a carbon $1s$ atomic orbital in the x-ray emitting atom. Because the one-center term is dominant, we can get an expression $T_j = \sum <1s|ez_1|2p_z> C_{ji}$, where the sum is run within the same atom. Since the term, $<1s|ez_1|2p_z>$, is common in all the x-ray transitions, the x-ray emission spectrum of C_{60} may be written as

$$F(h\nu) = \sum_{i\in 2p}^{occup.} |C_{ji}|^2 \, \delta(E_j - h\nu)$$

where E_j is the relative energy of the j-th MO, $h\nu$ the x-ray energy, δ the delta function, and *occup.* indicates occupied orbitals. We do not need to include the polarization of photons when the sample is homogeneous or randomly oriented. The height of the vertical lines in Fig. 5 represents $|C_{ji}|^2$, *i.e.* the carbon $2p$ net atomic orbital population. The thin solid line is the convoluted result with 0.5-eV-FWHM (full width at the half maximum) Lorentzian function to mimic the x-ray hole lifetime width. The agreement between the calculation and the experiment is satisfactory as is shown in Fig. 5. The $|C_{ji}|^2$ was calculated here for the ground state of C_{60}. The satisfactory agreement between the x-ray emission spectrum and the ground state DOS indicates that the x-ray emission spectra represent the ground state $2p$ DOS of C_{60}. Usually, the x-ray emission spectra of those compounds which have not partially filled valence shells can be satisfactorily reproduced by the ground state

local and partial electron density of states. The x-ray emission spectra of transition-metal compounds, rare-earth compounds, and multiply ionized species are treated differently as is described below.

3. X-ray emission spectra and atomic site determination

Boron suboxide The second successful example of the application of the DV-*Xα* method is the atomic site determination of boron suboxide ($B_{12}O_2$) [23]. We could determine the place of two

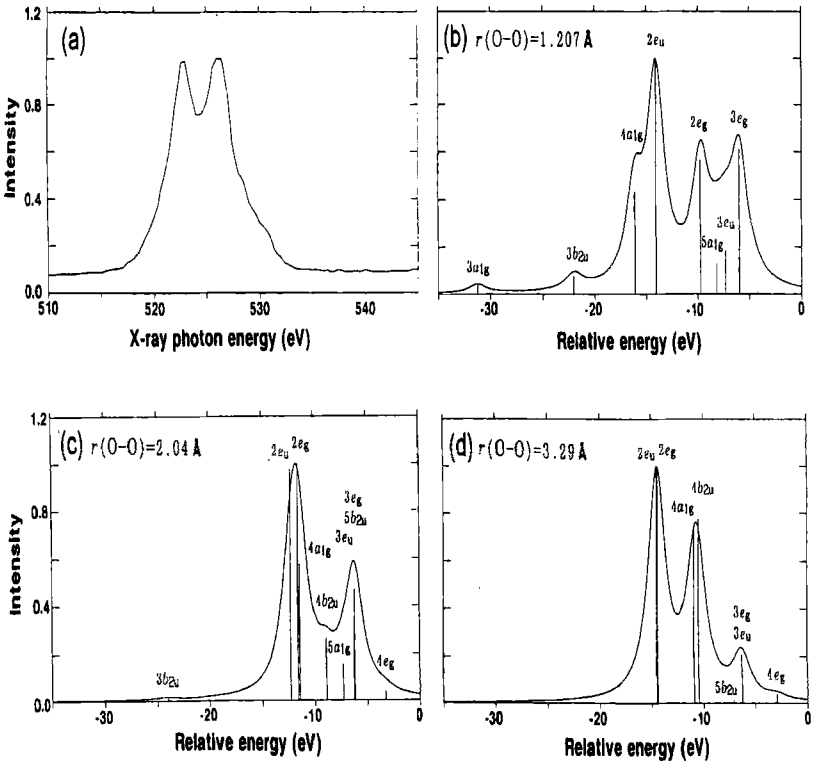

Fig. 6 (a) Measured oxygen *Kα* x-ray emission spectrum of $B_{12}O_2$. Calculated oxygen 2*p* DOS with O-O distances being 1.2 Å (b), 2.0 Å (c), and 3.3 Å (d). (Taken and modified from Kawai *et al.* [23].)

oxygen atoms in the rhombohedral boron unit cell by comparing the measured O $K\alpha$ (K-$L_{2,3}$) spectrum (Fig. 6a) with the DV-$X\alpha$ calculation where the adjustable parameter was the oxygen Cartesian coordinates. The calculated O $2p$ DOS was very sensitive to the oxygen coordinate as shown in Figs. 6b-d. When the O-O distance was shorter than 3 Å, the agreement between calculation and experiment was not satisfactory. When the O-O distance was 3.0-3.5 Å, then the agreement was satisfactory. This O-O distance indicated that the oxygen is situated at the center of gravity of boron triangle as is shown in Fig. 7. A small cluster (B_3O-B_3O) was used in this calculation where B_3 forms a triangle as is shown in Fig. 7 (small solid spheres in Fig. 7). It is well known that the boron triangle forms a three-center bond.

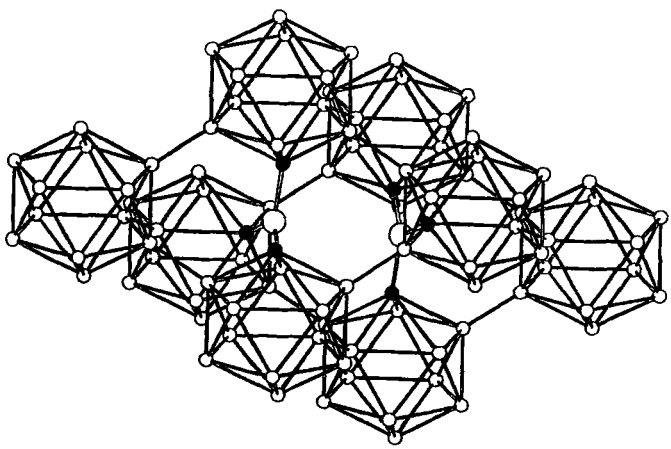

Fig. 7 Determined crystal structure of $B_{12}O_2$. (Taken from Kawai *et al.* [23].)

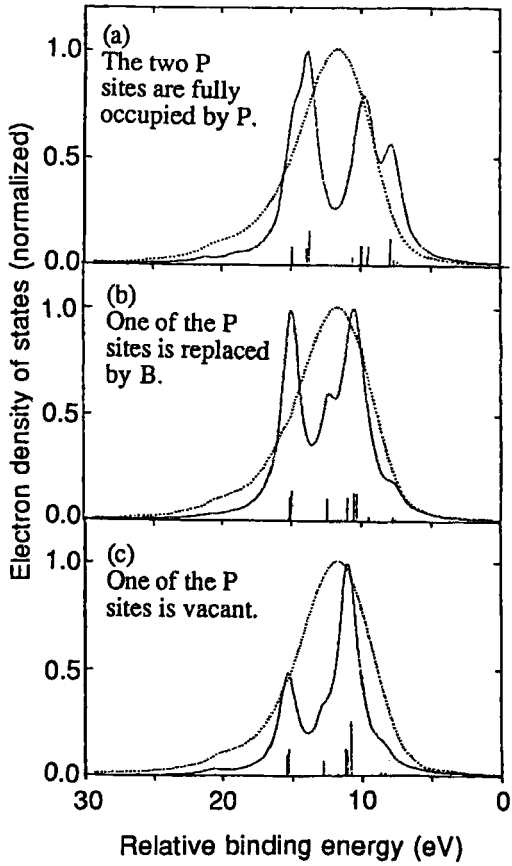

Fig. 8 Comparison of the measured P 3*p* DOS of $B_{13}P_2$ (dotted line) with the calculation (solid line). (Taken from Maeda *et al.* [24].)

$B_{13}P_2$ The crystal structure of $B_{13}P_2$ has determined to be the α-rhombohedral boron structure with two phosphorus atoms (partly replaced by boron) in a unit cell from x-ray diffraction. Maeda *et al.* [24] measured P 3*p* DOS of $B_{13}P_2$ by P $K\beta$ (K-$M_{2,3}$) x-ray emission spectroscopy. They also calculated the P 3*p* DOS using three

models of $B_{13}P_2$: (a) the two P sites were fully occupied by P atoms, (b) one of the P sites was replaced by B, and (c) one of the P sites was vacant. The calculated P 3*p* DOS were compared with the measured P 3*p* DOS as is shown in Fig. 8. It is found from Fig. 8 that the experimental DOS has been reproduced by the model (c). Neither the models (a) nor (b) gave satisfactory agreement with the measured x-ray spectrum. Consequently it was concluded that one of the P sites was vacant and was not replaced by B atom, and that the crystal structure of $B_{13}P_2$ was that shown in Fig. 9.

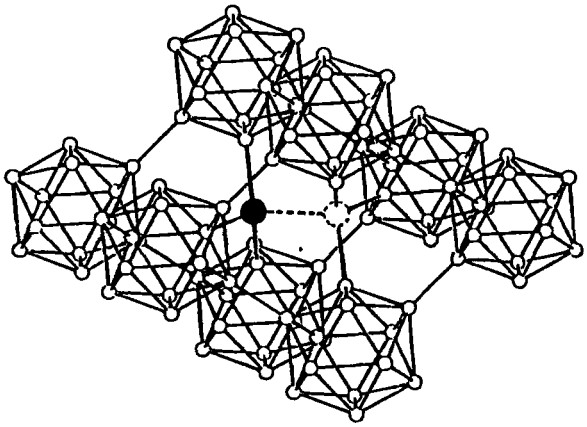

Fig. 9 Structure of $B_{13}P_2$: open circle, B; solid circle, P; dotted circle, vacant.

4. Resonant x-ray spectra and dangling bond density

Hexagonal boron nitride Resonant x-ray emission or resonance x-ray Raman scattering has recently been often studied using synchrotron radiation facilities. A successful example of the application of the DV-*Xα* method to the x-ray spectra is this resonance x-ray emission spectra of hexagonal boron nitride (*h*-BN).

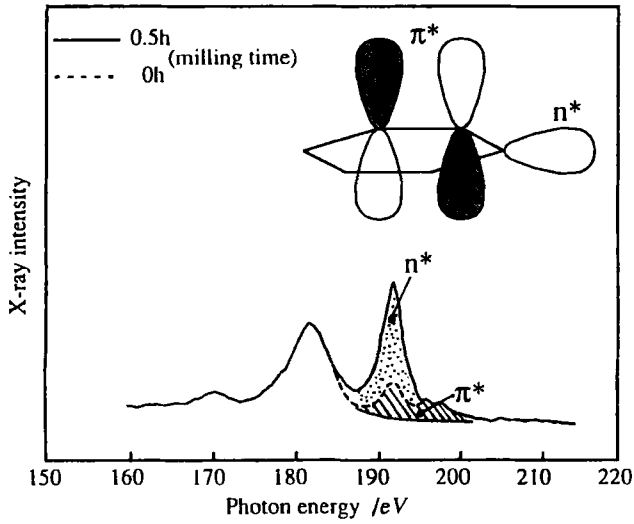

Fig. 10 Boron *Kα* and resonance scattering spectrum of *h*-BN. Hatched: π* peak, dotted: n* peak. π* and n* orbitals are schematically shown. (Taken from Kawai *et al.* [25].)

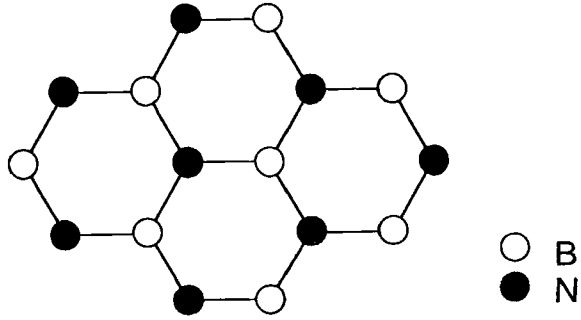

Fig. 11 Model cluster of *h*-BN for the DV-*Xα* calculation.

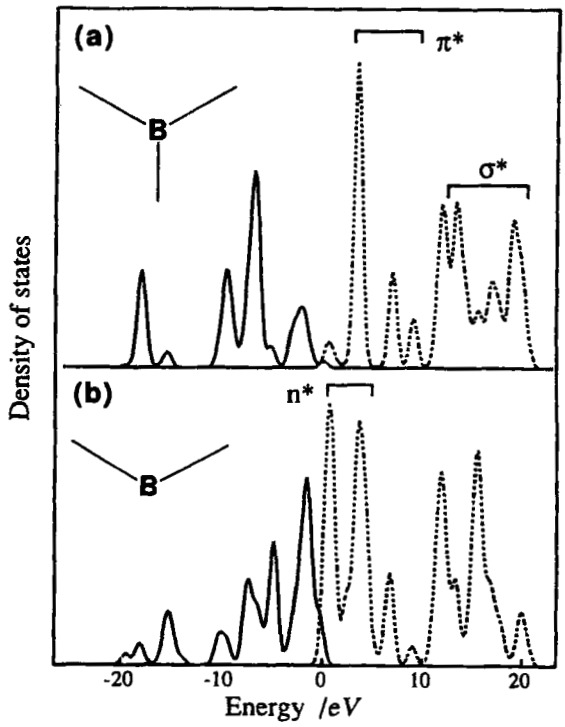

Fig. 12 Calculated boron $2p$ DOS of (a) three-fold coordination boron and (b) two-fold coordination boron. Solid line: occupied orbital, and dashed line: unoccupied orbital. (Taken from Kawai *et al.* [25].)

Figure 10 shows the measured resonant x-ray fluorescence spectra of *h*-BN [25, 26]. The excitation energy was 193 eV using an undulator beam line at the Photon Factory, National Laboratory for High Energy Physics, Tsukuba, Japan. The peaks at 170 and 182 eV are ordinary $K\alpha$ x-ray emission, and peak at 193 eV is the resonance x-ray emission. The difference of the two measurements

in Fig. 10 was the milling time of the *h*-BN powders. The powder crystal size of *h*-BN as received was 1000 Å. It became 100 Å after the powder was ground in a ball mill for 0.5 h. When the cluster size was small, the scattering peak intensity was strong, and when the cluster was large, the scattering peak was weak as is shown in Fig. 10.

The electronic structure of *h*-BN was calculated using a model cluster shown in Fig. 11 by the DV-*Xα* method. In this cluster, boron atoms are classified into two kinds: one is three-fold coordination and the other is two-fold coordination. The three-fold coordination boron represents the bulk boron, and the two-fold represents the boron at the end of a cluster. Calculated 2*p* DOS of these two kinds of boron are plotted in Fig. 12, where we find the change of π^* and σ^* orbitals (three-fold coordination) into n* orbitals (two-fold coordination). Here the n* represents a non-bonding orbital or a dangling bond. The schematic illustration of these orbitals is shown in the inset of Fig. 10. The energy of the resonance peak in Fig. 10 is identical to that of the n* peak in Fig. 12. As the cluster size becomes small, the ratio of the two-fold coordination relative to the three-fold coordination in a cluster becomes large. Consequently the ratio of the number of n* orbitals relative to the number of π^* and σ^* orbitals becomes large. Thus the increase of intensity due to the decrease of cluster size has been rationalized using the electronic structure calculation of *h*-BN cluster. The resonance peak intensity has been quantitatively related to the cluster size by Muramatsu *et al.* [26].

5. Comaprison between GAUSIAN and DV-*Xα*

S_8 Figure 13 shows the calculated sulfur 3*p* DOS of S_8 molecule compared with measured S *Kβ* (*K*-$M_{2,3}$) x-ray emission spectrum[27].

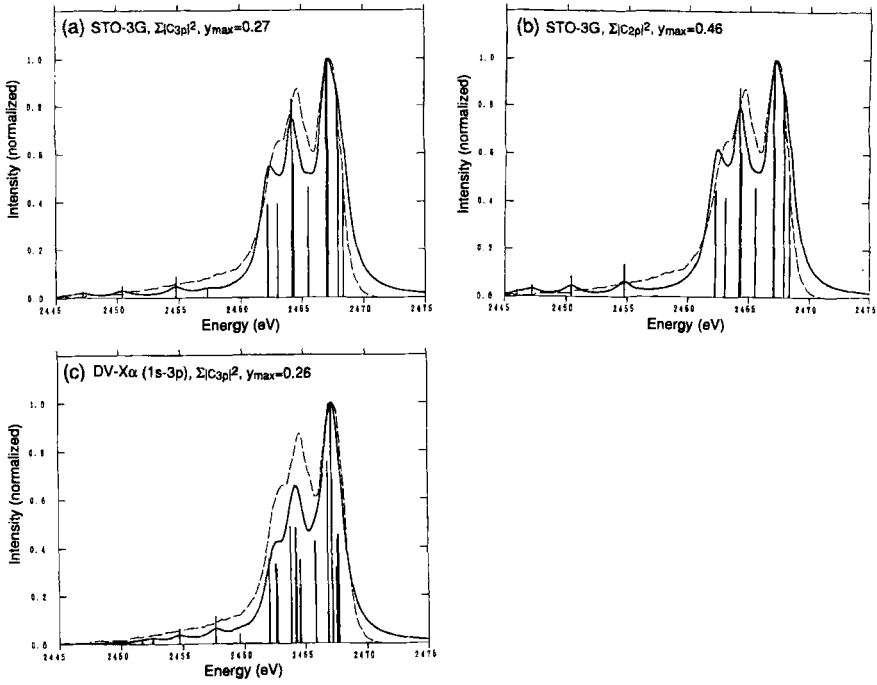

Fig. 13 (a) Calculated sulfur $3p$ DOS by STO-3G using GAUSSIAN 90, (b) $2p$ DOS by STO-3G, and (c) $3p$ DOS using the DV-$X\alpha$ method. y_{max} indicates the maximum hight of the $3p$ or $2p$ net atomic orbital population. (Taken and modified from Kawai and Hashimoto [27].)

Strictly speaking, the $3p$ and $2p$ net atomic orbital populations calculated by the STO-3G basis using the GAUSSIAN 90 are plotted in Figs. 13a and b, respectively. The maximum values of $|C_{ji}|^2$ for $3p$ and $2p$ net atomic populations are also indicated in Figs. 13a and

b. The maximum for $2p$ population is 0.46 whereas that for $3p$ population is 0.27. This indicates that the mixing of $2p$ orbital into the valence MO is too strong for STO-3G basis, and thus we can not directly estimate the electric dipole matrix element $<1s|ez_1|3p>$ using the STO-3G basis functions. On the other hand, the calculated maximum values of $3p$ and $2p$ net atomic populations using the DV-$X\alpha$ method was 0.26 (Fig. 13c) and 0.00 (not shown in Fig. 13), respectively. This indicates that our physical consensus of the mixing of $3p$ and $2p$ atomic orbitals into the valence orbitals agrees with the DV-$X\alpha$ calculation. The FORTRAN program named SXS is provided for the calculation of electric dipole matrix elements. Though I have not used SXS subroutine (to calculate the electric dipole matrix element $<1s|ez_1|3p>$) of the DV-$X\alpha$ method in the present paper because of simplicity, the x-ray intensity is able to be more quantitatively calculated with the use of SXS.

It should be noted here that $|<1s|ez_1|2p>|^2$ is two orders of magnitude greater than $|<1s|ez_1|3p>|^2$, thus very small mixing of $2p$ into $3p$ dominant valence levels is a source of numerical error for the estimation of dipole matrix element.

6. Core hole effect

S8 It is found from the comparison of the calculated $3p$ DOS (ground state $3p$ DOS) with the measured S $K\beta$ x-ray emission in Fig. 13c, that the low-energy structure (2461-2466 eV, bonding orbitals) seems to be too weak for the calculation, or the structure at 2467 eV (non-bonding orbital) seems to be too strong. To clarify the origin of this discrepancy, Uda [28] calculated the $3p$ DOS of sulfur for the ground state (Fig. 13c) and the $1s^{-1}$ core hole state (Fig. 14).

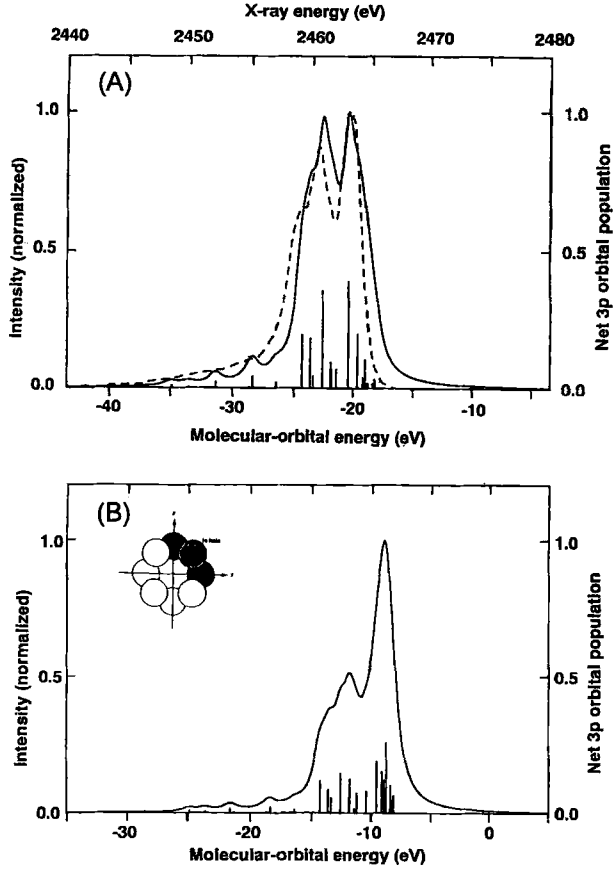

Fig. 14 Calculated sulfur $3p$ DOS using the DV-$X\alpha$ method for $1s^{-1}$ hole state. (a) S $3p$ DOS of the hole atom site, and (b) S $3p$ DOS of the neighbor S site in S_8 molecule. (Taken from Uda [28].)

The $3p$ DOS in Fig. 14A is the local DOS of the sulfur atom which has the $1s^{-1}$ hole. Comparing Fig. 13c and 14A, the bonding electrons are attracted by the core hole, and the low-energy structure (2461-2466 eV) becomes stronger in the core hole state. If the core hole is 0.5 (Slater's transition state), interpolation of Figs.

13c and 14A gives the close intensity of the low energy structure to the experiment. The $3p$ DOS in Fig. 14B is the local DOS of the neighbor sulfur atoms to the core-hole-having sulfur atom. It is found from Fig. 14B that the number of bonding electrons of the neighbor atoms are smaller than the ground state because they are attracted by the core-hole atom.

It is true that, strictly speaking, the ground state DOS does not represent the x-ray emission spectra because of the relaxation and correlation effects by the holes included in the x-ray transition, but the ground state DOS is the first approximation and a good approximation for the x-ray emission spectra. This is chiefly because the correlation and the relaxation energies are opposite but similar values with respect to the x-ray transition holes.

7. Cluster size for the calculation of infinite solids

Cu_2O The cluster size, when we calculate an infinite solid, is an important parameter using the cluster approximation. The size of the cluster or the termination method of the cluster (the charge of a cluster) has the largest effect on the accuracy of the DV-$X\alpha$ calculation.

Figure 15 is the results of cluster choice for the calculation of oxygen $2p$ DOS of Cu_2O solid by Sakai [29]. Figure 15A is the O $2p$ DOS of $(OCu_4)^{2+}$ cluster (center oxygen and the nearest neighbor copper atoms); the agreement between the calculation and the experiment is not satisfactory. Figure 15B is the O $2p$ DOS of the center oxygen of the cluster $(O_5Cu_4)^{6-}$; the agreement between the calculation and the experiment is satisfactory. The oxygen is anion and thus the electron clouds expand as far as the nearest neighbor anion, and they strongly hybridize each other. Thus we have found in our experience that the calculation of anion DOS requires a

cluster which includes the next nearest neighbor atoms (usually they are nearest neighbor anions), and cation DOS calculation requires only the nearest neighbor atoms (usually they are anions). The DOS calculated using such a cluster always agrees satisfactorily with experiment in our experience.

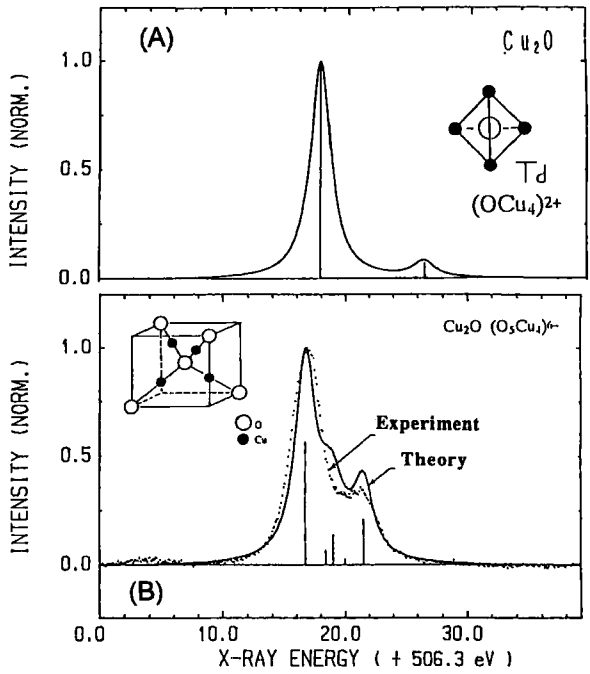

Fig. 15 Effect of cluster choice on the calculation of oxygen $2p$ DOS (oxygen $K\alpha$ x-ray emission spectrum) of Cu_2O. The 2p net atomic orbital population is broadened by 2.0-eV-FWHM Lorentzian function. (Taken from Sakai [29].)

8. Avoided crossing

One of the largest problem in x-ray emission spectroscopy was in the Cu $K\alpha_{1,2}$ (K-$L_{3,2}$) x-ray spectra. The high resolution measurement of Cu $K\alpha_1$ (K-L_3) indicated that the line width was not

significantly different between CuO and Cu_2O [30]. The valence electron configurations of CuO and Cu_2O are $3d^9$ and $3d^{10}$, respectively. Thus the x-ray emission spectral line shape of CuO should be broadened by the multiplet structure due to $1s\,2p^6\,3d^9$ $(^{1,3}D) \rightarrow 1s^2\,2p^5\,3d^9$ $(^{1,3}PDF)$. The calculated line width of CuO was twice as large as that of Cu_2O. However the line width was identical as is described above. The Cu $K\alpha_1$ line shape is important because the wavelength of Cu $K\alpha_1$ is the standard measure of x-ray crystallography [31].

The solution of this problem was in the charge transfer mechanism of Cu $2p$ x-ray photoelectron spectra (XPS) proposed by Kotani and Toyozawa [32], Asada and Sugano [33], Larsson [34], and van der Laan *et al.* [35]. They explained the strong "shake-up" satellite of Cu $2p$ XPS by the charge transfer.

It is very interesting to note that a similar idea to the charge transfer of the transition-metal compounds was independently proposed by Benka *et al.* [36], Urch [37], and Hartmann [38] for the interpretation of the chemical effect of shake-off satellites (transition between multiply ionized states) [39] in x-ray emission spectroscopy.

We have applied the charge transfer for the interpretation of shake-off satellites [40, 41], where the intensity modifications due to the chemical bonding was quantitatively reproduced by the Fock matrix elements calculated by the DV-$X\alpha$ method.

Table 1. Calculated valence charges of CuO and Cu_2O.

	Nominal electron configuration	Ground state	$1s^{-1}$ hole state
CuO	$3d^9$	$Cu^{+1.40}$	$Cu^{+0.79}$
Cu_2O	$3d^{10}$	$Cu^{+0.89}$	$Cu^{+0.62}$

We also applied the charge-transfer effect to the interpretation of the identical line width of Cu $K\alpha_1$ [42]. Table 1 is the calculated results of valence ($3d$ and $4s$) charges of CuO and Cu_2O for the ground state and the Cu $1s^{-1}$ hole state; Cu in CuO solid is charged +1.40, while Cu in Cu_2O charged +0.89. These charges are reasonable values from a chemical point of view; nominally Cu^{2+} and Cu^{+} are effectively $Cu^{+1.40}$ and $Cu^{+0.89}$, respectively, in solids. However, these effective charges become +0.79 (CuO) and +0.62 (Cu_2O) in the $1s^{-1}$ core hole states. This is because, for CuO, one $3d$ hole is filled by the electron which is transferred from the oxygen site because it is attracted by the Cu $1s^{-1}$ hole potential. On the other hand, Cu_2O electrons do not move because the Cu $3d$ orbitals are filled. Thus the effective charge of Cu_2O does not change remarkably, but the effective charge of CuO reduces as half as that of the ground state, when the core electron is photoionized from the Cu atom. Consequently, the Cu charge of CuO is similar to that of Cu_2O in the core hole state. This is the reason that the Cu $K\alpha_1$ does not show the multiplet splitting in experiment.

The charge-transfer effect can be schematically illustrated as Fig. 16, where one of the $2p$ electrons of CuO is photoionized and the Cu $3d$ orbital becomes deeper than ligand (oxygen) $2p$ orbital because of core hole potential. The center Cu $3d$ orbital and surrounding oxygen $2p$ orbitals (a linear combination of oxygen $2p$ orbitals) do not cross each other when they have a same symmetry (avoided crossing). This avoided crossing will transfer the valence $3d$ hole into the oxygen $2p$. The degree of avoidance can be estimated by the transfer matrix element (β). Thus the probability of hole transfer from Cu to O can be calculated by the DV-$X\alpha$ method. Table 2 shows the calculated MO coefficients and overlap integrals for the ground state and the $1s^{-1}$ hole state.

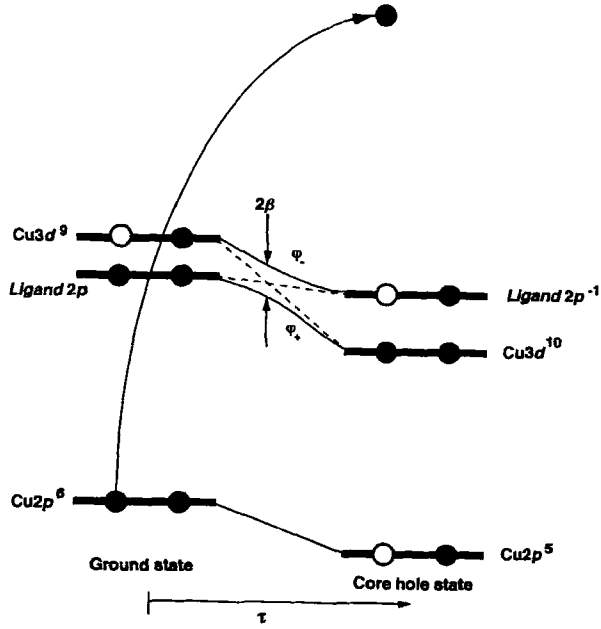

Fig. 16 Charge-transfer mechanism of CuO $2p$ electron photoionization. When the Cu $3d$ and the ligand (oxygen) $2p$ orbitals are strongly the hybridized, the same symmetry orbitals repulsive each other with twice their transfer integral (2β) , and the $3d$ hole is transferred to oxygen site after the photoionization of $2p$ electron. The order of molecular orbitals are changed before and after the photoionization. (Taken from Kawai *et al.* [44].)

It is found that the orbital character of $3b_{1g}$ and $4b_{1g}$ exchanges each other going from the ground state to the $1s^{-1}$ hole state. But it is also found that the hybridization between d and p is very strong for both the ground state and the $1s^{-1}$ hole state. This character exchange should be considered, in fact, by the total wavefunctions [33, 34] as is schematically shown in Fig. 17. Here the core-hole-state wavefunctions (Φ_m and Φ_s), which are orthogonal each other,

are the rotation of the ground state wavefunctions (Φ_1 and Φ_2); the rotation angle is larger than 45°. In other words, the core-hole-state wavefunctions are expressed by the configuration interactions (CI) of the ground state wavefunctions. The rotation angle, which can be converted into the CI coefficients can also be calculated by the DV-$X\alpha$ method. Charge-transfer effect on the line shape of x-ray emission spectra has been published for Ni [43], Cu [42, 44, 45], and Fe [46].

Table 2. Molecular orbital coefficients of planar $[CuO_4]^{6-}$ cluster calculated by the DV-$X\alpha$ method (d = |Cu3d>, p = |O2p>).

$d_{x^2-y^2}$	Ground state	$1s^{-1}$ hole state
$3b_{1g}$	$0.52d + 0.82p$	$0.90d + 0.34p$
$4b_{1g}$	$0.89d - 0.72p$	$0.46d - 1.03p$
$<d\|p>$	0.17	0.14

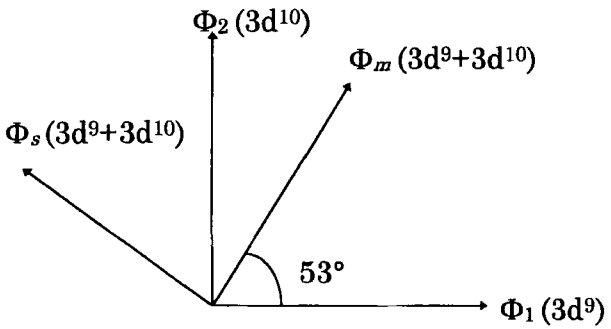

Fig. 17 The exchange of molecular orbitals is schematically illustrated by the rotation of total wavefunctions.

9. Concluding remarks

The calculation of the x-ray emission spectra are now not a difficult target for the DV-$X\alpha$ method. The development of experimental method using the synchrotron radiation now provides circularly and linearly polarized x-ray spectra, spin-selective x-ray spectra, and resonance x-ray spectra. These x-ray spectra will be calculated by the present DV-$X\alpha$ method without any revision of the FORTRAN code. When the agreement between the experiment and the calculation is not satisfactory in the x-ray spectra, the only thing we must do is to check the experiment or to check the cluster model we used in the calculation.

Acknowledgements The author wishes to express his gratitude for the guidance and encouragement received from Profs. Y. Gohshi, C. Satoko, K. Morokuma, M. Uda, and H. Adachi. Thanks are also due to C. Suzuki, M. Sakai and E. Uda, who collaborated with the author during master course students, for the use of their figures in their master theses. This work was partially supported by Grant-in-Aid for Scientific Research No. 08405042 from the Ministry of Education, Science and Culture, Japan.

References

[1] J. Kawai, Y. Gohshi, and Y. Nihei, *Adv. X-Ray Chem. Anal. Japan*, **19**, 1 (1988) (in Japanese).

[2] J. Kawai, *Adv. X-Ray Anal.* **34**, 91 (1991).

[3] J. Kawai, *Nucl. Instrum. Methods Phys. Res.* **B75**, 3 (1993).

[4] J. Kawai, *Nucl. Instrum. Methods Phys. Res.* **B87**, 88 (1994).

[5] J. Kawai, I. Tanaka, and H. Adachi, *Bunseki Kagaku*, **44**, 251 (1995).

[6] J. Kawai, *Hoshasen Kagaku*, **56**, 2 (1993) (in Japanese).

[7] S. Shin, *Synchrotron Radiation News*, **8**, 16 (1995).

[8] H. Adachi, M. Tsukada, and C. Satoko, *J. Phys. Soc. Japan*, **45**, 875 (1978).

[9] C. Satoko, M. Tsukada, and H. Adachi, *J. Phys. Soc. Japan*, **45**, 1333 (1978).

[10] H. Adachi, S. Shiokawa, M. Tsukada, C. Satoko, and S. Sugano, *J. Phys. Soc. Japan*, **47**, 1528 (1979).

[11] D. E. Ellis and G. S. Painter, *Phys. Rev.* **B2**, 2887 (1970).

[12] F. W. Averill and D. E. Ellis, *J. Chem. Phys.* **59**, 6413 (1973).

[13] A. Rosén, D. E. Ellis, H. Adachi, and F. W. Averill, *J. Chem. Phys.* **65**, 3629 (1976).

[14] D. E. Ellis, H. Adachi, and F. W. Averill, *Surf. Sci.* **58**, 497 (1976).

[15] J. C. Slater, *Quantum Theory of Molecules and Solids*, Vol. 4, McGraw-Hill (1974).

[16] C. Suzuki, *Master Thesis, Kyoto University, Department of Metallurgy* (1995) (in Japanese).

[17] H. Nakamatsu, *Oyo Buturi*, **62**, 1138 (1993) (in Japanese).

[18] Y. Saito, K. Kurosawa, H. Shinohara, S. Saito, A. Oshiyama, Y. Ando, and T. Noda, *J. Phys. Soc. Japan*, **60**, 2518 (1991).

[19] J. Kawai, K. Maeda, M. Takami, Y. Muramatsu, T. Hayashi, M. Motoyama, and Y. Saito, *J. Chem. Phys.* **98**, 3650 (1993).

[20] J. Kawai and M. Motoyama, *Phys. Rev.* **B47**, 12988 (1993).

[21] R. Manne, *J. Chem. Phys.* **52**, 5733 (1970).

[22] D. S. Urch, *J. Phys.* **C3**, 1275 (1970).

[23] J. Kawai, K. Maeda, I. Higashi, M. Takami, Y. Hayasi, and M. Uda, *Phys. Rev.* **B42**, 5693 (1990).

[24] K. Maeda, J. Kawai, T. Isomura, and H. Adachi (unpublished).

[25] J. Kawai, S. Tadokoro, Y. Muramatsu, S. Kashiwai, H. Kohzuki, M. Motoyama, H. Kato, and H. Adachi, *Physica* **B208/209**, 251 (1995).

[26] Y. Muramatsu, M. Oshima, J. Kawai, S. Tadokoro, H. Adachi, A. Agui, S. Shin, H. Kato, H. Kohzuki, and M. Motoyama, *Phys. Rev. Lett.* **76**, 3846 (1996).

[27] J. Kawai and K. Hashimoto, *Adv. X-Ray Chem. Anal. Japan*, **23**, 151 (1992) (in Japanese).

[28] E. Uda, *Master Thesis, Waseda University, Department of Materials Science and Engineering* (1993) (in Japanese).

[29] M. Sakai, *Master Thesis, University of Tokyo, Department of Industrial Chemistry* (1992) (in Japanese).

[30] P. H. Citrin, P. M. Eisenberger, W. C. Marra, T. Åberg, J. Utriainen, and E. Källne, *Phys. Rev.* **B10**, 1762 (1974).

[31] R. D. Deslattes, A. Henins, and E. G. Kessler, Jr. *Proc. Symp. On Accuracy in Powder Diffraction held at NBS*, NBS Special Publication 567, p. 55, Gaithersburg (1980).

[32] A. Kotani and Y. Toyozawa, *J. Phys. Soc. Japan*, **37**, 563, 912 (1974).

[33] S. Asada and S. Sugano, *J. Phys. Soc. Japan*, **41**, 1291 (1976).

[34] S. Larsson, *Chem. Phys. Lett.* **40**, 362 (1976).

[35] G. van der Laan, C. Westra, C. Haas, and G. A. Sawatzky, *Phys. Rev.* **B23**, 4369 (1981).

[36] O. Benka, R. L. Watson, and R. A. Kenefick, *Phys. Rev. Lett.* **47**, 1202 (1981).

[37] D. S. Urch, *J. Chem. Soc. Chem. Commun.* 526 (1982).

[38] E. Hartmann, *J. Phys. B: At. Mol. Phys.* **19**, 1899 (1986).

[39] T. Åberg, *Phys. Rev.* **156**, 35 (1967).

[40] J. Kawai, C. Satoko, K. Fujisawa, and Y. Gohshi, *Phys. Rev. Lett.* **57**, 988 (1986).

[41] J. Kawai, C. Satoko, and Y. Gohshi, *Spectrochim. Acta*, **42B**, 1125 (1987).

[42] J. Kawai, Y. Nihei, M. Fujinami, Y. Higashi, S. Fukushima, and Y. Gohshi, *Solid State Commun.* **70**, 567 (1989).

[43] J. Kawai, M. Takami, and C. Satoko, *Phys. Rev. Lett.* **65**, 2193 (1990).

[44] J. Kawai, K. Maeda, K. Nakajima, and Y. Gohshi, *Phys. Rev.* **B48**, 1281 (1993).

[45] J. Kawai, K. Maeda, K. Nakajima, and Y. Gohshi, *Phys. Rev.* **B52**, 6129 (1995).

[46] J. Kawai, C. Suzuki, H. Adachi, T. Konishi, and Y. Gohshi, *Phys. Rev.* **B50**, 11347 (1994).

X-Ray Absorption Near Edge Structure Study and DV-Xα Calculations on Some Square-planar Copper(II) Complexes with Macrocyclic Ligands

Seiichi Yamashita, Manabu Fujiwara, Yuko Kato
Toshio Yamaguchi, and Hisanobu Wakita
Department of Chemistry
Fukuoka University, Nanakuma, Jonan-ku, Fukuoka 814-01, Japan

Hirohiko Adachi
Department of Material Sciences and Engineering
Kyoto University, Kyoto 606-01, Japan

Abstract

The electronic states of copper(II) ions containing the square-planar tetraaza or diazadioxa macrocyclic copper(II) complexes abbreviated as Cu(N_4-Paen), Cu(N_4-[14]-ph-NO_2), Cu(N_4-[14]-Me,-NO_2), Cu(N_4-[14]-Me), Cu(N_2O_2-ph), Cu(N_2O_2-ph-Me), Cu(N_2O_2-Me,-ph-NO_2), Cu(N_2O_2-Me), where Pa, [14], ph, and Me represent pyrrolemethylamine, 14-membered macrocycle, phenyl, and methyl groups, respectively, were investigated in the solid state by means of X-ray absorption near edge structure (XANES). The peaks in the measured XANES spectra shifted to the lower energy side with increasing the electron density of a central copper(II) ion. The molecular orbital calculations for the tetraaza copper(II) complexes were carried out by the DV-Xα method, and their theoretical XANES spectra, atomic-charges, and bond-charges were estimated. The peaks of the measured XANES spectra could be assigned to the electron transition mainly from Cu1s orbital to Cu4p and/or Cu4s orbitals from comparison with the theoretical spectra. The values of the atomic-charge of the copper atoms and the bond-charge of the Cu-N bonds in the complexes are consistent with their peak positions in the measured XANES spectra.

ADVANCES IN QUANTUM CHEMISTRY, VOLUME 29

0065-3276/97 $25.00

1. Introduction

Metal complexes with a large organic ligand such as phthalocyanines and porphyrins are interesting for their characteristic, spectroscopic, and electronic properties, and numerous analogous compounds have been prepared and investigated on their chemical properties such as selectivity for metal ions or models of metal enzymes. Especially, the macrocyclic ligands have the complexing affinity for a particular transition metal ion; secondly, the structure change before and after the complex formation may be small; thirdly, the coordination bond in the complex is very stable and inert and hence many of the complexes keep firmly the coordination structure of square-planar for each central metal ion. For example, it was reported that the macrocyclic copper(II) complexes studied in this paper(Fig.1) have four-coordinated, stable square-planar structure in both crystal and solution.[1] In addition, the macrocyclic ligand complex differs from the corresponding uncyclic ligand complex on the electronic state and molecular structure because the former has the cyclic conjugated system around the central metal ion. It will be possible to know the nature of the complex molecules and to design the novel complexes and ligands having the superior properties, if both the electronic state and the local structure of their central metal ions can be determined under the same conditions.

XAS(X-ray absorption spectroscopy) is known as an X-ray analytical technique to determine the local structure of a desired atom under any sample condition such as in crystal, amorphous, and solution. On the characteristics of this technique, XAS has been well employed to characterize the state around the metal atom in metal complex molecules and thus includes the analytical ability to get information mentioned above. An X-Ray absorption spectrum obtained from XAS measurements is divided into two regions; the XANES(X-ray absorption near edge structure) region at the near X-ray absorption edge and the XAFS(X-ray absorption fine structure) region over the absorption edge. By the XAFS method, the structural information is obtained. Many XAFS studies have been reported because the XAFS structure analysis has become a routine work. However, on the analysis of the spectrum in the XANES region, there are only a few recent works on the extraction of the stereochemical information using the multiple scattering theory[2] and the assignment of peaks in the spectrum using the polarized XANES spectrum measurement[3]. Unfortunately, there is no perfect XANES theory, so that recent research objects were limited the analysis of the X-ray absorption spectra of light elements and of small simple molecules.[4]

At the rising part of the absorption edge, X-ray absorption spectrum is known to be

affected by the electronic state of the absorption atom in the macrocyclic copper(II) complexes(shown in Fig.1) which have four-coordinated and square-planar structures. In the present report the correlation between the XANES spectra of the complexes and the electron-donating abilities of the macrocyclic ligands in the complexes is studied. In addition, some peaks in the XANES spectra are assigned on the basis of the results of the molecular orbital calculation using the DV-Xα method.[5)]

2. Experimental

2. 1. Sample Preparation

A series of macrocyclic copper(II) complexes (Fig.1) were prepared according to methods described in the literature[1)]. The prepared complexes were recrystallized and identified by ^{1}H- and ^{13}C-NMR and IR spectrometries.

2. 2. X-Ray Absorption Measurements

X-Ray absorption measurements were performed at the BL-7C station of the Synchrotron Radiation Research Facili1ty(the Photon Factory) in the National Laboratory for High Energy Physics(KEK). X-Ray absorption data were collected in the range from ca.8970eV to ca.9020eV around copper *K*-edge(8981.83eV). The time to collect X-ray photons was 2 seconds at each measuring point. Crystalline samples of the complexes were measured in a pellet form after powdering crystals with an agate mortar.

2. 3. Molecular Orbital Calculations

Molecular orbital calculation by using the DV-Xα method for the tetraaza macrocyclic copper(II) complexes were performed with an FACOM-780/10S computer. The reliable crystal parameters of the molecular structures of the copper(II) complexes have not yet been reported. Therefore, their atomic positions of the macrocyclic ligands were estimated from similar structures in reported analogous complexes.

For the Cu-N bond distances within the copper(II) complexes was used an average value(1.98Å) obtained from XAFS analysis for the macrocyclic copper(II) complexes. The

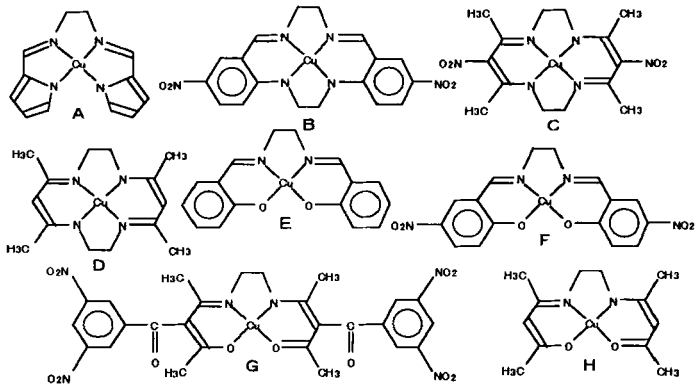

Fig. 1. Molecular structures of the macrocyclic copper(II) complexes investigated.

Table 1. The Reduction Half-wave Potential of the Macrocyclic Copper(II) Complexes shown in Fig.1

	Complex	$E_{1/2}$[1] / V
A	[Cu(N_4-Paen)]	-0.74
C	[Cu(N_4-[14]-Me, -NO_2)]	-1.23
D	[Cu(N_4-[14]-Me)]	-2.26
E	[Cu(N_2O_2-ph)]	-1.21
H	[Cu(N_2O_2-Me)]	-1.50

1) unit vs. S.C.E.

Table 2. Position and Shape of the XANES Peaks in the Macrocyclic Copper(II) Complexes

	Complex	Energy / eV		
		Peak 1	Peak 2	Peak 3
A	Cu(N_4-Paen)	8977.4 SP[1]	8981.9 SS[2]	8986.2 LS[3]
B	Cu(N_4-[14]-ph-NO_2)	8978.6 SP	8981.9 SS	8984.4 LP[4]
C	Cu(N_4-[14]-Me, -NO_2)	8978.3 SP	————	8983.4 LP
D	Cu(N_4-[14]-Me)	8977.7 SP	————	8982.8 LP
E	Cu(N_2O_2-ph)	8977.1 SP	————	8985.0 SS
F	Cu(N_2O_2-Ph-Me)	8978.0 SP	————	8984.7 LS
G	Cu(N_2O_2-Me, -Ph-NO_2)	8977.4 SP	————	8983.4 LP
H	Cu(N_2O_2-Me)	8977.4 SP	————	8983.4 LP

1) small peak, 2) small shoulder, 3) large shoulder, 4) large peak.

point group symmetries are C_{2v} for complexes **A** and **B**, and D_{2h} for complexes **C** and **D**(Fig.1). Numerical atomic orbitals taken into account in the calculations are 1s to 4p orbitals for Cu atom, 1s to 2p orbitals for C, N, and O atoms, and 1s orbital for H atom. The DV-Xα calculations were repeated until the difference of charges became less than 0.01 electron, where the charges were calculated from the Mulliken population analysis. The values of the ionization energies of 2p orbitals for N and Cu atoms were calculated from the DV-Xα calculation and compared with those measured by XPS measurements. The measured values were estimated as each ground state orbital energy, the calculated values agreed well with the estimated values to estimated at ground state orbital energy.

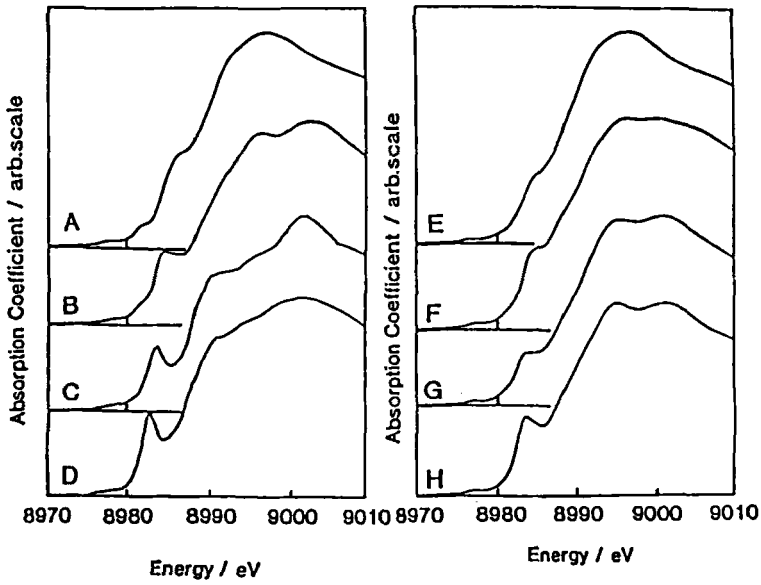

Fig. 2. XANES spectra of the macrocyclic copper(II) complexes.

3. Results

3. 1. XANES Analysis

For the tetraazacopper(II) complexes, the reduction potentials[6] of complexes **A**, **C**, and **D** are given in Table1. These values were obtained in DMF at 25°C by the polarographic method with a dropping mercury electrode and a mercury pool as the working and counter

electrodes, respectively. As is seen in Table1, all values are negative and become to more negative in order of **A>C>D**; these results indicate that the electron donating ability of the ligands to a central copper(II) ion is stronger in order of **A<C<D**. The XANES spectra of complexes **A**, **B**, **C**, and **D** are shown in Fig.2, and the positions and shapes of peaks in the spectra are listed in Table2. Three peaks are recognized in all spectra, where they are called the first peak at 8978eV, the second one at 8981eV, and the third one in the region from 8983 to 8986eV. The energy values of the first peak are almost the same. For the second peak, however, the peak intensities become smaller in order of **A<B<C** and the peak positions of **A**, **B**, and **C** shift(called the XANES shift in this paper) to the lower energy side from **A** to **C**. The third peak of **A**, **B**, **C**, and **D** shifts to lower energy from **A** to **D** and the peaks become sharper. This tendency corresponds to the result of the electron donating ability of the ligand to its central copper in complexes **A**, **C**, and **D**.

For the diazadioxacopper(II) complexes(Fig.1), the reduction potentials[6] of complexes **E** and **H** are listed in Table1. As is seen in Table1, the electron donating ability of ligand **H** is stronger than that of **E**. The XANES spectra of complexes **E**, **F**, **G**, and **H** are shown in Fig.2, and the energy values and shapes of the peaks in the spectra are listed in Table2. The energy values of the first peaks in the four spectra are almost the same as the case of those of tetraazacopper(II) complexes. The third peaks have only a little shift in complexes **E** and **F**, but its shape for complex **H** is sharper than that for complex **G**. The energy value of the third peak for **E**(or **F**) is lower than that of **G**(or **H**). Therefore, the electron donating ability of each ligand to a central copper ion in the diazadioxacopper(II) complexes may be similar with each other for complexes **E** and **F**, for complexes **G** and **H**, but a little weaker for complex **F** than that for complex **G**.

For both diazadioxa and tetraaza complexes, the third peaks in the XANES spectra shift to the lower energy region with increasing electron donating ability of the ligands, that is, with increasing the electron density of a central copper(II) ion. In addition, for the tetraaza complex **C** and diazadioxa complex **E**, though their reduction potentials are nearly equal, the third XANES peak of complex **C** has sharper shape and lower energy value than complex **E**. This result indicates that the XANES spectrum may be affected by not only the electron density of a central copper(II) ion but also other factors such as the type of donor sets coordinating to a central copper(II) ion.

3. 2. Molecular Orbital Calculations

Table 3. Atomic Position of the Macrocyclic Copper(II) Complexes Using the DV-Xα Calculations

Complex A

Atom		Position / A		
		X	Y	Z
1	Cu	0.00	0.00	0.00
2	N	1.40	1.40	0.00
3	N	1.40	-1.40	0.00
4	N	-1.40	1.40	0.00
5	N	-1.40	-1.40	0.00
6	C	2.60	0.70	0.00
7	C	-2.60	0.70	0.00
8	C	0.70	2.60	0.00
9	C	-0.70	2.60	0.00
10	C	2.60	-0.70	0.00
11	C	3.65	-1.60	0.00
12	C	3.10	-2.85	0.00
13	C	1.70	-2.75	0.00
14	C	-2.60	-0.70	0.00
15	C	-3.65	-1.60	0.00
16	C	-3.10	-2.85	0.00
17	C	-1.70	-2.75	0.00

Complex B

Atom		Position / A		
		X	Y	Z
1	Cu	0.00	0.00	0.00
2	N	1.40	1.40	0.00
3	N	1.40	-1.40	0.00
4	N	-1.40	1.40	0.00
5	N	-1.40	-1.40	0.00
6	C	2.70	1.24	0.00
7	C	3.40	0.00	0.00
8	C	2.70	-1.24	0.00
9	C	-2.70	1.24	0.00
10	C	-3.40	0.00	0.00
11	C	-2.70	-1.24	0.00
12	C	0.70	2.60	0.00
13	C	0.70	-2.60	0.00
14	C	-0.70	2.60	0.00
15	C	-0.70	-2.60	0.00
16	C	3.40	-2.48	0.00
17	C	4.91	-2.48	0.00
18	C	5.61	-1.24	0.00
19	C	4.91	0.00	0.00
20	C	-3.40	-2.48	0.00
21	C	-4.91	-2.48	0.00
22	C	-5.61	-1.24	0.00
23	C	-4.91	0.00	0.00
24	N	7.12	-1.24	0.00
25	N	-7.12	-1.24	0.00
26	O	7.56	-0.12	0.00
27	O	-7.56	-0.12	0.00
28	O	7.56	-2.36	0.00
29	O	-7.56	-2.36	0.00

Complex C

Atom		Position / A		
		X	Y	Z
1	Cu	0.00	0.00	0.00
2	N	1.40	1.40	0.00
3	N	1.40	-1.40	0.00
4	N	-1.40	1.40	0.00
5	N	-1.40	-1.40	0.00
6	C	2.70	1.24	0.00
7	C	3.40	0.00	0.00
8	C	2.70	-1.24	0.00
9	C	-2.70	1.24	0.00
10	C	-3.40	0.00	0.00
11	C	-2.70	-1.24	0.00
12	C	0.70	2.60	0.00
13	C	0.70	-2.60	0.00
14	C	-0.70	2.60	0.00
15	C	-0.70	-2.60	0.00
16	C	3.56	2.44	0.00
17	C	3.56	-2.44	0.00
18	C	-3.56	2.44	0.00
19	C	-3.56	-2.44	0.00
20	N	4.88	0.00	0.00
21	O	5.32	1.12	0.00
22	O	5.32	-1.12	0.00
23	N	-4.88	0.00	0.00
24	O	-5.32	1.12	0.00
25	O	-5.32	-1.12	0.00

Complex D

Atom		Position / A		
		X	Y	Z
1	Cu	0.00	0.00	0.00
2	N	1.40	1.40	0.00
3	N	1.40	-1.40	0.00
4	N	-1.40	1.40	0.00
5	N	-1.40	-1.40	0.00
6	C	2.70	1.24	0.00
7	C	3.40	0.00	0.00
8	C	2.70	-1.24	0.00
9	C	-2.70	1.24	0.00
10	C	-3.40	0.00	0.00
11	C	-2.70	-1.24	0.00
12	C	0.70	2.60	0.00
13	C	0.70	-2.60	0.00
14	C	-0.70	2.60	0.00
15	C	-0.70	-2.60	0.00
16	C	3.56	2.44	0.00
17	C	3.56	-2.44	0.00
18	C	-3.56	2.44	0.00
19	C	-3.56	-2.44	0.00

To perform more detailed investigation for the XANES peaks, molecular orbital calculations of the complex molecules were carried out, and the first, second and third peaks in the XANES spectra were assigned by comparing them with the corresponding calculated XANES spectra.

The XANES peaks of the tetraazacopper(II) complexes in Fig.2 are sharper than those of the diazadioxacopper(II) complexes, so that it is convenient to compare the observed spectra with the calculated ones. For these reasons, molecular orbital calculations of the complexes **A**, **B**, **C**, and **D** were carried out by the DV-Xα method. The atomic positions used on each molecular model of the macrocyclic copper(II) complexes in these calculations are given in Table3. The electron density distribution maps were calculated and are shown in Fig.3.

In Fig.3, the tetraazacopper(II) complexes have cyclic conjugated systems and each central copper(II) ion is surrounded by a doughnut-type and overlapping electron clouds formed by its macrocyclic ligand. In addition, for the N donor atoms of the ligand in each complex, the electron density distribution of the N atoms are not spherical but a symmetrical. For example, as for the complex **A**, the electron distributions of N atom at an ethylene chain side and N atom in a pyrrole ring are different from each other. This may reflect the fact that the latter N atom belongs to a pyrrole ring. For the coordinating N atoms in complexes **B**, **C**, and **D**, the electron distributions of these N atoms lie to the part of a propylene chain rather than to the part of a conjugated ethylene chain. This result indicates that the chemical bond between the coordinating N atom and C atom in the propylene moiety is stronger than that between the N atom with the C atom in the ethylene moiety. This seems reasonable from chemical structures of the ligands. For the nitro groups in complexes **B** and **C**, it is also recognized that the N and O atoms of the nitro group form a highly conjugated system from the result of electron density distribution around the group.

The charges of all atoms except for hydrogen atoms and of bonds in the copper(II) complexes were calculated by the DV-Xα method. The resulting charge maps are shown in Fig.4. The atomic-charge values in Fig.4 are the sum of the atomic orbital populations for each atom, and the bond-charge values are the sum of the overlap populations of molecular orbitals for each bond. A large atomic-charge value indicates high electron density on itself, and also a large bond-charge value indicates high covalency of its chemical bond. As is seen in the charge map, an atomic-charge value of the central copper atom increase in the order of **A<B<C<D**. In addition, for the N donor atoms in four copper(II) complexes, the bond-charge value of the N-C bond between the N donor atom and C atom in the ethylene chain is smaller than that of another N-C bond between the N donor atom and C atom in the propylene chain.

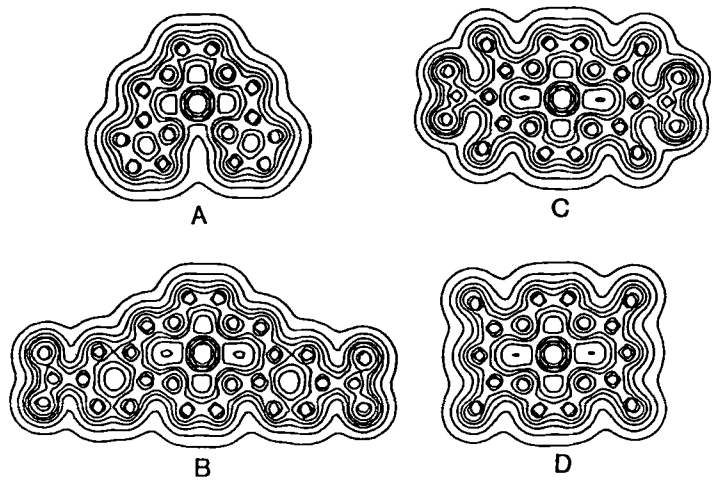

Fig. 3. Electron density distribution maps of the tetraazacopper(II) complexes.

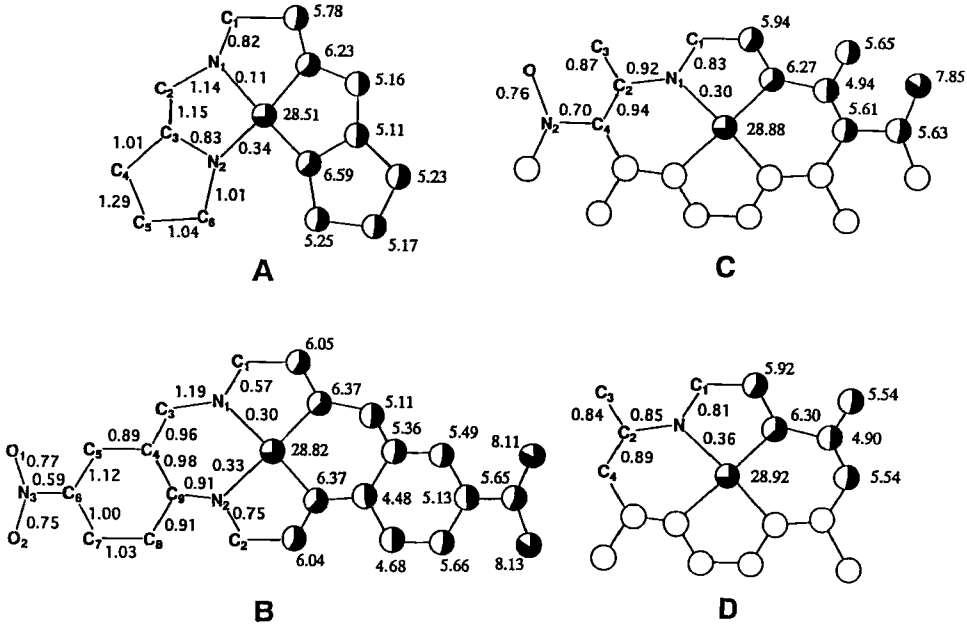

Fig. 4. Charge maps of the tetraazacopper(II) complexes. Numerical values near circles and element symbols represent atomic- and bond-charge values, respectively. Circles give the ratio of the atomic-charge (normalized at 40 for a copper atom and *10* for other atom).

This result indicates that the covalency of the latter bond is higher than the former one. In other word, the bond order of the latter one is higher than that of the former one. For the complexes **B** and **C**, the atomic-charge values of N and O atoms of the nitro group in complex **B** are 5.7 and 8.1, and those in complex **C** are 5.6 and 7.9, respectively. These indicate that the polarizability of the N-O bond in complex **C** is smaller than that in complex **B**. The atomic-charge values of C1 atom of the ethylene chain in complexes **B**, **C**, and **D** increase in the order of **B>C>D**. This order also shows about ones of C3 atom in complex **B** and of C2 atom in complexes **C** and **D**. This results indicate a flow of electron from the carbon atoms to the copper atom through the coordinated N atoms.

3. 3. Assignments of XANES Peaks

It is well known that the fine structure of the *K* absorption edge arises from the photoelectric effect of a 1s orbital electron of an absorption atom. It is obvious that the peaks in the rising part on XANES spectra are ascribed to the electron transition from an inner shell orbital to higher molecular orbitals (called as 1s electron transition in this report). Therefore, to estimate the probabilities of the 1s electron transition by an electronic dipole theory, theoretical XANES spectrum can be calculated using molecular orbital calculations.[4)]

From the results of DV-Xα calculations of the tetraazacopper(II) complexes, some energy levels of calculated molecular orbitals and their atomic orbital components are listed in Table4. The 1s molecular orbitals are $1a_1$, $1a_1$, $1b_{1g}$, and $1b_{1g}$ for complexes **A**, **B**, **C**, and **D**, respectively. The values of probability of the 1s electron transition were estimated from these 1s molecular orbitals and their main atomic orbitals(over 10%). All molecular orbitals of the four copper(II) complexes below ca.-5eV include a Cu3d atomic orbital as a main component; while almost all ones over ca.-3eV include a Cu4p atomic orbital as a main component. For each molecular orbital, the probability of the electron transition was calculated according to the electronic dipole theory.[4)] The peak positions of the absorption spectra were estimated from the transition energies. Each peak was replaced by a Gaussian with half-width of 1.2eV, is shown in Fig.5 with the measured XANES curves.

On the basis of the results in Fig.5 and Table5, the first peak at ca.-8eV in the measured XANES curve of complex **A** can be assigned to 1s electron transition mainly to $28a_1$ orbital. This orbital is composed mainly of Cu3d atomic orbital. The second peak at ca.-5eV can be assigned to the mixture of 1s electron transitions mainly to $26a_2$ and $9b_1$ orbitals. Each orbital is composed mainly of 2N2p and 4C2p atomic orbitals, respectively. The third peak at ca.-1eV

Table 4. Atomic Core Levels of Various Copper Complexes for Ground State

Complex	E[1]	Atomic orbital (rate[2] / %)	
A	-8744.67	Cu 1s	(100.0)
	-1046.65	Cu 2s	(100.0)
B	-8752.03	Cu 1s	(100.0)
	-1043.82	Cu 2s	(100.0)
C	-8745.92	Cu 1s	(100.0)
	-1042.77	Cu 2s	(100.0)
D	-8742.85	Cu 1s	(100.0)
	-1045.70	Cu 2s	(100.0)

1) average energy level of molecular orbital at up- and down-spins, 2) rate of composition of molecular orbital.

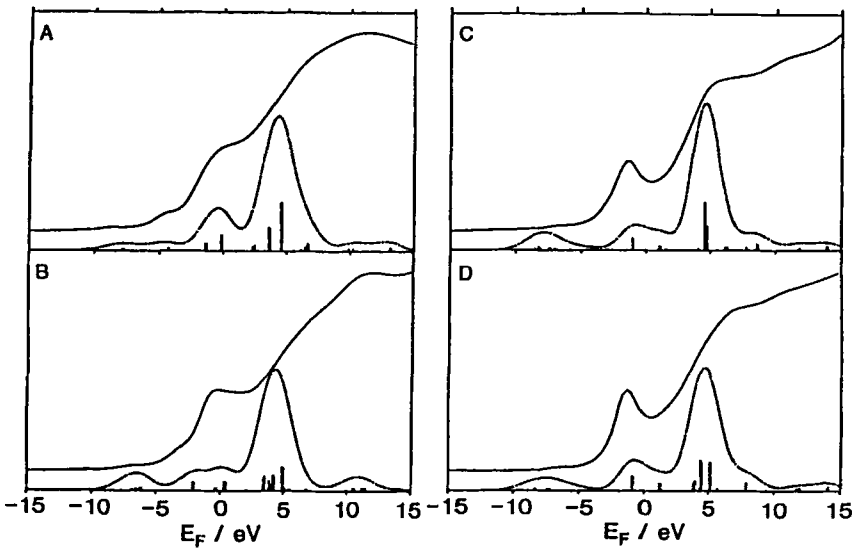

Fig. 5. Theoretical and measured XANES curves of the tetraazacopper(II) complexes. Bar chart represents the electron transition probability. E_F; relative energy value calculated from the Fermi level of each complex, solid line; measured XANES curve, chain line; theoretical XANES curve.

can be assigned to the mixture of transitions mainly to $10b_1$ and $11b_1$ orbitals. Both orbitals are composed mainly of Cu4p atomic orbital. For complex **B**, the first peak in the measured XANES curve is assignable to a mixture of transitions to $46a_1$ and $48a_1$ orbitals consisting of Cu3d atomic orbitals, the second peak to 1s electron transition to $15b_1$ orbital composed mainly of Cu4p atomic orbital, and the third peak to $17b_1$ and $50a_1$ orbitals including Cu4s and Cu4p atomic orbitals. For complex **C**, the first peak in the measured XANES curve can be assigned to transitions to $22b_{1g}$, $23b_{1g}$, and $24b_{1g}$ orbitals including with Cu3d and Cu4s atomic orbitals; the third peak can be assigned to 1s electron transition to $9a_u$ orbital composed mainly of Cu4p atomic orbital. For complex **D**, the first peak can be assigned to transitions to some orbitals composed of Cu3d and Cu4s orbitals and 2p atomic orbitals of light atoms, and the third peak can be assigned to 1s electron transition transmitted to $7a_u$ orbital composed mainly of Cu4p atomic orbital.

4. Discussion

For the diazadioxa and tetraazacopper(II) complexes, from the reduction potential values in Table1, the XANES spectra in Fig.2, and the XANES peak positions in Table2, the third XANES peaks at 8983-8986eV shift to the lower energy side as the reduction potential values become more negative. This XANES shifts for the tetraaza complexes are more remarkable than those for the diazadioxa complexes. In general, the coordinating ability of N donor atom to a transition metal ion is larger than that of O donor atom, and the electron-attracting effect of O atom is stronger than that of N atom. Therefore, the electron donating ability of N donor atom in the ligand to a central copper(II) atom is affected more strongly by the presence of substituent groups in the ligands than that of O atom. From the probability of 1s electron transition for the tetraaza complexes given in Table5, it is evident that the XANES shift of the third peak arises from the change of the probability of the 1s electron transition to some molecular orbitals rather than from the energy shift. For reasonable assignments of XANES peaks the above mentioned careful discussions should be needed. The peak shifts in XANES spectra give information on the electronic transfer from ligand to central metal in metal complexes.

As is seen in Fig.1, the nitro group within complex **C** is attached to the conjugated propylene chain, but that within complex **B** is not. There is a aromatic ring among them. Complex **C** has four methyl groups as an electron-releasing group. Thus, concerning the

Table 5. Electron Transition Probability from 1s Orbital and Component Ratio of Atomic Orbital Buildup a Molecular Orbital

Complex A (Sym. C_{2i})

E[1]	O[2]	M[3]	Atomic orbital (rate[4]) / %							
			1 Cu	2 N	3 N	4 C	5 C	7 C	8 C	9 C
-7.751	1.05	$28a_1\downarrow$	3d(66)			2p(11)	2p(13)			
-7.677	0.92	$28a_1\uparrow$	3d(55)			2p(17)	2p(14)			
-4.848	0.69	$26a_2\downarrow$	3d(10)	2p(29)		2p(16)	2s(12)			
							2p(13)			
-4.648	0.74	$26a_2\uparrow$		2p(29)		2p(14)	2s(14)			
							2p(16)			
-4.335	1.40	$9b_1\downarrow$	4p(13)	2p(18)		2p(28)		2p(14)		2p(14)
-4.270	1.51	$9b_1\uparrow$	4p(14)	2p(19)		2p(25)		2p(13)		2p(13)
-1.430	3.79	$10b_1\downarrow$	4p(30)						2p(24)	2p(19)
-1.312	4.08	$10b_1\uparrow$	4p(31)						2p(24)	2p(18)
-0.180	8.41	$11b_1\downarrow$	4p(54)		2p(13)					2p(17)
-0.110	8.30	$11b_1\uparrow$	4p(53)		2p(14)				2p(10)	2p(18)
0.387	0.42	$32a_1\downarrow$	4s(62)							
0.482	0.40	$32a_1\uparrow$	4s(62)							

Complex B (Sym. C_{2i})

E[1]	O[2]	M[3]	Atomic orbital (rate[4]) / %							
			1 Cu	2 N	4 C	5 C	9 C	10 C	11 C	12 C
-6.514	2.47	$46a_1\uparrow$	3d(42)				2p(15)			2p(22)
-6.272	2.12	$48a_1\downarrow$			2s(11)					
						2p(41)				
-6.158	3.20	$48a_1\uparrow$	3d(22)		2p(25)					2p(12)
-2.197	8.80	$15b_1\downarrow$	4p(69)			2p(10)				
-2.107	8.79	$15b_1\uparrow$	4p(69)			2p(10)				
-0.420	2.78	$17b_1\downarrow$	4p(18)		2p(17)			2p(14)	2p(15)	
-0.315	2.93	$17b_1\uparrow$	4p(19)	2p(11)	2p(20)			2p(13)	2p(11)	
0.288	9.05	$50a_1\downarrow$	4s(53)							
0.410	9.03	$50a_1\uparrow$	4s(53)							

Complex C (Sym. D_{2h})

E[1]	O[2]	M[3]	Atomic orbital (rate[4]) / %				
			1 Cu	4 C	5 C	6 C	8 O
-8.469	1.11	$22b_{1u}\uparrow$	3d(37)		2p(24)		2p(20)
-8.220	1.87	$23b_{1u}\downarrow$	3d(38)			2s(11)	2p(26)
						2p(16)	
-7.390	1.10	$24b_{1u}\uparrow$	3d(21)		2p(46)		
			4s(14)				
-7.366	1.09	$24b_{1u}\downarrow$	3d(20)		2p(49)		
			4s(15)				
-1.057	6.11	$9a_u\downarrow$	4p(73)	2p(12)			
-1.038	6.20	$9a_u\uparrow$	4p(74)	2p(11)			

Complex D (Sym. D_{2h})

E[1]	O[2]	M[3]	Atomic orbital (rate[4]) / %				
			1 Cu	2 N	3 O	4 C	5 C
-8.379	1.72	$17b_{1u}\downarrow$	3d(58)				2p(28)
-8.283	2.18	$17b_{1u}\uparrow$	3d(69)				2p(21)
-7.337	1.85	$18b_{1u}\downarrow$	3d(37)			2p(10)	2p(31)
				4s(12)			
-7.175	1.30	$18b_{1u}\uparrow$	3d(24)			2p(20)	2p(32)
-6.958	1.07	$14b_{2u}\downarrow$		2p(18)			2p(55)
-6.726	1.07	$14b_{2u}\uparrow$		2p(16)			2p(58)
-0.952	11.86	$7a_u\downarrow$	4p(67)		2p(13)	2p(15)	
-0.895	12.05	$7a_u\uparrow$	4p(67)		2p(13)	2p(16)	

1) energy level of molecular orbital, 2) electron transition probability, 3) symmetry symbol (↑ ;up-spin, ↓ ;down-spin), 4) molecular component ratio of atomic orbitals buildup a molecular orbital.

electron donating abilities of each ligand to each central copper(II) ion the electron-attracting effect of the nitro group in complex **B** is probably weakened by the presence of the aromatic ring, but that of the nitro group in complex **C** is weakened by the electron donating effect of the four methyl groups. As an aromatic ring in general has electron-attracting ability, the electron donating ability of the ligand in complex **C** is expected to be stronger than that in complex **B**. This is supported from the result of the present molecular orbital calculations, that is, the calculated atomic-charge values of the central copper(II) ion suggest that the electron donating ability for complex **B** is stronger than that of complex **C**.

For four tetraazacopper(II) complexes, the atomic-charge values on the central copper(II) ion obtained from the results of the molecular orbital calculations indicate that the electron donating ability of each ligand to each central copper(II) ion increases in the order of **A<B<C<D**, and the electron attracting ability of Cu-N bonds increases in the order of **A<B<C<D**. Nevertheless, the atomic-charge values on the coordinating N donor atoms are similar for four complexes. The results of the calculations indicate that desirous electrons are supplied to the coordinating N donor atoms from the conjugated chelate system in the complexes. Resultingly, the XANES shift of the third peaks in the XANES spectra are correlated not with the atomic-charge of the coordinating N donor atoms immediately but with both atomic-charge on the central copper(II) ion and the Cu-N bond-charge. A similar correlation can be expected for the second XANES peak assignable to the 1s electron transition to molecular orbitals composed mainly of 2p atomic orbital of the ligand, and the third XANES peak due to the some transitions from 1s orbital to molecular orbitals composed mainly of 4s and 4p atomic orbitals of the central copper atom. The fact that the second peak does not shift more significantly than the third peak can be explained in term of the electron transition to the coordinating N donor atom.

When copper(II) complexes of a certain ligand with and without a substituent group are formed, it is clear that their electron structures rearrange. The difference of the electronic structures between these complexes, thus, can be detected as the changes of the energy positions and/or the shapes of the second and/or third peaks in their XANES spectra.

The assignments of the XANES spectra in this report give very useful information to discuss these XANES spectra and also others. The discussion on the electronic state and structure of macrocyclic copper(II) complex has been done from the point of organoelectronic theory. It is very important for the studies on the macrocyclic complexes to determine the electronic state of the complex by X-ray absorption spectroscopy.

References

1) M. Fujiwara, *Doctoral Thesis, Osaka University*, **1987**.

2) T. Miyanaga, I. Watanabe, S. Ikeda, K. Tashiro, and T. Fujikawa, *Bull. Chem. Soc. Jpn.*, **61**, 3199 (1988).

3) N. Kosugi, H. Kondoh, H. Tajima, and H. Kuroda, *Chem. Phys.*, **135**, 149 (1989).

4) H. Adachi and K. Taniguchi, *J. Phys .Soc. Jpn.*, **49**, 1944 (1980); H. Nakamatsu, T. Mukoyama, and H. Adachi, *Chem. Phys.*, **143**, 221 (1990).

5) H. Adachi, M. Tsukada, and C. Satoko, *J. Phys. Soc. Jpn.*, **45**, 875(1978); M. Valli, S. Matsuo, H. Wakita, T. Yamaguchi, and M. Nomura, *Inorg. Chem.*, 35, 5642 (1996).

6) G. S. Patterson and P. H. Holm, *Bioinorg. Chem.*, **4**, 257 (1975).

Scattered-wave description of inner-shell processes in small molecules and clusters

EBERHARD HARTMANN and CHRISTA LAUTERBACH

Institute of Surface Modification,
Permoserstr.15, D-04303 Leipzig, Germany

Abstract

Due to the muffin-tin approximation of the local multi-centre potential, the applicability of the scattered-wave (SW) method is limited to relatively small and high-symmetry clusters and molecules. On the other hand, it is the prerequisite for generalizing the in-out integration scheme of atomic one-electron wavefunctions to the multi-centre case. This approach furnishes the multi-centre electronic structure in a particular atom sphere in its single-centre representation. Thus atomic transition-matrix elements can be readily rescaled in terms of near-nucleus electron amplitudes.

The potential of the SW approach to systematize inneratomic properties and processes can be easily illustrated by reconsidering chemically induced nuclear lifetime variations which, among others, are of relevance to the calibration problem of Moessbauer isomer shifts. Highly excited atom states carrying single or multiple vacancies in inner shells form another promising subject of SW simulations. In the latter case the results of a DV-Xα study of the K-shell x-ray satellite intensities of metal fluorides can be used for a comparative assessment of both methods.

ADVANCES IN QUANTUM CHEMISTRY, VOLUME 29

0065-3276/97 $25.00

1 Application of the scattered-wave method in inner-shell physics

In view of numerous advanced approaches to the electronic structure, with the discrete-variational (DV) method as a prominent representative, the question inevitably arises about the actual assessment of customary descriptions as they are provided, among others, by the $X\alpha_{MT}$-SW calculations [1]. With regard to the latter method, it is particularly the muffin-tin (MT) approximation of the local potential which limits the applicability of the SW codes to relatively small and high-symmetry molecules and clusters. On the other hand, this locally increased symmetry is the necessary prerequisite for the functioning of the scattered-wave method: In each particular atom sphere, the determination of a one-electron wavefunction starts with a radial outward integration from the nucleus to the sphere boundary. Then, with the aid of analytical partial solutions in the intersphere region (where the potential is assumed to be a constant average), an attempt is made to match all the partial waves at the given test energy. Thus, the multiple-scattering approach is highly reminiscent of Hartree's atomic in-out integration scheme where the "partial waves" are matched at the classical turning point. Therefore the SW description can be considered the most obvious multi-centre generalization of the aforementioned atomic single-centre approach.

The single-centre representation of the multi-centre one-electron wavefunctions in each atom sphere is of particular advantage in a study of properties or processes where the investigator's attention is focused on the near-nucleus region of the atom under consideration: A particular atom in its environment - such emphasis is made either if vacancies are accommodated in localized states of inner shell, or if short-range nucleus-electron interactions govern the processes under consideration. Thanks to the universal radial shape of both atomic single-centre and molecular multi-centre electron wavefunctions in the near-nucleus formation region of the relevant interaction integrals, all that has to be done is to rescale atomic matrix elements in terms of these nucleus-near amplitudes. This empirical approach has been verified both for nucleus-electron interactions [2] and vacancy-rearranging processes [3]. From the very beginning, this rescaling procedure comprises interatomic contributions which in LCAO studies originate from those orbitals which are centered at neighbouring atoms. These interatomic contributions efficiently compete with intraatomic transition probabilities [4] and, hence, considerably complicate the treatment. In order to maintain the same description level as in LCAO treatments, the angular-momentum expansion in SW studies must be extended to higher l values, which suggests the use of a symmetry-adapted basis set of partial waves. At first sight, this seems to require too much effort but it is largely repaid by the resulting clearness both in the problem formulation and the analysis of results. Moreover, thanks to this extended basis of l-type partial waves, polarizational charge fractions such as d- or even f-type valence charge fractions on main-group atoms are taken into consideration from the onset. Admittedly, SW treatment also involves a disadvantage: The one-electron energies are searched as

the zeroes of the scattering-matrix determinant and tremendous complications can arise with sign change through poles or with nearly degenerate energy levels.
Furthermore, vacancies can be easily introduced by just choosing appropriate occupation numbers. An early analysis of satellite and hypersatellite x-ray transitions [5] has shown that transition states, midway between initial and final states with averaged occupation numbers, make it possible to account for electron relaxation. This physical phenomenon occurs above all in configurations carrying multiple vacancies, irrespective of the way in which the latter have been produced: either directly in the strongly ionizing ion-atom collisions or in the course of the vacancy-multiplying deexcitation cascade following single-vacancy creation by e.g. inner-shell photoionization.
Naturally, the localization of the formation region of the interaction integrals in the vicinity of the nucleus brings relativity into play. As the atomic treatment of the interactions is carried out at a relativistic level, and rescaling of the matrix elements is done non-relativistically, a comparison of near-nucleus relativistic wavefunctions with non-relativistic ones enables the investigator to account for relativity in a fashion reminding of the Shirley-factor technique. This technique, however, does not comprise direct relativistic effects on chemical binding [6]. Fully relativistic SW variants exist (e.g., see [7] and refs. cited therein) but semirelativistic (SR) prescriptions (e.g., see /8/) do not only direct the computational effort towards the most essential effects but, moreover, provide a clearer and denser idea of the subject under consideration.
Further extension of methodological discussion seems quite pointless here. Instead, the usefulness of the SW method should be exemplified by a brief review of some of its applications to environmental effects on nucleus-shell interactions and the processes of creation and decay of inner-shell vacancies.

2 Environmental effects on the nucleus - electron interactions

In the seventies, investigations of the chemically induced variations of nuclear decay rates were established as a fruitful field of experimental research [9]. The main deficiency, however, was the insufficient theoretical understanding of experimental findings, precluding their efficient use in solving the Moessbauer isomer-shift (IS) calibration problem and deriving full information on higher-order nuclear processes. At that time pertinent modelling was mainly done within atomic single-centre descriptions in terms of effective charges or effective configurations. Thus, considerable effort has been invested in inferring effective occupancies from a great block of experimental data. But this approach of "configuration trajectories" [10] must inevitably fail if minor polarization of the valence electron cloud dominates the environmental effect considered.
For illustration, let us consider the internal conversion (IC) of ^{99m}Tc: In this atomic transition, by the E2 symmetry of the nuclear deexcitation, p-type electrons are

much more efficiently involved than d electrons. Therefore, a polarization of the 4d valence band, leading to a stabilization of a minor p-type valence charge fraction, could prevail over the more obvious effect of a d-type valence charge delocalization. With the aid of the SW method we have been able to devise the first, to our knowledge, explicit multi-centre picture of the lifetime variations of the IC (^{99m}Tc), with this particular IC nuclide being embedded in tetrahedral oxy-complex and octahedral halogen-complex ions as well as in the metallic state ([2], cf. also [11]). Indeed partial contributions to the IC lifetime variations were found which stem from valence-shell polarization (p_{val}), valence charge delocalization (d_{val}) and reorganization of the upper core (3p, 3d, 4p). Fortunately, in [2] we did not confine ourselves to publishing the largely integral lifetime variations but, in addition, we reported the spectroscopic data which were amenable to experimental verification by conversion electron spectroscopy. The satisfying agreement of experimentally recorded conversion electron spectra with our SW predictions encouraged the spectroscopists to employ the SW method (SR variant) in further interpretation of their measured spectra as well [12].
An analogous SW analysis of chemically induced lifetime variations has been carried out for the nuclear electron capture (EC) for ^{54,51}Cr [13]. The small collection of theoretical and experimental data in table 1 discloses the urgent need for further experimental research.

Table 1: Composite of our own SW data [14] on the chemically induced variations of the EC decay constant λ of ^{51}Cr with the corresponding SR-SW results [13] (in parentheses, the *Bahcall correction factors* have been introduced by us, for the sake of comparability).

$\Delta\lambda / \lambda$ [EC(^{51}Cr)] $\times 10^4$	3s	s_{val}	total
Cr_2O_3 / $CrCl_3$	1.5	1.0	2.5
CrO_4^{2-} / $CrCl_3$	1.9 (.9×*1.23*)	3.3 (2.6×*1.34*)	5.2 (4.6) / 5.3±2. [15]

Theoretically derived nucleus-near electron densities are of great relevance to the calibration problem of Moessbauer IS which provide a measure of the product of the relative change $\Delta R/R$ of the nuclear charge radius and the electron contact densities. To facilitate a conversion of IS data to density units, inferring contact densities from other experimental sources still represents the unrivalled calibration scheme. Among these experimental approaches, the measurements of EC lifetime variations seem to yield the most direct information on contact densities. However, EC lifetime could be potentially altered, in addition to changes in electron contact densities, through varying electron binding energies as well as exchange and overlap factors [15, 16]. SW simulations of various clusters carrying Sn, Te and I

atoms, enabled systematization of all relevant experimental EC, IC and IS data. For a more detailed illustration of the latter I case, fig. 1 shows the calculated relative differences of the I electron contact densities ρ (second scale) together with measured Moessbauer isomer shifts IS (top). The correlation between these values furnishes the alteration $\Delta[r^2]$ of the mean-square nuclear charge radius occurring in the isomeric transition of ^{129}I. The lower part of fig.1 likewise reveals a rather satisfying agreement between the SW predictions for the EC decay constant variations $\Delta\lambda/\lambda$ and the ratio of conversion electron emission α_{val}/α_{4s} which have been measured for the nuclides ^{123}I, ^{125}I and ^{129}I, respectively.

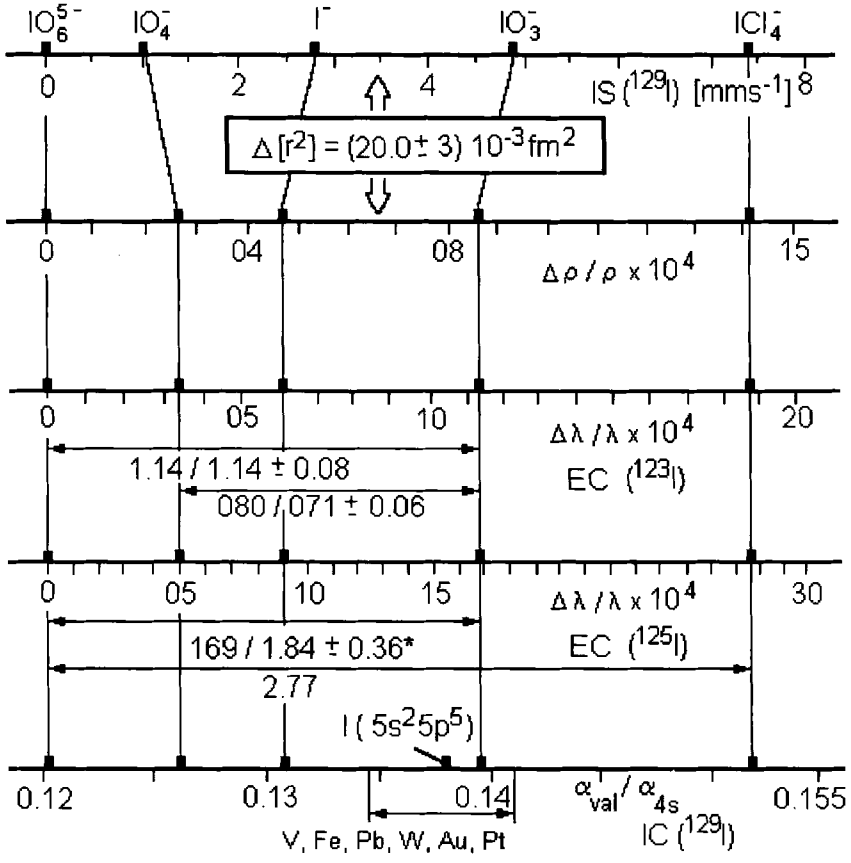

Fig. 1: Systematics of electron contact densities and pertinent properties; as for details, cf. [17].

In this systematization the contributions to EC lifetime variations through electron binding energies ΔE_i and exchange and overlap corrections ΔB_i were ignored. The results did not only encourage a proposal of new "best values" $\Delta R/R$ for the Moessbauer nuclides ^{119}Sn, ^{125}Te and $^{127,129}I$ [17] but, moreover, led to a reconsideration of the presumable environmental effects on EC lifetime through binding-energy shifts and varying exchange and overlap: For instance, the improved analysis of the Bahcall factors B_i [18] directs the attention to shake which, admittedly, is small in the main K capture channel [19]. Electron capture from outer shells, however, is connected with a higher shake probability, and the ΔB_i effect has been successfully correlated with shake. Thus, the SW treatment of IC and EC decay variations has proved its systematizing potential and, in order to devise a first picture of qualitatively new phenomena, application of the simple SW method still remains recommendable. For instance, nuclear excitation by electron transition (NEET) has recently gained some practical relevance [20], and the potentially pronounced environmental effects on this particular atomic transition might represent a promising subject of further SW studies. Discussion of the nucleus-electron interactions, however, is now dominated by more sophisticated methods: augmented plane wave (APW) [21] for crystalline samples and DV-Xα calculations for molecules; in our context the self-consistent charge (SCC-Xα) routine is worth mentioning as a strongly simplified and very efficient derivative of the DV description [22]. Obviously, introduction of empirical parameters into schemes devised on the basis of first principles seems to represent a wide-spread recipe for extending the applicability to larger systems (e.g., as for density functional schemes cf. [23]).

3 Creation and decay of highly excited atom states carrying inner-shell vacancies

3.1 Effect of excitation mode and chemical surroundings on single-hole filling

Although forming a homogeneous scattering process, the fate of highly excited atom states can be approximately described in the consecutive phases of ionization, relaxation and decay. Chemical surroundings and the special mode of excitation can jointly cooperate to affect the atom considered in each of these three stages, thus bringing on pronounced differences in the measured deexcitation spectra. There are numerous x-ray and electron spectroscopic methods with single or, at the utmost, two vacancies in the pertinent initial and final states: XES, XAS (XANES), AES, etc. Here, due to the relatively small inneratomic positive charge, the relaxation phenomena are less pronounced and, consequently, application of the SW method appears less fruitful than in the discussion of (satellite) transitions occurring in configurations carrying several vacancies. Nevertheless, some interesting results have been obtained: (i) The pronounced difference in the K_β/K_α x-ray

intensity ratio $R_{\beta\alpha}$, as it has been measured for 3d emitter atoms after photoionization and EC, could mainly be traced back to the excess 3d electron of the EC mother atom and, in addition, to different shake probabilities [24] (cf. [19] for the latter aspect). (ii) As for the chemical effects on the K x-ray deexcitation we found a pattern which is highly reminiscent of the variations of IC (^{99m}Tc) as discussed above: Polarization of the upper valence states of prevailing d-type character leads to varying admixtures of p character and a resulting direct enhancement of the Kβ line ($K\beta_5$, enlisted as p_{val} in table 2). Varying delocalization of d-type valence charge leads to contraction of the upper core (particularly 3p).

Table 2: Variations (percentages) of the K x-ray intensity ratio $R_{\beta\alpha}$ for some Cr and Mn compounds ([14], with the SR-SW results [25] again in parentheses).

$\Delta R_{\beta\alpha}$	3p		p_{val}		total			
Cr_2O_3/CrO_4^{2-}	.0	(-.1)	-.8	(-1.1)	-.8	(-1.2)	-2.2±2. [26]	-11.6±1.8 [27]
$CrCl_3/CrO_4^{2-}$	-1.0	(-2.0)	-2.5	(-1.6)	-3.5	(-3.6)	-2.7±2. [28]	
$Cr(CN)_6^{3-}/CrO_4^{2-}$	-3.1		2.1		-.9			
$Cr(CO)_6/CrO_4^{2-}$	-3.8		1.8		-1.9			
MnO/MnO_4^-	1.1	(.2)	-3.7	(-2.6)	-2.7	(-2.4)		
MnS/MnO_4^-	.6	(-.5)	-3.7	(-2.9)	-3.2	(-3.4)		
$MnCl_2/MnO_4^-$	.7		-3.1		-3.7		-2.2±2. [26]	

Although this picture was found to be in a satisfying agreement with SR-SW calculations, further extension of these studies appears quite pointless now because more accurate DV-Xα modelling of this topic has been carried out in the mean time (e.g., see [29]). The application of the latter method could lead to a final decision as to the extent of cooperation between polarization (p_{val}) and core reorganisation (3p) in shifting the ratio $R_{\beta\alpha}$, and as to whether the interpretation of these variations as pure valency effects [27] is on safe grounds.

The SW method could also make a valuable contribution to an understanding of XANES spectra (e.g., the symmetry effects in high-symmetry molecules. [30]), and more specialized versions are still within the pertinent methodical standard [31]. Our simple dense SW approach, however, is at present only efficient in devising some group addidivity concepts for the photoabsorption spectra of complex compounds [32]. In view of the high precision of *ab initio* calculations for relatively small molecules [33] and the DV-Xα method for molecules and solids [34], further application of the standard SW method requires special justification. An analogous assessment of methods also applies to the interpretation of Auger spectra [35].

3.2 Vacancy-induced variation of valence-electron structure

3.2.1 Covalent systems

Satellite and hypersatellite spectra were expected to contain enhanced chemical information because in the pertinent KL^n and K^2L^n vacancy configurations the valence electrons, thanks to reduced electronic screening, could have a particularly strong effect on energies and intensities of the satellite lines. For Si emitter atoms in prevailing tetrahedral coordination, for instance, the valence states form three separate bands, V_1 ($1a_1$, $1t_2$), V_2 ($2a_1$, $2t_2$) and V_3 ($1e$, $3t_2$, $1t_1$) which reveal a pronounced atomic-orbital mixture in the ground state. If Si K- and L-shell vacancies increase electron binding on the central Si atom, a marked purification of the electron orbitals takes place: $1a_1$ and $1t_2$ attain pure Si 3s and 3p character, respectively (see fig. 2).

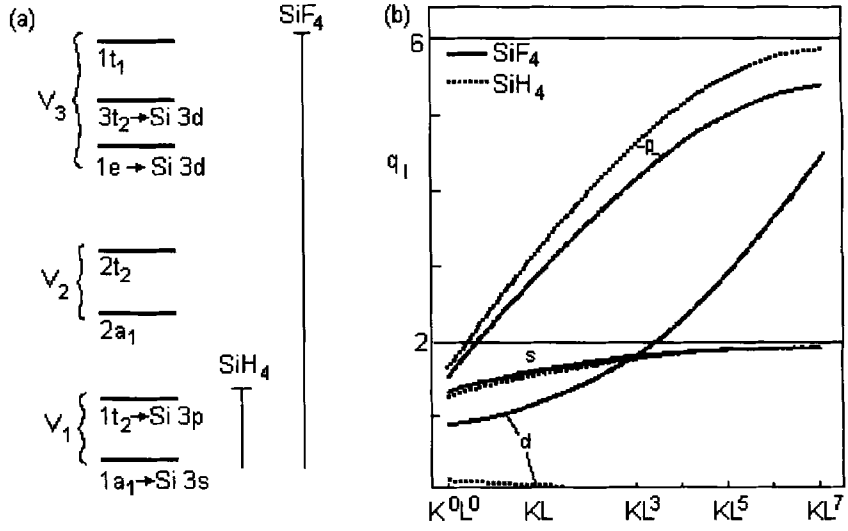

Fig. 2: Schematic illustration of the valence electron structure of light and heavy Si-bearing molecules (a) and the Si l-type valence charge fractions in dependence on inner-shell vacancy configuration (b); cf. [36].

The V_2 states transform into ligand states (lig. p_π) and, finally, the lower two V_3 states ($1e$ and $3t_2$) are converted into Si 3d states. In retrospect, this finding seems quite evident: The valence electrons, under joint binding force of the atomic charge Z and the n_v vacancies, attain a valence electron structure of a correspondingly heavier ($Z+n_v$) atom. These pseudo-alchemical features in the interatomic relaxation obviously blur the chemical differences occurring in the ground state of the covalent target system and

thus inevitably the question arises about the reasons for the chemical effects on heavy-ion induced x-ray satellite spectra. This leads one to reconsider dynamic screening of the projectile which, in dependence on the electron density of the target, alters the charge state of the projectile and, hence, its ionizing potential. Furthermore, in a recent atomic generalization [37] of the multi-centre case studies, an empirical approach [38] has been verified according to which single-hole standard K x-ray fluorescence yields were used to infer ionization cross sections or elemental abundance from heavy-ion-induced x-ray satellite spectra. The differences found between the electron structures of atoms (C, Si), light molecules (CH_4, SiH_4,) and many-electron systems (CF_4, SiF_4) comprise the aspect of the significantly different distribution of the valence electrons over the valence states: $2s^2 2p^2$, $1a_1^2 1t_2^6$ and $1a_1^2 1t_2^6\ 2a_1^2 2t_2^6\ 1e^4 3t_2^6 1t_1^6$, respectively. This should have consequences for non-radiative filling through the C KLL Auger two-electron transitions: One-centre estimates [39] furnished the Auger probabilities (C 1s linewidths) 56, 96 and 63 meV for the sequence C, CH_4, and CF_4, respectively, thus reflecting the electronegativity aspect. However, the corresponding multi-centre results (53, 75, 88 meV [40]) reflect the statistical distribution effect in a more accentuated way. In experimental determinations of the 1s linewidths tremendous difficulties are encountered. Therefore, further theoretical analysis should be done, using more accurate methods (e.g. DV-Xα). However, it should be mentioned that the experimental Si 2p linewidths in the SiX_4 molecules (X=H, F) [41] speak in favour of the multi-centre results [40].

Modelling the vacancy-multiplying deexcitation cascade following Ar K-shell photoionization, we obtained the charge stage spectra with slight improvements as compared with the literature standard (cf. [42] and refs. cited therein). However, a much more detailed validation of the theoretical data becomes feasible if consecutive decay channels are investigated by spectroscopic means. Indeed, Ar $L_{23}VV$ Auger spectra recorded after K-shell photoionization [43, 44], revealed a complicated satellite structure which, both by energy and intensity, could be labelled according to the pertinent spectator-vacancy configurations [42, 44]. An extension of these $L_{23}VV$ Auger satellite studies to S, H_2S and SF_6 could provide an assessment of the environmental effects on these Auger satellite spectra [42]: A growing broadening of the satellite structures was obtained by the convolution of a growing number of valence states and, in case of SF_6, participation of d-type valence electrons leads to increased intensities of higher-energy satellite structures. These chemical effects were found to reveal poor specific information on the chemical state so that they provide only a weak basis for chemical speciation.

3.2.2 Ionic systems

Despite the strong environmental effects on satellite spectra of covalent systems, SW calculations on next-neighbour clusters of ionic alkaline and alkaline earth fluorides have been carried out with rather modest expectation. Then, we were surprised to be

faced with strong covalent effects which occurred when the ionic F levels came to cross the cationic levels (cf. fig. 3).

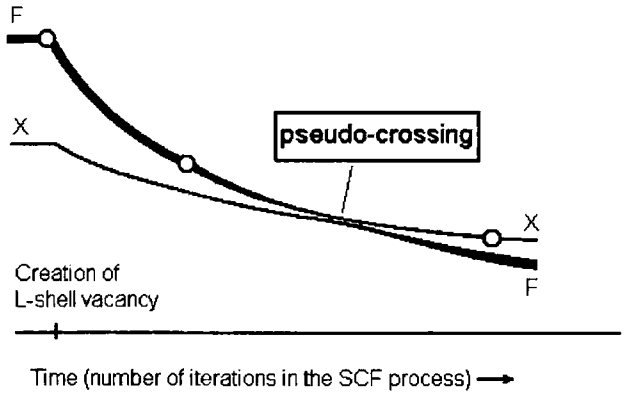

Fig. 3: Schematic illustration of adiabatic pseudocrossing with character exchange (occurring between anionic (F) and cationic (X) levels; cf. [36]).

Having in mind that two levels of the same symmetry, when driven by a single-parameter force under adiabatic conditions, are not allowed to cross in their approach (see basic sources, e.g. [45]), various types of level-crossing effects appear conceivable: (i) A growing nuclear charge Z of a free emitter atom can act as such a single-parameter drive, (ii) for an atom which is embedded in an ionic solid, in a series of either central atoms or ligands, resonant level-crossing conditions can be adjusted through a suitable combination of atomic numbers ($Z_{c.a.}$, Z_{lig}), and (iii) for a given ($Z_{c.a.}$, Z_{lig}) combination, level matching can be achieved by increasing electron binding at the central atom through a suitable number of vacancies.

As an example of resonance effects (i) the resonant sharp KM_1M_{45} intensity peaking can be quoted which occurs at Z=63 where the pertinent two-hole levels come to cross [46]. Resonant effects (iii) were addressed in terms of *resonant electron transfer* [47], *temporary covalency* [48], *pseudo-crossing* [49] and *avoided crossing* [50]. In the SW simulation [49] of the multiple-vacancy states F KL^n in ionic compounds, a transitory covalency was found to achieve the same pseudo-alchemical transmutation as it is produced in covalent systems by charge flows via covalent bonds. This transmutation even leads to an F M-shell population which even gives rise to a satellite (KL^n) Kβ x-ray emission [51]. The strong effects of the multiple vacancies produced in ion-atom collisions, encouraged re-consideration of the effect of the common "methodical" (non-spectator) vacancies occurring in the initial and/or final states of single-hole filling. In ionic fluorides we found resonant effects on the F K x-ray fluorescence yield and F KLL Auger spectra [3], with the latter being experienced in covalent satellites observed in KF and SrF_2 [52]. In the context of the effect of active vacancies on the valence-

electron structure, a DV-Xα study [53] is of particular interest: Even spin-unrestricted calculations had to be carried out in order to trace the violation of the Van Vleck theorem by the $K\alpha_1$ linewidths of octahedrally coordinated Fe atoms back to an influence of the Fe K-shell vacancy on valence-electron structure.

In the context of creation and decay of inner-shell vacancies no explicit evidence has been given so far in literature for the possibility (ii) to achieve resonant level matching. A recent DV-Xα analysis of the F KL^n x-ray satellite emission from various metal fluorides XF_2 (X = Mg. Fe, Co, Ni, Zn) [54], however, seems to contain this aspect: For a methodological comparison we reconsidered this matter with the aid of the SW approach and represented these metal fluorides by clusters which were further simplified as compared with [54] ($FX_3(D_{3h})$-cluster instead of C_{2v}). As a result of this slight modification, the F $2p_\sigma$ (strongly interacting with X $3d_\sigma$ in the FX_3 plane) and the weakly interacting F $2p_\pi$ electrons now transform according to different irreducible representations (e′ and a_2'', respectively), and the σ-type resonance effects between the upper e′ state of the Zn 3d band and the e′ from F 2p become visible in the ground state (left-hand side in Fig. 4).

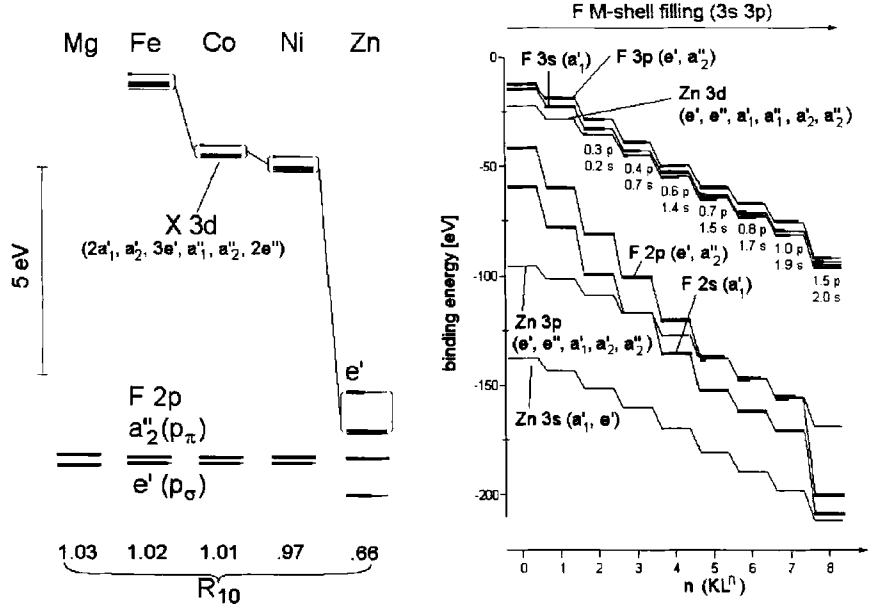

Fig. 4: Valence electron structure of various metal fluorides XF_2, represented by $(FX_3)^{5+}(D_{3h})$-clusters (on the left) and of ZnF_2 in dependence on growing number of F K- and L-shell vacancies.

In contrast to the DV-Xα ground-state discussion, outer-shell vacancies are now created through a two-step mechanism: In a first step they are accommodated with approximately equal probabilities in both e´ resonance levels of a mixed F and Zn character. Then, in the course of the relaxation occurring in response to stronger binding due to vacancies, the two resonance states again separate and are transformed back into F 2p and Zn 3d (cf. left part of Fig. 4) and, in effect, the e´ vacancies are transferred either to F or Zn (from lowest and highest e´, respectively).
Thus, the SW treatment furnishes an idea of the F KL^n x-ray emission, in which resonance effects (ii) in the ground state cooperate with relaxation in the K-shell ionized state to reduce the KL^1/KL^0 x-ray intensity ratio R_{10} in the series of metal fluorides. It would be interesting to fit the SW and the DV-Xα results into a convergent idea of the environmental effects considered. By the way, an increasing number of vacancies produces resonance effects (iii) between F 3s, 3p and Zn 3d, leading to a considerable F M-shell population (cf. right part of Fig. 4). Note that this M-shell population, thanks to more weakly bound X 3d for the lighter cations, would occur in a more pronounced way and already at a lower satellite order n, thus giving rise to stronger effects on satellite intensity distribution recorded after the impact of more strongly ionizing heavy-ion projectiles.

4 Methodological conclusion

Thanks to its unambiguous single-centre representation of the electron wavefunctions in the sphere of the atom considered, the simple and dense SW approach allows the application of matrix-rescaling techniques and evades the difficulties of interatomic contributions. Moreover, owing to the physical transparency and simplicity, the SW method can easily be applied by experimentalists at a relatively low level of specialization, thus ensuring close proximity between theory and experiment. Therefore, in the past the SW method has shown special usefulness in systematizing environmental effects on localized inner-shell processes. As the comparative DV-Xα and SW treatments of the metal fluorides XF_2 show, the SW method can well compete even with advanced approaches in an initial stage of research where the basic features of qualitatively new inner-shell phenomena are to be delineated. In a more profound discussion of refined details, either with respect to small and complicated chemical differences between measuring samples or to spectral details such as multiplett-coupling or multielectron effects, it is increasingly dominated by more elaborate methods such as DV-Xα and, for small systems, by *ab initio* calculations.

The authors thankfully acknowledge financial support by *Deutsche Forschungsgemeinschaft* through *Bonn SFB 334* and stimulating discussions with many colleagues.

References

[1] J. W. D. Conolly and K. H. Johnson *Chem. Phys. Lett.*, vol. 10, p. 616, 1971;
D. A. Case *Ann. Rev. Phys. Chem.*, vol. 33, p. 151, 1982.

[2] E. Hartmann, R. Der, and M. Nagel *Z. Physik A*, vol. 290, p. 349, 1979;
E. Hartmann and G. Seifert *phys. stat sol. (b)*, vol. 100, p. 589, 1980.

[3] E. Hartmann and R. Der *J. Phys. B*, vol. 21, p. 1751, 1988.

[4] F. P. Larkins and T. W. Rowlands *J. Phys. B*, vol. 19, p. 591, 1986.

[5] K. D. Sen *J. Phys. B*, vol. 11, p. L577, 1978.

[6] J. P. Desclaux and P. Pyykkö *Relativistic theory of atoms and molecules*, Pergamon, Oxford, 1981.

[7] C. Y. Yang *Relativistic Effects in Atoms, Molecules and Solids*, (G.L. Malli, ed.), Plenum, New York, 1983.

[8] V. Heera, G.Seifert, and P.Ziesche *J. Phys. B*, vol. 17, p. 519, 1984; *phys. stat. sol. b*, vol. 118, p. K107, 1983; vol. 119, p. K1, 1983.

[9] K.-P. Dostal, M. Nagel, and D. Pabst *Z. Naturforsch.*, vol. 32a, p. 345, 1977.

[10] L. I. Molkanov, Yu. S. Grushko, I. M. Band, G. A. Shadrina, and M. B. Trzhaskovskaya *Zh. Eksp. Teor. Fiz.*, vol. 70, p. 2218, 1976.

[11] O. Dragoun *Adv. Electron. Electron Phys.*, vol. 60, p. 1, 1983.

[12] V. N. Gerasimov, A. G. Zelenkov, V. M. Kulakov, V. A. Pchelin, M. V. Sokolovskaya, A. A.Soldatov, and L. V. Chistyakov *Zh. eksp. teor. fiz.*, vol. 82, p. 362, 1982; vol. 86, p. 1169, 1984.

[13] I. M. Band, A. P. Kovtun, and M. B. Trzhaskovskaya *Izv. Akad. Nauk SSSR*, vol. 47, p. 2137, 1983.

[14] E. Hartmann *ZfI-Mitteilungen*, vol. 73, p. 85, 1983.

[15] S. Kakiuchi and T. Mukoyama *Bull. Inst. Chem. Res.*, Kyoto Univ., vol. 59, p. 27, 1981.

[16] K. Makariunas *Phys. Lett.*, vol. 91A, p. 249, 1982.

[17] E. Hartmann and W. Winkler *Hyperfine Interactions*, vol. 61, p. 1435, 1990.

[18] E. Vatai *Nucl. Phys. A*, vol. 402, p. 541, 1970.

[19] T. Mukoyama and Y. Ito *Nucl. Instr. Meth. B*, vol. 87, p. 26, 1994.

[20] F. F. Karpeshin, I. M. Band, M. B. Trzhaskovskaya, and M. A. Listengarten, *Phys. Rev. Lett. B*, vol. 372, p. 1, 1996.

[21] D. Singh *Plane waves, pseudopotentials and the LAPW method*, Kluwer, Dordrecht, 1991;
L. Chow, P. A. Deane, J. N. Farrell, P. A. Magill, and L. D. Roberts *Phys. Rev. B*, vol. 33, p. 3039, 1986;
B. Dufek, P. Blaha, and K. Schwarz *Phys. Rev. Lett.*, vol. 75, p. 3445, 1995.

[22] M. Grodzicky, V. Männig, A. X. Trautwein, and J. M. Friedt *J. Phys. B*, vol. 20, p. 5595, 1987.

[23] G. Seifert, D. Porezag, and Th. Frauenheim *Int. J. Quant. Chem.*, vol. 58, p. 185, 1996.

[24] E. Arndt, G. Brunner, and E. Hartmann *J. Phys. B*, vol. 15, p. L887, 1982.
[25] I. M. Band, A. P. Kovtun, M. A. Listengarten, and M. B. Trzhaskovskaya *J. Electron Spectr. Rel. Phen.*, vol. 36, p. 59, 1985.
[26] Y. Tamaki, T. Omori, and T. Shiokawa *Jpn. J. Appl. Phys.*, vol. 17, p. 425, 1978; *Radiochem. Radioanal. Lett.*, vol. 37, p. 39, 1979.
[27] F. Folkmann *Nucl. Instr. Meth. B*, vol. 109/110, p. 39, 1996.
[28] A. Freyer and H.-J. Thomas, unpublished remeasurement, 1984.
[29] E. Uda, J. Kawai, and M. Uda *Nucl. Instr. Meth. B*, vol. 75, p. 24, 1993.
[30] K.-H. Hallmeier, R. Szargan, A. Meisel, E. Hartmann, and E. S. Glushkin *Spectrochim. Acta*, vol. 37A, p. 1049, 1981.
[31] P. Kizler *Phys. Lett. A*, vol. 172, p. 66, 1992;
A. V. Soldatov, T. S. Ivanchenko, S. D. Longa, Y. Iwamoto, and A. Bianconi *Phys. Rev. B*, vol. 50, p. 5074, 1994;
S. I. Zabinsky, J. J. Rehr, A. Ankudinov, R. C. Albers, and M. J. Eller *Phys. Rev. B*, vol. 53, p. 2995, 1995.
[32] A. Pantelouris, J. Hormes, C.Günther, E.Hartmann, F. Frick, and M. Jansen *J. Am. Chem. Soc.*, vol.118, p. 6954, 1996.
[33] A. Koch and S. D. Peyerimhoff *Z. Physik D*, vol. 23, p. 239, 1992; *Chem. Phys.*, vol. 172, p. 21, 1993.
[34] H. Ishikawa, K. Fujima, and H. Adachi *J. Chem. Phys.*, vol. 94, p. 6740, 1991;
I. Tanaka, J. Kawai, and H. Adachi *Phys. Rev. B*, vol. 52, p. 733, 1995;
I. Tanaka, J. Kawai, and H. Adachi *Sol. State Commun.*, vol. 93, p. 533, 1995;
T. Ikeda, Y. Ohmura, H. Nakamatsu, and T. Mukoyama *J. Phys. Soc. Jpn.*, vol. 64, p. 2669, 1995.
[35] B. Schimmelpfennig, B. Nestmann, and S. Peyerimhoff *J. Electron Spectr. Rel. Phen.*, vol. 74, p. 173, 1995;
F. O. Gottfried, L. S. Cederbaum, and F. Tarantelli *Phys. Rev. A*, vol. 53, p. 2118, 1996.
[36] E. Hartmann *J. Phys. B*, vol. 20, p. 475, 1987.
[37] C. Günther, E. Hartmann, F. von Busch, and J. Hormes *J. Phys. B*, vol. 27, p. 1055, 1994.
[38] V. Horvat, G. Sampoll, K. Wohrer, M. Chabot, and R. L. Watson *Phys. Rev. A*, vol. 46, p. 2572, 1992.
[39] M. Coville and T. D. Thomas *Phys. Rev. A*, vol. 43, p. 6053, 1991.
[40] E. Hartmann *J. Phys. B*, vol. 21, p. 1173, 1988.
[41] R. Püttner; M. Domke, K. Schulz, and G. Kaindl *Chem. Phys. Lett.*, vol. 250, p. 145, 1996.
[42] C. Günther, E. Hartmann, and C. Lauterbach *Nucl. Instr. and Meth. B*, vol. 98, p. 74, 1995; *Nucl. Instr. and Meth. B*, vol. 109/110, p. 42, 1996
C. Günther, thesis, Leipzig, 1996.

[43] S. H. Southworth, M. A. McDonald, T. LeBrun, and Y. Azuma *Proc. 16th Int. Conf. on X-Ray and Inner-Shell Processes X93*, (L. Sarkadi and D. Berenyi, eds.), Debrecen, p. 346, 1993.
[44] F. von Busch, J. Doppelfeld, C. Günther, and E. Hartmann *J. Phys. B*, vol. 27, p. 2151. 1994.
[45] L. D. Landau, E. M. Lifschitz *Theoretical Physics*, vol. 4, *Quantum Mechanics*, section 11.76, State Publ., Moscow, 1963.
[46] M. H. Chen, B. Crasemann, and H. Mark *Phys. Rev. A*, vol. 27, p. 1213, 1983.
[47] O. Benka, R. L. Watson, and R. L. Kennefick *Phys. Rev. Lett.*, vol. 47, p. 1202, 1981.
[48] D. S. Urch *J. Chem. Soc.*, Chem. Commun., p. 526, 1982.
[49] E. Hartmann *Proc. Int. Conf. on X-Ray and Inner-Shell Processes X93*, (A. Meisel and J. Finster, eds.), Leipzig, p. 297, 1984; *J. Phys. B*, vol. 19, p.1899, 1986.
[50] J. Kawai *Nucl. Instr. Meth. B*, vol. 75, p. 3, 1993.
[51] O. Benka, R. L. Watson, B. Bandong, and K. Parthasaradhi *Phys. Rev. A*, vol. 29, p. 123, 1984.
[52] O. Benka and M. Uda *Phys. Rev. Lett.*, vol. 56, p. 1667, 1986.
[53] J. Kawai, C. Suzuki, H. Adachi, T. Konishi, and Y. Goshi *Phys. Rev. B*, vol. 50, p. 347, 1994.
[54] M. Mochizuki, T. Yamamoto, S. Nagashima, and M. Uda *Nucl. Instr. Meth. B*, vol. 109/110, p. 31, 1996.

RESONANT ORBITAL REARRANGEMENT DURING F 1s IONIZATION OR DECAY PROCESS

M. Uda[a,b], T. Yamamoto[a] and T. Takenaga[a]

[a]Department of Materials Science and Engineering, Waseda University
3-4-1 Ohkubo, Shinjuku-ku, Tokyo 169, Japan
[b]Laboratory for Materials Science and Technology, Waseda University
2-8-26 Nishiwaseda, Shinjuku-ku, Tokyo 169, Japan

ABSTRACT

A new concept, a resonant orbital rearrangement ROR, has been introduced to explain an anomalously weak intensity of F Kα X-ray emitted from a K^1L^1 doubly ionized state and an unassigned M peak in KVV Auger spectra of KF. ROR has been used for explaining resonance between HOMO at K^0L^0 and LUMO at K^1L^0 states during F 1s ionization or X-ray and Auger decay processes, where K^mL^n denotes m and n vacancies on K and L shells, respectively. Molecular orbitals describing the K^mL^n state were calculated by the DV-Xα method. Ionization cross sections, F Kα X-ray energies and X-ray transition probabilities were calculated using the semi-classical approximations (SCA), the Slater's transition state method and the dipole approximation, respectively. In the present study we found excellent linearities between ROR probabilities and the M line intensities, and between fluorescence yields for a K^1L^1 doubly ionized state and relative X-ray intensities of (K^1L^1 / K^1L^0). Here X-ray and Auger emission spectra were studied, which were emitted from the alkali-metal fluorides, i.e. NaF, KF, RbF and CsF. All the intensities of F Kα X-rays and KVV Auger electrons have successfully been explained for the first time.

ADVANCES IN QUANTUM CHEMISTRY, VOLUME 29

0065-3276/97 $25.00

INTRODUCTION

Fine structures of photoelectron, Auger electron and X-ray spectra emitted from molecules through the transition from valence to inner-shells are sensitive to the change in chemical environments surrounding the atom of interest, and then have been used extensively for studies of electronic structures of chemical compounds[1-9]. For obtaining these spectra, photons, electrons and accelerated ions have been employed as excitation sources. However different kinds of excitation methods make explanations of the fine structures and/or satellite structures of Auger and X-ray spectra complicated. This is a main cause why intensity distributions of these spectra can not be discussed quantitatively.

If inner-shell electrons are removed from the atoms, characteristic X-ray and Auger electrons are emitted during the filling process of the electron vacancies by the outer-shell electrons. When the electrons to fill the vacancies are localized on the valence shell, pronounced chemical bond effects are expected to be observed. As the origin of the chemical bond effects on the fine structures of Auger and X-ray spectra, two principal causes can be considered, (a) outer-shell vacancy distributions generated at the time of collision change with bonding structures of molecules [10], (b) prior to Auger and X-ray emissions, the rearrangement of molecular orbitals or of the vacancy distributions occurs.

One of the simple examples of the orbital rearrangements is the change in the energy of Auger electrons emitted from atoms bound in solid, which is higher than that of Auger electrons emitted from free atoms [11]. The main cause of this energy shifts is the extra-atomic relaxation of atomic orbitals or reconstruction of molecular orbitals for screening the created double-hole final states. The configuration and vibronic interactions, electron transfer [12,13], and so on are also kinds of the molecular orbital rearrangements.

In photoelectron, Auger and X-ray spectroscopies, the frozen core and sudden approximations have frequently been used for their simplicity. However, interesting chemical bond effects in Auger and X-ray spectra have not yet been explained by such over simplified approximations. The representatives are remarkable changes in satellite intensity distributions appeared in X-ray and Auger spectra emitted from a series of fluorides [14-20]. Introduction of a new concept of

the orbital rearrangement prior to Auger and X-ray emissions is indispensable for explaining dramatic changes in the satellite intensities of X-ray and Auger spectra. In this paper "resonant orbital rearrangement; ROR" has newly been proposed to explain anomalous behavior of the satellite intensities on F KVV and F Kα spectra. The new concept is also promising to understand much lower intensities of K satellites emitted from low Z elements such as O, N, C, ··· and of L satellites emitted from transition metals.

EXPERIMENT AND DATA PROCESSING

Fluorescent F Kα X-ray spectra emitted from NaF, KF, RbF and CsF were measured using a flat crystal spectrometer, Philips PW1480. Radiations emitted from a thin scandium anode, evaporated on a molybdenum matrix and operated at 50kV and 60mA, were adopted as an incident photon source. Fluorescent X-rays thus induced from the samples were collimated by a series of Soller slits. A thallium acid phthalate (TAP) (001) flat crystal (2d = 25.750Å) was used as an analyzing crystal. Vacuum was kept less than 5 Pa during measurements. All the samples were prepared in the form of pellets by pressing their fine powders in Ar atmosphere to prevent chemical reactions of them with moisture in air. Diameters and thicknesses of the resulting pellets were about 3cm and 0.5cm, respectively. Before and after X-ray measurements, all the samples used were confirmed by X-ray diffraction to be free from contaminations.

Observed F Kα X-ray spectra emitted from the alkali-metal fluorides are shown in Fig. 1(a) and (b). Here X0, X1 and X2 are emitted from initial states of K^1L^0, K^1L^1 and K^1L^2, where K^1L^n denotes one K and n L vacancies. Change in the intensities of the first satellite lines (X1) is distinct, which are situated on the high energy sides of diagram lines (X0). Photon induced F KVV Auger spectra emitted from the same series of alkali-metal fluorides observed by Benka and Uda [9] were processed here by subtracting back grounds due to energy-loss electrons, and are shown in Fig. 1(c). The Auger spectra are composed of the diagram lines (A = $2s^22p^4(^1D + {}^1S)$, C = $2s^12p^5(^3P)$, D = $2s^12p^5(^1P)$ and E = $2s^02p^6(^1S)$) and satellite lines (B = $2s^22p^3$ ($^4S+^2D+^2P$) and M : not assigned).

The observed F Kα fluorescent X-ray, 5.5MeV He^+ induced X-ray and F KVV Auger spectra were deconvoluted to each component by the least-square fitting using the Lorentzian and Gaussian distribution functions for X-ray and Auger spectra, respectively. Resulting intensities of these components

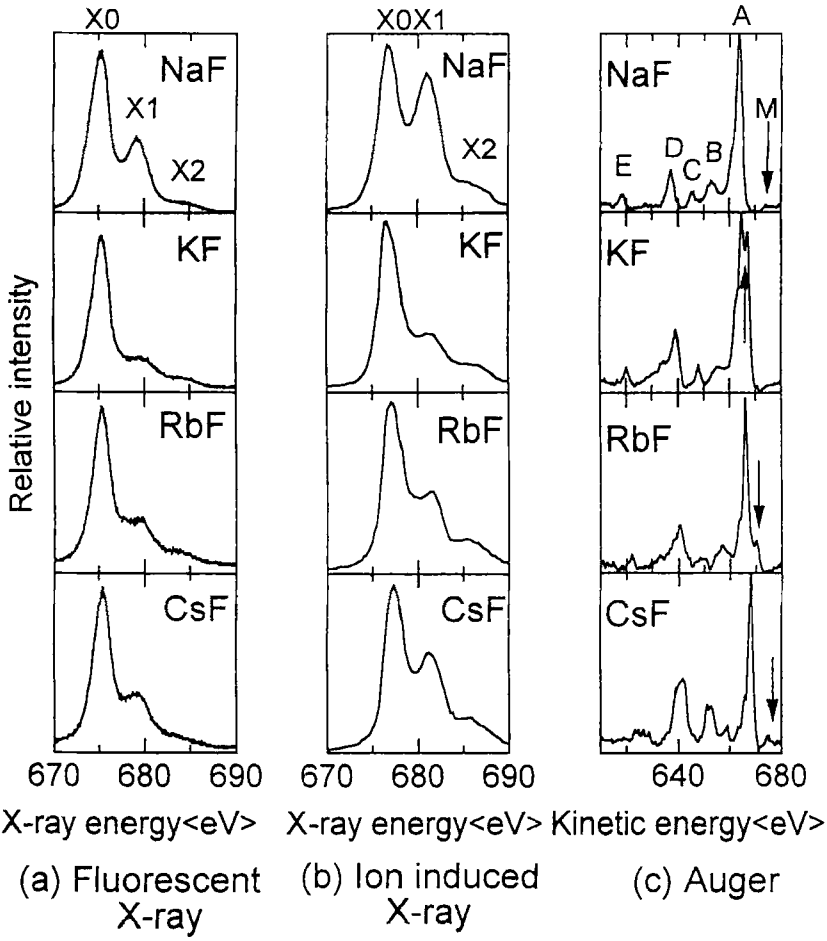

FIGURE 1. Observed F Kα (a) fluorescent X-ray, (b) ion induced X-ray [14], and (c) KVV Auger spectra [15] emitted from a series of alkali-metal fluorides.

are summarized on Table 1. The remarkable change in intensities of the X1 satellite lines in both photon and ion induced X-ray spectra and of the M lines in the Auger spectra is obvious.

TABLE 1. Observed intensity of each component in F Kα fluorescent X-ray, ion induced X-ray [14] and KVV Auger [15] spectra, which were deconvoluted by the least-square fitting using the Lorentzian distribution functions for X-ray spectra and Gaussian distribution functions for Auger spectra, respectively.

	Fluorescent X-ray			Ion induced X-ray			Auger					
	X0	X1	X2	X0	X1	X2	E	D	C	B	A	M
NaF	100	39.0	2.0	100	80.7	6.5	6.5	19.8	5.6	10.7	100	1.4
KF	100	16.0	5.1	100	28.6	13.3	5.7	58.0	6.2	8.6	100	68.0
RbF	100	25.6	6.8	100	41.6	13.3	4.7	52.5	10.0	16.2	100	6.2
CsF	100	29.8	5.5	100	54.5	12.6	11.5	75.8	32.5	7.2	100	14.6

OUTER-SHELL ORBITAL REARRANGEMENT DURING F 1s IONIZATION

Within the simplest picture for isolated atoms, ionized and excited states are initial ones for X-ray and Auger transitions. However, in molecules the orbital rearrangement following ionization and electronic excitation occurs in general due to the interaction of an inner-shell hole with the molecular field. This makes structures of the X-ray and Auger spectra complicated.

The Auger electrons and characteristic X-rays are emitted from initial states with one inner-shell vacancy or sometimes with several vacancies in inner- and outer-shells, where the initial states are formed by ionization and excitation of inner- and outer-shell electrons. In ionization of the isolated atom, constituents of all the atomic orbitals except for an ionized electron remain unchanged after

ionization, though all the energy levels for the atomic orbitals become deeper, due to decrease in the screening effect, than those before ionization. We call hereafter such reconstruction of the orbitals as the orbital rearrangement or relaxation. However, in ionization of molecules the orbital rearrangement at the outer-shells is not straightforward.

The molecular orbitals of the outer-shells are composed of atomic orbitals both of the atom of interest and surrounding atoms, and then their numbers are not a few. This leads to introduce the complicated orbital rearrangement or the change in orbital constituents. On the other hand, in most of the atomic spectroscopies such as the X-ray photoelectron spectroscopy (XPS), the Auger electron spectroscopy (AES) and the X-ray fluorescence (XRF), this kind of the orbital rearrangement is not taken into account because it does not lead, in general, to significant misunderstanding or wrong explanation of observed spectra. However, remarkable chemical bond effects appeared in X-ray [14,16-20] and Auger [15] satellite intensity distributions request employment of the orbital rearrangement. The X-ray and Auger spectra emitted from F^- ions in a series of fluorides, shown in Fig.1, are typical examples of the chemical bond effects. The remarkable change in the intensities of the M lines in the Auger spectra [15] and of the X1 lines in X-ray spectra has not yet, however, fully been understood by existing concepts.

We introduce here a new concept, i.e. resonant orbital rearrangement (ROR), to explain intensities of the M and X1 lines. If fluorine and metal atoms form a molecule or a fluoride, molecular orbitals at a K^0L^0 state can be described by linear combinations of atomic orbitals of both atoms, as shown in Fig.2 schematically, where K^0L^0 denotes zero electron vacancy state both on K and L shells. When an electron in a molecular orbital mostly composed of an F 1s component at the K^0L^0 state is ionized, the structure of the molecular orbitals for these fluorides is reconstructed before Auger electron and X-ray emissions. Rearrangement processes during F 1s ionization are schematically shown in Figs.2 ~4. The simplest case is parallel displacements of all the energy levels to deeper ones shown in Fig.2 by the mode 1, leading to form a K^1L^0 state. Second, an electron at the highest occupied molecular orbital (HOMO) or near the orbital is shaken-off due to sudden change in the Coulomb potential caused by ionization of

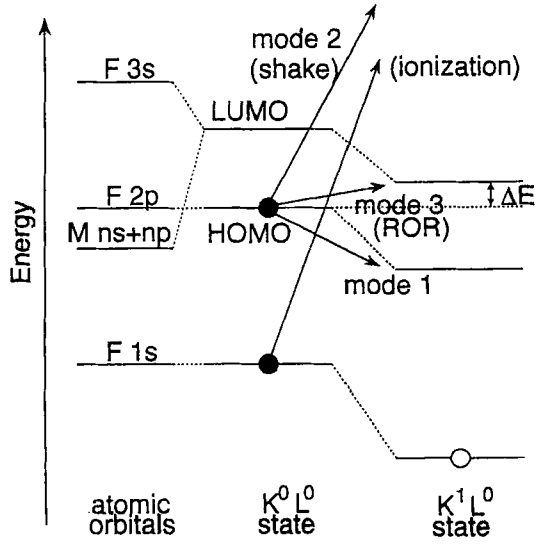

FIGURE 2. The shaking and orbital rearrangement processes following inner-shell (F1s) ionization.

the F 1s electron, making a K^1L^1 doubly ionized state written by the mode 2 in Fig.3. If the energy level of HOMO at the K^0L^0 state is almost the same as that of the lowest unoccupied molecular orbital (LUMO) at the K^1L^0 state as shown in Fig.2, resonance occurs between these two states. In other words, such resonant orbital rearrangement (ROR) produces a state with each one vacancy in the F K and L shells and with one excited electron in LUMO, shown in Figs.3 and 4 as the modes 3_1 and 3_2. This is a kind of virtual dipole excitation of the electron with 2p nature at HOMO to LUMO with 3s nature on the F^- ion.

The mode 1 is relevant to emissions of the A, C, D and E Auger and X0 X-ray diagram lines, and the mode 2 is relevant to emissions of the B Auger and X1 X-ray satellite lines, respectively. The mode 3 is divided into two, i.e. 3_1 and 3_2 which might relevant to Auger emissions of the F 2p or HOMO electron

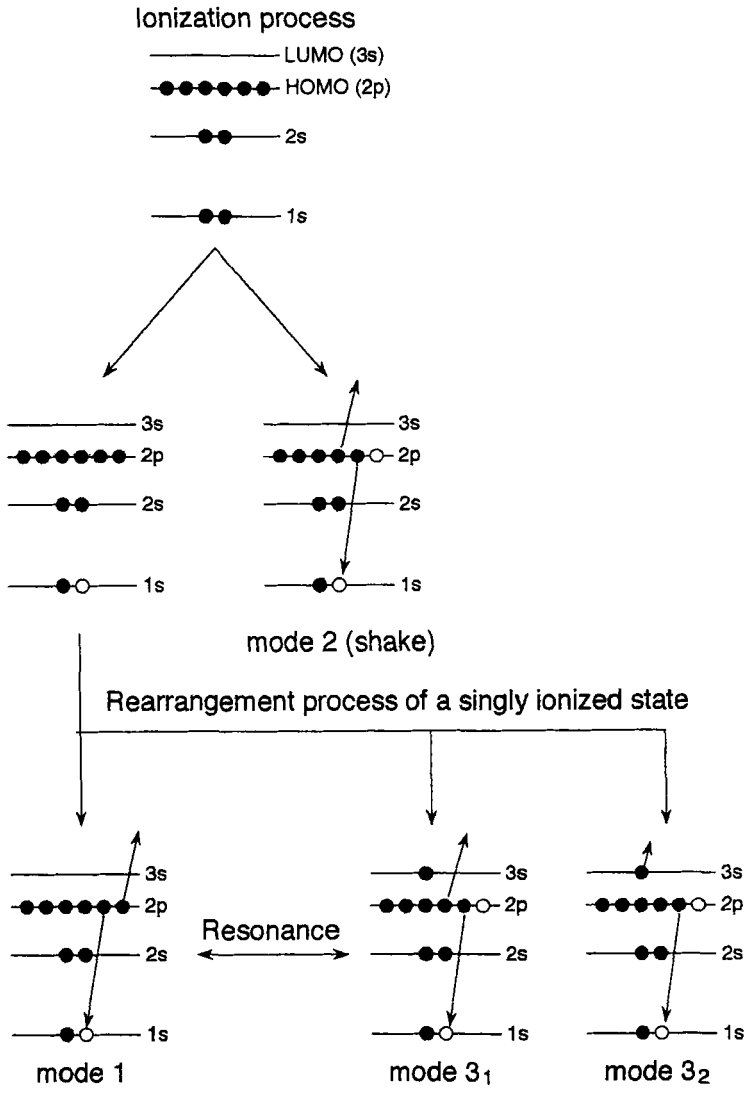

FIGURE 3. Ionization, shaking and orbital rearrangement processes of the F^- ion in a fluoride at the time of Auger electron emissions.

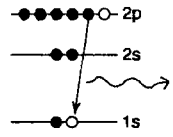

mode 2 (shake)

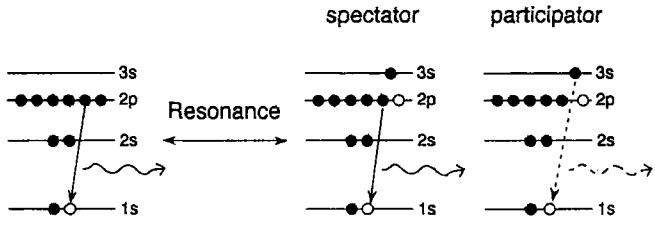

mode 1 mode 3_1 mode 3_2

FIGURE 4. F K X-ray emissions after the orbital rearrangement in a fluoride.

(corresponding to the spectator transition), and of the excited electron with 3s nature (corresponding to the participator transition), respectively. The mode 3_1 is to be relevant to productions of the B Auger and X1 X-ray satellite lines. Here the mode 3_2 is assumed to be relevant only to an emission of the M Auger line but not to an emission of an X-ray line, if based on the atomic scheme, because the excited electron to LUMO has 3s nature in this rearrangement scheme, as shown in Figs.3 and 4.

The rearranged electron from HOMO at the K^0L^0 state to LUMO at the K^1L^0 state has possibility, in the molecule but not in the atom, to fill the F 1s

vacancy through the mode 3_2 by emitting X-ray via the participator transition. To estimate a contribution of the mode 3_2 to the X-ray emission, first we calculated molecular orbitals of these fluorides by employing the DV-Xα method[21]. In this calculation the basis sets were chosen as 1s-3s for F, 1s-3p for Na, 1s-4p for K, 1s-5p for Rb and 1s-6p for Cs, respectively. A potential well of 0.9 a_0 and -3.0 Hartree in width and depth, respectively was also used. Here a_0 is an atomic distance between M and F, and clusters used for all the fluorides are $(M_6F)^{5+}$ with the Oh symmetry, where M represents Na, K, Rb or Cs. Energy levels and electronic constituents obtained by the above molecular orbital calculations are schematically shown for the K^0L^0 and K^1L^0 states in Figs.5 (a)(b)~8(a)(b). Here percentages written in these figures mean the orbital populations in the Muliken population analysis scheme.

Second, difference energies between the satellite and the diagram lines in the F Kα fluorescent X-rays in Fig.1 (a) were calculated adopting the Slater's transition state method [22,23]. A calculation procedure is shown in Fig.9 schematically. Here all the electrons and vacancies concerned with transitions are counted as one half instead of one in this transition state method. The observed and calculated difference energies are summarized on Table 2. The X-ray energies expected from the mode 3_2 were calculated here to be about 23eV larger than that caused by the mode 1. However no additional peak around this energy range was found in our experimental spectra (not shown in Fig.1 (a)).

Third, an X-ray transition probability through the mode 3_2 in Fig. 4 was calculated by use of the dipole approximation, giving less than 10^{-5} of the X-ray transition probability of the mode1. This means that the X-ray transition resulted from the mode 3_2 is mostly forbidden because the rearranged electron from HOMO at the K^0L^0 state to LUMO at the K^1L^0 state is characterized with F 3s nature on the F^- ion, but not on the surrounding atoms, even in the molecular orbital scheme, and then its contribution to X-ray emissions can be ignored. On the other hand, the mode 3_2 must be, in the Auger transition, taken into account because any restriction on an orbital angular momentum does not exist in this transition. Such results are also consistent with previous assumptions, i.e. the excited electron to LUMO being characterized with 3s nature in the atomic scheme.

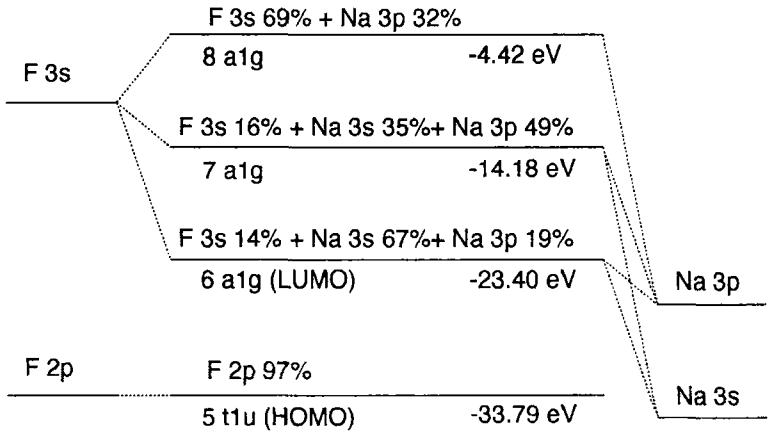

(a) K^0L^0

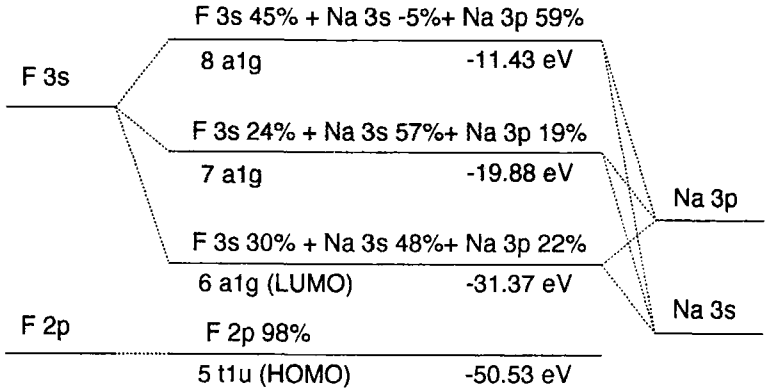

(b) K^1L^0

FIGURE 5. Molecular orbitals of NaF at (a) K^0L^0 and (b) K^1L^0.

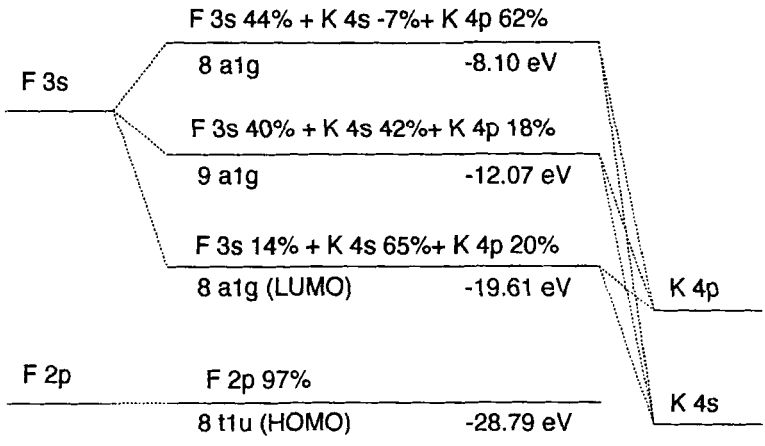

(a) K^0L^0

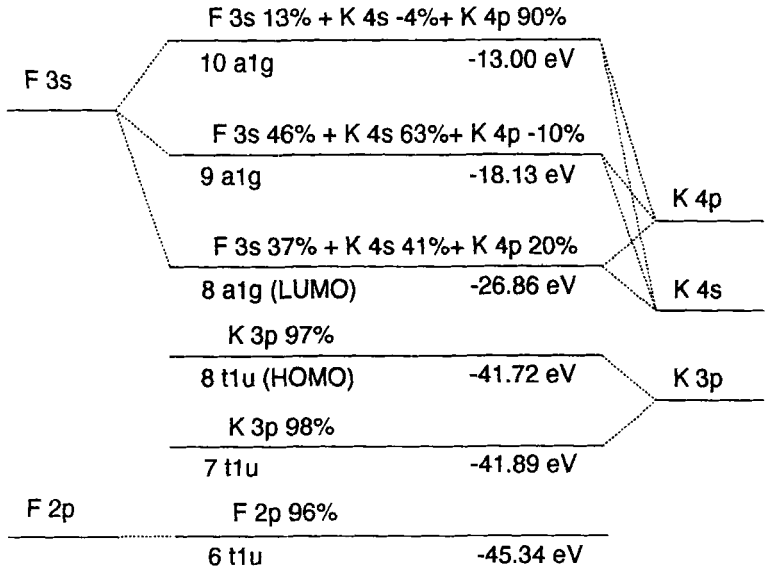

(b) K^1L^0

FIGURE 6. Molecular orbitals of KF at (a) K^0L^0 and (b) K^1L^0.

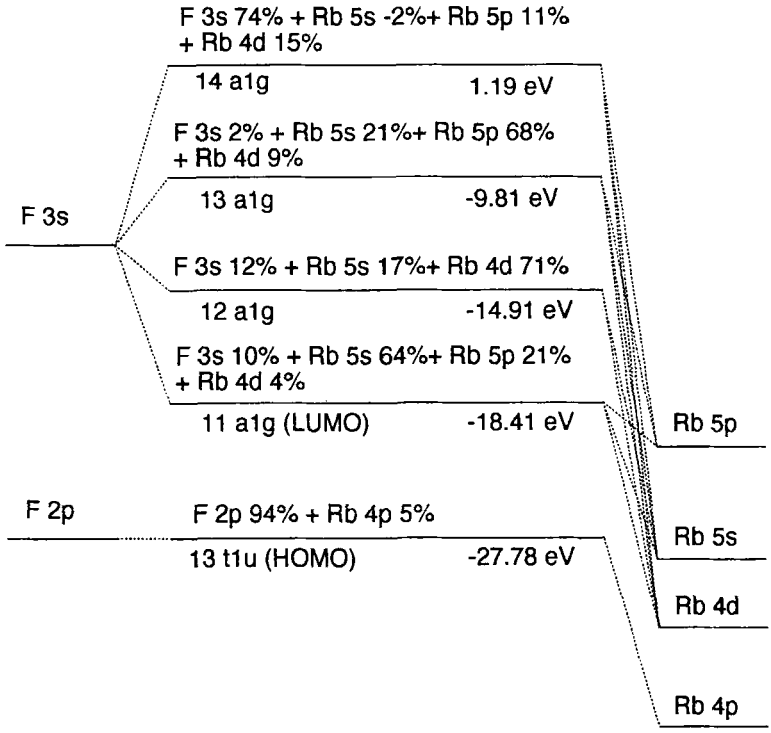

FIGURE 7(a). Molecular orbitals of RbF at K^0L^0.

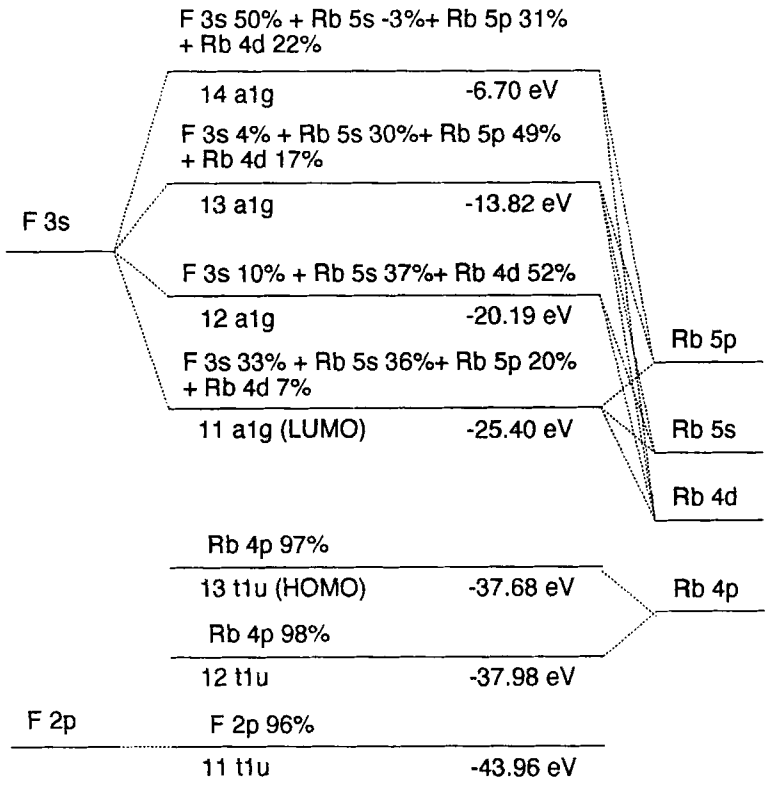

FIGURE 7(b). Molecular orbitals of RbF at K^1L^0.

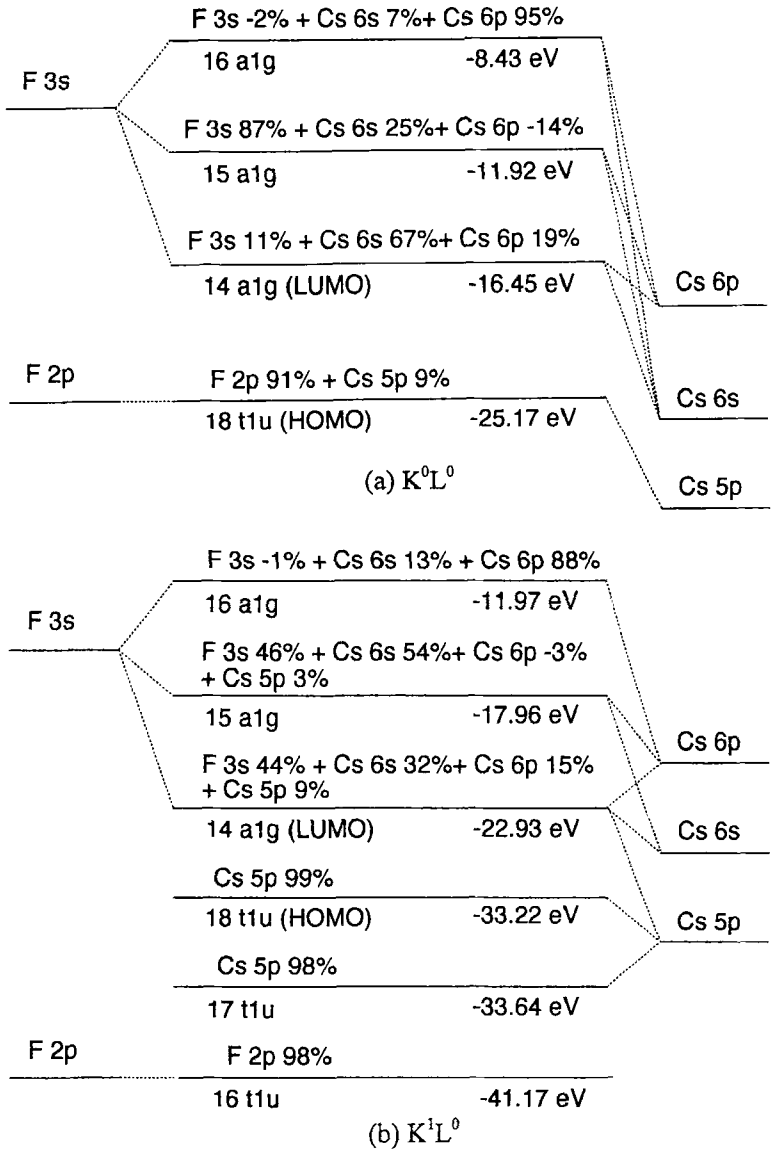

FIGURE 8. Molecular orbitals of CsF at (a) K^0L^0 and (b) K^1L^0.

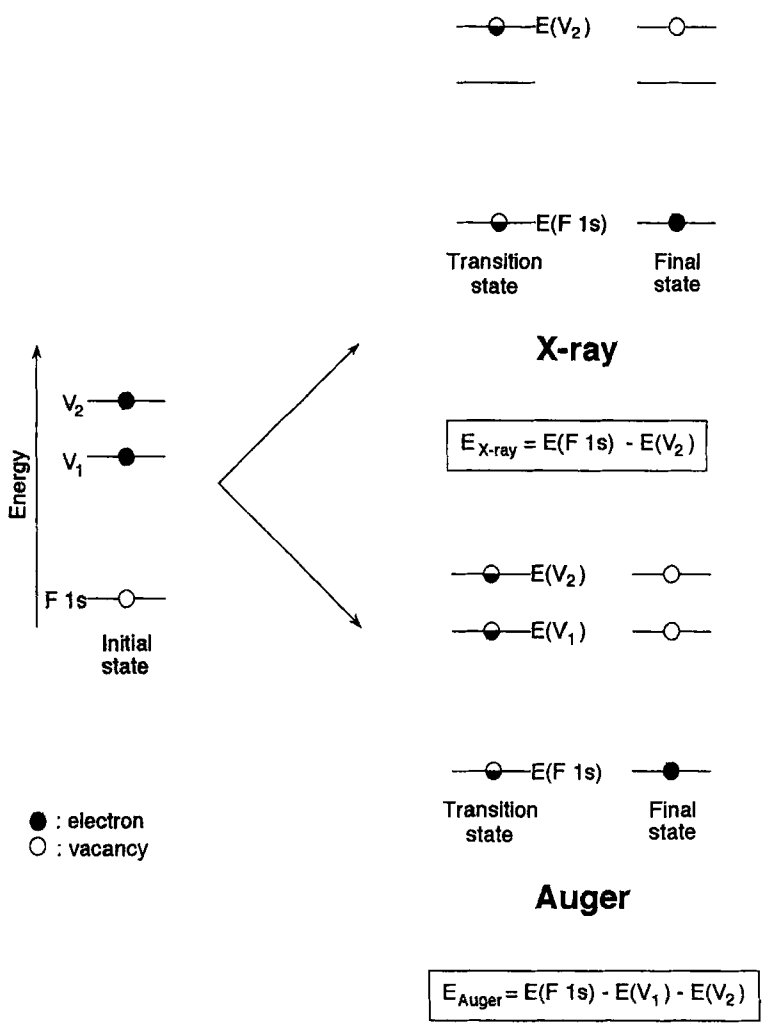

FIGURE 9. Schematic diagram to calculate X-ray and Auger electron energies. All the electrons concerned with the X-ray and Auger transitions are to be counted as an one half in the transition state method.

TABLE 2. Observed and calculated difference energies of the satellite lines (X1) and diagram lines (X0) in F Kα fluorescent X-ray spectra emitted from alkali metal fluorides.

	observed	calculated		
	$\Delta\varepsilon_{obs}$ <eV> $= E_{X1} - E_{X0}$	$\Delta\varepsilon_{calc}$ <eV> from mode 2	$\Delta\varepsilon_{calc}$ <eV> from mode 3_1	$\Delta\varepsilon_{calc}$ <eV> from mode 3_2
NaF	4.2	2.4	2.6	23.2
KF	4.8	3.4	3.4	23.6
RbF	4.2	3.0	3.1	23.6
CsF	4.0	3.7	3.7	22.3

DECAY PROCESS OF THE ELECTRON IN HOMOAT THE K^0L^0 STATE DURING F 1s IONIZATION

In most cases, as already stated, the electron in HOMO at the K^0L^0 state moves to HOMO at the K^1L^0 state after F 1s ionization and excitation. However, if the energy level of HOMO before ionization or at the K^0L^0 state is almost the same as that of LUMO at the K^1L^0 state, a new state can also be produced, which has each one vacancy in K and L shells and also with one excited electron in LUMO. We called such a decay process as "resonant orbital rearrangement (ROR)". To discuss a degree of the resonance quantitatively, we define an energy difference ΔE as a gap energy, as shown in Fig. 2, between HOMO at the K^0L^0 ground state and LUMO at the K^1L^0 singly ionized state. Here HOMO at the K^0L^0 state is mostly composed of F 2p electrons, and LUMO at the K^1L^0 state contains, at least in part, a component of the F 3s orbital, as can be seen in Figs. 5~8. Then the resonant orbital rearrangement probability P_{ROR} is written as

$$P_{ROR} \propto \frac{a(\hbar/2\tau)^2}{(\Delta E)^2 + (\hbar/2\tau)^2} \qquad (1)$$

if we use the Breit-Wigner resonance formula for describing ROR. Here a is a constant and τ is the life time of the resonance state relevant to the emission of the M Auger line, which can be approximated by the life time of F 1s vacancy, i.e. 2.4×10^{-13}sec. ΔE can be read out from Figs. 5~8, which is of the order of electron volts. $\hbar/2\tau$ is now 1.4×10^{-3} eV, which is much smaller than ΔE here estimated and then can be ignored in eq. (1), leading to $P_{ROR} \propto (\Delta E)^{-2}$. This means that the M Auger line intensity or M/A should be proportional to the orbital rearrangement probability. Relationships between observed M/A in Fig. 1(c) and $(\Delta E)^{-2}$ here calculated are shown in Fig. 10, whose linearity is satisfactory, suggesting that the newly defined concept, ROR, is acceptable at least in the energetic scheme.

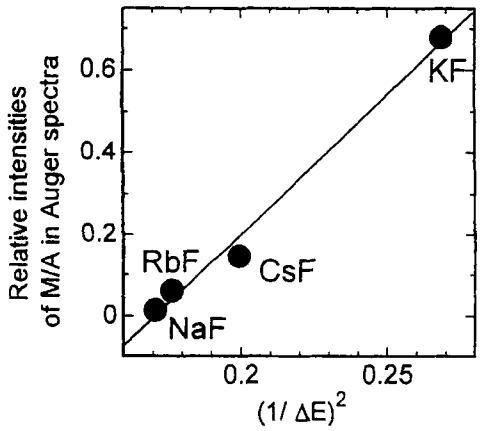

FIGURE 10. Relationships between observed M/A in Fig.1 (c) and $(\Delta E)^{-2}$.

Next we discuss the change in the fluorescence yields for the doubly ionized states, in order to explain the chemical bond effects in the satellite intensities of X1 lines in the F Kα fluorescent X-ray spectra. Here we assumed that the fluorescence yield is divided into two, i.e. one for the diagram lines of X0 and A,

C, D and E, and the other for the satellite lines of X1, and B and M. The fluorescence yield Y_{X0} for the diagram line is expressed as

$$Y_{X0} = \frac{\eta X_{X0}}{A_{A,C,D,E} + \eta X_{X0}} \tag{2}$$

where X_{X0} is the observed intensity of the X0 diagram line in the F Kα fluorescent X-ray spectra shown in Fig. 1(a), $A_{A,C,D,E}$ the sum of those of A, C, D and E lines in the F KVV Auger spectra shown in Fig. 1 (c), and η the detection efficiency of X-rays relative to Auger electrons in our experimental setups. The fluorescence yield Y_{X1} for the X1 satellite line is also expressed as

$$Y_{X1} = \frac{\eta X_{X1}}{A_{B,M} + \eta X_{X1}} \tag{3}$$

where X_{X1} is the observed intensity of X1 line, and $A_{B,M}$ the sum of the B and M intensities. From these two equations, Y_{X1} can be rewritten as

$$Y_{X1} = \frac{\dfrac{X_{X1}}{X_{X0}}}{\dfrac{1 - Y_{X0}}{Y_{X0}} \times \dfrac{A_{B,M}}{A_{A,C,D,E}} + \dfrac{X_{X1}}{X_{X0}}} \tag{4}$$

This equation now does not contain η being a function of experimental conditions.

We also assumed that the fluorescence yield for the diagram line is independent of chemical environments, i.e. Y_{X0}=0.013 obtained for the isolated F atom by Krause[24]. This is because the effective number of electrons on F L shells in the alkali-metal fluorides is almost the same, i.e. 7.5~8.0, and then the K^0L^0 ground state is almost the same for all the fluorides used.

The fluorescence yields for the X1 satellite lines, estimated from eq. (4), are summarized on Table 3. The relationships between the fluorescence yields and

the relative intensities of X1/X0 in the F Kα fluorescent X-ray spectra are shown in Fig. 11. We see good linearity between these two.

TABLE 3. Fluorescence yields for X1 satellite lines in F Kα fluorescent X-ray spectra obtained by eq. (4) and difference energies between LUMO at the K^1L^0 state and HOMO at the K^0L^0 state.

Compounds	Fluorescence yield Y_{X1}	ΔE <eV>
NaF	0.053	2.42
KF	0.0047	1.93
RbF	0.025	2.38
CsF	0.038	2.24

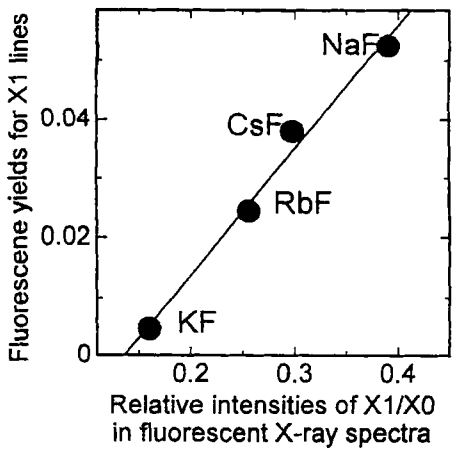

FIGURE 11. Relationship between the fluorescence yields for X1 satellite lines and the relative intensities of X1/X0 in fluorescent X-ray spectra.

As can be seen from Fig. 10, the Auger M line intensity becomes, through the mode 3_2, large for large ROR probability or for small ΔE defined in Fig. 2. This leads, in the first approximation, to reduction in the fluorescence yield Y_{X1} and then also reduction in the intensity ratio of X1/X0 as shown in Fig. 11, though the fluorescence yield is, strictly speaking, a function both of Auger and X-ray yields. Thus chemical bond effects in the satellite intensities of the X1 lines in the F Kα fluorescent X-ray spectra emitted from the alkali-metal fluorides have now successfully been explained.

In the case of ion impacts, the excitation processes are more complicated than those for the photon impacts, which are schematically shown in Fig. 12. The K^1L^0, K^1L^1 and K^1L^n ionized states are mainly produced through the direct Coulomb potential acting between projectiles and orbital electrons on the target atom, where $n \geqq 2$. Then the single and double ionization cross sections due to the direct Coulomb potential, σ^{DC}_{K1L0} and σ^{DC}_{K1L1}, can be calculated using the single center model in the semi-classical approximation (SCA) frame. A calculating

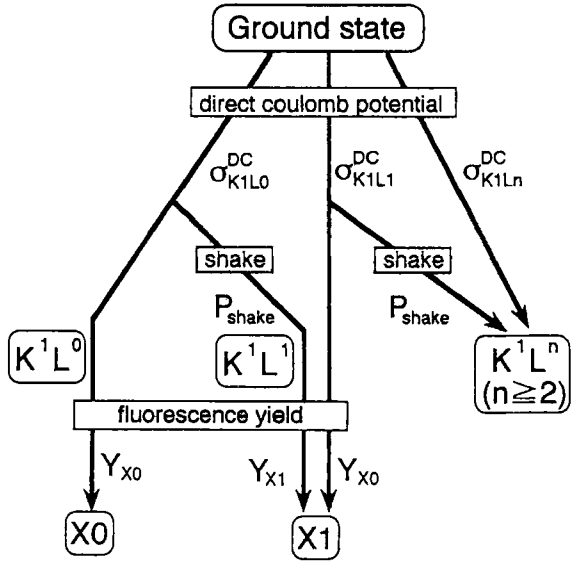

FIGURE 12. Schematic diagram for the excitation processes in the case of ion impacts.

procedure was proposed by the present authors [10]. In addition to the above direct Coulomb ionization, we have to consider an indirect ionization, i.e. the shake-off in the case of the ion impacts too. In other words parts of the Coulomb ionized states go to higher ionized states due to the shaking process. Then the cross sections σ_{K1L0} and σ_{K1L1} to produce the K^1L^0 and K^1L^1 states are written as the sum of contributions from the direct Coulomb potential and the shaking process. If we assume that the shaking probabilities are the same for both cases of $K^1L^0 \rightarrow K^1L^1$ and $K^1L^1 \rightarrow K^1L^2$, the cross section are written as

$$\sigma_{K1L0} = \sigma_{K1L0}^{DC}(1 - P_{shake}) \tag{5}$$

and

$$\sigma_{K1L1} = \sigma_{K1L1}^{DC}(1 - P_{shake}) + \sigma_{K1L0}^{DC} P_{shake} \tag{6}$$

where P_{shake} is the shaking probability calculated for the isolated F atom by Mukoyama and Taniguchi [25], i.e. P_{shake}=0.1845. Each of the ionized states emits an X-ray according to each fluorescence yield. Here the fluorescence yield for the X0 diagram line was assumed to be independent of chemical species of fluorides and the same as that for the isolated F atom, i.e. Y_{X0}=0.013 [24].

On the other hand, fluorescence yields for the X1 lines in the case of the ion impacts were assumed to be Y_{X1} only for $K^1L^0 \rightarrow K^1L^1$ through the shake process. Here Y_{X1} was determined from the photon induced X-ray spectra. However, for the K^1L^1 state produced through the direct Coulomb interaction, Y=0.013 was adopted because the direct Coulomb ionization is not accompanied with the orbital rearrangement. These considerations give the total X-ray production cross sections for the X0 and X1 lines, σ_{X0} and σ_{X1},

$$\sigma_{X0} = Y_{X0}\sigma_{K1L0}^{DC}(1 - P_{shake}) \tag{7}$$

and

$$\sigma_{X1} = Y_{X0}\sigma^{DC}_{K1L1}(1 - P_{shake}) + Y_{X1}\sigma^{DC}_{K1L0}P_{shake} \quad (8)$$

Calculated relative cross sections for X1/X0 with the aid of eqs. (7) and (8) are compared with the observed ones in Fig. 13. Agreement between experiments and calculations is satisfactory. This means that even on the ion induced F Kα X-ray spectra, ROR plays one of the most important role in the chemical bond effects on the X1 satellite intensities.

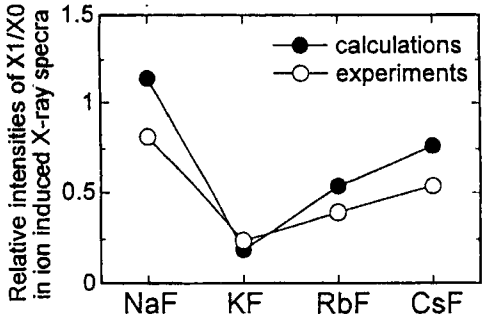

FIGURE 13. Comparisons of relative intensities of X1/X0 in ion induced X-ray spectra between experiments [14] and calculations.

EXTENDED ROR TO RESONANT AUGER SPECTRA

An inner-shell electron can be excited by photoabsorption to a bound state below the ionization threshold. From such an excited state Auger electrons are also emitted. This makes the structure of Auger spectra simple because the spectra are free from the shake-off peak due to multiple ionization. Aksela et al. [26] have studied F KVV Auger spectra emitted from a series of fluorides by use of the synchrotron radiation. Spectra taken from LiF and KF are shown in Figs. 14~16 as typical examples.

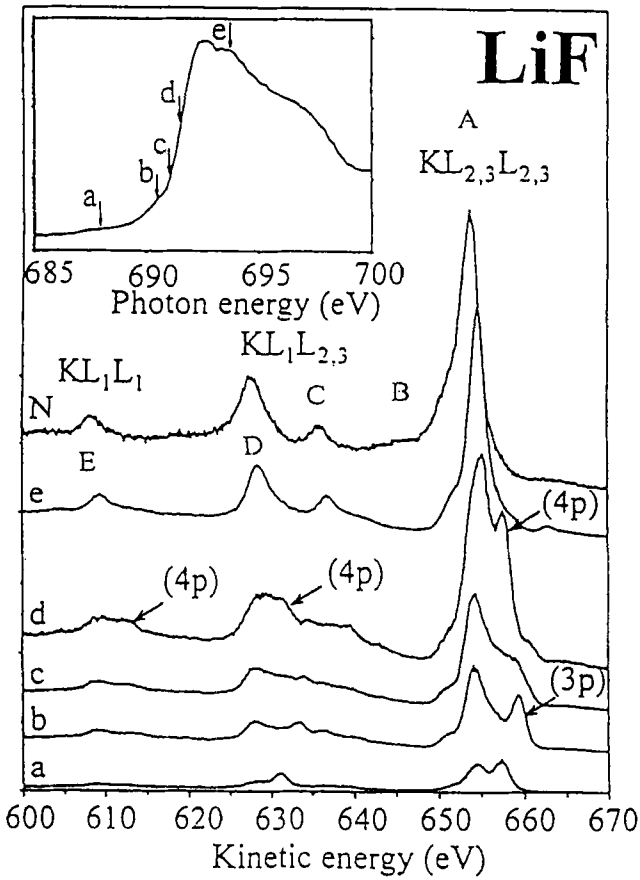

FIGURE 14. Normal (denoted by N) and resonant Auger spectra of LiF. Inset shows the total electron yield spectrum of LiF at the F K edge. Labels a-e indicate the mean photon energies where the electron spectra were recorded. The normal Auger electron spectrum was taken at hν = 800 eV. (by Aksela et al. in Phys. Rev. B49 (1994-I) pp. 3117 [26])

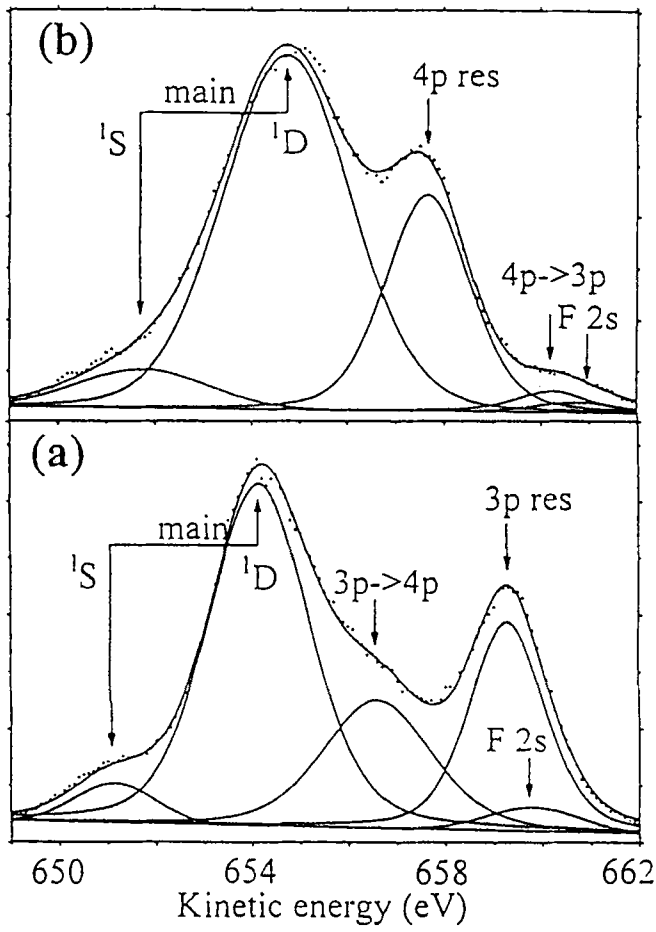

FIGURE 15. (a) F $KL_{2,3}L_{2,3}$ resonant Auger spectrum of LiF [26] taken at the mean photon energy b of Fig.14, decomposed into the line components. Fluorine 2s is indicated by F 2s. (b) F $KL_{2,3}L_{2,3}$ resonant Auger spectrum of LiF taken at the mean photon energy d of Fig. 14. (by Aksela et al. in Phys. Rev. B49 (1994-I) pp.3118[26])

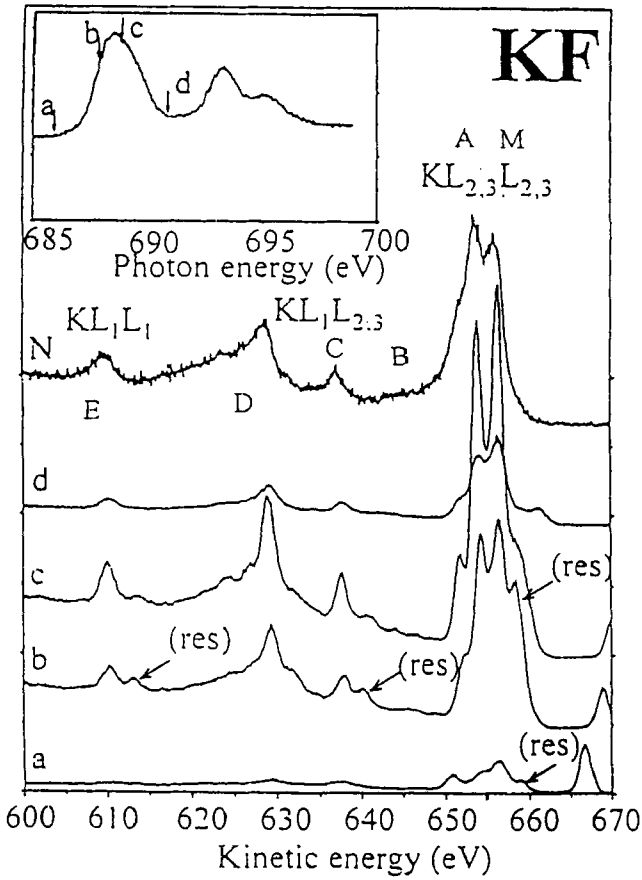

FIGURE 16. Normal and resonant Auger spectra of KF. The inset depicts the total electron yield spectrum of KF at the F K edge. (by Aksela et al. in Phys. Rev. B49 (1994-I) pp.3120 [26])

They succeeded to explain extra peaks appeared in the spectra to be caused by electrons resulted from the spectator Auger transitions. Here the F 1s electron is resonantly excited to 3p and 4p, noted as (3p), (4p) and (res) in Figs. 14 and 16. In addition new peaks due to the shake were also found in Fig. 15(a) and (b) noted as $3p \rightarrow 4p$ and $4p \rightarrow 3p$, which are originated from the spectator transitions accompanied by the shake-up from 3p to 4p and the shake-down from 4p to 3p during Auger decay. As can be seen in Fig. 14 for LiF the intensities of the shake peaks are much smaller than those of the main or diagram A and resonant (3p) and (4p) peaks. This is also true for KF as shown in Fig. 16. Here the same Auger notations (A, B, C, D, E and M) as in Fig. 1(c) are given in Fig. 14 for LiF and in Fig. 16 for KF, together with the resonant Auger peaks (np). Aksela et al. [20] did not, however, pay attention on the origin of the M peak observed at the high energy side of the diagram line A with comparable intensity in KF.

Fortunately from the above experiments an important conclusion can be drawn. ROR here proposed is distinguished from the shake because intense additional lines observable at the high energy side of the peak A must be observed from all the fluorides if the M peak were emitted through the shake process but not through ROR. This is not indeed the case. In addition the diagram A line gives continuous energy shift passing through b, c, d and N in Fig. 14 but the M line energy is almost independent of the excitation photon energies as shown in Fig. 16, indicating that the M line is not induced through the excitation process but is relevant to the decay process, i.e. ROR.

Sairanen et al. [27] observed F KVV Auger lines emitted from gaseous KF, giving only the diagram lines but no M line. They did not give any satisfactory explanation for the lack of the M line. We calculated MO of gaseous or di-atomic KF at K^0L^0 and K^1L^0 states as shown in Fig. 17 (a) and (b). Here gaseous KF has a shorter atomic distance (4.10 a.u.) than that of solid (5.05 a.u.). ΔE for gaseous KF was larger than that of solid (2.46 vs. 1.93eV), leading to off-resonance between HOMO at K^0L^0 and LUMO at K^1L^0 states in gaseous KF. This must give the weak M line. Thus ROR can explain all the experimental results on the resonant Auger spectra emitted from the fluorides satisfactorily.

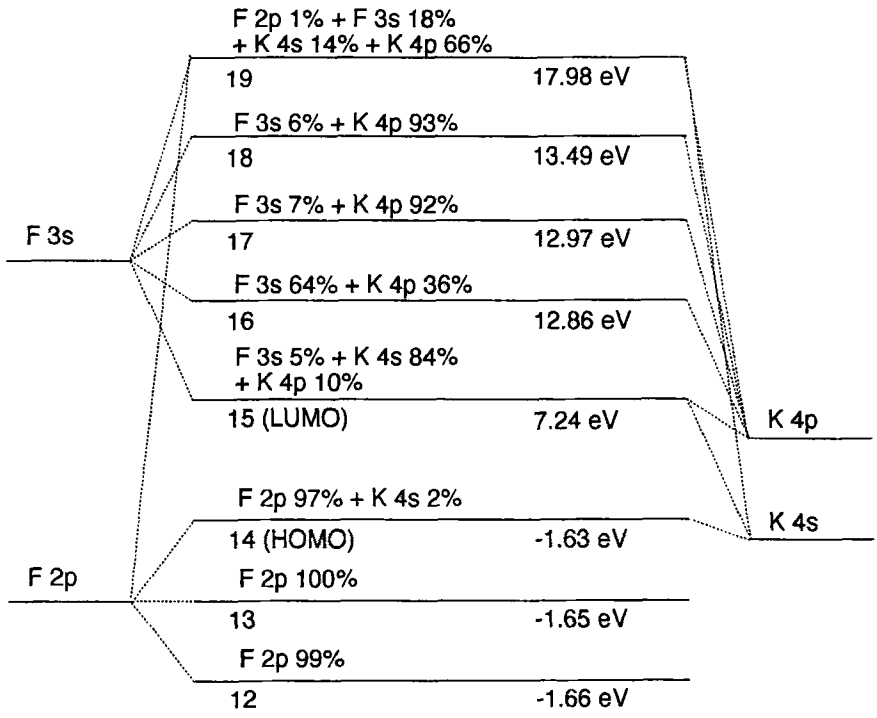

FIGURE 17(a). Molecular orbitals of gaseous or di-atomic KF at K^0L^0.

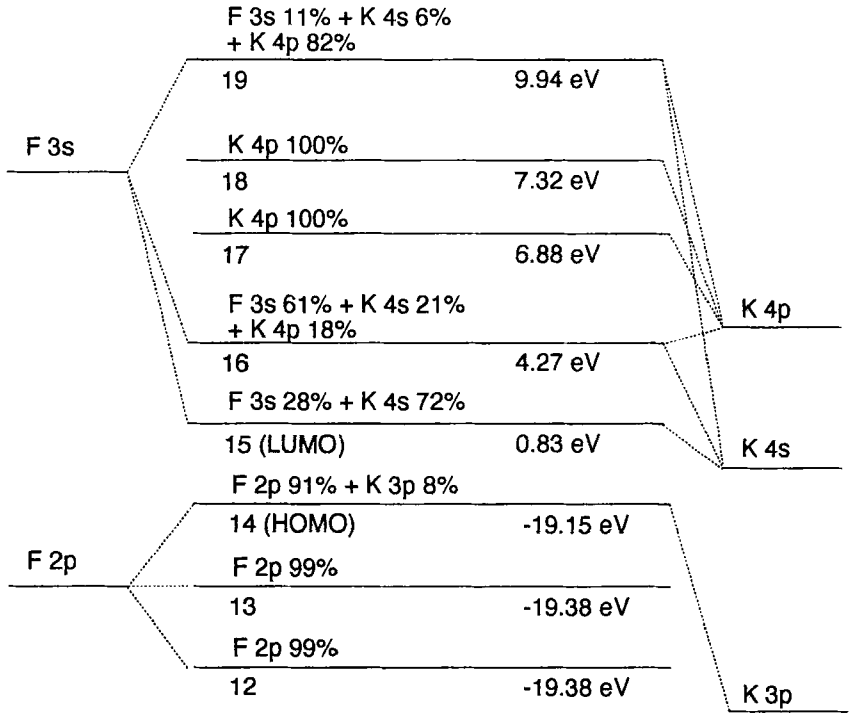

FIGURE 17(b). Molecular orbitals of gaseous or di-atomic KF at K^1L^0.

From the discussions of this chapter, origin of the M line in the F KVV Auger spectrum is now well understood, which is the resonant orbital rearrangement, ROR.

ACKNOWLEDGMENT

The Authors would like to thank Profs. T. Mukoyama, Kyoto University, and A. Koyama, RIKEN, for their fruitful discussions.

REFERENCES

[1] K. Siegbahn, C. Nordling, A. Fahlman, R. Nordberg, K. Hamrin, J. Hedman, G. Johansson, T. Bergmark, S. E. Karlsson, I. Lindgren and B. Lindberg, "ESCA Atomic, Molecular and Solid State Structure Studied by Means of Electron Spectroscopy" Nova Acta Regiae Soc. Sci. Upsaliensis. Ser. IV, Vol 20 (1967).

[2] K. Siegbahn, C. Nordiling, G. Johansson, J. Hedman, P. F. Heden, K. Hamrin, U. Gelius, T. Bergmark, L. O. Werme, R. Mann and Y. Baer, "ESCA - Applied to Free Molecules" (1969), North-Holland Publ. Co., Amsterdam.

[3] C. R. Brundle and A. D. Baker, "Electron Spectroscopy: Theory, Techniques and Applications" (1979), Academic Press, London, New York and San Francisco.

[4] B. K. Agarwal, "X-ray Spectroscopy - An Introduction" (1979), Springer-Verlag, Berlin, Heidelberg, New York.

[5] A. Meisel, G. Leonhardt and R. Szargen, "X-ray Spectra and Chemical Binding" (1989), Springer-Verlag, Berlin, Heiderberg, New York, London, Paris, Tokyo and Hong-Kong.

[6] Derek J. Fabian, "Soft X-ray Band Spectra and The Electronic Structure of Metals and Materials" (1968), Academic Press, London and New York.

[7] J. Kawai, Y. Goshi and Y. Nihei, Adv. X-ray Chem. Anal. Japan **19** (1987) 1.

[8] C. L. Briant and R. P. Messmer, "Auger Electron Spectroscopy" (1988), Academic Press, inc., Boston, San Diego, New York, Berkeley, London, Sydney, Tokyo and Toronto.

[9] Michael Thompson, Mark D. Baker, Alec Christie and Julian F. Tyson, "Auger Electron Spectroscopy" (1985), John Wiley & Sons, New York, Chichester, Brisbane, Toronto and Singapore.

[10] M. Mochizuki, T. Yamamoto, S. Nagashima and M. Uda, Nucl. Instr. Meth. **B109/110** (1986) 31.

[11] S. Aksela, R. Kumpula, H. Aksela and J. Väyrynen, Phys. Scr. **25** (1982) 45.

[12] F. P. Larkins and T. W. Rowlands, J. Phys. **B19** (1986) 591.

[13] F. P. Larkins and R. A. Phillips, J. Chem. Phys. **88** (1988) 5323.

[14] O. Benka, R. L. Watson and R. A. Kenefick, Phys. Rev. Lett. **47** (1980) 1202.

[15] O. Benka and M. Uda, Phys. Rev. Lett. **56**, (1986)1667.

[16] M. Uda, H. Endo, K. Maeda, Y. Awaya, M. Kobayashi, Y. Sasa, H. Kumagai and T. Tonuma, Phys. Rev. Lett. **42** (1979)1257.

[17] M. Uda, H. Endo, K. Maeda, Y. Sasa and M. Kobayashi, Z. Phys. **A300** (1981) 1.

[18] M. Uda, O. Benka, K. Fuwa, K. Maeda and Y. Sasa, Nucl. Instr. and Meth. **B22** (1987) 5.

[19] O. Benka and M. Uda, Phys. Rev. Lett. **56** (1986) 54.

[20] R. L. Watson, A. K. Leeper, B. J. Sonobe, T. Chino and F. E. Jenson, Phys. Rev. **A15** (1977) 914.

[21] H. Adachi, M. Tsukada and C. Satoko, J. Phys. Soc. Jpn. **49** (1978) 875.

[22] J. C. Slater, Quantum Theory of Molecules and Solids, The Self-Consistent Field for Molecules and Solids (McGraw-Hill, New York, 1974) vol. 4.

[23] H. Adachi and K. Taniguchi, J. Phys. Soc. Jpn. **49** (1980) 1944.

[24] M. O. Krause, J. Phys. Chem. Ref. Data **8** (1979) 307.

[25] T. Mukoyama and K. Taniguchi, Phys. Rev. **A36** (1987) 693.

[26] H. Aksela, E. Kukk, S. Aksela, A. Kikas and E. Nõmmiste, Phys. Rev. **B49** (1994-I) 3116.

[27] O. P. Sairanen, H. Aksela, S. Aksela and M. Hottoka, Chem. Phys. Lett. **215** (1993) 353.

Charge Transfer in Al-Ni alloys: a Spin Selective Study

Zs. Kovács, L. Kövér[+] and H. Adachi[++]

Department of Experimental Physics, Lajos Kossuth University,
Debrecen, Bem tér 18/a, Hungary
[+] Institute of Nuclear Research of Hungarian Academy of Sciences
H-4001 Debrecen, P.O.B.51 Hungary
[++] Department of Materials Science and Engineering, Kyoto University,
Yoshida - honmachi, Kyoto 606, Japan

Abstract

Charge transfer between the constituent atoms is thought to be important for the stability of crystal structures. In our previous work [1] the transferred charge in the case of Al_3Ni and $AlNi_3$ was estimated from Auger parameter measurements. In the present study, performing non relativistic spin-restricted and spin-unrestricted DVX_α molecular orbital calculations of model cluster we obtain more detailed information on the particular orbitals involved in the charge transfer processes.

Introduction

Charge transfer between the constituent atoms of crystal structures is thought to determine the stability of these structures [2] and therefore the knowledge of the direction and magnitude of the transferred charges is especially important in the case of metal alloys. Electronegativity difference between the components of binary alloys leads to changes in the electronic configuration from that of free atoms. Analyzing alloy-pure metal Auger parameter shifts of the component atoms has been proved to be a useful method for providing an insight into the energy and spatial dependence of the valence electron density of states of alloys and revealing the relationship between the physical and electronic structures of alloy systems [3]. Depending on the change in the potential at the core-ionized atom, Auger parameter shifts can be used for the separation of the initial and final state contributions to core level chemical shifts [4] and for the estimation of changes in the local charge and relaxation energies. The method developed by Thomas and Weightman for the determination of charge transfer in alloys [5] from Auger parameter shifts, is based on potential parameters obtainable from atomic structure calculations. In this work we present non relativistic spin-restricted and spin-unrestricted DVX_α molecular orbital calculations for Al_3Ni and $AlNi_3$ alloys for obtaining

ADVANCES IN QUANTUM CHEMISTRY, VOLUME 29

0065-3276/97 $25.00

detailed information on the particular orbitals involved in the charge transfer processes.

Computational method

Tables I and II contain the positions of atoms in atomic units for the two alloys. In the cluster type DV-X_α calculation we have 16 atoms for the Al_3Ni cluster and 14 atoms for the $AlNi_3$ cluster. It is difficult to increase the number of atoms especially in the case of Al_3Ni cluster due to the orthorhombic structure. For these compounds we used the sphere radii of the constituent atoms given by Slater [6]. The values of the sphere radii influence the determination of the charge transfer inside the cluster. For the numerical iteration the self-consistent-charge scheme [7] was used. In the SCC calculations, the HFS potential in the cluster is gained by a sum of the Coulomb potentials which is constructed by overlapping of the atomic Coulomb potentials and adding the statistical exchange potential proportional to the 1/3 power of molecular charge. As a first iterative point, the SCF atom charges and wavefunctions of the ground state configuration are used. Molecular orbitals are represented by linear combinations of the numerical single site orbitals (SSO). The overlap and Hamiltonian matrix elements of the secular equation are computed by means of the discrete variational (DV) method, then following diagonalisation the eigenvalues and eigenfunctions are obtained. The exchange scaling factor α is taken to be 0.7 for all calculations. Basis sets including 1s to 3d, 1s to 4p for Al and Ni, respectively, are used. In the DV procedure a number of sampling points N=500 for each atom is required to obtain an accuracy of 0.1 Ry for valence energies. In order to compare the calculated HFS results with electron binding energies in the XPS measurements, one should calculate one-electron orbital energies for the "transition state" which can be compared with the ionization state energies [6]. The level structure of the cluster is given in the density of states (DOS) profiles obtained by replacing each discrete level by a Lorentzian with a width of 2.0 eV, weighted by the degeneracy of the orbital. The total DOS may be compared to photoemission spectra for the occupied region and to electron energy loss spectra for $E > E_f$ as a rough approximation neglecting transition probabilities. The DOS diagram can be also compared with those from band structure calculations. In order to obtain atomic orbitals with large quantum numbers a spherical potential was superimposed upon the atomic potential as follows:

$$V^{\nu}_{sso}(\mathbf{r}) = \begin{cases} V^{\nu}_{a} - V^{\nu}_{s} & \text{if } r < R^{\nu}_{s} \\ -c/\mathbf{r} & \text{if } r \geq R^{\nu}_{s} \end{cases}$$

where V_a^ν(r is the superimposed potential of the νth atom, V_s^ν the depth of the potential well and R_s^ν its radius. The Coulomb potential -c/r is assumed outside of the sphere. The constant c is adjusted in order to link the two potentials at r=R_s^ν. The atomic orbitals did not vary appreciably with the parameters of the added potential. Charge distributions were computed using the DVX_α cluster MO model [8], with experimental lattice constants [12,13] for the cubic-ordered (O_h) intermetallic compound $AlNi_3$ alloy and for the orthorombic (DO_{20}) structure Al_3Ni.

Table I. The position of atoms in the Al_3Ni cluster [9, 10] in atomic units.

Atom	x	y	z
Ni	0.000	0.000	0.000
Ni	3.273	6.931	8.092
Ni	6.246	0.000	3.546
Ni	9.520	6.931	4.546
Al-1	1.499	6.931	3.273
Al-1	1.774	0.000	4.819
Al-1	7.746	6.931	0.272
Al-1	8.021	0.000	7.819
Al-2	3.810	2.731	0.809
Al-2	3.810	11.132	0.809
Al-2	5.709	4.200	5.355
Al-2	5.709	9.663	5.355
Al-2	10.057	2.731	2.736
Al-2	10.057	11.132	2.736
Al-2	11.956	4.200	7.283
Al-2	11.956	9.663	7.283

Table II. The position of atoms in the $AlNi_3$ cluster [11] in atomic units.

Atom	x	y	z
Ni	0.000	3.3712	0.000
Al	3.3712	3.3712	3.3712

Methods of interpretation

Alloy-metal Auger parameter shifts were obtained from the measured Auger kinetic and photoelectron binding energies using the definition given by Williams and Lang [12]:

$$\Delta\xi(j) = \Delta E_k(ijj) - \Delta E_b(i) + 2\Delta E_b(j) \tag{1}$$

where $\Delta E_k(ijj)$ is the environmentally induced shift in the kinetic energy of an Auger transition involving the i and j core levels and ΔE_b is the difference in the binding energy of a core level between two environments. If ΔE_b is similar for all core levels, (1) corresponds to the conventional definition of the Auger parameter shift $\Delta\alpha' = \Delta E_k(ijl) + \Delta E_b$ (core). For estimating charge transfer from analyzing the final state Auger parameter shifts $\Delta\xi$ between a pure metal and a binary alloy, it can be shown [5] that

$$\Delta\xi = \Delta[q\frac{dk}{dN} + (k - 2\frac{dk}{dN})(\frac{dq}{dN}) + \frac{dU}{dN}] \tag{2}$$

where q is the valence charge, k is the change in the potential in the core when a valence electron is removed, N is the occupancy of core orbitals and U is the contribution from the chemical environment. It is assumed that k and q depend linearly on N. Because of the efficient screening , $\Delta(dU/dN) = 0$ and due to the on-site core hole screening $(dq/dN) = 1$ comparing two metals $\Delta(dq/dN) = 0$, giving

$$\Delta\xi = \Delta q(\frac{dk}{dN}) \tag{3}$$

for the case when the valence electrons belong to a single band. The parameter dk/dN can be obtained from the results of atomic structure calculations for free atoms [13]. For Al the parameters of an improved model (assuming k depending linearly on q and N) are available [14]. From this model

$$\Delta\xi = \Delta q * b \tag{4}$$

(4) where b is a model parameter obtained from atomic structure calculations [14].

Results and discussion

Table III. contain the alloy-metal Auger parameter shifts computed from the corresponding measured Auger kinetic energy and photoelectron binding energy shifts using the formula (1) [1]. The estimated accuracy of the values is 0.06 eV. In Table IV the values of the transferred charge q, calculated from (3) and (4) using the parameters $dk/dN = -2.3$ for Ni [13] and $b_p = -3.18$ for Al [14] are presented, together with the values obtained from the cluster MO theory [1]. A more detailed description of the non spin polarised DVX_α calculation of the AlNi systems can be found in our earlier work[1, 15]. The difference between the recent and the previous calculation is that in the case of Al_3Ni alloy the atomic positions reflect the true (and not a Cu_3Au like structure) positions of the atoms in cluster (see Table I). Hence the derived transferred charge in the case of Al_3Ni alloy is considerably different from that of our previous calculation. The results of the spin polarised DVX_α calculation can be compared with the calculations published earlier [16]. Present calculations were performed using the cluster type DVX_α approximation for spin-polarised electrons developed by Adachi et al. [17]. In the case of Al_3Ni the value of the magnetic moment from our calculation is zero, in agreement with the results published earlier [16], and with the observation.

Table III. Measured Auger parameter shifts, (alloy-metal, eV) [1].

	$AlNi_3$	Al_3Ni
Al($\Delta\xi(2p)$)	-1.19	-1.6
Ni($\Delta\xi(3p)$)	L_3 0.37; L_2 0.12	L_3 0.44; L_2 0.24

Table IV. Transferred charges Δq (alloy-metal, e)

alloy	Al_3Ni	Al_3Ni	$AlNi_3$	$AlNi_3$
	Exp. [1]	Theory	Exp. [1]	Theory
Al	0.50	0.028[2]	0.37	0.60[2]
Ni	-0.15[1] (-1.5[2])	-0.085	-0.11[1] (-0.12[2])	-0.20

[1] Average of values obtained from $\Delta\xi$ (3p, L_3MM) and $\Delta\xi$ (3p, L_2MM).
[2] Derived on the basis of charge conservation.

In the case of $AlNi_3$ alloy our self-consistent calculations give a rather small spin-magnetic moment, for each Ni atom :

$$\sigma_0^{Ni-s} = 0.033\ \mu_B/atom$$

$$\sigma_0^{Ni-p} = 0.025\ \mu_B/atom$$

$$\sigma_0^{Ni-d} = 0.032\ \mu_B/atom$$

through polarisation of the s,p,d valence electrons and for each Al atom:

$$\sigma_0^{Al-s} = 0.027\ \mu_B/atom$$

$$\sigma_0^{Al-p} = 0.075\ \mu_B/atom$$

through a small polarisation of the s and p electrons.

$$\sigma_0^{j-l} = Q_l^{\downarrow}(j) - Q_l^{\uparrow}(j)$$

where $Q_l^i(j)$ is the spin-i charge of angular momentum l on site j, μ_B is the Bohr magneton. All other valence states give a negligible polarisation. Comparing the results of our calculation with the earlier [16] one we find the same polarisation value ($0.032\mu_B$) in the case of Ni d valence electron. The earlier calculation is based on band structure model which use expansions of the Bloch functions in terms of linear combination of energy-independent augmented spherical waves (ASW) [16]. In these calculations [16] the Al p charge through polarisation was found to be $\sigma_0^{Al-p} = -0.003\ \mu_B/atom$, a value of opposite sign.

It can be seen from Table III that the experimental Auger parameter shifts are rather small ones, especially in the case of Ni, indicating the necessity of high accuracy energy measurements which is difficult at high kinetic energies. In the case of $AlNi_3$ our experimental results and the atomic structure model (Table IV) gives a charge transfer of 0.37 e from the Al to the Ni [1], the direction of this charge transfer agrees with the expectations regarding the difference in the electronegativity of Al and Ni. The value obtained from the Ni Auger parameter shifts is consistent with this transferred charge as well as with the charge conservation. Although the MO theory predicts a small charge transfer similarly to our results, it gives a factor of two higher values. It should be mentioned, however, that the absolute differences are not too large ones regarding the experimental error and the systematic errors of the approximations used in the atomic structure model and in the cluster MO calculations. In the case of Al_3Ni alloy the direction of the charge transfer is correctly given by our measurements (similarly to the prediction of the theory), and it indicates a larger electron transfer to Ni than in the case of the $AlNi_3$ alloy, in contradiction with our present MO calculation (Table IV).

Table V. Change in the Ni valence charge relative to the pure Ni.

	Al_3Ni	$AlNi_3$ (up)	$AlNi_3$ (down)
ΔQ(Ni 3d)	0.079	-0.025	0.002
ΔQ(Ni 4s)	0.124	-0.007	-0.026
ΔQ(Ni 4p)	-0.195	0.116	-0.141

$$\Delta Q(\mathrm{Ni}3d) = Q_{\mathrm{Al_3Ni}}(\mathrm{Ni}) - Q_{\mathrm{Ni}}(\mathrm{Ni})$$
$$\Delta Q(\mathrm{Ni}4s) = Q_{\mathrm{Al_3Ni}}(\mathrm{Ni}) - Q_{\mathrm{Ni}}(\mathrm{Ni})$$
$$\Delta Q(\mathrm{Ni}4p) = Q_{\mathrm{Al_3Ni}}(\mathrm{Ni}) - Q_{\mathrm{Ni}}(\mathrm{Ni})$$

Table V contain the alloy-metal change in the Ni valence charge relative to the pure Ni. It can be seen from the table that the largest charge transfer occurs to Ni 4s orbitals in the case of Al_3Ni alloy. Figure 1. shows the level structure and spin components for the $AlNi_3$ alloy. In Figure 2. the density of states (DOS) for the $AlNi_3$ is shown. The up spin component of the density of states are slightly shifted compared to the down spin component, causing the non-zero magnetic moment of $AlNi_3$ alloy.

In summary, our estimation for charge transfer in $AlNi_3$ alloy correctly gives the direction and the magnitude of the transferred charge comparing with the results from the cluster MO theory and the result is consistent with the

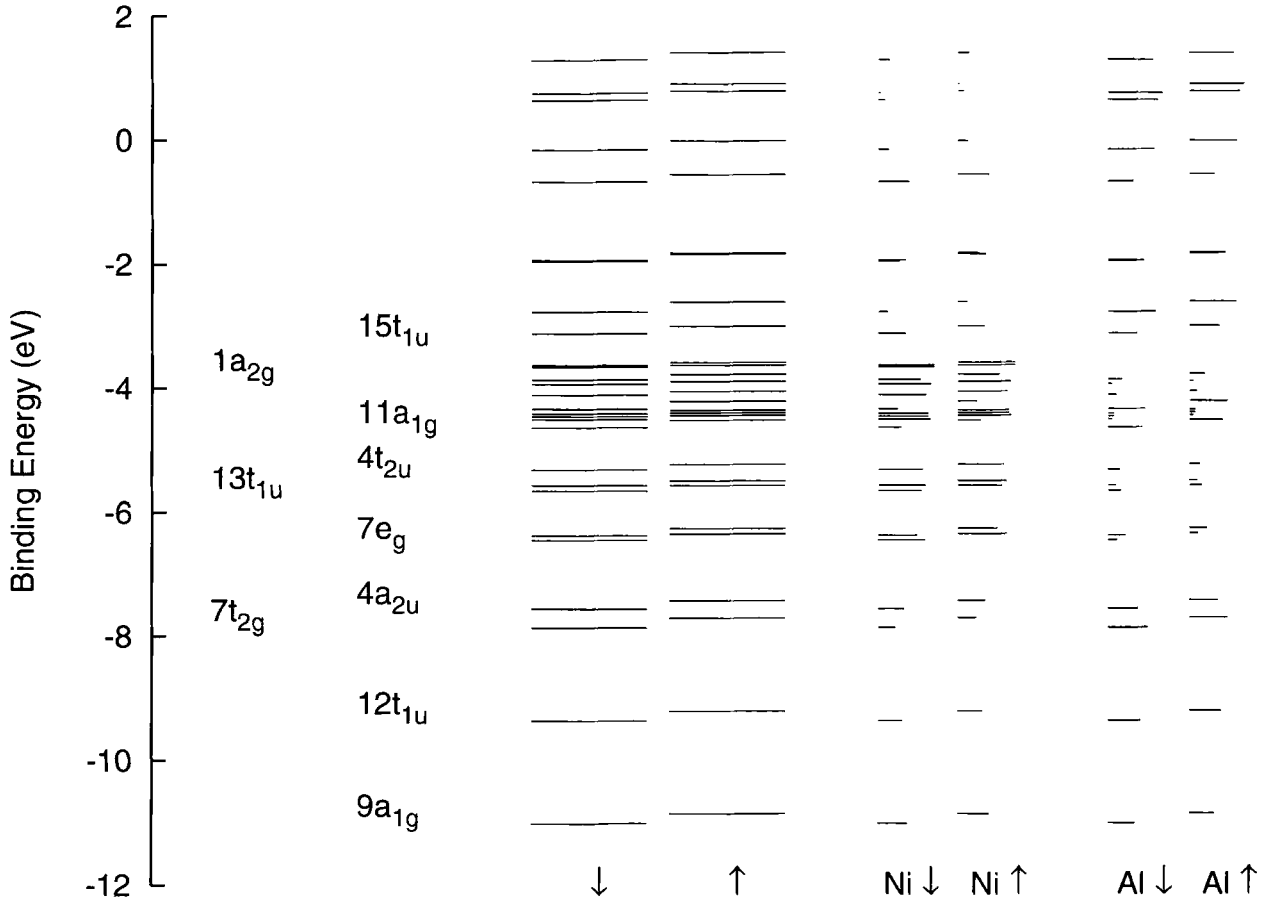

Figure 1. Molecular orbital levels and spin components for $AlNi_3$ alloy

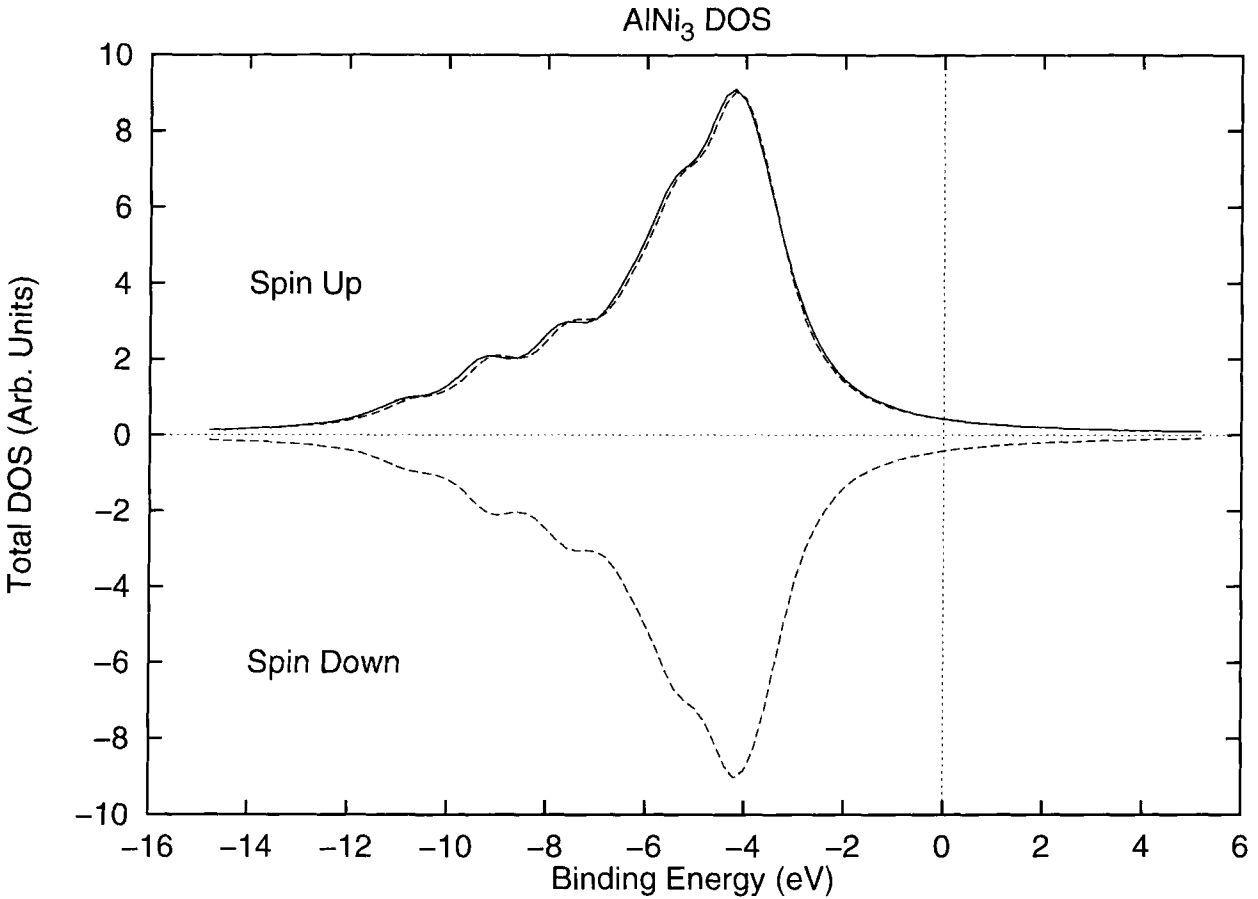

Figure 2. DOS for $AlNi_3$ alloy and spin components

charge conservation. We have found the same polarisation value ($0.032\mu_B$) as obtained earlier from band structure calculation [16] in the case of Ni d valence electrons. The experimental magnetic moment is an order of magnitude smaller for $AlNi_3$ than for Ni, this fact is demonstrated with DVX_α calculations. In the case of Al_3Ni the DVX_α calculation gives a zero magnetic moment. For Al_3Ni our charge estimation indicates a smaller charge transfer however, larger discrepancies occur between the theoretical and experimetal data (Table IV), possibly partly due to the neglection of the on site configuration changes in Ni. The potential model can not give the spin charge transfer, hence the DVX_α calculation can provide a good starting point to develop a spin polarised potential model.

Acknowledgments
This work was supported by the research projects: COST/D5/0001/94 (CEC), OTKA T007274 and T016636.

References

[1] L. Kövér, Zs. Kovács, R. Sanjinés, P. Weightman, G. Margaritondo, D. Varga, J. Pálinkás and H. Adachi, In B. Reihl and D. Briggs, Editors, *Proceedings of the Conference ECASIA-95*, page 448. Wiley and Sons, (1996).

[2] L. Pauling, *The Chemical Bond, Structure and Dynamics.* Academic Press, (1992).

[3] P. Weightman, R. J. Cole, N. J. Brooks and J. M. C Thorton, *Nuclear Instr. and Methods in Physics Research B.*, **97**, 472, (1995).

[4] R. J. Cole D. A. C. Gregory and P. Weightman, *Phys. Rev. B*, **49**, 5657, (1994).

[5] T.D. Thomas and P. Weightman, *Phys. Rev. B*, **33**, 5406, (1986).

[6] J.C.Slater, *Quantum Theory of Molecules and Solids*, volume **2** . McGraw-Hill, New York, (1960).

[7] A.Rosén, H. Adachi and D.E.Ellis, *Molecular Phys.*, **33** , 199, (1977).

[8] H.Adachi, T. Tanabe and S. Imoto, *Japanese Journal of Applied Physics*, **17** , 49, (1978).

[9] P. Villars and L.D.Calvert, *Pearson's Crystallographic Data for Intermetallic Phases.* American Society for Metals, Ohio, (1985).

[10] G. Cubiotti, E. E. Krasovskii, O. V. Slobodyan ,Yu. N. Kucherenko and V. N. Antonov. *J. Phys., Condens. Matter*, **7**, 4865, (1995).

[11] K-H Hellwege, *Landolt-Börnstein New Series Group III, Structure data of crystals, vol 6.* Springer Verlag, Heidelberg, (1971).

[12] A. R. Williams and N. D. Lang, *Phys. Rev. Lett.*, **40**, 954, (1978).

[13] D.A.C. Gregory, A.D. Laine. P.S. Fowles. A. Takahashi and P. Weightman, *J. Phys. C*, **5**, 3843, (1993).

[14] N.J. Brooks, M.D. Jackson, R.J. Cole and P. Weightman. *Surface Rev. Letters*, in press.

[15] Zs.Kovács, L.Kövér, D.Varga, P.Weightman, J.Pálinkás and H.Adachi. *Phys. Rev. B*, **54**, (1996).

[16] D.Hackenbracht and J.Kübler, *J. of Physics F*, **10**, 427, (1980).

[17] H.Adachi, M. Tsukada and C. Satoko, Discrete Variational X_α cluster calculation. *Journal of the Phys. Soc. of Japan*, **45** , 875, (1978).

Core-electron binding energy shifts in aluminium

G. Paragi, I. K. Gyémánt, Zs. Varga
Department of Theoretical Physics, József Attila University
Szeged, Hungary

Abstract

Theoretical 1s, 2s, 2p core-electron binding energies are presented for the Al atom in free space and in $AlAl_{12}$ and $AlAl_{12}Al_6$ clusters. The binding energies have been calculated by the self-consistent field scattered-wave method, using various exchange-correlation potentials. The atom/cluster binding-energy shifts have been obtained both from Slater's transition-state energies (STS) and from total-energy differences (ΔSCF). Relying upon these results we could examine, how the binding energy changes with increasing the size of the cluster, and we could compare the effect of the different potentials.

1. Introduction

It was realised early, that the core level energies depend on the chemical environment of the atom and are systematically several eV lower in conducting solids than in free atoms. Measurements and calculations on the atom/molecule binding-energy shifts indicate that binding energy shifts reflect not only the ground-state charge-distribution of the molecule, but also the energy associated with the rearrangement of the passive electrons in the final state, and the results show that without final state-effects the core level binding energies would be higher in the molecule, than in the atom.

The core-level binding energy is defined as:

$$E_c = E_f(n_c - 1) - E_i(n_c)$$

where „ i " and „ f " refer to initial and final state, „ E " means the total energy and „ n_c " is the initial occupancy of the core level c . The difference between core-level binding energy in the cluster (molecule, solid) and in the free atom gives the core-level binding energy shift (Δ) .

Various theoretical models, such as the " excited-atom approach " [1] and the thermochemical model [2,3] have been proposed for the determination of these shifts. A model based on the density-functional theory has been suggested and applied for the analysis of core hole screening in simple metals by Ambladh and von Barth [4] and by Williams and Lang [5]. Spin-polarised density-functional

ADVANCES IN QUANTUM CHEMISTRY, VOLUME 29

0065-3276/97 $25.00

conduction-electron screening calculation have been performed for core ionisation by Nieminen and Puska [6] and Rantala [7].

2. Model and Method

In our calculations four kinds of exchange potentials have been used, the Xα with Schwarz's parameter, the Gunnarsson-Lundqvist [8], the Langreth-Mehl [9] and the Perdew-Yue [10] potential. The expression of these potentials can be found in the appendix. The Xα and the Gunnarsson-Lundqvist (GL) potentials are within the Local Density Approximation (LDA) while the Langreth-Mehl (LM) and the Perdew-Yue (PY) potentials are based on the Generalized Gradient Approximation (GGA). We have successfully tested these potentials for several atoms and some small molecules.

The geometry of the $AlAl_{12}$ cluster corresponds to an Al atom and its 12 nearest neighbours in bulk Al of *fcc* structure with the lattice const of 7.64 bohr. In the calculations we used overlapping atomic spheres (the overlap is 15%), where the radius of atomic region (for all Al atoms) is 3.1063 bohr, and the cluster was placed into an outer sphere, with a radius of 8.1034 bohr. For the $AlAl_{12}Al_6$ cluster the radius of the outer region is 10.3411 bohr. In the interatomic and outer sphere region we used the same α parameter as in the atomic region. We should mention that the scheme of the overlapping sphere has, although not completely rigorous advantage over the muffin-tin methods. Nonempirical criteria for atomic sphere overlap, based on electron counting and the virial theorem , have been suggested by Norman [11] .

The SCF criteria were 10^{-5} relative change in the total potential in all cases. This implies 1-2 eV inaccuracy in the total energy, that is why we used an alternative approximation, the so called Slater's transition state (STS) approach.

The definition of the binding energy shift is given by the difference:

$$\Delta = E_c^{atom} - E_c^{cluster}$$

where E_c^{atom} and $E_c^{cluster}$ are the core-level binding energies in the atom and in the cluster respectively and calculated by difference of the total energies (ΔSCF) [12] , [13]. The inaccuracy of the total energy of the cluster is 0.001% in calculation. Using Slater's transition-state energies the binding energy shift is defined as :

$$\delta = |\varepsilon_c^{atom}| - |\varepsilon_c^{cluster}|$$

where ε_c indicate the Kohn-Sham orbital energy calculated with half integer occupation (the so called Slater's transition state energy [12] , [13]). There are practically no inaccuracy in ε_c , so the inaccuracy in δ depends only on the quality of the STS approximation.

3. Results and Discussion

In Table I we present results for the free Al atom core-level binding energies

obtained by using various exchange-correlation potentials. The reference 1s binding energy of a free Al atom has been obtained from the thermochemical model combined with X-ray data [14]. The 2s and 2p data were obtained from photoemission experiments which were performed on samples of aluminium prepared with clean surface in ultrahigh vacuum [15].

Table I. ΔSCF and STS core-level binding energies (E and $|\varepsilon|$, respectively) for free Al atom, using various exchange and correlation potentials. (all energies are in eV) in comparison with reference data. (Detailed information and explanation of abbreviations see in the text.)

orb.		Xα	G.-L.	L.-M.	P.-Y.	ref.
1s	E_{1s}	1575.60	1569.80	1573.62	1578.21	1568.8 [14]
	$\lvert\varepsilon_{1s}\rvert$	1577.46	1571.56	1575.75	1580.15	1558.2 [16]
2s	E_{2s}	120.06	119.63	118.85	119.10	117.99 [15]
	$\lvert\varepsilon_{2s}\rvert$	121.70	121.09	120.57	120.50	
2p	E_{2p}	83.34	83.12	81.26	81.65	72.84 [15]
	$\lvert\varepsilon_{2p}\rvert$	84.99	84.42	83.20	83.16	

Note: Experimental reference data [15, 16] is referred to Fermi level.
The value of the work function is approximately 4eV in Al

We can see from Table I that the Gunnarsson - Lundqvist potential gives the best result comparing with reference data. This is in contrast with the expectations, because GGA potentials resulted better agreement with experimental data in DFT calculations for several atoms [10] .

We had convergence problem in cluster calculation with the Langreth - Mehl potential, though we tested our model successfully for such a small molecule as SF_6. The convergence problem may be connected with the poor asymptotic behaviour of the LM potential, namely that the energy diverges when r tends to infinity.

The Perdew-Yue potential works well for $AlAl_{12}$, and in this manner we could compare the results of the LDA and the GGA approximations. In Table II we show the calculated binding energies for $AlAl_{12}$, and the core-level shifts are presented in Table IV. We can see both in table I and II that in case of the 1s orbital, the core-level binding energy strongly depends on the choice of the exchange and correlation potential. The 1s orbital is near to the nucleus so the electron density is large here and therefore the differences in the exchange and correlation potentials (cf. Table III.) have large effects on this orbital. For 2s and 2p orbitals the binding energies are not so sensitive, because these orbitals are not so near to the nucleus. Though neither experimental nor theoretical results have been reported for Al clusters, both theoretical and experimental data are available for atom/metallic aluminium core-level shifts.

Table II. Al core-level binding energies (in eV) in $AlAl_{12}$ cluster calculated using various exchange potentials (notation see at Table I) .

orb.		Xα	G.-L.	P.-Y.	ref.
1s	E_{1s}	1572	1566.784	1575.01	–
	$\|\varepsilon_{1s}\|$	1570.86	1566.57	1575.28	
2s	E_{2s}	118.167	117.6686	117.0.97	–
	$\|\varepsilon_{2s}\|$	116.6	117.267	117.097	
2p	E_{2p}	81.336	80.94	79.655	–
	$\|\varepsilon_{2p}\|$	79.77	80.49	79.526	

The differences between the results obtained for $AlAl_{12}$ cluster with various potentials, show similar tendencies as for Al atom, but for the cluster the variation of calculated binding energies is less than in the atomic calculations. The reason for the differences between STS and ΔSCF values is that, though the SCF criterion were the same in every case (0.001% relative change in the potential) , the total energy could change a few eV per iteration. We have examined the difference between the value of GGA and LDA exchange potential, and Table III shows some potential data at different radial distances. At first sight it seems that close to the nucleus, the difference is larger, but the difference relative to the total potential energy is always the same order of magnitude (about 0.1%)

Table III Values of the different exchange and total potentials in the central atomic sphere of the $AlAl_{12}$ cluster at sample points (in a.u.) .

Radial	X α		G. L.		P. Y.	
distance	$-V_{xc}$	$-V_{tot}$	$-V_{xc}$	$-V_{tot}$	$-V_{xc}$	$-V_{tot}$
0.00188	23.66	13743.80	21.98	13742,30	71.66	13791.80
0.00377	23.28	6838.30	21.63	6836.80	45.35	6860.40
0.05648	14.81	394.30	13.86	393.55	15.04	394.70
0.06024	14.35	365.96	13.40	365.22	14.46	366.20
0.19579	5.68	81.20	5.44	81.09	5.40	81.14
0.20332	5.50	76.90	5.30	76.80	5.16	76.70
0.48949	3.47	18.10	3.40	18.00	3.37	18.10
0.50455	3.38	17.09	3.30	17.05	3.27	17.08
1.16724	1.09	2.69	1.15	2.70	1.08	2.71
1.22748	1.01	2.34	1.07	2.35	1.02	2.39
2.97457	0.59	0.06	0.69	0.067	0.57	0.04
3.09506	0.57	0.058	0.67	0.07	0.55	0.08

Table IV ΔSCF and STS core-level binding energy shifts for $Al/AlAl_{12}$

calculated with various exchange potentials (in eV) . In the last column (ref.) Al/metal shifts are referred to.

orb.		Xα	G.-L.	P.-Y.	ref.
1s	Δ	3.32	3.02	3.20	6.15 [7]
	δ	6.60	4.99	4.87	6.3 [6]
2s	Δ	1.89	1.96	2.00	5.71 [7]
	δ	5.10	3.82	3.40	
2p	Δ	2.00	3.48	1.99	5.74 [7]
	δ	5.20	3.93	3.63	5.8 [6]

We have to mention, that no experimental and - to our knowledge - no other calculated values are available for Al/$AlAl_{12}$ binding energy shifts. In the last column of Table IV we presented empirical and calculated values for the Al/metal shifts. According to the relatively great (1-2 eV) uncertainty in the total energy, we regard the STS results as more consistent approximations. Further, each calculation shows, that the 2s and the 2p core-level shifts are nearly equal, but the shift of the 2p is always a little bit larger. The GL and the PY shifts are nearly equal, and are slightly different from the Xα results.

Core-level biding-energies and biding-energy shifts for $AlAl_{12}Al_6$ cluster are presented in Table V.

Table V. $AlAl_{12}Al_6$ STS core-level binding energies ($|\varepsilon|$), and core-level shifts with Xα exchange potential (in eV)

core level	$\|\varepsilon\|$	δ
1 s	1573.24	4.22
2 s	119.15	2.55
2 p	82.29	2.70

We can see from table V , that the shifts are smaller then in $AlAl_{12}$. The formal explanation for the decrease of core-electron binding energy shifts is that the interatomic region in $AlAl_{13}Al_6$ is much bigger than in $AlAl_{12}$. That is the reason why the constant potential (which is the volume average for the interatomic region of the total potential) is 1-2 eV deeper in case of $AlAl_{12}$ than in $AlAl_{13}Al_6$. This can cause approximately the same (1 eV) amount of " muffin tin " type difference in the binding energies and therefore in the shifts . An explanation based on physical argument is what follows: The electrons of the first 12 neighbouring Al atoms screen the effect of the central nucleus, and as a result the core electrons binding energies decrease. The 6 Al-atoms in the second shell will reduce the

screening effect of the screening electrons. So the binding energy shift will be smaller in $AlAl_{13}Al_6$ than in $AlAl_{12}$

Calculations with GL and PY are in progress and results for $AlAl_{12}Al_6$ will be presented in an other paper. From Table V one can see, that our previous statements about 2s, 2p core level shifts hold in this case too.

In conclusion we note that the STS approximation gives a proper estimate of the binding energies and has the advantage to the ΔSCF calculations of avoiding the subtraction of two large and uncertain quantities. (Total energies that may be of the order of several thousand eV, with 0.001% uncertainty.) Another experience is that the GGA approximation has not improved the results for binding energies, and in addition its convergence feature is less effective. We can see that we have to increase the size of the cluster because the atom/cluster shift may not tend to the value of the atom/metal shift monotonously with increasing cluster size.

References:

[1] R.E. Watson, M.L. Perlman, and J.F. Herbst, Phys. Rev. B13 2358 (1976)
[2] B Johansson and N. Mårtensson, Phys. Rev. B21 4427 (1980)
[3] P. Steiner, S. Hüfner, N. Mårtensson, and B. Johansson, Sol. State Comm. 37 73 (1981)
[4] C.O. Ambaladh and U. von Barth, Phys. Rev. B33 3307 (1976)
[5] A.R. Williams and N.D. Lang, Phys. Rev. Lett. 40, 954 (1978)
[6] R.M. Nieminen, M.J. Puska, Phys. Rev. B25 67 (1982)
[7] T Rantala, Phys. Rev. B28 3182 (1983)
[8] O. Gunnarsson and B.I. Lundqvist, Phys. Rev. B13 4274 (1976)
[9] D.C. Langreth and M.J. Mehl Phys. Rev. B28 1809 (1983)
[10] J.P. Perdew and W. Yue, Phys. Rev. B33 8800 (1986)
[11] J.G. Norman, Jr. J. Chem. Phys. 61 4630 (1974)
[12] J.C. Slater: " The Self-consistent Field for Molecules and Solids " Vol. 4. McGraw-Hill Book Co. , New York, 1974
[13] J.C. Slater: " The calculation of Molecular Orbitals " John Wiley and Sons, New York, 1979
[14] S. Aksela, R Kumpula, H. Aksela, J. Väyrynen: Phys. Scripta 25, 45 (1982)
[15] L. Ley *etal*: Phys. Rev. B11,. 600 (1975)
[16] J.E. Castle *etal.* J. Elec. Spectr. , 16 97 (1979)

Appendix :

Here we present the form of the potentials, what we used in calculation where ρ means the electron density :

- Xα potential:

$$V_x = -6\alpha(3 / (4\pi) \rho)^{1/3}$$

- Gunnarsson-Lundqvist Local Density Approximation :

$$V_x = -aX(1+(b/X) \ln(1+cX))$$

where: a=2.797 , b=0.07788 , c=7.9043 , $X=(4\pi\rho)^{1/3}$

- Langreth-Mehl Generalized Gradient Approximation :

$$V_x = A_x\rho^{1/3}\left[\tfrac{4}{3}F - ts^{-1}\frac{dF}{ds}\right]$$

where: $F(s) = 1+1.521(0.0864\, s^2)$ and $A_x = -\frac{3}{4}\left(\frac{3}{\pi}\right)^{1/3}$, $s=\frac{\nabla\rho}{2k_f\rho}$,

$t = (2k_f)^{-2}\rho^{-1}{}^2\rho$, $k_f = (3\pi^2\rho)^{1/3}$

- Perdew-Yue Generalized Gradient Approximation:

$$V_x = A_x\rho^{1/3}\left[\tfrac{4}{3}F - ts^{-1}\frac{dF}{ds} - \left(u - \tfrac{4}{3}s^3\right)\frac{d}{ds}\left(s^{-1}\frac{dF}{ds}\right)\right]$$

where: $F(s) = (1+0.0864\, s^2/m + b\, s^4 + c\, s^6)^m$ $u=(2k_f)^{-3}\rho^{-2}\times\nabla\rho\,|\,\nabla\rho\,|$
m=1/15, b=14, c=0.2 and A_x, s , t , k_f are same like in L.-M. potential

Analysis of Core-Hole Effect in Cation $L_{2,3}$-Edge of MgO, α-Al_2O_3 and SiO_2 Based on DV-Xα Cluster Calculations

Kazuyoshi Ogasawara, Isao Tanaka and Hirohiko Adachi

Department of Materials Science and Engineering
Kyoto University
Sakyo-ku, Kyoto 606-01, JAPAN

Abstract

In order to clarify the effect of a core hole in the cation $L_{2,3}$-edge of electron energy-loss near-edge structures (ELNES) and X-ray absorption near-edge structures (XANES), the photoabsorption cross section (PACS) and the partial density of stats (PDOS) are calculated for MgO, α-Al_2O_3, SiO_2 (α-quartz) based on the DV-Xα cluster calculations in the absence and presence of a core hole. It is found that the PDOS is a good approximation of the PACS and the major spectral features are well reproduced by the Slater's transition state, in which one half of a core electron is excited to an unoccupied orbital. The absolute transition energy calculated by the spin-polarized transition state is in excellent agreement with those estimated from the XANES spectra. The strongest peak that appears near the Al $L_{2,3}$-edge is found to originate from the presence of a core hole. Such an effect is less significant in MgO and α-quartz. The electronic relaxation due to the presence of a core hole was characterized by the localization of unoccupied molecular orbitals and evaluated quantitatively by calculating the localization index of these orbitals. The difference in the magnitude of core-hole effects in these oxides were well understood by the difference in the structural and chemical environment of excited atoms such as cation-cation distances and the coordination numbers.

ADVANCES IN QUANTUM CHEMISTRY, VOLUME 29

0065-3276/97 $25.00

1 Introduction

Recent technological improvements enable one to obtain electron energy-loss spectra (EELS) with spatial resolution comparable to chemical bond length in solid matter [1]. On the electron energy-loss process, an electron is excited from a core level to an unoccupied orbital leaving a core hole. The structures in the first 30 eV just above the energy-loss edge are called electron energy-loss near-edge structures (ELNES). When the signal is collected only in the small scattering angle as is the case for an ordinary spectrometer equipped in a transmission electron microscope, the transition is dominated by the electric dipole selection rule. Under these conditions, the ELNES is identical to the near-edge structures of X-ray absorption spectra (XANES or NEXAFS) [2]. If the unoccupied band structure remains rigid during the electronic transition, the ELNES spectrum should reflect the density of states (DOS) at the excited atom projected in a certain symmetry according to the selection rule (partial density of states or PDOS). Since the DOS at a probe atom is sensitive to the surrounding atoms and their arrangement, the ELNES can be potentially a powerful tool to reveal the local structural and chemical environment around a particular atomic species. The ELNES spectra often exhibit a specific structures reflecting a local site symmetry and it is called a "coordination fingerprint" [3]. However, it is obviously more efficient to calculate the spectra based on a reliable theoretical method.

For this purpose, theoretical calculations with various degrees of approximations have been employed. Among them, three different approaches are the most widely used. First one is the molecular orbital (MO) calculations using the multiple scattering (MS)-Xα method originally developed by Johnson [4]. Second is the multiple-scattering approach based on the Korringa-Kohn-Rostocker (KKR) band theory as used in the ICXANES computer code by Durham and coworkers [5], [6]. This method will hereafter be called simply as MS-calculation. Although these calculations have been successful in

many systems, they calculate the multiple scattering phenomena by imposing a muffin-tin potential on the structure in question. Such potential is not a good assumption for systems having highly covalent directional bonding or large open interstitial space. Moreover, the calculated results are pointed out to be dependent on the choice of muffin-tin potential [7]. Third is the band-structure calculation using "extended basis-sets", which have been successfully reproduced the XANES for some oxides [8], [9].

Despite the potential, experimental spectra of ELNES and XANES have not been fully utilized in order to monitor the local structural and chemical environment. One of the major reasons is the presence of "core-hole effects" which leads to a redistribution of the PDOS features [10]. In other words, the presence of this effect has been considered as a bottleneck for the full interpretation of the experimental spectra. For example, O'Brien *et al.* compared their XANES spectra of MgO, α-Al_2O_3 and $MgAl_2O_4$ at cation $L_{2,3}$-edge with theoretical DOS obtained by band calculations, but their unoccupied DOS did not reproduce the experimental spectra [11]. Thus, the origin of the major spectral features was concluded to be the formation of a core exciton, *i. e.*, a bound state of the excited electron due to the presence of a core hole.

In order to investigate such local electronic relaxations, discrete variational (DV)-Xα cluster calculation [12],[13] is one of the most powerful methods. Since all of the core orbitals are used in the calculation, the electronic structures in the presence of a core hole can be calculated self-consistently. We have recently demonstrated that our DV-Xα cluster calculations well reproduce the core-hole excitonic features in the Al $L_{2,3}$-edge of the α-Al_2O_3 [14]. This indicates that the redistribution of the electronic structure is well reproduced by the DV-Xα calculations. The spectral features at cation $L_{2,3}$-edge ELNES and XANES of MgO and SiO_2 are also well reproduced by the calculation including a core hole, but they are well reproduced even by the ground state calculations [15]-[17]. Therefore, the cation PDOS in the unoccupied band is virtually rigid during the electronic transition in these oxides. However, it is

important to evaluate the limitation to use the ground state calculation for the interpretation of experimental spectra.

Another open question is the accuracy of using the PDOS as an approximation of the photoabsorption cross section (PACS). There should be some uncertainty in the calculated PDOS depending upon the choice of the basis-set. The ambiguity can be reduced if the PACS is calculated directly from first principles using wave functions obtained by a self-consistent calculation.

In this paper, we present the PDOS and PACS calculated by the DV-Xα method for model clusters of MgO, α-Al_2O_3 and SiO_2 (α-quartz) at the ground state, intermediate state (Slater's transition state) and the final state of the transition. The major spectral features in the cation $L_{2,3}$-edge ELNES and XANES spectra are well reproduced by the Slater's transition state. Absolute transition energy calculated by the spin-polarized transition state agrees well with those estimated from the XANES spectra. A significant core-hole effect appear when the unoccupied orbital localizes drastically during the transition. The degree of localization was evaluated quantitatively by calculating the localization index of the unoccupied molecular orbital. The characteristics of the core-hole effect in these oxides are well understood by the difference in the structural and chemical environment, especially by the cation-cation interaction such as the cation-cation distance and the coordination numbers. The origin of the large core-hole effect in α-Al_2O_3 is ascribed to the presence of an exeptionally short cation-cation bond with rather large cation-cation overlap population.

2 Computational Procedures

First principles MO calculations were done by the Hartree-Fock-Slater (HFS) method using the DV-Xα method. The DV-Xα method was first developed to solve the energy-band problems by D. E. Ellis and G. S. Painter [18] and was then applied to the cluster calculation by F. W. Averill and D. E. Ellis [19]. Self-consistent calculations were developed by A. Rosén *et al.*

[20]. We use a modified version of this program, in which the numerically generated basis functions can be optimized corresponding to the change of molecular charge density for each iteration. The details of this program have been described by H. Adachi *et al.* [12]. In the HFS method, the exchange and correlation energies are taken into account by the use of Xα potential given by Slater [21] as

$$V_{xc\uparrow} = -3\alpha[\frac{3}{4\pi}\rho_{\uparrow}(\mathbf{r})]^{1/3}, \tag{1}$$

where $\rho_{\uparrow}(\mathbf{r})$ is the local charge density at point $\mathbf{r}$ for electrons with up spin. In the present calculation, α was fixed at 0.7, which was found empirically as most appropriate [22]. The MOs were constructed by linear combination of numerically generated atomic orbitals (AOs);

$$\phi_l(\mathbf{r}) = \sum_i C_{il}\chi_i(\mathbf{r}), \tag{2}$$

where $\chi_i(\mathbf{r})$ denotes the AOs and C_{il} is the coefficient of the ith AO in the lth MO. All integrations are made in a numerical manner. The numerical basis functions were obtained by solving the radial part of the Schrödinger equations. The radial part of the basis functions are thus flexible to chemical environment. A spherical potential well was imposed for the generation of atomic orbitals, however, it is confirmed that the calculated PDOS and PACS are almost independent on the choice of the potential well, if the width and the depth of the well are chosen in a certain range [17]. Thus the present calculation is practically free from any adjustable parameters.

The oscillator strength for the electric dipole transition for the photon absorption between states p and q is given by

$$I_{pq} = \frac{2}{3}\Delta E \mid \langle q \mid \mathbf{r} \mid p \rangle \mid^2 . \tag{3}$$

where ΔE represents the transition energy. In the present work, I_{pq} is obtained directly by the numerical integration of the dipole matrix. In the DV numerical integration scheme, all integrals in equation (3) can be calculated easily as the weighted sum of integrands at sample points [23]. One can therefore avoid

computational difficulties associated with the multicentre integration. The photoabsorption cross section (PACS) is proportional to the oscillator strength.

The PDOS and PACS were calculated for MgO, α-Al_2O_3 (corundum), and SiO_2 (α-quartz) using the model clusters of $(Mg_{13}O_{14})^{2-}$, $(Al_8O_{33})^{42-}$ and $(Si_5O_{16})^{12-}$, respectively. The stereoscopic views of these clusters are shown in Fig. 1. They are constructed based on the crystal data and point charges are located at the external atomic sites so as to produce the effective Madelung potential. A cation atom is put at the center of the cluster which is surrounded by one cation shell and two anion shells. The symmetry used in the calculations are O_h for $(Mg_{13}O_{14})^{2-}$, C_3 for $(Al_8O_{33})^{42-}$ and C_2 for $(Si_5O_{16})^{12-}$, respectively. Nearly minimal basis-sets are used in order to clarify the simple relationship between spectral features and chemical bondings. Basis-sets are 1s - 2p for O and 1s - 3d for Mg, Al and Si. The number of sample points used in the calculations are one thousand times the number of atoms within the cluster.

Calculations are made for three electronic configurations, namely ground state (GS), final state (FS) with the presence of a core hole, and the Slater's transition state (TS) in which one half of an electron is removed from the core orbital to fill an unoccupied orbital [21]. These electronic configurations are illustrated schematically in Fig. 2. The number of electrons in a cluster is the same for all three states. In the HFS method, one electron MO energy is given by a partial derivative of the HFS total energy with respect to the occupation number of the MO (Janak's theorem). Thus, the ith MO energy is expressed as

$$\varepsilon_i = \frac{\partial E}{\partial f_i}, \tag{4}$$

where E is the total energy and f_i is the number of electrons in the ith MO. This is different from the Hartree-Fock (HF) MO energy, which is the finite difference of the HF total energies between two states where the occupation number of the MO differs by one (Koopmans' theorem). If we denote the total energy of many-electron system with f_i electrons in the ith orbital and f_j electrons in the jth orbital by $E(f_i, f_j)$, the total energy of the ground

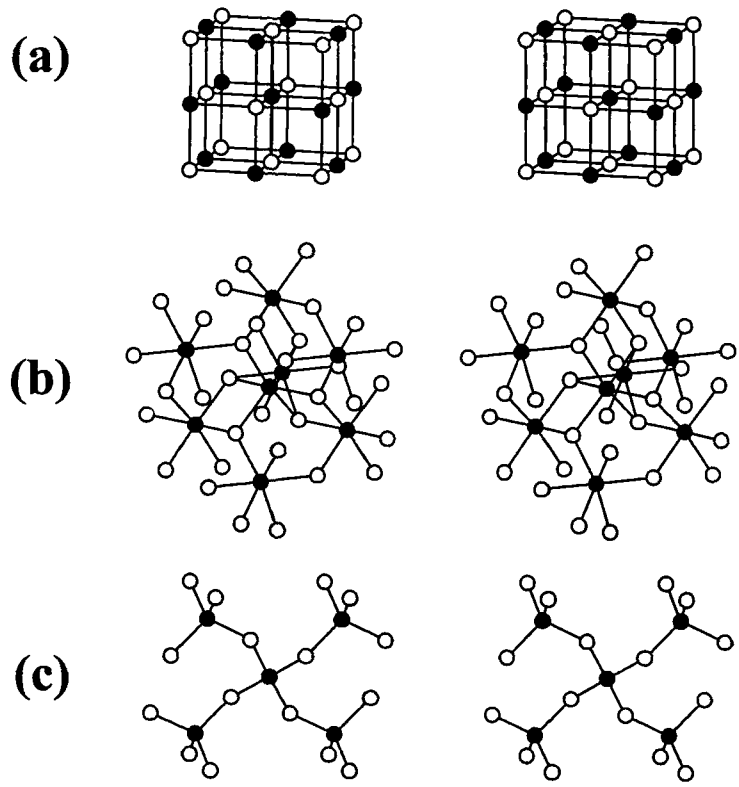

Figure 1: Stereoscopic views of (a) $(Mg_{13}O_{14})^{2-}$, (b) $(Al_8O_{33})^{42-}$ and (c) $(Si_5O_{16})^{12-}$ clusters.

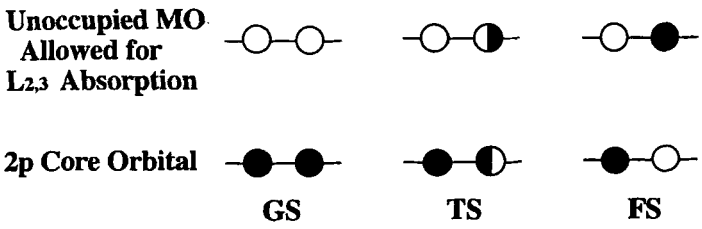

Figure 2: Schematic illustration of ground state (GS), Slater's transition state (TS) and final state (FS) electronic configurations.

state, transition state and final state can be expressed as $E^{GS} = E(f_0, 0)$, $E^{TS} = E(f_0 - 1/2, 1/2)$ and $E^{FS} = E(f_0 - 1, 1)$, respectively, where the ith orbital corresponds to the 2p core orbital, the jth orbital corresponds to the unoccupied orbital and f_0 is the number of electrons in the ith orbital at ground state. Thus, the total energy of the initial state can be expanded around $f_i = f_0 - 1/2$ and $f_j = 1/2$ as,

$$\begin{aligned} E^{GS} = E^{TS} &+ \frac{1}{2}\frac{\partial E}{\partial f_i}\Big|_{\substack{f_i = f_0 - 1/2 \\ f_j = 1/2}} + \frac{1}{8}\frac{\partial^2 E}{\partial f_i^2}\Big|_{\substack{f_i = f_0 - 1/2 \\ f_j = 1/2}} \\ &- \frac{1}{2}\frac{\partial E}{\partial f_j}\Big|_{\substack{f_i = f_0 - 1/2 \\ f_j = 1/2}} + \frac{1}{8}\frac{\partial^2 E}{\partial f_j^2}\Big|_{\substack{f_i = f_0 - 1/2 \\ f_j = 1/2}} \\ &+ \cdots . \end{aligned} \tag{5}$$

The total energy of the final state is also expanded similaly as,

$$\begin{aligned} E^{FS} = E^{TS} &- \frac{1}{2}\frac{\partial E}{\partial f_i}\Big|_{\substack{f_i = f_0 - 1/2 \\ f_j = 1/2}} + \frac{1}{8}\frac{\partial^2 E}{\partial f_i^2}\Big|_{\substack{f_i = f_0 - 1/2 \\ f_j = 1/2}} \\ &+ \frac{1}{2}\frac{\partial E}{\partial f_j}\Big|_{\substack{f_i = f_0 - 1/2 \\ f_j = 1/2}} + \frac{1}{8}\frac{\partial^2 E}{\partial f_j^2}\Big|_{\substack{f_i = f_0 - 1/2 \\ f_j = 1/2}} \\ &+ \cdots . \end{aligned} \tag{6}$$

Thus the difference in the total energy between the initial state and the final

state can be calculated as,

$$E^{FS} - E^{GS} = \frac{\partial E}{\partial f_j}\Big|_{\substack{f_i = f_0 - 1/2 \\ f_j = 1/2}} - \frac{\partial E}{\partial f_i}\Big|_{\substack{f_i = f_0 - 1/2 \\ f_j = 1/2}} + \cdots$$

$$= \varepsilon_j^{TS} - \varepsilon_i^{TS} + \cdots. \tag{7}$$

Since the second-order terms cancells each other and only the third-order and higher-order terms follow the explicitly written terms, the diference in the total energy between the initial state and final state can be well approximated by the difference in the one-electron MO energy obtained by the Slater's transition state. The single calculation at the transition state is computationally more convenient than having to make a separate calculation of the total energies of initial and final states. Additionally, the transition state calculation has a great advantage, since electronic relaxation associated with the transition can be evaluated self-consistently.

The overlap population between ith AO and jth AO at the lth MO is given by

$$Q_{ij}^l = C_{il}C_{jl}\sum_k \omega(\mathbf{r}_k)\chi_i(\mathbf{r}_k)\chi_j(\mathbf{r}_k), \tag{8}$$

where $\mathbf{r}_k$ is one of the sampling points and $\omega(\mathbf{r}_k)$ is the integration weight or reciprocal of the sample point density at $\mathbf{r}_k$. The sum with respect to j provides the orbital population Q_i^l of ith AO at the lth MO, *i. e.*,

$$Q_i^l = \sum_j Q_{ij}^l. \tag{9}$$

Localization index for each MO, L_l, given by

$$L_l = \sum_i (Q_i^l)^2, \tag{10}$$

was computed in order to evaluate the spacial extension of the lth MO among different atomic sites. The sum without squaring is unity, *i. e.*,

$$\sum_i Q_i^l = 1. \tag{11}$$

The definition of the localization index is the same as that used by Ching *et al.* [24]. It has a value ranging from $1/N$ and 1, where N is the total number of AOs. L_l is unity when the l-th MO is perfectly localized and $1/N$ when perfectly delocalized.

3 Results and Discussion

3.1 MgO

For the $(Mg_{13}O_{14})^{2-}$ cluster in O_h symmetry, the LUMO allowed for the $L_{2,3}$ absorption is $12a_{1g}$. Therefore, $(2p)^{5.5}(12a_{1g})^{0.5}$ and $(2p)^{5.0}(12a_{1g})^{1.0}$ configurations were used for the transition state and final state calculations. Following the electric dipole selection rule, the cation 2p core electron is excited to occupy the cation s and d unoccupied orbitals, which brings about the ELNES or XANES spectra at the cation $L_{2,3}$-edge. Since we use nearly minimal basis-sets throughout the present work for simplicity, a sum of cation 3s and 3d PDOS is shown as an approximation of theoretical spectrum. A numerical calculation of the PACS is also carried out directly for comparison.

The calculated PDOS and PACS are shown in Fig. 3 and Fig. 4, respectively. These curves are made by broadening of discrete energy eigenvalues by a Lorentzian of 0.5 eV (FWHM). Peaks found in the calculated spectra are labeled alphabetically in order of increasing energy. The MO energy relative to the 2p core orbital was used as the transition energy, and the horizontal scale of the calculated spectra is translated. The Mg-(3s + 3d) PDOS and the Mg $L_{2,3}$-edge PACS are found to be almost the same. This fact confirms that the present PDOS is a good approximation of the theoretical PACS.

The Mg $L_{2,3}$-edge experimental ELNES and XANES spectra have been measured by Lindner *et al.* [25] and O'Brien *et al.* [11], respectively, as shown in Fig. 3. Two experimental spectra exhibit similar structures except peak A, which is much smaller in the ELNES than in the XANES.

The splitting between peak B and peak C increases as the core hole is in-

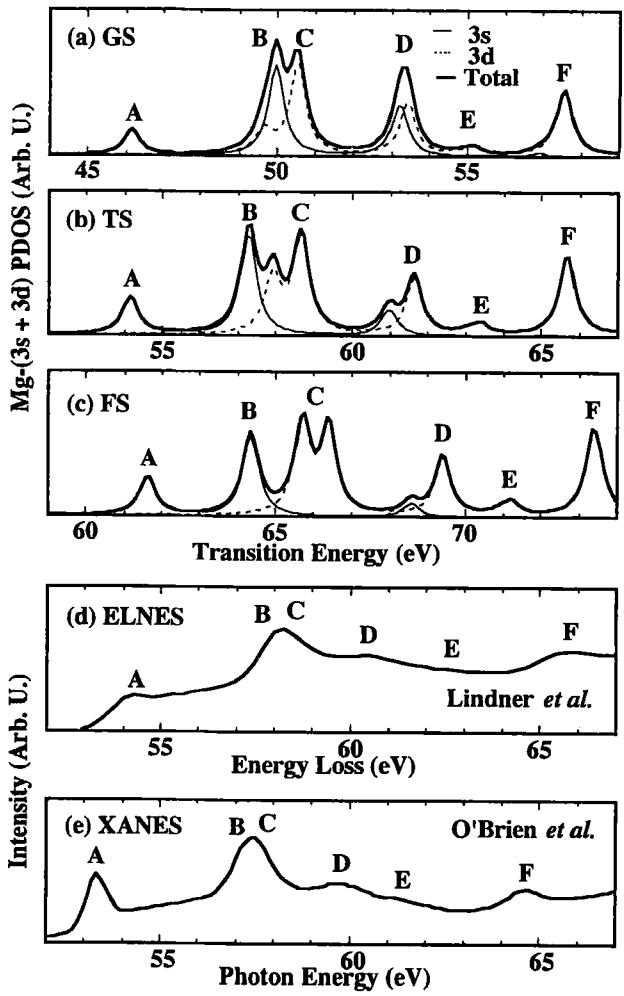

Figure 3: The sum of Mg-3s and 3d unoccupied partial density of states (PDOS) calculated for MgO using the $(Mg_{13}O_{14})^{2-}$ cluster at (a) ground state (GS), (b) Slater's transition state (TS) and (c) final state (FS). (d) Experimental ELNES and (e) experimental XANES reported in Refs. [25] and [11].

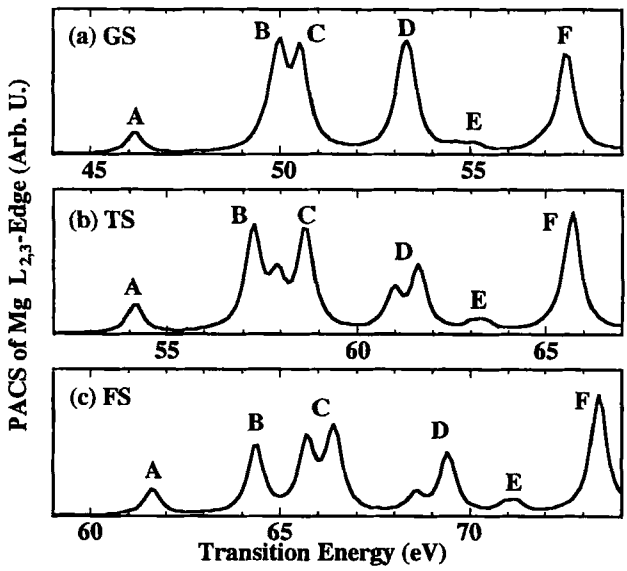

Figure 4: Mg $L_{2,3}$-edge photoabsorption cross section (PACS) calculated for MgO using the $(Mg_{13}O_{14})^{2-}$ cluster at (a) ground state (GS), (b) Slater's transition state (TS) and (c) final state (FS).

troduced. Considering that peak B and C can be regarded as one peak with appropriate broadening of each peak, the PDOS calculated by the transition state agrees well with the experimental ELNES and XANES spectra. However, the experimental spectrum can be reproduced even by the ground state calculation as reported previously [15]. This indicates that the core-hole effect is not significant in MgO.

Theoretical spectra of ELNES and XANES of MgO were obtaind by Lindner *et al.* [25] using the MS-calculation. They couldn't reproduce peak A and attributed it to the formation of a core exciton. In our calculations, however, peak A is well reproduced even by the ground state calculation as shown in Fig. 3. This is not a surprising result, since a core-exciton state in this case is essentially a state at the bottom of the normal 3s band which is slightly

localized due to the presence of a core hole.

Lindner *et al.* succeeded to reprodece other major features in the experimental spectra when a 6-shell cluster composed of 80 atoms was used [25]. They concluded that it was necessary to use a cluster of such size to describe the bulk electronic properties of MgO. In the present calculation, however, we have used a cluster consisting of only 27 atoms (3-shell cluster) in order to obtain good agreement with experiments. Although only 1s - 3d atomic orbitals are used in this calculation, the higher energy features (< 50 eV) can be reproduced by the expansion of the basis-set [15]. Thus, we can conclude that fine structure of ELNES, and therfore conduction-band structue, is determined even by such a small cluster. In addition to the necessity of using many atoms to obtain a good theoretical spectra, results of multiple-scattering type calculations were dependent on the choice of muffin-tin parameters. Weng and Rez [7] used a cluster of 6 to 10 shells (84 and 174 atoms) to obtain a theoretical spectrum of O K-edge of MgO, CaO and SrO. The calculation did not well reprodece the experimental spectra when the muffin-tin potential was not optimized. On the other hand, we have also reproduced the O K-edge spectra using a cluster consisting of only 27 atoms [15]. The smaller cluster size required for the calculation is computationally very convenient and is one of the advantages of the DV-Xα method.

So far we neglected the spin polarization of the electrons in order to save the computational task. When a core hole is introduced, however, the magnitude of exchange potential for up-spin electrons is different from that for down-spin electrons. Thus the spin polarization should be taken into account in order to evaluate the exchange potential properly. In this case, the electronic configuration in the Slater's transition state is expressed as $(2p\uparrow)^{2.5}(12a_{1g}\uparrow)^{0.5}$ $(2p\downarrow)^{3}(12a_{1g}\downarrow)^{0}$ for MgO and the calculated transition energy at peak A becomes 53.6 eV, which is in good agreement with the experimental value estimated from the XANES spectrum (53.4 eV). The theoretical transition energy and experimental ones at peak A for MgO, α-Al_2O_3 and SiO_2 (α-quartz) are

Table 1: The list of theoretical and experimental values of the transition energy at peak A for MgO, α-Al_2O_3 and SiO_2 (α-quartz). ΔE^s and ΔE^{ns} are the values calculated by the Slater's transition state with and without spin polarization, respectively. ΔE^X and ΔE^E are the values estimated from the XANES and the ELNES, respectively.

	MgO	α-Al_2O_3	SiO_2 (α-quartz)
ΔE^{ns} (eV)	54.1	79.9	107.4
ΔE^s (eV)	53.6	79.0	106.4
ΔE^X (eV)	53.4	78.5 ($2p_{1/2}$) 78.9 ($2p_{3/2}$)	106.4 ($2p_{1/2}$) 105.8 ($2p_{3/2}$)
ΔE^E (eV)	54.3	79.6	—

summarized in Table 1.

3.2 α-Al_2O_3

For the $(Al_8O_{33})^{42-}$ cluster in C_3 symmetry, the LUMO allowed for the $L_{2,3}$ absorption is 72a. Therefore, $(2p)^{5.5}(72a)^{0.5}$ and $(2p)^{5.0}(72a)^{1.0}$ configurations were used for the transition state and final state calculations. The PDOS and PACS are calculated in the same way with the case of MgO, and the results are shown in Fig. 5 and Fig. 6. The Al-(3s + 3d) PDOS and Al $L_{2,3}$-edge PACS are found to be almost the same. Thus the PDOS is also a good approximation of the theoretical PACS in this case.

The Al $L_{2,3}$-edge experimental ELNES and XANES have measured by Bruley *et al.* [26] and O'Brien *et al.* [11], respectively, as shown in Fig. 5. Two experimental spectra exhibit similar structures, however, the energy resolution is higher in the XANES. The absolute transition energy is different by 0.6 eV; its reason is not clear. Splitting of peak A is found only in the XANES, which is attributable to the spin-orbit splitting components, $2p_{3/2}$ and $2p_{1/2}$. In order to confirm this, we calculated the spin-orbit splitting of 2p orbital for a free Al atom using a relativistic Hartree-Fock-Slater method (Dirac-Fock-Slater

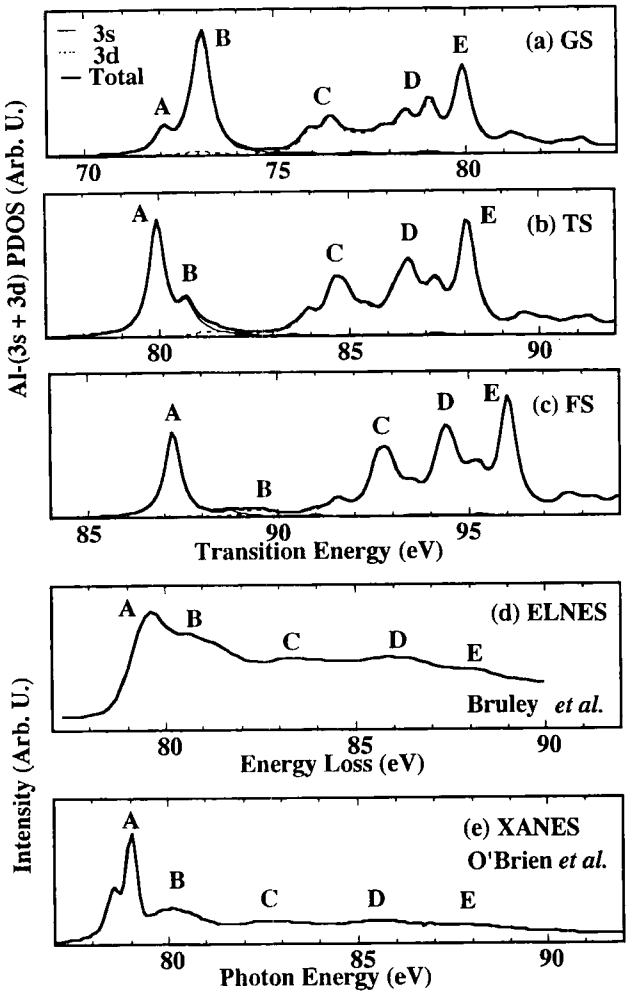

Figure 5: The sum of Al-3s and 3d unoccupied partial density of states (PDOS) calculated for α-Al_2O_3 using the $(Al_8O_{33})^{42-}$ cluster at (a) ground state (GS), (b) Slater's transition state (TS) and (c) final state (FS). (d) Experimental ELNES and (e) experimental XANES reported in Refs. [26] and [11].

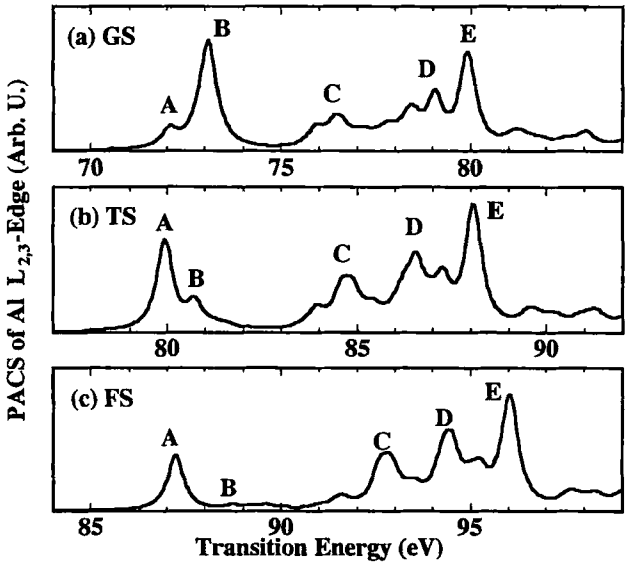

Figure 6: Al $L_{2,3}$-edge photoabsorption cross section (PACS) calculated for α-Al_2O_3 using the $(Al_8O_{33})^{42-}$ cluster at (a) ground state (GS), (b) Slater's transition state (TS) and (c) final state (FS) electronic configuration.

method). The calculated splitting was 0.45 eV, which agrees well with the experimental splitting (0.4 eV).

Both of PDOS and PACS structures, especially the shape of the first peak near the edge, are found to be significantly dependent on the electronic configuration. The intensity ratio of peaks A and B in the experimental spectra is best reproduced by the transition state calculation. The ground state calculation shows much smaller intensity of peak A than that of the experimental spectrum, and the final state calculation exhibits much greater intensity of peak A. Thus, the core-hole effect is very significant in this material. Three-peak feature of higher energy peaks (C, D and E) is well reproduced by the calcuation irrespective of the electronic configuration. However, the energy

separation between the first peaks (A, B) and the second peaks (C, D and E) is larger by 1.5 eV in the theoretical spectrum at the transition state than the experimental spectrum. The small discrepancy seems to be general in the minimal basis-set calculations. However, the systematic discrepancy does not affect our peak assignments at all. Peak A and B originate from Al-3s orbitals and C, D and E are ascribed to Al-3d orbitals.

The absolute transition energy obtained by the present transition state calculation overestimates the experimental XANES by 0.9 eV at peak A. If the spin polarization is taken into account, however, the discrepancy decreases. In this case, the electronic configuration in the Slater's transition state is expressed as $(2p\uparrow)^{2.5}(72a\uparrow)^{0.5}$ $(2p\downarrow)^{3}(72a\downarrow)^{0}$ and calculated transition energy at peak A becomes 79.0 eV, which is in excellent agreement with experimental values estimated from the XANES spectrum (78.5 eV for $2p_{1/2}$ component and 78.9 eV for $2p_{3/2}$ component) as listed in Table 1.

3.3 SiO_2(α-quartz)

For the $(Si_5O_{16})^{12-}$ cluster in C_2 symmetry, the LUMO allowed for the $L_{2,3}$ absorption is 54a. Therefore, $(2p)^{5.5}(54a)^{0.5}$ and $(2p)^{5.0}(54a)^{1.0}$ configurations were used for the transition state and final state calculations. In this case, the spectra were broadened by a Lorentzian of 1.0 eV (FWHM) taking into account the widths of observed peaks. The Si-(3s + 3d) PDOS and the Si $L_{2,3}$-edge PACS are shown in Fig. 7 and Fig. 8. It is found that the PDOS is also a good approximation of the theoretical PACS in SiO_2.

The experimental XANES spectrum has been reported by Li *et al.* [13] as shown in Fig 7, where the horizontal scale was calibrated by the data obtained by O'Brien *et al.* [28]. As in the case of α-Al_2O_3, the splitting of peak A is attributable to the spin orbit splitting. The calculated splitting of 2p orbital for a free Si atom using the Dirac-Fock-Slater method is 0.66 eV, which agrees well with the experimental splitting (0.6 eV).

As already described in our previous report [16], there is a good one-to-one

correspondence between Si $L_{2,3}$-edge XANES spectrum and Si-(3s + 3d) PDOS calculated by the transition state configuration. As shown in Fig. 7, however, the spectral shapes of the Si-(3s + 3d) PDOS are not affected significantly when the core hole is introduced. Thus, the experimental spectrum is well reproduced even by the ground state calculation. The presence of a core hole does not always change the electronic structure of unoccupied band remarkably. Since the core hole effect originates from the electronic rearrangement or relaxation during the transition, a significant effect appears only when the unoccupied band structure is susceptible to the rearrangement. In the case of α-quartz, such electronic relaxation is not significant.

Fujikawa made multiple-scattering type calculation to reproduce the Si $L_{2,3}$-edge XANES of SiO_2 [29]. McComb *et al.* [30] also conducted similar calculations using a SiO_4 cluster. These types of calculations, however, do not agree well with experimental spectra unless both large clusters composed of nearly 100 atoms and a large number of basis functions were used. On the other hand, in the present calculation, we use a minimal basis-set which is necessary to reproduce the valence band structure. The cluster size we have chosen is also the minimal one necessary to distinguish different SiO_2 polytypes.

As in the case of α-Al_2O_3, the absolute transition energy at peak A obtained by the present transition state calculation is overestimated by 1.0 eV. The discrepancy can be also reduced if the spin polarization during transition is taken into account. In this case, the electronic confiuration in the Slater's transition state is expressed as $(2p\uparrow)^{2.5}(54a\uparrow)^{0.5}$ $(2p\downarrow)^{3}(54a\downarrow)^{0}$ and the calculated transition energy at peak A becomes 106.4 eV, which is in excellent agreement with the experimental values estimated from the XANES spectrum (106.4 eV for $2p_{1/2}$ component and 105.8 eV for $2p_{3/2}$ component) as listed in Table 1.

3.4 Electronic Relaxations during Transition

Since Al is located between Mg and Si in the periodic table, the exceptional photoabsorption spectrum of α-Al_2O_3 at the Al $L_{2,3}$-edge cannot be explained

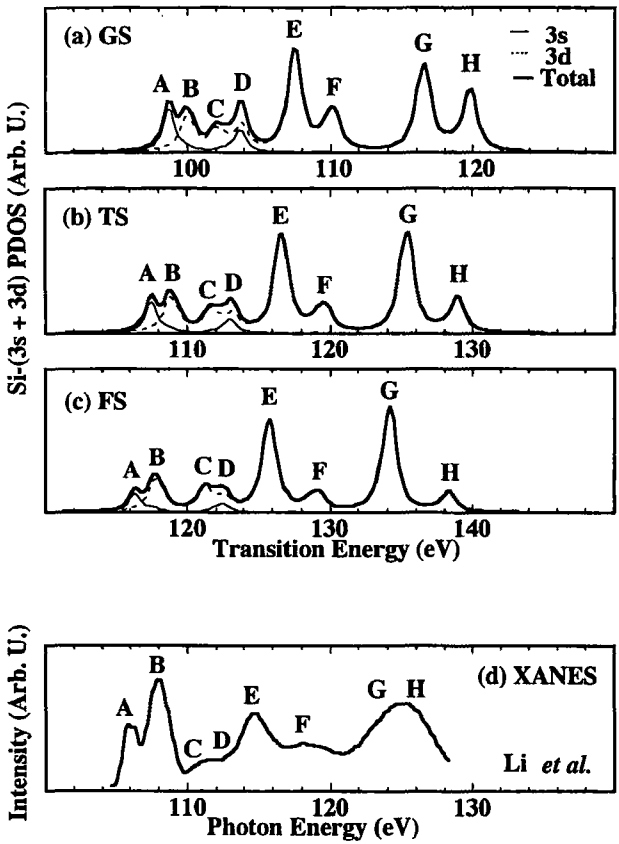

Figure 7: The sum of Si-3s and 3d unoccupied partial density of states (PDOS) calculated for SiO_2 (α-quartz) using the $(Si_5O_{16})^{12-}$ cluster at (a) ground state (GS), (b) Slater's transition state (TS) and (c) final state (FS). (d) Experimental XANES reported in Ref. [27].

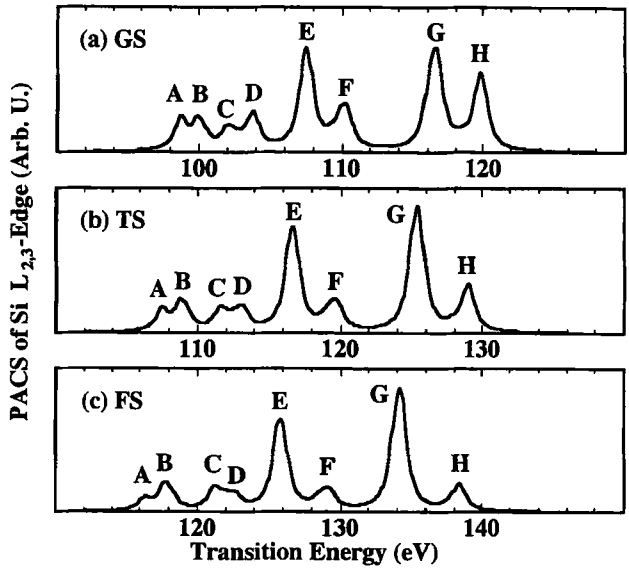

Figure 8: Si $L_{2,3}$-edge photoabsorption cross section (PACS) calculated for SiO_2 (α-quartz) using the $(Si_5O_{16})^{12-}$ cluster at (a) ground state (GS), (b) Slater's transition state (TS) and (c) final state (FS).

simply by the nature of the Al atom itself. We have to consider the environment of the excited atom in detail. Since all of these compounds are typical insulators having fully oxidized cations, their primary bonding mechanisms are the same. However, small difference in their chemical environment may change the excited state structures notably.

Contour maps of the LUMOs in the $(Mg_{13}O_{14})^{2-}$, $(Al_8O_{33})^{42-}$ and $(Si_5O_{16})^{12-}$ clusters at three electronic configurations are shown in Fig. 9. These MOs are responsible for peak A in the experimental spectra. At the ground state, they are mainly composed of a cation 3s orbital overlapping with its neighboring cation 3s orbitals. On the formation of a core hole, the nuclear potential is temporarily deepened. As a result, electrons tend to be bound to the nucleus. As can be seen in Fig. 9, the 72a orbital of the $(Al_8O_{33})^{42-}$ cluster is most

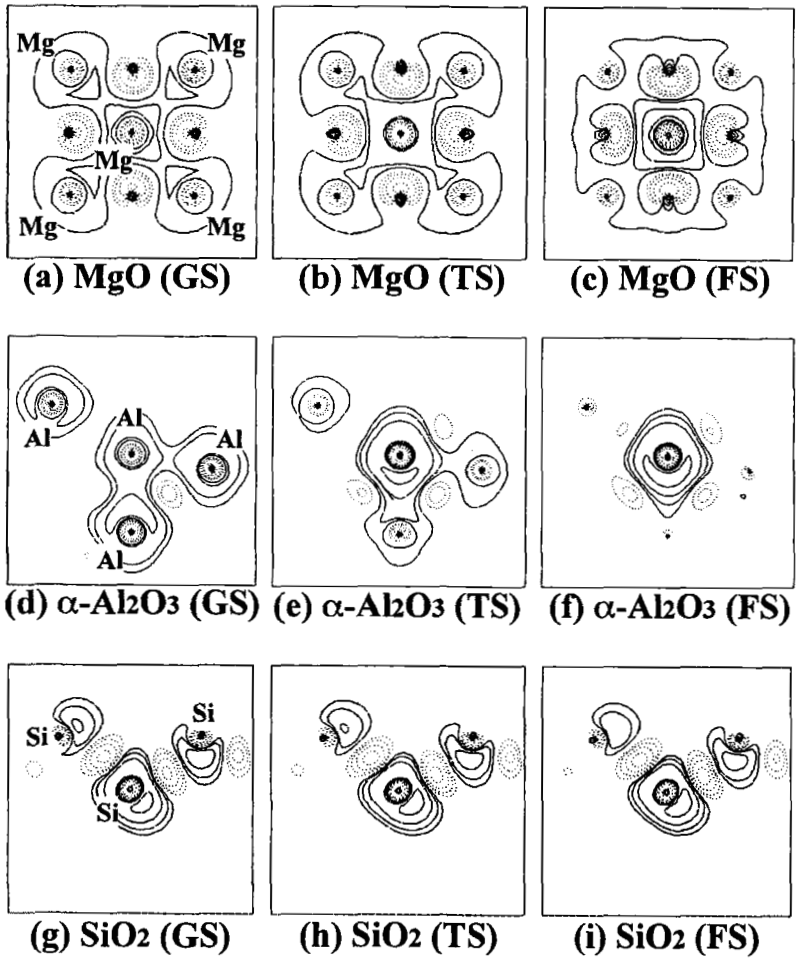

Figure 9: Contour maps of the $12a_{1g}$ orbital in the $(Mg_{13}O_{14})^{2-}$ cluster at (a) ground state (GS), (b) transition state (TS) and (c) final state (FS). Contour maps of the 72a orbital in the $(Al_8O_{33})^{42-}$ cluster, at (d) GS, (e) TS and (f) FS. Contour maps of the 54a orbital in the $(Si_5O_{16})^{12-}$ cluster at (g) GS, (h) TS and (i) FS.

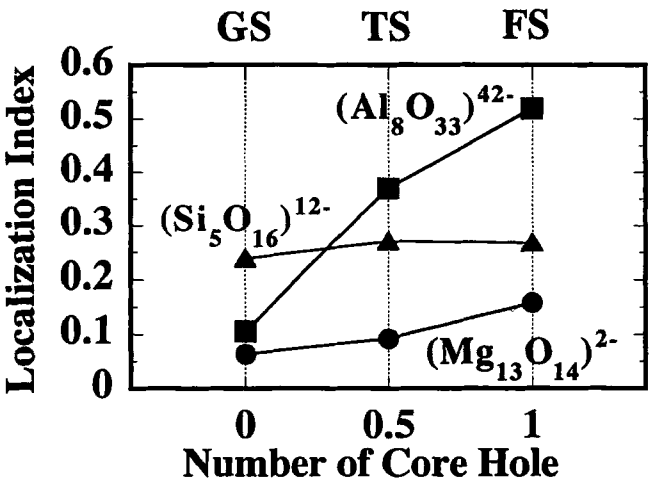

Figure 10: Localization index of the $12a_{1g}$ orbital in the $(Mg_{13}O_{14})^{2-}$ cluster (solid circles), the 72a orbital in the $(Al_8O_{33})^{42-}$ cluster (solid squares) and 54a orbital in the $(Si_5O_{16})^{12-}$ cluster (solid triangles) at ground state (GS), transition state (TS) and final state (FS).

significantly influenced by the presence of a core hole, and a strong localization occurs at the final state of the transition. The localization of $12a_{1g}$ orbital in the $(Mg_{13}O_{14})^{2-}$ cluster is much weaker even at the final state. In the case of the $(Si_5O_{16})^{12-}$ cluster, the 54a orbital is somewhat localized even at the ground state, but the degree of localization is not affected by the presence of a core hole. The magnitude of the localization can be quantified by the localization index of these MOs. The calculated values of localization index are displayed in Fig. 10. Significant localization of the 72a orbital of the $(Al_8O_{33})^{42-}$ cluster during the transition process can be seen. This is the phenomenological origin of the notable core-hole feature in α-Al_2O_3 near the Al $L_{2,3}$-edge.

The localization due to the formation of a core hole is expected to be greater

Table 2: Cation-cation distances, coordination numbers and calculated overlap populations of the LUMO allowed for the $L_{2,3}$ absorption in MgO, α-Al_2O_3 and SiO_2 (α-quartz).

	cation-cation distance (nm) and coordination number	cation-cation overlap population
MgO	0.2978 × 12	0.055
α-Al_2O_3	0.2653 × 1	0.142
	0.2792 × 3	0.046
	0.3223 × 3	0.008
SiO_2 (α-quartz)	0.3061 × 4	0.043

when the overlapping between these neighboring cation AOs is stronger. The overlap population between the neighboring cation orbitals for the LUMO at the ground state configuration is calculated and shown in Table 2 together with the corresponding cation-cation distances. The overlap population between the neighboring cation orbitals are found exceptionally strong for one special Al-Al bond in α-Al_2O_3 : It is 0.2653 nm, which is about 10 - 20 % shorter than the other cation-cation bonds in the other two compounds. It is natural to expect that the overlapping of cation orbitals is strong only for this particular bond. As a matter of fact, the localization associated with the formation of a core hole occurs significantly only in α-Al_2O_3 near the Al $L_{2,3}$-edge. In the case of MgO and SiO_2, the effect of a core hole is small, because the overlapping between the neighboring cation orbitals are relatively small. Due to the longer cation-cation distance and smaller coordination number, the magnitude of localization at ground state is somewhat larger in SiO_2 than in MgO

4 Summary and Conclusion

In summary, the cation $L_{2,3}$-edge ELNES and XANES of three oxides are found to be well reproduced by the first principles molecular orbital calculations using model clusters composed of a cation atom with one cation shell

and two oxygen shells. Absolute energy, as well as fine-structures of cation $L_{2,3}$-edge, in the range of < 30 eV from the conduction-band edge are well reproduced by the DV-Xα calculation. Advantages of the DV-Xα method can be summarized as follows: (1) Calculations are essentially free from any adjustable parameters. (2) Absolute values of the transition energy can be obtained accurately using the "spin-polarized Slater's transition state" method. (3) The cluster size necesary to reproduce the fine structure of the spectrum is much smaller than that required for the MS calculations. (4) A core hole can be included in the self-consistent calculation. By comparing the spectra calculated with different electronic configurations, the strongest peak that appears in the spectrum of α-Al_2O_3 is found to be due to the presence of an Al-2p core hole. The origin of the significant core-hole excitonic feature in α-Al_2O_3 is ascribed to the presence of exceptionally short Al-Al bond in the α-Al_2O_3 structure, which brings about strong overlapping of the neighboring cation orbitals.

Acknowledgments

This work was supported by Grant-in-Aid for Scientific Research from the Ministry of Education, Sports, Science and Culture of Japan.

References

[1] M. Disko, C. C. Ahn and B. Fultz edited., *Transmission Electron Energy Loss Spectrometry in Materials Science* (TMS, Warrendale, 1992).

[2] J. Stöhr, *NEXAFS Spectroscopy* (Springer, Berlin, 1992).

[3] R. Brydson, H. Sauer, W. Engel, J. M. Thomas and E. Zeitler, J. Chem. Soc., Chem. Commun., 1010 (1989).

[4] K. H. Johnson, Advances in Quantum Chemistry (Edited by P. -O. Loewdin). Academic Press, New York (1973).

[5] P. J. Durham, J. B. Pendry and C. H. Hodges, Comput. Phys. Commun., **25**, 193 (1982).

[6] D. D. Vvedensky, D. K. Saldin and J. B. Pendry, Comput. Phys. Commun., **40**, 421 (1986).

[7] X. Weng and P. Rez, Phys. Rev., **B39**, 7405 (1989).

[8] M. T. Czyzyk, R. A. D. Groot, G. Dalba, P. Fornasini, A. Kisiel, F. Rocca and E. Burattini, Phys. Rev., **B39**, 7405 (1989).

[9] F. M. F. Groot, J. Faber, J. J. M. Michiels, M. T. Csysyk, M. Abbate and J. C. Fuggle, Phys. Rev., **B48**, 2074 (1993).

[10] S. T. Pantelides, Phys. Rev., **B11**, 2391 (1975).

[11] W. L. O'Brien, J. Jia, Q. -Y. Dong, T. A. Callcott, D. R. Mueller, D. L. Ederer and C. -C. Kao, Phys. Rev., **B47**, 15482 (1993).

[12] H. Adachi, M. Tsukada and C. Satoko, J. Phys. Soc. Jpn., **45**, 875 (1978).

[13] D. E. Ellis, H. Adachi and F. W. Averill, Surface Sci., **58**, 497 (1976).

[14] I. Tanaka and H. Adachi, Phys. Rev., **B54**, 4604 (1996).

[15] I. Tanaka, J. Kawai and H. Adachi, Solid State Commun., **93**, 553 (1995).

[16] I. Tanaka, J. Kawai and H. Adachi, Phys. Rev., **B52**, 11733 (1995).

[17] I. Tanaka and H. Adachi, J. Phys. D., **29**, 1725 (1996).

[18] D. E. Ellis and G. S. Painter, Phys. Rev., **B2**, 2887 (1970).

[19] F. W. Averill and D. E. Ellis, J. Chem. Phys., **59**, 6412 (1973).

[20] A. Rosén, D. E. Ellis, H. Adachi and F. W. Averill, J. Chem. Phys., **65**, 3629 (1976).

[21] J. C. Slater, *Quantum Theory of Molecules and Solids*, Vol. 4 (McGraw-Hill, New York, 1974).

[22] C. Satoko, M. Tsukada and H. Adachi, J. Phys. Soc. Jpn., **45**, 1333 (1978).

[23] H. Adachi and K. Taniguchi, J. Phys. Soc. Jpn., **49**, 1944 (1980).

[24] W. Y. Ching, L. W. Song and S. S. Jaswal, Phys. Rev., **B30**, 544 (1984).

[25] T. Lindner, H. Sauer, W. Engel, and K. Kambe, Phys. Rev., **B33**, 22 (1986).

[26] J. Bruley, M. -W. Tseng and D. B. Williams, Microsc. Microanal. Microstruct., **6**, 1 (1995).

[27] D. Li, G. M. Bancroft, M. Kasrai, M. E. Fleet, X. H. Feng, K. H. Tan and B. X. Yang, Solid State Commun., **87**, 613 (1993).

[28] O'Brien, J. Jia, Q. -Y. Dong and T. A. callcott, Phys. Rev., **B44**, 1013 (1991).

[29] T. Fujikawa, J. Phys. Soc. Jpn., **52**, 4001 (1983).

[30] D. W. McComb, P. L. Hansen and R. Brydson, Microsc. Microanal. Microstruct., **1**, 213 (1992).

Concluding Remarks

M. Uda

Department of Materials Science and Engineering,
School of Science and Engineering, Waseda University,
3-4-1 Okubo, Shinjuku-ku, Tokyo 169, Japan

The first international workshop on the Discrete Variational Xα method was held on September 2 and 3, 1996 with great success in Debrecen, Hungary, which was well organized by active members of ATOMKI in Hungarian Academy of Science, especially by L. Kövér. The memorial year of 1996 for our DV-Xα society coincided fortunately also with 1100 years of the Hungarian independence. This seems to celebrate the independence or distinguishability of the DV-Xα method from the other numerous molecular orbital calculation methods.

It is worth noticing that wide varieties of topics from such scientific fields as atomic physics, relativistic effects, photoelectron, X-ray and Auger processes, metal physics, chemical bonding affects, solid state chemistry and the others were presented in the first workshop. This was perfectly astounding because most calculating methods of the molecular orbitals have been applied only to specialized fields in which a researcher, who has proposed and formulated the calculating method, has been involved.

Developing stages of the DV-Xα method are divided into four. Firstly, the preliminary DV-Xα method has been developed by Ellis and Painter, which was applied to the band calculations [D. E. Ellis and G. S. Painter: Phys. Rev. **B2** (1976) 2887]. Secondly, Adachi proposed to introduce the self-consistent procedure in it and Ellis named such a revised method as a self-consistent charge (SCC) method. They have worked together with Rosén during their stay in

ADVANCES IN QUANTUM CHEMISTRY, VOLUME 29

0065-3276/97 $25.00

Northwestern University and applied the method to elucidate electronic structures of solid surface and of simple molecules [D. E. Ellis, H. Adachi and F. W. Averill, Surf. Sci. **58** (1976) 497; T. Tanabe, H. Adachi and S. Imoto, Jpn. J. Appl. Phys. **15** (1976) 1865; A. Rosén, D. E. Ellis and H. Adachi and F. W. Averill, J. Chem. Phys. **65** (1976) 3629]. Thirdly, Adachi has started, after coming back from Northwestern University, to improve the DV-Xα program in Japan. Important modifications were found in employment of the atomic orbitals calculated at each iteration as new basis functions for the next iteration, and also in proper arrangement of the program which enables nonprofessionals to handle it easily [H. Adachi , M. Tsukada and C. Satoko, J. Phys . Soc. Jpn. **45** (1978) 875]. In addition, the program was improved so as also to calculate intensity distributions of soft X-ray spectra reflecting molecular orbital components [H. Adachi and K. Taniguchi, J. Phys. Soc. Jpn. **49** (1980) 1944]. Lastly, personal computers have been introduced to the DV-Xα calculations, which have led to almost unlimited numbers of applications of such a powerful and versatile method not only to fundamental sciences but also to industrial purposes. This is a brief story why the DV-Xα method has been developed in Japan explosively within the last decade.

The Society for the Discrete Variational Xα, starting with 20 members, was established in 1988 in Japan and is now organized by more than 350 scientists and engineers. They are physicists, chemists, material scientists, advanced engineers, and so on, who come from universities, research institutes, industries and others. These wide varieties of inquisitive scientists have often used the DV-Xα in the frontier science fields together with the well established fields for better understings of quantum phenomena behind them. Some active members of the Society for the DV-Xα discussed at the 8th annual meeting in Fukuoka, Japan, in 1995 how the DV-Xα is developing and in what direction. Our conclusion was that very lively and successful works have been going on to investigate electronic

structures or transitions in molecules or atomic aggregates, and then it is untimely to confine our interests to the subject at hand but goes with the tide to extend scientific fields and to call for all scientists over the world who are interested in the DV-Xα method. For the convenience of European scientists, Debrecen in Hungary was selected as the first international conference location, where several active members have already used the DV-Xα program and also where R. Gaspar in the Lajos Kossuth University first developed the local-density approximation in 1954. The program developed by Adachi is now available for every scientists to calculate the molecular orbitals and their associates. The programs written by Ellis, Rosén and Fricke have been used in U.S.A., Brazil, China, Sweden, Germany, and so on.

Lastly, the author expects continuation in harmony of familial and competitive atmosphere in the Society for the Discrete Variational Xα. The second workshop will be held in 1999.

Index

C

D

E

F

G

H

I

J

K

L

M

N

O

P

Q

R

S

T

V

X

Z